ANALYSIS OF FIRST PASS MYOCARDIAL PERFUSION ~~WITH~~ IMAGING WITH MAGNETIC RESONANCE ~~IMAGING~~

Nicholas Akbar Ablitt

A Thesis submitted to the University of London
for the degree of Doctor of Philosophy

Department of Computing
Imperial College of Science, Technology and Medicine
2004

BRITISH LIBRARY

IMAGING SERVICES NORTH

Boston Spa, Wetherby
West Yorkshire, LS23 7BQ
www.bl.uk

BEST COPY AVAILABLE.

VARIABLE PRINT QUALITY

BRITISH LIBRARY

IMAGING SERVICES NORTH

Boston Spa, Wetherby
West Yorkshire, LS23 7BQ
www.bl.uk

ORIGINAL COPY TIGHTLY BOUND

Abstract

Early diagnosis and localisation of myocardial perfusion defects is an important step in the treatment of coronary artery disease. Thus far, coronary angiography is the conventional standard investigation for patients with known or suspected coronary artery disease and it provides information about the presence and location of coronary stenoses. In recent years, the development of myocardial perfusion CMR has extended the role of MR in the evaluation of ischaemic heart disease beyond the situations where there have already been gross myocardial changes such as acute infarction or scarring. The ability to non-invasively evaluate cardiac perfusion abnormalities before pathologic effects occur, or as follow-up to therapy, is important to the management of patients with coronary artery disease. Whilst limited multi-slice 2D CMR perfusion studies are gaining increased clinical usage for quantifying gross ischaemic burden, research is now directed towards complete 3D coverage of the myocardium for accurate localisation of the extent of possible defects.

In 3D myocardial perfusion imaging, a complete volumetric data set has to be acquired for each cardiac cycle in order to study the first pass of the contrast bolus. This normally requires a relatively large acquisition window within each cardiac cycle to ensure a comprehensive coverage of the myocardium and reasonably high resolution of the images. With multi-slice imaging, long axis cardiac motion during this large acquisition window can cause the myocardium imaged in different cross-sections to be mis-registered, *i.e.*, some part of the myocardium may be imaged more than twice whereas other parts may be missed out completely. This type of mis-registration is difficult to correct for by using post-processing techniques. The purpose of this thesis is to investigate techniques for tracking through plane motion during 3D myocardial perfusion imaging, and a novel technique for extracting intrinsic relationships between 3D cardiac deformation due to respiration and multiple 1D real-time measurable surface intensity traces is developed. Despite the fact that these surface intensity traces can be strongly coupled with each other but poorly correlated with respiratory induced cardiac deformation, we demonstrate how they can be used to accurately predict cardiac motion through the extraction of latent variables of both the input and output of the model. The proposed method allows cross-modality reconstruction of patient specific models for dense motion field prediction, which after initial modelling can be use in real-time prospective motion tracking or correction.

In CMR, new imaging sequences have significantly reduced the acquisition window whilst maintaining the desired spatial resolution. Further improvements in perfusion imaging will require the application of parallel imaging techniques or making full use of the information content of the *k*-space data. With this thesis, we have proposed RR-UNFOLD and RR-RIGR for significantly reducing the amount of data that is required to reconstruct the perfusion image series. The methods use prospective diaphragmatic navigator echoes to ensure UNFOLD and RIGR are carried out on a series of images that are spatially registered. An adaptive real-time re-binning algorithm is developed for the creation of static image sub-series related to different levels of respiratory motion. Issues concerning temporal smoothing of tracer kinetic signals and residual motion artefact are discussed, and we have provided a critical comparison of the relative merit and potential pitfalls of the two techniques. In addition to the technical and theoretical descriptions of the new methods developed, we have also provided in this thesis a detailed literature review of the current state-of-the-art in myocardial perfusion imaging and some of the key technical challenges involved. Issues concerning the basic background of myocardial ischaemia and its functional significance are discussed. Practical solutions to motion tracking during imaging, predictive motion modelling, tracer kinetic modelling, RR-UNFOLD and RR-RIGR are discussed, all with validation using patient and normal subject data to demonstrate both the strength and potential clinical value of the proposed techniques.

Acknowledgements

I'd like to thank my mother who unfortunately passed away in the fist year of this PhD. From her own academic achievements under more difficult circumstances, she provided inspiration for me.

Within the research group the work of Dr Robert Merrifield, Dr Paramate Horkaew and Marcus Ellington provided valuable tools for the development and validation of my own work. Collaboration with colleagues at the Cardiovascular Magnetic Resonance unit of the Royal Brompton Hospital provided a valuable source of knowledge and technical expertise. Dr David Firmin, Dr Andrew Elkington, Dr Jennifer Keegan and Dr Dudley Pennell with a tremendous amount of help more recently from Dr Jonathan Lyne. I'd like to extend special thanks to Dr Peter Gatehouse whose patience as well as honest critical appraisal was always well received.

For the development and validation of many of these techniques, I would like thank my many friends at the Imperial College Boat Club for volunteering their time and cardiovascular systems. My time spent at the boat club with a mentor in Bill Mason is perhaps all that has kept me sane at times, providing a valuable escape from the demands of academic research.

Last but no means least I would like to thank my supervisor Professor Guang-Zhong Yang who has guided me throughout the course of this PhD. His scientific standard and integrity, as well as the time he was able to put into developing my skills, I hope, are reflected in this work. During the time I have spent here, the research group has grown tremendously and I'm sure will benefit students for many years to come.

This project would not have been possible without the funding provided from the UK Engineering and Physical Sciences Research Council.

Table of Contents

Chapter 1 : Introduction **26**

Chapter 2 : The Clinical Background of Myocardial Perfusion Imaging **33**

2.1 Introduction 33
- 2.1.1 The basic structure of the heart and its function 34
- 2.1.2 Coronary artery disease (CAD) 36
- 2.1.3 Ischaemia and myocardial infarction 37
- 2.1.4 Myocardial territory linked to coronary blood supply 40
- 2.1.5 Collateral circulation 41
- 2.1.6 Diagnosis and prognosis 42

2.2 Perfusion imaging: what is available? 44
- 2.2.1 Single-Photon Emission Computerised Tomography (SPECT) 44
- 2.2.2 Positron Emission Tomography (PET) 46
- 2.2.3 Echocardiography 49
- 2.2.4 Computed Tomography (CT) 51
- 2.2.5 Cardiovascular magnetic resonance imaging 52

2.3 Myocardial Perfusion CMR 53
- 2.3.1 First pass myocardial perfusion imaging, Gd-DTPA late enhancement, and BOLD 53
- 2.3.2 Imaging sequence design 58

2.4 Conclusion 62

Chapter 3 : Exploiting the Information Content of *k*-space Data **63**

3.1 Introduction 63

3.2 *k*-space data acquisition 64

3.3 Prior information driven reduced *k*-space encoding 65
- 3.3.1 Keyhole imaging 65
- 3.3.2 Block Regional Interpolation Scheme for *K*-space (BRISK) 67
- 3.3.3 Temporal filtering methods for reduced FOV imaging 68
- 3.3.4 Broad-use Linear Acquisition Speed-up Technique (BLAST) 69
- 3.3.5 Locally focused and reduced field of view imaging 71
- 3.3.6 Locally focused imaging with volume selective RF Excitation 73

3.4 Parallel imaging techniques 75
- 3.4.1 SiMultaneous Acquisition of Spatial Harmonics (SMASH) 75
- 3.4.2 SENSitivity Encoding for fast MRI (SENSE) 78

3.5 Conclusion 80

Chapter 4 : Management of Cardiac and Respiratory Motion **82**

4.1 Introduction 82

4.2 Cardiac contractile motion 83

4.3 Respiratory motion 84
- 4.3.1 Measurement of respiratory motion 86
- 4.3.2 Pattern of free breathing respiratory motion 88
- 4.3.3 Hysteresis effects of free breathing 89
- 4.3.4 Upward creep during breath holds 91

4.4 Respiratory adapted imaging 91

4.4.1 Respiratory motion control in CMR 91
4.4.2 Navigator echoes for prospective respiratory motion compensation 92
4.4.3 Phase encode reordering 93
4.4.4 Adaptive respiratory gating 95
4.5 Motion decoupling and image registration 98
4.5.1 Motion correction in first pass myocardial perfusion MRI 98
4.5.2 Post processing and image registration 98
4.6 Adaptive slice tracking for perfusion imaging 106
4.7 Conclusions 110
Chapter 5 : Predictive Motion Modelling 112
5.1 Introduction 112
5.2 Materials and methods 117
5.2.1 Deformation recovery with 3D free-form image registration 117
5.2.2 Predictive motion modelling and PLSR 118
5.2.3 Image acquisition 125
5.2.4 Validation 127
5.3 Results 128
5.4 Discussions and conclusions 136
Chapter 6 : Respiratory Reordered-UNFOLD 139
6.1 Introduction 139
6.2 The principal of UNFOLD 140
6.3 Correcting respiratory motion for artefact suppression with UNFOLD 146
6.3.1 Correcting rigid body translation 147
6.3.2 Correcting for shear motion 149
6.3.3 UNFOLD reconstruction with myocardial perfusion imaging 151
6.4 RR-UNFOLD for MR myocardial perfusion imaging 152
6.4.1 Unaliasing by Fourier-encoding the overlaps using the temporal dimension 152
6.4.2 Respiratory reordered UNFOLD (RR-UNFOLD) 152
6.4.3 Image reconstruction after re-binning 155
6.4.4 Restoration of tracer kinetic signal 158
6.4.5 Image acquisition 158
6.4.6 Error analysis 159
6.5 Results of RR-UNFOLD 161
6.6 Discussion and conclusions 171
Chapter 7 : RR-RIGR for Myocardial Perfusion Imaging 175
7.1 Introduction 175
7.2 Theoretical background of RIGR 176
7.3 Assessment of RIGR for contrast enhanced imaging 180
7.3.1 Reconstruction of synthetic myocardial perfusion data 180
7.3.2 RIGR for myocardial perfusion with free breathing 189
7.4 RR-RIGR for myocardial perfusion imaging 191
7.4.1 Comparison of RR-RIGR with RR-UNFOLD 193
7.5 Discussion and conclusions 198

Chapter 8 : Tracer Kinetic Modelling and Perfusion Analysis 200
8.1 Introduction 200
8.1.1 Extracellular versus intravascular contrast agent 201
8.1.2 Tracer kinetics and compartment modelling 202
8.1.3 Single compartment modelling 203
8.1.4 Multi-compartment modelling 205
8.1.5 Factor analysis 205
8.2 Issues related to perfusion quantification 207
8.2.1 The deconvolution problem 207
8.2.2 Perfusion indices 208
8.2.3 Perfusion plug in for CMRtools 210
8.3 Clinical case studies 212
8.3.1 Patient 1 212
8.3.2 Patient 2 219
8.3.3 Patient 3 224
8.4 Interstudy reproducibility 229
8.5 Conclusions 231
Chapter 9 : Discussions and Conclusions 232
9.1 Effective cardiac motion modelling 233
9.2 Fast image acquisition in the presence of respiratory motion 234
9.3 Future work 236
Appendix A :The NIPALS algorithm 239
A.1 MATLAB implementation 239
Appendix B :PLSR with a 2D CMR myocardial perfusion sequence 240
B.1 Introduction 240
B.2 Materials and methods 241
B.2.1 Myocardial motion prediction 241
B.2.2 PLSR implementation 242
B.2.3 Validation and *in vivo* data acquisition 244
B.3 Results 244
B.4 Discussion and conclusions 246
Appendix C :Levenberg-Marquardt minimisation 248
Appendix D :Journal Publications 249
D.1 Predictive cardiac motion modeling and correction with partial least squares regression ... 249
D.2 Respiratory reordered UNFOLD perfusion imaging 260
D.3 Accurate assessment of the arterial input function during high-dose myocardial perfusion cardiovascular magnetic resonance 270
References 278

Acronyms

AIF	Arterial Input Function
BLAST	Broad-use Linear Acquisition Speed-up Technique
BRISK	Block Regional Interpolation Scheme for *k*-space
CAD	Coronary Artery Disease
CMR	Cardiovascular Magnetic Resonance
CT	Computed Tomography
EBCT	Electron Beam CT
ECG	ElectroCardioGraphy
EPI	Echo Planar Imaging
FFD	Free-Form Deformation
FGRE-ET	Fast GRadient Echo with an Echo Train readout
FISP	Fast Imaging with Steady-State Precession
FLASH	Fast Low-Angle SHot
FOV	Field Of View
HLA	Horizontal Long Axis
LAD	Left Anterior Descending
LCX	Left CircumfleX
LV	Left Ventricle
MBF	Myocardial Blood Flow
MPR	Myocardial Perfusion Reserve
MR	Magnetic Resonance
MRI	Magnetic Resonance Imaging
NIPALS	Nonlinear Iterative PArtial Least Squares
PCA	Principal Components Analysis
PET	Positron Emission Tomography
PLSR	Partial Least Squares Regression
PSF	Point Spread Function
RCA	Right Coronary Artery
RF	Radio Frequency
RIGR	Reduced-encoding Imaging by Generalised-series Reconstruction
ROI	Region Of Interest
RR-RIGR	Respiratory Reordered RIGR
RR-UNFOLD	Respiratory Reordered UNFOLD
RV	Right Ventricle
SENSE	SENSitivity Encoding for fast MRI
SMASH	SiMultaneous Acquisition of Spatial Harmonics
SNR	Signal to Noise Ratio
SPECT	Single Photon Emission Computed Tomography
TR	Time to Repetition
UNFOLD	Unaliasing by Fourier-encoding the Overlaps Using the Temporal Dimension
VLA	Vertical Long Axis

List of Figures

Figure 2-1 The basic anatomy of the heart and relative position of the left and right ventricles. The coronary arteries running along the epicardial surface provide vital blood supply to the myocardium in order to maintain its function. 35

Figure 2-2 A schematic diagram of the coronary tree, showing the relative position of the major coronary arteries, based on a figure used by the AHA [19] 36

Figure 2-3 A schematic representation of the 17-segment model defined by the AHA. 41

Figure 2-4 A schematic illustration of collateral circulation with a healthy artery supplying a neighbouring ischaemic region, adapted from [27]. 42

Figure 2-5 An example of a single photon emission computed tomography myocardial perfusion image. Three short axis and two long axis views are shown at rest above and corresponding images during stress below. 46

Figure 2-6 An example PET myocardial perfusion image showing viable myocardium identified by preserved glucose uptake (with permission from *Camici* [42]). The use of PET allows quantitative analysis of FDG uptake suggesting the viability of the tissue in question. A cut of point of 0.25 *μmol/g/min* is routinely used. 47

Figure 2-7 The graph shows the signal recovery curve of the septal region pointed to by the arrow, and the *x* and *y* axes represent time in *ms* since the annihilation of the myocardium and video intensity respectively. 49

Figure 2-8 An image series a typical first pass CMR perfusion study showing the transit of contrast bolus. From the top left going across, initially the nulled signal before the contrast agent (Gd-DTPA) enters the RV, followed by the contrast agent exiting the RV and entering the LV. The last few rows show the contrast agent exiting the LV and entering the myocardium of the LV. The observed enhancement within the myocardium is small and minor defects are often difficult to observe by eye. 55

Figure 2-9 BOLD imaging at 3T. Courtesy Shea S, D. Li. Northwestern University. 57

Figure 2-10 Long axis view of the LV showing the late enhancement associated with the transmural infarction. On the right an image from a TrueFISP (Fast Imaging with Steady-State Precession described in section 2.3.2) cine series for assessing morpho-dynamics of the LV. 58

Figure 2-11 An example sequence of FLASH myocardial perfusion images. 59

Figure 2-12 An example sequence of Hybrid EPI myocardial perfusion images. 61

Figure 3-1 *k*-space filling strategies. 64

Figure 3-2 The reference and dynamic images from a dynamic image series, and the corresponding dynamic information captured by the central lines in *k*-space. The dynamic image is also shown reconstructed with only ¼ of the available information, by using the keyhole technique RIGR, respectively 66

Figure 3-3 A $1/3^{rd}$ BRISK sampling scheme for 16 cardiac phases. Each of the 12 *k*-space sections represents a block of *k*-space (*e.g.* 10 lines for a 120^2 matrix) with grey shading showing sampling for a particular image acquisition. On the left the block number is shown, on the right the number of times each block is sampled and below the frame number. 68

Figure 3-4 (a) An example of the applied resolution constraint $r(y)$ for the derivation of basis functions. (b) the corresponding distribution of eigenvalues of the covariance matrix. (c) the selection of near optimal solutions of k_y phase encoding steps using the sequential back selection algorithm. In (c), the deleted encoding steps are represented as black strips superimposed on the normalised average mean square error of v_m, where lighter shades indicate larger errors (E^*). With permission from Yang *et al* [130]. 74

Figure 3-5 The effect of using reduced encoding on a 3D phantom data set. (a) the original fully encoded image. (b) and (c) the reconstructed results using locally focused encoding and zero filling, respectively. With permission from Yang *et al* [130]. 75

Figure 3-6 Linear combinations of component coils approximating spatial harmonics of frequency $\sin \Delta k_y$ for SMASH imaging, adapted from a figure by Sodickson *et al* [131]. For this example, six phase array coils are used modelled by Gaussian functions and depicted in the figure as separate weighted sensitivity profiles by red lines. The blue line represents the combined sensitivity profile of all six coils and the dashed black line the sinusoidal weighting function. 77

Figure 3-7 The use of temporal filtering to adaptively acquire sensitivity profiles for adaptive TSENSE imaging. Based on a figure by Kellman *et al* [143]. 80

Figure 4-1 Five cross-sectional images of the LV demonstrating the contractile motion of the heart 84

Figure 4-2 A coronal view of the heart showing the effect of respiratory induced cardiac motion. The four images (a), (b), (c) and (d) show four stages of the respiratory motion from end inspiration to end expiration. All these images are gated to the same ECG R-wave delay. 85

Figure 4-3 Column positioning of diaphragmatic navigator echoes. The transverse view (a) shows the two intersecting planes angled to avoid interference with the heart, intersecting at the dome of the right hemi-diaphragm. In the coronal (b) and sagittal (c) views, the location of the column is shown. 88

Figure 4-4 Diaphragmatic navigator traces for four subjects over a period of 120 cardiac cycles. A clear cyclical pattern can be seen in all four subjects, although regions of non-uniform breathing can be seen in (b) and (d). The range of observed motion of the navigator reading varies amongst subjects from 10 *mm* in (a) and (c) to around 20 *mm* in (d). 89

Figure 4-5 Example path of breathing measured at boundaries of the diaphragm and the heart with an observed hysteresis effect. Based on figure by Nehrke *et al* [166]. 90

Figure 4-6 A phantom evaluation of locally focused encoding and adaptive respiratory gating. (a) conventional respiratory gating with full phase encoding, (b) adaptive respiratory gating with locally focused encoding reducing the imaging time, and (c) as with (b) but with an increase in imaging time from 238 *s* to 328 *s*. With permission from Yang *et al* [130]. .. 97

Figure 4-7 The effect of in-plane motion on the resulting intensity time curves. Prior to registration, the signal time curve from the selected point shows significant variation through time moving from the blood pool to the myocardium, the cyclic nature of which is primarily due to respiratory motion. After registration the same pixel is located within the myocardium throughout the sequence. This produces a much smoother intensity time curve giving a more accurate measurement of the required myocardial tissue. 99

Figure 4-8 Two frames from a short axis cardiac gated sequence. (a) is used as a reference to which (b) is transformed. (c) shows the displacement of a 9×9 control point grid, overlaid on the reference image. (d) is the deformed version of (b) by using the B-spline deformation field. 102

Figure 4-9 A comparison of the probability distribution of two images both before and after registration. A green (reference) and magenta (transform) overlay shows the difference between the two images. The joint probability distribution is plotted for each intensity within the image. 105

Figure 4-10 Schematic illustration of the basic procedures used for prospective tracking of through plane cardiac motion. Cine myocardial tagging is performed on both the VLA and HLA of the LV from which the positions of the tracking planes are derived. Shown on the above diagram we see the locations of the planes both before (dark) and after (light) the relocation due to the results of the tracking. Large displacement can be seen, particularly during phase 2 of the three-phase cine sequence. 107

Figure 4-11 The absolute difference in measured regional error of three slices acquired during one cardiac cycle for five subjects. The apical slice was acquired first within the cardiac cycle and the basal slice last. The resulting error without motion tracking is shown and is generally greatest during the mid phase of the cardiac cycle. 108

Figure 4-12 Using a special test pulse sequence shows the effectiveness of slice tracking for two subjects above. Signals form the myocardium should remain uniform and enhanced if the imaging planes are accurately tracked over time. This can clearly be seen for the tracked sequence while on the untracked the correct tissue is not imaged during phase 2 and 3..... 109

Figure 4-13 An example of the effect of cardiac contraction on the imaging of multi-slice short axis planes. Image (a) shows three tags across the VLA of the LV, and (b) shows their deformation after 202 *ms*. The most basal of the three slices is shown after 202 *ms* without tracking (c) and with tracking (d). 110

Figure 5-1 An example of the extent of respiratory induced cardiac motion. Three views of the heart are shown along three orthogonal axes. For each view (Volume A) is end-expiration and (Volume B) is end-inspiration at the same stage of the cardiac cycle. Also shown is the location of the myocardium at the two extremes (Myocardium). Large translation and deformation of the shape of the LV is observed. This displacement can be as much as 15*mm* 114

Figure 5-2 A diagrammatic representation of the proposed predictive motion modelling scheme. Initial 2D/3D imaging is used along with real-time measurable inputs to create a motion model that can be used as the input to the imaging system for achieving real-time motion adaptation 117

Figure 5-3 An example data set illustrating the basic concept of PLSR. The input data has two variables x_1 and x_2 and these are plotted against the output variable y. The solid circles show the primary mode of variation in X while the open circles show the secondary mode of variation. After applying PCA on X, it is found that the solid circles represent around 99% of the variation. The graph shows that although the solid circles represent the majority of the variation within X they do not help to describe the variation in Y. In fact the variation present in the open circles, while only representing 1% of the variation in X, is the only useful information in describing the variation in Y. 121

Figure 5-4 A systematic representation of the intrinsic relationship between the p intensities used as an indicator and the q displacements as the response used in the learning and predication. This relationship is shown in terms of the matrices **X** and **Y** for m frames of a sequence. **C** is the coefficient matrix which when combined with the input **X** is able to predict the response matrix **Y**, **E** represents noise and higher order terms that are not accounted for in the above relationship. 122

Figure 5-5 A schematic diagram of the PLSR method used for deformation modelling and prediction. In this example, multiple measurements of surface intensity distributions are used as the input, from which latent variables factors are extracted. A similar process is also applied to the observed output data, in this case the deformation vectors of the heart derived from the control vertices of the free-form image registration algorithm. A model that establishes the intrinsic correlation between **T** and **U** is then derived. At the prediction stage, 3D myocardial deformation is directly predicted from the intensity patterns measured at the chest wall, which can be performed in real-time. 124

Figure 5-6 A pseudo code representation of the NIPALS algorithm. 124

Figure 5-7 A schematic diagram showing the image acquisition and reconstruction procedure for the 3D imaging method with retrospective respiratory gating used in this study. ECG gating was used to acquire data at the same phase (early diastole) of the cardiac cycle. Prior to image data acquisition, a navigator echo was used to locate the position of the dome of the diaphragm. The figure shows the over-sampling of one data segment twenty times and the corresponding navigator locations. The full 3D acquisition requires a total of 28 data segments (14 slices × 2 segments per slice). Over-sampling the data by a factor of 20 ensured that 3D datasets could be reconstructed at a number of positions through the respiratory cycle. 126

Figure 5-8 A visual representation of the motion of the heart due to respiration. The solid surface of each 3D reconstruction represents the endocardial surface at end-expiration and the meshed surface delineates the endocardial border due to respiration corresponding to diaphragm displacements of 5, 15, and 25 *mm*, respectively. The corresponding mid-ventricular short axis slice of each 3D volume is shown on the top row of the figure. 128

Figure 5-9 2D deformation vectors of a mid-ventricular slice at the same phase of different cardiac cycles with varying levels of respiration motion, and an associated intensity trace measured at the surface of the chest. (a) The deformation vectors corresponding to cardiac cycles 6, 11, and 23, as marked by the dashed lines on (c) and (b) the deformation vectors corresponding to cardiac cycles 8, 12, and 18, as marked by the solid lines on (c). These images highlight the potential inconsistencies of using single movement traces of the chest wall to predict respiratory induced cardiac deformation as in (a) the associated cardiac deformation is different despite the fact that the intensity patterns measured at the chest wall are identical. For (b), however, there is a much closer correlation between the deformation vectors and surface traces. 129

Figure 5-10 Subtraction error for PLSR by using a single chest trace compared to using all the 16 chest traces measured. Results were calculated as the mean square error of voxel intensity values (ranging from 0-255) for the selected region containing the heart. A value of 1.00 indicates the same result as using all 16 traces. 130

Figure 5-11 Subtraction error relative to the registration result for MLR and PLSR when different numbers of input traces are used. The graph shows the error range corresponding to different permutations of a given number of traces. 131

Figure 5-12 Deformation patterns of layer 3, 5 and 7 of the final 9×9×9 grid of a subject studied. For each image, the vectors were calculated from the PLSR coefficient matrix by keeping the first three principal components. Each row of this image represents the in-plane deformation captured by the 1st, 2nd, or 3rd principal component, where the motion vectors were amplified by 10 times for the 2nd and 3rd rows of each image as the corresponding vectors were much smaller than those captured by the first principal component. For each layer, the columns show the mean ± standard deviation of the in-plane deformation. 132

Figure 5-13 An example of the results derived from the proposed 3D motion prediction method. Images (a1) and (a2) represent the mid-ventricular slices of a subject at different phases of the respiratory cycle with the corresponding subtraction result shown in (a3). The 3D rendition shown in (a4) highlights the amount of cardiac motion and deformation involved, where the solid and meshed surfaces represent the endocardial border of (a1) and (a2), respectively. The second row shows the result of using direct 3D free-form image registration to the two 3D image volumes with (b2) representing the final warped mid-ventricular slice. Images (b3) and (b4) show the residual error by image subtraction and 3D rendering. The third row illustrates the same result as that of the second row but with PLSR motion prediction, demonstrating the ability of the proposed technique in accurate 3D motion prediction. 134

Figure 5-14 The overall residual error and standard deviation of the proposed motion prediction technique for all the 10 subjects studied by using the leave-one-out test. The analysis cover the entire respiration range and the corresponding 3D image registration results are provided as a reference. Results were calculated as the mean square error of voxel intensity values (ranging from 0-255) for the selected region covering the heart. 135

Figure 5-15 The subtraction error after sequential removal of traces used for learning and prediction relative to the use of all 16 traces. The best and worst case is shown with all possible error values for the different number of traces shaded in between. Results were calculated as the mean square error of voxel intensity values (ranging from 0-255) for the selected region containing the heart. A value of 1 indicates no improvement due to registration. 136

Figure 6-1 The Cartesian sampling function on the left gives a PSF shown in the middle after inverse Fourier transform. This replicates the imaged object (in this case a circle) as shown on the right. Two points are shown P_0 and P_1. P_0 originating from the 0th peak of the PSF and P_1 from the 1st peak of the PSF. 141

Figure 6-2 By increasing the distance between the lines in the sampling function, the distance between the peaks of the PSF is reduced in an inversely proportional manner. This leads to the reconstruction of the imaged object overlapping in the under-sampled direction. The points P_0 and P_1 now lie in the same position in the spatial image domain due to the two replicas of the imaged object sharing some of the same pixels in the image domain. 141

Figure 6-3 The images above show the effect described previously in sub-sampling the information in *k*-space. As shown, the *k*-space coverage in (a) is sufficient to produce image (b) without noticeable artefact due to wrap around. By reducing the sampling density by a factor of two in (c), the resulting constructed image has the image data overlapping from above and below in (d) producing significant artefact and error. 142

Figure 6-4 By shifting the sampling function in the phase encode direction through time (from dashed to full for instance) a phase ramp in the PSF is produced. This phase shift is passed on to the image domain so as points P_0 and P_1 may once again be distinguished. 143

Figure 6-5 A shift in the phase encode direction of half a line results in a π phase shift for each of the secondary peeks in the PSF. The point P_1 is now π degrees out of phase with the point P_0. 143

Figure 6-6 When applying the sampling function shown in Figure 6-5 to a stationary image sequence, it has the effect of producing two spikes in the temporal frequency domain, the DC component centred on 0 and the oscillating component at the Nyquist frequency. These two components may be easily separated to distinguish points P_0 and P_1. 144

Figure 6-7 A schematic illustration showing the basic effect due to sub-sampling of the Cartesian space. (a) and (b) are two sequential acquisitions through time with the corresponding even and odd *k*-space information shown on the left. The sampling function has been shifted in the phase encode direction by half a line. This leads to a π phase shift in the PSF for the secondary peaks. The result is shown with the resulting pixel intensities in regions C and D alternating between the magnitude of +a and –a, where all lower case variables are complex. When reconstructed, overlapping pixels such as those in E and F that alternate between the magnitude of 2a and 0 are created in the image domain. In this simple case, the complete reconstruction of the object is obtained by summing the two images either in the frequency domain or in the image domain. 144

Figure 6-8 With full sampling the temporal spectra for two points in image space are shown. (a) represents dynamic information, while (b) represents a static or more slowly varying point. Through under sampling in *k*-space the PSF moves closer and these two points are represented by the same pixel in image space (c). Through the temporal phase shift in the sampling pattern used with UNFOLD (b) has been shifted to the edge of the spectra, allowing the information from pixel (a) and (b) to be distinguished in post processing with temporal filtering. 145

Figure 6-9 With full sampling the temporal spectra for two points, (a) and (b), in image space are shown both containing significant dynamic information resulting in broad temporal spectra. Through under sampling in *k*-space, the PSF moves closer and these two points are represented by the same pixel in image space (c). Even though the sampling pattern is able to shift the information for pixel (b) to the edge of the temporal spectra, it is not sufficient to successfully distinguish the two points (a) and (b). 146

Figure 6-10 A synthetic (above) and real (below) stationary image sequence sub-sampled in *k*-space by a factor of two with UNFOLD applied. The right column shows the corresponding results when one of the image frames is translated by 5 pixels in the phase encode direction. 147

Figure 6-11 A single frame from an under sampled static image series with up to (a) 0, (b) 5, (c) 10 and (d) 15 pixels of random motion applied in the phase encode direction to each of the frames before applying 2 x UNFOLD. 148

Figure 6-12 The effect of shear distortion on UNFOLD. On the left, two synthetic images reconstructed from complete *k*-space information are shown. On the right the same objects are reconstructed from *k*-space data under-sampled by 2 in the phase encode direction. 149

Figure 6-13 Seven frames of a synthetic image series. All images are identical except for the central frame that has undergone shear distortion before being converted to *k*-space. The left column shows the result of full *k*-space image reconstruction, whereas the middle and right columns show the results of 2 × UNFOLD without and with distortion correction. 150

Figure 6-14 A central reconstruction of a circle is shown with overlapping PSF replicas due to sub sampling of the *k*-space data. In (a), a circle is shown on a rectangular background with the arrow showing the spatial difference in location between neighbouring replicas of the same point on the imaged object. In (b) the imaged object has undergone a shear transformation and in (c) the resultant image has undergone the reverse shear transformation to correct the central replica. 151

Figure 6-15 A schematic diagram showing the algorithm used for the binning and odd/even alternation used for RR-UNFOLD. 154

Figure 6-16 A sample navigator trace with a respiratory window of 5 *mm* for each of the bins used for RR-UNFOLD. A new bin is created in real-time at the first instance of a navigator edge being located within the specified window and from there, each further instance of a navigator edge within the required bin alternates the acquisition of odd (O) and even (E) *k*-space encoding steps. When a new bin is created, the first image is always chosen to be in sequence, in terms of odd/even *k*-line coverage, with the previous image regardless of respiratory position. 155

Figure 6-17 A schematic diagram showing all the processing steps involved in pre-processing the *k*-space data within each bin before UNFOLD reconstruction is applied. 157

Figure 6-18 The sequence timing diagram used for the acquisition of the patient data. The top figure shows the time in microseconds since the last R wave on the horizontal axis, the figure below shows the detail during the acquisition of the navigator, application of the saturation pulse and the start of the image data acquisition. 160

Figure 6-19 The average diaphragmatic respiratory navigator histogram for all 10 patients during the 120 cardiac cycle pre-scan, and 50 cardiac cycle perfusion scan. Diaphragmatic respiratory positions are normalised between 0 (end inspiratory) and 1 (end expiratory) with 0.1 bin widths. 161

Figure 6-20 Example diaphragmatic respiratory navigator histograms for three patients during the 120 cardiac cycle pre-scan and 50 cardiac cycle perfusion scan. Diaphragmatic respiratory positions are measured in *mm* with 2 *mm* bin widths, smaller values represent end inspiration and greater values end expiration. 162

Figure 6-21 The ratio of subtraction errors between RR-UNFOLD and conventional UNFOLD for the patients with no pre-scan binning (a) and binning based on a preliminary pre-scan (b) studied when different respiratory window sizes/number of bins are selected. In both figures, the same *k*-space data with extra central lines were used for RR-UNFOLD and conventional UNFOLD techniques. The subtraction error is the sum of mean square pixel subtraction errors for the whole sequence. The solid curve demonstrates the mean error ratio for all 10 subjects and the vertical bars indicate the standard deviation amongst subjects. An error ratio of less than 1.0 indicates an improved artefact suppression of the RR-UNFOLD technique against normal UNFOLD. 163

Figure 6-22 An example of the image artefact introduced by different reconstruction techniques, showing original fully encoded images – first column, conventional UNFOLD reconstructed images – second column, difference between the original and UNFOLD reconstructed images – third column, RR-UNFOLD reconstructed images (prior to tracer intensity correction) – fourth column, and the difference between the original and RR-UNFOLD reconstructed images – fifth column, respectively. For both UNFOLD and RR-UNFOLD, a two-fold reduction in phase encoding steps was used. 164

Figure 6-23 ROI signal intensity curves showing the effectiveness of signal intensity correction by the introduction of extra central *k*-space encoding lines for RR-UNFOLD. The three intensity curves of each figure show the signal derived from images with and without central *k*-space encoding measured within the blood pool and myocardium, respectively, compared to those from the original fully encoded perfusion image sequence. 165

Figure 6-24 The ratio of subtraction errors between RR-UNFOLD and conventional UNFOLD for the normal subjects (a) and patients (b) studied when different respiratory window sizes are used for each bin. In both figures, the same *k*-space data with extra central lines were used for RR-UNFOLD and conventional UNFOLD techniques. The subtraction error is the sum of mean square pixel subtraction errors for the whole sequence. The solid curve demonstrates the mean error ratio for all 10 subjects and the vertical bars indicate the standard deviation amongst subjects. An error ratio of less than 1.0 indicates an improved artefact suppression of the RR-UNFOLD technique. 166

Figure 6-25 The reduction in error (mean and standard deviation of the 10 patients studied) represented as a ratio of RR-UNFOLD against normal UNFOLD when different numbers of extra central *k*-lines are used. 168

Figure 6-26 Four frames from a perfusion sequence of a patient showing the image artefact introduced by using different reconstruction techniques, showing original fully encoded images – first column, conventional UNFOLD reconstructed images – second column, conventional UNFOLD with extra central *k*-lines – third column, RR-UNFOLD reconstructed images (prior to tracer intensity correction) – fourth column, and RR-UNFOLD – fifth column, respectively. Rows (a)-(d) show the results for different time frames and the corresponding subtraction errors compared to the original fully encoded image. 169

Figure 6-27 Perfusion index for normalised slope from Fermi deconvolution curve fitting calculated for 6 mid-ventricular segments of a patient demonstrating the effect of RR-UNFOLD and conventional UNFOLD for myocardial perfusion quantification. Relative values between reduced *k*-space reconstructions and the original data are shown for UNFOLD and RR-UNFOLD, where 1.0 indicates no change in perfusion index. With UNFOLD, the derived perfusion index has an error range of 25%-71%, whereas for RR-UNFOLD the error range is kept within 14%. 170

Figure 6-28 The relative error in perfusion index after applying the same processing steps as in Figure 6-27 to all the 10 patients studied by using the UNFOLD and RR-UNFOLD techniques, respectively. The mean absolute perfusion index errors and minimum/maximum absolute perfusion index errors are shown for each patient. 170

Figure 6-29 The ratio of subtraction errors between RR-UNFOLD and conventional UNFOLD for the normal subjects (a) and patients (b) studied when different numbers of bins are selected following an initial pre-scan. The first of the two methods divides the respiratory range evenly while the second selects bins to divide the histogram distribution from the pre scan evenly. 172

Figure 7-1 Two images from a synthetic myocardial perfusion sequence. The reference image is an image from late in the sequence and the dynamic image as the contrast agent enters the myocardial tissue. In the dynamic image a transmural defect is shown in the infero-septal wall (pointed by the arrow). The graphs show the pixel intensity values for the line shown down the image in the phase encode direction. The most notable difference between the reference and dynamic image in the graph is enhancement of the blood pool of the LV and hypo-enhancement of the transmural perfusion defect (phase encode line ~70). 181

Figure 7-2 Reconstruction of the dynamic image from Figure 7-1 by using only 16 of the 128 phase encode lines. The top graph and image show a simple Fourier transform of the central 16 lines, the middle graph and image show the replacement of the central 16 lines of the dynamic image into the remaining lines of the reference image from Figure 7-1. The bottom graph and image show reconstruction using the RIGR technique from the central 16 lines of the dynamic image with basis functions derived from the reference image. While significant artefact is shown throughout the image with all three reconstructions, the RIGR technique provides visibly clearer myocardial borders. For display purposes, the images on the right have been cropped and this region is shown as dotted lines on the graphs on the left 182

Figure 7-3 Reconstruction of the dynamic image from Figure 7-1 by using only 32 of the 128 phase encode lines. The top graph and image show a simple Fourier transform of the central 32 lines, the middle graph and image show the replacement of the central 32 lines of the dynamic image into the remaining lines of the reference image from Figure 7-1. The bottom graph and image show reconstruction using the RIGR technique from the central 32 lines of the dynamic image with basis functions derived from the reference image. While all three techniques are able to distinguish the transmural defect, RIGR provides visibly sharper edges to the LV blood pool with significantly less artefact. For purposes, display the images on the right have been cropped and this region is shown as dotted lines on the graphs on the left 183

Figure 7-4 Two images from a synthetic myocardial perfusion sequence. The reference image is an image from late in the sequence and the dynamic image as the contrast agent enters the myocardial tissue. In the dynamic image a subendocardial defect is shown in the antero-lateral wall (pointed by the arrow). The graphs show the pixel intensity values for the line shown across the image in the phase encode direction. The most notable difference between the reference and dynamic image in the graph is the enhancement of the blood pool of the LV and hypo-enhancement of the subendocardial perfusion defect (phase encode line ~85). 184

Figure 7-5 Reconstruction of the dynamic image from Figure 7-4 by using only 16 of the 128 phase encode lines. The top graph and image show a simple Fourier transform of the central 16 lines, the middle graph and image show the replacement of the central 16 lines of the dynamic image into the remaining lines of the reference image from Figure 7-4. The bottom graph and image show reconstruction using the RIGR technique from the central 16 lines of the dynamic image with basis functions derived from the reference image. For display purposes, the images on the right have been cropped and this region is shown as dotted lines on the graphs on the left 185

Figure 7-6 Reconstruction of the dynamic image from Figure 7-4 by using only 32 of the 128 phase encode lines. The top graph and image show a simple Fourier transform of the central 32 lines, the middle graph and image show the replacement of the central 32 lines of the dynamic image into the remaining lines of the reference image from Figure 7-4. The bottom graph and image show reconstruction using the RIGR technique from the central 32 lines of the dynamic image with basis functions derived from the reference image. It is clear that the RIGR technique provides a clearer endocardial border in the LV with fewer artefacts in the blood pool than the keyhole technique and is also able to distinguish the subendocardial defect from the dynamic image in Figure 7-4. For display purposes, the images on the right have been cropped and this region is shown as dotted lines on the graphs on the left. 186

Figure 7-7 The effect of small detail in the reference image on the reconstruction quality of the keyhole and RIGR methods. Series 1,2 and 3 are identical but for the contrast of the subendocardial defect in the reference image. With RIGR, due to the way that the basis functions are derived, when the high-resolution details are not clearly present in the reference image, significant blurring can be observed. This is evident from the above figure in the clarity of the small subendocardial border reconstructed. Depending on the size of the *k*-space used, the RIGR method is generally suitable for depicting small dynamic regions. 188

Figure 7-8 Seven frames from a first pass myocardial perfusion sequence acquired during free breathing. Each frame is shown with the value of the diaphragmatic respiratory navigator acquired directly preceding the image acquisition. The fully encoded reconstruction with 112 phase encode lines and the RIGR reconstruction using only 28 dynamic phase encodings are shown side by side with the direct subtraction image showing resulting artefact. At the bottom, the static reference image (frame 50) is also shown. 190

Figure 7-9 For a single subject shown in Figure 7-8, the diaphragmatic respiratory navigator reading, and the subtraction error result from a fully encoded image sequence is shown for each cardiac cycle. 191

Figure 7-10 Seven frames from a first pass myocardial perfusion sequence acquired during free breathing. Each frame is shown with the central value of the respiratory bin used for reconstruction of the image. The fully encoded reconstruction with 112 phase encode lines and the RR-RIGR reconstruction using only 28 dynamic phase encodings are shown side by side. The RR-RIGR image is reconstructed with the static data from the final frame within its respiratory bin, not necessarily frame 50. Frame 20 and 26 use frame 50 for reconstruction resulting in exactly the same reconstruction as in Figure 7-8. It is clear that significantly fewer artefacts are created using this technique as shown in frames 29, 32, 35 and 38. This is further highlighted by the difference images on the right. 192

Figure 7-11 Mean square subtraction error is shown for each frame of the myocardial perfusion sequence reconstructed with the RIGR technique using 28/112 dynamic phase encode lines. Two variations of this are shown, the method without binning uses the final frame (50) as a static reference image for the calculation of the required basis functions for the generalised series reconstruction. With RR binning, the data is separated into 5 *mm* bins and the final image from each of these bins is used as a static reference image 193

Figure 7-12 Seven frames from a first pass myocardial perfusion sequence acquired during free breathing (subject 1). The fully encoded reconstruction with 112 phase encode lines is shown on the left. A reconstruction using RR-UNFOLD with 56 lines and 6 extra central phase encode lines is shown together with the subtraction difference image from the full reconstruction. Also shown is a RR-RIGR reconstruction using only 56 dynamic phase encodings. From the subtraction images the difference in the artefact created by the two techniques is clear. 194

Figure 7-13 Mean square subtraction error is shown for each frame of the myocardial perfusion sequence reconstructed with the RR-UNFOLD and RR-RIGR using approximately half of the phase encode lines. It is clear that the error created differs between the two techniques. 195

Figure 7-14 Eight frames from a first pass myocardial perfusion sequence acquired during free breathing (subject 2). The fully encoded reconstruction with 112 phase encode lines is shown on the left. A reconstruction using RR-UNFOLD with 56 lines and 6 extra central phase encode lines is shown together with the subtraction difference image from the full reconstruction. Also shown is a RR-RIGR reconstruction using only 56 dynamic phase encodings. 196

Figure 7-15 Mean square subtraction error is shown for each frame of the myocardial perfusion sequence reconstructed with the RR-UNFOLD and RR-RIGR using approximately half of the phase encode lines. In this case the error created from the RR-RIGR technique is clearly less than from the RR-UNFOLD technique........ 197

Figure 8-1 The basic perfusion model. The time intensity signal from the blood pool of the LV (b) is combined with the curve for the tissue impulse response (r) to give the time intensity signal from the myocardium. The blood pool signal is considered as the input to the system and the myocardial signal the output. The impulse response has a small time delay representing the time taken for the agent carrier to travel to the entrance of the coronary arteries........ 203

Figure 8-2 The Fermi function. This represents the impulse response of the washout properties of the contrast agent through the myocardium. The value of τ_d represents the delay due to the time taken for the bolus of contrast agent to pass from the blood pool of the LV to the entrance to the coronary arteries........ 204

Figure 8-3 (a) Eight image frames from a synthetic perfusion sequence showing both subendocardial and transmural perfusion defects. (b) The derived factor images show different tracer characteristics of the myocardium and the locations of the defects (d1 and d2, pointed by the arrows). 207

Figure 8-4 The deconvolution problem represented through time intensity curves. Given the blood pool signal and the myocardial signal as the input and output to the system. It can be seen that the myocardial signal is the result of combining the blood pool signal with the unknown system characteristics through convolution. To obtain these system characteristics, a simple deconvolution could be performed. In this case, we show the result to be dominated by noise due to the inherent differentiation process involved. It is because of this that the model fitting approach is required. 208

Figure 8-5 Example screenshots of the Perfusion plug-in for CMRtools. Myocardial borders are delineated in (a) followed by motion correction (b), ROI delineation (c) in this case 6 radial segments divided into endo- and epicardium with a circle selecting the blood pool region. Corresponding signal-time measurements are graphically shown in (d) with the blood pool region shown in red and the selected myocardial region in green. In the final stage, this data is used to calculate myocardial perfusion indices (e) and displayed in a bullseye plot (the subendocardium is currently displayed). For the region selected, the myocardial perfusion index is shown at both rest and stress along with the corresponding curves and the final myocardial perfusion reserve index (MPRi). 10 of the 12 measurements are shown with a scroll bar to view the remaining data entries.. 211

Figure 8-6 A summary of SPECT findings for patient 1. Four views are shown, at the top eight time series images at stress and rest of a basal slice, below stress and rest of a mid ventricular slice then a HLA view and a VLA view. At stress, there is absent uptake in the antero-apical region with severe reduction of uptake in the septum and moderate reduction in the whole of the inferior wall. Antero-lateral uptake is normal. Following rest injection the antero-apical region and septum improve partially and the inferior wall returns to normal.213

Figure 8-7 X-ray angiography of the left coronary artery of patient 1, showing the LAD sub-totally occluded whilst the LCX is unobstructed... 214

Figure 8-8 X-ray angiography of the RCA of patient 1, showing the proximal occlusion as marked by the arrow. 215

Figure 8-9 Images from the first pass MR perfusion sequence of patient 1 showing hypo-perfusion of the anterior, inferior and septal walls, predominantly in the subendocardium.216

Figure 8-10 The bullseye plots of the first pass perfusion distribution corresponding to results in Figure 8-9 of patient 1. Severely reduced MPR Index (MPRi) values for the inferior wall is seen in the basal slice spreading around to the septal wall in the mid ventricular slice.. 217

Figure 8-11 The intermediate modelling results for Segment 2 of Figure 8-9 of patient 1, demonstrating normal perfusion uptake of this subendocardial segment. 218

Figure 8-12 The intermediate modelling results for Segment 4 of Figure 8-9 of patient 1, demonstrating hypo-enhancement in the inferior wall... 218

Figure 8-13 Late enhancement images of patient 1 at five weeks following presentation with ventricular fibrillation and myocardial infarction, showing septal hypo-enhancement. In the context of a recent infarction, this demonstrates microvascular obstruction and is therefore the territory responsible for their presentation.. 219

Figure 8-14 SPECT assessment of patient 2 showing partial thickness basal inferior myocardial infarction with moderate inducible ischaemia of the mid and apical inferior wall. The views on the left show from the top, apical, mid ventricular and basal short axis slices of the LV, followed by a HLA and VLA view. In the central column bullseye plots, and on the right a 3D visualisation of the LV are shown with a measure of reversibility based on the rest and stress findings. 220

Figure 8-15 MR first pass perfusion assessment of patient 2 with arrows identifying hypo-perfusion of the inferior, infero-septal and lateral walls at stress. 221

Figure 8-16 Bullseye plots from the MR assessment of patient 2 clearly showing the subendocardial perfusion defect in the inferior wall spreading to the infero-septal wall and lateral wall of the mid ventricular slice (shown as the inner ring). 222

Figure 8-17 Late enhancement images of patient 2 showing subendocardial infarction of the inferior wall. The arrows identify the late enhancement in the (a) short axis basal slice (b) short axis mid slice (c) LV outflow tract and (d) VLA views. 223

Figure 8-18 CMR perfusion images of patient 3 obtained with the TSENSE EPI sequence. Images taken during adenosine hyperaemia show an area of hypo-perfusion within the inferior and infero-septal wall in the basal and mid ventricular slices. In the basal slice this extends further in to the septum and antero-septal wall. Therefore the distribution of this inducible defect would suggest that more than one coronary territory is affected, most likely the RCA and to a lesser extent the LAD vessel. 224

Figure 8-19 Polar plots of MPRi values for patient 3 graphically illustrate the severe inducible hypo-perfusion of the inferior and infero-septal walls in green, particularly at the base of the ventricle. Furthermore, they also depict the less severe inducible hypo-perfusion of the septum and anterior wall, particularly at a mid ventricular level 225

Figure 8-20 Late enhancement images for patient 3 showing subendocardial infarction of the inferior wall. The arrows identify the late enhancement in the (a) short axis basal slice (b) short axis mid slice 226

Figure 8-21 Left anterior oblique (a) and right anterior oblique (b) projections of the RCA of patient 3. Showing occlusion of the main vessel (1), and a large collateral vessel (2) that distally refills the occluded vessel (3) 227

Figure 8-22 Left anterior oblique cranial (a) and left anterior oblique (b) projections of the LAD artery of patient 3. Arrows 1 and 2 depict 50% of luminal diameter stenoses of the mid and proximal vessel respectively. 228

Figure 8-23 A scatterplot of the global MPRi measurement, calculated by the maximum upslope of the myocardial signal normalised against the maximum upslope of the blood pool signal. 230

Figure 8-24 A scatterplot of the global MPRi measurement, calculated by Fermi deconvolution. The reproducibility of MPRi was similar in normal volunteers and in patients with CAD (CoV 21% vs 23%, P=0.88). 230

Chapter 1 : Introduction

Early diagnosis and localisation of myocardial perfusion defect is an important step in the treatment of Coronary Artery Disease (CAD). Thus far, coronary angiography is the conventional standard investigation for patients with known or suspected CAD and it provides information about the presence and location of coronary stenoses. For prognostic evaluation, as well as monitoring the efficacy of interventional measures of these patients, myocardial perfusion imaging plays an important role in establishing the ischaemic burden and the viability of ischaemic myocardium. Single Photon Emission Computed Tomography (SPECT) with thallium-201 or technetium-99m labelled compounds is the most widely used imaging modality for assessing regional myocardial perfusion. The technique, however, is affected by attenuation artefact from soft tissue and has relatively poor spatial resolution. Although it is possible to overcome these problems by the use of Positron Emission Tomography (PET) with ^{13}N labelled ammonia or ^{15}O labelled water, the method is more expensive and not widely available [1,2]. The main strength of PET is its ability to accurately quantify perfusion in addition to other metabolic activities. Perfusion studies are performed through the administration of a radionuclide tracer that decays with the emission of a positron. The main limitation of this method is blurring caused by cardiac contraction and respiratory induced distortion, thus limiting the transmural sensitivity of the technique [3,4]. In addition, the radionuclide tracers emit a significant radiation burden to the patient. As an alternative, echocardiography can also be used for perfusion quantification, with which the blood flow through the myocardium is determined by the use of sonicated micro bubbles as a contrast agent. This method, however, is only recently applied to myocardial perfusion imaging and the improvement in Signal-to-Noise Ratio (SNR) is a significant hurdle to overcome before the technique can be routinely applied [5,6].

In recent years, the development of myocardial perfusion Cardiovascular Magnetic Resonance (CMR) has extended the role of Magnetic Resonance (MR) in the evaluation of ischaemic heart disease beyond the situations where there have already been gross myocardial changes such as acute infarction or scarring. The ability to non-invasively evaluate cardiac perfusion abnormalities before pathologic effects occur, or as follow-up to therapy, is important to the management of patients with CAD. Early reperfusion of ischaemic myocardium has been shown to have a positive reversal effect on the ischaemic myocardium, which reduces mortality and morbidity. Differentiation of ischaemic but viable myocardium from infarcted regions requires detailed global quantitative assessment and modelling of myocardial perfusion characteristics. CMR allows for the acquisition of images of the myocardium with relatively high spatial resolution, thus allowing the transmural extent of myocardial ischaemia to be determined. Thus far, the common technique used for assessing myocardial perfusion based on first pass techniques with CMR is fast gradient echo (turboFLASH) [7,8,9], other techniques include TrueFISP [10], and Echo-Planar Imaging (EPI) sequences [11,12]. Quantitative results have been achieved in animal studies with intravascular agents (polylysine-Gd-DTPA) as a macromolecular blood pool marker [13] and conventional extracellular agents (Gd-DTPA) for human studies [7,14-16]. Whilst limited multi-slice 2D CMR perfusion studies are gaining increased clinical usage for quantifying gross ischaemic burden, research is now directed towards complete 3D coverage of the myocardium for accurate localisation of the extent of possible defects. The aim of this thesis is to address major technical issues concerning accurate myocardial perfusion quantification with motion modelling, rapid image acquisition and tracer kinetic modelling. The work reported in this thesis involves extensive phantom and *in vivo* clinical validation.

In Chapter 2, the clinical background of myocardial perfusion imaging is provided. It gives an overview of the basic pathophysiology of myocardial infarction and the development of imaging techniques, MRI in particular, for quantifying myocardial perfusion abnormalities. In this chapter, we describe the basic cause of CAD and the outcome of ischaemia and myocardial infarction. For providing a better understanding of the complexity of myocardial perfusion, we summarise the linkage between myocardial territory and coronary blood supply, and the importance of collateral circulation. In this chapter, we have also provided a relatively comprehensive comparison of the relative strength and potential pitfalls of different imaging techniques for quantifying myocardial perfusion, highlighting the potential of CMR perfusion and the technical challenges we have to overcome.

One of the pre-requisites of accurate myocardial perfusion imaging is to ensure a comprehensive coverage of the Left Ventricle (LV). In order to track the transit of the contrast bolus, it is required that the entire volume of interest be imaged within each cardiac cycle, preferably during a short acquisition window of 200-300 *ms*. In practice, this is a challenging task and compromises are usually made favouring SNR over myocardial coverage, or spatial resolution over temporal resolution. With many of the faster imaging sequences already approaching established limits of neuromuscular stimulation and Radio Frequency (RF) heating, further improvements in perfusion imaging will have to rely on exploiting the full information content of the *k*-space data. In Chapter 3, we review some of the commonly used *k*-space acquisition techniques that have been developed over the years. They include Keyhole imaging, Block Regional Interpolation Scheme for *k*-space (BRISK), temporal filtering methods for reduced field-of-view imaging, locally focussed imaging, and Broad-use Linear Acquisition Speed-up Techniques (BLAST). In this chapter, we have also described the basic concept of parallel imaging techniques including SiMultaneous Acquisition of Spatial Harmonics (SMASH) and SENSitivity Encoding for fast MRI (SENSE), and outlined their potential value in myocardial perfusion imaging.

Differentiation of ischaemic but viable myocardium from infarcted regions requires detailed global quantitative assessment and modelling of myocardial perfusion characteristics. This requires the development of a spatially and temporally registered imaging strategy for complete 3D coverage of the myocardium. In 3D myocardial perfusion imaging, a complete volumetric coverage can involve a large data acquisition window within each cardiac cycle. When using multi-slice imaging, cardiac motion during this large acquisition window can cause the myocardium imaged in different image planes to be mis-registered, *i.e.*, some part of the myocardium may be imaged twice whereas other parts may be missed out completely. This type of mis-registration is difficult to correct for by using post-processing techniques. In Chapter 4, we examine in detail the effect of cardiac motion and respiratory induced cardiac distortion to myocardial perfusion quantification. In practice, the effect of respiratory motion is particularly problematic to CMR and we discuss some of the current state-of-the-art techniques in respiratory motion management. We describe the normal patterns observed in free-breathing respiratory motion, and issues related to respiratory drift and hysteresis. In this chapter, we review some of the major techniques used for respiratory adapted imaging including the design of diaphragmatic navigator echoes and different phase encode reordering techniques. We also provide a motion decoupling strategy to ensure during myocardial perfusion imaging the same material is covered by each of the imaging slices, which greatly simplifies subsequent quantitative perfusion analysis.

In Chapter 5, one of the most significant contributions of this thesis is introduced. It describes a novel predictive motion-modelling technique that uses multiple surface traces to derive a free form motion model of cardiac deformation due to respiration. The predictive motion modelling method developed is designed for extracting intrinsic relationships between 3D cardiac deformation due to respiration and multiple 1D real time measurable surface intensity traces. The strength of this approach is that it does not require interleaved acquisition of navigators, and thus significantly simplifies the pulse sequence design. Furthermore, it makes the technique easily transportable to other imaging modalities. For myocardial perfusion, it will allow cross modality comparison of transmural Myocardial Blood Flow (MBF) distributions, particularly with 3D PET. The problem with using surface measured signals, however, is that they are strongly coupled with each other but poorly correlated with respiratory induced cardiac deformation. Numerically, this can create significant problems for recovering the inherent model that explains the causality between respiratory motion and surface deformations. In this chapter, a new technique of predictive cardiac motion modelling and correction based on Partial Least Squares Regression (PLSR) has been developed. The key steps of the method involve initial subject specific modelling of cardiac deformation with 2D/3D imaging of the anatomical structure combined with in situ real-time measurable inputs. Registration based on Free-Form Deformation (FFD) or finite element modelling is used to recover the underlying spatio-temporal deformation of the anatomical structure. The causality between tissue deformation and real-time measurable signals, such as surface deformation, is then extracted through the use of PLSR. At the prediction stage, real-time measurable inputs are used to predict cardiac deformations without the need for further 2D/3D imaging so that adaptive imaging can be performed in real-time to track the anatomical regions of interest.

In order to further increase the scan efficiency of myocardial perfusion imaging, Chapter 6 introduces a novel respiratory reordering scheme to reduce motion artefact with the use of the already established Unaliasing by Fourier-encoding the Overlaps Using the Temporal Dimension (UNFOLD) technique. The principle of UNFOLD is based on temporal filtering to resolve spatial aliasing within the Field Of View (FOV) caused by a reduction in the density of *k*-space sampling. The method assumes that the dynamic structure under consideration is slowly varying throughout the imaging series, and therefore can be represented by a narrow range of low frequency components in the temporal frequency domain. Unfortunately, due to respiration, significant motion and wraparound artefact can be introduced to myocardial perfusion imaging. The method developed in this chapter performs prospective respiratory reordering during data acquisition so that multiple synchronised sequences can be obtained. Issues related to dynamic bin allocation and UNFOLD reconstruction are discussed, and the proposed technique has been validated with both patient and normal subject data.

From detailed numerical analysis, it was apparent that with UNFOLD, a certain amount of temporal smoothing is involved despite the use of continuous sampling of the central *k*-space data. To assess this problem, we compare in Chapter 7 the use of Reduced-encoding Imaging by Generalised-series Reconstruction (RIGR) as an alternative to UNFOLD. RIGR attempts to minimise the total number of spatial encodings required for acquiring the dynamic image data sets. The suitability of the method to the imaging task as with other reduced encoding methods for dynamic imaging is based on the assumption that during the acquisition of dynamic image data, the high-resolution data remains static. The high-resolution static image is therefore built into a set of basis functions of generalised series constrained to the low-resolution dynamic images. The dynamic images can then be reconstructed with relatively few extra phase encoding steps. In this chapter, we describe the use of RIGR combined with prospective respiratory reordering for handling cardiac motion. The technique is similar in spirit to that described in Chapter 6, and our emphasis is placed on the comparison of relative merit and potential pitfall of the RIGR approach, particularly in the localisation of small endocardial defects.

To outline the clinical value of the techniques proposed, particularly the use of tracer kinetic modelling, we provide in Chapter 8 detailed quantitative analysis results involved in this thesis. In this chapter, we also outline some of the clinical background of extracellular versus intravascular contrast agent, tracer kinetics and compartment modelling, as well as the main issues related to perfusion quantification. We provide detailed quantitative analysis of three patients with comparative results from X-ray coronary angiography and SPECT, outlining the clinical value of the proposed CMR technique. To further assess the reproducibility of the method, results from a further study involving seven normal volunteers and nine patients with CADs are also provided. We conclude in Chapter 9 some of the remaining issues that need to be addressed in future research in CMR perfusion imaging, particularly the accurate measurement of the arterial input function for perfusion quantification.

Most parts of this thesis are published in peer-reviewed academic journals and conference proceedings/presentations. They include:

Motion Decoupling

Ablitt NA, Gao JX, Yang GZ, Motion Decoupling and Registration for 3D Magnetic Resonance Myocardial Perfusion Imaging, International Conference on Computational Science (3) 2002: 285-294.

Ablitt NA, Gatehouse PD, Gao JX, Firmin DN, Yang GZ, Cardiac Motion Tracking for 3D Myocardial Perfusion Imaging, Proc Intl Soc Mag Reson Med 10 (2002) 1615.

Predictive Motion Modelling

*Ablitt NA, Gao JX, Keegan J, Stegger L, Firmin DN, Yang GZ, Predictive cardiac motion modeling and correction with partial least squares regression. IEEE Trans Med Imaging. 2004 Oct;23(10):1315-24. (Appendix D.1)

Ablitt NA, Gao JX, Stegger L, Keegan J, Firmin DN, Yang GZ, Predictive cardiac motion modelling and correction, Computer Aided Radiology and Surgery 2003, International Congress Series 1256 (2003) 1179-1184.

Gao JX, Ablitt NA, Elkington A, Yang GZ, Deformation Modelling Based on PLSR for Cardiac Magnetic Resonance Perfusion Imaging, MICCAI (1) 2002: 612-619.

Ablitt NA, Gao JX, Keegan J, Firmin DN, Stegger L, Yang GZ, Predictive Motion Modelling for Adaptive Imaging, Proc Intl Soc Mag Reson Med 11 (2003) 1570.

Gao JX, Ablitt NA, Yang GZ, Self-Adaptive Free-form Registration for First Pass Myocardial Perfusion Imaging with PLSR, Proc Intl Soc Mag Reson Med 10 (2002) 1610.

Ablitt NA, Gao JX, Elkington AG, Pennell DJ, Yang GZ. Predictive Registration for Myocardial Perfusion Imaging, Euro CMR 2002.

Ablitt NA, Gao JX, Gatehouse PD, Firmin DN, Pennell DJ, Yang GZ, Adaptive Free-Form Registration for First Pass MR Myocardial Perfusion Imaging, SCMR 2002.

Respiratory Reordering

*Ablitt NA, Gatehouse PD, Firmin DN, Yang GZ, Respiratory reordered UNFOLD perfusion imaging. J Magn Reson Imaging. 2004 Nov;20(5):817-25. (Appendix D.2)

---

* indicates peer reviewed academic journals

Ablitt NA, Gatehouse PD, Yang GZ, RR-UNFOLD: Respiratory Reordered UNFOLD for First Pass Myocardial Perfusion Imaging, Proc Intl Soc Mag Reson Med 12 (2004).

Ablitt NA, Gatehouse PD, Merrifield R, Yang GZ, Respiratory Reordered RIGR for First Pass CMR Perfusion Imaging, Proc Intl Soc Mag Reson Med 13 (2005).

Tracer Kinetic Modelling

*Gatehouse PD, Elkington AG, Ablitt NA, Yang GZ, Pennell DJ, Firmin DN. Accurate assessment of the arterial input function during high-dose myocardial perfusion cardiovascular magnetic resonance. J Magn Reson Imaging. 2004 Jul;20(1):39-45. (Appendix D.3)

*Elkington AG, Gatehouse PD, Ablitt N, Yang GZ, Firmin DN, Pennell DJ. Interstudy reproducibility of quantitative perfusion Cardiovascular Magnetic Resonance, (under review) J Magn Reson Imaging.

Gatehouse PD, Elkington AG, Ablitt NA, Yang GZ, Pennell DJ, Firmin DN. Dual T1-sensitivity quantitative high-dose first-pass Gd-DTPA myocardial perfusion. Proc Intl Soc Mag Reson Med 12 (2004).

Elkington AG, Gatehouse PD, Ablitt NA, Firmin D, Yang GZ, Pennell DJ. Myocardial perfusion reserve using a novel dual acquisition Cardiovascular Magnetic Resonance sequence, SCMR 2003.

Elkington AG, Gatehouse PD, Ablitt NA, Firmin D, Yang GZ, Pennell D. Interstudy reproducibility of myocardial perfusion reserve using a novel dual acquisition Cardiovascular Magnetic Resonance sequence, SCMR 2003.

Elkington AG, Gatehouse PD, Ablitt NA, Yang GZ, Pennell DJ. A novel approach to measuring myocardial perfusion with cardiovascular magnetic resonance: the potential advantages of a double bolus technique, Euro CMR 2002.

---

* indicates peer reviewed academic journals

Chapter 2 : The Clinical Background of Myocardial Perfusion Imaging

2.1 Introduction

CAD is the leading cause of death in the developed world. Statistics published by the American Heart Association [17] for 2001 show that in the United States, 64.4 million Americans had one or more forms of cardiovascular disease. Amongst them, 13.2 million are diagnosed with coronary heart disease (CAD), 7.8m having had a myocardial infarction. Cardiovascular disease claimed 931,108 lives in America, nearly 40 percent of all fatalities. The totals for other cases of mortality are: Cancer 553,768, Accidents 101,537, Alzheimer's disease 53,852, and HIV (AIDS) 14,175.

For many years, researchers have been investigating ways of improving the diagnosis and treatment of CAD. Earlier diagnosis has the potential to prevent irreversible damage or possible death. Thus far, coronary angiography is the gold standard test for the diagnosis of CAD, providing information on the presence and location of coronary stenoses. For prognostic evaluation of these patients, as well as monitoring the efficacy of interventional measures, myocardial perfusion imaging plays an important role in establishing the ischaemic burden and myocardial viability. SPECT with thallium-201 or technetium-99m labelled compounds is the most widely used imaging modality for assessing regional myocardial perfusion. Its importance in clinical practice is evident, with approximately 7 million examinations yearly in the USA alone. The technique, however, is affected by attenuation artefact from soft tissue and has relatively poor spatial resolution. Although it is possible to overcome some of these problems by the use of PET with ^{13}N labelled ammonia or ^{15}O labelled water, this method is more expensive and not widely available. Furthermore, both techniques involve ionising radiation. With recent advances in ultra-fast MR imaging, the potential of using contrast enhanced MRI to assess myocardial perfusion has been increasingly recognised. The purpose of this chapter is to provide an overview of the basic pathophysiology of myocardial infarction and the development of imaging techniques, MRI in particular, for the quantification of myocardial perfusion abnormalities.

2.1.1 The basic structure of the heart and its function

The heart is a complex organ that maintains a supply of oxygenated blood flowing throughout the body and is similar in size to a clenched fist. The heart muscle, termed myocardium, is where the pumping force originates. But the heart could not function without the valves, coronary arteries and the conductive properties of the tissues. From a basic anatomical perspective, the heart is divided into four chambers including the two atria and two ventricles, as shown in Figure 2-1. The left and right sides of the heart are separated by the septum. The right atrium receives oxygen-depleted blood from the body via the superior and inferior venae cavae, which is then transferred to the right ventricle (RV) and pumped into the pulmonary artery. From here, the blood is circulated through the lungs and re-oxygenated. The left atrium receives the returning oxygen-rich blood from the pulmonary veins. It is transferred to the LV through the mitral valve and then pumped via the aorta and branching arteries throughout the body. The LV has stronger and thicker muscle as it is must exert greater pressure to pump the blood around the body than the RV to the lungs.

Cardiac muscle fibres differ from other muscle fibres within the human body in both size and structure. The fibres consist of elongated cells with central nuclei and branching attachments, making up three quarters of the volume and one third of all cells within the myocardium. The cells are relatively small, typically measuring around 110 μm long and 15 μm wide. Cardiac myocytes join with one another end to end through intercalated discs that provide structural as well as electrical coupling between cells. This mass of interconnected myocytes can in theory be treated as a single muscle cell or a functional syncytium.

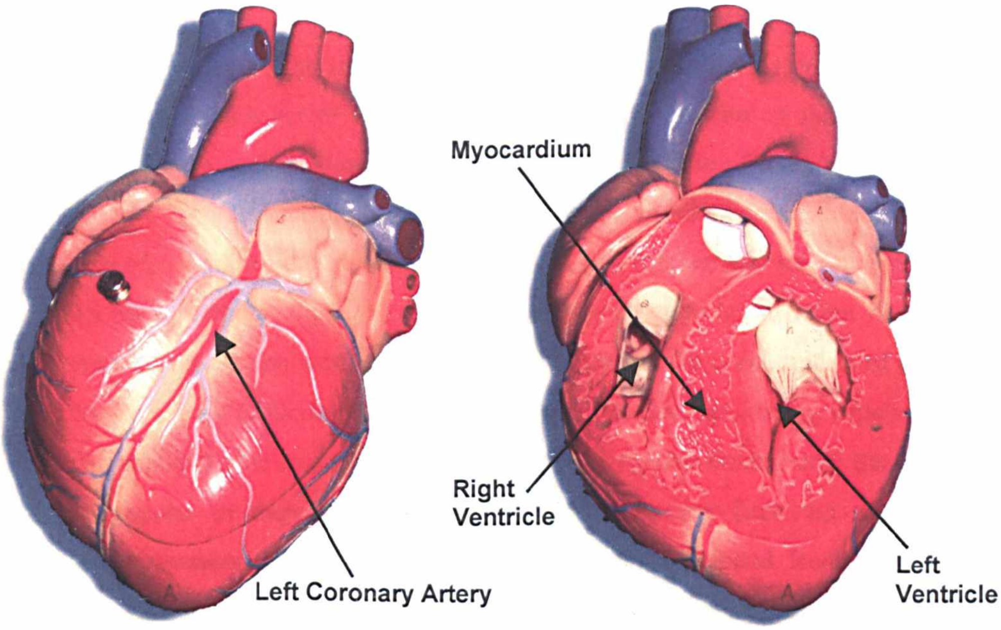

Figure 2-1 The basic anatomy of the heart and relative position of the left and right ventricles. The coronary arteries running along the epicardial surface provide vital blood supply to the myocardium in order to maintain its function.

Cardiac myocytes also have unique characteristics in the activation of their contraction. Whereas muscle fibres generally require neuronal stimulation, cardiac myocytes are activated by cardiac pacemaker cells without neuronal activation. This produces a regular activation of contraction and the relatively long action potentials (200-350 *ms*) avoid additional stimuli creating contraction out of synchrony with the cardiac cycle. Critically, cardiac myocytes are unable to regenerate by division so when damaged by disease or injury, permanent loss of function occurs. In principle, it is the contractile proteins within cardiac muscle cells that activate contraction. Through a cross-bridge mechanism, linking myosin and actin filaments, an energy-dependent process is activated by calcium. Three proteins troponin C, troponin T and troponin I are involved. An increase in cytosolic calcium causes troponin C to bind with calcium, and a "pull" effect (contraction) is produced. Conversely, a lowering of cytosolic calcium concentration causes the release of calcium from troponin C, resulting in cardiac muscle relaxation [18].

In order to contract, a constant blood supply from the coronary arteries is essential. The myocardium has a dedicated blood supply, the coronary arteries arising from the aorta just above the aortic valve. The Right Coronary Artery (RCA) supplies the RV and the Left CircumfleX (LCX) and Left Anterior Descending (LAD) supplies blood to the LV and septum. These divide into vessels with a smaller diameter and better coverage supplying the entire myocardium at capillary level. An illustration of the coronary tree is shown in Figure 2-2. Contraction will be impaired when the blood supply to the myocardium is inhibited such as by coronary heart disease. The supply of oxygen to the myocardium is predominately via coronary blood flow. The level of which is determined by a number of factors including systemic blood pressure, and anatomical factors such as the calibre of the coronary arteries and arteriolar bed. The myocardium has a high density of capillaries able to provide sufficient levels of oxygen to the myocardial tissue. At rest the demand for oxygen and the time available for its supply allow the coronary arteries to provide sufficient oxygen for myocardial contraction. As the workload of the heart increases the combination of a greater demand for oxygen and a reduction in relative time spent in diastole (during which MBF to the LV is at its greatest), due to an increased frequency of cardiac contraction, the coronary arteries must respond to their demand. Regulation of coronary flow via dilation and contraction of the coronary arteries occurs in response to oxygen demand. Reduced coronary flow can cause reduced blood supply to certain areas of the myocardium and when the myocardial oxygen supply-demand relationship decreases to a critical level, myocardial ischaemia occurs.

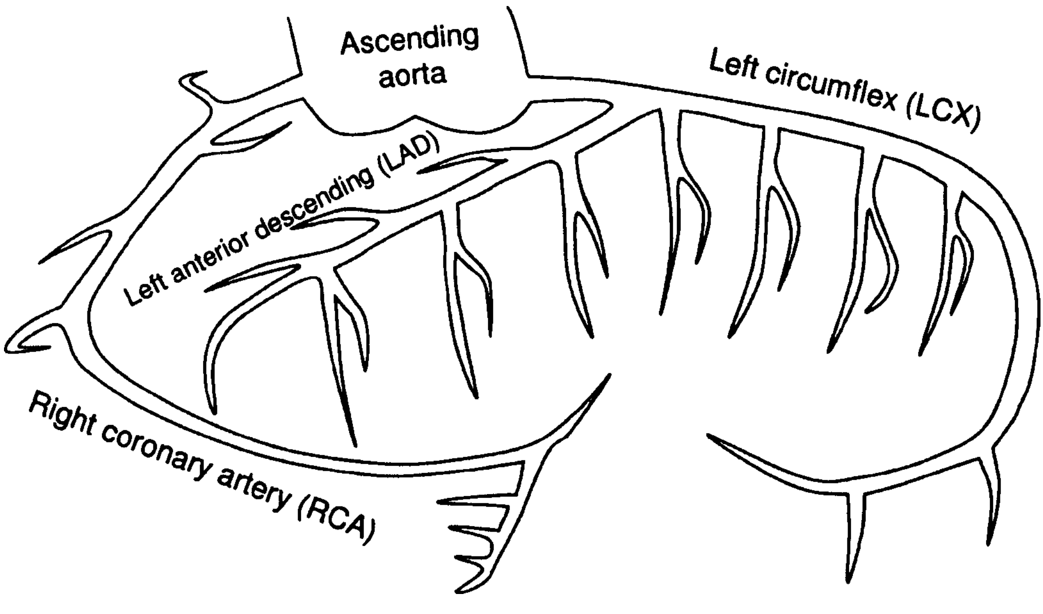

Figure 2-2 A schematic diagram of the coronary tree, showing the relative position of the major coronary arteries, based on a figure used by the AHA [19].

2.1.2 Coronary artery disease (CAD)

CAD results in the narrowing and eventual occlusion of coronary arteries due to atheroma, caused by the deposition of cholesterol and lipids within the arterial walls. Atherosclerosis is the process involving the deposition of fatty substances, cholesterol, calcium and other materials on the inner lining of typically large and medium sized arteries. Atherosclerosis can affect any blood vessel, beginning at an early age and developing over years, and eventually causes the artery to narrow and stiffen. These plaques in time may rupture, and a process called thrombosis occurs causing blood clots that may further impair blood flow or break off and affect blood flow further along the coronary tree. The process of thrombosis may occlude the vessel resulting in a myocardial infarction or "heart attack". The causes and pathogenesis of atherosclerosis are so far not completely understood. CAD occurs to some degree as a natural result of aging. There are several known "risk factors" that may result in its development at a younger age. Some of these risk factors may be modified, and some cannot. Factors such as a family history of CAD in a first-degree relative at a younger age are known to affect the likelihood of early onset. Aging itself, and the female menopause are also influential. Risk factors that may be modified include smoking, diabetes, high cholesterol, blood pressure, weight and lifestyle.

In general, a mild narrowing of the coronary artery will not usually cause any symptoms. If the vessel becomes narrowed by around half or more, there can be a reduction in blood flow during periods of activity when the demand for blood supply are greater. When the vessel is narrowed by around 90% or more there is the potential for a lack of blood supply at rest. When the vessel becomes 100% closed, a heart attack ("myocardial infarction") may occur. On the other hand, if the vessel closes gradually, the muscle may obtain flow from other vessels through collateral flow. Typically, mild blockages will permit an adequate blood supply to the myocardial territory served by the artery. With moderate blockages, there may be insufficient blood flow under increased demand such as exercise. In these cases, one may experience chest discomfort (angina) due to inadequate blood flow. Permanent muscle damage does not occur following anginal symptoms in isolation, and may in fact train the myocardium for a decreased blood supply by inducing subcellular changes. In fact, the majority of ruptures that lead to infarction are of plaques that do not cause stenosis. Stenotic plaques have a thick fibrous cap, which possibly act as a protection against rupture.

2.1.3 Ischaemia and myocardial infarction

Ischaemia is a shortage of oxygen resulting in cellular dysfunction, which can have both short and long term effects. A short period of ischaemia, lasting only several minutes, is usually reversible. A long-term period (30-40 *min*) of ischaemia, however, can lead to permanent myocardial injury and cell death. In certain cases, persistent severe ischaemia may not necessarily result in myocardial infarction but can cause marked contractile abnormalities. Despite the restoration of perfusion to these areas of the myocardium, abnormalities may persist for days or even weeks before normal functionality is restored. This is referred to as myocardial stunning. Hibernating myocardium refers to a more chronic myocardial oxygen deficiency. The function of the myocardium is reduced which mirrors the available oxygen supply. This can form a new state of equilibrium without resulting in necrosis. Restoration of coronary flow to this region of tissue can lead to the return of normal functionality. Many people have no symptoms despite having a substantial blockage. They can still be shown to have insufficient blood supply with exercise or stress tests, but simply don't experience a symptom of angina as others do. This is termed "asymptomatic ischaemia".

Myocardial infarction is the death or irreversible injury of myocardial tissue (necrosis), resulting from an occlusion of coronary flow and thereby a localised deprivation of oxygen. The characteristic symptom of myocardial infarction is severe and persistent angina (chest pain). The time taken for an infarct to develop varies depending on that myocardium's current perfusion characteristics. It has been shown that when there is little collateral flow and high oxygen uptake within the myocardium this time period can be as short as 20-60 minutes. This may be extended to between 2 and 6 hours in situations where the collateral flow is high and the myocardial oxygen uptake is low [20]. In general, myocardial infarction occurs initially within the subendocardium, as it lies furthest away from the epicardial arteries. This, together with transmural metabolic differences, is thought to explain the pattern seen in the progression of myocardial infarction, developing from the subendocardium to the subepicardium in a manner described as an advancing wave front.

The consequence of myocardial infarction is the altered function of the heart. With time the necrotic myocardium is infiltrated by fibroblasts; cells that form a scar tissue with the myocardium. This results in remodelling of the myocardium. Ventricular remodelling is a significant factor in the process resulting in heart dysfunction and eventually failure. Molecular changes occur in the remodelling of both the structure and function of the heart, resulting in compensatory myocyte hypertrophy or left ventricular dilation. The ventricle becomes dilated and more spherical, and by Laplace's law there is an increase in wall stress, increasing the workload on the myocytes. With ventricular dilation, cardio-myocytes operate with less efficiency since the same amount of contractile force generates less pressure, and thus flow. Therefore, even normal myocytes can suffer from increased work due to decreased efficiency. This can result in fatigue, which may lead to functional and structural failure [18].

Prolonged severe ischaemia may eventually lead to cell death. The manner of death and the processes involved are an important element in both the diagnosis and treatment of myocardial infarction. While it was previously believed that all cell death took place via necrosis, it is now known that this is not the case. Necrosis may be described and classified into two different types. The first of these is called coagulation necrosis. This is commonly found in the centre of a developing infarct, and characterised by a swollen and indistinct appearance. Amorphous dense bodies form within mitochondria inhibiting the production of ATP within the cell, resulting in a critical energy deficit. Blebs and holes appear within muscle cell membranes. Due to increased membrane permeability intracellular enzymes and proteins escape into the extracellular space. These enzymes and proteins may be used as clinical markers in detecting myocardial infarction. Contraction band necrosis is found near the border of the infarct. The main feature of which is hypo contraction of the contractile elements.

Apoptosis results in cell death through a different process. A genetically programmed series of biochemical events leads to the shrinkage of the cell. While intracellular degeneration takes place the, sarcolemma remains intact. The nucleus is split into fragments, with little damage to the mitochondria taking place. Phagocytes, in a waste clearing process called phagocytosis, absorb these fragments, termed apoptotic bodies. Genes control apoptosis, either promoting or suppressing its activation. There are a number of reasons why the body deliberately activates the death of cells, such as aging. The genes that control its activation are believed to be present in a variety of tissues and many act as a form of tumour suppression. The exact conditions under which apoptosis take place are unclear. It is known that necrosis takes place after a period of prolonged severe ischaemia. There is evidence that apoptosis takes place during longer sustained periods of ischaemia exceeding 2 to 3 hours, and also during reperfusion after shorter periods of ischaemia [21]. The two differing modes of cell death are significant as the diagnosis and possible treatment of cell death will no doubt differ.

At a microscopic level, as an infarct progresses cardio-myocytes die rapidly and contractions stops within one minute. However, adjacent living cells rhythmically tug at the ends of the paralysed fibres. This results in thinning at the site of infarction [22]. Electron microscopy shows that ischaemic damage in contractile cells will form transverse contraction bands of hyper-contracted sarcomeres. Therefore, wavy fibres are an initial sign of infarction, prior to the occurrence of necrosis [23]. When flow is obstructed through an artery, it will develop alternative routes in and/or around ischaemic tissue. At the start of infarction, all infarcts are of a reddish hue, because the dead tissue is soaked with blood. Its capillaries and other vessels tend to be paralysed or over-dilated. This will evoke an acute inflammatory reaction within hours, spearheaded by a wave of polymorphonuclear phagocytes. The capillaries connected with the infarcted tissue may be sealed off by thrombosis. About one day later, the infarction turns white, as the red blood cells haemolyse and haemoglobin diffuses away. The final result is a fibrous scar formed over the following weeks. Ultimately the time course of these changes is determined by the flow, collateral supply and the myocardium itself.

To say that a certain area of myocardium is viable indicates that whatever its current contractile status, function will improve if blood flow is improved. This means that cells within the area are alive. The ability to distinguish between myocardium that has the potential to regain normal function, and tissue which is permanently scarred and unable to regain full functionality, is a major challenge in cardiac medicine. The identification of reversible dysfunction is essential in the early management of heart failure, and has the potential to reduce both morbidity and mortality in this condition. There are a number of different strategies for imaging viable myocardium based on myocardial perfusion techniques. These are gaining clinical recognition in that they provide both a qualitative and quantitative assessment of the dynamic behaviour of the heart.

2.1.4 Myocardial territory linked to coronary blood supply

Clinically, to link coronary blood supply to a particular myocardial territory, it is useful to use a standardised representation. The epicardial coronary arteries consist of the left coronary artery and RCA. The left main stem is the common origin of the two major left sided coronary vessels, the LAD and LCX. The right coronary descends and becomes the posterior descending artery. Anatomically, these main arteries lie in the atria-ventricular grooves that separate the heart chambers. The left main and its branches usually provide most of the blood supply to the LV. In the LV, the anterior wall is adjacent to the chest wall, the septal divides the LV and RV, the posterior (inferior) at the back and lateral away from the RV. The LAD supplies anterior septum, anterior wall and in most cases apex possibly right around to the most apical portion of the posterior and lateral walls, whereas the LCX supplies the lateral wall. The RCA, which runs down the groove between the LV and RV, supplies blood to most of the RV and a portion of the inferior wall. Each of these arteries branch into smaller vessels to penetrate the heart muscle. Each individual person has a unique coronary artery tree. The number and placement of branches can vary greatly.

Figure 2-3 illustrates the standard 17-segment model for the LV as proposed by AHA [24]. The model divides the entire ventricle into 4 major cross-sections along the long axis starting from the base to the apex of the LV. Within each cross-section, the short axis cross section of the LV is further divided into approximately equal volume segments. In relation to the coronary structure mentioned above, the LAD normally supplies regions 1, 2, 7, 8, 13, 14 and 17 and can also supply 6, 12, 15, and 16 depending on the subject. The LCX generally supplies 5, 6, 11, 12, and 16, while the RCA 3, 4, 9, 10 and 15 and also sometimes region 2.

Anatomical variability in the regions of myocardial territory supplied by the different coronaries is normal amongst different subjects. The inferior wall is essentially supplied by the dominant vessel, defined as which ever gives off the posterior descending artery this is either the RCA (2/3 of the population) or LCX (the remaining 1/3). Some people have virtually no RCA or LCX and supply is dominated by whichever is present.

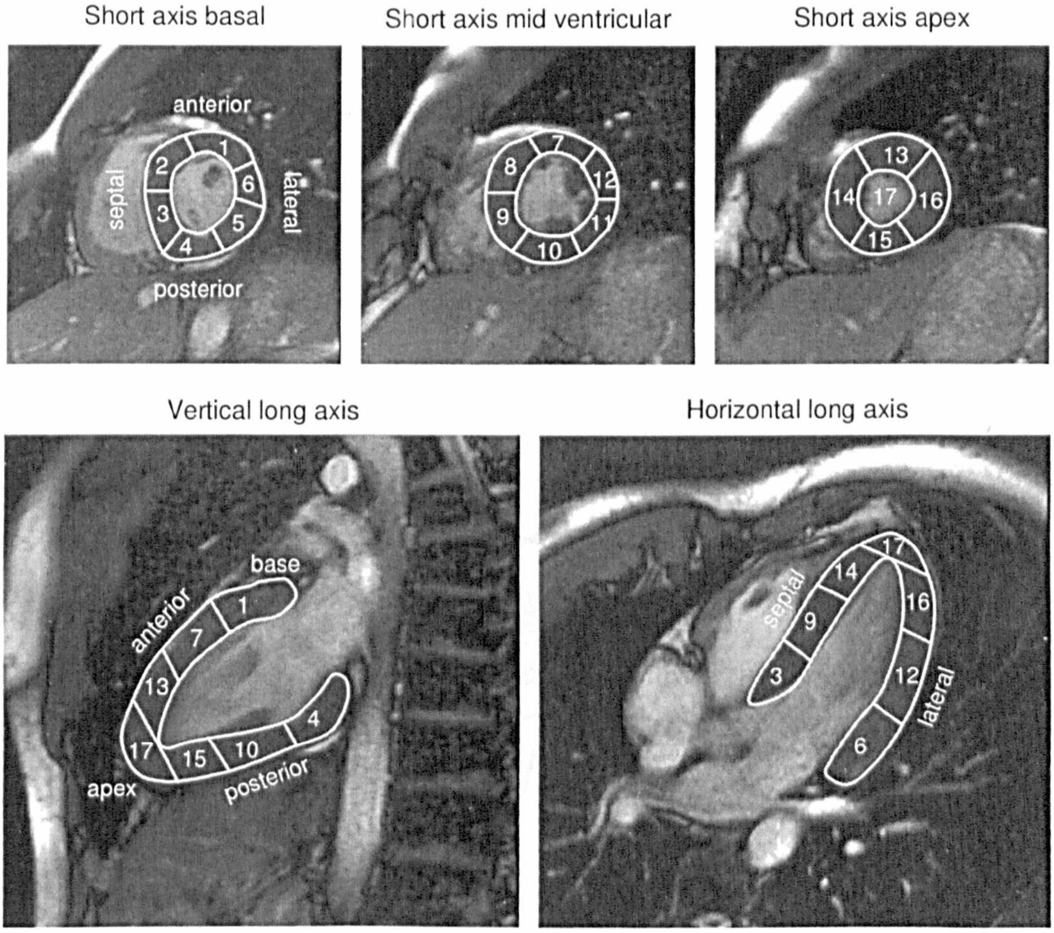
Short axis basal

Short axis mid ventricular

Short axis apex

Vertical long axis

Horizontal long axis

Figure 2-3 A schematic representation of the 17-segment model defined by the AHA.

2.1.5 Collateral circulation

To understand the basic pathophysiology of myocardial perfusion it is also important to understand collateral perfusion. Coronary artery branches may interconnect through arteries called intra-coronary collaterals. Collateral circulations are alternate routes of blood supply to the major feeding artery. When a collateral vessel in the heart enlarges, blood flows from one coronary artery to an adjacent one or further downstream on the same artery. Experiments show that in dogs, a sufficient coronary constriction would stimulate collateral growth over 4-5 days that prevents myocardial infarction when the constricted artery is completely blocked. This "detour" around a blockage restores the blood flow to part of the vessel. In this case, ischaemia and contractile dysfunction only appear after the collateral flow to the myocardium is curtailed. Thus, collateral circulation is helpful in protecting the myocardial muscle from dying if the normal blood supply is cut off [25].

This alternative route of supply of blood to the myocardium introduces a further delay in first pass myocardial perfusion and must be considered in the analysis of myocardial perfusion reserve. However, with high spatial and temporal resolution MR images, these effects can be quantified [26]. Recently development of new model independent deconvolution techniques aim to cope with this delay [27]. Fuchs *et al* [28] recently carried out a pig experimental study, showing that bone marrow cells injected trans-endocardially will enhance collateral perfusion and myocardial function in ischaemic myocardium. This result correlates the conclusion by Rajanayagam *et al* [29], who in 2000 carried out a dog study and found that administration of basic fibroblast growth factor by the intra-coronary route, an intervention that is feasible in patients, improves collateral development in dogs.

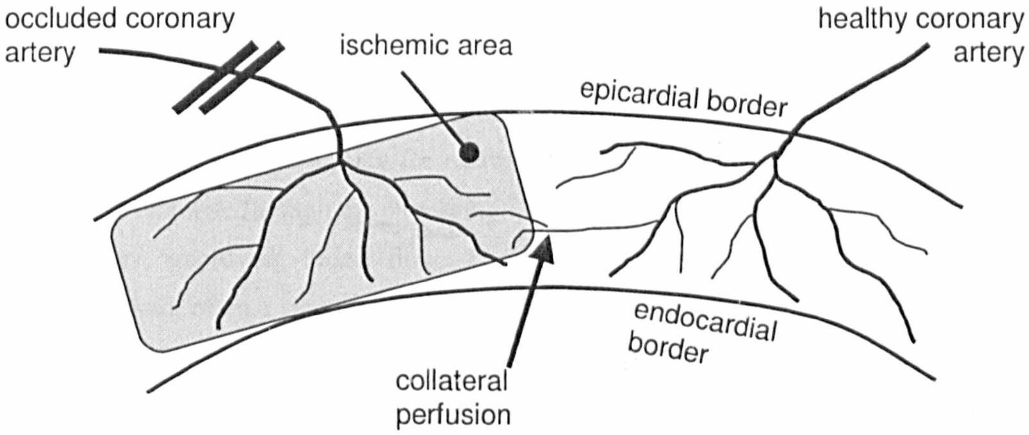

Figure 2-4 A schematic illustration of collateral circulation with a healthy artery supplying a neighbouring ischaemic region, adapted from [27].

2.1.6 Diagnosis and prognosis

The prognosis of CAD is highly variable, and depends on many factors. The key issue is how well the heart muscle is functioning and how many vessels are diseased and to what degree. The long-term prognosis is influenced by many factors, including a history of smoking and management of blood pressure and cholesterol, which may include diet and exercise programs. Clinically, the diagnosis of CAD is complicated and generally not limited to a single test. The choice of test is often dependent upon a number of factors, particularly the severity of the symptoms and the likelihood of CAD being present. ElectroCardioGraphy (ECG) is the most commonly used technique for recording the electrical activity of the heart, which can detect abnormal heartbeats, some areas of damage, heart enlargement and if stress (exercise) ECG is performed inadequate blood flow can be detected. The limitation of the technique, however, has long been recognised. It was found that the diagnostic abilities of exercise ECG were limited. The occurrence of false negative responses for patients with clinically suspected coronary disease is high, and false positive responses frequent in asymptomatic patients (particularly females) leading to unnecessary further tests. An ECG cannot assess myocardial viability, only the likely presence of ischaemic heart disease and possible hypertrophy; however, it is neither very specific nor sensitive. It was further found that surface exercise ECG has limitations in localising ischaemia to specific areas of the myocardium. This led to research into alternative methods of assessing myocardial ischaemia and viability, particularly non-invasive imaging techniques.

The treatment of CAD in severe cases may require an operation to either bypass or open an artery and improve blood flow. This is usually done to ease severe chest pain, or to clear major or multiple blockages in blood vessels that are causing angina. Two commonly used procedures are coronary angioplasty and coronary artery bypass grafting:

- *Coronary angioplasty.* In this procedure, a fine tube or catheter is threaded into an artery and then a wire into the narrowed coronary vessel. A balloon is then passed over this wire through the narrowing. The balloon is inflated to open and stretch the artery, improving blood flow. The balloon is then deflated, and the catheter removed, often a stent is inserted to keep the artery open after angioplasty. In about 15% of those who have angioplasty, the blood vessel becomes narrowed again within 6 months and may undergo a repeat procedure.
- *Coronary artery bypass graft operation.* The procedure uses a piece of vein taken from the leg, or of an artery taken from the chest or wrist. This graft is then attached to the coronary artery below the narrowed area and the aorta above, thus making a bypass around the blockage. Sometimes, more than one bypass is needed. Bypass surgery may be indicated for various reasons including anatomy that is not suitable for angioplasty or where a valve is also required

Other procedures that may be used to remove narrowing in the coronary arteries include atherectomy where the plaque is burred or shaved off by using a rotary drill bit, and laser atherectomy. The described procedures relieve the symptoms of CAD but do not cure the disease. Lifestyle changes must still be followed and any necessary medications must continue to be taken.

2.2 Perfusion imaging: what is available?

Myocardial perfusion imaging is becoming a valuable method in the evaluation of CAD. Perfusion imaging provides several important haemodynamic parameters; including blood flow, volume, and mean transit time, which is the average time it takes a tracer molecule to pass through the target tissue. When the coronary artery narrows due to cardiac disease, the related perfusion image uptake will differ from normal. If this narrowing is severe enough, the corresponding perfusion images will show significant abnormality. However, when the narrowing is slight, the corresponding variation in perfusion uptake will be difficult to detect. In order to detect a stenosis at an early stage, perfusion images under pharmacological vasodilatation or physical stress are performed. Induction of hyperaemia or maximal vasodilation is to increase the divergence between areas supplied by normal flow and those supplied by stenosed arteries. Imaging methods may be used to detect and distinguish between different aspects of coronary heart disease, including ischaemia, myocardial viability and the detection of scar tissue.

For the accurate assessment of sub endocardial perfusion defects, a resolution of at least 2-3mm is required across the myocardium. In clinical practice, SPECT typically has a resolution of ~10 *mm* which is then interpolated to a higher resolution. PET has a similar resolution, generally at around ~4-8 *mm*. EBCT, on the other hand, can achieve a much higher resolution of 0.7-1.5 *mm*, whereas contrast echo is around 1-2 *mm*. MRI is able to achieve an in plane resolution of ~2 *mm* (typically with a 128 × 128 matrix size). When slices are acquired in the short axis of the LV, it is sufficient to assess sub-endocardial perfusion defects.

2.2.1 Single-Photon Emission Computerised Tomography (SPECT)

With SPECT, images are formed from gamma and X-ray photons emitted from radioactive tracers. The system uses the principle of mechanical collimation where a lead collimator with an array of holes is used to allow photons travelling in a preferential direction to interact with a scintillation crystal. A lead septa is used to block other photons whose direction of travel is not in the preferential direction. The photons with this directionality are recorded at multiple locations around the organ being imaged and subsequently reconstructed using filtered back projection. By using a rotating gamma camera, SPECT can take images from between 32 to 64 views with a large FOV, *i.e.* 180- to 360-degree. After image processing, the myocardium can be assessed in different imaging planes including the short, horizontal and vertical axes. In addition to myocardial perfusion, SPECT can also provide information about regional wall motion, thickening and the ejection fraction of the

LV when gated with the ECG. An example set of SPECT images at both rest and stress is shown in Figure 2-5.

The use of SPECT for myocardial perfusion quantification has a long clinical history. Early studies in the 1980s have assessed the capabilities for predicting cardiac events after uncomplicated myocardial infarction by comparing pre-discharge exercise thallium-201 scintigraphy with coronary angiography [30]. The results indicated that sub maximal exercise 201Tl scintigraphy could distinguish between high and low risk groups after uncomplicated acute myocardial infarction before hospital discharge. A large multi-centre study investigated risk stratification and survival after myocardial infarction [31]. It was found that there is a progressive increase in cardiac mortality during one year as the ejection fraction fell below 40%. A study involving 1,600 patients analysed the incremental prognostic power of the clinical history, exercise electrocardiography and myocardial perfusion scintigraphy in suspected CAD [32]. A strategic model was subsequently developed that stratified individual patient risk for subsequent coronary events, at one third of the cost of performing both stress tests in all patients. Kaul *et al* [33] studied the prognostic utility of the exercise thallium-201 test in ambulatory patients with chest pain, in comparison with cardiac catheterisation. The number of diseased vessels was found to be the single most important determinant of future events, but it was found that the combination of non-invasive measures with exercise thallium-201 was equally powerful. More recently Machecourt *et al* [34] studied the prognostic value of thallium-201 SPECT myocardial perfusion imaging according to the extent of a myocardial defect. It was found that for patients with stable angina, normal thallium SPECT was able to indicate those patients at low risk. It was also found that the extent and severity of the myocardial defect is an important prognostic factor, providing additional information compared with other clinical variables and exercise ECG. A similar study by Hachamovitch *et al* [35] looked at the incremental prognostic value of myocardial perfusion SPECT for the prediction of cardiac death. SPECT was found to provide incremental prognostic information toward the identification of cardiac death. Additionally, it was concluded that patients with mildly abnormal scans after exercise stress are at low risk for cardiac death but intermediate risk of nonfatal myocardial infarction and thus may benefit from a non-invasive strategy. For patients who are unable to exercise, Vernai *et al* [36] investigated the diagnosis of CAD by controlled coronary vasodilatation with adenosine and thallium-201 scintigraphy. In general, more reproducible results have been found using pharmacological stress in comparison with exercise, and the technique is now widely used.

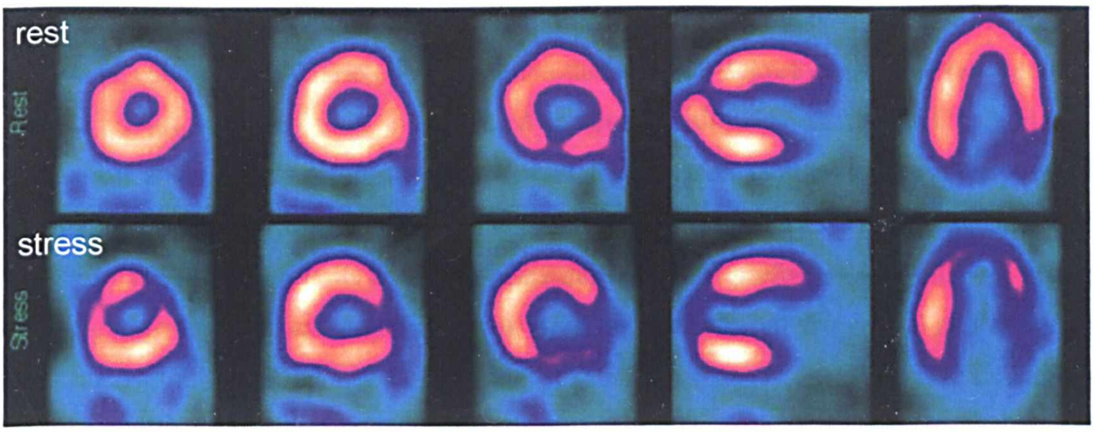

Figure 2-5 An example of a single photon emission computed tomography myocardial perfusion image. Three short axis and two long axis views are shown at rest above and corresponding images during stress below.

While the value of SPECT for the management of patients with CAD is well recognised, it is still limited by image artefacts [37,38]. One of the most common artefacts seen in SPECT is a consequence of the non-uniform reduction of photon activity caused by soft tissue motion. This attenuation artefact can cause apparent perfusion defects in the resulting images. False positive perfusion evaluations may result in further diagnostic studies, potentially increasing the risk to the patient, healthcare time and expenditure. Methods to circumvent this drawback include cardiac gated SPECT where end diastolic images have been found to display more ischaemic defects than standard summed images [39]. The problems with this method arise from the low count obtained from gated imaging, limiting the analysis of rest and stress perfusion in a single day ^{99m}Tc-sestamibi injection protocol, when performed over 2 days where high doses of radionuclide can be used for both rest and stress this problem can be significantly reduced. However, the time involved for the patient, carer and hospital department is not insignificant. Advances in camera instrumentation and software development, however, offer the potential to correct non-uniform photon attenuation. A method that involves the acquisition of transmission data and construction of an attenuation map to correct for non-uniform photon attenuation [40] was recently assessed with a large-scale clinical trial [41], and found to significantly improve the normalcy rate without a decline in overall sensitivity. However, this technique is not 100% reliable, the limited resolution and lack of temporal information (as SPECT is not a first pass technique) restrict the diagnostic capabilities.

2.2.2 Positron Emission Tomography (PET)

PET systems create images based on the principle of electronic collimation. Positrons (or positive electron antiparticles) emitted from these short-lived radionuclides interact with electrons within a few millimetres and are annihilated with conversion of mass into energy in the form of two photons. These photons are emitted at a 180-degree angle from one another. The electro-magnetic radiation is measured externally, allowing spatial and quantitative information about the location and quantity of the positron emitter to be obtained. The distribution of this positron emission can be measured as a function of time. The main strength of the technique is its ability to accurately quantify perfusion and other metabolic activities. However, the technique involves radiation hazards and the spatial and temporal resolution is limited. PET is currently the standard, and most accepted determinant of myocardial viability. Perfusion scans are combined with an assessment of the fuel substrate uptake. To this end, a tracer called Fluorodeoxyglucose (FDG) is commonly used, which allows an assessment of regional glucose metabolism. In non-viable necrotic myocardium, fuel substrate uptake is diminished along with myocardial perfusion. In viable tissue, although the perfusion is diminished the fuel substrate uptake is not diminished, sometimes being even enhanced, leading to "flow-metabolism" mismatch, which is easy to identify. Figure 2-6 shows an example PET myocardial perfusion image, which demonstrates viable myocardium identified by preserved glucose uptake.

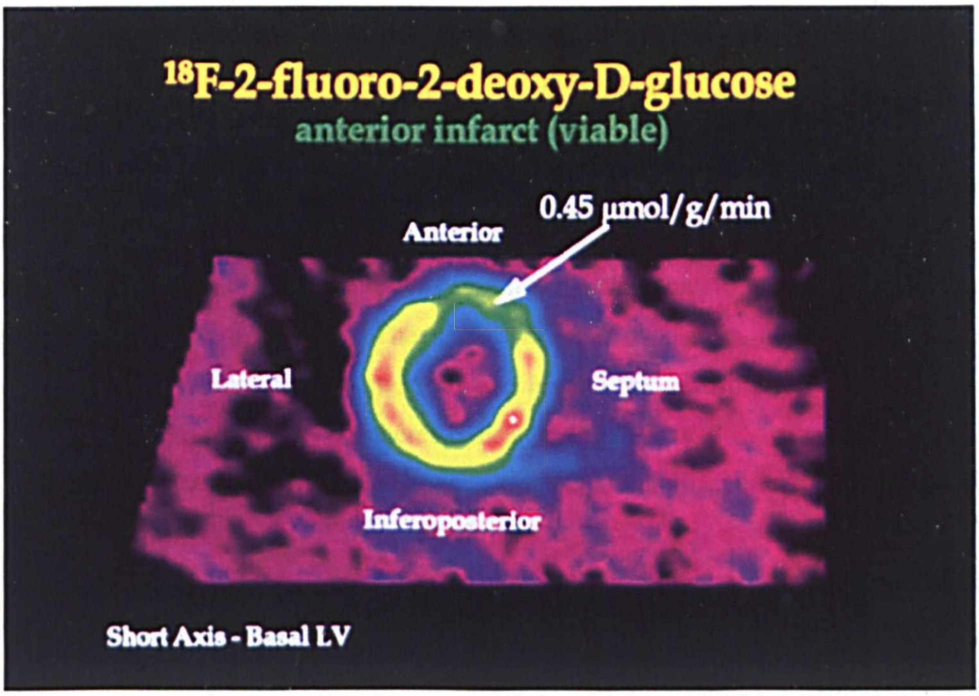

Figure 2-6 An example PET myocardial perfusion image showing viable myocardium identified by preserved glucose uptake (with permission from *Camici* [42]). The use of PET allows quantitative analysis of FDG uptake suggesting the viability of the tissue in question. A cut of point of 0.25 *µmol/g/min* is routinely used.

An assessment by Huang *et al* [1] looked at the *in vivo* quantitative measurement of MBF with ^{15}O water and positron computed tomography in comparison with quantitative *in vitro* microspheres, with results correlating well over the sample flow range. Bergman *et al* [43] subsequently extended this technique for completely non-invasive measurement of blood flow. This involved a parameter estimation procedure whereby the effects of limited tomographic spatial resolution and cardiac motion were compensated for within the operational flow model. The method was also validated with microspheres in dogs, and its success permits measurement of absolute MBF in humans with ^{15}O labelled water. A similar study using ^{15}O labelled water for the measurement of absolute blood flow addressed the issue of quantification in relation to the partial volume effect [44]. The partial volume effect is a phenomenon caused by a voxel representing the average of all signals emitted from its volume. With limited resolution this leads to a single voxel representing more than one tissue type, thus causing blurring at tissue boundaries. The technique was based on a new model involving the concept of tissue fraction, defined as the fraction of the tissue mass in the volume of the region of interest. The results were consistent with coronary angiographic findings. An alternative method of tracer administration for the quantification of MBF works through inhalation of ^{15}O labelled carbon dioxide [45]. This tracer has previously been used for labelling the blood pool in ^{15}O water scans.

The modelling of tracer kinetics can be carried out through the modification of a single tissue compartment model for the measurement of MBF [3]. For assessment in humans, it was found that models containing components for blood flow, fraction of water exchanging tissue and spill over arterial blood volume, provided the most accurate and reproducible results. A variety of different tracers are available. A direct comparison of ^{13}N ammonia and ^{15}O water as tracers for the quantification of MBF, with quantification of regional blood flow by microspheres was performed [2]. The study was carried out on dogs with appropriate compartment models and the correction for two *in vivo* tracers. Both tracers were found to show good correlation with microspheres over a wide range of flow values. The ^{15}O water values showed slightly better correlation with microspheres. Nitzsche *et al* [4] performed a similar study on humans in 1996, finding similar results from the two tracer agents in this study, although doubts arose over the seemingly similar heterogeneity of myocardial segments with the ^{15}O technique therefore putting weight behind the ^{13}N tracer. Iida *et al* [46] performed a comparison of ^{15}O water bolus injection with slow infusion and ^{15}O carbon dioxide slow inhalation for assessing MBF. The results concluded that the ^{15}O water bolus injection was able to provide the most accurate results for MBF and perfusable tissue fraction.

To generate myocardial images directly from the dynamic ^{15}O water scan, Hermansen *et al* [47] proposed a technique that does not need ^{15}O carbon monoxide blood pool scan, which is normally required for defining the region of interest. The new technique iteratively reconstructs the images by means of a linear dimensional reduction of the dynamic sinograms. No significant difference was found between the MBF values measured from regions of interest within the traditional method and that measured from the factor images. A comparison of administration protocols revealed the acceptability of the intravenous administration of ^{15}O labelled water as opposed to the more invasive arterial cannulation [48]. The development of a four-parameter protocol was required and the model proved effective in resolving issues related to the signal from the septum, both with fitting and the over estimation of the tissue fraction in the septum seen with ^{15}O carbon inhalation.

2.2.3 Echocardiography

Ultrasonography is a well-established imaging technique in cardiology, which makes use of high frequency sound waves rather than ionising radiation. An ultrasound transducer generates sound waves, which are propagated through the body tissue. The sound waves travel at varying speeds due to the different tissue types, and are reflected back by tissue interfaces. The transducer also has the ability to receive the echoes of the sound waves and it is these that are used to create the images.

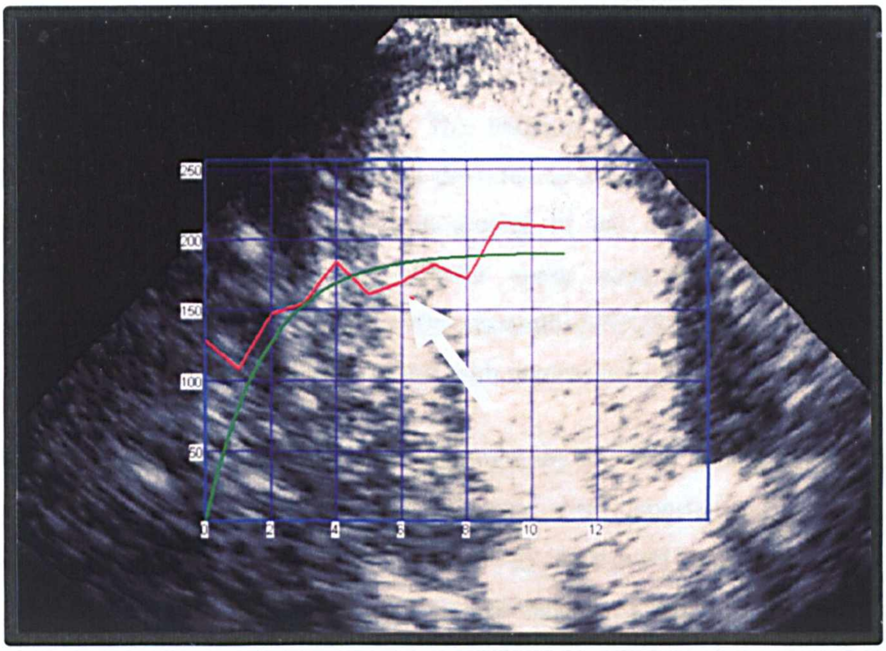

Figure 2-7 The graph shows the signal recovery curve of the septal region pointed to by the arrow, and the *x* and *y* axes represent time in *ms* since the annihilation of the myocardium and video intensity respectively.

The use of echocardiography for myocardial perfusion is relatively new. Kaul *et al* [49] performed a preliminary assessment of regional MBF with contrast two-dimensional echocardiography. Microbubbles were used as the contrast agent in dogs with artificial occlusions in the coronary arteries. The study indicates that the measurement of the transit time of microbubbles through the myocardium can accurately reflect regional MBF. Previous studies have also investigated myocardial perfusion immediately after thrombolysis to provide an indication of the recovery of left ventricular function in patients with anterior myocardial infarction [50]. Myocardial contrast echocardiography was performed before and immediately after reflow (when coronary blood supply to the myocardium is restored) with an intra-coronary injection of microbubbles. It has also been shown that angio-graphically successful reflow may not represent successful myocardial reperfusion in patients with acute myocardial infarction, whereas residual contrast defect in the risk area immediately after reflow are a predictor of poor functional recovery of the post-ischaemic myocardium. Subsequent animal studies have further investigated the characterisation of spatial patterns of flow within the re-perfused myocardium [51]. In patients, Ragosta *et al* have investigated the microvascular integrity as an indicator for myo-cellular viability with recent myocardial infarction [52]. This result was significant as it demonstrated a link between microvascular patency and myocardial cellular viability after acute myocardial infarction in humans. Meza *et al* have studied the effectiveness of combining dobutamine echocardiography and myocardial contrast echocardiography in differentiating post-ischaemic from infarcted myocardium [53]. To assess the accuracy of myocardial contrast echocardiography with the more widely used SPECT approach, Kaul *et al* [54] studied the relative merit of the method compared to Tc-99m sestamibi SPECT. The location and physiological relevance of abnormalities was found to be similar to that provided by SPECT, demonstrating the clinical potential of myocardial contrast echocardiography in the non-invasive assessment of myocardial perfusion in humans. A similar study compared myocardial contrast echocardiography with NC100100 and Tc-99m sestamibi SPECT for the detection of resting myocardial perfusion abnormalities in patients with myocardial infarction [55].

Recent studies in myocardial contrast echocardiography are now aiming to quantify MBF through the destruction of microbubbles administered with a constant rate venous infusion [56]. The microbubbles are destroyed by a high-energy ultrasound burst and their myocardial reappearance rate at steady state gives a measure of mean myocardial microbubble velocity. This combined with concentration measured at steady state will then give a measure of MBF. The texture and intensity of opacification of myocardial segments during myocardial contrast echocardiography have also been investigated [57]. The study was carried out on canine models and defects in opacification confirmed the presence of infarcted tissue. It is suggested that the texture of infarcted but also opacified myocardium may assist in the determination of segmental viability after reperfusion.

Recent advances in microbubble design and detection have made low power real-time intravenous myocardial contrast echocardiography feasible [5]. By using this technique, microbubble replenishment rate and peak intensity after bubble destruction by high-energy ultrasound have proven to provide reliable parameters of regional microcirculatory flow [58,59,60]. Before being used in routine clinical practice, larger studies must be performed to confirm these findings and further research is required to provide accurate quantitative values for MBF.

2.2.4 Computed Tomography (CT)

The use of Computer Tomography (CT) for myocardial perfusion imaging has become possible with the advent of Electron Beam CT (EBCT) in the early 80s. With electron beam CT, electromagnetic coils are used to focus the electron beam targeted towards stationary tungsten rings creating the X-rays. In this way, a series of temporal X-ray images with high-resolution in multiple planes can be produced. CT perfusion assessments have been validated both in human [61] and animals, and the results have shown good correlation at both rest and under adenosine vasodilatation. Although CT has been shown to underestimate absolute myocardial perfusion, and thus myocardial perfusion reserve at high blood flow rates [62-64], the method has shown promising clinical value. It allows quantitative analysis of perfusion states up to approximately 4 $mLmin^{-1}g^{-1}$ using central intravenous contrast administration [65].

Among the existing studies performed with EBCT, Rumberger *et al* [66] looked at normal and pharmacologically increased myocardial perfusion in the posterior papillary muscle in canine experiments. The study, however, did not investigate myocardial ischaemia but EBCT myocardial flow quantification. Martin Rodriguez-Porcel *et al* [67] recently used EBCT to study the effect of hypercholesterolemia on myocardial perfusion and permeability response to increased cardiac demand. They found that hypercholesterolemia is associated with blunted myocardial perfusion and increased vascular permeability. In another study, Da Silva *et al* [68] used conventional CT combined with SPECT in pigs to study absolute *in vivo* Tc-99m sestamibi uptake. In order to measure radionuclide uptake, they proposed a co-registered X-ray CT image technique that leads to more accurate results [69]. Budoff *et al* further compared exercise EBCT with stress Tc-99m sestamibi SPECT in a patient group and found regional wall motion assessed by EBCT to be as sensitive and more specific than SPECT myocardial perfusion imaging in identifying obstructive CAD [70]. With the increasing capability of CT imaging techniques, particularly ultra-fast volume CT, it is expected that the technique will make further impact to quantitative myocardial perfusion imaging.

2.2.5 Cardiovascular magnetic resonance imaging

As the main technique of choice for myocardial perfusion imaging, the limitations of the previously mentioned SPECT technique are well known. The technique has relatively poor resolution, and is associated with significant radiation burden and a prolonged visit in hospital for the patient (typically 4-6 hours). In recent years, myocardial perfusion CMR is emerging as a promising alternative due to its high spatial resolution. It enables for the first time, the definition of subendocardial perfusion defects [71], which occur much earlier in the course of development of CAD, or associated with functional microvascular disorders such as Syndrome-X [72]. Myocardial perfusion CMR involves no radiation burden and is ideally suited to repeated studies and research. Magnetic Resonance Imaging (MRI) is based on the principle of nuclear magnetic resonance, a technique of spectroscopy used to find microscopic properties of molecules. The nuclear part of the name is dropped in clinical settings as it leads to confusion with the harmful radioactive isotopes used in nuclear medicine. The potential for MRI arises from the presence of nuclei possessing spin within the region of interest. Spin refers to the way in which the protons of certain atoms orbit around the nuclei. This creates a small magnetic field around the nucleus of the atom. The primary nucleus possessing spin used in MRI is the Hydrogen nucleus or proton, which is found in abundance in the human body (approximately 63% of human body) particularly in water and fat. The first successful demonstrations of nuclear spin were by two separate groups led by Felix Block at Stanford University and Edward Purcell at Harvard in 1946. Paul Lauterbur obtained the first 2D MR image in 1973, which subsequently earned him the Noble Prize in 2003.

A bulk of water contains a large quantity of atoms, and the resulting net magnetisation is zero. However, when the object is placed within a magnetic field, a non-zero magnetization (net magnetisation) will occur with the same direction as the external magnetic field. In this case, when an RF (radio frequency) pulse with the resonant frequency of the nuclei, known as the Larmor frequency, is applied, the spins will be excited and tipped to a certain angle according to the power of the RF pulse. A 90° RF pulse will tip the spins into a transverse plane with respect to the longitudinal direction of the external magnetic field. When the pulse is switched off, the spins begin to relax, dissipating the absorbed energy and recovering to the initial equilibrium state. There are two kinds of relaxation. The first one is the spin-lattice relaxation, or longitudinal relaxation. The relaxation is exponential with a time constant T1, the time it takes for the longitudinal magnetisation to recover to 63% of its equilibrium value after it has been exposed to a 90° pulse. T1 relaxation results in the recovery of longitudinal magnetisation due to energy dissipation within the surrounding lattice. The second relaxation is called spin-spin relaxation, or transverse relaxation, which is again exponential and characterized by the time constant T2. T2 relaxation is caused by the de-phasing of all spins that were previously coherent (in phase) when excited by a RF pulse, due to interactions between the magnetic fields of adjacent nuclei. T1 and T2 independently depend upon several parameters. For example, while the strength of the external magnetic field influences both T1 and T2, the influence on T2 is less crucial than for T1. Experiments show that in a solid, T2 is significantly shorter than T1. In mobile fluids however, T1 and T2 are nearly equal. The difference between T1 and T2 within different materials and environments is the very foundation for MRI to distinguish between different kinds of material in human body. That is, by detecting the signal re-emitted by the system under investigation, relaxation times T1 and T2 can be measured. Alternatively, imaging sequence parameters can be adjusted to produce so-called T1-weighted or T2-weighted images.

The assessment of myocardial perfusion using CMR has been based on first pass techniques using fast gradient echo (turboFLASH) [7,73-75] or EPI sequences [12,76,77]. Quantitative results have been achieved in animal studies with an intravascular agent (polylysine-Gd-DTPA) [13] as a macromolecular blood pool marker. At the same time, semi-quantitative results have also been established in humans with a conventional extra cellular agent (Gd-DTPA) [78,79]. Either approach will have an impact on the detailed characterisation of the relationship between functional and perfusion abnormalities.

For myocardial perfusion CMR, a contrast agent is required so that its arrival, up-slope, and washout may be studied. While this has to be injected into the patient, the tracer is inert and is far less hazardous than the radioactive isotopes required in nuclear medicine. For the analysis of perfusion images there are a number of different indices that must be obtained from the data. This allows the data to be studied in more depth than is permitted through visual analysis alone. Signal time curves are obtained based on the localised intensity of the myocardium within the image. The time to peak intensity for the myocardium supplied by the diseased vessel is longer relative to the normally perfused myocardium. Additionally, the peak intensity is lower and the curve is shallower than that for the normal tissue.

2.3 Myocardial Perfusion CMR

2.3.1 First pass myocardial perfusion imaging, Gd-DTPA late enhancement, and BOLD

A variety of techniques exist for the detection of CAD, many of these involve *in vivo* imaging of the cardiovascular system. The obvious approach is to image the coronary artery directly for the detection of narrowing or occlusion. This, however, is a difficult task due to the small dimension of the coronary vessels and its tortuous path, coupled with complex cardiac and respiratory induced motion. An alternative approach is to detect the defects in myocardial perfusion resulting from coronary blockage. First pass MR perfusion imaging is a non-invasive method, which follows the passage of a bolus of contrast agent from the superior vena cava, to the right heart, through the lungs and to the left heart. The bolus is injected directly into a peripheral vein and a sequence of images is obtained to show the dynamic passage of the tracer as shown by a series of images in Figure 2-8.

For quantitative perfusion analysis, Wilke *et al.* investigated the correlation between MBF in dogs at rest and during hyperaemia using myocardial perfusion CMR with radiolabelled microspheres as a reference [7]. CMR was performed using a Turbo FLASH sequence with a 180-degree inversion pre-pulse, and a Gd-DTPA bolus injected into the left atrium with images acquired every heartbeat. This study demonstrates that different transmural and regional myocardial perfusion levels may be quantified from the signal intensity time curves. It was found that the detection of myocardial hypo-perfusion improved significantly after the administration of dipyridamole as a means of inducing stress. The study also revealed the correlation between the mean transit time calculated from the signal intensity time curve, and the absolute MBF derived from the microsphere data [73]. Quantitative perfusion analysis was demonstrated with intravascular relaxation agents and heavily T1-weighted ultra fast gradient echo sequences. In parallel to Wilke's work, Larsson *et al* studied an alternative quantification procedure [78]. This involved the study of Gd-DTPA diffusion across the capillary membrane in the human myocardium. A turbo-FLASH sequence was used for imaging the passage of the contrast agent, the results being comparable to those obtained with PET and invasive animal studies. This work also presented a method of obtaining an input function non-invasively.

The mid nineties saw the start of attempts at quantifying MBF from myocardial perfusion CMR. Semi-quantitative analysis on first pass images was assessed with mean transit times derived from intravenous catheter bolus injection and signal time curves [13,75,74]. As with previous studies, the analysis of the signal time curves involved the use of compartment modelling, which is a further developed spatially distributed model. Larsson also extended his initial modelling to take into account the fast and slow water exchange between compartments, enabling further parameters of cardiac perfusion to be obtained [14].

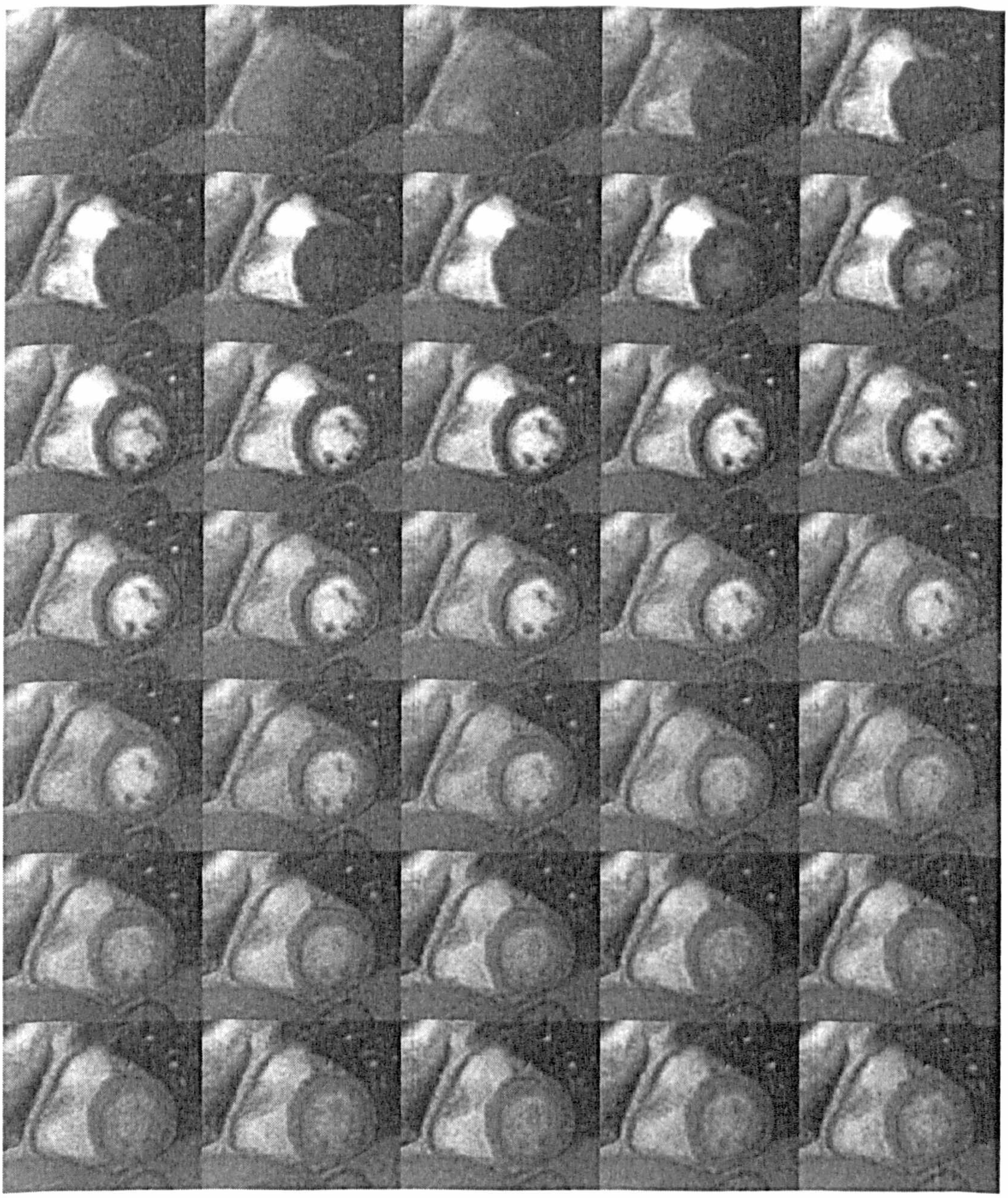

Figure 2-8 An image series a typical first pass CMR perfusion study showing the transit of contrast bolus. From the top left going across, initially the nulled signal before the contrast agent (Gd-DTPA) enters the RV, followed by the contrast agent exiting the RV and entering the LV. The last few rows show the contrast agent exiting the LV and entering the myocardium of the LV. The observed enhancement within the myocardium is small and minor defects are often difficult to observe by eye.

In terms of imaging sequence design, extensive research has also been conducted to investigate alternative CMR imaging sequences for MR perfusion studies, particularly the use of echo-planar imaging for improved spatial coverage. Schwitter *et al.* assessed normal myocardial perfusion with ECG gated multi-shot echo planar imaging as opposed to the more traditional T1-weighted fast gradient-echo imaging [12]. Between five and seven slices were obtained for every two heartbeats with promising results. Beache *et al.* looked at imaging perfusion defects with susceptibility-enhanced T2-weighted echo-planar imaging [76]. An investigational T2/T2* contrast agent (Dysprosium-DTPA bis (methylamide)) was used showing the potential for characterisation of myocardial perfusion defect. A further study looked at the use of interleaved gradient echo echo-planar imaging [77]. This allowed for improved cardiac coverage while maintaining the acquisition characteristics required for performing a quantitative first-pass perfusion study.

In myocardial perfusion imaging, the contrast agents can be classified into two types: susceptibility agents and relaxation agents. Dysprosium-DTPA-BMA is a typical susceptibility agent. It acts like a super-paramagnetic particle, inducing large fluctuations of magnetization between blood and intracellular compartments. As a result, spins will de-phase quickly, *i.e.*, the T2 and T2* decay time can be reduced. Thus, T2-weighted contrast enhanced MR images may be obtained. Gadolinium-diethylenetriamine pentaacetic acid (Gd-DTPA) is the most common relaxation agent currently available for clinical use. Its paramagnetic property disturbs the relaxation of the surrounding water protons, resulting in both T1 and T2 shortening effects, but particularly in T1 relaxation time. Thus, T1-weighted contrast enhanced MR images may be obtained.

For the T1-weighted technique for myocardial perfusion imaging, a short axis slice of the LV shows the perfusion of a ring of the myocardium. A single sequence gives the passage of the bolus from the RV, to the blood pool of the LV, and finally to the myocardium of the LV. Up to three or four separate slices may be simultaneously obtained to achieve a greater coverage of the myocardium after a single injection. The first pass of a bolus through the coronary artery to regions of the myocardium show significantly decreased signal intensity in hypo-perfused regions [80] compared with normally perfused regions. This differing myocardial enhancement is often visible when looking at the series of MR images. However, intensity differences rapidly decrease as the MR-contrast media reaches all the interstitial spaces. Therefore, only the first pass is of interest for directly assessing the perfusion characteristics of the myocardium.

While first pass imaging is commonly used in myocardial perfusion assessment, recently alternative techniques have been developed. Instead of administering a perfusion contrast agent, the Blood Oxygen Level Dependent (BOLD) effect can be used as a surrogate for evaluating coronary flow. This is because deoxyhaemoglobin is paramagnetic, as opposed to oxyhaemoglobin, which is diamagnetic. The presence of deoxyhaemoglobin causes spin de-phasing within a voxel, which effectively shortens T2 or T2* and thus reduces the signal from T1 or T2* weighted sequences. An example of BOLD imaging at 3T is shown in

Figure 2-9. The effect has the potential to allow investigation of myocardial perfusion reserve because changes in blood flow result in changes in the venous blood oxygen levels. Previous studies have demonstrated an increased T2* and T2 weighted signal with increased blood flow owing to a reduced deoxyhaemoglobin level [81-89]. The quantitative signal change is very small and difficult to distinguish from motion and other artefacts, for this reason the majority work has been carried out with a high field strength to enhance the BOLD effect [81-83,88,89]. Additionally, much of the work has concentrated on global changes in order to average out the artefactual changes [81,82,84-89]. The potential of this completely non-invasive method will depend on the development of techniques with reduced artefacts to allow observation of regional differences in blood flow at commonly used field strengths [90].

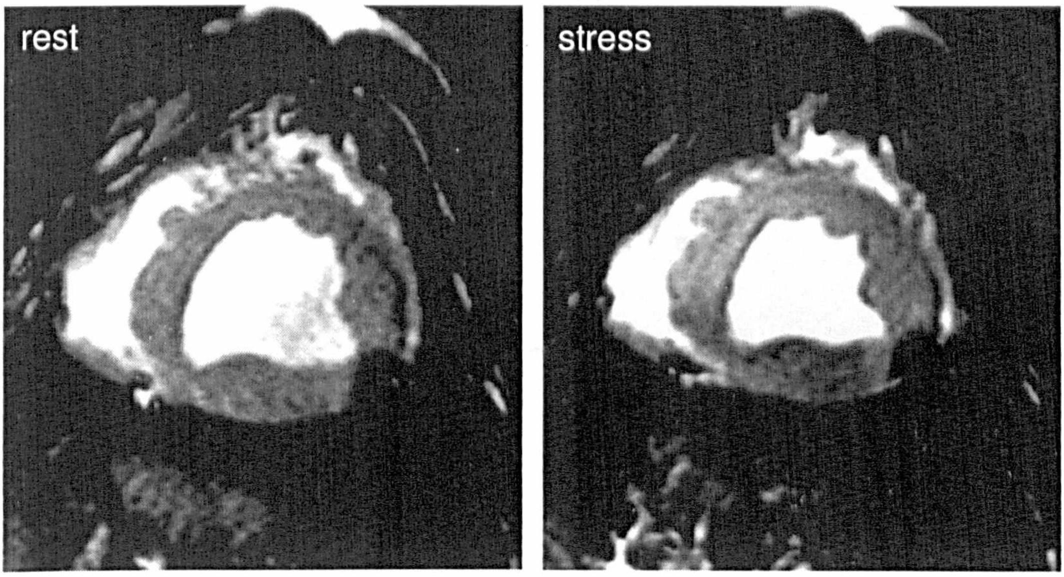

Figure 2-9 BOLD imaging at 3T. Courtesy Shea S, D. Li. Northwestern University.

Another important development in cardiac MR, which is very much a by-product of first pass myocardial perfusion imaging, is late enhancement Gd-DTPA imaging. The technique has been found to be particularly useful in distinguishing infarcted regions within the myocardium. With this technique, the images of the heart are taken approximately 20 minutes after the contrast agent has been injected into the bloodstream. During this period, the contrast agent is typically washed out of the healthy myocardium by the circulation of blood. The agent is also largely filtered out of the bloodstream within this time in a natural process passing through the kidneys. From the acquired images, the infarcted (scarred) regions may be distinguished by their delayed but sustained enhancement relative to the healthy myocardium. This is due to the contrast agent being unable to wash out of the scarred myocardium. This method is of great use in assessing the viability of myocardium post infarction and has shown good correlation concerning location and extent of infarcts with PET findings [91].

An example patient data set is shown in Figure 2-10, where a large transmural hyper-enhanced anterior infarct is seen. The ability of this method to assist in assessment of CAD makes the first pass imaging even more valuable. In addition to the benefits of first pass imaging, the potential for combining late enhancement along with regional wall analysis provides the promise of combining assessment of myocardial viability into a single patient examination.

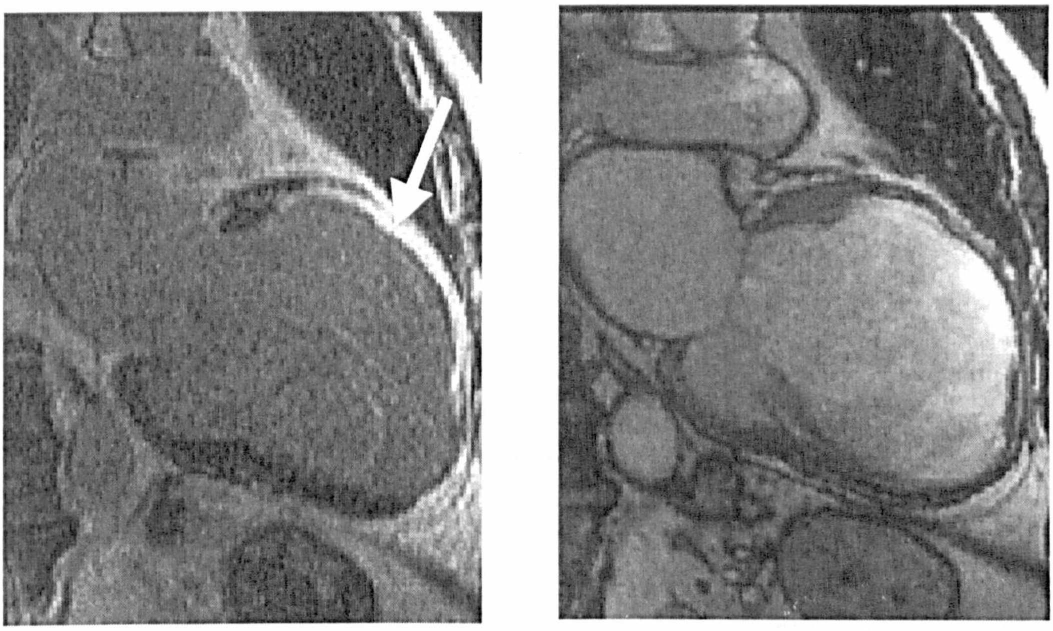

Figure 2-10 Long axis view of the LV showing the late enhancement associated with the transmural infarction. On the right an image from a TrueFISP (Fast Imaging with Steady-State Precession described in section 2.3.2) cine series for assessing morpho-dynamics of the LV.

2.3.2 Imaging sequence design

The ability for accurate quantification of myocardial perfusion with CMR is closely coupled with the imaging sequence design. For myocardial perfusion analysis, the optimisation of image acquisition speed to provide adequate temporal resolution is critical [92]. There are a number of reasons for this. First, the contrast agent has a relatively short period of time passing through the myocardium (20-60 seconds). During this time a temporal sequence of the entire region of interest must be obtained at a sufficient temporal resolution so that the reconstructed images can accurately depict the change in contrast agent concentration over time. Second, for a complete depiction of myocardial perfusion distribution, slices covering the entire 3D volume of the heart are required for each cardiac cycle. Although it is possible to acquire the perfusion images during diastole when the cardiac motion is minimal, the acquisition window within each cardiac cycle need to be made as small as possible, typically around 200-300 *ms* to avoid motion artefact and mis-registration. Thus far, a number of different image acquisition sequences have been used both in routine clinical practice and in research studies. In the following section, we will summarise some of the common sequences that have been used.

Fast Low-Angle Shot (FLASH)

Fast Low-Angle Shot (FLASH) imaging is a well-established technique first developed in 1986 by Frahm, Haase and colleagues [93,94]. The technique uses excitation pulses with small flip angles to reduce the TR, thus allowing images to be acquired significantly faster. In MR imaging, the signal is based on the recovery of magnetization to its equilibrium state. When the recovery time is excessive, the time taken to produce sufficient signal is correspondingly long in order to allow the magnetization to fully recover to equilibrium. In cardiac imaging, however, short acquisition time is crucial because of the dynamic nature of the heart. One way to shorten the acquisition time is to reduce the recovery time and in FLASH imaging, this can effectively be achieved by tipping the magnetization with an angle α less than 90°, so that its longitudinal magnetization component will not require as much recovery to an equilibrium state, although this will reduce the signal since it is proportional to $\text{Sin}(\alpha)$.

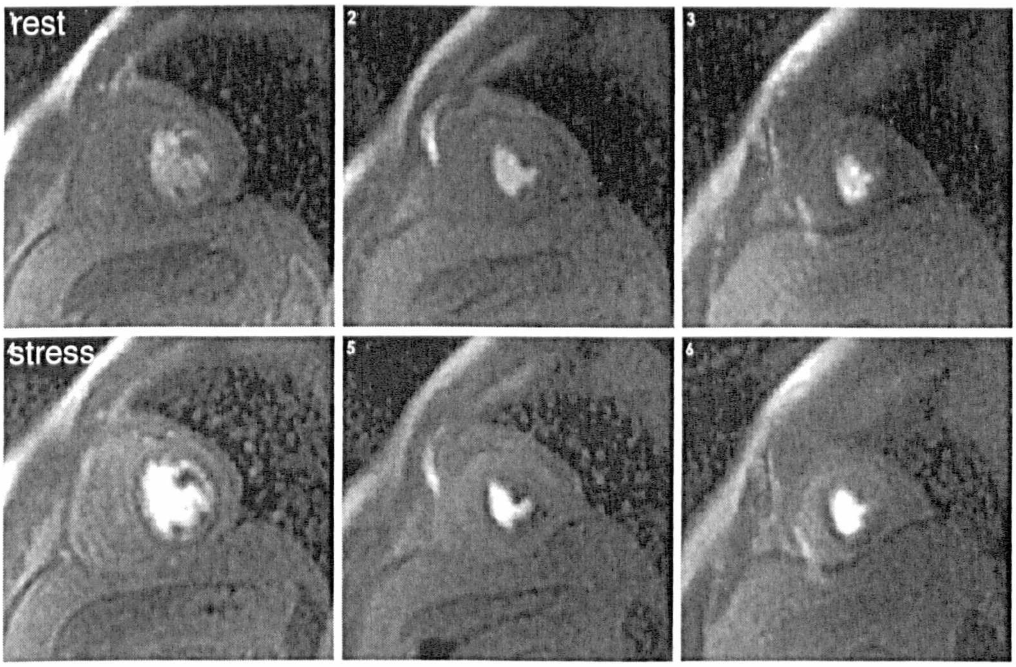

Figure 2-11 An example sequence of FLASH myocardial perfusion images.

The FLASH sequence uses a de-phasing gradient followed by a frequency encoding or read-out gradient, which is turned on during signal acquisition. During the application of this gradient waveform, the signal is re-phased to produce an echo known as the gradient echo.

Echo Planar Imaging (EPI)

EPI is a fast imaging technique capable of obtaining the whole of *k*-space within one TR (Time to Repetition, the time between two consecutive RF pulses measured in milliseconds) cycle with single RF excitation. Peter Mansfield, also a Nobel Laureate in 2003, first proposed this method in 1977, using a single excitation pulse followed by the rapid switching of a strong gradient to generate a train of gradient echoes. This echo series was encoded with different phases, from which an image could be reconstructed. With EPI, the sampling period is normally reduced and the bandwidth correspondingly increased, allowing a complete low-resolution image to be acquired within 50-80 *ms*. In general, EPI has reduced SNR because of the bandwidth. Another disadvantage of EPI is the rapid switching of large gradients, which can generate potentials and electric currents in the body that can introduce nerve stimulation. Safety guidelines have been established to avoid this problem although the heart is particularly safe as its stimulation thresholds are greater than elsewhere in the body. Unlike the line-by-line filling of *k*-space with conventional methods, with EPI the *k*-space is filled cycling backwards and forwards in the frequency encoding direction. EPI images are commonly associated with geometrical distortion and large susceptibility artefact due to the way that the images are acquired.

A variation of single shot EPI is called interleaved or hybrid EPI first developed around 1992 [77,95-99], which collects data in multiple passes through the *k*-space. For example, two shot interleaved EPI effectively collects every other line in the first pass, and then collects the remaining lines in the second pass. This method is a good compromise between the gradient echo and single shot EPI methods. It permits the optimisation of the imaging sequence for a given imaging period, normally used to produce better temporal and spatial resolution than FLASH, and with reduced imaging artefacts over single shot EPI. For the purposes of 3D myocardial perfusion imaging, multiple slices are required for full coverage of the myocardium. In this case, multi-slice interleaved EPI may be used. In the case of two shot EPI, every other line of *k*-space is filled for each slice on the first shot, followed by the remaining lines being filled on the second shot. Schwitter *et al* [12] used an ECG-gated multi-shot echo-planar imaging sequence, together with the use of intrinsic T_1 weighting produced by a repetition time equal to the cardiac cycle for myocardial perfusion imaging. They reached a homogeneous enhancement throughout the LV myocardium, with improvement of approximately 50% for the optimum contrast dose of 0.05 *mmol/kg* Gd-

DTPA. They subsequently [100] applied a multi-slice hybrid echo-planar pulse sequence [77] to a total of 48 patients and healthy subjects. Results were analysed by signal intensity up-slope for 32 regions within each heart and compared with those obtained from PET (sensitivity and specificity of 91% and 94%, respectively) and coronary angiography (sensitivity and specificity of 87% and 85%, respectively).

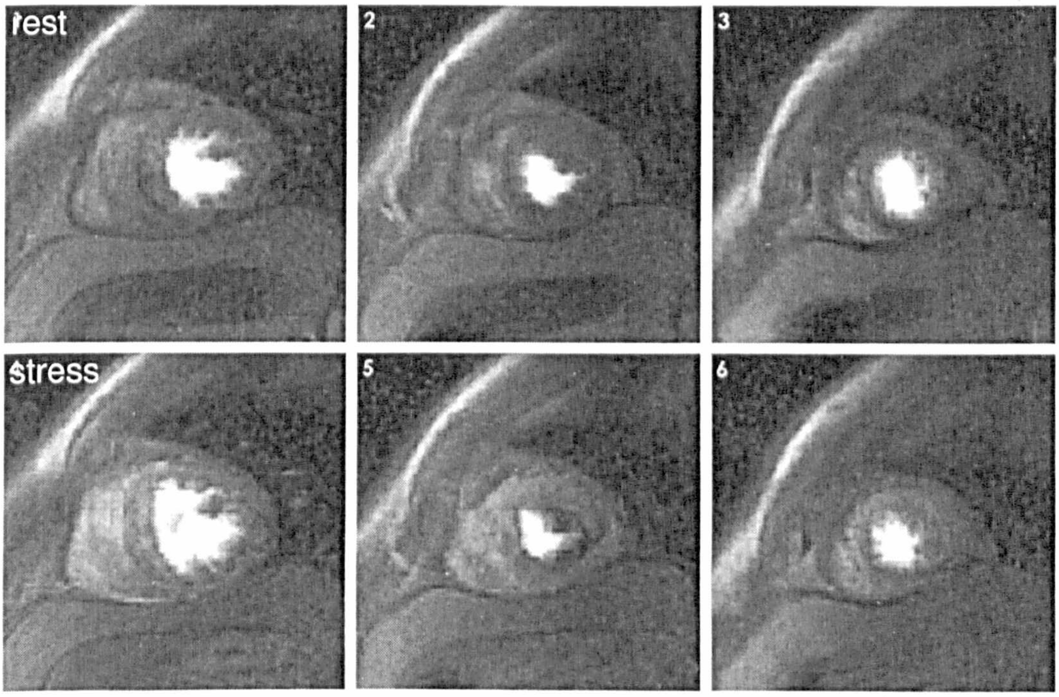

Figure 2-12 An example sequence of Hybrid EPI myocardial perfusion images.

TrueFISP (Fast Imaging with Steady-State Precession)

True Fast Imaging with Steady-State Precession (FISP) is another gradient echo pulse sequence with which TR is normally much shorter than the T1 and T2 relaxation times of the tissue. Therefore, there is little time for the magnetization to decay before the next RF pulse is switched on. This results in two signals, one is the free induction decay, and the other is the steady state signal made up of the residual transverse magnetization component. Steady state sequences can be classified as coherent, incoherent and SSFP (Steady State Free Precession) pulse sequences, according to whether they use one or both of these signals. Following the development of high performance scanners over the last few years, the majority of MRI scanner manufacturers have implemented this technique in various forms. GE have named it FIESTA and Philips named it balanced FFE, dubbed from Fast Field Echo. In Japan, Hitachi called it GFEC (Gradient Field Echo with Contrast) and Shimadzu called it SSFP, the name originally given to the rapid repetition steady state sequences during the early development of MRI. Siemens used the name TrueFISP, as the sequence is a variation on the FISP sequence originally described by Oppelt [101] in 1986. TrueFISP enables the use of high RF flip angles to achieve high SNR and good T2 or T2* contrast. This produces high contrast between myocardium and blood in the intra-ventricular cavity, which is crucial for accurately assessing ventricular function.

Steady state sequences using balanced gradients have recently been introduced into routine clinical imaging [102] with benefits in both imaging time and quality. T1 weighted images suitable for myocardial perfusion imaging can be obtained with saturation prepared TrueFISP [10], and when compared with a saturation prepared TurboFLASH sequence, the method has shown improved image quality and a higher spatial resolution. In addition, the sequence preserves the linear relationship between contrast agent concentration and signal intensity, a requirement of quantitative perfusion analysis. However, there are still concerns with this imaging sequence because of the susceptibility artefacts. The successful elimination of these may be possible with the advances in hardware and further research in this area.

2.4 Conclusion

The diagnosis of CAD is possibly the most important area of current medical research throughout the developed world. First pass perfusion analysis provides a promising method for diagnosing the effects on myocardial perfusion directly relating to reductions in blood flow due to CAD. While different imaging modalities are currently in clinical use and the subject of further research, MR perfusion imaging is emerging as a promising technique for high-resolution dynamic contrast imaging which has the potential to distinguish sub endocardial perfusion defects. Compared to other parallel techniques, MR myocardial perfusion imaging is less harmful than X-ray angiography and more sensitive than SPECT and echocardiography. Further development in CMR will allow the possibility of combining complete cardiac studies including perfusion, morpho-dynamics, contractility, and viability into single imaging sessions. Clinically, a variety of MR imaging sequences are in current use, with significant compromises made between SNR, myocardial coverage and sensitivity to motion. Limitations of clinical hardware and patient nerve stimulation make further increases in data acquisition speed troublesome. This makes the efficient use of the information content of the acquired data crucial to dynamic studies such as first pass myocardial perfusion.

Chapter 3 : Exploiting the Information Content of *k*-space Data

3.1 Introduction

In Chapter 2 we have outlined the basic clinical background of myocardial perfusion and the relative merit of different imaging approaches. The prerequisite of detailed quantitative analysis of regional perfusion characteristics is a comprehensive coverage of the myocardium. In order to track the transit of the contrast bolus, it is required that the entire volume of interest is imaged within each cardiac cycle, preferably during a short acquisition window of 200-300 *ms*. Compromises are generally made favouring SNR over myocardial coverage, or spatial resolution over temporal resolution. Despite the use of rapid imaging sequences such as hybrid-EPI with the state-of-the-art MR hardware as described in Chapter 2, it remains difficult in practice to achieve the simultaneous improvement in spatio-temporal resolution required. With many of the faster imaging sequences already approaching established limits of neuromuscular stimulation and RF heating, further improvements in perfusion imaging will rely on alternatives such as parallel imaging [103] or making full use of the information content of the *k*-space data. In this chapter, we will look at the information content of *k*-space and describe ways of exploiting the redundancies carried within to speed up the data acquisition process.

3.2 *k*-space data acquisition

Frequency analysis of measured MR signals permit the localisation of magnetic spins within a magnetic field varying linearly across an object. Acquiring such data in two dimensions, however, is not possible due to the intrinsically one-dimensional signal acquired from the combined magnetic field gradients. For image acquisition in higher dimensions, the magnetic field gradient is varied through time so that data can be acquired in a variety of trajectories to complete the required *k*-space. For MR, *k*-space is a two-dimensional frequency domain that is related to image space through 2D Fourier transform. In MR imaging, data is acquired in raw *k*-space commonly one line at a time, where each line is traversed by frequency encoding. This can be performed very quickly, and in rectilinear sampling we move from one line to the next by the use of phase encoding. In practice, the *k*-space can be sampled in a number of different ways. Figure 3-1 provides several examples used by common MR imaging techniques including Cartesian, radial, spiral and EPI. From an information point of view, the centre of *k*-space represents low frequency components, which in image space corresponds to background contrast levels and slow spatially varying signal. Moving out towards the edge of *k*-space, the higher frequencies capture edge details of the objects. With sufficient encoding, *k*-space can accurately represent all of the information in image space to single pixel resolution. The size and spacing of points within *k*-space determines the resolution and FOV of the represented image. In MR, *k*-space is a complex 2-D array that is representative of the individual waveforms that can be combined to form an image. The location of a point within *k*-space determines the scalar frequency in the two dimensions, and thus the combined vector frequency (or more correctly wave number, which is equal to the number of complete wave cycles that exist in one metre of linear space). The magnitude of a point in *k*-space determines the amplitude of the wave described, and the phase determines the phase of the waveform within the image. To an extent, every single point in *k*-space contributes to the whole of the corresponding image. Depending on the imaging task and acquisition procedure, the relative significance of different points within *k*-space to the final image can vary widely.

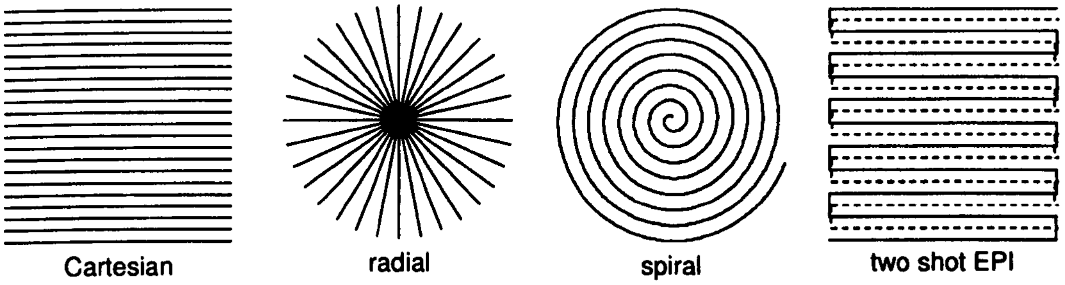

Figure 3-1 *k*-space filling strategies.

3.3 Prior information driven reduced *k*-space encoding

The use of prior information in the acquisition strategy can exploit the redundancy of *k*-space values in representing the image, or series of images. This is of particularly importance where the further development of fast image acquisition is limited by hardware constraints. For dynamic imaging, a variety of methods have been developed, which either exploit correlations in *k*-space (partial Fourier, reduced FOV, parallel and prior information driven *e.g.* BLAST), in time (keyhole, view sharing and UNFOLD) or in both *k*-space and time (cardiac UNFOLD, *k-t* BLAST) also known as *k-t* space. The term *k-t* space refers to the higher dimension *k*-space through time axes as described by Xiang and Henkel [104], where x and f are the conjugate axes of k and t after inverse Fourier transformation. For dynamic studies where improvements in the image resolution are desired, it is generally preferable that the reduction in *k*-space acquisition should be the same for each cardiac phase. This allows consistent spatial coverage as well as maintaining the temporal resolution of the imaging sequence. An exception to this is where the reference static images are acquired either prior or subsequent to the main dynamic imaging scan. Simple partial Fourier reconstruction algorithms [105] such as half *k*-space sampling, makes uses of the conjugate symmetry of *k*-space that equates to a 180° rotation of each point in *k*-space, theoretically resulting in the same reconstructed image, although the reuse of noise contamination results in a decrease of SNR by a factor of $\sqrt{2}$. In practice, however, *k*-space data replacement or interpolation is more commonly used for dynamic imaging.

3.3.1 Keyhole imaging

Keyhole imaging is a straightforward example of data sharing for dynamic imaging. As mentioned before, the central low frequency *k*-space information generally determines the contrast and low frequency details of the image, which in dynamic imaging typically represents regional intensity variations. Keyhole imaging therefore makes use of a high-resolution static reference image to supplement the low-resolution dynamic *k*-space information by only updating the central portion of the *k*-space for each time frame [106,107]. While the method provides visually similar results as to full *k*-space coverage, the amount of *k*-space that may be substituted needs careful consideration. Early studies provided three to five fold speed increases, but the result was dependent on the size of the Region Of Interest (ROI) being studied. With keyhole imaging, data inconsistencies can be expected between the extrapolated data and the measured data. These include amplitude discontinuities and phase incoherence that can give rise to Gibbs artefact and blurring. In a study of quantitative dynamic contrast imaging results indicated that the minimum keyhole size used should be restricted by the approximate minimum size of the expected lesions. This restriction applies even with the use of reconstruction algorithms that offer improved image resolution [108]

By following the similar principal of *k*-space data replacement, a more elegant solution to dynamic imaging with static reference scans is RIGR [109]. The method attempts to minimise the total number of spatial encodings required for acquiring the dynamic image data sets. The suitability of the method to the imaging task as with keyhole imaging is based on the assumption that during the acquisition of dynamic image data, the high-resolution data remains static. The high-resolution static image is built into a set of basis functions of generalised series constrained to the low-resolution dynamic images. The high-resolution dynamic images can then be reconstructed with relatively few extra phase encoding steps. The RIGR method alleviates some of the problems associated with keyhole imaging through the use of the generalised series reconstruction. Figure 3-2 demonstrates an image frame from a dynamic sequence as reconstructed by the keyhole and RIGR methods respectively. It is evident that the Gibbs artefact and blurring have been reduced significantly by RIGR. With the MR community, the RIGR method has been compared rigorously with other parallel techniques, including the Singular Value Decomposition (SVD) method [110] which in a similar manner acquires a high-resolution reference image followed by reduced encodings for the dynamic data. With SVD, the method uses spatially selective RF pulses allowing the acquisition of SVD encoded dynamic data. Remaining points within the *k*-space are then either zero filled [110] or substituted with values from the reference data [111]. The SVD method is found to optimise the data acquisition for the reference image but copes poorly with new dynamic image features, which renders the technique unsuitable for myocardial perfusion studies.

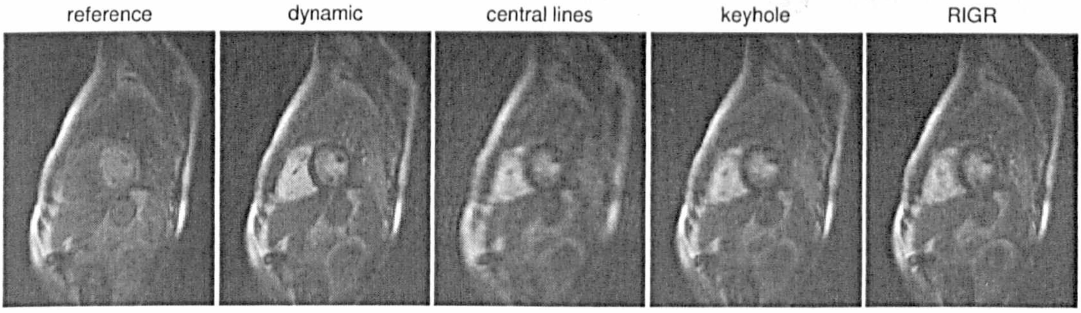

Figure 3-2 The reference and dynamic images from a dynamic image series, and the corresponding dynamic information captured by the central lines in *k*-space. The dynamic image is also shown reconstructed with only ¼ of the available information, by using the keyhole technique RIGR, respectively.

3.3.2 Block Regional Interpolation Scheme for *K*-space (BRISK)

BRISK is a technique that exploits inter-frame correlations to realise acquisition time reductions [112]. The technique is particularly suited for cardiac imaging and exploits *a priori* information of the imaging system to construct a prospective sparse sampling scheme. The theory behind the technique can be explained by analysing *k*-space maps derived from the inverse Fourier transform of the modulus images. The 1D Fourier transform for each pixel of a sequence of these Fourier images produces a number of Fourier coefficients for each pixel dependent on the number of images in the sequence. Through this, a set of *k*-space Fourier coefficient images can be created. From the first *k*-space map representing DC information, or *k*-space information which remains the same through the sequence of images, to the later maps representing the information which varies rapidly through the sequence of *k*-space images, it was found that the most significant data contracted towards the centre of the *k*-space map. This is not surprising as it conforms to the previous observation used by keyhole and RIGR. However, the extent to which this contraction of the energy to the centre of the *k*-space maps in the higher coefficients is dependent on the relative change between images within the sequence. A sequence of images where each frame is independent of one another would result in no contraction between frames, and conversely if there were no change between frames then only the first coefficient map would contain image information.

Figure 3-3 shows an example BRISK sampling scheme with a 2/3rd reduction in sampled *k*-space points. While the central blocks are sampled for every image acquisition, the outer blocks are sampled less frequently so as only 4 of the total 12 *k*-space blocks are acquired for each image acquisition. Comparing this with the Fourier coefficients mentioned earlier, the entire of *k*-space is sampled at least once during the total sequence, which is suitable for the zeroth coefficient. For the 2nd coefficient for instance which requires at least 4 samples based on the Nyquist theorem, the central 6 blocks are sampled, so 50% of *k*-space. Fourier interpolation between frames is used to fill in the missing *k*-space information. This sampling scheme allows for a reduction in acquisition time or corresponding increase in image resolution. The technique has been demonstrated on both simulation and real data, with 25% and 50% reductions in *k*-space acquisition [112]. The 25% scan showed some ringing artefact on the simulation scan around the aortic vessel but the myocardial borders were well represented, while on the real data some ringing artefact is apparent originating from the myocardial borders. This is because images measured with a limited number of Fourier harmonics are imperfect. This can cause high-frequency oscillations at the edges, and the reconstructed image can exhibit some noticeable spatial intensity variations at object boundaries. In the case shown in Figure 3-3 the artefact is also due to uncompensated respiratory motion making the high frequency information unsuitable for the dynamic data. When 50% BRISK coverage was used, however, it was sufficient to represent all the relevant image information.

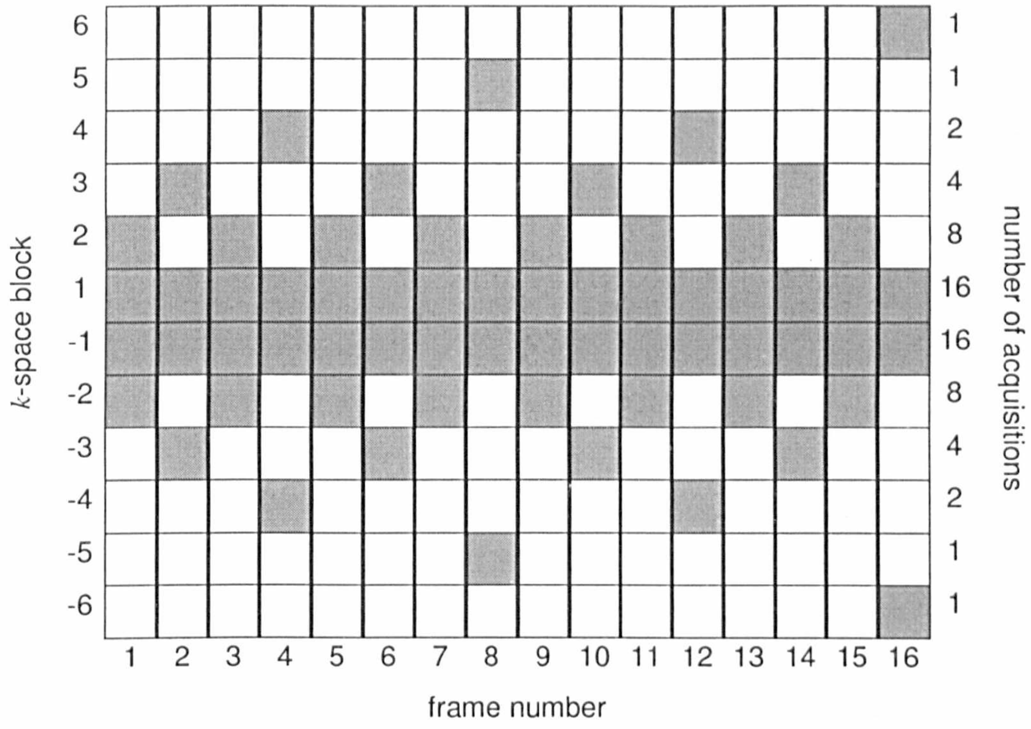

Figure 3-3 A 1/3rd BRISK sampling scheme for 16 cardiac phases. Each of the 12 *k*-space sections represents a block of *k*-space (*e.g.* 10 lines for a 120^2 matrix) with grey shading showing sampling for a particular image acquisition. On the left the block number is shown, on the right the number of times each block is sampled and below the frame number.

3.3.3 Temporal filtering methods for reduced FOV imaging

UNFOLD [113] is an imaging technique that uses temporal redundancies to reduce the required data acquisition in dynamic MRI. During the acquisition stage, a reduction in the dynamic FOV corresponds to a reduction in *k*-space sampling. Due to aliasing, this results in representations of the imaged object in the image domain no longer occupying spatially distinct points. The introduction of a phase shift in the time domain effectively labels the overlapping components in the time domain so as they can be distinguished in post processing with the use of a Fourier transform through time. The UNFOLD technique to a certain extent allows relocation of spatial information within *k-t* space to achieve a more efficient encoding.

Cardiac applications of UNFOLD are particularly useful for cine imaging where images containing a mixture of dynamic and non dynamic regions which may be represented spatially by the same pixel in image space but separated in the time domain [113]. The method can also be applied to breath hold myocardial perfusion imaging [114,115] where the chest wall and back are static (or close to), with the cardiac region being dynamic due to the uptake of contrast agent. In this case, where no motion was present on a canine study the method performed well with once again a 2-fold reduction in image acquisition data. On patients, the results were generally good with the exception where respiratory motion resulted in significant artefact in the reconstructed image. The UNFOLD method causes a temporal smoothing which also has the effect of causing spatial blurring in regions where spatial motion occurs. Although this may appear visually pleasing, it is at the expense of image resolution. It has been proposed [115] that the use of registration either in the image or frequency domain before the application of UNFOLD could reduce the effects of this problem although the successful implementation of this has yet to be seen.

UNFOLD is applicable when the nature of the imaging allows two spatial points to share the same temporal bandwidth without overlap. In addition, it is essential that sufficient prior knowledge about the shape of the temporal spectra is available to separate the individual contributions of the two points. Selective Line Acquisition Mode (SLAM) [116] is a recent variation of the UNFOLD technique similar to 2xUNFOLD with the acquisition of alternating even/odd phase encode lines. SLAM uses a less complex method of estimating the information lost due to insufficient sampling, by interpolating missing lines from the neighbouring frames. In a comparative study of temporal filtering methods for myocardial perfusion it was reported that the SLAM technique is actually equivalent to UNFOLD if a Hanning filter is used for the temporal filtering step. Results presented showed similar results between the two techniques with only subtle changes dependent on the filter chosen. An extension of SLAM uses a technique similar to those used in other reduced FOV imaging where a reference image is used after the SLAM technique has been applied. This can bring a further 3 fold reduction in *k*-space sampling, and the method is cunningly called Reconstruction by Estimation of Lines and Inhibition of Fold-in (RELIF) [117]. It is potentially applicable to breath hold cardiac perfusion studies but is reliant on there being no motion in the chest wall and such a large reduction in data acquisition results in a ~50% loss in SNR.

3.3.4 Broad-use Linear Acquisition Speed-up Technique (BLAST)

In an attempt to unify the description of image acquisition methods that aim to reduce the amount of data required for *k*-space reconstruction, a common equation is used to describe the use of prior information. BLAST is an image acquisition technique that is developed from the analysis of this common equation and uses the estimated amount of change within the FOV as prior information to reduce the redundancy in *k*-space information that remains static through time. The single common equation takes into account both static and dynamic components and is described here based on the original description by Tsao *et al.* [118]. The single common equation for many prior information driven acquisition methods:

$$\rho(\mathbf{x}) = R_{static}(\mathbf{x}) + R_{dynamic}(\mathbf{x}) \cdot \sum_{l=1}^{N_{terms}} c_l \varphi_l(\mathbf{x}) \tag{3.1}$$

where $\rho(\mathbf{x})$ is the reconstructed image. The c_l 's are the unknown basis coefficients to be determined from the MR data. The number of basis coefficients, N_{terms}, is less than or equal to the number of MR measurements so that there are more equations than unknowns. R_{static}, $R_{dynamic}$ and $\varphi_l(\mathbf{x})$ are the static reference image, dynamic image and basis functions respectively. Given this equation, it can be seen that methods that involve zero filled *k*-space such as RIGR and SVD effectively discard the R_{static} component (or set this to 0) in the common equation. Alternative techniques such as keyhole [106] or RIGR with two reference images [119] include a baseline image for $R_{static}(\mathbf{x})$.

In BLAST, a full resolution baseline image is initially acquired from which the user highlights regions where changes are likely to occur. $R_{static}(\mathbf{x})$ is then made equal to this baseline image and $R_{dynamic}$ a probabilistic map defined by the user from the baseline image. The basis functions $\varphi_l(\mathbf{x})$ are chosen to be the Fourier basis designed to match the *k*-space sampling pattern allowing the method to be used with any sampling pattern. Given a uniform probabilistic map BLAST becomes equivalent to keyhole imaging [106]. If a binary probabilistic map is used, the method becomes equivalent to reduced FOV imaging [120,121] and if precise information is known about the magnitude of change then the method is equivalent to RIGR with two reference images [119].

An extension to this method termed *k-t* BLAST [122] has been applied to 3D cardiac cine imaging [123]. This method differs in the dimension that the probabilistic information determines the reconstruction of under sampled *k*-space information. Rather than using a user defined probabilistic map of changes in the image space, *k-t* BLAST computes a similar map from a low-resolution fully sampled data set in *k-t* space. Acquisition efficiency is increased by applying sparse sampling to *k-t* space in a sheared grid pattern (chosen as it allows the tightest packing of signal replica in *x-f* space). The low-resolution image is used to determine a reconstruction filter from the signal distribution in *x-f* space. During the high-resolution acquisition, the sparse sampling results in multiple replicas in *x-f* space. In image space, these overlapping reconstructions occur due to the pattern of the point spread function. By multiplying the under sampled high resolution data, with the filter determined from the low-resolution data, these overlapping reconstructions can be eliminated.

In the study by Kozerke *et al.* [123], the use of *k-t* BLAST with cine 3D imaging of the heart allowed for whole heart coverage in a single breath hold with both high spatial and temporal resolutions. For use in myocardial perfusion imaging, there are many issues that must be addressed. The dynamic low resolution image would need to be performed with the use of contrast agent and would have to take into account the passage of contrast agent into regions of the anatomy with blood flow other than just the heart. This creates a greater dynamic field than is present in cardiac cine imaging. In addition, performing myocardial perfusion assessments with breath holds for the duration of the scan is practically difficult. The contrast enhancement along with the respiratory motion makes the optimisation of *k-t* BLAST to myocardial perfusion imaging a difficult prospect.

3.3.5 Locally focused and reduced field of view imaging

Locally focused imaging [124,125] is a method that enables the encoding of variable resolution across an MR image so as the regions containing more detailed features may be imaged at a higher resolution. While Fourier series have spatially uniform wave functions, giving uniform resolution across the entire FOV, alternative non-Fourier functions may be defined that allow variation in the resolution across the image. With conventional 2D Cartesian sampling this can be used in the phase encode direction to reduce the required sampling by as much as 50%. An example of this technique is LOFT (Locally Focused Tomography) [125] that applies a complete orthonormal set of non-Fourier functions that vary more slowly in homogenous regions of the image. The image is represented by a truncated series of these functions, more efficiently representing the data than a Fourier series representation. The method is applied in the phase encode direction of Cartesian *k*-space, reducing the total number of phase encode steps required to represent the imaged data. Artefacts produced by this method are generally limited assuming no hard edges are found outside of the regions in focus. Regions within the image can be of arbitrary size and resolution, thus the ability to optimise the scanning process is dependent on the prior knowledge of the image features. This technique can be expanded into 2D [126] allowing sparsely sampled imaging with single shot spiral trajectories.

While the locally focused imaging technique can be applied quite generally, the complexity in determining the optimal set of functions and mathematical computation required can prove difficult in setup and reconstruction. A variation on this [120] provides for a more straightforward locally focused imaging setup with the ability to perform high resolution imaging in regions of high spatial variability and low resolution imaging in regions of low spatial variability. This is achieved by acquiring two image data sets. A low-resolution image is acquired covering the entire FOV and a high-resolution image with a reduced FOV to contain the high spatially variable image data. The resulting images are overlaid onto one another to remove aliasing artefacts due to *k*-space under-sampling, and provide a complete image with variable spatial resolution. The drawback of this technique is that it does not allow for arbitrarily shaped regions although the significance of this is dependent on the imaging task at hand. The method has been applied to dynamic imaging [121] where reduced *k*-space acquisition for the dynamic images limits the FOV that may accurately be reconstructed through time. The differences between dynamically acquired phase encode lines and lines acquired in the static reference image are calculated and the portion representing the reduced FOV in image space is added to the dynamic reconstruction. An improvement upon the expected reduction in SNR has been achieved [127] through using all of the acquired data to estimate the static outer region of the image.

Rapid dynamic imaging has also been achieved through a reduction in the FOV with polar *k*-space sampling [128]. An initial optimally sampled image is acquired as a reference image followed by dynamic images with angular under-sampling restricting the dynamic FOV to a circular region with the full FOV. The reference images corresponding *k*-space diagonals are then subtracted from the dynamic image to obtain a difference image. This difference image is added to the optimally sampled reference image to obtain a full FOV dynamic image. The size of the dynamic FOV is directly proportional to the number of equally spaced *k*-space diagonals. The method is dependent on the region outside of the dynamic circular FOV being static although is shown to be robust to small amounts of motion with small streaking artefacts in the dynamic FOV.

A hybrid technique for dynamic imaging [129] has been developed which combines characteristics of reduced FOV imaging and keyhole imaging. Reduced FOV imaging is performed with full sampling of dynamic central phase encode lines to provide additional information about the low frequency changes in the full FOV. This helps in dealing with changes in the region outside of the reduced FOV such as background changes in signal intensity from dynamic contrast enhanced studies. This is shown to effectively correct for background signal intensity changes in cerebral perfusion studies, although is unlikely to be able to effectively deal with motion due to respiration in cardiac studies. This is due to the spatial motion of edge structures outside of the central FOV, such as chest wall and diaphragm motion, which cannot accurately be represented with low frequency *k*-space information.

3.3.6 Locally focused imaging with volume selective RF Excitation

The above locally focussed imaging scheme can be further enhanced by using volume selective RF excitation such that simultaneous improvement in spatio-temporal resolution is possible [130]. The method uses 2D spatially selective RF pulses to limit the imaging FOV to cover only the object of interest. This allowed an increase in the spacing of the sampling function without the introduction of wraparound into the central FOV. The method also facilitates real-time tracking, which has important implications in coronary imaging.

By considering the characteristics of the RF excitation profile, the method proposed by Yang *et al* [130] uses a set of training images, each with varying spatial resolution related to the spatial characteristics of the 2D RF pulse to determine an optimal set of phase encoding steps. It can be proved that for all possible images with variable spatial resolution in k_y, the positive eigenvalues of the covariance matrix of the training images determine that only M phase encoding steps are required to accurately derive the remaining phase-encoded signals. In practice the actual number required may be greater than this and a near optimum solution can be derived through the sequential back selection algorithm. Based on these lines, the remaining k_y lines can be estimated using the least mean squares estimate:

$$f(i\Delta k_y) = \sum_{m=1}^{M} (v_m U_{im}) \tag{3.2}$$

where i is the k_y encoding step being estimated, U_{im} a unitary matrix for diagonalising the covariance matrix and v_m the projection of the image onto the mth basis function as in:

$$v_m = \sum_{i \in \{L\}} \left[(R^+ R)^{-1} R^+\right]_{mi} f(i\Delta k_y) \tag{3.3}$$

where **L** are the measured phase encoded signals and R is an $L \times M$ matrix with elements $R_{im} = U_{im}$ for $i \in \{L\}$. R^+ represents the complex conjugate transpose of R.

An example of the resolution constraint placed upon the derivation of the basis functions is shown in Figure 3-4 (a), where the maximum resolution along y is 1 *mm*. The resolution towards the edge of the image reduces quite dramatically with uniform resolution in the central region. In Figure 3-4 (b), the distribution of eigenvalues corresponding to the covariance matrix is shown with 41 values being non-zero. To ensure numerical stability only 20 encoding steps were discarded with 44 remaining. Figure 3-4 (c) illustrates the process involved with the iterative steps shown on the vertical axis and the phase encoding steps shown on the horizontal axis. The iterative process calculates the mean square error of the reconstruction for the removal of each k_y index and at each step deletes the k_y index that has the least detrimental effect. In Figure 3-4 (c) the deleted k_y indexes are represented by black lines with the upper most point showing the point at which it was deleted. The iterative process is repeated until only 44 encoding steps remain. Figure 3-5 shows this acquisition profile applied to a phantom data set, comparing the full acquisition (a) with the reduced encoding (b) and a low pass filtering method zero filling the outer 20 k_y encoding lines of the original 3D data set (c). A 30% reduction in imaging time results in comparable images with only a small loss in SNR, whereas the low pass filtering in (c) destroys minute image detail due to the uniform resolution of the image.

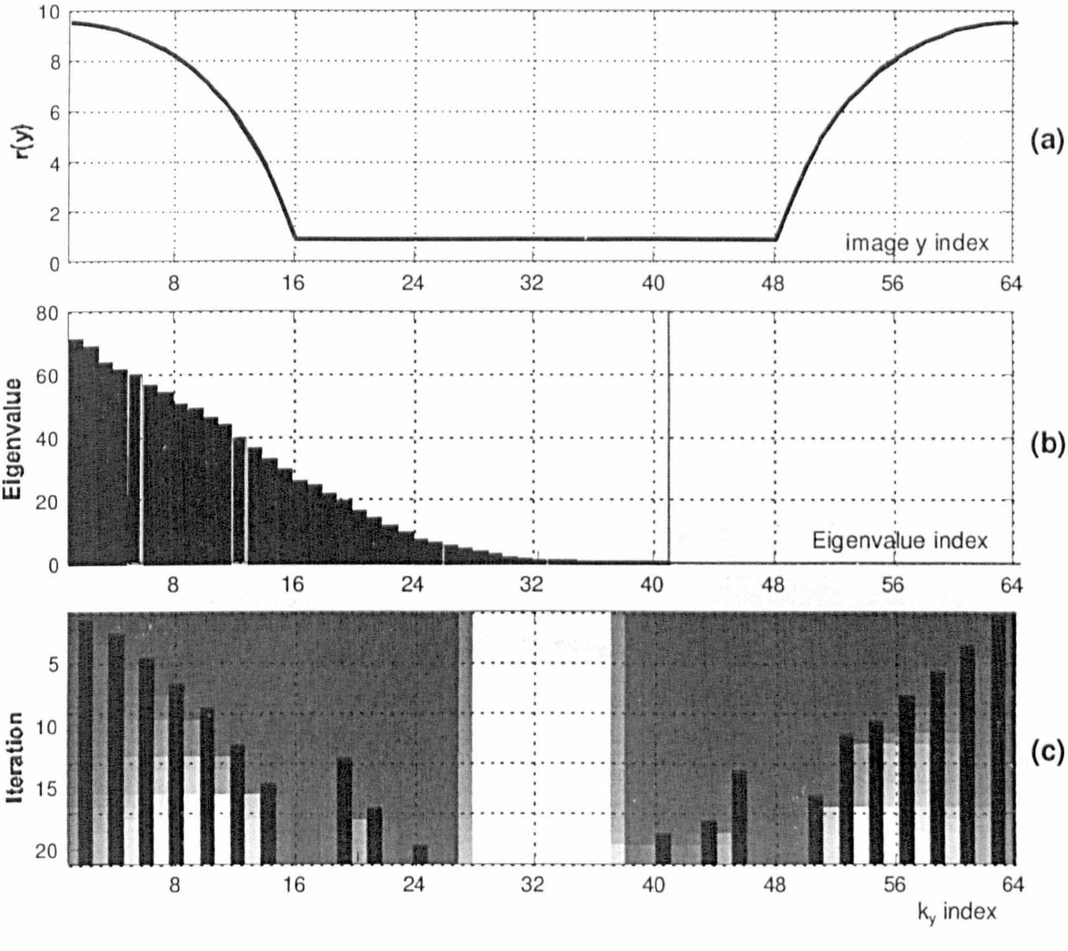

Figure 3-4 (a) An example of the applied resolution constraint *r(y)* for the derivation of basis functions. (b) the corresponding distribution of eigenvalues of the covariance matrix. (c) the selection of near optimal solutions of k_y phase encoding steps using the sequential back selection algorithm. In (c), the deleted encoding steps are represented as black strips superimposed on the normalised average mean square error of v_m, where lighter shades indicate larger errors (E^*). With permission from Yang *et al* [130].

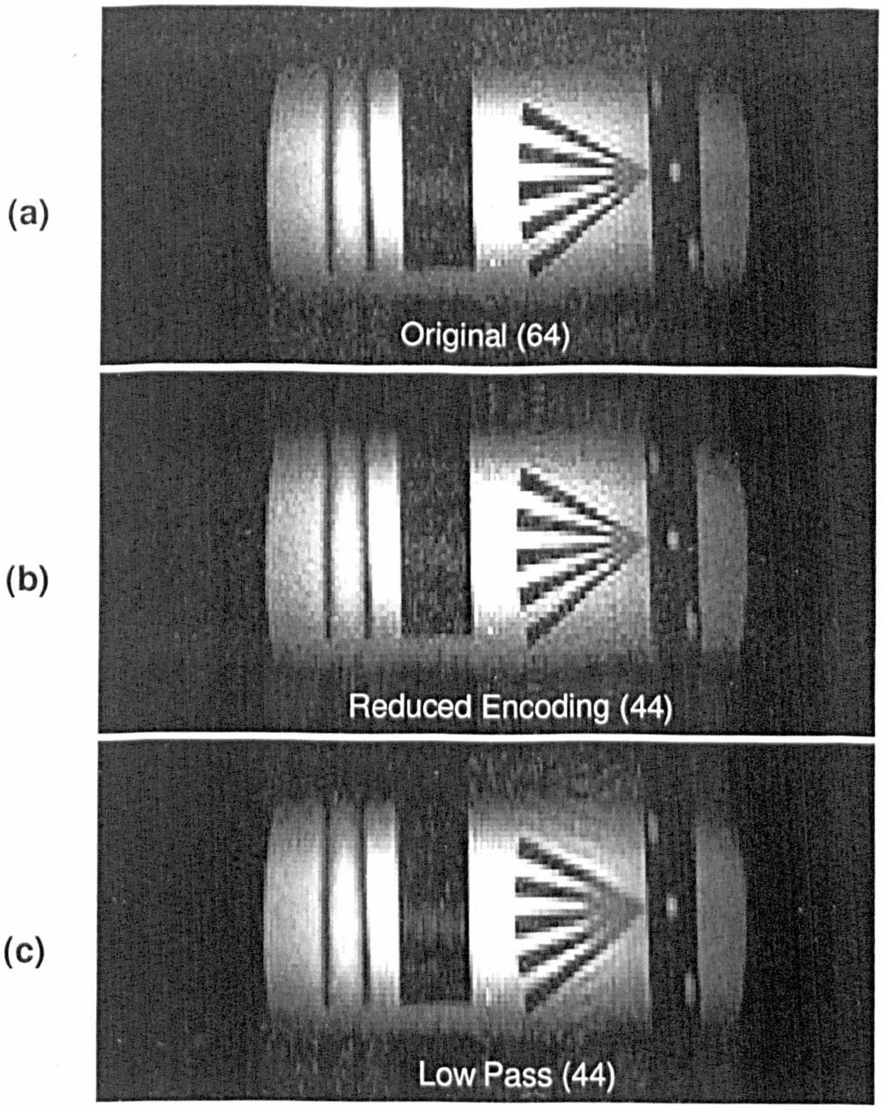

Figure 3-5 The effect of using reduced encoding on a 3D phantom data set. (a) the original fully encoded image. (b) and (c) the reconstructed results using locally focused encoding and zero filling, respectively. With permission from Yang *et al* [130].

3.4 Parallel imaging techniques

3.4.1 SiMultaneous Acquisition of Spatial Harmonics (SMASH)

The use of parallel imaging in MR is relatively new. The method uses the spatial characteristics of the phase array coils for minimising the acquisition time. Thus far, a number of parallel imaging techniques have been proposed. Most of these techniques, however, are originated from the SMASH and SENSE methods. SMASH [131] is a partially parallel imaging technique that makes use of the multiple coils generally used in MRI to encode Fourier lines in spatial harmonics of the receiver coils signals. This allows the recovery of additional *k*-space lines in the post processing stage reducing the number of *k*-

lines that are required and thus increasing the efficiency of the imaging process. MR receiver coils have spatial variation in their sensitivity, which for a standard circular surface coil is monotonic in all directions with distance from the coil. The combination of multiple coils may be used to create a sinusoidal spatial sensitivity profile and suitable modulations in the amplitude of this can replace the phase or frequency encoding normally produced by magnetic field gradients. An example of spatial harmonics approximated from the combination of six-coil phased array is shown in Figure 3-6. In its simplest form, a linear array of surface coils can be used to synthesise various sinusoidal sensitivity variations. This synthesis is performed in post processing and the sinusoidal variation shifts the data acquired from the combination of receiver coils in *k*-space. It can be seen that the number of spatial harmonics that can be successfully synthesised determines the number of *k*-lines that can successfully be reconstructed for each phase encoding gradient acquired. The range of harmonics that may effectively be synthesized is dependent on the width and spacing of the individual component coils spatial sensitivities. The method has been applied to cardiac imaging [132] to obtain images with reduced breath hold duration, enhanced spatial resolution, and increased temporal resolution.

For single shot imaging, the SMASH theory has been described in [133] and is used as a basis for our description below. By using the standard Fourier sequence, the obtained MR signal may be written as:

$$S(k_x, k_y) = \int\int dx\, dy\; C(x, y)\rho(x, y)\exp\{-ik_x x - ik_y y\} \tag{3.4}$$

where $C(x, y)$ is the RF coil sensitivity profile and $\rho(x, y)$ the spin density. By exploiting the variation in the coil sensitivity profile, SMASH is able to effectively acquire multiple phase-encode lines at once. If a multi-coil array is used which is linear in its arrangement it becomes possible to use linear combinations of component coil sensitivities to generate composite sensitivity profiles, taking the form of complex exponentials such that:

$$C_m^{comp}(x, y) = \sum_{k=1}^{L} n_l^{(m)} C_1(x, y) = \exp\{-im\Delta k_y y\} \tag{3.5}$$

where $l = 1,2,\ldots L$, $\Delta k_y = 2\pi / \mathrm{FOV}$ and L is the total number of coils in the array. n_l are the set of complex weights required to generate the mth harmonic $\exp(-im\Delta k_y y)$. The composite sensitivities are thus arranged to be spatial harmonics of the imaged FOV. By using the sensitivity profile in equation (3.5) the signal measured in (3.4) now becomes:

$$
\begin{aligned}
S_m^{comp}\left(k_x,k_y\right) &= \sum_{l=1}^{L} n_l^{(m)} S_l\left(k_x,k_y\right) \\
&= \int\!\!\int dx\,dy \sum_{l=1}^{L} n_l^{(m)} C_l(x,y)\rho(x,y)\exp\{-ik_x x - ik_y y\} \\
&= \int\!\!\int dx\,dy\, C_m^{comp}(x,y)\rho(x,y)\exp\{-ik_x x - ik_y y\} \\
&= \int\!\!\int dx\,dy\, \rho(x,y)\exp\{-ik_x x - i\left(k_y + m\Delta k_y\right)y\} \\
&= S\left(k_x, k_y + m\Delta k_y\right)
\end{aligned}
\tag{3.6}
$$

In this manner, linear combinations of the component coil signals produce an effective phase encode shift of $m\Delta k_y$. Through the use of an appropriate coil arrangement and weights, a reduced number of phase encodings may be acquired, and in post processing, the remaining information can be calculated through linear combinations of the component coil signals.

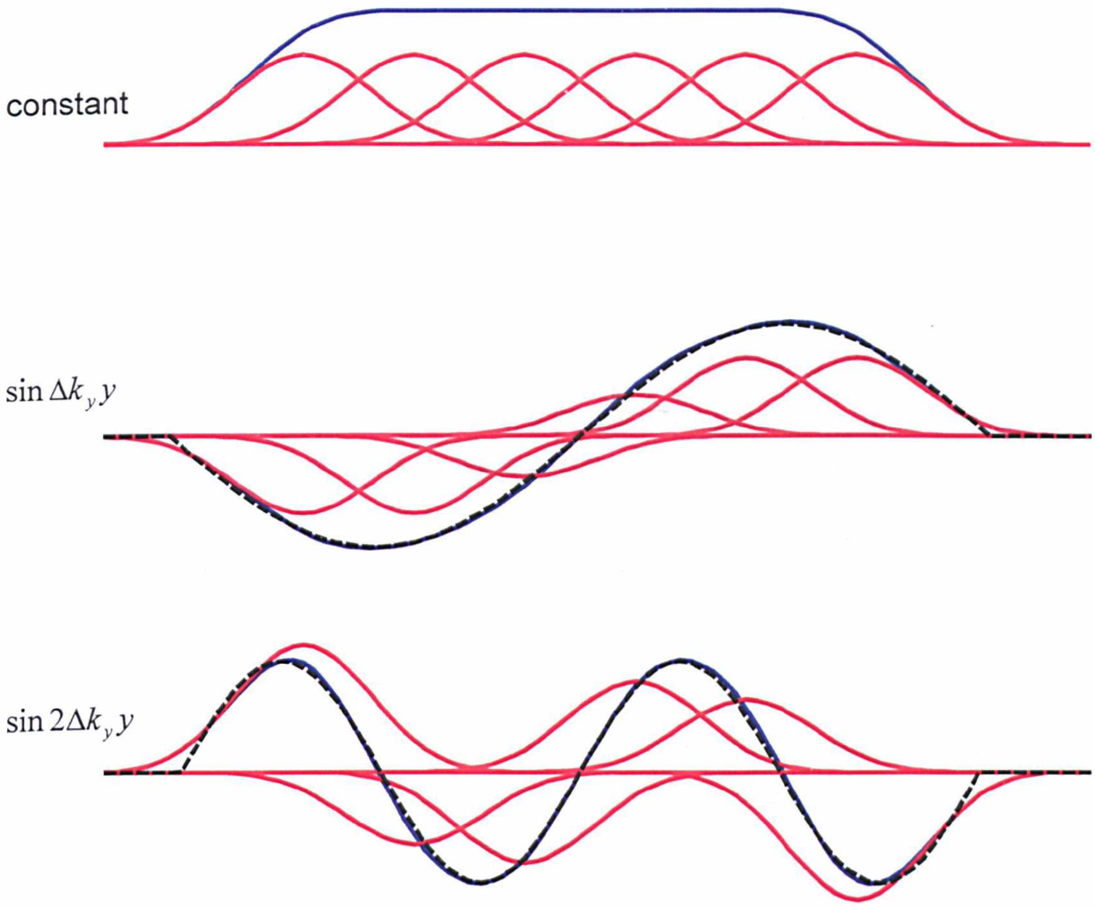

Figure 3-6 Linear combinations of component coils approximating spatial harmonics of frequency $\sin \Delta k_y$ for SMASH imaging, adapted from a figure by Sodickson *et al* [131]. For this example, six phase array coils are used modelled by Gaussian functions and depicted in the figure as separate weighted sensitivity profiles by red lines. The blue line represents the combined sensitivity profile of all six coils and the dashed black line the sinusoidal weighting function.

Recent advances in the determination of spatial harmonics and reconstruction procedure have allowed the technique to be applied to a greater variety of imaging planes and along with developments in hardware design allow for a wide range of coil geometries [134-136]. Automatic sensitivity calibration techniques using central *k*-space lines while marginally reducing the efficiency extinguish the need for calibration images [137,138].

SMASH may be combined with UNFOLD to further increase the *k*-space encoding efficiency [139]. A two fold acceleration from SMASH can be combined with a two fold acceleration from UNFOLD for a combined four fold acceleration. A variety of methods of performing this exist but are based around sampling every fourth line, recovering another one or two lines through SMASH, and then applying UNFOLD to estimate the remaining lines. The method uses a cross-shaped support region and the more dynamic portion of the FOV can occupy no more than half of the FOV.

3.4.2 SENSitivity Encoding for fast MRI (SENSE)

SENSE is a parallel imaging technique that uses the knowledge of the sensitivities of the elements of a phased-array coil to correct for aliasing artefact due to a reduction in the sampling FOV. For each of the receiver coil array elements a reduced FOV aliased image is reconstructed. Depending on the individual coil sensitivities, the contribution of different signals to an individual pixel varies in a manner, which to an extent can be determined from the prior sensitivity scans. The basic method is shown in the equations below taken from the original paper by Pruessmann *et al* [140]. For an individual pixel, let n_P denote the number of pixels superimposed and n_C the number of coils used. The vector **a** is the collection of complex image values the chosen pixel has in intermediate images and the complex coil sensitivities at the n_P superimposed positions form an $n_C \times n_P$ sensitivity matrix **S**:

$$\mathbf{S}_{\gamma\cdot p} = s_\gamma(\gamma_\rho) \tag{3.7}$$

where the subscript γ indexes the coils and ρ the superimposed pixels, the vector γ_ρ denotes the position of the pixel ρ, and s_γ is the spatial sensitivity of the coil γ. The sensitivity matrix S is used to calculate the unfolding matrix **U**:

$$\mathbf{U} = \left(\mathbf{S}^H \Psi^{-1} \mathbf{S}^H\right)^{-1} \mathbf{S}^H \Psi^{-1} \tag{3.8}$$

where the superscript H indicates the transposed complex conjugate, and Ψ is the $n_C \times n_C$ receiver noise matrix, which describes the levels and correlation of noise in the receiver channels. Using the unfolding matrix, signal separation is performed by

$$\mathbf{v} = \mathbf{U}\mathbf{a} \tag{3.9}$$

where the resulting vector $\mathbf{v}$ has length n_P and lists separated pixel values for the originally superimposed positions. The procedure is repeated for each pixel within the reduced FOV to produce a non-aliased version of the full FOV. The number of receiver coils used limits the theoretical maximum reduction factor. The number of pixels n_P must not exceed the number of coils n_C so as the matrix inversions in Equation (3.8) can be performed.

The method compares favourably to the SMASH technique described above. With SMASH, the discrete Fourier transform is applied as a last step in the reconstruction approach, while with SENSE the separate coil images are reconstructed as the first stage. The SENSE technique is also more forgiving and straightforward in the determination of coil set up and imaging plane orientations. The requirement for a preliminary reference scan is weaker with SMASH, as described previously this can be performed as part of the actual imaging scan with a small amount of extra data, whereas with SENSE full sensitivity profiles must be acquired. The major limiting factor of SENSE is noise with the SNR reducing with the increasing level of aliasing, thus limiting the acceleration factor. A comparison of SMASH and SENSE [141] found that SMASH showed significantly higher artefacts at all levels of acceleration. SENSE demonstrated good SNR at low levels of acceleration although as the acceleration increased this tended to increase rapidly.

SENSE has been applied to real time cardiac imaging [142] providing a three-fold increase in image acquisition efficiency with a six-element receiver coil array. This allows for 27 *msec* scan times with a resolution of 2.6 *mm*. Importantly for cardiac imaging, the use of SENSE reduces the acquisition time and thus artefacts due to motion of the heart during acquisition. SENSE has also been combined with UNFOLD and named TSENSE [143] due to the temporal filtering which takes place with UNFOLD. The initial purpose of this is for artefact suppression as the temporal filtering deals well with reducing artefact due to incorrect sensitivity profiles, and the use of the SENSE method relaxes the requirement for a limited dynamic region within the FOV that is associated with UNFOLD. In addition, the use of temporal filtering allows for the reconstruction of sensitivity profiles from reduced *k*-space data before applying TSENSE making the method adaptive and more robust to motion. A schematic diagram of this is shown in Figure 3-7.

A combination of TSENSE and UNFOLD in a hybrid approach has been used for real time cardiac imaging [144], differing from the previous TSENSE approach in its selective use of adaptive TSENSE and UNFOLD for different coils. In practice this amounts to using adaptive TSENSE where suitable and UNFOLD on frames with unstable sensitivity maps or unsuitable coils configurations. The use of UNFOLD as the final step in adaptive TSENSE (as shown in Figure 3-7) was optional as while being successful at reducing artefact it has a temporal blurring effect which was noticeable in some of the studies. TSENSE has been applied to first pass myocardial perfusion imaging with slice interleaving of a hybrid EPI imaging sequence [145]. Two-fold acceleration allowed 8 slices to be acquired each cardiac cycle with acceptable results. UNFOLD has been used in a similar way to reduce artefact in SMASH as well as partial Fourier imaging [146].

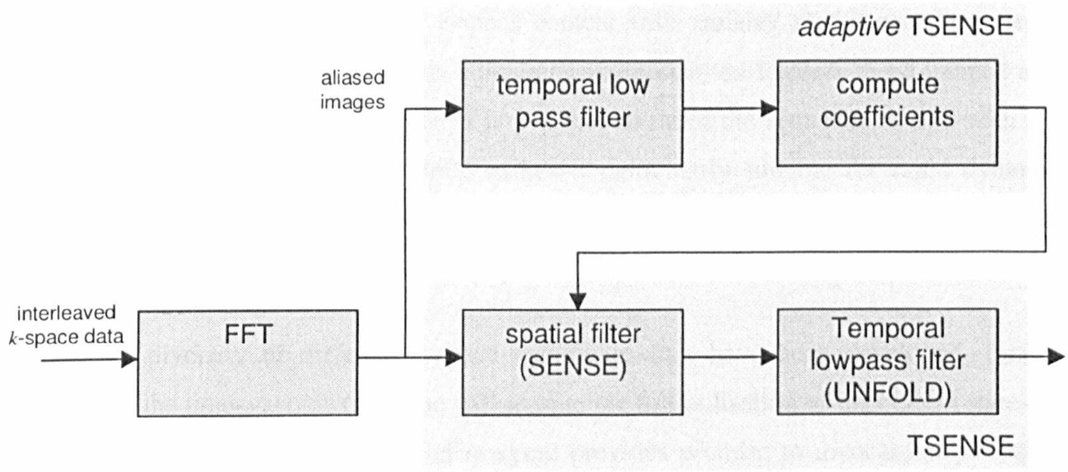

Figure 3-7 The use of temporal filtering to adaptively acquire sensitivity profiles for adaptive TSENSE imaging. Based on a figure by Kellman *et al* [143].

3.5 Conclusion

In this chapter, we have outlined some of the major techniques used in MR for improving the overall acquisition efficiency by exploiting the information content of the *k*-space data. The majority of techniques achieve reductions in *k*-space acquisition based on prior knowledge of the imaging task. For dynamic imaging, this mainly includes the temporal characteristics of the imaging structure. The keyhole technique described is simple to implement and it has been widely used in a number of cardiac imaging applications. However, the method has several drawbacks including the amplitude discontinuities and phase incoherence that can give rise to Gibbs artefact and blurring. RIGR is a more elegant way of minimising the *k*-space data and it is best applied when the spatial details of the image remain static throughout the acquisition period. BRISK, on the other hand, exploits inter-frame correlation of the dynamic sequence and is particularly suited to high temporal resolution cine imaging. When applied to perfusion imaging, a number of issues may arise due to the rapid change in blood pool contrast details and inconsistency of respiratory induced cardiac deformation at different cardiac cycles. The use of UNFOLD is similar to that of RIGR, which requires temporal alignment of the anatomical details. The method, however, is particularly efficient and simple to implement, and therefore can have significant potential to myocardial perfusion if respiratory motion can be effectively controlled or tracked during imaging.

In this chapter, we have also described BLAST, which is an image acquisition technique that uses the estimated amount of change within the FOV as prior information to reduce the redundancy in *k*-space information that remains static through time. In BLAST, a full resolution baseline image is initially acquired from which the user highlights regions where changes are likely to occur. The locally focussed imaging techniques we described are advanced methods for exploiting the *k*-space content with variable spatial encoding across the imaging FOV. This allows regions containing more detailed features to be imaged at a higher resolution. With this technique, it is possible to tailor the sequence design with the specific coverage of the *k*-space, which makes it particularly suitable for rapid dynamic imaging. The feasibility of incorporating selective volume excitation further enhances the flexibility of the technique.

Despite the diversity of different *k*-space techniques that have been developed, further reduction of the image acquisition time will require the full utilisation of the current state-of-the-art MR imaging hardware. Parallel imaging provides promise to myocardial perfusion studies as improvements in efficiency and resolution are achieved without necessary assumptions about the content of the image [103]. This provides the possibility of greater coverage of the myocardium, allowing more accurate analysis of the underlying physiological characteristics. Recent developments including the foundations of generalised parallel imaging [147] together with dedicated coil array designs offer the potential to achieve accelerations approaching the theoretical maximum (equal to the number of receiver coils). With developments in parallel imaging, techniques allowing for auto-calibration [148,149] and the prospect of the latest MRI hardware offering a greater number of receiver channels the development of parallel imaging is expected to progress rapidly in the coming years. For this thesis, however, we will focus on the development of efficient *k*-space coverage and the effect of respiratory induced cardiac motion on these methods.

Chapter 4 : Management of Cardiac and Respiratory Motion

4.1 Introduction

Differentiation of ischaemic but viable myocardium from infarcted regions requires detailed global quantitative assessment and modelling of myocardial perfusion characteristics. This requires the development of a spatially and temporally registered imaging strategy for complete 3D coverage of the myocardium. Quantitative analysis demands the localisation of regions of myocardial tissue throughout the passage of the contrast bolus. This process, however, is complicated by both cardiac and respiratory motion. As mentioned in Chapter 1, in 3D myocardial perfusion imaging a complete volumetric data set has to be acquired for each cardiac cycle, and this can result in 50-100 such 3D data sets for studying the first pass of the contrast bolus. To ensure a comprehensive coverage of the myocardium and reasonably high resolution of the images, a typical data acquisition window of 100-200 *ms* per slice, and thus an overall acquisition time of more than 600 *ms* is required for each cardiac cycle. When using multi-slice imaging, cardiac motion during this large acquisition window can cause the myocardium imaged in different image planes to be mis-registered, *i.e.*, some part of the myocardium may be imaged twice whereas other parts may be missed out completely. This type of mis-registration is difficult to correct for by using post-processing techniques. Direct application of the techniques mentioned in Chapter 3 that exploit the redundancies in information content in the perfusion sequence; can introduce significant artefacts due to respiratory induced cardiac motion. In this chapter, we will discuss the nature of cardiac and respiratory motion associated with myocardial perfusion imaging, and outline necessary strategies that can be employed to minimise this effect.

4.2 Cardiac contractile motion

The heart contracts in a cyclical pattern as deoxygenated blood flows into the heart. An example of the motion is shown in Figure 4-1. This cycle persists in a semi-autonomous state without interruption through a healthy individuals life. While the frequency of this contraction varies, the motion is predictable and at rest corresponds to around 70 beats per minute. It is not possible to suspend or control this motion non-invasively, so imaging must be performed with consideration for this effect. In CMR, ECG gating is typically used to ensure the *k*-space data is acquired in synchrony with the cardiac motion. Typically, ECG gating triggers the acquisition of MR image data to a pre-defined gating delay after the R-wave [150], allowing images to be acquired with a pseudo stationary cardiac contractile position over repeated cardiac cycles. This technique is now widely used in MRI and offers a robust solution for cardiac imaging. Cardiac gating facilitates segmented imaging, where *k*-space data is acquired over multiple cardiac cycles, as well as simplifying the analysis of dynamic imaging such as first pass myocardial perfusion studies.

One of the major issues related to ECG gating is the difficulty in acquiring late diastolic images. This has motivated extensive research in the development of retrospective gating techniques [151]. Research has also been conducted in the practicality of surface electrode ECG, particularly in high-field and fetal cardiac imaging applications. It has been demonstrated that it is possible to use data directly acquired with MR to perform cardiac gating. For example, an under-sampled radial *k*-space acquisition has been used to measure a real-time image-derived flow-gating waveform, from which the gating times are derived. These gating times are used to reconstruct a conventional gated-segmented image series by combining the real-time data from multiple heartbeats. A number of other self-gated acquisition techniques have also been proposed [152], which directly extract motion synchronization signal from the same MR signals used for image reconstruction. The strategies used with self-gated signals from data acquired using radial *k*-space include echo peak magnitude, kymogram, and 2D correlation. Self-gated techniques represent a valuable advance in clinical MRI because they enable the acquisition of high temporal and spatial resolution cardiac cine images without the need for ECG gating and with no loss in imaging efficiency.

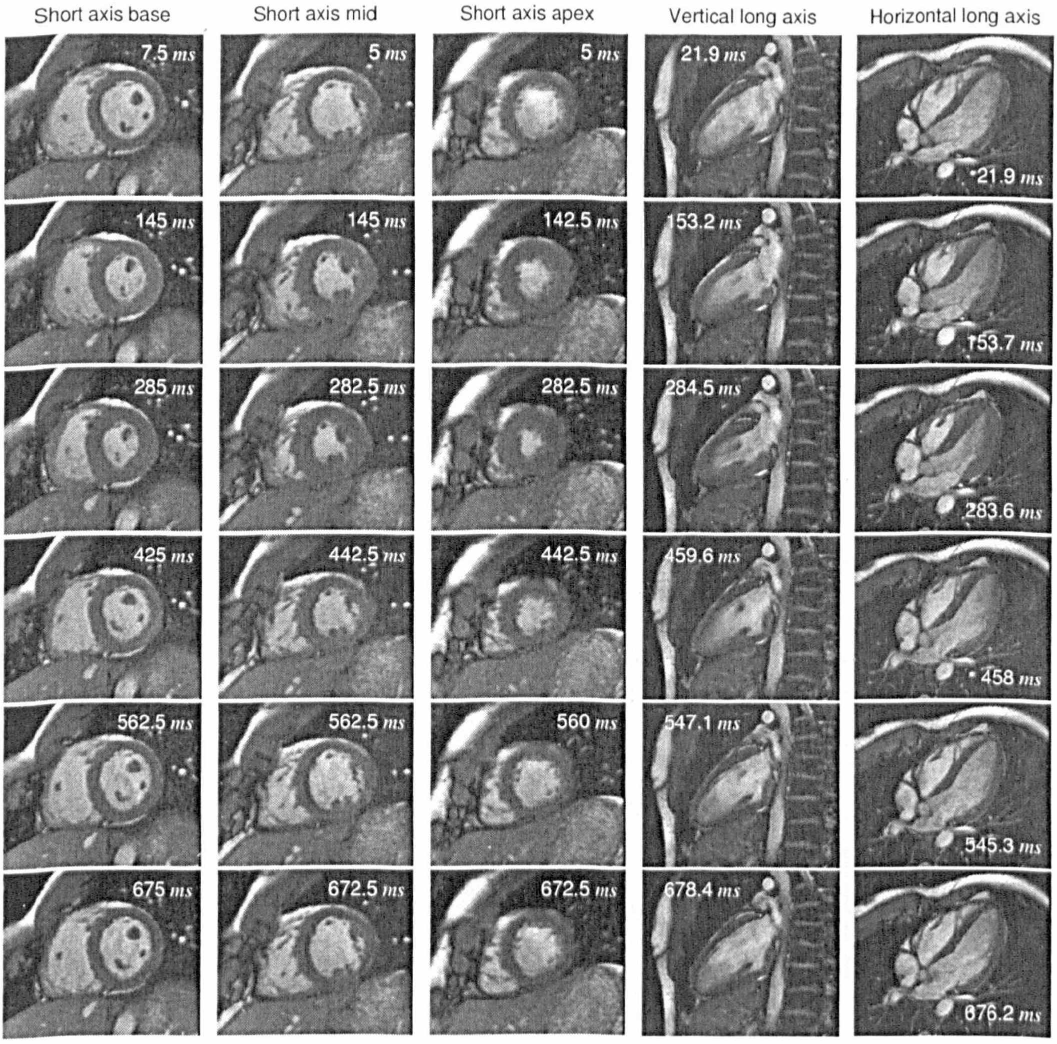
Short axis base
Short axis mid
Short axis apex
Vertical long axis
Horizontal long axis
7.5 ms
5 ms
5 ms
21.9 ms
21.9 ms
145 ms
145 ms
142.5 ms
153.2 ms
153.7 ms
285 ms
282.5 ms
282.5 ms
284.5 ms
283.6 ms
425 ms
442.5 ms
442.5 ms
459.6 ms
458 ms
562.5 ms
562.5 ms
560 ms
547.1 ms
545.3 ms
675 ms
672.5 ms
672.5 ms
678.4 ms
676.2 ms

Figure 4-1 Five cross-sectional images of the LV demonstrating the contractile motion of the heart.

4.3 Respiratory motion

Respiratory induced cardiac motion is a major problem that has troubled the CMR community for many years. Unlike cardiac motion, respiratory induced motion has poor inter-cycle consistency. This makes gating at different phases of the respiratory cycle particularly difficult. A coronal view of the chest in a sequence of respiratory positions is shown in Figure 4-2, demonstrating the typical range of motion. Although motion of the heart due to respiration acts predominantly in the cranio-caudal (head to foot) direction, supplementary translational motion in the other two directions must not be ignored. Furthermore, there is also a degree of rotation of the heart that varies amongst subjects [153]. The degree of non-rigid deformation is found to vary amongst subjects and where present is most significant in the apex of the LV, the right atrium and in the region of the RCA. Due to this non-rigid motion, the use of translational or affine motion correction on its own is not enough. This makes the correction of respiratory motion through prospective or retrospective correction in *k*-space insufficient. The variation in the degree and nature of motion found in the cardiac region due to respiration makes the use of a statistical population models difficult, and therefore subject specific motion modelling and correction is currently seen as the most viable option. The use of breath holds has traditionally allowed the acquisition of data with reduced respiratory motion artefact. Breath-holds, however, are difficult to sustain and upward creep can affect the acquired results. In recent years, the monitoring of respiratory motion through the use of navigator echoes has been used in coronary imaging to drive simple respiratory motion models.

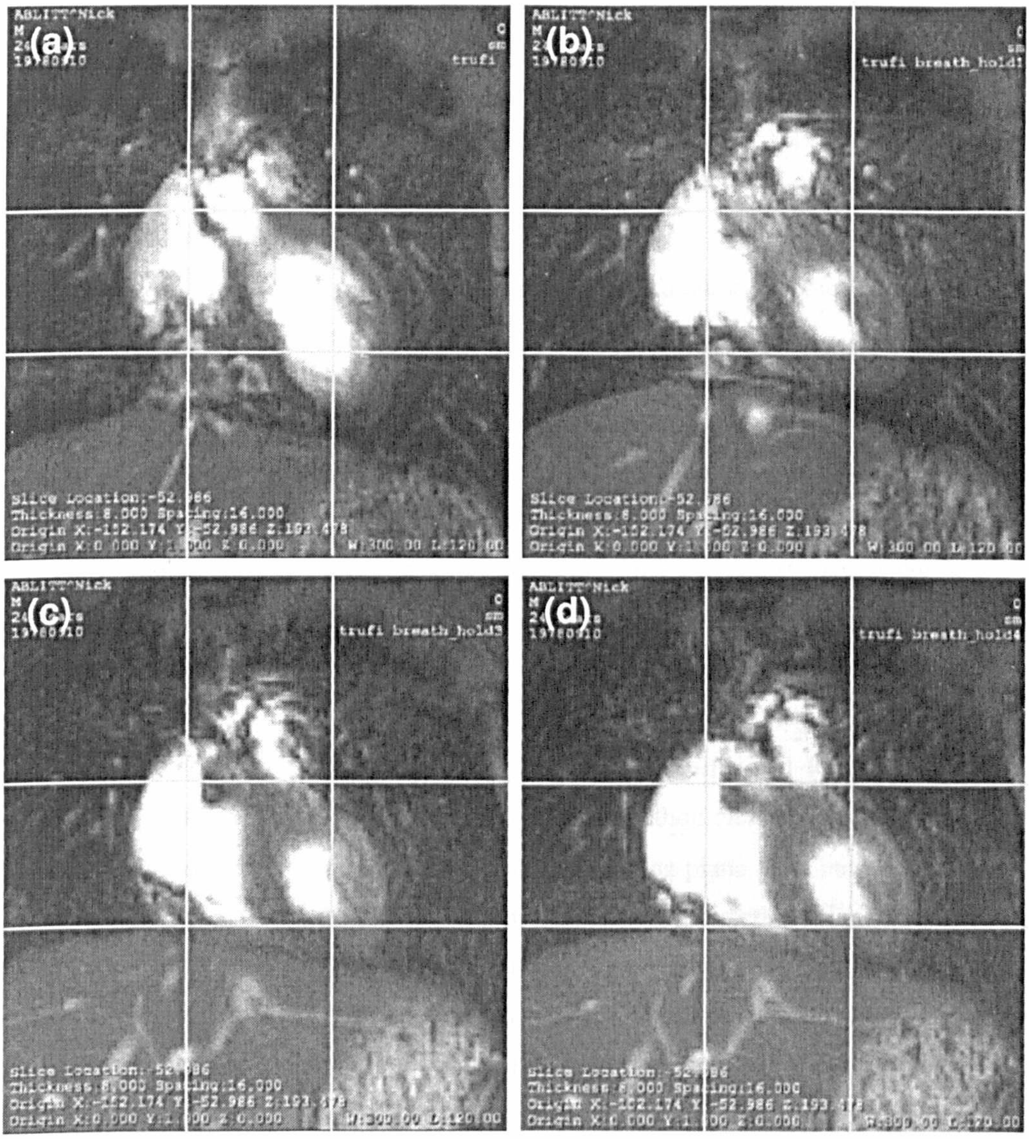

Figure 4-2 A coronal view of the heart showing the effect of respiratory induced cardiac motion. The four images (a), (b), (c) and (d) show four stages of the respiratory motion from end inspiration to end expiration. All these images are gated to the same ECG R-wave delay.

4.3.1 Measurement of respiratory motion

For the measurement of respiratory motion, a reliable marker strongly correlated to the motion of the heart is required. Traditionally methods of directly monitoring respiration with a belt or bellows have been used [154]. Other methods of measuring respiratory motion include the monitoring of ECG demodulation, where an optically coupled ECG sensor is used to reduce interference from MR [155].

Existing research has shown that the diaphragm can have a range of motion 4 to 5 times greater than that of the chest wall [156]. Due to the location of the heart within the chest cavity resting on the diaphragm, the motion of the diaphragm is a sensitive measure of respiratory motion. Navigator echoes are an MR technique for acquiring signal from a column of material running perpendicular to the direction of motion, with the use of a readout gradient along its length [157]. The use of a Fourier transform on the measured data provides a well-defined edge that gives a scalar value of respiratory position. The acquisition takes minimal time and can be interleaved with the imaging sequence, allowing real time measurement of respiratory position throughout the acquisition, which is essential for prospective respiratory motion compensation.

There are two methods that have been applied for the generation of a navigator echo. The spin echo technique uses two planes, one excited by a 90° RF pulse and the other by a 180° RF pulse. The intersection of these orthogonal planes is positioned on the diaphragm and a spin-echo signal is acquired for measurement. This method is robust and produces a well-defined column. However, care must be taken when using this technique to ensure that the planes do not intersect with the region of interest for the interleaved image acquisition. A further disadvantage of this method is the speed with which the measurement can be repeated. An alternative technique uses a selective two-dimensional RF pulse to excite a circular column intersecting with the diaphragm. This method can be repeated more rapidly and has less intrusion on the interleaved acquisition imaging plane. This method, however, is more sensitive to problems such as shimming errors (corrections for magnetic field inhomogeneities), which can cause blurring and distortion in the measured column [158]. In practice, both techniques have been used extensively in coronary angiography studies with great success [159-161]. The additional respiratory information that these navigator echoes provide can serve two purposes; it can be either used to prospectively adjust the acquisition or to correct for the motion in post processing.

It is important to note that the positioning of the navigator column affects the measured motion. The right dome is higher than the left, with the regions undergoing coherent motion but to different degrees [162]. Motion of the diaphragm is greater when measured posteriorly than anteriorly (motion measured anteriorly is 56% of that measured posteriorly [163]). While the greater motion is desirable measured posteriorly, a more accurate lung diaphragm border for edge detection is achieved at the peak of the dome, enabling the column to be perpendicular to the diaphragm edge. This variation in measurements makes the use of diaphragmatic navigators for motion modelling heavily dependent on the location of the measured column. A typical positioning for a spin echo navigator column is shown in Figure 4-3, with two planes carefully positioned to avoid interference with the heart and intersecting at the dome of the right hemi diaphragm, as shown in the transverse view (a). The positioning of the column is shown in the coronal (b) and sagittal views (c) at the dome of the right hemi diaphragm.

The timing of navigator acquisition can be an important parameter, but may often be limited by the system being used. Pre-navigators (acquired after the ECG trigger before image data acquisition) are the most efficient for prospective respiratory information, although can be vulnerable to sudden changes in respiration between the navigator and the image acquisition. Pre and post-navigators (within each cardiac cycle before and after image data acquisition) provide added assurance of respiratory position although come at the cost of scan efficiency. For free breathing studies, the post scan is generally superfluous, although for multiple breath holds pre and post-navigators are desirable.

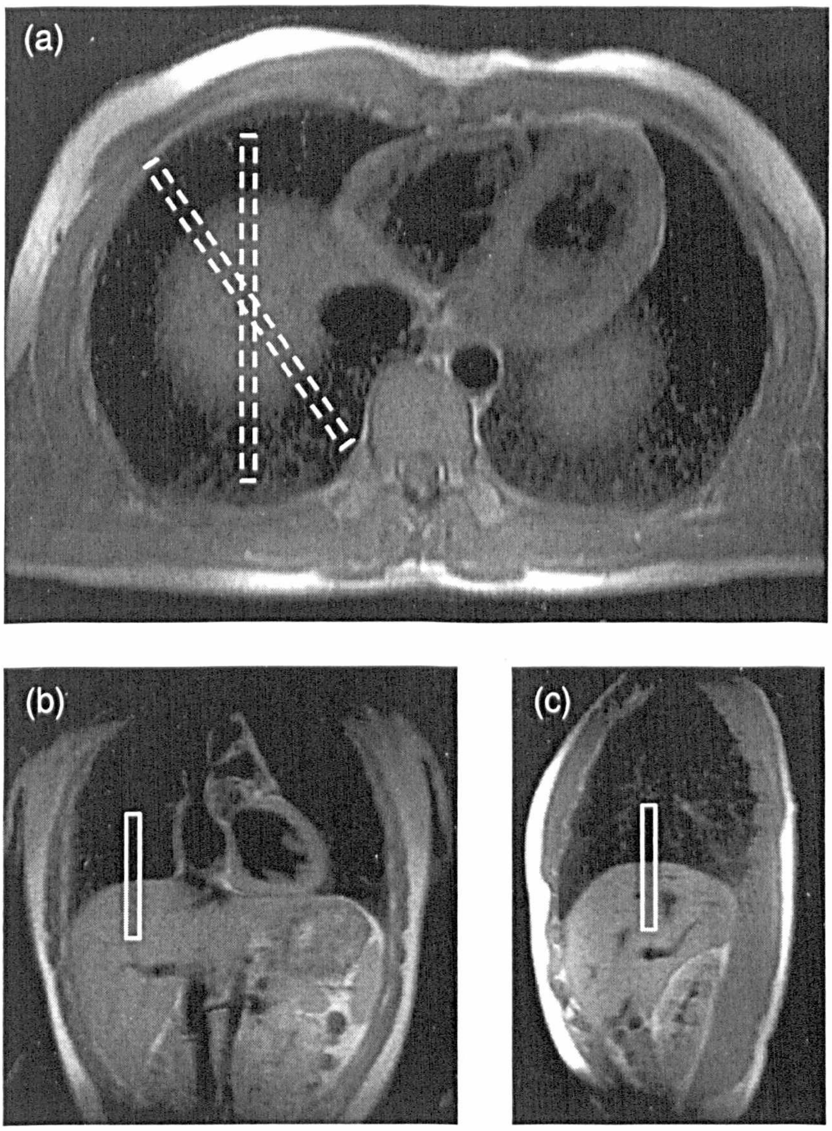

Figure 4-3 Column positioning of diaphragmatic navigator echoes. The transverse view (a) shows the two intersecting planes angled to avoid interference with the heart, intersecting at the dome of the right hemi-diaphragm. In the coronal (b) and sagittal (c) views, the location of the column is shown.

4.3.2 Pattern of free breathing respiratory motion

Research has shown that the pattern of respiration varies among different subjects and through time. As shown in Figure 4-4, natural free breathing often has a delay at end expiration (higher values). The end expiratory position has been shown to be held for longer in free breathing and more stable in position than the end-inspiratory position [164]. While the pattern is cyclical alterations or aberrations to this pattern are common, these can be due to coughs or natural variation due to physiological requirements. A general drift in position is found to occur over time, most commonly upwards at end expiration [164]. This change in end expiratory position can be seen in Figure 4-4, where in (b) an upward movement is visible. In addition, alteration in breathing pattern is common when the patient is made aware of their breathing pattern, or interestingly instructed to breathe normally. Inspiratory velocities are generally greater than expiratory [165] and this is also apparent in Figure 4-4.

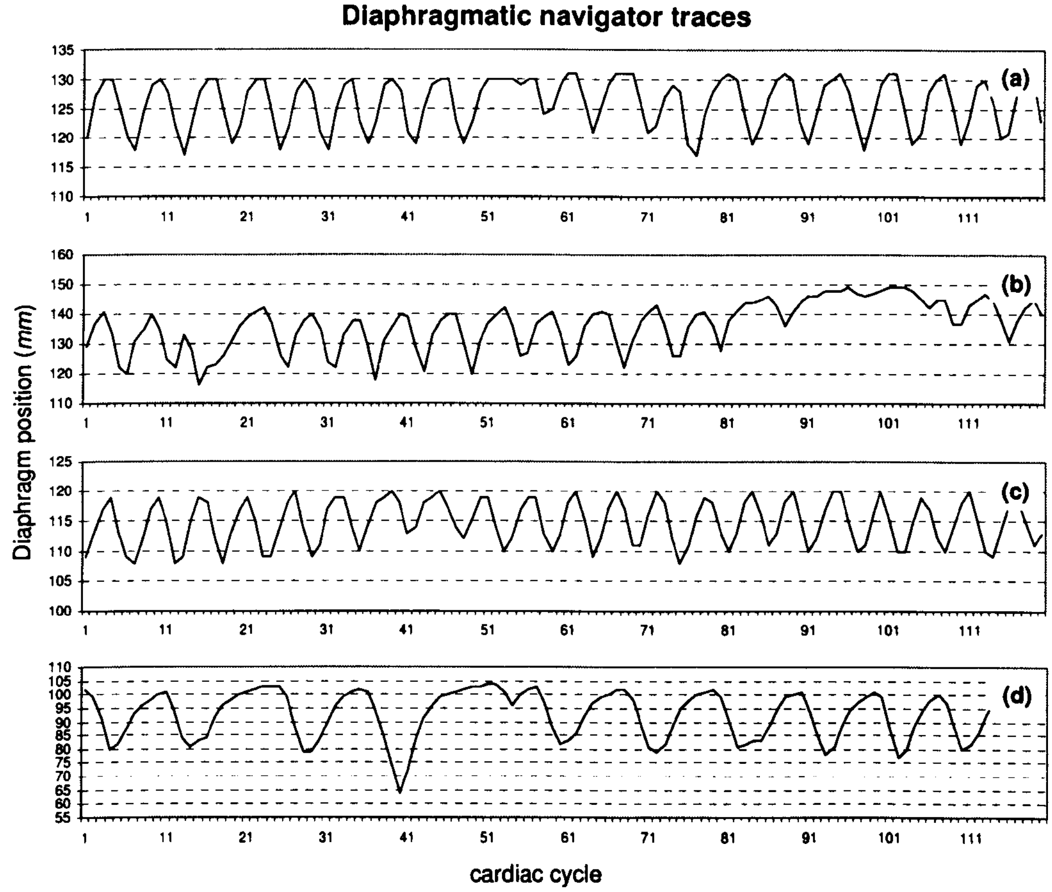

Figure 4-4 Diaphragmatic navigator traces for four subjects over a period of 120 cardiac cycles. A clear cyclical pattern can be seen in all four subjects, although regions of non-uniform breathing can be seen in (b) and (d). The range of observed motion of the navigator reading varies amongst subjects from 10 *mm* in (a) and (c) to around 20 *mm* in (d).

4.3.3 Hysteresis effects of free breathing

In order to establish the relative motion of anatomical positions due to respiration, a study of free breathing cardiac MR imaging was performed. Multiple navigators corresponding to the dome of the right hemi-diaphragm, the LV, the chest wall and the abdominal wall were simultaneously measured [166]. A linear relationship between heart motion and diaphragm motion was generally observed with the slope varying between 0.46 and 0.99. In many cases a hysteretic loop was present with a delay in the respiratory motion of the heart relative to the diaphragm. The degree of this was subject specific and independent of the cardiac phase. An example of the path traced from a breathing pattern with a significant hysteresis effect is shown in Figure 4-5. The breathing pattern is shown to follow an anti-clockwise direction due to a delay in the motion of the heart relative to that of the diaphragm. This delay was found in the small study performed by Nehrke *et al* [166] to be as long as 0.6 seconds.

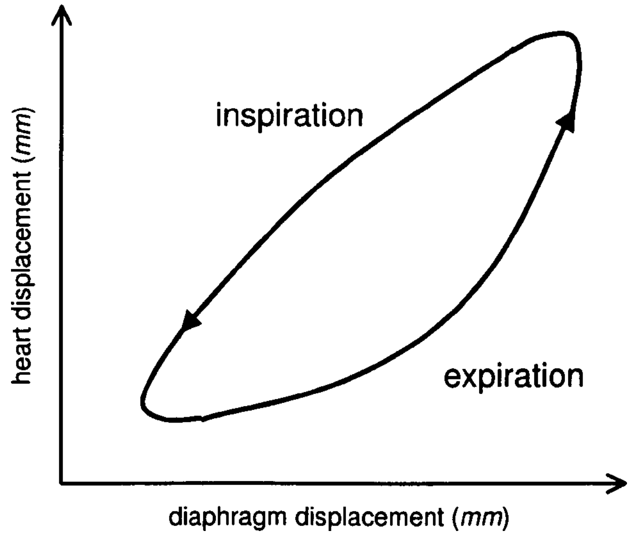

Figure 4-5 Example path of breathing measured at boundaries of the diaphragm and the heart with an observed hysteresis effect. Based on figure by Nehrke *et al* [166].

Cardiac cine images acquired on the same patients highlighted similar problems. Without the use of respiratory phase ordering, patients who had previously showed strong hysteric effects from the navigator study showed discontinuities in the cine images. The cine images were further separated into inspiratory and expiratory acquisition. Results showed a difference in the shape of the diaphragm between inspiration and expiration that in certain cases lead to a tilting of the heart resting on the diaphragm. This tilting effect, albeit being small, could lead to errors in high-resolution cardiac imaging. The exact reason for this hysteresis effect is not fully known. Possible reasons include the viscoelastic properties of the lungs acting as a damper on the motion of the heart, or the activation of different muscle groups during inspiration and expiration. The difference in the shape of the diaphragm, observed on the cine images, possibly gives credence to the latter reason.

In cardiac MRI, the hysteresis effect can cause significant issues with the accuracy and reliability of respiratory compensated imaging schemes. This is of most concern in high-resolution applications such as coronary imaging. The placement of the navigator directly through the wall of the heart would eliminate the effect, but is impractical due to the considerable destructive effect the pencil beam would have on the imaging volume. In preliminary studies the introduction of a delay of the heart in relation to the diaphragm has been shown to help alleviate this problem [166], although it is required to be subject specific due to the individual characteristics of the patients breathing.

4.3.4 Upward creep during breath holds

In an ideal situation, a breath hold results in the freezing of the respiratory position for its duration. In practice, this is not the case with limitations on the duration of feasible breath holds. Upward creep is an effect that has previously been described in SPECT imaging [167] where it was found to occur during breath holds following physical activity. Upward creep is the movement of the diaphragm and heart in the direction of the head through the duration of a patient induced suspension in breathing. The measurement of diaphragm position through the duration of a breath hold allows for the more accurate assessment of upward creep [165]. The occurrence of such motion has been explained by relaxation of inspiratory muscles and changes in lung volume due to greater oxygen uptake than carbon dioxide secretion during the breath hold. The velocity of upward creep at end expiration is relatively constant at an average of 0.15 *mm/sec* and at end inspiration more variable in the range of 0.1-7.9 *mm/sec*. This results in a displacement during 20 seconds of suspended breathing, 25% of that recorded during free breathing when measured at the diaphragm. In the SPECT study, the occurrence of upward creep was found to be significantly reduced if imaging was performed 15 minutes post exercise. These findings highlight problems encountered with breath hold imaging, regardless of the patients health and willingness to suspend breathing for the duration of the scan. While measures can be taken to reduce the likelihood of its effects, breath hold imaging cannot be assumed to completely resolve the problems of respiratory motion.

4.4 Respiratory adapted imaging

Respiratory induced cardiac deformation is a significant source of error in CMR and also one of the main limiting factors for PET and 3D echo-cardiography [168-170]. In CMR, particular problems are encountered in contrast imaging of the coronary arteries. While small effects of respiratory deformation can be acceptable for more general imaging tasks. When imaging small anatomical structures such as the coronary arteries, bulk cardiac motion can cause ghosting, blurring and image degradation. Due to this, many of the developments for the monitoring and control of respiration have been made in coronary imaging, providing a range of solutions which are potentially of value to problems encountered with respiratory motion in myocardial perfusion imaging.

4.4.1 Respiratory motion control in CMR

With MRI, a number of methods can be employed to account for the respiratory motion of the heart. These range from periods of suspended breathing during the image acquisition, to methods of following this motion during the acquisition, or methods to correct for the motion in post processing.

Respiratory motion may be ignored if images are acquired during a period of suspended breathing [171]. The breath hold is often taken at end expiration to provide better consistency between repeated breath-holds. This method, however, has drawbacks in addition to upward creep described earlier. The duration that a patient is able to hold their breath is finite and often the patient suffers considerable discomfort performing this. For high-quality high-resolution imaging, breath-holds can be long and inappropriate for cardiac patients, particularly those with coexistent pulmonary disease [164]. With myocardial perfusion imaging in particular, the use of adenosine or other stress agents can provide additional discomfort for the patient, thus further reducing the likelihood of a successful breath hold. The effect that the suspended breathing has on the normal operation of the heart must also be considered [172,173]. A reduction in venous return to the heart due to increased pleural pressure can potentially affect the results of cardiac studies acquired during breath holds.

4.4.2 Navigator echoes for prospective respiratory motion compensation

The use of navigator echoes for prospective respiratory gating and motion compensation requires real time feedback from the reconstruction computer to drive the scanner. This requires real-time signal processing and MR hardware capable of reconstructing navigator data in real time. Currently, scanner hardware is capable of performing this reconstruction and feedback in less than 50 *ms*. Whereas during breath hold acquisitions, limited time is available to acquire images at will, with the ability to measure respiratory position, data may be acquired over an extended period of time when the respiratory and cardiac cycle coincide [154,174-176]. This, however, is an extremely inefficient method of acquiring data as the frequency at which these two cyclic patterns meet requires either large gating windows or increasingly long scan times. A development of this allows for multiple breath holds, with monitoring of respiratory position and feedback to the patient [177]. This has been used for coronary imaging using either bellows [178] or navigator echoes [159,179] to measure respiratory position, providing consistent respiratory position for imaging while significantly improving the scan efficiency in comparison with respiratory gating techniques. For CAD patients, however, some difficulty is found in cooperating with respiratory feedback systems to accurately repeat breath holds [180].

A further drive in CMR towards enhanced spatial resolution and scan efficiency with improved motion adaptation is the recent development in prospective motion tracking [181].

In its basic form, real-time slice-following is used to shift the imaging slice for each data segment according to the respiratory position, as determined by the preceding navigator echoes [130,160,182]. In coronary imaging, it has been shown that the superior-inferior (SI) motion of the coronary artery origin, relative to that of the diaphragm, is linear with that of the RCA origin, being on average approximately 0.6 times that of the diaphragm [156]. Tracking is consequently frequently implemented with a fixed correction factor of 0.6 [183,184], despite evidence that there is considerable variability between subjects [156,183,185,186]. The alternative is to implement subject-specific SI correction factors calculated as the shift in the position of the origin of the artery of interest between small inspiratory and expiratory breath-hold acquisitions relative to that of the diaphragm, as measured by interleaved navigator echoes or by direct imaging [187]. Anterior-posterior motion of the arteries is currently either ignored or assumed to be a fixed percentage (20%) of that occurring in the SI direction [156]. In most studies, left-right motion is assumed to be negligible. It has been recognised that due to a failure of the linear model, or due to the use of inaccurate correction factors relating the motion of the artery to that of the diaphragm, many of the existing techniques for adaptive tracking only permit modest increases in navigator window width.

The effectiveness of the adaptive motion correction method is therefore limited by the presence of structures with motion characteristics different from that of the coronary artery. To avoid these problems and make prospective tracking more practical, a locally focused imaging technique has been proposed which uses elaborated RF pulses to excite only the 3D volume of interest [130,160,185]. Since only the volume of interest is excited and imaged, respiratory synchronised uniform motion of the coronary artery and its surrounding vessels can be assumed. An adaptation of the reduced FOV method described in Chapter 3 caters for cyclic motion [188]. This is achieved by using navigators to consider the motion occurring outside of the reduced FOV but within the full imaging FOV. Prior to the scan, static reference data is acquired over a number of cyclic motions to build up a set of reference data for multiple positions. During the reconstruction stage, dynamic data is supplemented by the reference scan information that is most suitable to the current dynamic data based on the navigator measurement.

4.4.3 Phase encode reordering

Fourier imaging techniques are particularly sensitive to motion, which may occur due to physiological function such as cardiac contraction, respiratory motion or direct patient movement on the couch. Phase encode reordering has been proposed to maximise the scan efficiency by considering the information content of the *k*-space data and avoiding sharp variations between adjacent *k*-space encoding steps. Traditionally, Cartesian phase encode sampling schemes operate by acquiring line-by-line from the bottom end of *k*-space to the top. With phase encode reordering schemes, respiration is monitored and an attempt is made to acquire lines of *k*-space with a shallow phase gradient between encoding steps, due to minimal respiratory movement between steps. The advantage of these techniques is that, in contrast to respiratory gating methods [174], usable data is acquired during each of the acquisition steps.

The first of these phase encoding algorithms is known as Respiratory Ordered Phase Encoding (ROPE) [189]. This method reorders the acquisition of *k*-space lines so as one extreme of phase encoding points in *k*-space represents end expiration and the other extreme end-inspiration with intermediate points smoothly varying in between. Through statistical analysis of the respiratory positions measured prior to the scan ROPE can effectively acquire phase encode lines to follow the required pattern. A development of this known as Centrally Ordered Phase Encoding (COPE) [190,191], which aims to acquire the central lines of *k*-space during full expiration, to minimise motion during the acquisition of the low frequency image information. For this method, no prior knowledge of respiratory pattern need be acquired during a pre-scan, as displacements towards end inspiration are arranged proportionally through the outer *k*-space in a symmetrical manner. This has the advantage of robustness against changes in breathing patterns, which even when small can introduce significant error. The incorrect mapping of phase encoding lines, that occurs when the probability profiles change, is the most common problem in phase-reordering algorithms. One further technique known as Hybrid Ordering of Phase Encoding (HOPE) [192] combines the two previous techniques mapping the most frequent respiratory positions to the centre of *k*-space (whether that is at end expiration or not) and attempts to obtain a smooth distribution either side for the outer regions of *k*-space. This technique is found to be the most adaptable to real breathing patterns and can be further improved if the mapping function is continually updated during the acquisition.

These techniques have been shown to improve image quality over conventional methods, and in combination with a navigator acceptance window allow for larger acceptance windows without sacrificing image quality. The methods, however, are still susceptible to changes in breathing patterns reducing the efficiency of the respiratory window. Phase ordering with Automatic Window Selection (PAWS) [193] is a navigator acceptance technique which requires no prior knowledge as the acceptance window is not pre defined. *k*-space is split into three bins and the first navigator reading determines the 0 point for acquisition of data. From there, data is collected to fill one of the three bins at each acquisition. Each respiratory position is associated with acquisition for one of the three bins, and the selection of this is rotated through the range of respiration. Given a navigator reading associated with one of the two outer bins data is collected from the outer edge moving towards the middle, while acquisition for the central bin works from the centre in the direction which would prospectively result in the earliest completion of *k*-space based on the data already at neighbouring respiratory positions. At termination, three neighbouring respiratory bins complete *k*-space, with uniform respiratory position during acquisition of the central region of *k*-space, and at most a jump of 2 steps for either of the outer regions of *k*-space. This method is resilient to changes in breathing patterns, requires no prior information or interaction from the operator and allows data acquired in the presence of respiratory motion to be acquired in the shortest possible time.

4.4.4 Adaptive respiratory gating

Similar to phase encode reordering algorithms, adaptive respiratory gating techniques combine traditional respiratory gating to localise the acquisition window to a narrow respiratory range with advanced algorithms for the determination of the gating threshold function [194]. This allows for variation of the gating threshold for different phase encoding steps with a narrower range of acceptable motion where most detrimental to image quality, and broader ranges of motion in less significant regions of *k*-space.

In Chapter 3, a locally focused imaging technique with RF excitation was described for coronary imaging [130]. The use of prospective gating significantly reduced the artefact from respiratory motion. Due to the large respiratory gating window (~5 *mm*) required to achieve acceptable scan efficiency, respiratory motion makes a large contribution to the error in the measured data. From Equation (3.3) of Page 73 the error introduced into v_m can be represented as:

$$\Delta v_m = \sum_{i \in \{L\}} \left[\left(R^{+} R \right)^{-1} R^{+} \right]_{mi} \Delta f\left(i \Delta k_y \right) \tag{4.1}$$

where $\Delta f\left(i \Delta k_y \right)$ is the error caused by noise and respiratory motion. By attempting to minimise the sum of these errors we can derive a weighting to represent the relative contribution that errors in each of the L measured k_y steps make to the estimated phase encode signals. This then permits an adaptive respiratory window to optimise the scan efficiency for each measured phase encode signal. The recorded diaphragmatic position for each phase encoding step was then used as a weighting function for performing a weighted least mean squares estimate of v_m by adapting Equation (4.1) as:

$$v_m = \sum_{i\in\{L\}} \left[\left(R^+ W R \right)^{-1} R^+ W \right]_{mi} f\left(i \Delta k_y \right) \tag{4.2}$$

where W is a $L \times L$ real positive diagonal matrix and

$$W_{ii} = 1 - \beta \frac{\left| p_i - p_{ref} \right|}{p_{\max}} \tag{4.3}$$

In Equation (4.3) β is a weighting parameter and p_i, p_{ref} and $p_{\max}$ represent the associated diaphragm displacement, the user defined reference position and the maximum allowed value, respectively. This method allowed for optimally efficient navigator acceptance windows for acquired phase encode lines. This is demonstrated on a phantom study in Figure 4-6 where the use of locally focused encoding and adaptive respiratory gating (b) significantly improves the result over full phase encoding with conventional respiratory gating, while also reducing the scan time. By increasing the scan time in (b) and reducing the available respiratory window, further improvement is made to the resulting reconstruction shown in (c). With this scheme, it has been demonstrated that it is possible to achieve an overall scan efficiency of 90% without sacrificing the image quality, compared to the 60% that is achievable using the conventional approaches [130]. For the phantom study a 3D database was created, by translating the phantom along the imaging y axis within the range of ±8 *mm* in 1 *mm* intervals. A 3D zonal echoplanar data set was acquired at each position with all raw *k*-space data indexed and stored.

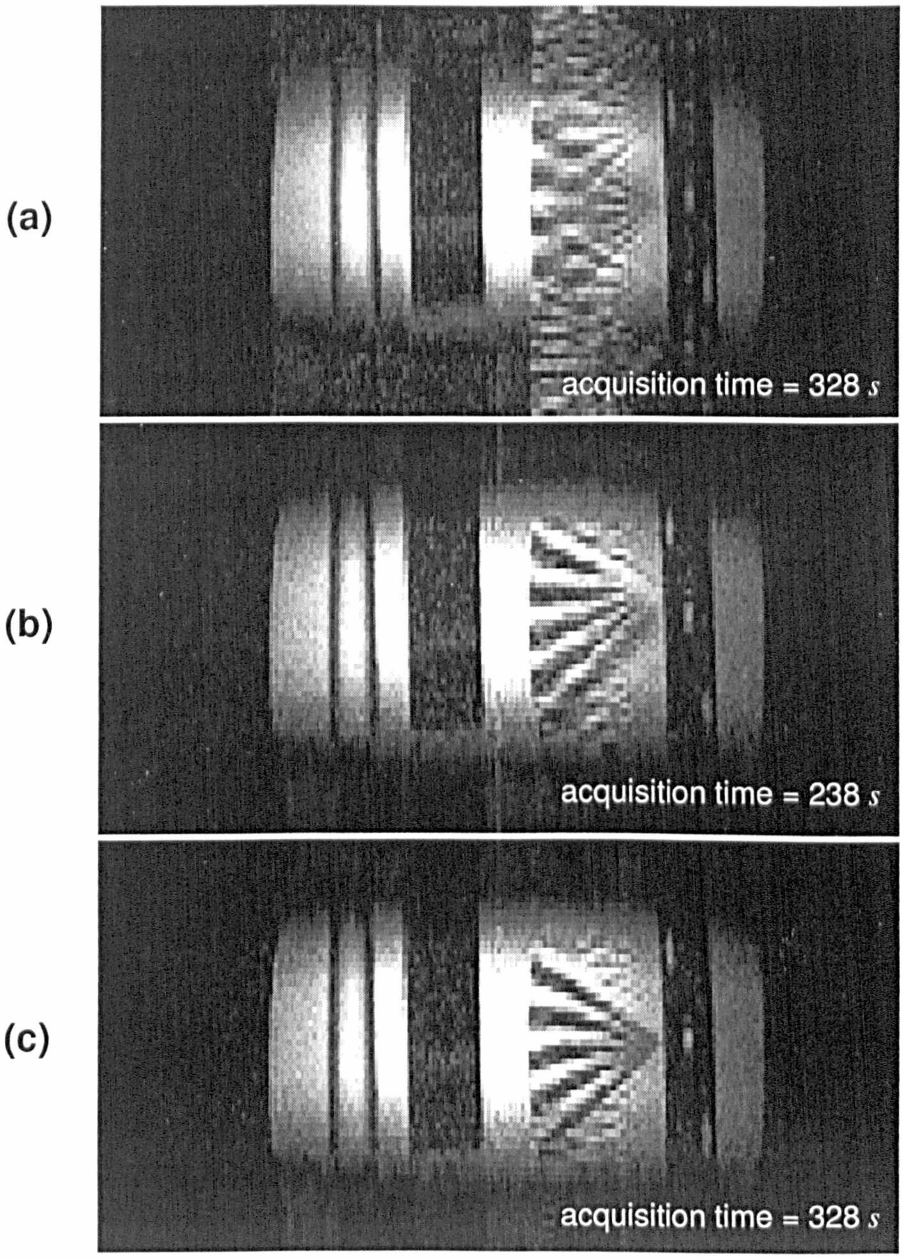
(a)
acquisition time = 328 *s*
(b)
acquisition time = 238 *s*
(c)
acquisition time = 328 *s*

Figure 4-6 A phantom evaluation of locally focused encoding and adaptive respiratory gating. (a) conventional respiratory gating with full phase encoding, (b) adaptive respiratory gating with locally focused encoding reducing the imaging time, and (c) as with (b) but with an increase in imaging time from 238 *s* to 328 *s*. With permission from Yang *et al* [130].

4.5 Motion decoupling and image registration

4.5.1 Motion correction in first pass myocardial perfusion MRI

Thus far, the use of breath holds is common in first pass myocardial perfusion imaging. Although useful, the length of the breath hold is often in excess of what a patient can reliably sustain and along with upward creep effects discussed earlier can be a source of error in later analysis. Additionally, when the breath hold fails the motion is often large as the patient recovers their breath, in excess of normal free breathing. The use of respiratory gating in conjunction with cardiac gating creates problems, as the frequencies of the two cyclic motions do not coincide resulting in infrequent imaging windows unlikely to coincide at critical points in the passage of contrast agent such as the up-slope of the blood pool and myocardium. Manual correction of image motion and similarly frame-by-frame manual delineation of ROI's, are current but labour intensive means of providing accurate signal time curves. A typical myocardial perfusion study can amount to over 100 images with both rest and stress images being considered. This creates a lengthy task for the analysis of the data and is likely to be a hindrance for the further advancement and clinical acceptance of quantitative analysis for MR myocardial perfusion studies. Automatic contour detection for registration and delineation is troublesome due to relative and absolute signal intensity variations between ventricles, myocardium and surrounding anatomy. The use of image registration can simplify the contour delineation process.

4.5.2 Post processing and image registration

The registration of cardiac images is a complex problem due to the deformable nature of the heart. The heart is a non-rigid structure that can be compressed and deformed through a combination of contraction and external forces due to respiration. In addition, surrounding visceral structures exhibit different forms of displacement and deformation. While rigid translation and global affine transformations can help correct for a large amount of cardiac displacement, they cope poorly with the deformation of the heart structure that can commonly occur due to respiration. In addition, the registration of images can be advantageous to cross modality complimentary assessments of cardiac structure and function. The effect of motion and deformation of the heart on subsequent signal time curve analysis is shown in Figure 4-7. Following registration, the point remains located in the myocardium, thus providing an accurate representation of regional myocardial perfusion.

In post processing any remaining motion following the image acquisition procedure may be resolved. This is often carried out at a separate location to the scanning, as it is not reliant on any real time collaboration with the scanning procedure. When describing image registration, the terms 'reference image' and 'transform image' are often used. The reference image is the model on which the registration is based. The transform image is then translated and rotated and deformed to undergo a transformation so that it is aligned to the reference image. Image registration is an extensively researched area in image processing and has often been applied to a variety of applications. The methods involved in image registration can be divided into two main categories, based on geometric image features, and voxel similarities respectively.

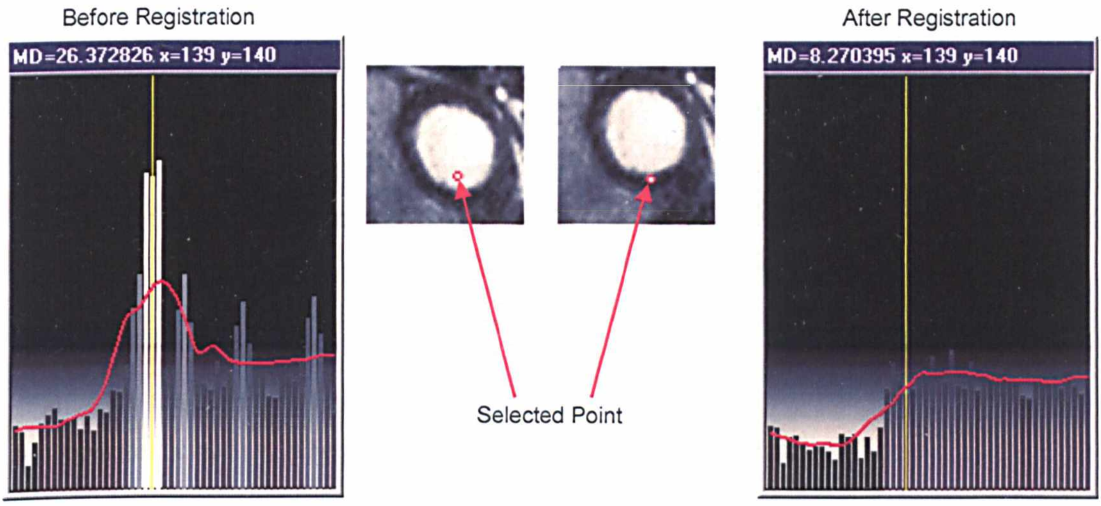

Figure 4-7 The effect of in-plane motion on the resulting intensity time curves. Prior to registration, the signal time curve from the selected point shows significant variation through time moving from the blood pool to the myocardium, the cyclic nature of which is primarily due to respiratory motion. After registration the same pixel is located within the myocardium throughout the sequence. This produces a much smoother intensity time curve giving a more accurate measurement of the required myocardial tissue.

Geometric feature based image registration

Registration using this method aims to align geometrically defined features within the transform image to corresponding features within the reference image. This includes edge and ridge based methods, and the alignment of known anatomical points. A shape-based method has been used on MR myocardial perfusion images by using the border of the LV and RV as well as the pericardium [195]. In addition, an active contours method with the myocardium defined in polar coordinates has been demonstrated [196]. Problems with such a system are significant. The methods are reliant on accurate localisation of features, the edges of which must be present throughout the sequence, which may not always be the case with the dynamic passage of the contrast agent. Perfusion defects may lead to new edges being created during critical periods of the first pass of contrast agent.

Voxel based image registration

For myocardial perfusion imaging, our aim is to align all images to a common model. This implies choosing a single reference image for the registration process. Due to the nature of the image acquisition, the most suitable image chosen as the reference image is the final one from the series. This is due to better contrast and enhancement than the initial frames.

The types of transformation applied can then be separated into rigid and affine transformations, and free form or fluid deformations.

Rigid and affine deformation

A rigid transformation is a transformation that preserves the distance between any two points within an image. A rigid transformation can be expressed as the combination of rotation, translation and reflection. This can effectively represent bulk motion of the imaged object although is unable to represent deformation of the image to be aligned.

An affine transformation results in coordinates which are a linear function of the original coordinates x and y. The general 2D affine transformation can be written as:

$$\mathbf{T}(x,y)=\begin{pmatrix}\theta_{11} & \theta_{12}\\ \theta_{21} & \theta_{22}\end{pmatrix}\begin{pmatrix}x\\ y\end{pmatrix}+\begin{pmatrix}\theta_{13}\\ \theta_{23}\end{pmatrix} \qquad (4.4)$$

where the coefficients θ parameterise the 6 degrees of freedom of the transformation. Affine transformations have the general property that parallel lines are transformed into parallel lines. Examples of affine transformations are translation, rotation, scaling, reflection and shear. The set of affine transformations can be expressed as a combination of these five transformations.

Affine transformations are able to deal with more complex motion such as basic compression or shear forces applied to a soft tissue structure such as the heart. A general affine transformation alone has been shown to significantly improve the analysis of myocardial perfusion [197]. Due to the non-uniformity of the structure of the heart, the exact deformation that may occur cannot be fully represented using global affine transformations.

Free form deformation (FFD)

FFD registration is a method that allows for elastic or fluid transformations. While rigid or affine transformations allow for misalignment due to changes in location or viewing angles, they do not perform well when a change in shape has occurred between the reference and transformed image. This is particularly true when the object is of a soft deformable nature. Free form transformations may be performed in a number of ways. The simplest method is to use a combination of local rigid and affine transformations [198]. A refinement of this performs the localised deformations using thin-plate splines for point-based elastic registration [199]. Control points are chosen uniformly across the image to form a grid like structure. The coordinates of these control points are then optimised so that the similarity measure between the two images is maximised.

More recently, the use of B-splines [200] for describing a continuous FFD in non-rigid image registration [201] has been investigated. B-splines are locally controlled, offering computational advantages over thin-plate splines as the number of control points increases. The approximating tensor product B-spline can be represented as:

$$T(u,v) = \sum_{i=1}^{m}\sum_{j=1}^{n} B_i(u)C_j(v)\mathbf{c}_{ij}\ , \quad \mathbf{c}_{ij} \in R^3 \tag{4.5}$$

where B_i and C_i are B-spline coefficients at control-points c_{ij} that minimise the sum of squared errors $\sum_{k=1}^{N}\left\|\mathbf{s}(\mathbf{u}_k) - \mathbf{x}_k\right\|^2$. When cubic B-spines are used [202], matrix $\mathbf{B}$ becomes

$$\mathbf{B} = \begin{bmatrix} B_1(u_1)C_1(v_1) & B_2(u_1)C_1(v_1) & \cdots & B_m(u_1)C_n(v_1) \\ \vdots & \vdots & & \vdots \\ B_1(u_N)C_1(v_N) & B_2(u_N)C_1(v_N) & \cdots & B_m(u_N)C_n(v_N) \end{bmatrix} \tag{4.6}$$

The uniform B-spline coefficients are formulated using the following set of bases:

$$\begin{aligned} B^{i-1} &= \frac{1}{6}(1-u)^3 & \qquad B^{i+1} &= \frac{1}{6}\left(-3u^3 + 3u^2 + 3u + 1\right) \\ B^{i} &= \frac{1}{6}\left(3u^3 - 6u^2 + 4\right) & \qquad B^{i+2} &= \frac{1}{6}u^3 \end{aligned} \tag{4.7}$$

An example of image registration performed using B-splines is shown in Figure 4-8. The control point displacement field is shown in image (c) which represents the motion from image (a) to image (b). The resulting transformed image is shown in (d).

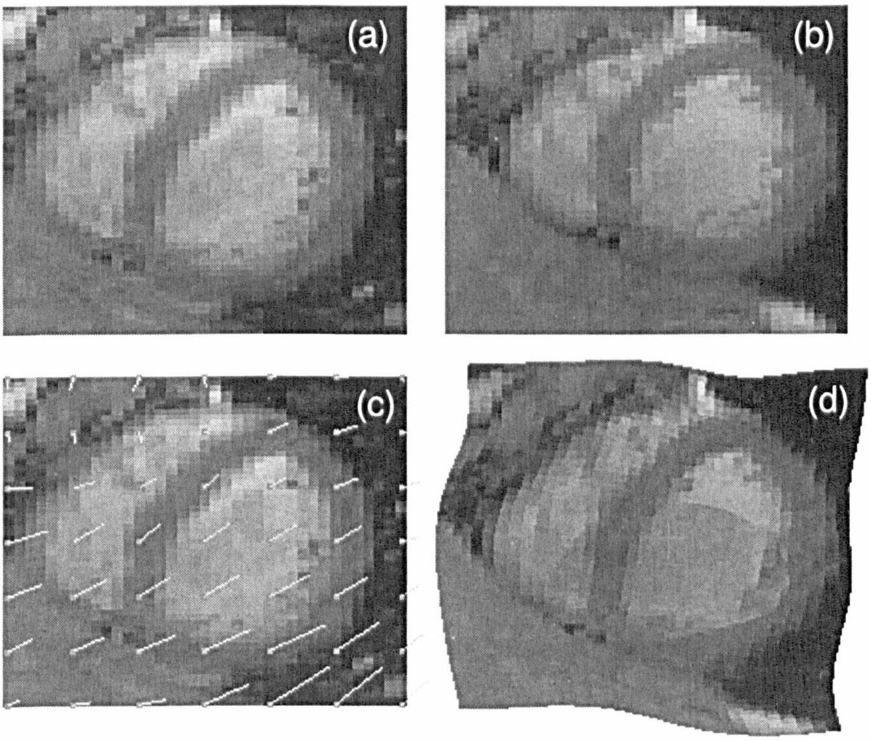

Figure 4-8 Two frames from a short axis cardiac gated sequence. (a) is used as a reference to which (b) is transformed. (c) shows the displacement of a 9×9 control point grid, overlaid on the reference image. (d) is the deformed version of (b) by using the B-spline deformation field.

In performing pixel-based registration, the choice of similarity measure is critical to the successful optimisation. There are two similarity measures most commonly used, these being cross correlation and normalised mutual information.

Cross correlation

Cross correlation is an optimal measure for the similarity of two images given a linear relationship between their intensities. The correlation coefficient is a normalised measure of cross correlation, and is defined as the ratio between the covariance of the two images, and the product of their respective standard deviations. For two images I_1 and I_2 and transform T, applied to I_2, the correlation coefficient C is defined as:

$$C = \frac{\sum_{x,y}\left(I_1(x,y)-\bar{I}_1(x,y)\right)\left(I_2(T(x,y))-\bar{I}_2(T(x,y))\right)}{\sqrt{\sum_{x,y}\left(I_1(x,y)-\bar{I}_1(x,y)\right)^2\sum_{x,y}\left(I_2(T(x,y))-\bar{I}_2(T(x,y))\right)^2}} \quad (4.8)$$

where $\bar{I}$ represents the mean of the corresponding image.

In general, the limitation of cross correlation as a similarity measure is the problems it has dealing with cross modality images. In first pass myocardial perfusion studies images, great variation in absolute and relative contrast and intensity need to be aligned, thus making cross correlation type similarity measures unsuitable.

Mutual Information

Mutual information is a method based on information theory that has been successfully applied to the alignment of MR images [203]. This is particularly useful when cross correlation fails, as no constraints are placed on the dependence of pixels between images. This has allowed the method to be applied in image alignment between different modalities [204]. Mutual information measures the ability of the model to predict the image, rather than making a pixel-by-pixel comparison, as is the case with cross correlation. The value of the mutual information measure depends upon the entropy and joint entropy of two random variables. In the case of image registration, these variables are the pixel intensities of the images.

If we assume that pixels are discrete random variables, then entropy can be defined as a measure of the randomness of the variables. Low entropy means that the average probability over the support set for given random variables is low. The entropy H of the discrete random variables X, can be defined as:

$$H(X) = -\sum_{x \in X} p\{x\} \log(p\{x\}) \tag{4.9}$$

Joint entropy can be used to measure alignment or similarity. Two identical samples will have lower joint entropy when aligned than when misaligned. Two constant regions will also have low joint entropy, which is not desirable. The joint entropy $H(X,Y)$ of the discrete random variables X, Y, can be defined as:

$$H(X,Y) = -\sum_{x \in X} \sum_{y \in Y} p\{x,y\} \log(p\{x,y\}) \tag{4.10}$$

While joint entropy may be used as a similarity measure, it does have limitations. This is due to its representation of two constant regions. If joint entropy alone were used as a similarity metric the registration may converge to a point where the background has been transformed so as to cover the whole image. In the majority of registration problems, this seriously reduces the stability of the procedure. To avoid this, we use mutual information. The mutual information I of images M and N based on pixel values m and n with discrete density p is:

$$I(M,N)=\sum_{m\in M}\sum_{n\in N}p\{m,n\}\log\frac{p\{m,n\}}{p\{m\}p\{n\}} \tag{4.11}$$

By maximising mutual information we minimise the information in the combined images with respect to that present in the two component images. Therefore we aim to have a large amount of information in the individual images while having little extra information in the combined images. So the mutual information can be viewed as a measure of the independence of the two variables M and N.

$I(M,N)$ can also be written as:

$$I(M,N)=H(X)+H(Y)-H(X,Y) \tag{4.12}$$

$$I(M,N)=H(X)-H(X|Y) \tag{4.13}$$

$$I(M,N)=H(Y)-H(Y|X) \tag{4.14}$$

where the conditional entropy $H(N,M)$ is defined as:

$$H(N|M)=-\sum_{m\in M}\sum_{n\in N}p\{m,n\}\log(p\{n|m\}) \tag{4.15}$$

The normalised mutual information [205] of the two images M and N based on their entropy H, and joint entropy $H(M,N)$ can then be defined as:

$$H(M,N)=\frac{H(M)+H(N)}{H(M,N)} \tag{4.16}$$

This differs from standard mutual information as it considers the amount of mutual information with respect to the information provided by the individual images. This favours transformations that maximise the proportion of information shared between the images, rather than favouring transformations that result in high marginal entropies of the two images.

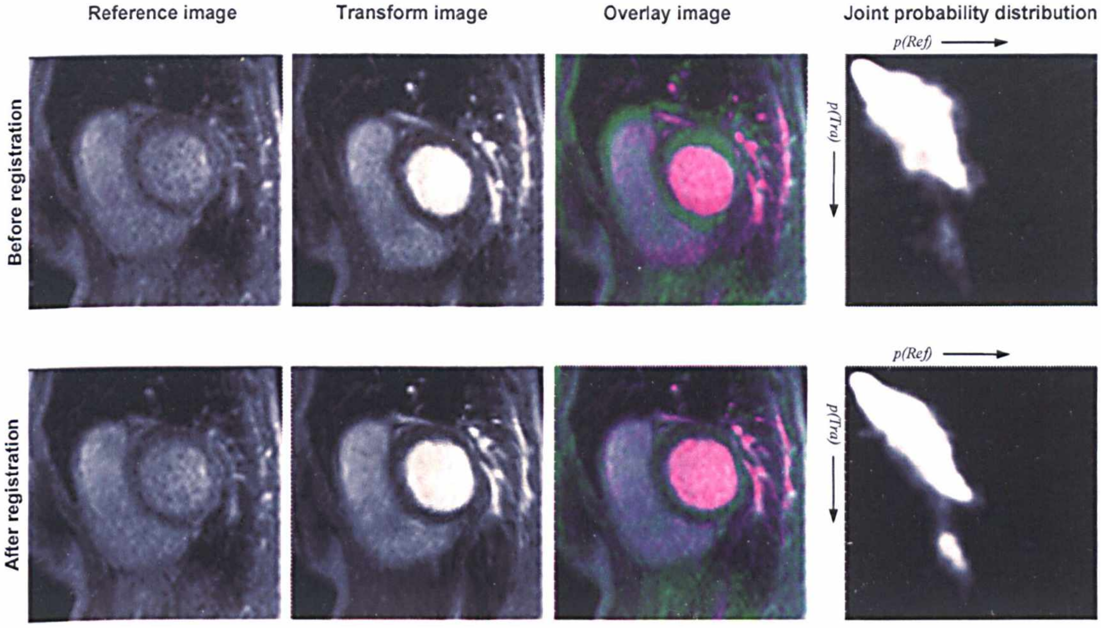

Figure 4-9 A comparison of the probability distribution of two images both before and after registration. A green (reference) and magenta (transform) overlay shows the difference between the two images. The joint probability distribution is plotted for each intensity within the image.

Figure 4-9 shows the result of free form 2D image registration. The reference image is fixed and the transform image undergoes a FFD to minimise a normalised mutual information function. The green magenta overlay shows the initial mis-registration and the result after the transformation. The two separate intensity images (the reference image being in green and the transform image in magenta) are combined through summation, where the equal combination of the two colours produces grey as shown in the myocardium after registration. The resulting magenta colour of the blood pool is due to the relative difference in contrast of the blood pool between the reference and transform image due to the high concentration of the contrast agent within the blood pool at the time of the acquisition of the transform image. The joint probability distribution represents the corresponding pixel intensities in the reference and transform image, with the joint probability of a pixel in the reference image having the intensity *p(Ref)* and the intensity *p(Tra)* in the transform image. If the two images are identical, the probability distribution would be a single diagonal line, in terms of mutual information the more compact the joint probability distribution the less information required to describe the relationship between the two images, *i.e.* the more similar they are.

The choice of optimisation scheme for the corresponding similarity measure as well as the smoothness constraint placed on the transformation, are important in both achieving the desired result as well as limiting the computation burden. This can be carried out with multi-resolution approaches where initially low-resolution images are used to perform coarse global optimisation before iteratively refining the resolution and the detail of the transformation. Rigid registration is more reliable and precise while non-rigid registration provides more accurate results, but is more susceptible to error and computationally expensive. Rigid registration relies on a larger region of the image to obtain a similarity measure, while the non-rigid approach uses a smaller region so is more susceptible to noise and changes between the reference and transform image, other than motion. With careful application, non-rigid free form registration is able to align myocardial perfusion images suitable for automatic analysis of the perfusion indices.

4.6 Adaptive slice tracking for perfusion imaging

To demonstrate the effect of cardiac motion on multi-slice perfusion imaging, we show in this section the amount of mis-registration introduced by the use of MR tissue tagging. As mentioned previously, in 3D myocardial perfusion imaging, a complete volumetric data set has to be acquired for each cardiac cycle, and this can result in 50-100 such 3D data sets for studying the first pass of the contrast bolus. To ensure a comprehensive coverage of the myocardium and reasonably high resolution of the images, a typical data acquisition window of 100-200 *ms* per slice, and thus the overall acquisition time of more than 600 *ms*, is required for each cardiac cycle to cover the entire volume of the LV. When using multi-slice imaging, cardiac motion during this large acquisition window can cause the myocardium captured in different image planes to be mis-registered, *i.e.*, some part of the myocardium may be imaged more than twice whereas other parts may be missed out completely. This type of mis-registration is difficult to correct for by using post-processing techniques. We show here how to use online slice tracking to alter the location of each imaging plane such that it always follows the same tissue of the myocardium throughout the perfusion imaging period.

Prior to perfusion imaging, a tagging sequence is used to highlight the short axis through plane motion of the heart. This consists of a Vertical Long Axis (VLA) and Horizontal Long Axis (HLA) tagged cine sequence within a single heartbeat, with the tag lines cutting through the short axis of the LV. An example of the tagged cine sequences with imaging planes overlaid is shown in Figure 4-10. The tags within these two cines are tracked throughout the cardiac cycle and a plane is fitted with least-mean-squares errors to the HLA and VLA short axis tag locations. The exact orientation of particular short axis planes within the myocardium is now known. Following from this, a standard multi-slice perfusion sequence is applied, which automatically adjusts the location and orientation of the imaging plane according to different trigger delays. The method assumes that the rate and extent of contraction of the LV is consistent between the motion tagging scan and subsequent perfusion imaging. The above procedures ensure that the through plane motion of the heart is captured during imaging. The decoupled in-plane motion can then be corrected for by using free-form 2D image registration techniques.

Images used for this study were obtained using a Siemens Sonata (1.5 *T*; 200 *T/m/s*; 40 *mT/m*) and a four-element phased-array receiver coil. The HLA and VLA tagged cine images were obtained in the same 16 cardiac cycle end-expiratory breath-hold, using segmented FLASH imaging. In each cardiac cycle, a multi-planar ("comb") saturation pulse was applied after the R-wave to tag three short-axis 2 *mm* slices with 15 *mm* gaps, followed by acquisition of the cine phases to image the moving tags, using a low flip-angle to minimise disruption of M_z. The cine phases were timed to cover central *k*-space at the same delay times after the R-wave as the slices of the perfusion sequence. The perfusion sequence was a 3-slice single-shot FISP sequence, obtaining an image every 156 *ms* starting at the R-wave trigger, and was obtained at end-expiration. For validating the motion tracking, no contrast agent was administered to the subjects, and therefore the magnetisation preparation (a saturation pulse) was switched off. Five asymptomatic subjects aged 24.4±7.3 were recruited for validating the proposed technique with informed consent.

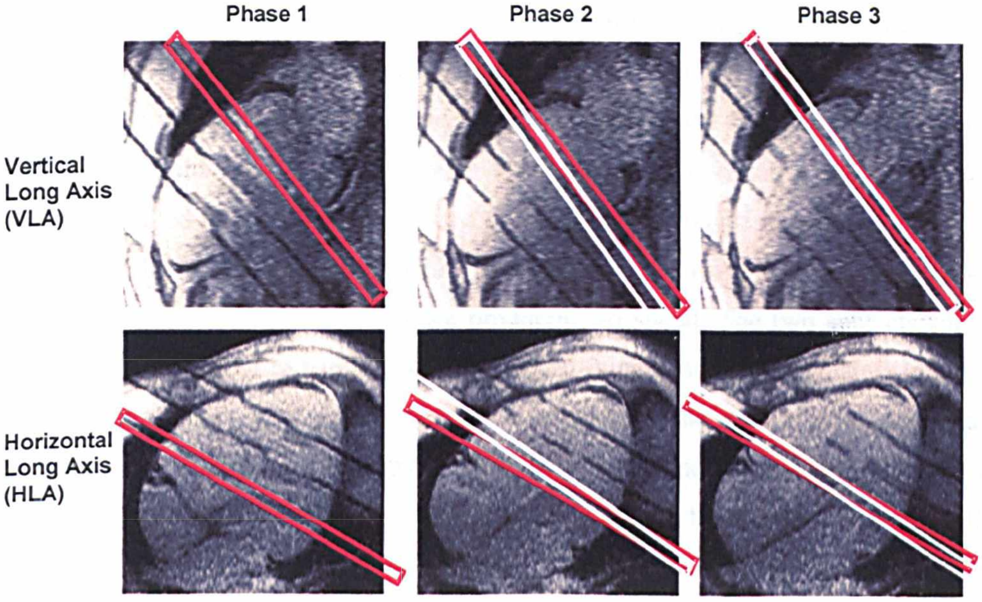

Figure 4-10 Schematic illustration of the basic procedures used for prospective tracking of through plane cardiac motion. Cine myocardial tagging is performed on both the VLA and HLA of the LV from which the positions of the tracking planes are derived. Shown on the above diagram we see the locations of the planes both before (dark) and after (light) the relocation due to the results of the tracking. Large displacement can be seen, particularly during phase 2 of the three-phase cine sequence.

As a comparison, the area of the myocardium of the LV was measured, with and without motion tracking, for each short axis slice of the five subjects studied. The three short axis slices were taken within the same cardiac cycle, with the most apical slice acquired first and the most basal slice last. The bar chart in Figure 4-11 indicates the absolute differences in measured regional errors in mm^2 without motion tracking.

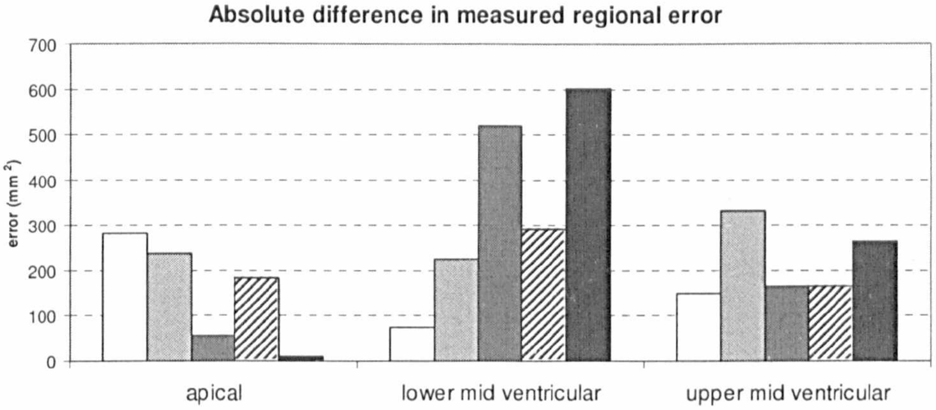

Figure 4-11 The absolute difference in measured regional error of three slices acquired during one cardiac cycle for five subjects. The apical slice was acquired first within the cardiac cycle and the basal slice last. The resulting error without motion tracking is shown and is generally greatest during the mid phase of the cardiac cycle.

Figure 4-12 demonstrates the effectiveness of the slice tracking procedure. A special test pulse sequence is used. Which through the subtraction of the two images, one acquired at phase 1 and the other during phase 2 and 3 with the application of a saturation band in the imaged plane at the start of each cardiac cycle, is able to visualise the error in slice alignment. A nulled image subtracted from a positive image produces a positive image, if the slices are misaligned the saturated plane moves out of the imaging plane and a positive image is subtracted from a positive image producing no signal. The two subjects show the misalignment caused due to cardiac contraction that is generally at its greatest in phase 2. With the tracking procedure applied, phase 2 clearly shows the correct slice of myocardial tissue being shown, although due to the shift in the image plane the surrounding tissue is no longer visible. The first subject clearly shows a rotation in the heart with the septal wall and RV moving through the imaged plane, whereas the second subject shows the whole plane shifting, particularly in phase 2.

Figure 4-13 shows an example of the effect of cardiac contraction on the imaging of multi-slice short axis planes. Image (a) shows three tags across the VLA of the LV, and (b) shows their deformation after 202 *ms*. Without motion tracking, the most basal imaging slice erroneously enters into the left atrium, as shown in (c). By using the proposed tracking technique, the correct short axis plane, as shown in image (d), is captured.

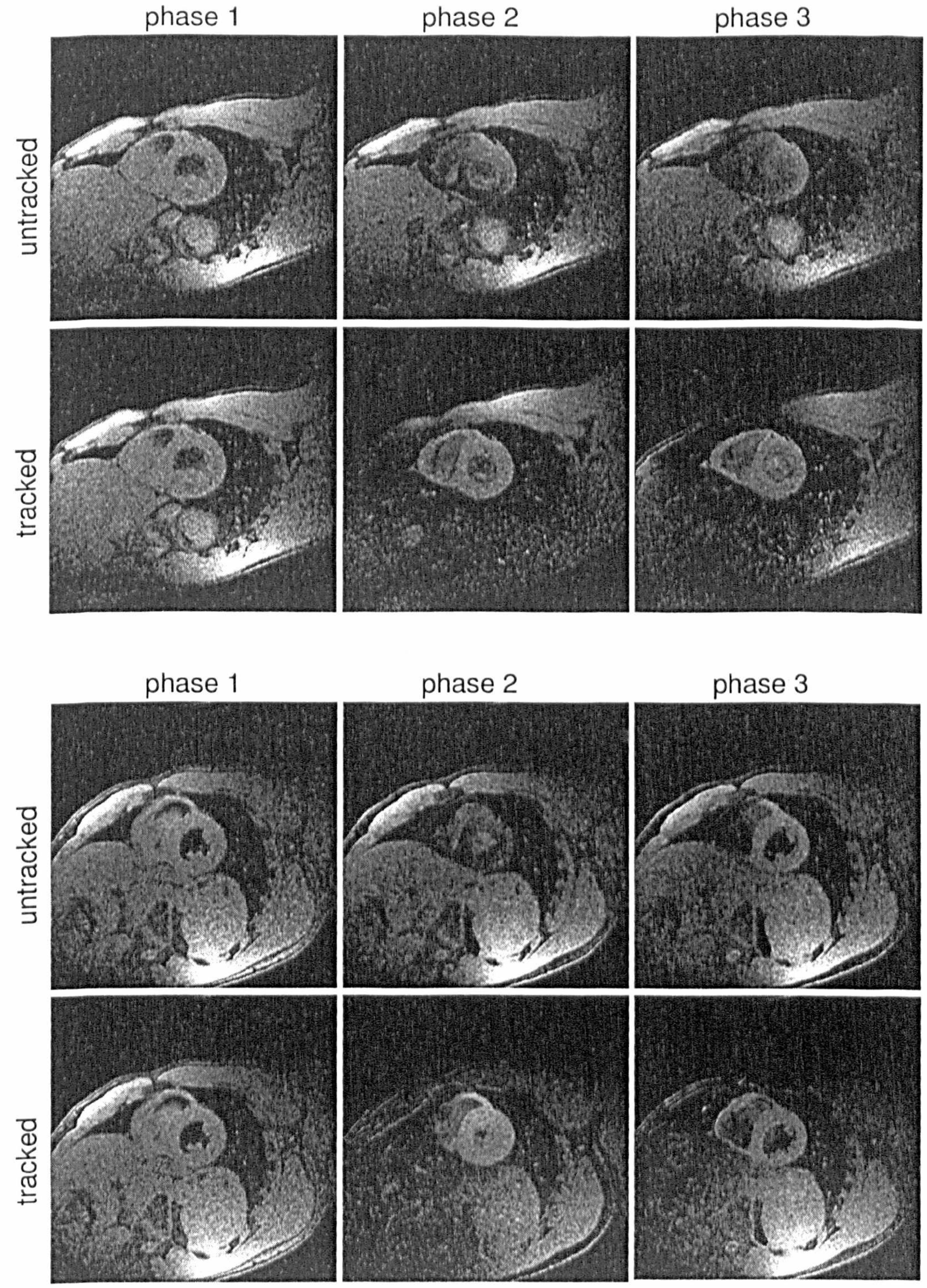
phase 1
phase 2
phase 3
untracked
tracked
phase 1
phase 2
phase 3
untracked
tracked

Figure 4-12 Using a special test pulse sequence shows the effectiveness of slice tracking for two subjects above. Signals form the myocardium should remain uniform and enhanced if the imaging planes are accurately tracked over time. This can clearly be seen for the tracked sequence while on the untracked the correct tissue is not imaged during phase 2 and 3.

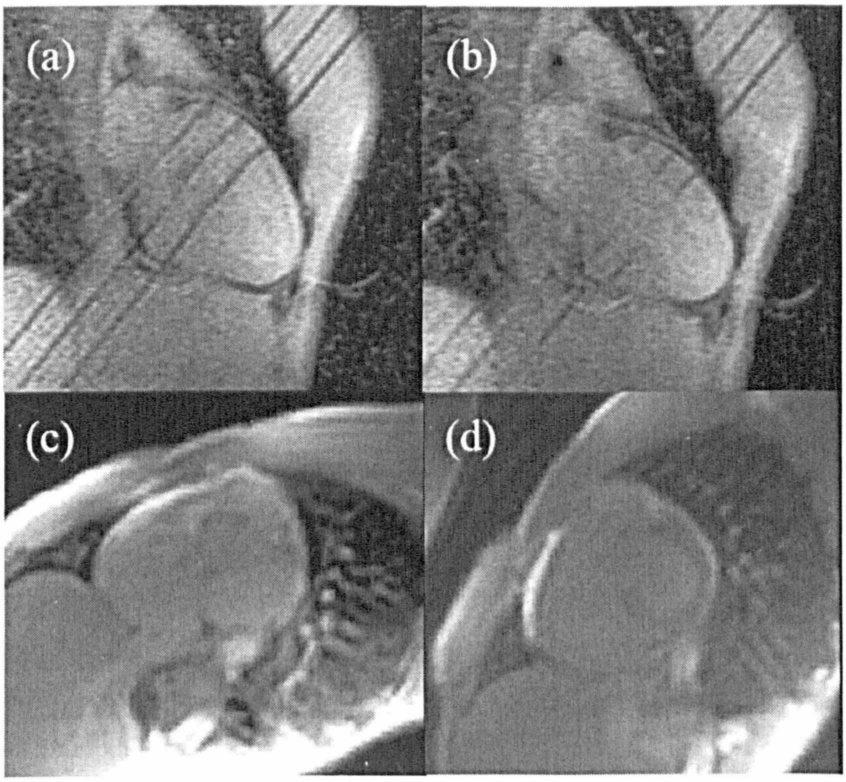

Figure 4-13 An example of the effect of cardiac contraction on the imaging of multi-slice short axis planes. Image (a) shows three tags across the VLA of the LV, and (b) shows their deformation after 202 *ms*. The most basal of the three slices is shown after 202 *ms* without tracking (c) and with tracking (d).

Motion tracking is important for 3D myocardial perfusion imaging. The use of slice tracking ensures regional contrast uptake variations are followed accurately over time. The current study indicates the gross error introduced if cardiac motion is ignored during the large acquisition window normally required in 3D perfusion imaging. Work in progress includes the incorporation of online correction of respiratory motion induced cardiac deformation by using subject specific motion calibration and real-time diaphragm navigator echoes, and assessing the relative significance of cardiac and respiratory motion induced errors to subsequent myocardial perfusion quantification.

4.7 Conclusions

In this chapter, we have discussed the basic patterns of respiratory motion and different methods that have been developed in linking *k*-space acquisition with respiratory dynamics. Techniques such as ROPE, COPE, and HOPE make use of *k*-space re-ordering to minimise motion artefact introduced due to motion discontinuities between adjacent *k*-space encoding steps. This in effect, turns high frequency artefact into local blurring of the imaging structure, which makes it much more acceptable for clinical examinations.

Traditionally, techniques based on navigator echoes follow the assumption that there is a linear or near linear relationship between the navigator trace and the movement of the visceral structure. Although positioning the navigator carefully through the dome of the diaphragm ensures good reproducibility of the technique, further studies have shown that for many subjects a single navigator echo may not be able to predict the expected cardiac deformation. This has motivated extensive research in the use of multiple navigators for coronary imaging [206,207]. These methods generally use three navigator echoes placed on the diaphragm and also on the walls of the heart. An implementation using a diminishing variance algorithm that effectively acts as an adaptive gating procedure has been proposed [206]. More recently principal components analysis has been applied to multiple navigators for predictive affine motion modelling of the coronaries [207].

In this chapter, we have presented an adaptive slice tracking method for adjusting the imaging plane dependent on the time past the ECG trigger. While this currently accounts only for cardiac contractile motion during breath hold, cardiac and respiratory tracking methods can be combined so as the scanner images the same slice of the myocardium through the series. This will significantly reduce the through plane motion due to cardiac contraction and respiratory motion, and may be able to reduce much of the in plane motion during the acquisition stage. The method while potentially effective is based on a uniform pattern of motion due to heart contraction and respiratory motion. This is not always the case during the actual scans. The breathing may be performed with more emphasis on the diaphragm or the rib cage, and the interaction between the cardiac and respiratory motion is not necessarily straightforward. Due to this further free form registration is required after the images have been acquired to account for localised deformation.

Chapter 5 : Predictive Motion Modelling

5.1 Introduction

In Chapter 4, we have outlined key technical issues related to cardiac and respiratory motion for myocardial perfusion imaging. The management of inconsistent physiological motion is one of the major considerations of high-resolution cardiac imaging. For different imaging modalities, the effect of patient motion and its associated artefacts are well recognised. In general, patient motion can be grouped into voluntary and involuntary motions. Voluntary motion includes unpredictable movements of the patient during data acquisition, which can be avoided with patient cooperation, improved couch design, or certain levels of straining. Involuntary motion, on the other hand, involves movements of the organs such as those due to cardiac and respiratory motion. It also includes motion that is induced by physiological loadings such as stress or exercise. For example, it is well known that during exercise the heart is displaced inferiorly against the diaphragm as the thorax expands, whereas during recovery the heart starts to "creep" back up into the thorax. This is called upward creep [167]. In practice, if the involuntary motion is cyclic, motion artefact can be eliminated through the use of effective gating. Acyclic motion, however, remains a major challenge to current imaging techniques. In SPECT, the effect of upward creep can lead to artefact manifesting as reversible defects in the infero-septal wall, and is often coupled with other image degrading factors such as attenuation, collimator-detector blurring and scatter [167]. For Intensity Modulated Radiation Therapy, a promising tool for dose escalation in the management of mobile thoracic and abdominal lesions, respiration-induced organ motion may greatly degrade the effectiveness and efficiency of the treatment [208-210]. Respiratory induced cardiac deformation is also one of the main limiting factors for PET and 3D echocardiography [168-170].

In cardiovascular MR, the effective management of acyclic motion due to respiration is driven by the ongoing demand for the assessment of cardiovascular anatomy and function with higher image resolution, particularly for examining vessel walls and small coronary arteries. Despite considerable advances in MR techniques over the last 10 years, imaging of the coronary arteries remains a technically challenging task, primarily due to the small size and tortuous pathways of the arteries coupled with complex cardiac and respiratory motions [211,212]. Whilst the effects of cardiac motion may be dealt with by acquiring data at mid-diastole when the heart is relatively stationary, respiratory motion is more difficult to control. Figure 5-1 depicts the extent of respiratory induced motion as measured from the three axes of the LV. The options available are to either acquire the data during a period of suspended breathing [171], or perform data acquisition during free breathing but with respiratory gating [154,174]. Although the former effectively freezes respiration, the need to limit the duration of data acquisition to that of a comfortable breath-holding period imposes significant limitations on the image quality obtainable both in terms of spatial temporal resolution and the SNR. The method also requires a certain level of patient co-operation that may not always be forthcoming, either due to illness or anxiety. The alternative technique of respiratory gating [154,174] requires the monitoring of respiratory patterns. Navigator echoes are an MR technique for acquiring signal from a column of material running perpendicular to the motion with the use of a readout gradient along its length [157]. Basic processing of the received signal enables the position of the moving edge to be determined. If the navigator echoes are interleaved with the imaging sequence, prospective decisions may be made either to retain or to discard the data acquired. This removes the need for patient co-operation but since imaging is now only performed during a small part of the respiratory cycle, the scan efficiency is considerably reduced. Although increasing the navigator acceptance window width increases the scan efficiency, this is at the expense of allowing data acquisition over a greater range of respiratory motion and is therefore to the detriment of image quality.

The strength and flexibility of CMR in providing *in situ* respiratory motion measurements has permitted the development of a number of more advanced techniques for adapting *k*-space data acquisition with different levels of respiratory induced motion. Phase encode reordering has been proposed to maximise the scan efficiency by considering the information content of the *k*-space data and avoiding sharp variations between adjacent *k*-space encoding steps [189,192,194]. All of these methods require online processing of the navigator signals and prospective adjustments of the phase encoding steps. This is made possible through recent advances in MR imaging hardware and computer architecture design. The use of phase encode reordering allows data acquisition even in the presence of larger cardiac deformation; therefore with less data being thrown away, greater scan efficiency can be achieved.

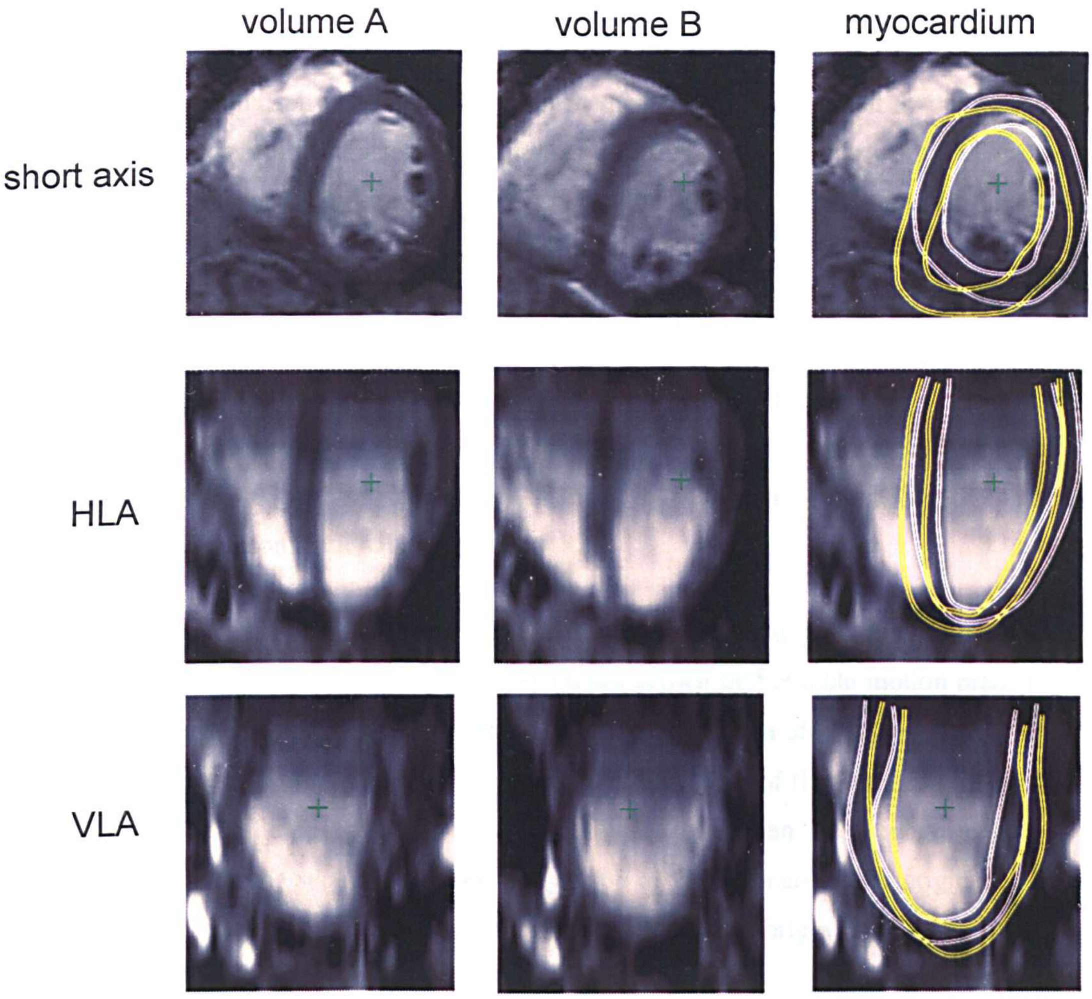

Figure 5-1 An example of the extent of respiratory induced cardiac motion. Three views of the heart are shown along three orthogonal axes. For each view (Volume A) is end-expiration and (Volume B) is end-inspiration at the same stage of the cardiac cycle. Also shown is the location of the myocardium at the two extremes (Myocardium). Large translation and deformation of the shape of the LV is observed. This displacement can be as much as 15*mm*.

A further drive in CMR towards enhanced spatial resolution and scan efficiency with improved motion adaptation is the recent development in prospective motion tracking [181]. In its simplest form, real-time slice following is used to shift the imaging slice for each data segment according to the respiratory position, as determined by the preceding navigator echoes [130,160,182]. The accuracy of this technique is critically dependent on the accuracy of the navigator echo to predict the cardiac motion. Furthermore, for this approach to be practical some major issues have to be considered. In 2D conventional imaging techniques, the size of the object or the effective response area of the RF coils governs the FOV. Under common image orientations, static and mobile visceral structures are both present. If the algorithm is designed to correct global rigid motion, then the static object will be portrayed as if it were moving synchronously with the mobile object, and thus may introduce 'pseudo motion' artefacts. This situation is more complicated when non-uniform motion of the objects within the FOV occurs, which is true for the case of coronary imaging. The effectiveness of the adaptive motion correction method is therefore limited by the presence of structures with motion characteristics different from that of the coronary artery. To avoid these problems and make prospective tracking more practical, a locally focussed imaging technique has been proposed which uses elaborated RF pulses to excite only the 3D volume of interest [130,182,185]. Since only the volume of interest is excited and imaged, respiratory synchronised uniform motion of the coronary artery and its surrounding vessels can be assumed. With this scheme, it has been demonstrated that it is possible to achieve an overall scan efficiency (percentage of acquired data which is suitable for image reconstruction) of 90% without sacrificing the image quality, compared to the 60% that is achievable using the conventional approaches [182].

Although imaging with real-time tracking and adaptation has shown great promise in a number of clinical applications, existing research has shown that reliable motion prediction is the key to the success of the imaging result. The implementation of adaptive tracking over such a large range of motion requires an accurate understanding of the intrinsic relationship between the motion of the target anatomical structure and respiration. In coronary imaging, it has been shown that the superior-inferior (SI) motion of the coronary artery origin, relative to that of the diaphragm, is linear with that of the RCA origin, being on average approximately 0.6 times that of the diaphragm [156]. Tracking is consequently frequently implemented with a fixed correction factor of 0.6 [183,184], despite evidence that there is considerable variability between subjects [156,183,184,186]. The alternative is to implement subject-specific SI correction factors calculated as the shift in the position of the origin of the artery of interest between small inspiratory and expiratory breath-hold acquisitions relative to that of the diaphragm, as measured by interleaved navigator echoes or by direct imaging [187]. Anterior-posterior motion of the arteries is currently either ignored or assumed to be a fixed percentage (20%) of that occurring in the SI direction [156]. In most studies, left-right motion is assumed to be negligible. It has been recognised that due to a failure of the linear model, or to the use of inaccurate correction factors relating the motion of the artery to that of the diaphragm, many of the existing techniques for adaptive tracking only permit modest increases in acceptable respiratory range.

The improvement of MR hardware has allowed rapid imaging of the entire cardiac structure with much reduced imaging time. This permits a more detailed assessment of the effect of cardiac motion and deformation in response to respiratory motion. Recent studies have confirmed the significance of inter-subject variability and the need for *in situ* subject specific motion modelling [153,213]. A prospective translational motion correction method based on image registration of 3D respiratory motion data has been used to derive more accurate and subject specific motion tracking for coronary imaging [153]. The use of diaphragmatic navigators is now a popular choice for coronary imaging and the adaptation of coordinated multiple navigator tracers is an ongoing research topic [206,207]. The quest for higher image resolution as required for vessel wall imaging has called for more sensitive real-time motion measurement techniques to be explored. In CMR, researchers are investigating the use of complementary MR-compatible sensing methods to perform real-time measurements of surface distortions due to respiration. The strength of these techniques is that they do not require the interleaved acquisition of navigators, and thus significantly simplify the pulse sequence design. Furthermore, it makes the technique easily transportable to other imaging modalities. The problem with these methods, however, is that surface measured signals are strongly coupled with each other but poorly correlated with respiratory induced cardiac deformation. Numerically, this can create significant problems for recovering the inherent model that explains the causality between respiratory motion and surface deformations. The purpose of this chapter is to present a new technique of predictive cardiac motion modelling and correction based on Partial Least Squares Regression (PLSR). PLSR is a recent technique that generalises and combines features from principal component analysis and multiple regression. It originated in Social Sciences and became popular in Chemometrics [214]. Its ability to extract correlation between input and output data that is itself highly collinear, allows it to deal with problems that would be inappropriate for multi linear or principal components regression. In imaging, it has also been used for analysing spatial patterns of functional brain images [215].

In Appendix B a predictive motion modelling technique using PLSR for 2D CMR myocardial perfusion imaging is presented and is based on previous investigations into this work. The predictive motion modelling method described in this chapter is designed for extracting intrinsic relationships between 3D cardiac deformation due to respiration and multiple 1D real time measurable surface intensity traces. By using reconstructed 3D image data sets, detailed numerical issues related to the technique are discussed and the effectiveness of the method is validated with data acquired from ten asymptomatic subjects using motion modelling for the entire respiratory range.

5.2 Materials and methods

The basic principle of the proposed method is shown in Figure 5-2, which outlines the key steps involved. The initial subject specific modelling of cardiac deformation involves 2D/3D imaging of the anatomical structure combined with *in situ* real-time measurable inputs. Registration based on FFD or finite element modelling can be used to recover the underlying spatio-temporal deformation of the anatomical structure. The causality between tissue deformation and real-time measurable signals, such as surface deformations, is then extracted through the use of PLSR. At the prediction stage, real-time measurable inputs are used to predict cardiac deformations without the need for further 2D/3D imaging so that adaptive imaging can be performed in real-time to track the anatomical regions of interest.

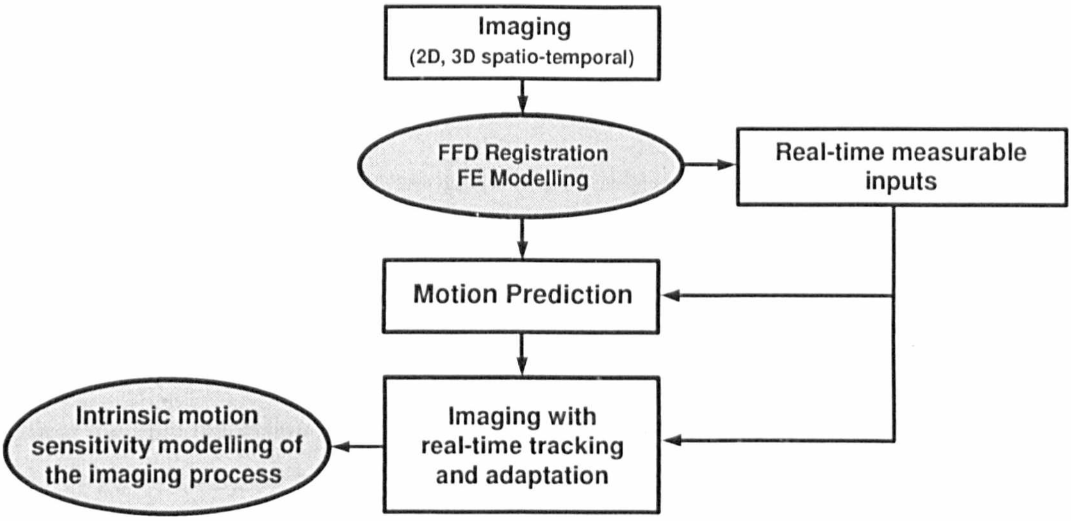
Imaging
(2D, 3D spatio-temporal)
FFD Registration
FE Modelling
Real-time measurable inputs
Motion Prediction
Intrinsic motion sensitivity modelling of the imaging process
Imaging with real-time tracking and adaptation

Figure 5-2 A diagrammatic representation of the proposed predictive motion modelling scheme. Initial 2D/3D imaging is used along with real-time measurable inputs to create a motion model that can be used as the input to the imaging system for achieving real-time motion adaptation.

5.2.1 Deformation recovery with 3D free-form image registration

To recover cardiac deformation and establish its intrinsic correlation with real-time measurable surface signals, 3D image volumes depicting different stages of the cardiac deformation due to respiration are used. The extraction of 3D deformation vectors was performed by using the free-form image registration method [201] as described in Chapter 4. With this technique, a hierarchical transformation model of soft tissue deformation is employed, in which the global motion of the heart is modelled by an affine transformation whereas local deformation is described by free-form deformation based on B-splines. The normalised mutual information [205] was used as a voxel-based similarity measure and registration was achieved by minimising a cost function that encapsulates contributions associated with both the smoothness of the transformation and the overall image similarity.

To ensure a good optimisation performance, the algorithm worked by decoupling global and local motion such that only the affine transformation parameters are optimised initially. This was then followed by optimising the non-affine transformation parameters at increasing levels of resolution of the control point mesh. For this study, no manual delineation of the cardiac border was performed on the 3D volume. To reduce the image registration time, however, the 3D volume is manually trimmed to a rectangle containing the heart at the full range of respiratory positions. The final number of control points used was 9×9×9 to cover the image volume, which gives the total degrees-of-freedom of 2187. With this registration approach, the deformation of each volume in relation to a selected reference volume was characterised by the movement of control vertices of the B-splines, the associated 729 3D vectors were used for the PLSR algorithm to determine their intrinsic relationship with real-time measurable signals associated with different levels of respiratory motion.

5.2.2 Predictive motion modelling and PLSR

The traditional approach of using navigator echoes only involves a single navigator trace and the prediction of cardiac deformation in this case can be achieved via simple correlation. Simple regression can be described as the relation between selected values of x and observed values of y. With this relation, probable values of y may be predicted from the observed value of x. For example linear regression may be represented in a form such as $y=ax+b$. Linear multiple regression is an extension of this where the value of one dependent variable may be predicted on the basis of two or more predictor variables *e.g.* $y=a_0+a_1x_1+a_2x_2 \ldots a_ix_i$. The drawbacks of this method are that it only can only predict a single dependent variable, and relies on the predictor variables being linearly independent. In order to predict two or more dependent variables an extension of multiple regression sometimes called multivariate regression may be used. If multiple traces are used and by assuming that the respiratory motion components detected are linearly independent, multivariate regression may be used. When multiple surface measurements are used, however, one can no longer guarantee that these measurements are mutually independent. If **X** is assumed to be the surface measurements at a given instant of the respiratory cycle (predictor) and **Y** to be the respiratory induced cardiac motion (response), there will be a significant amount of redundancies in both **X** and **Y**. This is because the FFD model used for deformation recovery involves uniformly sampled control vertices and some of the vertices may be strongly correlated depending on the cardiac structure being covered. Conversely, the placement of surface measurements for real-time monitoring of respiratory motion is difficult to control and redundancies are inevitable.

The goal of PLSR is to predict **Y** from **X** and to describe their common structure. When **X** is full rank, this can be accomplished by using ordinary Multi Linear Regression (MLR). In practice, **X** is likely to be singular due to multi-collinearity of the predictors and the regression approach is no longer feasible. To avoid this problem, one can either use step-wise methods to eliminate some predictors or apply principal component analysis to the **X** matrix to extract the principal components of **X** as regressors on **Y**. Although the orthogonality of the principal components eliminates the multi-collinearity problem, the issue of choosing an optimum subset of predictors remains. By contrast, PLSR regression finds components from **X** that are also relevant for **Y**. Specifically, PLSR searches for a set of components called latent vectors that perform a simultaneous decomposition of **X** and **Y**, with the constraint that these components explain as much as possible of the covariance between **X** and **Y** [216]. Figure 5-3 illustrates a sample data set similar in spirit to the one used in [217] where 22 sample readings corresponding to input **X** with dimensions x_1 and x_2 are used. The corresponding matrices are given by Equations (5.1) to (5.6) as shown below.

$$\mathbf{X} = \begin{bmatrix} -5 & -5 \\ -4 & -4 \\ -3 & -3 \\ -2 & -2 \\ -1 & -1 \\ 0 & 0 \\ 1 & 1 \\ 2 & 2 \\ 3 & 3 \\ 4 & 4 \\ 5 & 5 \\ 0.5 & -0.5 \\ 0.4 & -0.4 \\ 0.3 & -0.3 \\ 0.2 & -0.2 \\ 0.1 & -0.1 \\ 0.0 & 0.0 \\ -0.1 & 0.1 \\ -0.2 & 0.2 \\ -0.6 & 0.3 \\ -0.4 & 0.4 \\ -0.5 & 0.5 \end{bmatrix} \qquad \mathbf{Y} = \begin{bmatrix} 0 \\ 0 \\ 0 \\ 0 \\ 0 \\ 0 \\ 0 \\ 0 \\ 0 \\ 0 \\ 0 \\ -10 \\ -8 \\ -6 \\ -4 \\ -2 \\ 0 \\ 2 \\ 4 \\ 6 \\ 8 \\ 10 \end{bmatrix} \tag{5.1}$$

Equation (5.1) shows the two matrices used in Figure 5-3 with **X** representing the input data and **Y** representing the response data. It is evident that the first 11 y samples are constant although much variation is seen in the corresponding x samples. This variation in x is therefore unrelated to the output y and can be considered as noise or interference. The variation seen in the last 11 samples, however, is more closely related to the variation seen in y.

$$PC = \begin{bmatrix} -7.07 & 0 \\ -5.66 & 0 \\ -4.24 & 0 \\ -2.83 & 0 \\ -1.41 & 0 \\ 0 & 0 \\ 1.41 & 0 \\ 2.83 & 0 \\ 4.24 & 0 \\ 5.66 & 0 \\ 7.07 & 0 \\ 0 & -0.707 \\ 0 & -0.566 \\ 0 & -0.424 \\ 0 & -0.283 \\ 0 & -0.141 \\ 0 & 0.0 \\ 0 & 0.141 \\ 0 & 0.283 \\ 0 & 0.424 \\ 0 & 0.566 \\ 0 & 0.707 \end{bmatrix} \qquad (5.2)$$

$$PCAaxis = \begin{bmatrix} 0.707 & -0.707 \\ 0.707 & 0.707 \end{bmatrix} \qquad (5.3)$$

$$\mathbf{X}^{\mathbf{T}}\mathbf{Y} = \begin{bmatrix} -22 \\ 22 \end{bmatrix} \qquad (5.4)$$

$$EV = \begin{bmatrix} 10.48 \\ 0.10 \end{bmatrix} \qquad (5.5)$$

$$\mathbf{XX}^{\mathbf{T}}\mathbf{Y} = \begin{bmatrix} 0 \\ 0 \\ 0 \\ 0 \\ 0 \\ 0 \\ 0 \\ 0 \\ 0 \\ 0 \\ 0 \\ -22.0 \\ -17.6 \\ -13.2 \\ -8.8 \\ -4.4 \\ 0.0 \\ 4.4 \\ 8.8 \\ 13.2 \\ 17.6 \\ 22.0 \end{bmatrix} \qquad (5.6)$$

By performing Principal Components Analysis (PCA) on the **X** matrix, it transpires that the principal modes of variation correspond to the diagonals of the plot of **X** shown in Figure 5-3. From the eigenvalues (Equation (5.5)) we see that the first principal component (the first column in Equation (5.2)) accounts for 99% of the variation in **X**, but is useless for predicting **Y**. A typical implementation of principal components regression would ignore the second PC (the second column in Equation (5.2)) because it only contributes 1% of the variation in **X**. In contrast, PLSR evaluates $\mathbf{X}^T\mathbf{Y}$ (Equation (5.4)) to calculate the required coefficients and the resulting $\mathbf{X}\mathbf{X}^T\mathbf{Y}$ matrix (Equation (5.6)) is equivalent to the second principal component of the PCA result. This is exactly what is needed for describing the variation in **Y**.

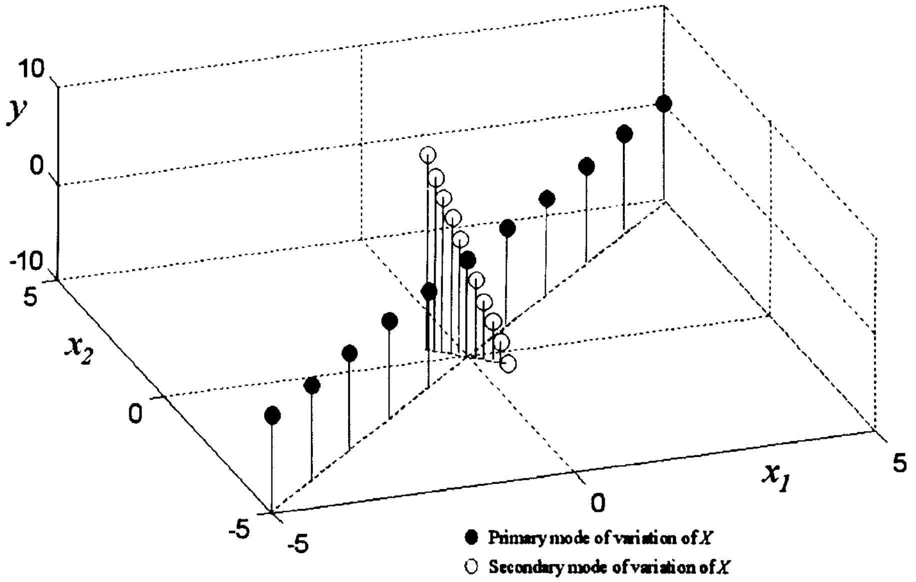

Figure 5-3 An example data set illustrating the basic concept of PLSR. The input data has two variables x_1 and x_2 and these are plotted against the output variable y. The solid circles show the primary mode of variation in X while the open circles show the secondary mode of variation. After applying PCA on X, it is found that the solid circles represent around 99% of the variation. The graph shows that although the solid circles represent the majority of the variation within X they do not help to describe the variation in Y. In fact the variation present in the open circles, while only representing 1% of the variation in X, is the only useful information in describing the variation in Y.

The use of principal components regression reveals the principal source of variation in **X** being contributed by those samples marked with solid colour in Figure 5-3. A close examination of these samples has shown that although they contribute to over 99% of the variation in **X**, the response of these samples are constant, and the variation in **X** is therefore not useful for predicting **Y**. By contrast, the somewhat smaller variation in samples marked with open circles have a more direct relationship with variation in **Y**, despite the fact that they only explain 1% of the variation in **X**. In practice, it is possible that significant information for describing the variation in **Y** may be hidden in **X** to the extent that principal components regression may exclude this information as noise. In PLSR, the direction in the space of **X** is sought, which yields the biggest covariance between **X** and **Y**. The method examines both the **X** and **Y** data and extracts the factors that are significant to both of them.

The factors extracted are in order of significance, by evaluating $\mathbf{X}^T\mathbf{Y}$, the primary factor with which **X** determines the variation in **Y** in Figure 5-3 corresponds to the open circles.

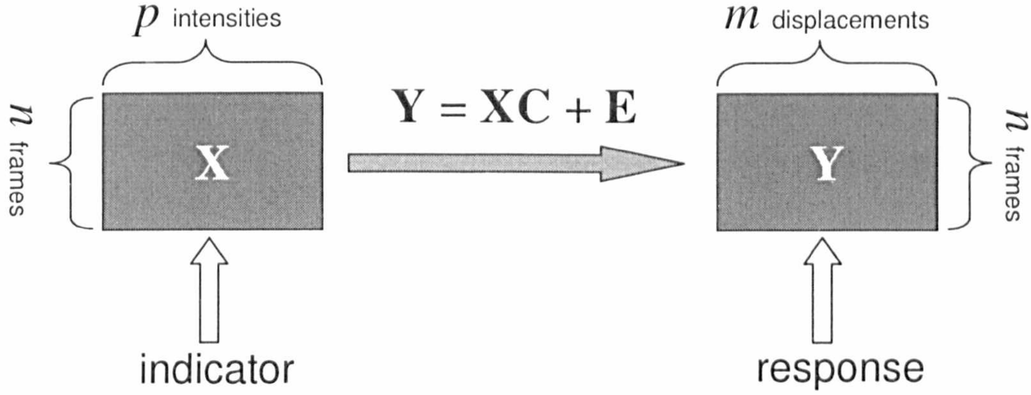

Figure 5-4 A systematic representation of the intrinsic relationship between the *p* intensities used as an indicator and the *q* displacements as the response used in the learning and predication. This relationship is shown in terms of the matrices **X** and **Y** for *m* frames of a sequence. **C** is the coefficient matrix which when combined with the input **X** is able to predict the response matrix **Y**, **E** represents noise and higher order terms that are not accounted for in the above relationship.

The intrinsic relationship of the key steps involved in the proposed framework for predictive motion modelling can be summarised in Figure 5-4. Let's assume that the dimension used to describe the distribution of myocardial deformation is *q* and the dimension used to describe each surface measurement for the respiratory motion is *p*. When a total number of *m* experiments are performed to extract the relationship between **X** and **Y**, the size of the matrices will be $m \times p$ and $m \times q$ for **X** and **Y**, respectively. With PLSR, both the predictor and response matrices are decomposed, such that

$$\mathbf{X}_c = \mathbf{T}\mathbf{P}^T + \mathbf{E} \tag{5.7}$$

and

$$\mathbf{Y}_c = \mathbf{U}\mathbf{Q}^T + \mathbf{F} \tag{5.8}$$

where **P** is the factor loading matrix and **Q** is the coefficient loading matrix and **E** and **F** are factors in **X** and **Y** that are not described by the PLSR model. In the above equations, $\mathbf{X}_c$ and $\mathbf{Y}_c$ represent the mean centred matrices of **X** and **Y**, respectively. PLSR tries to find a score vector $\boldsymbol{t}$ in the column space of $\mathbf{X}_c$ and a score vector $\boldsymbol{u}$ in the column space of $\mathbf{Y}_c$ such that

$$\mathbf{t} = \mathbf{X}_c\mathbf{w} \tag{5.9}$$

$$\mathbf{u} = \mathbf{Y}_c\mathbf{q} \tag{5.10}$$

to give the maximal squared covariance for $(\mathbf{u}^T\mathbf{t})^2$. That is, the process aims to maximise $(\mathbf{q}^T\mathbf{Y}_c{}^T\mathbf{X}_c\mathbf{w})^2$ subject to $|\mathbf{w}| = |\mathbf{q}| = 1$. The solution to this equation is given by an eigenvalue problem of $\mathbf{X}_c^T\mathbf{Y}_c$, *i.e.*,

$$\mathbf{X}_c^T\mathbf{Y}_c\mathbf{Y}_c^T\mathbf{X}_c\mathbf{w} = \lambda\mathbf{w} \tag{5.11}$$

where λ is the eigenvalue associated with **w**. In essence, the method searches for a set of latent vectors that performs a simultaneous decomposition of **X** and **Y** with the constraint that these components explain as much as possible of the covariance between **X** and **Y**. Rather than linking measurements **X** and **Y** directly, the method tries to establish the inner relationships between latent variables **T** and **U**, derived from **X** and **Y** respectively, *i.e.*,

$$\mathbf{U} = \mathbf{TB} + \mathbf{U}_\mathbf{E} \tag{5.12}$$

where **B** is a diagonal matrix that has the regression weights as the diagonal elements and $\mathbf{U}_\mathrm{E}$ is an error term similar to **E** and **F** above. When these error terms are ignored, the predicted value of $\mathbf{Y}_c$ can be calculated as

$$\mathbf{Y}_c = \mathbf{TBQ}^T \tag{5.13}$$

Figure 5-5 gives a schematic diagram showing how the PLSR framework is applied to the current framework for predicting myocardial deformation. The method allows for a large number of predictor variables to be used even when the principal modes of variation of the response variables are limited. It is particularly useful when the data involved is highly collinear as it accounts for redundancies in both the predictor and responses. The basic principle of PLSR was developed in 1960 by Herman Wold [218] as an econometric technique but is often used by chemical engineers and chemotricians. Numerically, the solution to the equations presented above can be solved iteratively through Nonlinear Iterative Partial Least Squares (NIPALS) method [214]. The pseudo code in Figure 5-6 represents the key computational steps of the NIPALS algorithm and our MATLAB (Mathworks, Natick, MA) implementation is provided in Appendix A. Each execution of the loop extracts a latent variable of the data. The loop terminates when the required number of latent variables are extracted or when A, M or B reduces to (or close to) zero, which implies the current number of factors suitably represents the data.

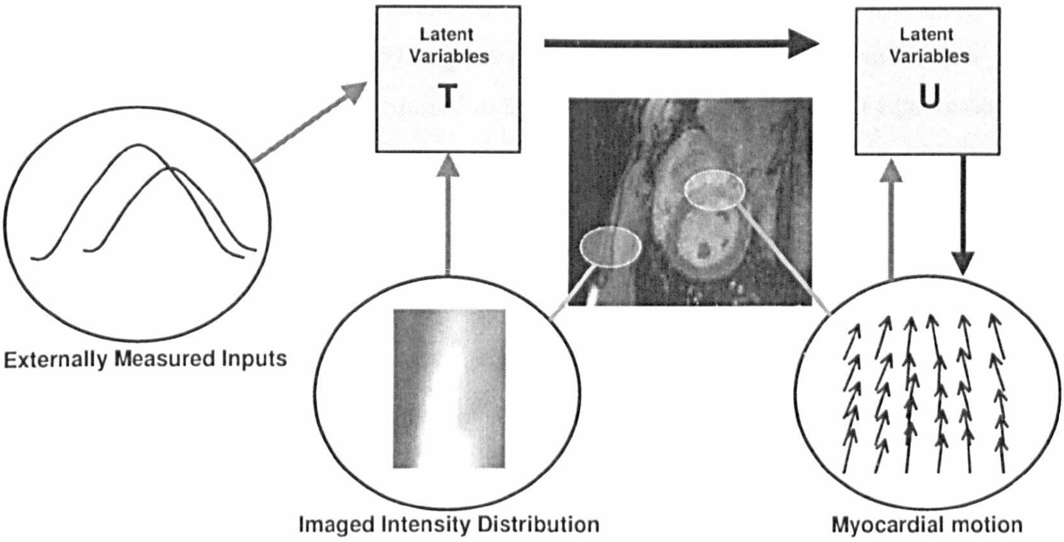

Figure 5-5 A schematic diagram of the PLSR method used for deformation modelling and prediction. In this example, multiple measurements of surface intensity distributions are used as the input, from which latent variables factors are extracted. A similar process is also applied to the observed output data, in this case the deformation vectors of the heart derived from the control vertices of the free-form image registration algorithm. A model that establishes the intrinsic correlation between **T** and **U** is then derived. At the prediction stage, 3D myocardial deformation is directly predicted from the intensity patterns measured at the chest wall, which can be performed in real-time.

```
Zero-mean and scale the input $\mathbf{X}$ and the output $\mathbf{Y}$.
Set starting matrix $\mathbf{M}=\mathbf{X}^T\mathbf{X}$, $\mathbf{A}=\mathbf{X}^T\mathbf{Y}$ and $\mathbf{B}=\mathbf{I}$.
For the required number of principal components
    Calculate the first eigenvector of $\mathbf{A}^T\mathbf{A}$, save as the first coefficient loading vector $q_1$, in row form
    Calculate the corresponding weighting vector $w_1=\mathbf{B}\mathbf{A}q_1$ in column form normalized as $w_k=w_k/||w_k||$;
    Calculate the first factor loading vector $p_1=\mathbf{M}w_1/f$ in column form, where $f=w_1^T\mathbf{M}w_1$, and then update the coefficient loading vector $q_1$ as $q_1=\mathbf{A}^T w_1/f$
    Exclude the extracted information from initial variance matrix $\mathbf{M}$, co-variance matrix $\mathbf{A}$ and unit matrix $\mathbf{B}$: $\mathbf{A}=\mathbf{A}-fp_1q_1$, $\mathbf{M}=\mathbf{M}-fp_1p_1^T$, $\mathbf{B}=\mathbf{B}-w_1p_1^T$;
    If either $\mathbf{A}$, $\mathbf{M}$ and $\mathbf{B}$ vanishes to zero then break from loop
End loop
```

Figure 5-6 A pseudo code representation of the NIPALS algorithm.

5.2.3 Image acquisition

To extract subject specific respiratory induced cardiac deformation patterns, ten normal subjects were recruited and underwent MR imaging on a Siemens Sonata MR scanner. The system has a field strength of 1.5T, a peak gradient strength of 40 *mT/m* and a slew rate of 200 *mT/m/ms*. All images were acquired in the supine. The duration of each examination was about 20 to 25 minutes, depending on the heart rate. After scout scans, a segmented 3D TrueFISP sequence was used to acquire short-axis image volumes in free breathing with navigator-echo and data over-sampling [219]. The imaging parameters used include an RF flip angle of 65°, in plane matrix size of 256×102, pixel size of 1.56 *mm* × 2.70 *mm* × 8.78 *mm*, and FOV of 400 *mm* × 275 *mm* × 123 *mm*. The 3D stack comprised of 14 short axis slices from the valve plane to the apex throughout the full respiratory range, covered by two *k*-space segments with 51 views per segment. This gave a total of 28 segments per 3D slab. Data acquisition was repeated 20 times for a total acquisition duration of 560 cardiac cycles. The image acquisition and reconstruction procedure used are schematically illustrated in Figure 5-7. A navigator echo, located perpendicular to the centre of the right hemi-diaphragm, preceded each segment. Data was acquired with four receiver coils. All raw data, including navigators, were stored and processed off-line. 3D datasets were generated at different respiratory positions by means of retrospective respiratory gating using purpose-built programs written in C and MATLAB (Mathworks, Natick, MA). For every acquired segment, the diaphragm position was determined from the preceding navigator echo. A one-dimensional Fourier transform of the navigator echo was smoothed by using an averaging filter (kernel size of 5), and a step function was iteratively fitted to the filtered data in the region of the liver-diaphragm-lung junction. The location of the step after the fitting procedure indicates the diaphragm position. In order to reconstruct a 3D data set for a given respiratory position, each segment contributing to the data set was chosen from the over-sampled data when the accompanying navigator echo yielded a diaphragm position nearest to the given respiratory level. The remaining over-sampled data was discarded. Images were then created from the raw data by using the 3D Fast Fourier Transform. Contributions from all coils were combined with an equal weight. Image sets were created for between six and seven different respiratory positions covering from end-inspiration to end-expiration.

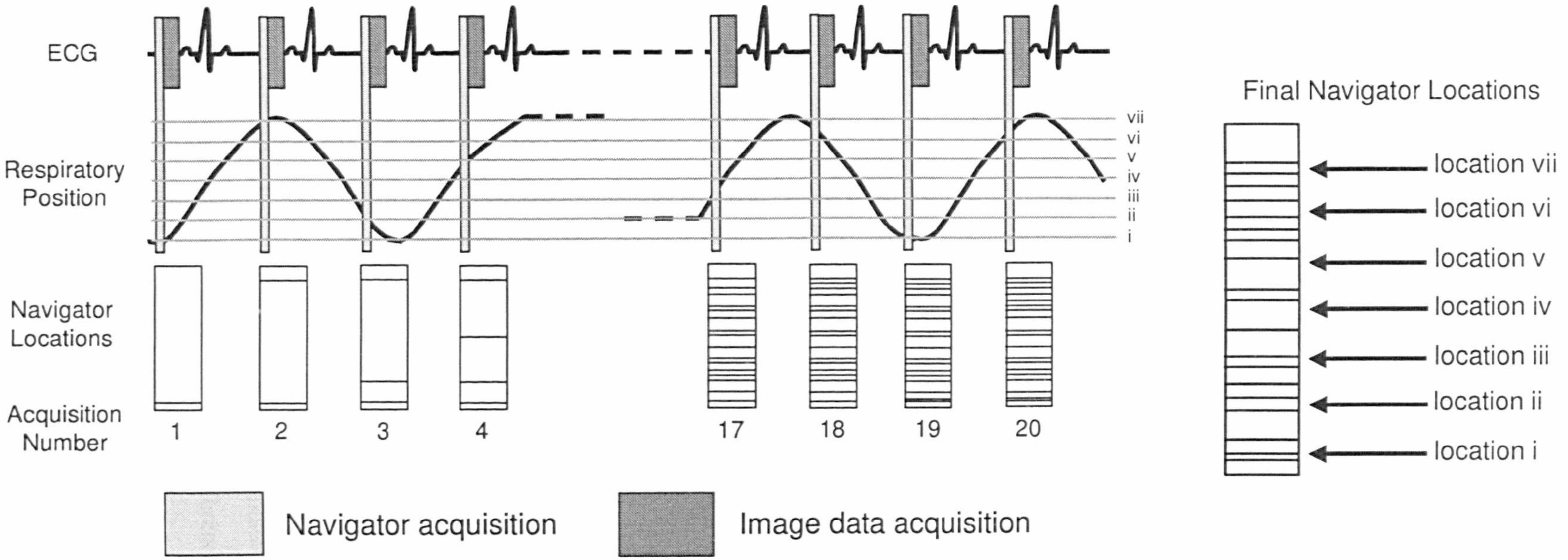
ECG
Respiratory Position
Navigator Locations
Acquisition Number
1
2
3
4
17
18
19
20
vii
vi
v
iv
iii
ii
i
Final Navigator Locations
location vii
location vi
location v
location iv
location iii
location ii
location i
Navigator acquisition
Image data acquisition

Figure 5-7 A schematic diagram showing the image acquisition and reconstruction procedure for the 3D imaging method with retrospective respiratory gating used in this study. ECG gating was used to acquire data at the same phase (early diastole) of the cardiac cycle. Prior to image data acquisition, a navigator echo was used to locate the position of the dome of the diaphragm. The figure shows the over-sampling of one data segment twenty times and the corresponding navigator locations. The full 3D acquisition requires a total of 28 data segments (14 slices × 2 segments per slice). Over-sampling the data by a factor of 20 ensured that 3D datasets could be reconstructed at a number of positions through the respiratory cycle.

5.2.4 Validation

In order to validate the proposed motion prediction scheme, multiple 1D intensity traces through the chest wall were used as the input signal to the PLSR model. Points lying on the chest wall were selected in a grid with around 25 *mm* spacing from the stack of 14 short axis slices, with traces measured directly from the imaging volume in parallel to the local intensity gradient. A total of 20 measurements were made for each subject, and these intensity values were concatenated as a row vector for matrix **X** of the PLSR model. In this study, between 5 and 7 image volumes were reconstructed for each subject to cover the entire range of respiration, this determines the number of rows used for matrices **X** and **Y** for motion prediction. The associated cardiac motion due to respiration was represented by the movements of the control vertices of the FFD model by the use of the 3D registration scheme described in section 5.2.1, for which the 3D volume corresponding to end-expiration was used as the reference. Since the control grid used was refined to 9×9×9, by concatenating all their deformation values together the number of columns of **Y** was therefore 729. In this study, motion prediction was performed separately for each of the three (*dx, dy, dz*) deformation components.

For each subject, the accuracy of the proposed motion prediction method was assessed. The basic form of cross-validation is to divide the acquired input-output data into two parts, one for training and the other for prediction. To avoid any bias in partitioning the data, multiple permutations of this division can be performed and averaged. In this chapter, leave-one-out cross-validation was used. The idea being to predict the output for each data set with learning based on both the input and output of all other data sets. The learning stage of the PLSR method was performed using all but one of the acquired respiratory positions for each result. From this learning phase the multiple navigator trace vector for the missing volume was used to predict the motion vectors for the missing image volume. This was carried out for all available volumes of each subject. In this way it is possible to assess the ability of the method to predict the correct motion characteristics for a respiratory position not involved in the learning phase. For quantitative assessment, the predicted motion vectors were used to warp the 3D volume so that normalized mean absolute difference could be calculated between the target and reference volumes. A small value represents a good motion prediction result.

5.3 Results

Figure 5-8 illustrates the amount of cardiac deformation that can be induced at different stages of the respiratory cycle. The solid shaded surfaces represent the reference endocardial border delineated from the 3D imaging volume corresponding to end-expiration. The meshed surfaces illustrate the deformation of the endocardial border due to respiration corresponding to diaphragm displacement values of 5, 15, and 25 *mm,* respectively. The corresponding mid-ventricular slices from which these meshed surfaces have been extracted are shown on the top row of Figure 5-8. The amount of cardiac motion is evident, including bulk motion, twisting and deformation. For this subject, the maximum cardiac displacement induced was about 15 *mm*.

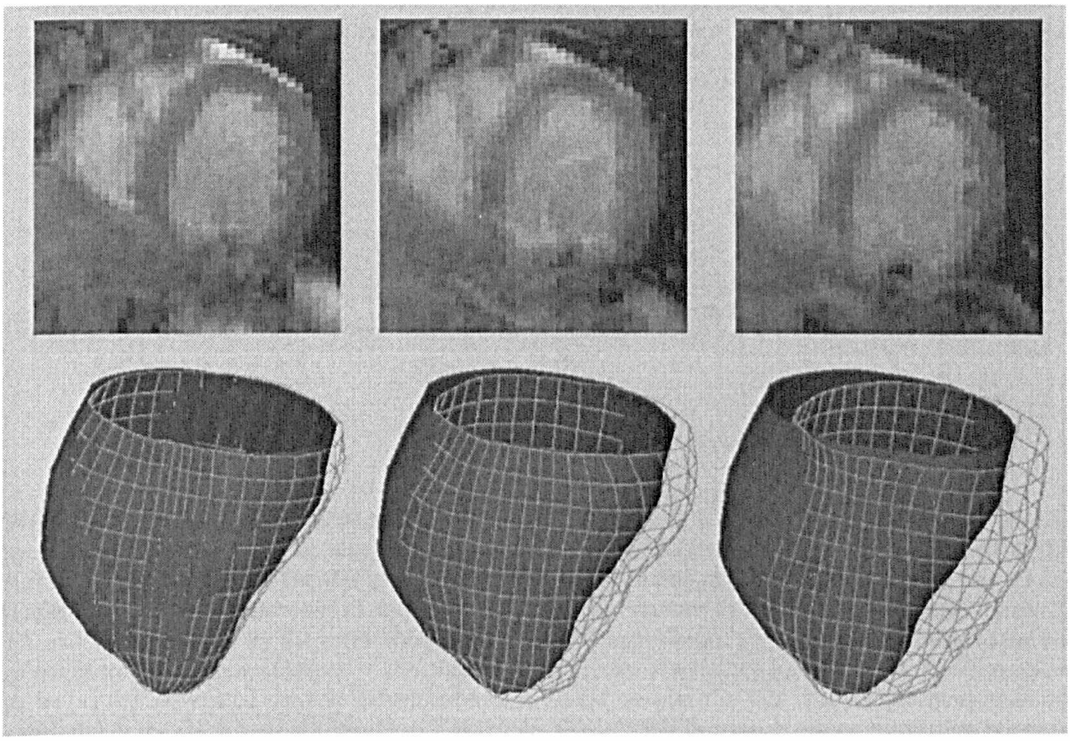

Figure 5-8 A visual representation of the motion of the heart due to respiration. The solid surface of each 3D reconstruction represents the endocardial surface at end-expiration and the meshed surface delineates the endocardial border due to respiration corresponding to diaphragm displacements of 5, 15, and 25 *mm*, respectively. The corresponding mid-ventricular short axis slice of each 3D volume is shown on the top row of the figure.

Figure 5-9 highlights the potential inconsistencies of using single movement traces of the chest wall to predict respiratory induced cardiac deformation. On the right, a sampled chest intensity trace over a number of cardiac cycles is shown (c). The top row shows the deformation vectors of the mid-ventricular slice corresponding to cardiac cycles 6, 11, and 23, as marked by the dashed lines on Figure 5-9 (c). It is evident that despite the fact that the intensity patterns measured at the chest wall correspond well, the associated cardiac deformation field while generally the same can be contrastingly different. At cardiac cycles 8, 12, and 18, once again with similar intensity patterns in (b) and marked with dashed lines in (c), the relationship between the corresponding motion fields is much more clear with 12 and 18 being practically identical. These results confirm the uncertainties of using limited measurements of the chest wall to predict respiratory induced cardiac deformation, as found in previous studies. For this reason, a combination of surface traces was used from a spread of locations. The use of PLSR allows the variation (or factors) from the multiple traces that are significant in determining the output to be extracted during the learning stage so that the prediction can be performed with a high level of confidence.

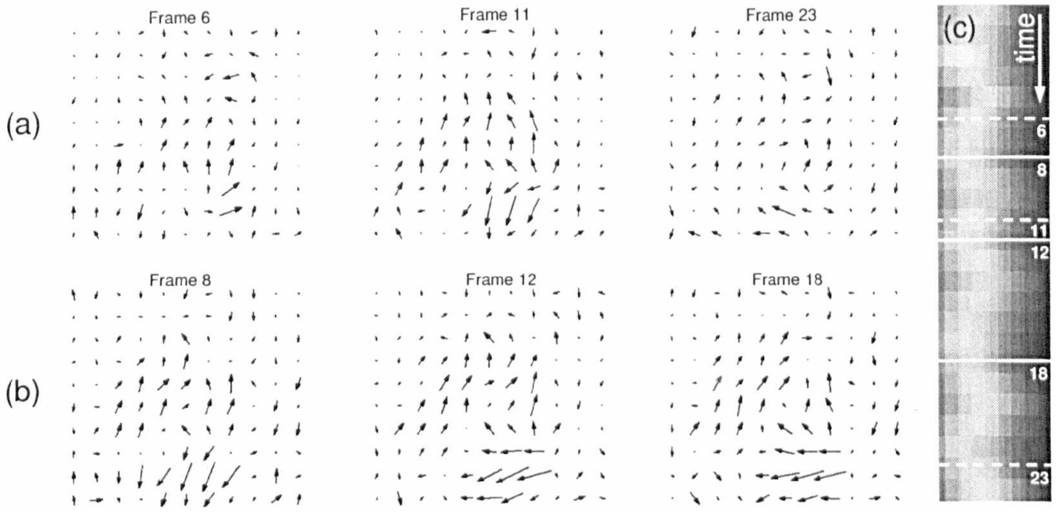

Figure 5-9 2D deformation vectors of a mid-ventricular slice at the same phase of different cardiac cycles with varying levels of respiration motion, and an associated intensity trace measured at the surface of the chest. (a) The deformation vectors corresponding to cardiac cycles 6, 11, and 23, as marked by the dashed lines on (c) and (b) the deformation vectors corresponding to cardiac cycles 8, 12, and 18, as marked by the solid lines on (c). These images highlight the potential inconsistencies of using single movement traces of the chest wall to predict respiratory induced cardiac deformation as in (a) the associated cardiac deformation is different despite the fact that the intensity patterns measured at the chest wall are identical. For (b), however, there is a much closer correlation between the deformation vectors and surface traces.

Figure 5-10 demonstrates the drawbacks of using a single chest trace for learning and prediction with PLSR. This is normalised against the use of all 16 traces and it is clear that no single trace is more effective at predicting the cardiac deformation as the combined result of all 16 traces, while some traces *e.g.* 7, is over 20% worse when pixel intensity subtraction error is measured.

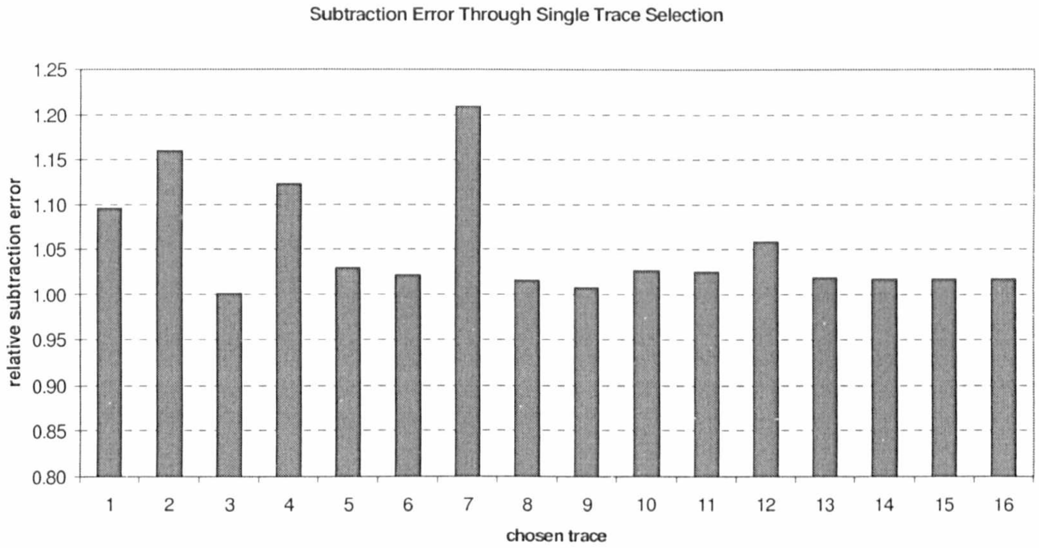

Figure 5-10 Subtraction error for PLSR by using a single chest trace compared to using all the 16 chest traces measured. Results were calculated as the mean square error of voxel intensity values (ranging from 0-255) for the selected region containing the heart. A value of 1.00 indicates the same result as using all 16 traces.

To assess the relative merit of the proposed PLSR method, detailed comparisons were made when different input traces are used for PLSR and Multi Linear Regression (MLR). The results presented in Table 5-1 are normalised with the residual errors achieved by 3D free form registration that is used as the gold standard for this study. A value of 1 therefore indicates the best possible motion prediction result. It is evident that with the PLSR approach the min/max error range is consistently small and it improves with the increasing number of tracers used. For MLR however, the error range is large and due to the co-linearity of the data when a large number of input variables are used, the result deteriorates. The analysis was also performed with an increasing number of chest traces as shown in Figure 5-11. For PLSR, the error range is consistently small and as more surface traces are used, the error range starts to decrease. For MLR, however, the error range varies and is significantly worse than that of PLSR. When all surface traces are used, the residual error is nearly 500% to that of using 3D registration due to the co-linearity of the input data.

Input Variables	32 1 trace	64 2 traces	96 3 traces	128 4 traces
MLR max	5.265	5.080	5.956	5.964
MLR min	1.380	1.889	2.247	3.943
PLSR max	1.176	1.121	1.086	1.079
PLSR min	1.053	1.052	1.054	1.051

Table 5-1 The maximum and minimum relative subtraction errors normalised against the registration result for MLR and PLSR with an increasing number of input variables. Results were calculated as the mean square error of voxel intensity values (ranging from 0-255) for the selected region containing the heart and normalised against the registration result.

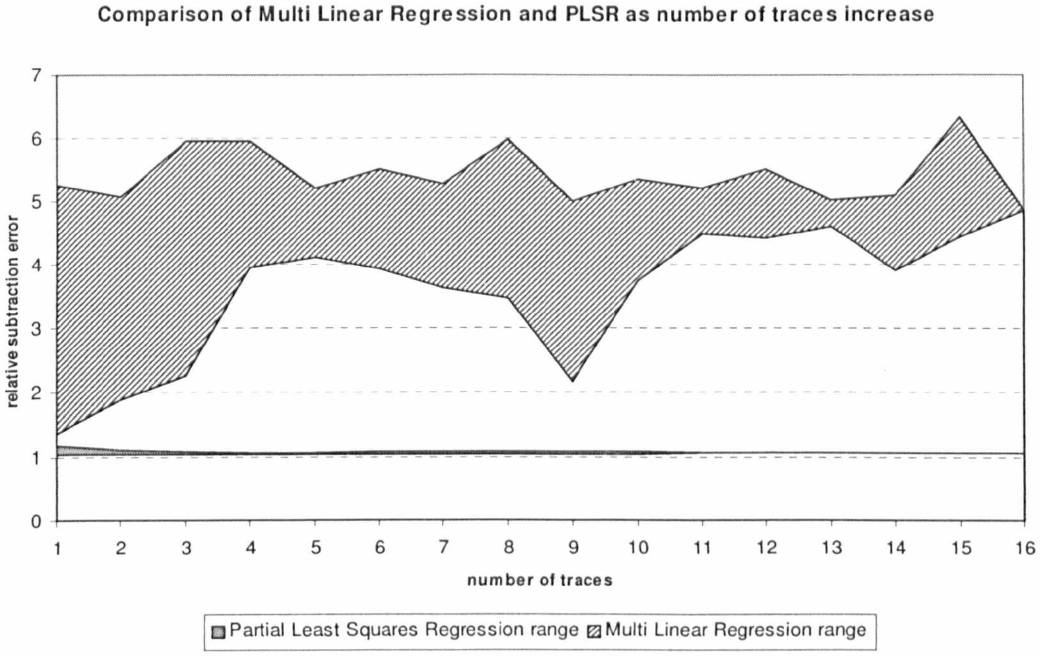

Figure 5-11 Subtraction error relative to the registration result for MLR and PLSR when different numbers of input traces are used. The graph shows the error range corresponding to different permutations of a given number of traces.

The proposed PLSR motion prediction technique was to rely on a large number of chest wall traces to extract their intrinsic correlation to cardiac deformations. As the inherent correlation among these traces could be significant, latent variables among these traces were extracted. For the corresponding deformation vectors of the cardiac structure, the movement of the deformation vectors of the control vertices of the FFD model were used. The same process of latent variable extraction was also applied to these deformation vectors. To illustrate the internal redundancies of the 3D deformation vectors, Figure 5-12 demonstrates the deformation patterns of layer 3, 5 and 7 of the final 9×9×9 grid of a subject studied. For each image, the vectors were calculated from the PLSR coefficient matrix by keeping the first three principal components. Each row of this image represents the in-plane deformation captured by the 1st, 2nd, or 3rd principal component, where the motion vectors were amplified by 10 times for the 2nd and 3rd rows of each image as the corresponding vectors were much smaller compared to those captured by the first principal component. For each layer, the columns show the mean ±standard deviation of the in-plane deformation. The first principal component is shown to carry most of the variation demonstrating that while a large number of input factors are acquired, the majority of this information is redundant with the third mode of variation having little effect on the final result.

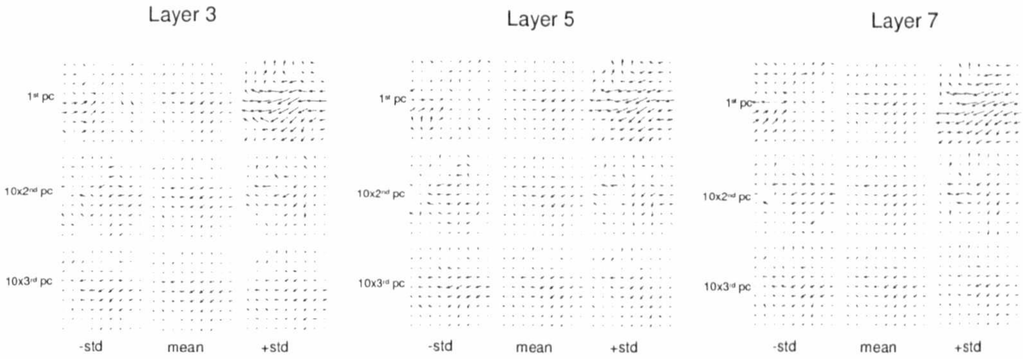

Figure 5-12 Deformation patterns of layer 3, 5 and 7 of the final 9×9×9 grid of a subject studied. For each image, the vectors were calculated from the PLSR coefficient matrix by keeping the first three principal components. Each row of this image represents the in-plane deformation captured by the 1st, 2nd, or 3rd principal component, where the motion vectors were amplified by 10 times for the 2nd and 3rd rows of each image as the corresponding vectors were much smaller than those captured by the first principal component. For each layer, the columns show the mean ± standard deviation of the in-plane deformation.

With the establishment of the PLSR model, it is now possible to accurately predict respiratory induced cardiac motion from multiple chest wall movement traces. Figure 5-13 shows an example result derived from the proposed 3D motion prediction method. Images (a1) and (a2) represent the mid-ventricular slices of a subject at different phases of the respiratory cycle, with the corresponding subtraction result shown in (a3). The 3D rendition shown in (a4) highlights the amount of cardiac motion and deformation involved, where the solid and meshed surfaces represent the endocardial border of (a1) and (a2), respectively. The second row of Figure 5-13 shows the result of using direct 3D free-form image registration on these two 3D image volumes. It is evident that the motion associated with Image (b2) has been corrected for, with the LV being warped to the correct position. The quality of the registration process can be seen from the direct subtraction result and 3D endocardial surface rendering. The final result derived from PLSR motion prediction is shown in the last row of Figure 5-13. The effectiveness of the prediction algorithm is evident by comparing the result to that derived from 3D image registration.

In order to demonstrate the fact that by using PLSR and multiple surface traces it is possible to derive results with similar accuracy to those derived by measuring diaphragmatic motions, Table 5-2 lists the mean residual errors by using these two approaches for the 10 subjects studied. In this Table, the residual error was measured as the normalised mean absolute intensity difference between the reference 3D image volume timed at end-expiration and the target 3D image volume timed at mid-respiration with 3D warping. The normalisation was achieved by dividing the mean absolute residual error of each method with the mean absolute error without motion correction. When applied to Figure 5-13, for example, the normalised error in Image (b2) is calculated as the mean absolute value of (b3) divided by that of Image (a3). A similar value can be derived for (c2) by normalising (c3) against (a3). This normalisation process is important as for each subject the range of pixel intensities can be contrastingly different depending on the attenuation used for the RF receiver coil and the reconstruction parameters used.

In Table 5-2, Rows P-chest and P-diaphragm represent results derived from motion prediction with PLSR from the chest wall and diaphragm, respectively. Despite the fact that the results derived from motion prediction are slightly poorer than that of 3D image registration, it is evident that the results from P-chest and P-diaphragm are very much similar justifying the use of chest traces only to drive the motion prediction model. For all the ten subjects studied, leave-one-out tests were performed for each subject with all the 3D volumes acquired corresponding to different respiratory positions. The overall errors produced by using the proposed motion prediction technique using 20 input traces located on the chest wall can be assessed in Figure 5-14, which provides the mean error and standard deviation for each subject based on the intensity difference criteria mentioned above. The corresponding results by using the 3D free-form image registration are also provided for each subject as a reference. No significant difference was found between the two techniques.

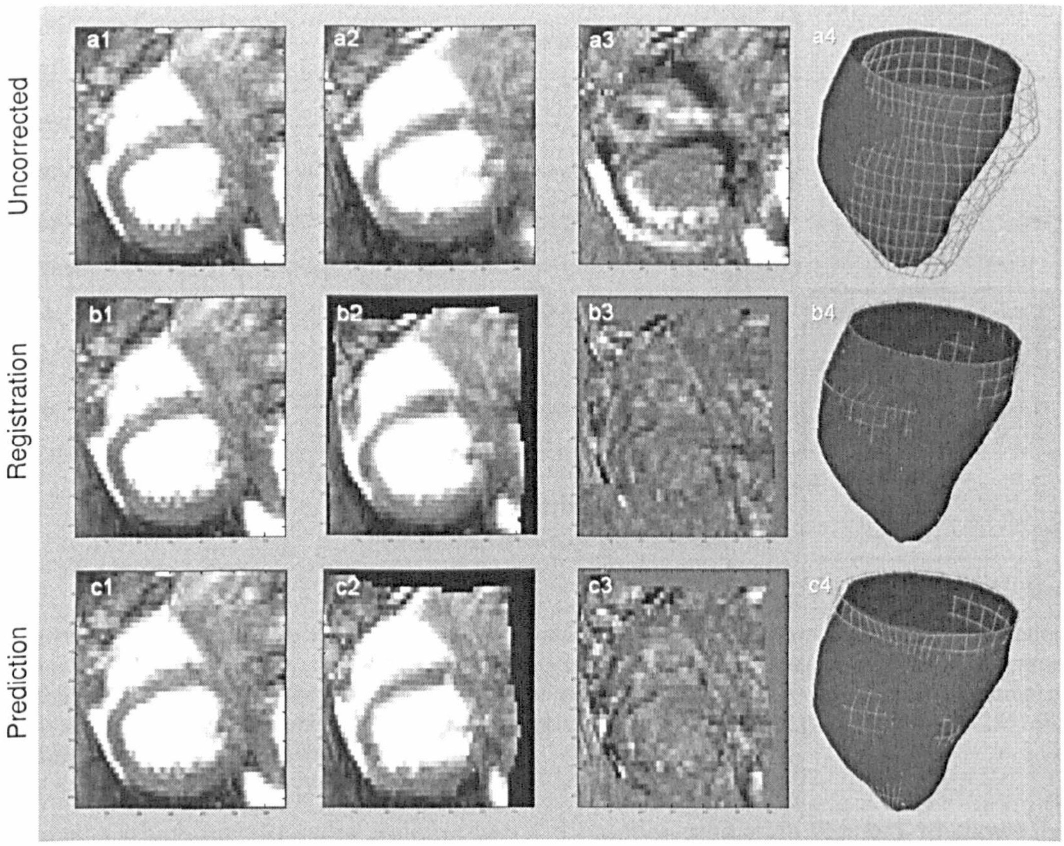

Figure 5-13 An example of the results derived from the proposed 3D motion prediction method. Images (a1) and (a2) represent the mid-ventricular slices of a subject at different phases of the respiratory cycle with the corresponding subtraction result shown in (a3). The 3D rendition shown in (a4) highlights the amount of cardiac motion and deformation involved, where the solid and meshed surfaces represent the endocardial border of (a1) and (a2), respectively. The second row shows the result of using direct 3D free-form image registration to the two 3D image volumes with (b2) representing the final warped mid-ventricular slice. Images (b3) and (b4) show the residual error by image subtraction and 3D rendering. The third row illustrates the same result as that of the second row but with PLSR motion prediction, demonstrating the ability of the proposed technique in accurate 3D motion prediction.

	1	2	3	4	5	6	7	8	9	10	**Mean**	**STD**
Registration	0.622	0.531	0.524	0.583	0.544	0.621	0.529	0.529	0.620	0.575	**0.568**	**0.042**
P chest	0.629	0.534	0.562	0.683	0.511	0.691	0.571	0.718	0.642	0.587	**0.617**	**0.065**
P diaphragm	0.624	0.531	0.572	0.750	0.553	0.662	0.550	0.718	0.643	0.587	**0.619**	**0.074**

Table 5-2 The mean residual error (normalised against no registration) and the standard deviation by using 3D image registration, 3D motion prediction with surface intensity traces (P chest) and the dome of the diaphragm (P diaphragm), for the 10 subjects studied. The results were derived from mid-respiration and end-expiration image volumes, and calculated as the mean square error of voxel intensity values (ranging from 0-255) for the selected region containing the heart. A value of 1 indicates no improvement due to registration.

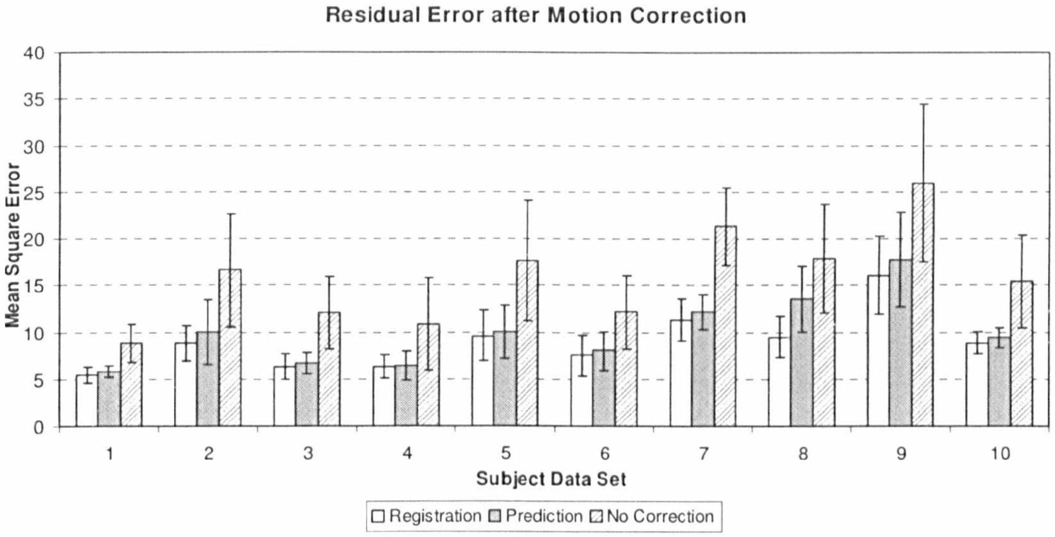

Figure 5-14 The overall residual error and standard deviation of the proposed motion prediction technique for all the 10 subjects studied by using the leave-one-out test. The analysis cover the entire respiration range and the corresponding 3D image registration results are provided as a reference. Results were calculated as the mean square error of voxel intensity values (ranging from 0-255) for the selected region covering the heart.

To assess which surface traces are most useful for motion prediction Figure 5-15 shows the range of subtraction error values with the removal of input chest traces. The initial value (1.00) is obtained with a leave-one-out test on all 10 subjects with 16 chest traces as input. Subsequently, traces are removed and a range of results are shown between the worst and best case. The optimal result is obtained with between 4 and 10 traces remaining, the error being around 97% of the error with all 16 traces used. Although being able to suggest the most useful traces for motion prediction for a particular subject at different phases of the respiratory cycle, it has been found that the permutation of the sensor position can vary across subjects. A poor selection of traces can result in a significantly worse result than from using all available traces. This justifies the use of PLSR in using a relatively large number of surface traces for reliable motion prediction despite the fact that they can be correlated and often individually of poor quality.

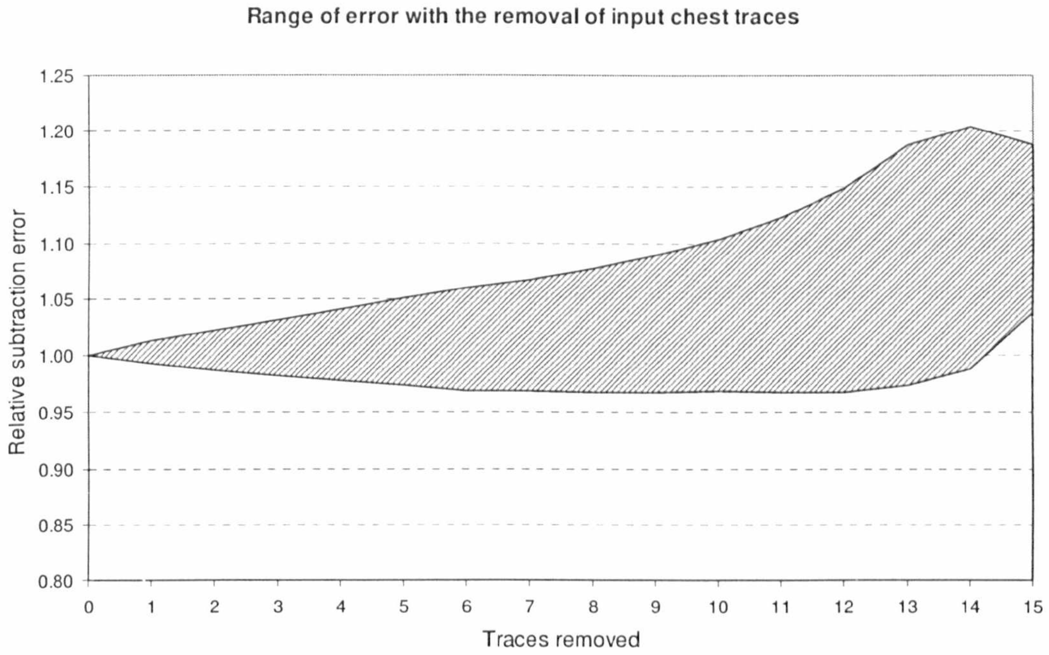

Figure 5-15 The subtraction error after sequential removal of traces used for learning and prediction relative to the use of all 16 traces. The best and worst case is shown with all possible error values for the different number of traces shaded in between. Results were calculated as the mean square error of voxel intensity values (ranging from 0-255) for the selected region containing the heart. A value of 1 indicates no improvement due to registration.

5.4 Discussions and conclusions

In this study, a new technique is presented based on surface measurable information for predicting respiratory induced cardiac deformation. The technique relies on multiple input traces to capture the intrinsic pattern of surface deformation related to cardiac deformation. The use of PLSR effectively resolves the problem encountered by traditional regression methods in that latent variables are used from both the input and output of the regression model to establish their inner relationships. Multi-collinearity or near-linear dependence of regressors is a significant problem in regression models. The strength of the proposed PLSR approach is that it not only effectively deals with high multi-collinearity of the measured signals from the chest, but also permits reliable motion prediction when the number of observations is significantly less than the observed variables as in this study where only 6-7 different 3D volumes corresponding to different respiratory positions were used. It must be mentioned, however, the method used is fundamentally a linear technique. While it is able to deal with non-rigid 3D motion, it is possible that for different subjects, a nonlinear relationship can exist between the measured respiratory traces and the deformation of the heart. This is true especially at the two extremes of the respiratory cycle. To cater for this problem, some of the developments in nonlinear and kernel based PLSR approaches may be used [220]. It is worth noting that hysteresis as observed in respiratory induced cardiac deformation was not assessed in this study. This effect is related to the different relationship between respiration and cardiac deformation during inspiration and expiration [166]. It is not studied here due to the nature of the over sampled retrospectively gated image acquisition. The use of a single diaphragmatic navigator to determine the respiratory gating precludes the hysteresis effect, and because of this, it is not possible to assess the ability of the current framework to cope with this effect.

Subject specific respiratory patterns are a significant problem for motion management in *in vivo* imaging. Although in MR the use of navigator echoes has already improved the quality of the images acquired, particularly for capturing small mobile structures such as the coronaries, its wide spread use is still hindered by its lack of general adaptivity to different imaging platforms. The results from this study suggest that being effectively a real-time technique, the proposed method is not only reasonably accurate, but also able to predict respiratory induced cardiac motion from purely surface measurable signals. The development of a general method for 3D motion prediction based on easily measured surface signals will have significant impact on motion tracked imaging in MR as well as for other parallel imaging modalities and the delivery of focused energy in the presence of physiological motion.

There are, however, a number of design issues related to the experiment that need to be recognised. Firstly, the image acquisition for this study was based on retrospective diaphragmatic gating for acquiring 3D volumes at different respiratory positions. The use of retrospective gating with over sampling has the advantage of being easy to implement and the data acquired corresponds to natural physiological states of the patient. The option of using breath holding was not adopted in this study as it could introduce artificial loadings to the visceral structure. The technique used, however, had a prolonged imaging time. A large over-sampling factor was used to ensure all *k*-space data, corresponding to different respiratory positions, was covered. Secondly, the use of diaphragmatic navigator echoes for predicting the deformation of visceral structures can itself have problems. It is possible that certain respiratory patterns can have different cardiac thoracic deformations despite the same navigator trigger response from the diaphragm. The use of 3D volumes acquired as such is not ideal but the alternatives are currently limited by methods of acquisition. It is expected that by the use of parallel imaging, the imaging time can be significantly reduced.

It is also important to note that in this study motion modelling and prediction are based on data that is simultaneously acquired. For the method to be used for cross modality motion prediction, *i.e.*, the use of MR for predictive motion modelling prior to PET imaging such that prospective motion correction can be applied, inter-scan inconsistencies of motion correlation will need to be further investigated. This analysis must be conducted in line with the choice of surface signal measurement techniques. In this study chest intensity profiles are used as a means of measuring local surface deformation. This is only to demonstrate the basic principle of the proposed motion prediction technique. In practice, more accurate imaging or non-imaging based techniques will need to be explored. These include the use of surface tension arrays to measure surface tension based on strain (*e.g.* chest belts incorporating strain gauges) rather than absolute positions, or by the use of other optical/ultrasound-based techniques. In these cases, modality compatibility is an important issue, especially for MR as the exclusion of ferromagnetic materials and the restriction on RF can introduce significant design problems. This is an important area to pursue given the current development in micro-sensor research.

It is worth noting that in the current study the optimum arrangement of surface sensing locations has not been investigated. A detailed analysis either to determine a suitable arrangement for all subjects or an efficient method of determining suitable locations on a subject specific basis can potentially minimize the number of physical sensors. In conclusion, an effective motion prediction technique has been demonstrated, which after initial modelling can be used in real-time prospective motion tracking. Detailed analysis of results from ten asymptomatic subjects demonstrate the accuracy and effectiveness of the proposed technique.

Chapter 6 : Respiratory Reordered-UNFOLD

6.1 Introduction

In Chapter 5, we have discussed the use of predictive motion modelling for handling respiratory motion. In parallel to this, we also have to address rapid data acquisition issues for efficient 3D coverage of the myocardium. In 3D myocardial perfusion imaging, a complete volumetric data set has to be acquired for each cardiac cycle in order to study the first pass of the contrast bolus. This normally requires a relatively large acquisition window within each cardiac cycle to ensure a comprehensive coverage of the myocardium and reasonably high resolution of the images. As mentioned in Chapter 4, with multi-slice imaging, long axis cardiac motion during this large acquisition window can cause the myocardium imaged in different cross-sections to be mis-registered, *i.e.* some part of the myocardium may be imaged more than twice whereas other parts may be missed out completely. This type of mis-registration is difficult to correct for by using post-processing techniques. New imaging sequences such as Fast Gradient Echo with an Echo Train readout (FGRE-ET) [77,99] have significantly reduced the acquisition window whilst maintaining the desired spatial resolution. Further improvements in perfusion imaging will require the application of parallel imaging techniques as mentioned in Chapter 3 [103] or making full use of the information content of the *k*-space data. View sharing is a common approach that involves the use of the similarity or redundancy in *k*-lines between images. Phase encode lines which through a Fourier transform represent image data that remains static across time can be acquired once and shared between multiple images. Techniques such as BRISK [112] and BLAST [118] can potentially be adapted for this purpose.

More recently, UNFOLD has been used for perfusion imaging [113,115]. The technique attempts to encode spatial information into redundant regions of *k-t* space. Initial experience has shown promising practical value of the technique for breath-hold myocardial perfusion imaging by doubling the scan efficiency, which can be used either to increase the spatial resolution/coverage or to decrease the acquisition window. For perfusion imaging with free breathing, however, the technique suffers from significant motion artefacts and blurring due to respiratory induced motion. In reality, the use of breath-holds are undesirable for patients with cardiac conditions as a first-pass perfusion series often involves tracking the contrast bolus over 50 cardiac cycles. Therefore, extensive improvement of the current UNFOLD framework is necessary before the technique can be practically used for myocardial perfusion imaging. The purpose of this work is to present a new prospective *k*-space reordering method for UNFOLD to eliminate respiratory induced motion artefact. The method uses real-time diaphragm navigator echoes [157], similar to those used in CMR coronary angiography [159-161], to ensure temporal filtering of UNFOLD is carried out on a series of images that are spatially registered. The method requires a prospective re-binning algorithm for the creation of multiple image sub-series related to different levels of respiratory motion. Issues concerning the temporal smoothing of tracer kinetic signals are discussed and a solution based on over-sampling of central *k*-space is provided. The strength of the technique is demonstrated with detailed error analysis for data acquired from 10 patients and 10 normal volunteers.

6.2 The principal of UNFOLD

As mentioned in Chapter 3, UNFOLD is a relatively new technique for MRI. It allows for a reduction in the required *k*-space sampling. The technique, however, comes at a price and as with many similar temporal filtering methods, this technique results in smoothing and a loss of SNR. This method was first published in 1999 by Madore *et al* and applied to cardiac imaging and fMRI. Its application is only of use with dynamic data sets as it is based on reducing redundancies in the time domain of the *k*-space sampling.

The principal of UNFOLD lies in a reduction of the FOV in the image plane containing dynamic information. This is achieved through a sparser sampling of *k*-space, which has the effect of wrapping around due to the aliasing within the FOV. These overlapped components are labelled in the time domain through adjustments in the dynamic sampling function. Subsequently these overlapped components may be 'unfolded' allowing the full FOV image to be reconstructed.

The density of the sampling function used to acquire the data determines the FOV of an MR image. As shown in Figure 6-1, the resultant Point Spread Function (PSF) should normally allow the imaged object to be uniquely contained within the FOV. By reducing the sampling function in the phase encode direction as shown in Figure 6-2, where the distance between *k*-space lines is increased, it has the effect of compacting the PSF such that the peaks are brought closer together. Given the same imaged object and choosing the same FOV as in Figure 6-1, the result is an overlapping of the object in the image domain. This reduces the effective FOV due to the aliased reconstruction encroaching on the central reconstruction. This is more clearly demonstrated in Figure 6-3 by taking away lines of the image in the frequency domain, overlapping of the reconstruction is introduced in the image domain.

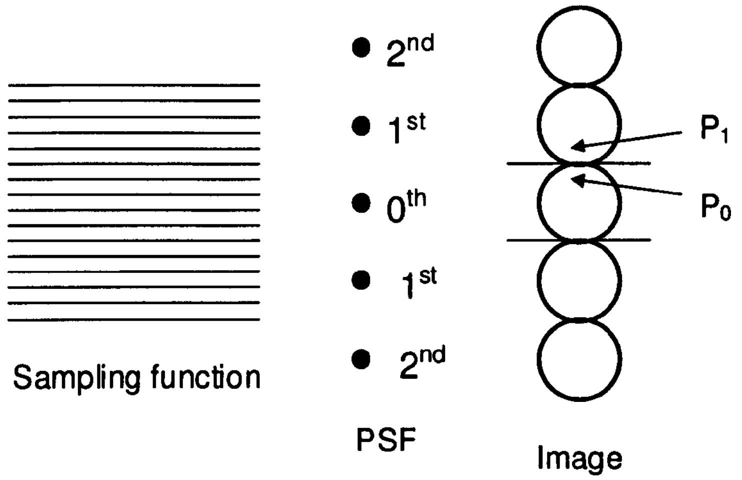

Figure 6-1 The Cartesian sampling function on the left gives a PSF shown in the middle after inverse Fourier transform. This replicates the imaged object (in this case a circle) as shown on the right. Two points are shown P_0 and P_1. P_0 originating from the 0th peak of the PSF and P_1 from the 1st peak of the PSF.

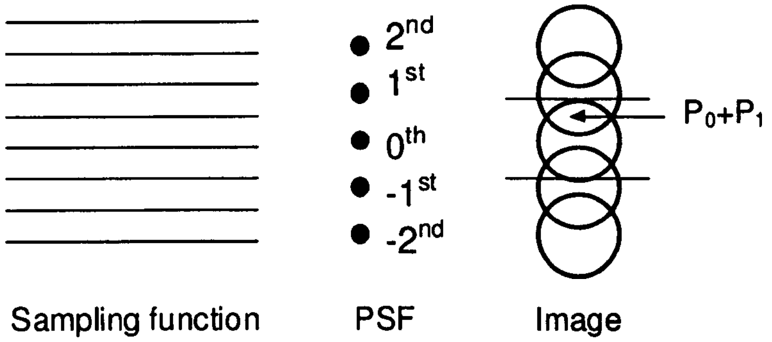

Figure 6-2 By increasing the distance between the lines in the sampling function, the distance between the peaks of the PSF is reduced in an inversely proportional manner. This leads to the reconstruction of the imaged object overlapping in the under-sampled direction. The points P_0 and P_1 now lie in the same position in the spatial image domain due to the two replicas of the imaged object sharing some of the same pixels in the image domain.

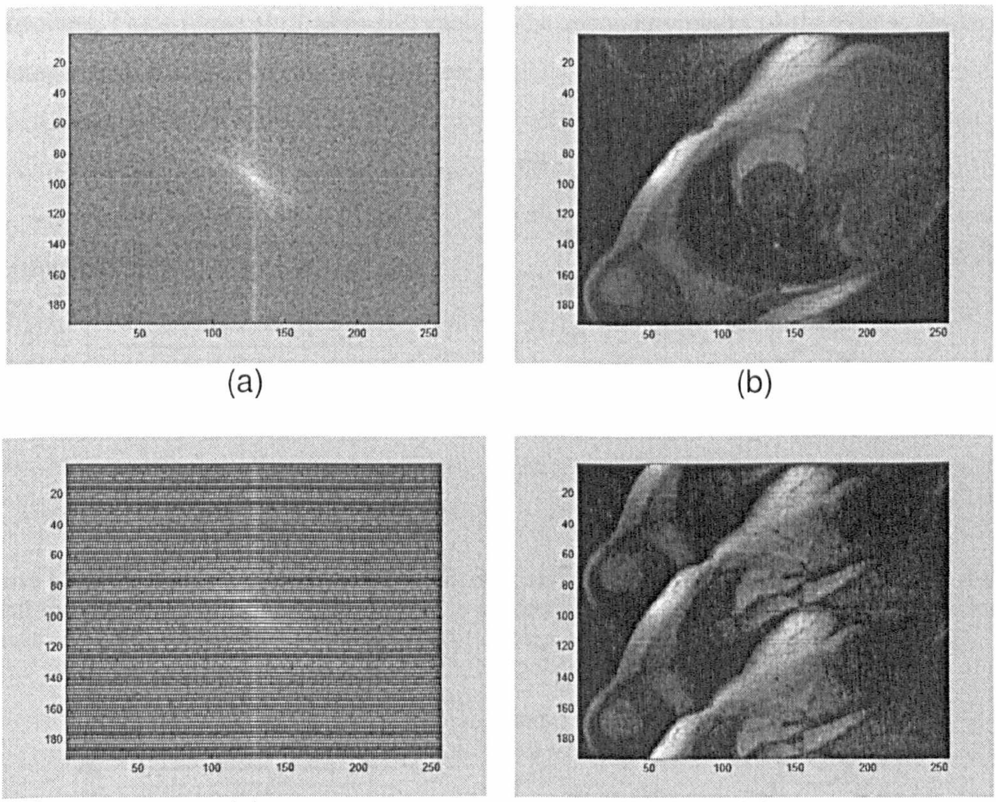

(a) (b)

(c) (d)

Figure 6-3 The images above show the effect described previously in sub-sampling the information in *k*-space. As shown, the *k*-space coverage in (a) is sufficient to produce image (b) without noticeable artefact due to wrap around. By reducing the sampling density by a factor of two in (c), the resulting constructed image has the image data overlapping from above and below in (d) producing significant artefact and error.

The important element in the UNFOLD process is how the sampling function is adjusted. By shifting the sampling function in the phase encode direction through time, a linear phase shift in the PSF is introduced. This has the effect of altering the phase of all but the central peak of the PSF. With this effect being passed on to the reconstructed image, it is possible to distinguish the central replica of the object from its overlapping copies. As shown in Figure 6-4, by shifting the sampling function by *f* of a line through time, a phase shift is created. In this way, pixels containing overlapped components may be separated into the individual elements from each reconstruction. This is possible as the time varying shift effectively labels the overlapped components by modulating their phase. In the case where the sampling function is shifted by half its spacing in the phase encode direction at each time frame, the signal of the overlapped component is modulated by the Nyquist frequency while the central replica is unchanged. The separation or 'unfolding' is achieved by filtering out the extra information contained at each the pixel location in the Fourier domain through time before performing the inverse Fourier transform to reconstruct the image without the overlapped component. For a phase shift of $f = 1/2$, each of the secondary peaks of the PSF is shifted by an integer multiple of π as shown in Figure 6-5.

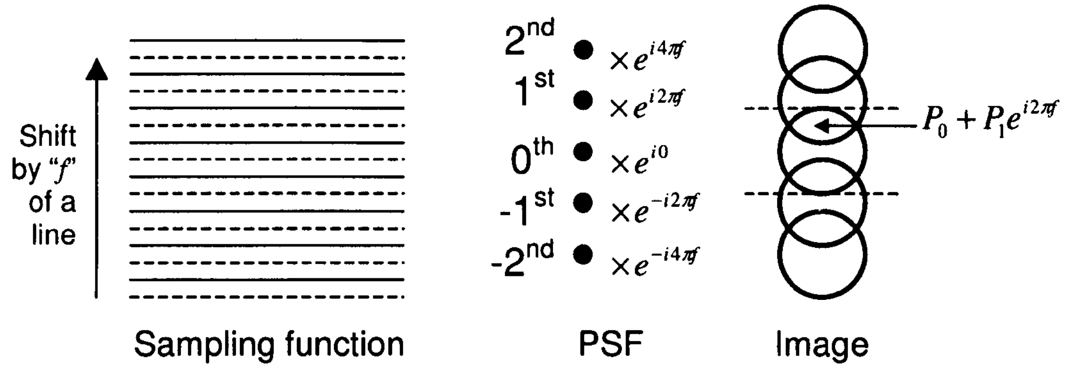
Shift by "f" of a line
2nd $\times e^{i4\pi f}$
1st $\times e^{i2\pi f}$
0th $\times e^{i0}$
-1st $\times e^{-i2\pi f}$
-2nd $\times e^{-i4\pi f}$
$P_0 + P_1 e^{i2\pi f}$
Sampling function
PSF
Image

Figure 6-4 By shifting the sampling function in the phase encode direction through time (from dashed to full for instance) a phase ramp in the PSF is produced. This phase shift is passed on to the image domain so as points P_0 and P_1 may once again be distinguished.

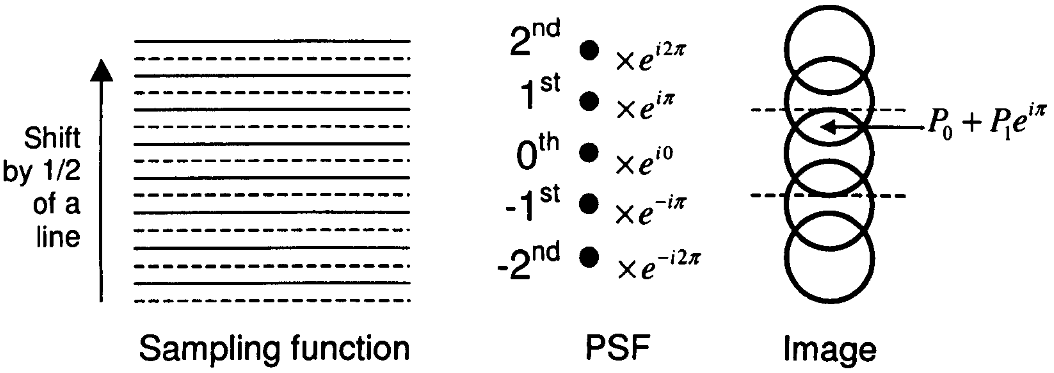
Shift by 1/2 of a line
2nd $\times e^{i2\pi}$
1st $\times e^{i\pi}$
0th $\times e^{i0}$
-1st $\times e^{-i\pi}$
-2nd $\times e^{-i2\pi}$
$P_0 + P_1 e^{i\pi}$
Sampling function
PSF
Image

Figure 6-5 A shift in the phase encode direction of half a line results in a π phase shift for each of the secondary peeks in the PSF. The point P_1 is now π degrees out of phase with the point P_0.

Figure 6-6 and Figure 6-7 demonstrate how this phase shift allows the reconstructed image to be separated in the time domain for a static sequence. Effectively, information is taken from the spatial domain and encoded into the time domain, where the phase shift allows this data to be reconstructed without spatial aliasing.

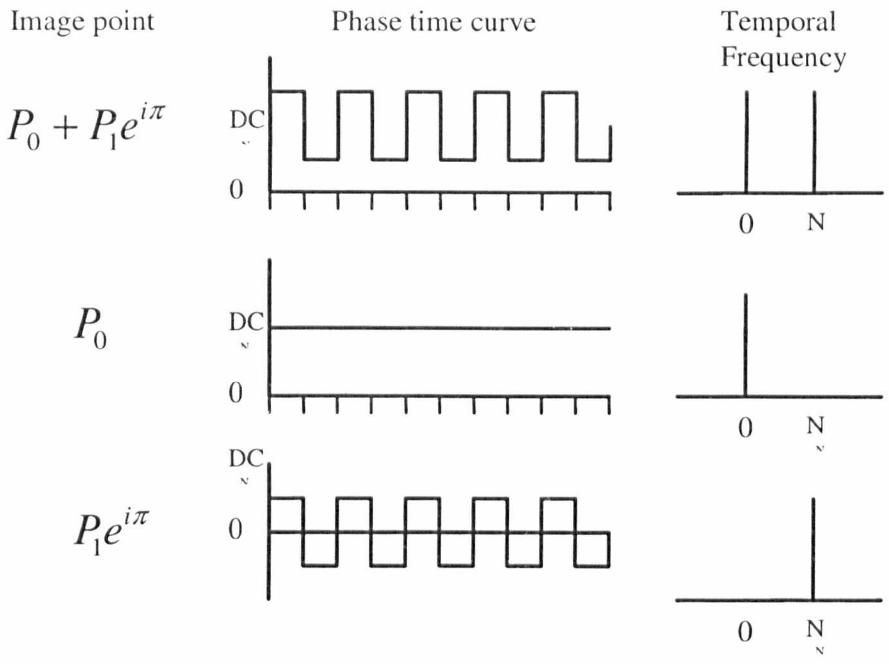
Image point
Phase time curve
Temporal Frequency
$P_0 + P_1 e^{i\pi}$
P_0
$P_1 e^{i\pi}$
DC
0
0
N

Figure 6-6 When applying the sampling function shown in Figure 6-5 to a stationary image sequence, it has the effect of producing two spikes in the temporal frequency domain, the DC component centred on 0 and the oscillating component at the Nyquist frequency. These two components may be easily separated to distinguish points P_0 and P_1.

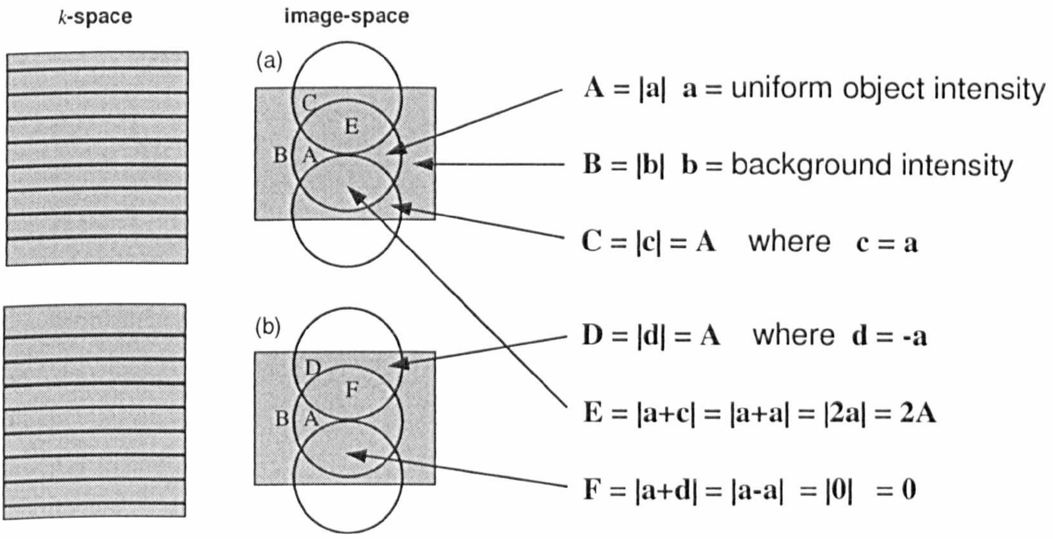
k-space
image-space
(a)
(b)
A
B
C
D
E
F
A = |a| a = uniform object intensity
B = |b| b = background intensity
C = |c| = A where c = a
D = |d| = A where d = -a
E = |a+c| = |a+a| = |2a| = 2A
F = |a+d| = |a-a| = |0| = 0

Figure 6-7 A schematic illustration showing the basic effect due to sub-sampling of the Cartesian space. (a) and (b) are two sequential acquisitions through time with the corresponding even and odd *k*-space information shown on the left. The sampling function has been shifted in the phase encode direction by half a line. This leads to a π phase shift in the PSF for the secondary peaks. The result is shown with the resulting pixel intensities in regions C and D alternating between the magnitude of +a and –a, where all lower case variables are complex. When reconstructed, overlapping pixels such as those in E and F that alternate between the magnitude of 2a and 0 are created in the image domain. In this simple case, the complete reconstruction of the object is obtained by summing the two images either in the frequency domain or in the image domain.

This technique, however, has limitations when performed on dynamic data sets. The movement of the structure will have a broadening effect of the PSF. When the movement across time is of low frequency as shown in Figure 6-8, the redundancy in the bandwidth of spectra (b) allows it to be combined with dynamic data as shown in (a) without interfering with each other. This, however, is not the case with Figure 6-9 as significant overlap exists in the temporal spectra and the resulting curves are unable to be separated through temporal filtering. A comparison of different temporal filtering methods has been carried out [115] and its suitability to perfusion studies assessed, the conclusion was that UNFOLD was suitable for myocardial perfusion studies assuming that large sudden motion throughout the frame due to respiration can be resolved.

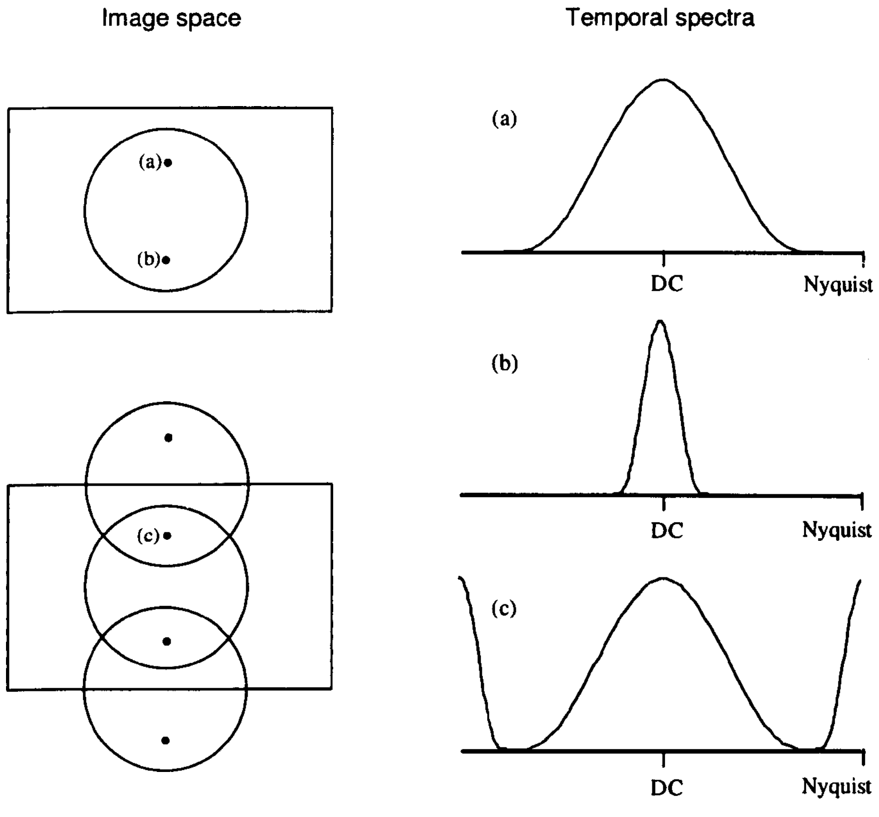

Figure 6-8 With full sampling the temporal spectra for two points in image space are shown. (a) represents dynamic information, while (b) represents a static or more slowly varying point. Through under sampling in *k*-space the PSF moves closer and these two points are represented by the same pixel in image space (c). Through the temporal phase shift in the sampling pattern used with UNFOLD (b) has been shifted to the edge of the spectra, allowing the information from pixel (a) and (b) to be distinguished in post processing with temporal filtering.

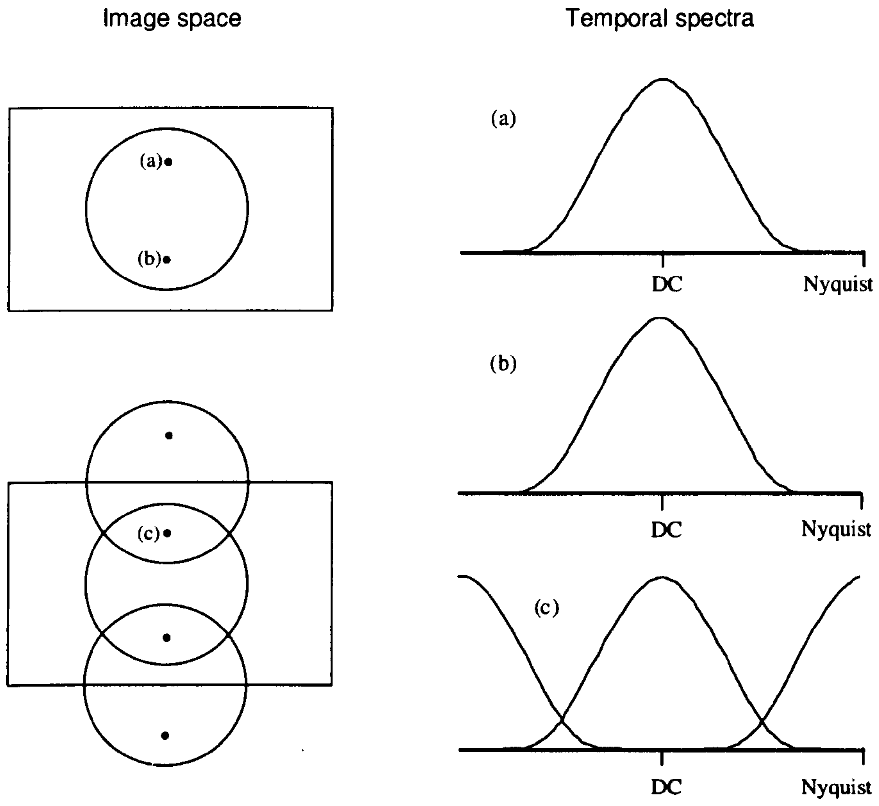

Figure 6-9 With full sampling the temporal spectra for two points, (a) and (b), in image space are shown both containing significant dynamic information resulting in broad temporal spectra. Through under sampling in *k*-space, the PSF moves closer and these two points are represented by the same pixel in image space (c). Even though the sampling pattern is able to shift the information for pixel (b) to the edge of the temporal spectra, it is not sufficient to successfully distinguish the two points (a) and (b).

6.3 Correcting respiratory motion for artefact suppression with UNFOLD

From the above discussion, it becomes apparent that motion within myocardial perfusion image sequences can make the use of UNFOLD for reduced *k*-space encoding problematic. With ECG gating we limit the bulk of this motion to respiratory induced motion. In this case, respiratory motion can have two effects; artefact edges may be wrapped around onto sensitive areas for perfusion analysis such as the myocardium. Additionally, the borders where motion has occurred can suffer from a temporal smoothing effect. While in plane respiratory motion can often be corrected for in post processing attempting to correct for this after the UNFOLD reconstruction of reduced *k*-space images results in artefact remaining in the image. One solution to this is to attempt to correct for the motion before UNFOLD is applied.

6.3.1 Correcting rigid body translation

UNFOLD is able to separate alternate PSF reconstructions in the temporal frequency domain. As mentioned earlier, the method relies on each pixel representing the same imaged structure through time. With the introduction of rigid body motion attempts at removing this artefact results in errors at the edges of the region subject to motion. This error is propagated through the image sequence due to the removal of high frequency components in the temporal frequency domain when applying UNFOLD. Figure 6-10 shows an example of this error on synthetic and real data. This is a static sequence only with one frame that has a sudden translational motion in the *y* direction. After UNFOLD, it can be seen that edge artefact is present due to the chest wall wrapping around into the central FOV. Figure 6-11 shows a similar effect from adding random motions in the phase encode direction to the complete sequence of images. It is apparent that as the degree of motion increases the level of artefact also starts to increase.

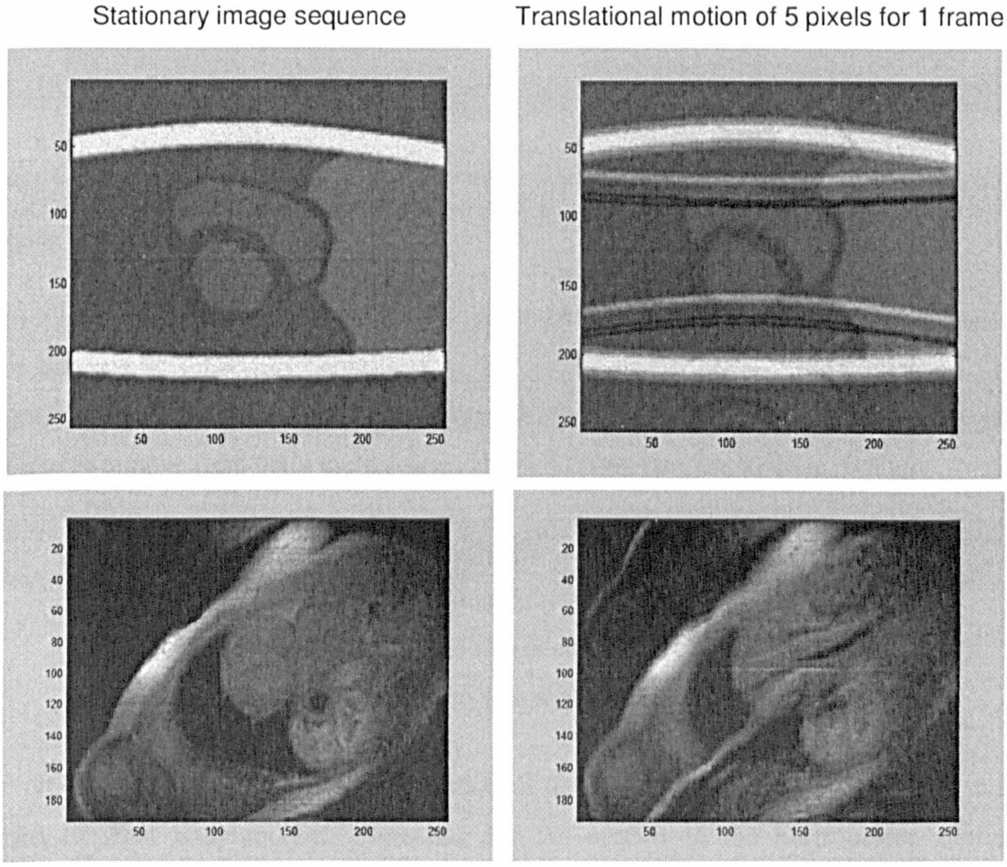
Stationary image sequence

Translational motion of 5 pixels for 1 frame

Figure 6-10 A synthetic (above) and real (below) stationary image sequence sub-sampled in *k*-space by a factor of two with UNFOLD applied. The right column shows the corresponding results when one of the image frames is translated by 5 pixels in the phase encode direction.

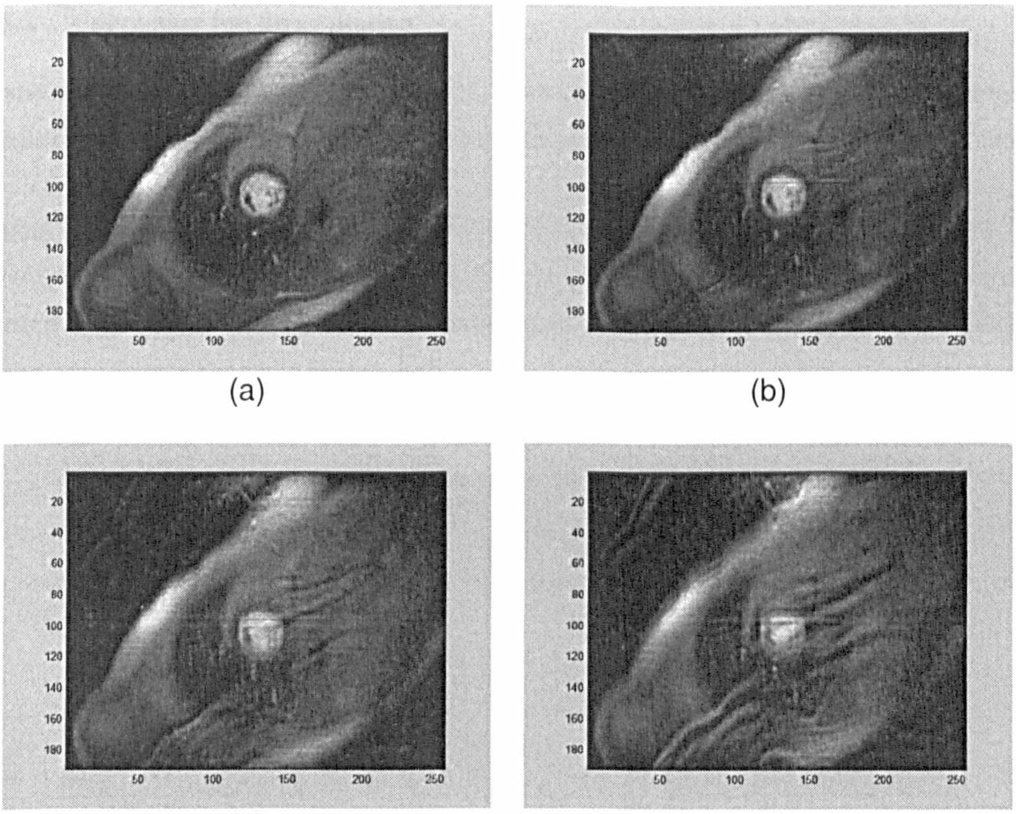

(a) (b)

(c) (d)

Figure 6-11 A single frame from an under sampled static image series with up to (a) 0, (b) 5, (c) 10 and (d) 15 pixels of random motion applied in the phase encode direction to each of the frames before applying 2 x UNFOLD.

With rigid body translation, correcting the motion before applying UNFOLD eliminates the error that would otherwise occur. The error present in Figure 6-10 and Figure 6-11 is completely removed if the motion is corrected for before applying UNFOLD. The steps required to remove rigid body motion from UNFOLD sub sampled *k*-space data are:

1. Apply inverse Fourier transform to data to obtain image series
2. Correct for rigid body motion through translation
3. Apply Fourier transform to obtain *k*-space information
4. Apply UNFOLD to *k*-space data series to obtain error free images

The problem with this method is that motion of the heart within the chest cavity does not consist of rigid body motion. Correcting for the motion of the heart before applying UNFOLD using rigid translation will create pseudo motion in the chest wall. To cope with more complex motion, free form deformation is required. This however can introduce significant problems as we illustrate below using a simple shear transform.

6.3.2 Correcting for shear motion

A shear transformation is part of a group of transformations known as affine transformations. While these are linear they are not required to preserve angles and distances between points.

Figure 6-12 shows a shear transformation applied to a rectangle and the effect this has on the reduced *k*-space reconstruction. It is important to realise that unlike rigid body translation, shear distortion does not result in the same points in overlapping PSF reconstructions sharing the same pixels, as shown in Figure 6-12.

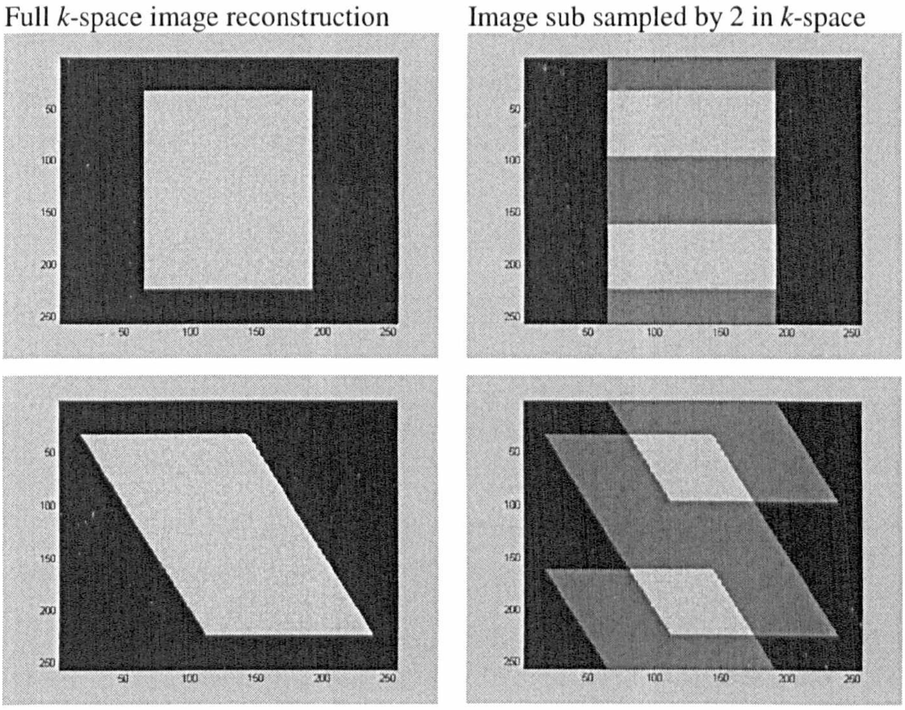
Full *k*-space image reconstruction

Image sub sampled by 2 in *k*-space

Figure 6-12 The effect of shear distortion on UNFOLD. On the left, two synthetic images reconstructed from complete *k*-space information are shown. On the right the same objects are reconstructed from *k*-space data under-sampled by 2 in the phase encode direction.

The difference in overlapping structure is highly significant in performing the UNFOLD reconstruction as shown in Figure 6-13. The left column shows the sequence of images reconstructed with full *k*-space data, the middle column with reduced *k*-space and UNFOLD reconstruction and the right hand column also with reduced *k*-space but with correction for the shear in frame 4 before UNFOLD reconstruction. Aliasing artefact can be seen in the UNFOLD reconstruction; the correction for the shear distortion in frame 4 before applying UNFOLD is not sufficient to remove the artefact. The issue is not with the central PSF reconstruction suffering from shear but of the outer reconstruction not being aligned with the central reconstruction.

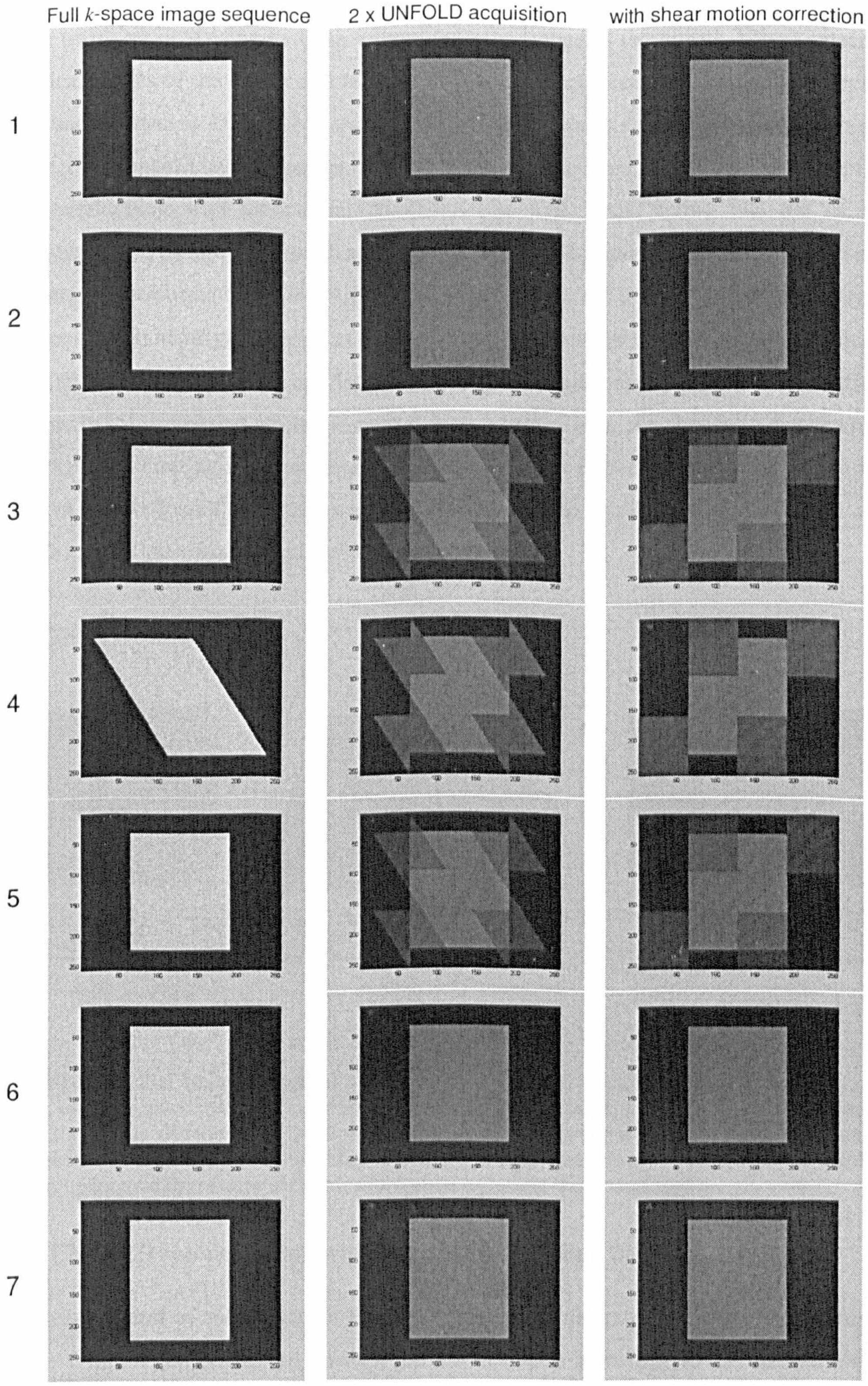
Full *k*-space image sequence
2 x UNFOLD acquisition
with shear motion correction
1
2
3
4
5
6
7
50
100
150
200
250

Figure 6-13 Seven frames of a synthetic image series. All images are identical except for the central frame that has undergone shear distortion before being converted to *k*-space. The left column shows the result of full *k*-space image reconstruction, whereas the middle and right columns show the results of 2 × UNFOLD without and with distortion correction.

In Figure 6-14, the circular object in (a) is imaged with insufficient density in the sampling function resulting in aliasing as wrap around onto the image of the object. This is observed as identical copies of the object overlapping with the central reconstruction of the object. In (b), the same object is imaged but the object has undergone a shear transformation before imaging. Once again identical copies of the image protrude from the top and bottom of the image, overlapping with the central reconstruction. The arrow shows that the relative position between PSF locations is preserved. In (c) the same acquisition as (b) is shown after undergoing a transformation before UNFOLD to correct for the shear in the object, warping the object back to its original shape as in (a). The central reconstruction is identical to that in the first slide, although the two overlapping reconstructions appear in transformed locations. The arrow in (c) shows that while the central replica is the same, the change in displacement of the PSF neighbouring replicas results in differing object points overlapping in the image domain in (c) compared with those in (a). This makes the application of UNFOLD with frames (a) and (c) in sequence subject to extensive artefact.

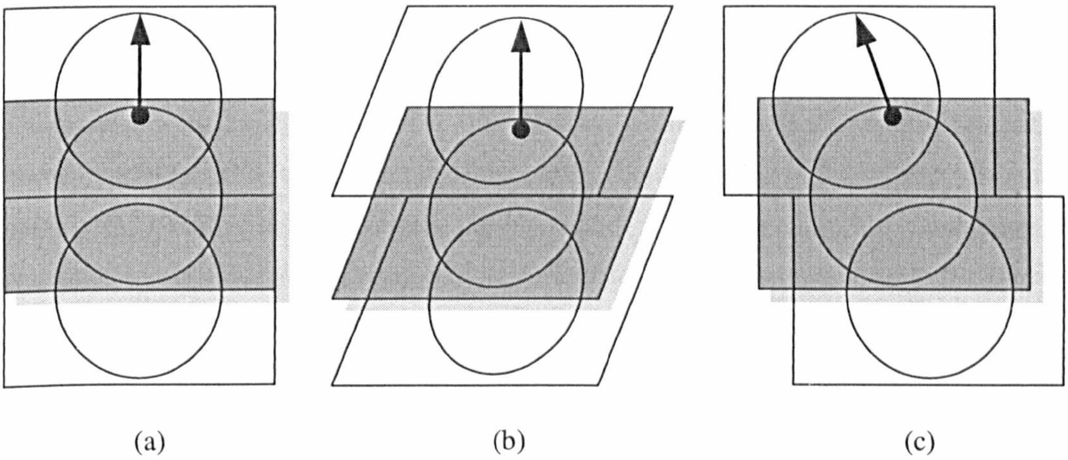

Figure 6-14 A central reconstruction of a circle is shown with overlapping PSF replicas due to sub sampling of the *k*-space data. In (a), a circle is shown on a rectangular background with the arrow showing the spatial difference in location between neighbouring replicas of the same point on the imaged object. In (b) the imaged object has undergone a shear transformation and in (c) the resultant image has undergone the reverse shear transformation to correct the central replica.

6.3.3 UNFOLD reconstruction with myocardial perfusion imaging

Respiratory motion as mentioned in Chapter 4, is unavoidable with myocardial perfusion imaging. While it can be limited through the use of breath holds due to the duration of the scan, the confidence in this being maintained for the full duration is limited. Although it is possible to correct for rigid body motion prior to applying UNFOLD to remove aliasing artefact, this is not a suitable model for cardiac respiratory motion. The use of locally focused imaging techniques [130] may permit the use of rigid body motion compensation and is an area for further investigation. As shown above, more complex forms of deformation are incompatible with the currently described method and do not assist in dealing with motion artefact in UNFOLD myocardial perfusion imaging. Due to the difficulty in correcting for motion artefact with UNFOLD perfusion imaging, an alternative method is investigated where UNFOLD is applied only to spatially static images, this eliminates the need to correct for motion before applying UNFOLD and for later analysis standard registration techniques may be performed after reconstructing the sequence with UNFOLD.

6.4 RR-UNFOLD for MR myocardial perfusion imaging

6.4.1 Unaliasing by Fourier-encoding the overlaps using the temporal dimension

It now becomes clear that the use of UNFOLD for myocardial perfusion imaging can be faced with two major problems. First, the transit of the contrast bolus within the blood pool at the up-slope of the contrast intake is rapid, which can result in sharp signal intensity changes. Second, respiratory induced cardiac deformation between cardiac cycles can be significant. Both of these introduce high temporal frequency components, thus compromising the basic condition for UNFOLD to be effective. The associated artefact is normally manifested as an attenuation of the contrast bolus signal and aliased edges from the chest wall as well as borders between the blood pool and myocardium. The elimination of respiratory motion and the restoration of tracer kinetics are therefore essential to performing UNFOLD for myocardial perfusion studies.

6.4.2 Respiratory reordered UNFOLD (RR-UNFOLD)

The main steps of Respiratory Reordered UNFOLD (RR-UNFOLD) involve the use of prospective diaphragmatic navigator echoes to split the perfusion imaging series into different sub-series (bins) so that within each bin the anatomical structures are spatially static. The only temporal change within the sub-series is a varying contrast uptake amongst different anatomical regions. There are a variety of methods for determining the limits of a bin. The most basic of these is to determine the limits of the respiratory range from a pre-scan, then divide this equally between the required number of bins. The creation of the bins can be done either through pre-scan or being dynamically created. The former requires the prior determination of the extent of the diaphragmatic motion to allocate a window width and location for each bin. The maximum and minimum values obtained from the preliminary navigator scan are used to obtain the respiratory range. This range is divided by the desired number of bins to give the bin window width, with the location equally spaced from the minimum navigator location. Additionally a bin is created below the minimum and above the maximum to contain any acquired images whose navigator location is outside the range of the pre-scans. This method is unlikely to result in an even distribution of the images amongst the bins due to the nature of breathing patterns that can change extensively during data acquisition. An accurate prediction of the bin allocation will require a longer pre-scan to build up statistical knowledge of the respiratory position.

Whilst the use of pre-scan may assist in the estimation respiratory motion, patients undergoing perfusion scans may often move or change their breathing pattern during data acquisition, particularly during the injection of the contrast bolus or Adenosine. We propose in this chapter an alternative that uses dynamic bin allocation during image acquisition. For each bin, a standard UNFOLD *k*-space acquisition is employed, where with two-fold speed-up, alternating odd-even *k*-line coverage is used for successive temporal frames. This process can be illustrated by the following pseudo code:

```
First image is acquired with odd k-lines
For all subsequent images
  Navigator location is compared with previous images working backwards
  If an image with the same navigator window value is found
    Image is acquired next in sequence with either odd/even k-lines
  Else this is the first occurrence of this navigator window value
    Image is acquired next in odd/even sequence from the previous image
```

For the first acquisition cycle, odd lines are obtained and inserted into a respiratory bin, subsequently depending on the respiratory navigator position; the associated *k*-space data is assigned to an appropriate respiratory bin. As the data collection progresses, the proposed technique acquires data sets with odd/even *k*-space coverage dictated by the RR-UNFOLD algorithm, and assigns them to the appropriate respiratory bins. There is no limit on how many images should be acquired for each bin, as the data collection process is prospective. This process is illustrated in Figure 6-15.

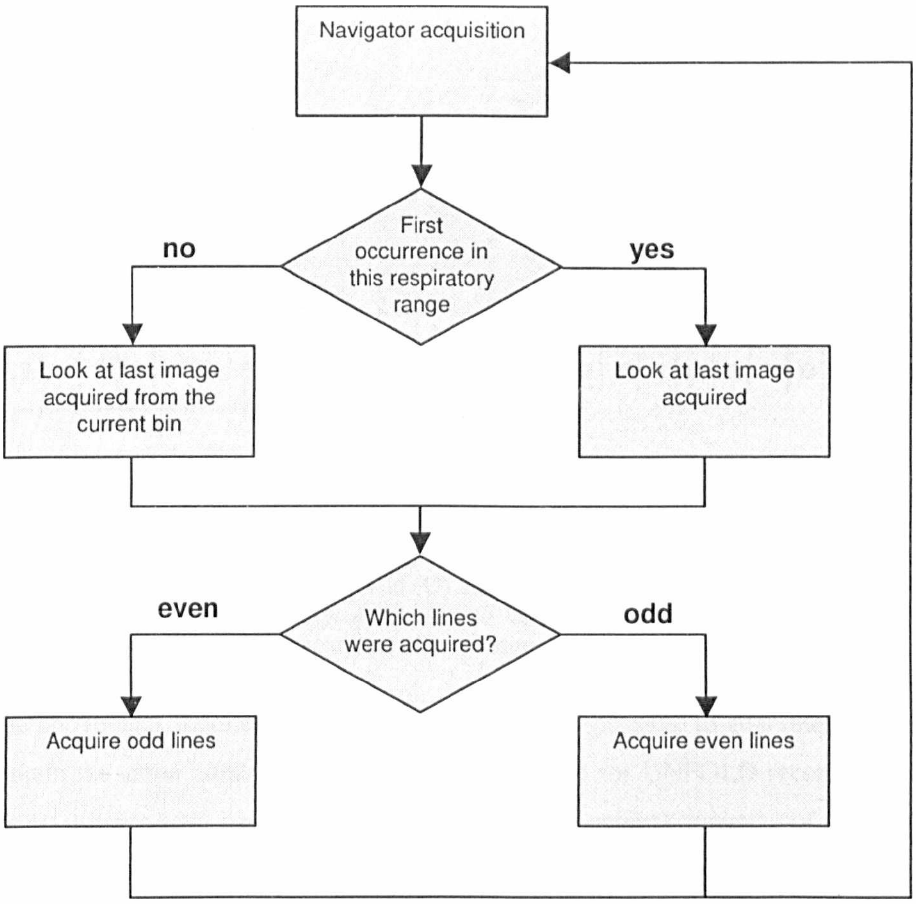
Navigator acquisition
First occurrence in this respiratory range
no
yes
Look at last image acquired from the current bin
Look at last image acquired
Which lines were acquired?
even
odd
Acquire odd lines
Acquire even lines

Figure 6-15 A schematic diagram showing the algorithm used for the binning and odd/even alternation used for RR-UNFOLD.

Figure 6-16 schematically illustrates how this algorithm is applied by using a diaphragm navigator trace where five respiratory bins are used to cover the entire respiratory range. It also demonstrates how different bins are created as time progresses. One important detail to notice is that when a new bin is created, the first image is chosen to be in sequence, in terms of odd/even *k*-line coverage, with the previous image regardless of respiratory position. For example, when bin 2 was first created, the first image used odd *k*-line coverage as the previous acquisition was for bin 1 and it used even *k*-line coverage. This is advantageous for dealing with bins with orphan frames (single frame within bin) during subsequent reconstruction.

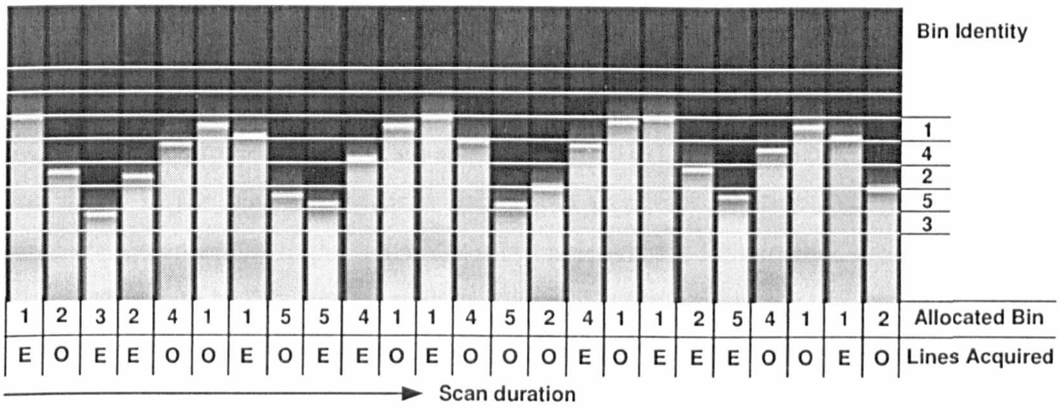

Figure 6-16 A sample navigator trace with a respiratory window of 5 *mm* for each of the bins used for RR-UNFOLD. A new bin is created in real-time at the first instance of a navigator edge being located within the specified window and from there, each further instance of a navigator edge within the required bin alternates the acquisition of odd (O) and even (E) *k*-space encoding steps. When a new bin is created, the first image is always chosen to be in sequence, in terms of odd/even *k*-line coverage, with the previous image regardless of respiratory position.

With the above data acquisition scheme, it is not always possible to guarantee that each bin will contain the same number of odd-even *k*-space pairs for UNFOLD reconstruction. It is possible to use pre-scan navigator echoes to obtain the general statistics of the respiratory pattern and the associated respiratory range so that the derived histogram can be used to equally distribute the raw *k*-space data among different bins. However, it is not practical in patient studies as the administration of Gd-DTPA and Adenosine for pharmacological stress can significantly alter the respiratory patterns of the patient during data acquisition. In this study, a fixed respiratory window size is used for dynamically creating all the necessary bins used for RR-UNFOLD as indicated in Figure 6-16. A typical respiratory window size is in the range of 5 *mm*, and with this approach the method is immune to respiratory drifts as new bins are created on the fly where necessary.

6.4.3 Image reconstruction after re-binning

The image series created by the above re-binning process cannot be used directly for reconstruction as non-uniform breathing patterns can result in bins with too few images for UNFOLD reconstruction. The number of bins created is dependent on the respiratory range of the subject during acquisition and the size of the window for each bin. Due to the way that UNFOLD is implemented, certain restrictions are imposed on the contents of each bin, *i.e.*, each bin must contain at least four images, fewer than this will make it impossible to separate the aliased image from the original image in the temporal frequency domain, as it becomes impossible to distinguish sufficient temporal frequencies. In addition, due to the way that Fourier temporal filtering is used each bin must contain an even number of images.

To correct for these problems where necessary each bin is supplemented with additional frames before applying the UNFOLD method. Since all bins are created dynamically during acquisition, there are four possible cases that need to be considered. The basic steps involved in the proposed method are shown in Figure 6-17. For example, when there is only one frame in the bin, images from the closest navigator position that are in odd-even sequence are appended to the bin. Since when a new bin is first created, the initial image is always chosen to be in sequence with the previously acquired image, the bin to be used for padding is often located at the next navigator window with variation in contrast agent bolus kept to a minimum. Further processing is then applied to ensure that the bin with padding has a minimum of four images with all the odd-even acquisition paired before conventional UNFOLD reconstruction is used. When there are only two images in the bin, the existing data in the bin is duplicated before reconstruction. The third case in Figure 6-17 deals with situations where there are an odd number of frames within the bin. In this case, the penultimate image is copied as the last image to complete the odd-even sequence. Finally, if none of the above applies, conventional UNFOLD reconstruction is applied directly.

The principle behind this post processing step is to increase the contents of a bin to a suitable size for UNFOLD to be successfully applied. This is achieved either through the reuse of current frames within the bin or the recruitment of frames from neighbouring bins. The frames recruited must adhere to the required phase shifting pattern selected during the acquisition, *i.e.*, in our case odd and even phase encode lines. From this, reconstructions for the frames originally contained within the bin are kept and reinserted into the final series, while those from additional 'borrowed' frames are discarded. In this way the result of the UNFOLD procedure is optimised for each bin by making use of the extra information present in the full series.

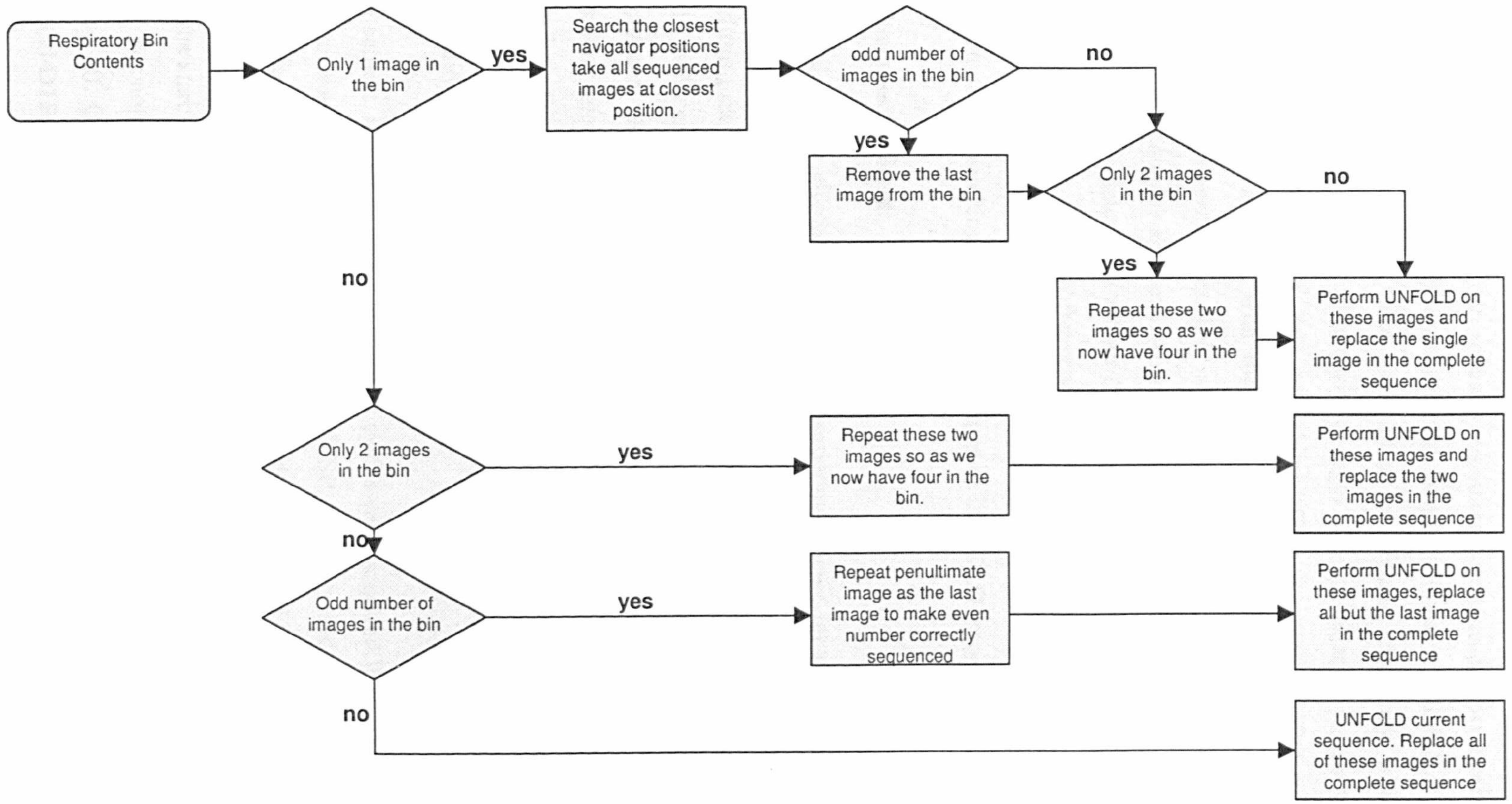
Respiratory Bin Contents
Only 1 image in the bin
yes
Search the closest navigator positions take all sequenced images at closest position.
odd number of images in the bin
no
yes
Remove the last image from the bin
Only 2 images in the bin
no
yes
Repeat these two images so as we now have four in the bin.
Perform UNFOLD on these images and replace the single image in the complete sequence
no
Only 2 images in the bin
yes
Repeat these two images so as we now have four in the bin.
Perform UNFOLD on these images and replace the two images in the complete sequence
no
Odd number of images in the bin
yes
Repeat penultimate image as the last image to make even number correctly sequenced
Perform UNFOLD on these images, replace all but the last image in the complete sequence
no
UNFOLD current sequence. Replace all of these images in the complete sequence

Figure 6-17 A schematic diagram showing all the processing steps involved in pre-processing the *k*-space data within each bin before UNFOLD reconstruction is applied.

6.4.4 Restoration of tracer kinetic signal

By splitting up the image series into spatially registered series, respiratory motion induced artefact can be eliminated in the reconstructed images. However, UNFOLD works by eliminating temporal changes in pixel intensity at the Nyquist frequency, which has the effect of smoothing out sharp signal intensity changes between adjacent images within each bin. With respiratory reordering, this smoothing effect is amplified for each bin, as successive images are acquired with the same respiratory position but not temporally immediately adjacent to each other. This is especially pronounced during contrast uptake, as by reordering the sequence sharper intensity changes have effectively been introduced. To reintroduce the correct intensities within the image, extra central phase encode *k*-lines are acquired to reintroduce the low frequency spatial intensity information. These can be substituted into the *k*-space series after the application of RR-UNFOLD to correct for excessive temporal smoothing due to out of sequence UNFOLD reconstruction.

6.4.5 Image acquisition

To study in detail the effectiveness of the re-ordering scheme for motion artefact removal and the robustness of the re-binning algorithm for free-breathing perfusion imaging, a true-FISP perfusion sequence was applied to 10 normal subjects (24 years +/- 3) and 10 patients (54 +/- 18) with clinical referrals for late gadolinium myocardial viability assessment with written consent. The navigator column was formed by intersection of 90 and 180-degree 10 *mm* thick slice selective RF pulses, positioned in the head-foot direction through the dome of the diaphragm. For navigator echoes, a frequency-encoded readout of 256 points was used to cover a 400 *mm* range, which was then interpolated to 1 *mm* resolution during reconstruction for display and edge position measurement.

For each subject, images covering 50 cardiac cycles were acquired. For each cardiac cycle, the navigator was followed by single slice TrueFISP, which, to avoid cardiac motion, ran as late as possible in the cardiac cycle, typically starting about 400 to 500 *ms* after the R-wave depending on the patient's R-R interval and R-R variability. Total image duration was 260 *ms* from the start of the non-selective saturation pulse to the end of a single-shot TrueFISP sequence. For normal volunteers Gd-DTPA was not used, and therefore the saturation pulse was turned off. Other imaging parameters include: 140 *ms* saturation recovery delay, 0.1 *mmol/kg* Gd-DTPA dose injected at approx 3 *ml/s* followed by 10 *ml* saline flush, 10 *mm* slice thickness, 40-60 degrees flip angle (SAR limited), 370 *mm* (FE) by 288 *mm* (PE) FOV (both scaled up sometimes for bigger patients), 144 (FE) by 112 (PE) un-interpolated unfiltered pixels in the image, full *ky* coverage in linear order over *ky* versus time, and 2.2 *ms* repeat time between the FISP RF-pulses. All images were acquired on a SIEMENS 1.5T Sonata scanner with a peak gradient strength of 40 *mT/m* and peak slew rate of 200 *mT/m/ms*.

The timing diagrams in Figure 6-18 shows the time since the last R wave on the horizontal axis. The diaphragmatic navigator runs just before the saturation pulse, it is therefore as up-to-date with respect to respiratory motion as is possible. The saturation pulse (at 464000-472000 *us*) for the T1-weighted perfusion TrueFISP perfusion image resets all longitudinal magnetization to 0, so the varying T1-recovery of different tissues give different brightness' in the TrueFISP image whose central raw data is acquired approx 140 *ms* (called TI) later. If the navigator hits any blood that enters the heart later, the saturation pulse to some extent acts as a reset for this. The TrueFISP image data acquisition takes 260 *ms*, plus 30 *ms* for the saturation and stabilisation at its beginning. For multi-slice acquisition, there would be one navigator and then for each slice a saturation pulse and data acquisition. Even though the saturation pulse is non-slice-selective by applying the saturation pulse again we ensure each slice has the same T1 sensitivity.

6.4.6 Error analysis

Validation of the proposed technique was performed in two stages. A detailed study of the technique on 10 normal subjects without the administration of contrast agent allowed for the assessment of RR-UNFOLD on the removal of motion artefact. Following this, the method was applied to 10 patients for further assessment of the quantitative errors associated with perfusion index calculation under normal CMR perfusion settings. The aim of the patient study is to determine the effects of the changing image intensity through time on the success of RR-UNFOLD. It also provides a means of determining the optimum number of extra central *k*-lines required to maintain the contrast agent intensity through time. For quantifying image artefact, the image series reconstructed with full *k*-space encoding was used as a gold standard and the sum of the squared subtraction error was calculated for different reconstruction methods used.

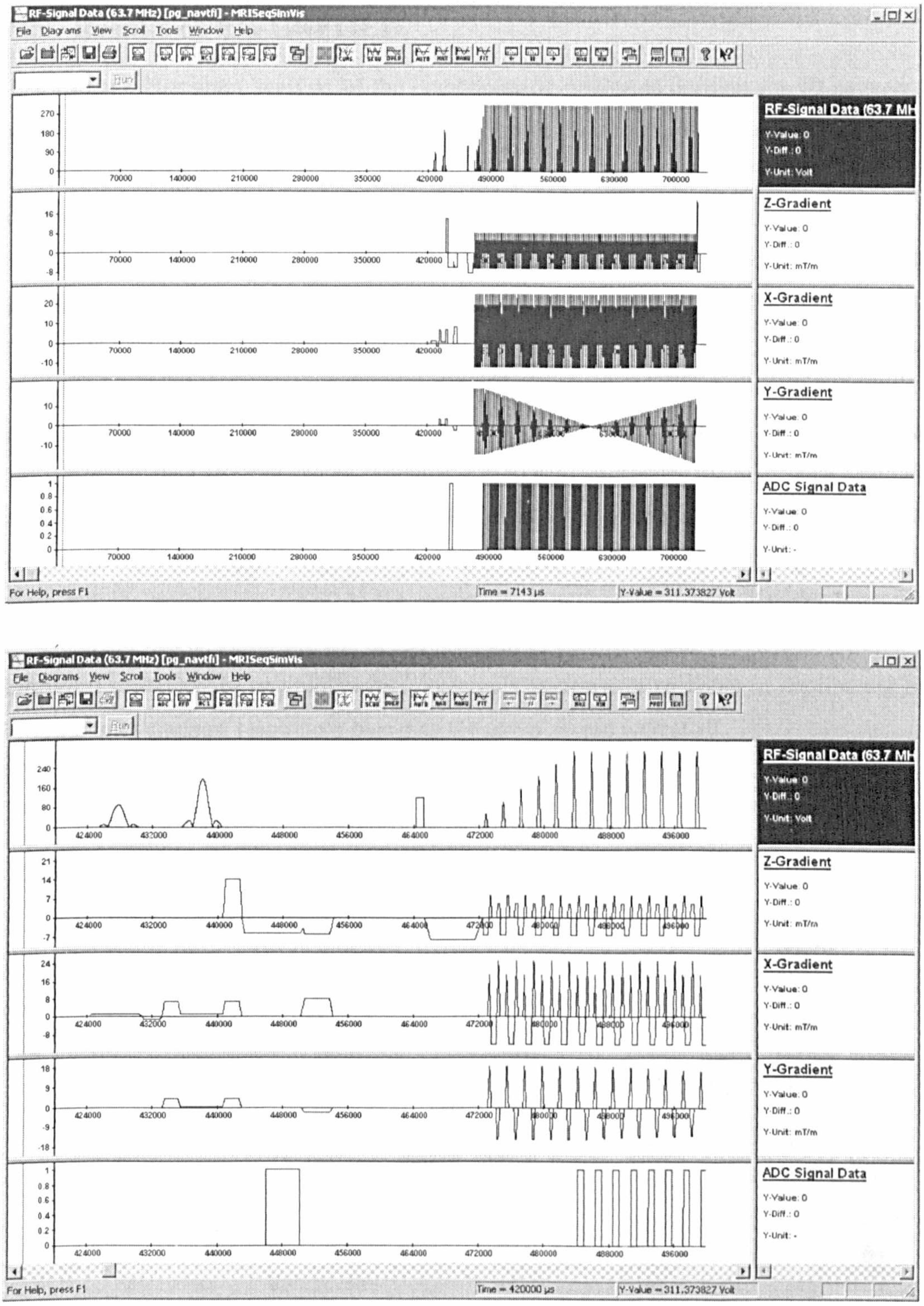
RF-Signal Data (63.7 MHz) [pg_navtfi] - MRISeqSimVis
File Diagrams View Scroll Tools Window Help
Run
270
180
90
0
70000
140000
210000
280000
350000
420000
490000
560000
630000
700000
RF-Signal Data (63.7 MH
Y-Value: 0
Y-Diff.: 0
Y-Unit: Volt
Z-Gradient
Y-Unit: mT/m
X-Gradient
Y-Gradient
ADC Signal Data
Y-Unit: -
For Help, press F1
Time = 7143 µs
Y-Value = 311.373827 Volt
424000
432000
440000
448000
456000
464000
472000
480000
488000
496000
Time = 420000 µs
Y-Value = 311.373827 Volt

Figure 6-18 The sequence timing diagram used for the acquisition of the patient data. The top figure shows the time in microseconds since the last R wave on the horizontal axis, the figure below shows the detail during the acquisition of the navigator, application of the saturation pulse and the start of the image data acquisition.

6.5 Results of RR-UNFOLD

The average histogram analysis of the diaphragmatic navigator position for 10 patients is shown in Figure 6-19, demonstrating the dwell time at end expiration observed with both the pre-scan method and the actual perfusion imaging. The histogram analysis of the diaphragmatic navigator for three patients is shown in Figure 6-20. Graph (a) shows a typical example with more acquisitions towards end expiration for both the pre-scan and the perfusion scan. In this case, the delay at end expiration is more pronounced during the actual perfusion scan. Graph (b) is more unusual with the patient appearing to pause at both end expiration and end inspiration, with the end inspiratory pause is more pronounced during the perfusion scan. This disagreement between the pre-scan and the actual scan is common amongst other data sets and can be explained due to natural changes in the patients breathing along with discomfort due to the intravenous contrast agent administration. Graph (c) shows an example where a significant drift is observed between the respiratory range of the pre-scan and the respiratory range of the perfusion scan measured with the diaphragmatic navigator. In this situation the use of the pre-scan to determine bin widths and location as discussed earlier could be problematic, potentially performing no better at distributing the image frames amongst respiratory bins than the use of no pre scan at all.

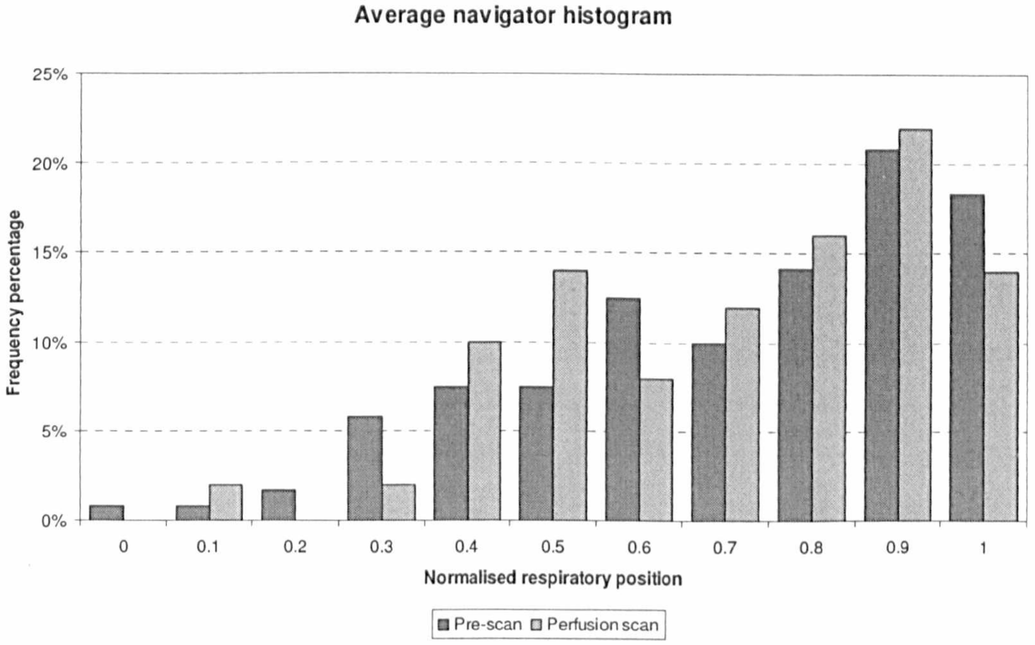

Figure 6-19 The average diaphragmatic respiratory navigator histogram for all 10 patients during the 120 cardiac cycle pre-scan, and 50 cardiac cycle perfusion scan. Diaphragmatic respiratory positions are normalised between 0 (end inspiratory) and 1 (end expiratory) with 0.1 bin widths.

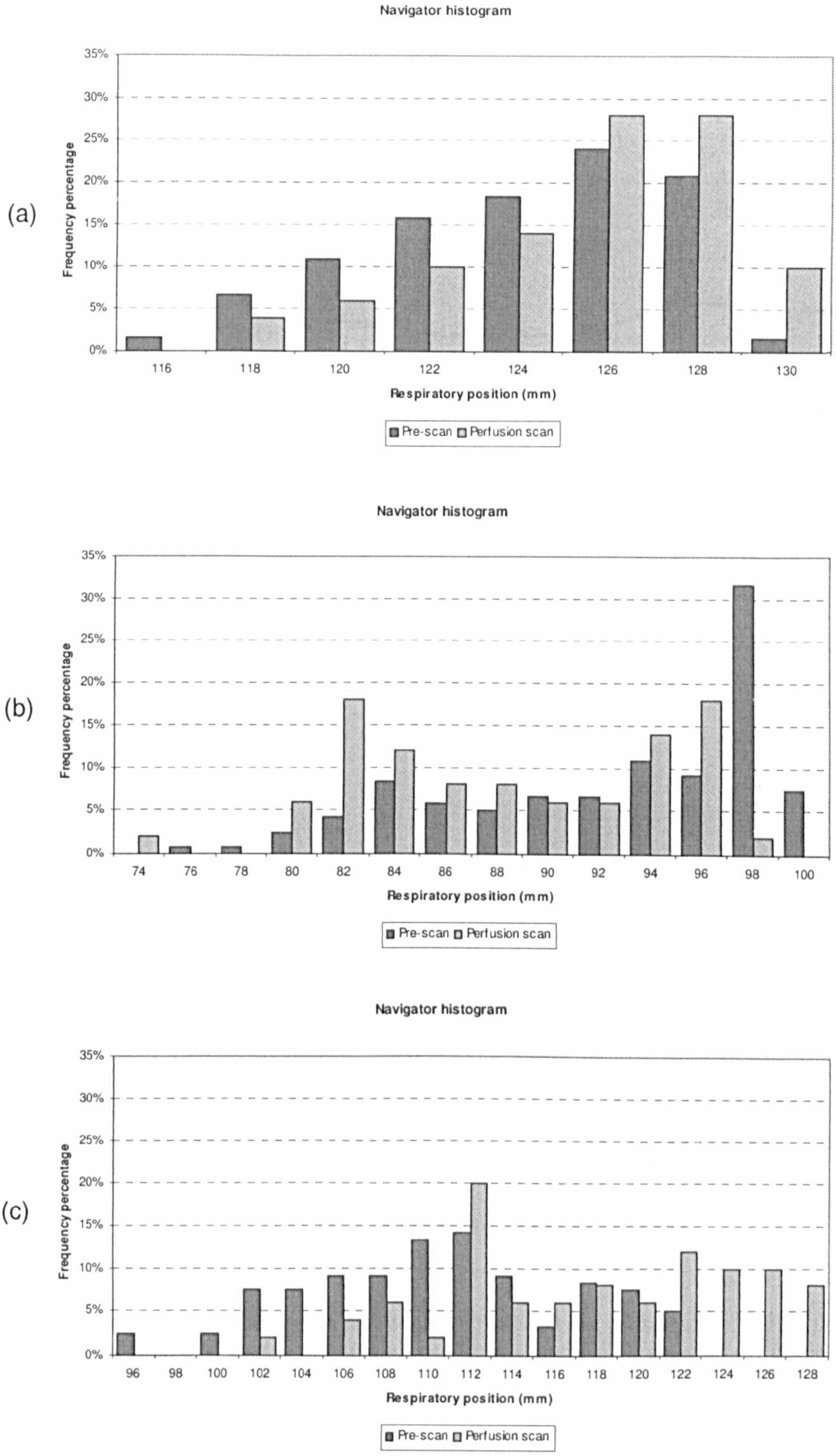

Figure 6-20 Example diaphragmatic respiratory navigator histograms for three patients during the 120 cardiac cycle pre-scan and 50 cardiac cycle perfusion scan. Diaphragmatic respiratory positions are measured in *mm* with 2 *mm* bin widths, smaller values represent end inspiration and greater values end expiration.

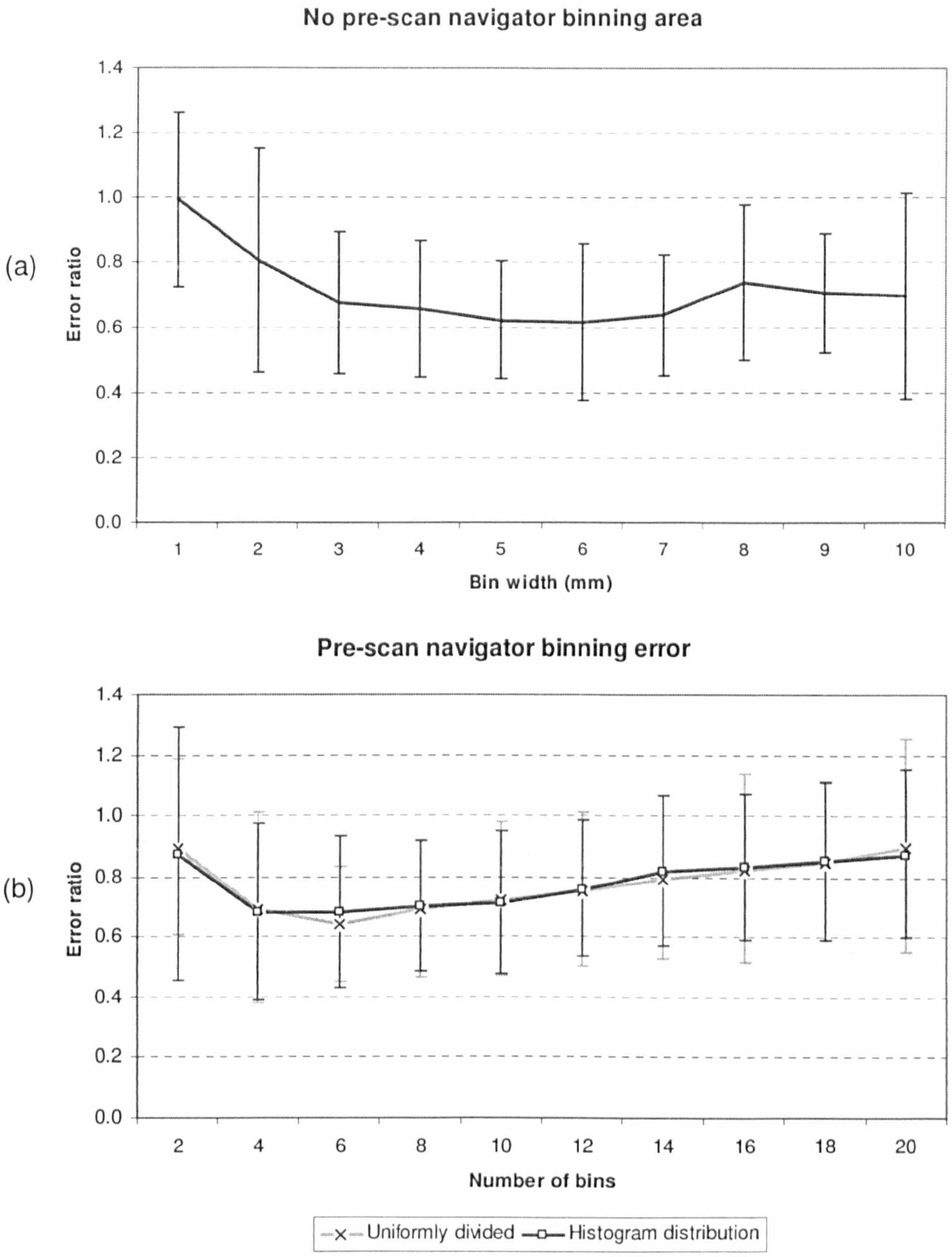

Figure 6-21 The ratio of subtraction errors between RR-UNFOLD and conventional UNFOLD for the patients with no pre-scan binning (a) and binning based on a preliminary pre-scan (b) studied when different respiratory window sizes/number of bins are selected. In both figures, the same *k*-space data with extra central lines were used for RR-UNFOLD and conventional UNFOLD techniques. The subtraction error is the sum of mean square pixel subtraction errors for the whole sequence. The solid curve demonstrates the mean error ratio for all 10 subjects and the vertical bars indicate the standard deviation amongst subjects. An error ratio of less than 1.0 indicates an improved artefact suppression of the RR-UNFOLD technique against normal UNFOLD.

Figure 6-21 demonstrates the effect of binning procedure on the performance of RR-UNFOLD when applied to 10 patients with the administration of contrast agent. As shown in (a) between 5 and 6 *mm* bin width with no pre-scan is able to reduce the error for RR-UNOLD to around 60% of that which is possible with UNFOLD. The two alternative binning procedures based on a pre scan in (b) produce very similar results. Optimal results are obtained with between 4 and 6 bins with RR-UNFOLD reducing the error to at best around 65%.

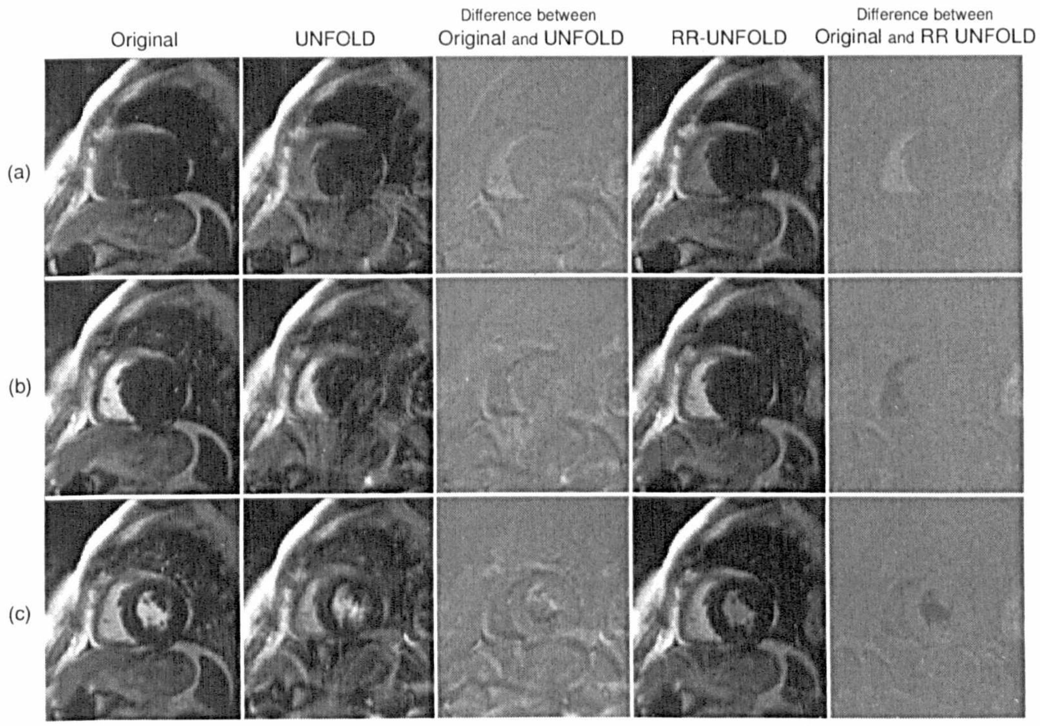
Original
UNFOLD
Difference between Original and UNFOLD
RR-UNFOLD
Difference between Original and RR UNFOLD
(a)
(b)
(c)

Figure 6-22 An example of the image artefact introduced by different reconstruction techniques, showing original fully encoded images – first column, conventional UNFOLD reconstructed images – second column, difference between the original and UNFOLD reconstructed images – third column, RR-UNFOLD reconstructed images (prior to tracer intensity correction) – fourth column, and the difference between the original and RR-UNFOLD reconstructed images – fifth column, respectively. For both UNFOLD and RR-UNFOLD, a two-fold reduction in phase encoding steps was used.

Figure 6-22 illustrates the image artefact introduced by applying the original UNFOLD and the proposed RR-UNFOLD methods (prior to intensity correction) to a perfusion sequence. It is evident that with UNFOLD significant motion blurring and artefact is present. Before the restoration of tracer kinetic signal, the proposed RR-UNFOLD method eliminates motion artefact and restricts the difference between the reconstructed images and those with fully encoded data only to temporal intensity attenuation. This attenuation can be corrected for by the use of extra central *k*-lines, which is demonstrated in Figure 6-23, where signal intensity curves from regions within the blood pool and myocardium are provided to illustrate the effectiveness of the proposed intensity correction method. It is evident that by using extra central *k*-lines with RR-UNFOLD, the reconstructed perfusion image series is very close to the result with full *k*-space encoding. In the examples shown in Figure 6-23, only 6 extra central *k*-lines were used, which represented a 45% reduction in image acquisition time.

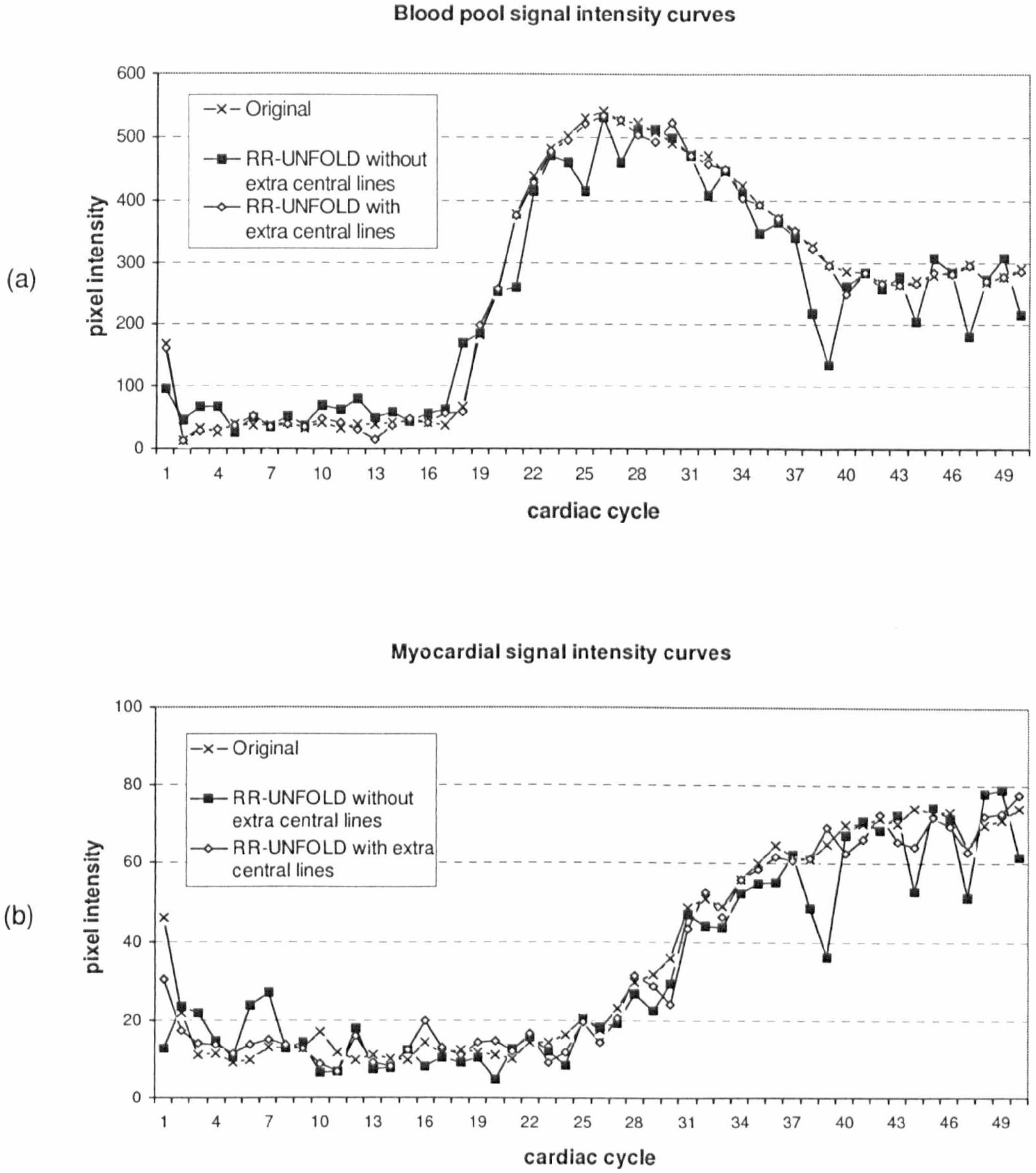

Figure 6-23 ROI signal intensity curves showing the effectiveness of signal intensity correction by the introduction of extra central *k*-space encoding lines for RR-UNFOLD. The three intensity curves of each figure show the signal derived from images with and without central *k*-space encoding measured within the blood pool and myocardium, respectively, compared to those from the original fully encoded perfusion image sequence.

To provide a more quantitative assessment of the errors introduced by the proposed RR-UNFOLD technique, the following experiments were conducted to analyse the effect of window width of each bin and the number of extra *k*-lines used for RR-UNFOLD reconstruction.

(a)

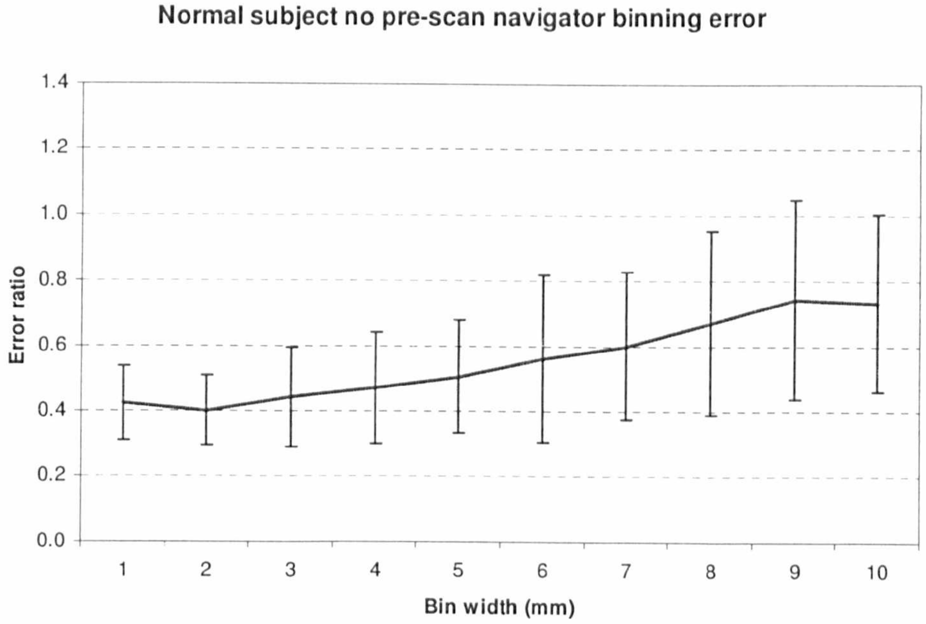

(b)

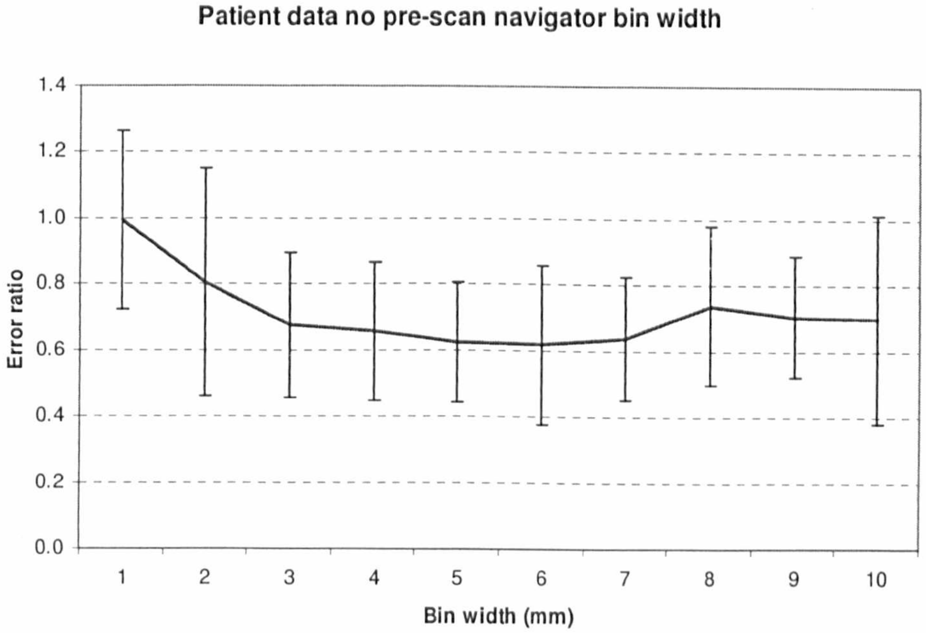

Figure 6-24 The ratio of subtraction errors between RR-UNFOLD and conventional UNFOLD for the normal subjects (a) and patients (b) studied when different respiratory window sizes are used for each bin. In both figures, the same *k*-space data with extra central lines were used for RR-UNFOLD and conventional UNFOLD techniques. The subtraction error is the sum of mean square pixel subtraction errors for the whole sequence. The solid curve demonstrates the mean error ratio for all 10 subjects and the vertical bars indicate the standard deviation amongst subjects. An error ratio of less than 1.0 indicates an improved artefact suppression of the RR-UNFOLD technique.

Figure 6-24 illustrates the amount of reduction in image artefact with RR-UNFOLD compared to UNFOLD when different window sizes (bin width) were used during data acquisition. To make a fair comparison, the extra central *k*-lines were also used for UNFOLD reconstruction and the ratio of image artefact between the two was used for Figure 6-24 (a) and (b). For normal volunteers with no Gd-DTPA injection, the amount of image artefact mainly reflects the effectiveness of the binning algorithm for respiratory motion correction, whereas for patients, this is associated with the combined effect of motion and contrast uptake restoration. As expected, smaller respiratory windows are advantages for motion correction, whereas for normal perfusion sequences in the presence of Gd-DTPA bolus, a window size of 5 *mm* is optimum. Overall, the average image artefact in the patient group was reduced to a mean of 60% ± 20 standard deviations across the 10 patients in comparison with the UNFOLD technique when the same amount of *k*-space encoding lines were used. This reduction in artefact in the patient group is likely to be significant for quantifying subtle perfusion defects in clinical applications.

The graph in Figure 6-25 illustrates the reduction in image artefact with RR-UNFOLD when different numbers of central *k*-lines, ranging from 1 to 20, were used for reconstructing the data sets for the 10 patients studied. For this analysis, the navigator window size used for each bin was fixed at 5 *mm*. As before, all values provided are represented as the amount of artefact reduction with RR-UNFOLD compared to normal UNFOLD. It is evident that the error reduces rapidly with the first 5 extra lines and after this point the reduction in image artefact is marginal. A good compromise between image quality and scan efficiency is to use 6 extra central lines for the present imaging sequence, at which point the artefact is reduced to 30% of the normal UNFOLD method.

To help relate the above image artefact ratio to the actual improvement in the visual quality of the reconstructed images, Figure 6-26 provides an example image series by using the optimum parameter settings determined above, *i.e.*, the navigator window size and the number of extra central *k*-lines were set to be 5 *mm* and 6, respectively. Four frames from a perfusion image series are shown for one of the patients studied. Each frame is reconstructed using five different methods with respective subtraction images demonstrating the difference between the original image and the reconstruction results. It can be seen that UNFOLD introduces a large amount of spatial motion artefact even with the addition of the 6 extra central *k*-lines. While RR-UNFOLD almost entirely eliminates this edge artefact, it suffers from low frequency image intensity artefact. Using RR-UNFOLD with the additional 6 extra central *k*-lines both types of artefact from the final reduced *k*-space reconstruction can be significantly reduced. This acquisition gives a 45% saving in *k*-space coverage with an average reduction in artefact of (72%±8%) over the UNFOLD method.

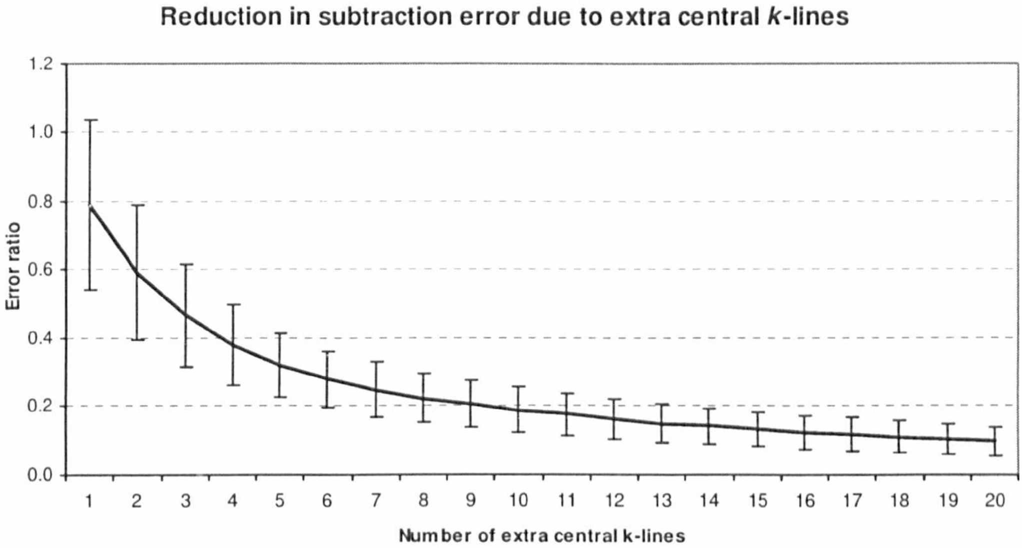

Figure 6-25 The reduction in error (mean and standard deviation of the 10 patients studied) represented as a ratio of RR-UNFOLD against normal UNFOLD when different numbers of extra central *k*-lines are used.

Finally, the effect of RR-UNFOLD on the accuracy of the derived perfusion index was analysed for the 10 patients studied. The image series were analysed by using CMRtools (Imperial College, London, UK) where a model-based approach based on Fermi deconvolution [15] was used to fit the signal time course curves. Six transmural ROI's were selected in addition to the blood pool from the short axis slice of the myocardium. The image series full *k*-space acquisition was then automatically aligned with image registration to correct for rigid body motion. Manual adjustment was applied when necessary if automatic registration was sub-optimal. The resulting time series curves were analysed by de-convolving the myocardial signal with that of the blood pool. The same analysis, including the same motion correction parameters, was applied to RR-UNFOLD reconstructed data. Normalised slope is used as the perfusion index for the 10 patients studied and Figure 6-27 gives regional values for one of the patients studied. It is evident that the error from normal UNFOLD ranges from 25% to 71%, whereas with RR-UNFOLD the maximum error is only 14%. Figure 6-28 illustrates the mean absolute perfusion index error using the conventional UNFOLD and the proposed RR-UNFOLD with a 5 *mm* bin width and 6 extra central lines for all of the 10 patients studied. The average error of the two techniques was 25% and 9% respectively.

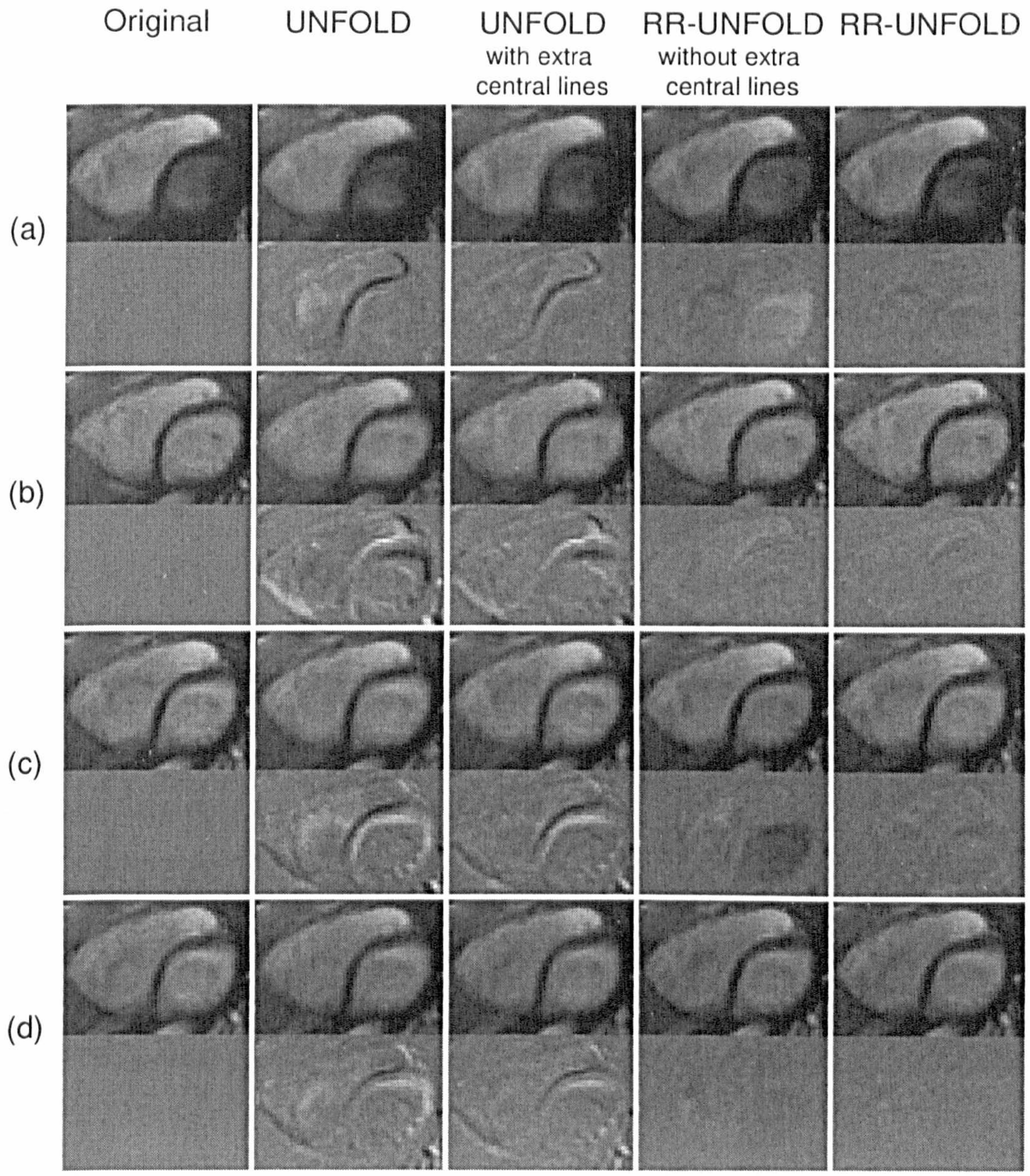
Original
UNFOLD
UNFOLD with extra central lines
RR-UNFOLD without extra central lines
RR-UNFOLD
(a)
(b)
(c)
(d)

Figure 6-26 Four frames from a perfusion sequence of a patient showing the image artefact introduced by using different reconstruction techniques, showing original fully encoded images – first column, conventional UNFOLD reconstructed images – second column, conventional UNFOLD with extra central *k*-lines – third column, RR-UNFOLD reconstructed images (prior to tracer intensity correction) – fourth column, and RR-UNFOLD – fifth column, respectively. Rows (a)-(d) show the results for different time frames and the corresponding subtraction errors compared to the original fully encoded image.

Segment	UNFOLD	RR-UNFOLD
1	1.25	0.95
2	1.42	1.14
3	1.28	1.00
4	1.32	1.03
5	1.36	1.00
6	1.71	1.05

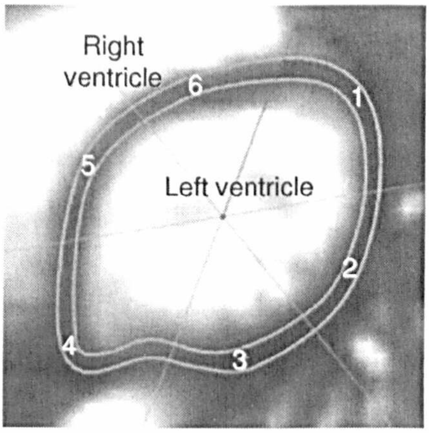

Figure 6-27 Perfusion index for normalised slope from Fermi deconvolution curve fitting calculated for 6 mid-ventricular segments of a patient demonstrating the effect of RR-UNFOLD and conventional UNFOLD for myocardial perfusion quantification. Relative values between reduced *k*-space reconstructions and the original data are shown for UNFOLD and RR-UNFOLD, where 1.0 indicates no change in perfusion index. With UNFOLD, the derived perfusion index has an error range of 25%-71%, whereas for RR-UNFOLD the error range is kept within 14%.

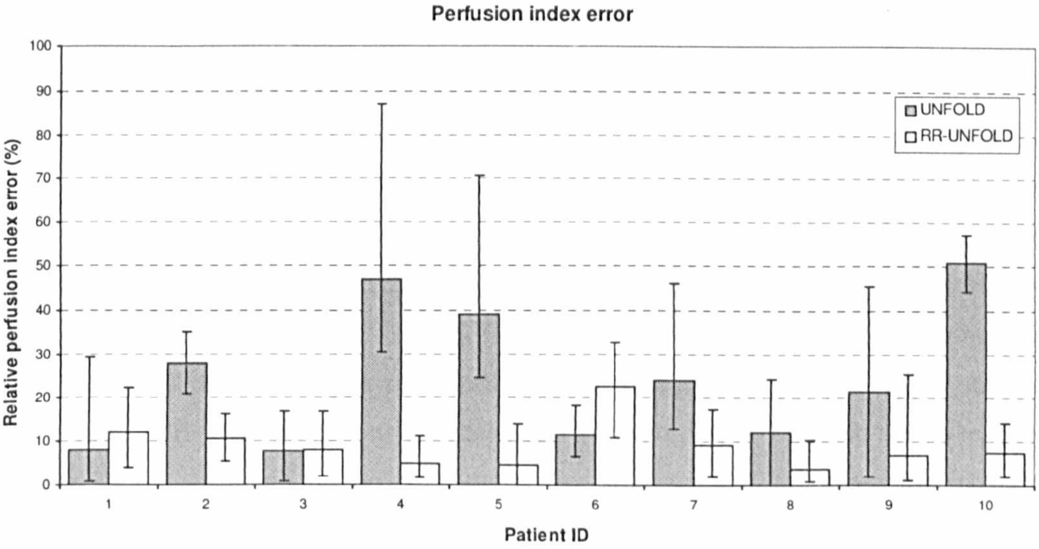

Figure 6-28 The relative error in perfusion index after applying the same processing steps as in **Figure 6-27** to all the 10 patients studied by using the UNFOLD and RR-UNFOLD techniques, respectively. The mean absolute perfusion index errors and minimum/maximum absolute perfusion index errors are shown for each patient.

6.6 Discussion and conclusions

In this study, a new RR-UNFOLD technique for myocardial perfusion imaging has been introduced. The relative strength and potential pitfalls of the techniques were assessed in detail, with results demonstrating the potential clinical value of the technique. The method achieved an overall 45% reduction in image acquisition time, whilst significantly reducing the image artefact compared to UNFOLD based on the TrueFISP perfusion sequence used. One of the major advantages of the proposed method is its simplicity, in terms of both respiratory motion correction and data reconstruction. The method only involves minor changes to sequence design if prospective navigator echoes are available on the CMR system. The re-binning algorithm proposed is straightforward to implement, and our study involving both normal subjects and patients demonstrates the robustness of the technique in dealing with different respiratory patterns.

For this study, the bin used for each image sub-series was created dynamically, thus making the technique resilient to changes in respiratory patterns. It is worth noting that for the results presented in the chapter, a fixed respiratory window was used for all the bins. The comparison of the different binning methods involved compiling results for a variety of different bin widths and number of desired bins. While the methods involving the pre-scan correctly allocated images to the relevant bins, the importance of this was found to be small. For the pre-scan methods, especially with the histogram the desired effect was to evenly spread the number of images in each bin. This was found to be of less importance than the respiratory range that a bin covered. The results for both pre-scan methods were very similar, on the normal subjects with no contrast agent the more bins that were used the better the result up to around 14 bins at which point the bin width came close to the 1 *mm* navigator resolution so the results were unaffected. This is shown in Figure 6-29 and can be compared with Figure 6-24 for the no pre scan method. The patients with contrast agent showed improvement as the number of bins increased up to around 6 bins, at which point the error increased as the small bin size affected the ability to accurately reconstruct the intensity change due to the passage of contrast agent. For the complete range tested between 2 and 20 bins for both pre-scan methods the RR-UNFOLD method with 6 extra central lines showed improvement in comparison with normal UNFOLD with 6 extra central lines.

(a)

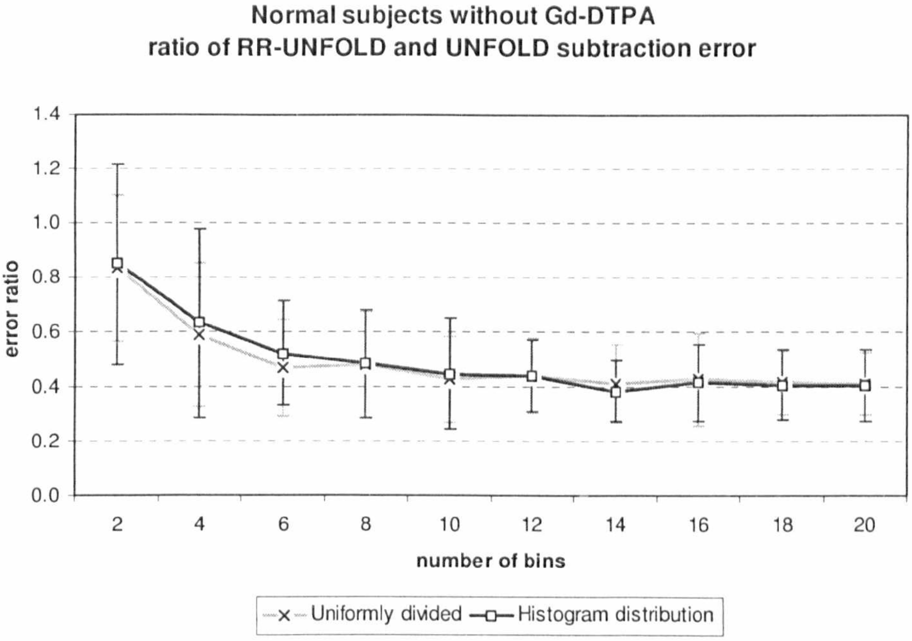

(b)

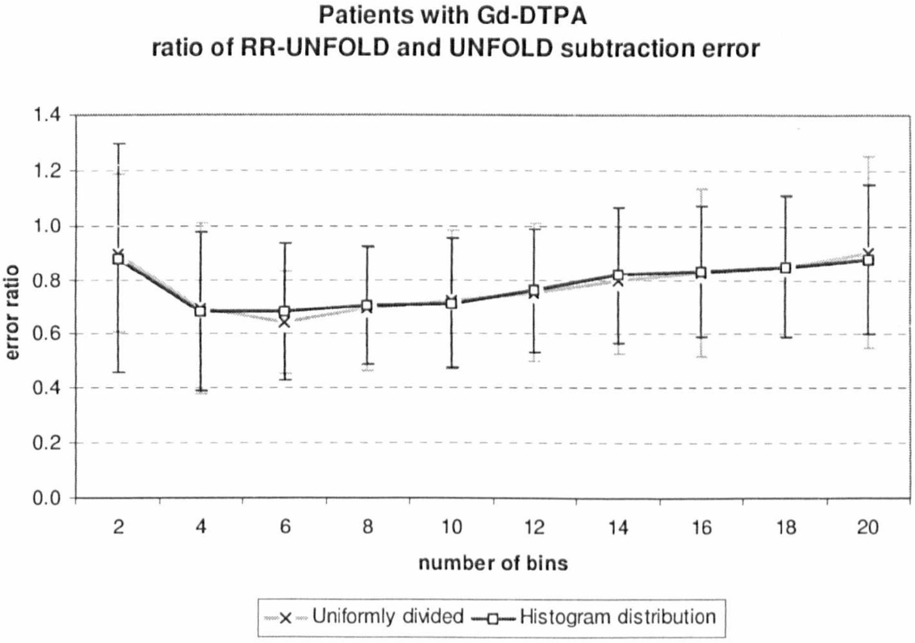

Figure 6-29 The ratio of subtraction errors between RR-UNFOLD and conventional UNFOLD for the normal subjects (a) and patients (b) studied when different numbers of bins are selected following an initial pre-scan. The first of the two methods divides the respiratory range evenly while the second selects bins to divide the histogram distribution from the pre scan evenly.

By creating bins in real time based on a predefined bin width, we are able to discard the preliminary navigator scan. This reduces the time that the patients must stay in the scanner. It also reduces the dependency on the relationship between the respiratory pattern of the pre-scan and the respiratory pattern of the actual scan. The results for this method were found to be more consistent than the pre-scan methods. Furthermore, it is also important to consider the respiration speed during data acquisition as for perfusion imaging the acquisition window is long compared to that of conventional imaging due to the complete spatial coverage required for every cardiac cycle. This effect is most pronounced at mid-respiration when the speed of the diaphragm movement is at its maximum. An optimised solution to these issues, however, is not trivial and will require prior knowledge of subject specific respiratory patterns. Although this information can be acquired, to some extent, by using pre-scans so that the respiratory patterns are monitored for a short period of time before actual perfusion imaging, it is difficult to put this into practice as respiratory patterns do change during the course of image acquisition, especially due to the use of pharmacological stress for assessing the perfusion reserve.

It is worth noting that although all results shown in this chapter are based on a TrueFISP perfusion sequence, the method is applicable to general perfusion sequences. Our results have shown that RR-UNFOLD significantly extends the applicability of UNFOLD to perfusion imaging, which brings a 40% reduction in image artefact (or 70% reduction if the extra central *k*-lines were not used for UNFOLD reconstruction). The scan efficiency achieved can either be used for extending the 3D spatial coverage or shortening the acquisition window of the perfusion sequence. Both are fundamental to the accuracy of the CMR technique in providing detailed information on regional myocardial perfusion abnormality. The reduction in acquisition window is particularly important to 3D perfusion imaging with multi-slice coverage as mis-registration due to materials moving in/out of the imaging plane caused by cardiac and respiratory induced long axis motion is particularly difficult to rectify, and cannot be restored by post-processing techniques. The proposed technique is therefore valuable for accurate perfusion quantification to extend the role of CMR in managing patients with suspected CAD and for follow-up in patients with known ischaemic defects.

While the results for RR-UNFOLD show marked improvements in accuracy for the perfusion index measured by normalised slope in comparison with UNFOLD, in two instances RR-UNFOLD actually produced greater error in the measured perfusion index value (patient 1 increasing from 8% to 12% and patient 6 from 12% to 23% as shown in Figure 6-28). In the case of patient 1 both UNFOLD and RR-UNFOLD provided acceptable error of around 10%. For patient 6 however the error is significant. This is attributed to the poor navigator trace from the patient which when used with RR-UNFOLD degrades the consistency of the *k*-space data and actually increases the image artefact.

In summary an effective way of extending the UNFOLD framework for myocardial perfusion imaging has been demonstrated. The strength of the technique is demonstrated with *in vivo* data acquired from both normal subjects and patients referred for myocardial viability assessment. The method brings near two-fold increase in imaging efficiency but with only minor deterioration in image quality compared to full *k*-space coverage. Furthermore, the method is relatively simple to implement and can be applied to most of the current state-of-the-art CMR scanners.

Chapter 7 : RR-RIGR for Myocardial Perfusion Imaging

7.1 Introduction

In Chapter 6, we have demonstrated the use of RR-UNFOLD for halving the image acquisition time for myocardial perfusion imaging. With prospective respiratory reordering, the technique has shown great promise in retaining tracer kinetic details in the presence of free-respiratory motion. From detailed numerical analysis, it was apparent that despite the use of continuous sampling of the central *k*-space data, a certain amount of temporal smoothing still remains. To circumvent this problem, we will introduce the use of Respiratory Reordered RIGR (RR-RIGR) for myocardial perfusion. The technique does not rely on temporal smoothing as redundancies in the spatial domain are exploited with the use of prior information obtained from a reference image.

As an alternative to the traditional keyhole method, RIGR has been applied to a range of dynamic imaging applications including functional brain imaging and contrast enhanced angiographic studies. Dynamic contrast studies of the brain are ideally suited for RIGR [221] due to the relatively static nature of the brain morphology. The reduction in imaging time allows for increased temporal resolution, or signal averaging for enhancing SNR [222]. RIGR has also been applied to other contrast enhanced dynamic studies such as those for breast tumours staging [223]. The method is applicable to data acquisition schemes that involve T1 or T2 weighted images, which typically require prolonged imaging time [221]. For example, the method has been used for dual contrast TrueFISP imaging [224] where pairs of contrasting RF flip angle images are used for automatic cardiac segmentation strategies. RIGR has also been applied to diffusion-weighted tensor imaging for the characterisation of myocardial fibre orientations [225].

Recent improvement in RIGR has reduced the computational complexity of the technique, which can potentially increase the practical value of the method in clinical settings [226]. In parallel to the use of Fourier encoding with RIGR, approaches using partial wavelet encoding have also been proposed. Rather than limiting the dynamic information to low frequency contrast changes, the use of wavelets allows for improved localisation of spatial changes thus permitting increased scan efficiency. To cater for global motion, an interesting variation of the RIGR technique has been proposed that builds a family of basis functions from rotated and translated versions of the high-resolution reference image [226]. The principle of maximum cross entropy is then used to determine the optimal set of basis functions for reconstruction of particular images.

In this chapter, we will describe the use of RIGR combined with prospective respiratory reordering for handling cardiac motion. The technique is similar in spirit to that described in Chapter 6, and our emphasis is placed on the comparison of relative merit and potential pitfalls of the RIGR approach, particularly in the localisation of small endocardial defects.

7.2 Theoretical background of RIGR

The generalised series approach is based on constrained image reconstruction as an alternative to Fourier encoding. In Fourier encoded images, the spatial resolution is primarily determined by the number of data points collected in *k*-space. For an $i \times j$ image dimension, $i \times j$ data points must be collected in *k*-space to avoid artefact and ensure accurate representation of features and relative intensity. This method of acquiring images takes no account of the relative amount of actual information that is required to form the image. For dynamic imaging, the efficient reduction in *k*-space sampling can be considered as the amount of new information provided from one image to the next.

Mathematically, the requirement of dynamic imaging can be defined as the acquisition of a sequence of Q images, denoted as $I_1(x)\ldots I_Q(x)$, with the aim of representing a time varying function $I(x,t)$ in a discrete manner. With the traditional Fourier transform based method, these Q data sets are independently acquired in *k*-space, denoted as $d_1(k)\ldots d_Q(k)$ such that

$$d_q(k) = \int_{-\infty}^{\infty} I_q(x) e^{-i2\pi kx} dx \tag{7.1}$$

where k is the spatial frequency variable. Assuming that N data points (or encodings) are sampled for each set at $k = n\Delta k$, where n is the encoding step and Δk the sampling spacing in k-space. The speed at which each image is acquired is limited by NT_R, where T_R is the repetition time.

RIGR attempts to minimise the total number of spatial encodings required for acquiring the dynamic image data sets [109]. The suitability of the method to the imaging task as with keyhole imaging is based on the assumption that during the acquisition of dynamic image data, the high-resolution data remains static. The high-resolution static image is built into a set of basis functions of a generalised series model, constrained to the low resolution dynamic images; the high resolution dynamic images can then be reconstructed with relatively few dynamic encodings. With keyhole imaging, data inconsistencies can be expected between the extrapolated data and the measured data. These include amplitude discontinuities and phase incoherence that can give rise to Gibbs artefact and blurring. With RIGR, these problems are avoided through the use of the generalised series reconstruction.

By following the original description by Liang *et al* [109], the general mathematical framework for the constrained image reconstruction can be described by the generalised series image function:

$$I_{GS}(x) = \sum_n c_n \varphi_n(x) \tag{7.2}$$

where $\varphi_n(x)$ are the set of basis functions chosen as an alternative to the sinusoidal functions used in the Fourier representation and c_n are corresponding coefficients. For dynamic imaging, we look at the class of basis functions formed from a family of constrained complex sinusoids,

$$\varphi_n(x) = C(x) e^{i2\pi n\Delta kx} \tag{7.3}$$

where the constraint function $C(x)$ is chosen to absorb available *a priori* information. The optimality of these basis functions can also be justified from the maximum cross-entropy principle. By treating the constraint function $C(x)$ as an initial estimate to a desired image function $I(x)$, the optimal reconstruction under this principal is the one that maximises the following cross entropy measure

$$-\int_{-\infty}^{\infty} I(x)\log\frac{I(x)}{C(x)}dx \tag{7.4}$$

subject to the data consistency constraints for the m encodings

$$d(m\Delta k)=\int_{-\infty}^{\infty} I(x)e^{-i2\pi m\Delta kx}dx \tag{7.5}$$

The solution to this constrained problem is

$$\tilde{I}(x)=C(x)\exp\left(\lambda_n\sum_n e^{i2\pi m\Delta kx}\right) \tag{7.6}$$

where λ_n are appropriate Lagrange multipliers. If $C(x)$ is a good estimate for $\tilde{I}(x)$, the exponential term can be reasonably approximated by the first two terms of its power series expansion, *i.e.*, $\exp(x)\approx 1+x$. In this case, $\tilde{I}(x)$ becomes

$$\begin{aligned}\tilde{I}(x)&\approx C(x)+\sum_n \lambda_n C(x)e^{i2\pi n\Delta kx}\\&=\sum_n[\delta(n)+\lambda_n]C(x)e^{i2\pi n\Delta kx}\end{aligned} \tag{7.7}$$

which when $c(n)=\delta(n)+\lambda_n$, where $\delta(n)$ is a unit impulse function with a value of 1 for $n=0$ and 0 otherwise, is identical to the GS model function $I_{GS}(x)$ defined in (7.2) and (7.3). In this way the GS model function can be viewed as an approximation to the maximal cross entropy solution. This approximation has the advantage of creating a linear problem (with $c(n)$ being determined by a set of linear equations), out of a highly non-linear one, enabling fast reconstruction of the resulting images.

By combining (7.2) and (7.3) we can rewrite the GS model as

$$I_{GS}(x)=C(x)\sum_n c_n e^{i2\pi n\Delta kx} \tag{7.8}$$

the resolution of $I_{GS}(x)$ is now therefore determined by the constraint function $C(x)$ rather than the number of dynamic encodings N_L acquired for the dynamic image. Given this, if a high-resolution image is acquired and used to determine the basis functions, only a few dynamic encodings are later required to reconstruct a high-resolution image. In practice a reference image can be acquired at any time, although to preserve sufficient consistency of high frequency information this should be during the same scanning session with minimum movement of the imaged subject. The reference image should have high SNR and similar contrast characteristics to the dynamic data.

The number of dynamic encodings N_L actually required to reconstruct the high-resolution dynamic data depends on the dynamic properties of the image. From equation (7.8) the Fourier series factor $\sum_n c_n e^{i2\pi n\Delta kx}$ is termed the contrast modulation function and the number of dynamic encodings directly determines the resolution of this function. If only a single dynamic encoding is used this acts as a global scaling factor, with more terms able to represent localised contrast changes. The boundary information built into the basis functions produces a more rapidly convergent model than in the Fourier series model, reducing the truncation artefact that is inevitable if too few dynamic encodings are acquired to provide sufficient resolution to the contrast modulation function. Given this model, three issues need to be addressed in using RIGR. These are the construction of the basis functions, the determination of the basis functions under the data consistency constraints, and the calculation of the image from the GS model.

With RIGR, the basis functions are uniquely determined by the constraint function $C(x)$. In the case of dynamic imaging with the high-resolution reference image $I_{ref}(x)$ acquired following the same protocol as the low-resolution dynamic images, $C(x)$ can be initially set to $I_{ref}(x)$ and be successively updated with the newly reconstructed GS image. This gives the following set of basis functions:

$$\varphi_n(x) = \left|I_{ref}(x)\right| e^{i2\pi n\Delta kx} \tag{7.9}$$

The GS coefficients c_n are determined by fitting the GS model to the reduced data sets to recognise the dynamic changes. By using the basis functions in (7.9), a dynamic image $I_q(x)$ is given by:

$$I_q(x) = \left|I_{ref}(x)\right| \sum_{n=0}^{N_L-1} c_n e^{i2\pi n\Delta kx} \tag{7.10}$$

From this we can provide the data consistency constraints for c_n as

$$\begin{aligned} d_q(m) &= \int_{-\infty}^{\infty} I_q(x) e^{-i2\pi m\Delta kx} dx \\ &= \left\{ \left|I_{ref}(x)\right| \sum_{n=0}^{N_L-1} c_n e^{i2\pi n\Delta kx} \right\} e^{-i2\pi m\Delta kx} dx \\ &= \sum_{n=0}^{N_L-1} c_n d_c(m-n), \quad 0 \le m \le N_L - 1 \end{aligned} \tag{7.11}$$

where $d_c(k)$ is the Fourier transform of $\left|I_{ref}(x)\right|$. The linear equations in (7.11) define a linear system of N_L equations in matrix form:

$$\mathbf{Hc} = \mathbf{d} \tag{7.12}$$

where $\mathbf{d} = [d_q(0), \ldots, d_q(N_L - 10)]^T$, $c = [c_0, \ldots, c_{N_L - 1}]^T$ and the coefficient matrix:

$$\mathbf{H} = \begin{bmatrix} d_c(0) & d_c(-1) & \cdots & d_c(N_L + 1) \\ d_c(1) & d_c(0) & \cdots & d_c(N_L + 2) \\ \vdots & \vdots & \ddots & \vdots \\ d_c(N_L - 1) & d_c(N_L - 2) & \cdots & d_c(0) \end{bmatrix} \tag{7.13}$$

The coefficient matrix **H** is ill conditioned and regularisation is required to provide a good solution and reduced sensitivity to noise. For the following investigations, we have used MRITool 2.0 [227], an implementation of the RIGR technique based on the above description.

7.3 Assessment of RIGR for contrast enhanced imaging

7.3.1 Reconstruction of synthetic myocardial perfusion data

In order to assess the general performance of RIGR for dynamic contrast enhanced data, a series of synthetic images were constructed. The synthetic data consisted of a single mid ventricular short axis slice of the heart with a resolution of 128×128. No motion was present and uniform regions of contrast varied through the sequence based on real data acquired from a patient. Figure 7-1 shows two frames from the sequence. The reference frame is from the end of the sequence as the contrast agent has distributed throughout the blood stream and the blood pools and the borders of the myocardium are clearly observed. Two perfusion defects are simulated, a transmural defect in the infero-septal wall that is still clearly visible in the reference frame, and a sub endocardial defect in the antero-lateral wall, which has almost disappeared. The dynamic image is from midway through the sequence as the contrast agent in the blood pool is leaving the LV and entering the myocardial tissue. At this point, the transmural defect is clearly highlighted and the subendocardial defect, which was hardly visible in the reference frame, is clearly visible.

The graphs in Figure 7-1 illustrate the pixel line intensity profile through the image in the phase encode direction. It is clear from the reference to the dynamic image that there is significant enhancement in the LV blood pool and also enhancement in the anterior myocardial wall and in the RV blood pool, while little enhancement is seen in the transmural defect in the infero-septal wall.

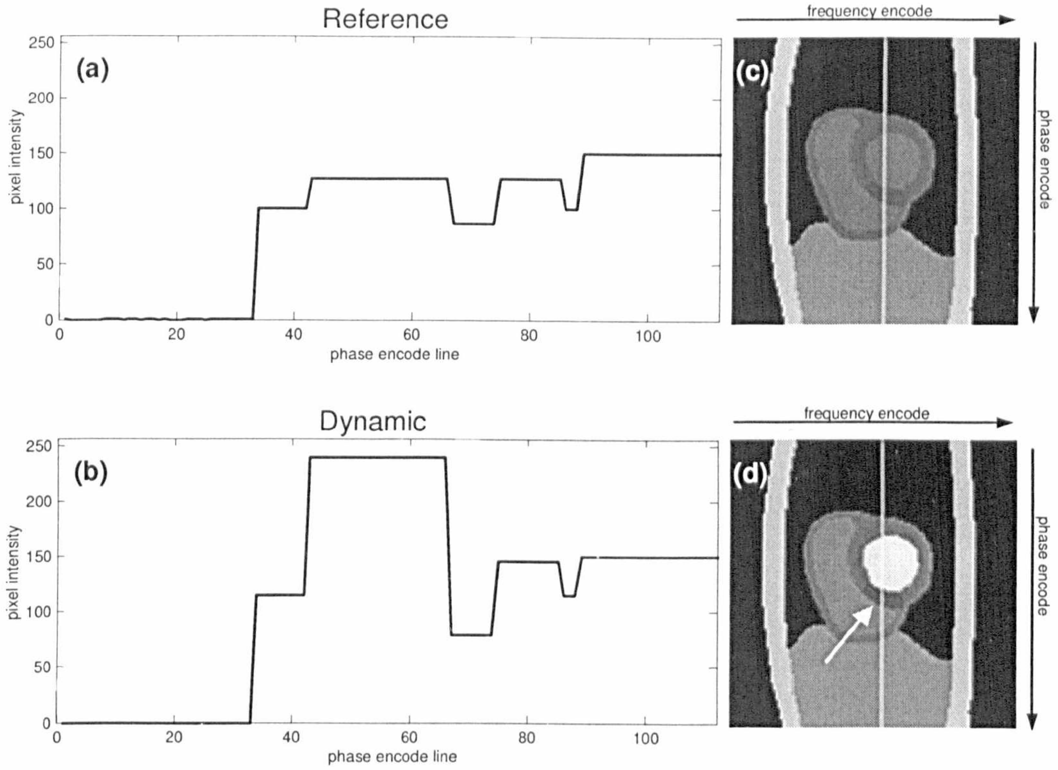

Figure 7-1 Two images from a synthetic myocardial perfusion sequence. The reference image is an image from late in the sequence and the dynamic image as the contrast agent enters the myocardial tissue. In the dynamic image a transmural defect is shown in the infero-septal wall (pointed by the arrow). The graphs show the pixel intensity values for the line shown down the image in the phase encode direction. The most notable difference between the reference and dynamic image in the graph is enhancement of the blood pool of the LV and hypo-enhancement of the transmural perfusion defect (phase encode line ~70).

In Figure 7-2, the same data set is shown with the dynamic image reconstructed using only the central 16 of the 128 dynamic phase encode steps. For display purposes, we have cropped the image to show the region of the heart. When the image is reconstructed using only the central 16 lines of *k*-space, the line profile is, as expected, over smoothed due to the lack of high frequency information. This translates to significant blurring in the phase encode direction. In Figure 7-2(b), the keyhole technique [106] is used with direct replacement of the central 16 phase encode lines from the reference image, supplemented with the remaining lines from the static reference image shown in Figure 7-1. This provides a noticeably improved result although a smearing artefact from the blood pool to the infero-septal wall can be observed. For Figure 7-2 (c), the RIGR technique is used with basis functions derived from the reference image in Figure 7-1, and once again the central 16 phase encode lines. This provides a sharper edge to the myocardium in the anterior wall although artefact is seen in the blood pool.

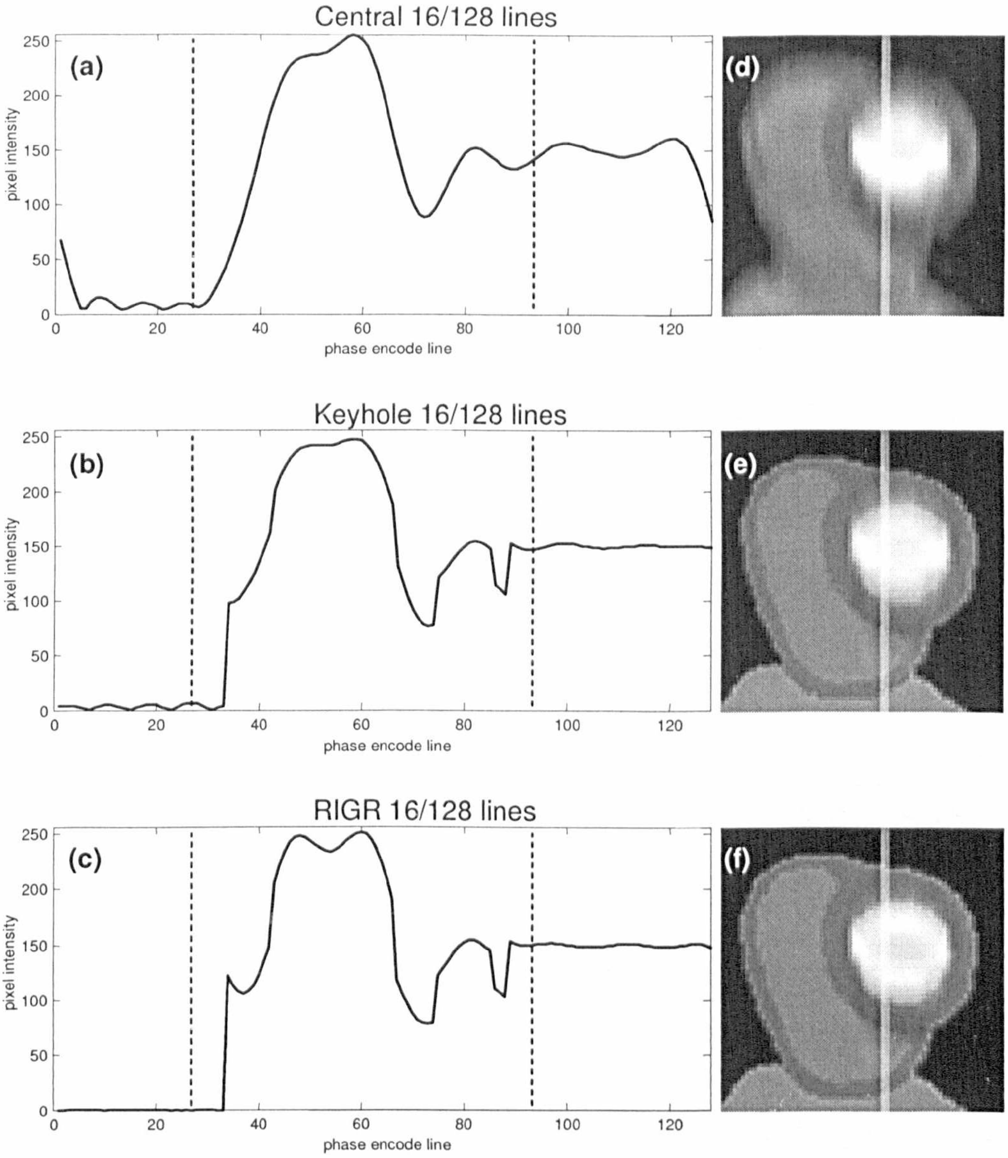

Figure 7-2 Reconstruction of the dynamic image from Figure 7-1 by using only 16 of the 128 phase encode lines. The top graph and image show a simple Fourier transform of the central 16 lines, the middle graph and image show the replacement of the central 16 lines of the dynamic image into the remaining lines of the reference image from Figure 7-1. The bottom graph and image show reconstruction using the RIGR technique from the central 16 lines of the dynamic image with basis functions derived from the reference image. While significant artefact is shown throughout the image with all three reconstructions, the RIGR technique provides visibly clearer myocardial borders. For display purposes, the images on the right have been cropped and this region is shown as dotted lines on the graphs on the left

In Figure 7-3, we perform the same process as with Figure 7-2 now doubling the number of central phase encode lines to 32. With only the central lines used, we now have a much more recognisable image although significant Gibbs artefact still exits. With the keyhole technique, much of the blurring has been removed although artefact is seen in the blood pool of the LV. By using the RIGR technique, this artefact is reduced and the myocardial boundaries are more clearly seen.

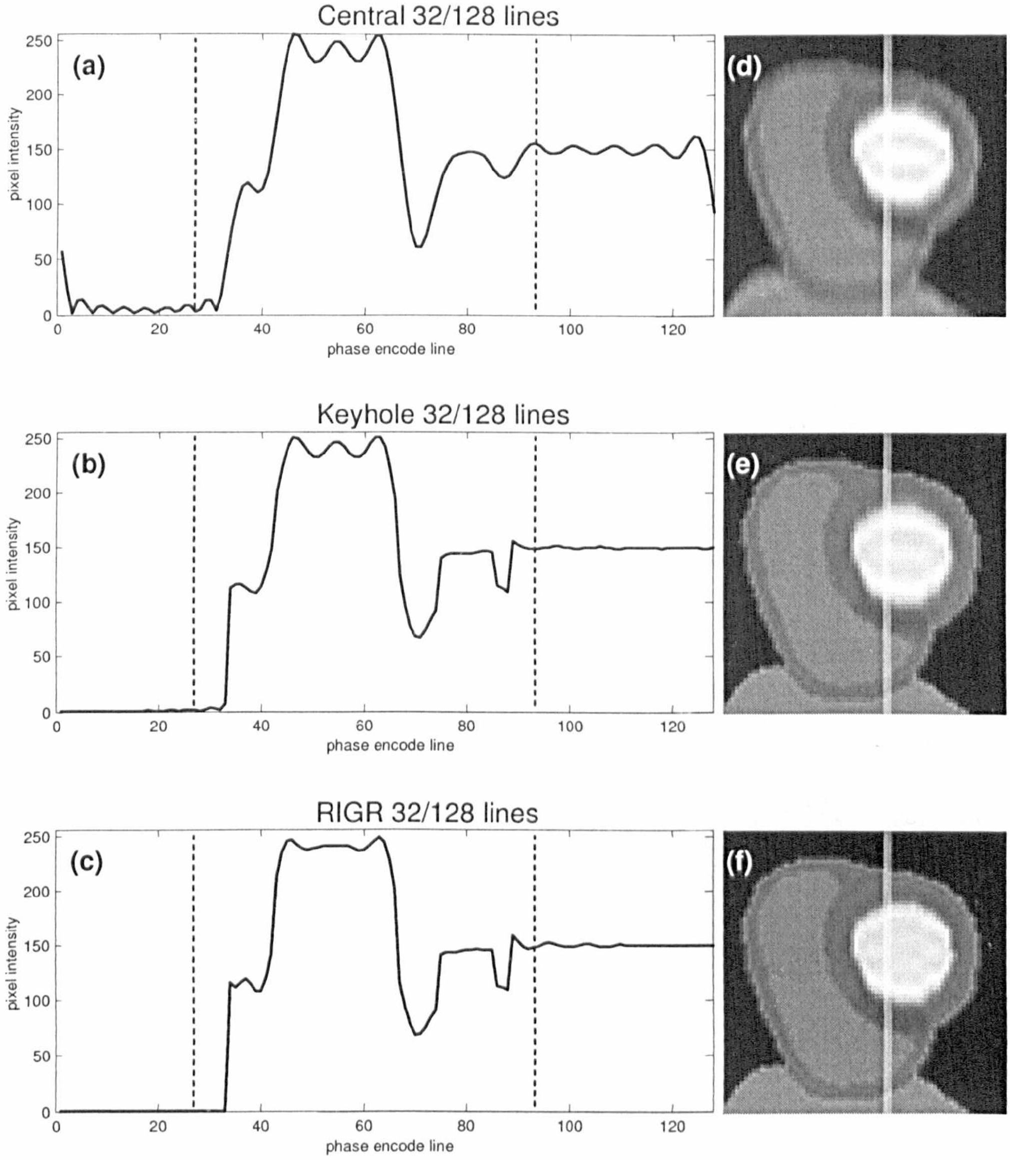

Figure 7-3 Reconstruction of the dynamic image from Figure 7-1 by using only 32 of the 128 phase encode lines. The top graph and image show a simple Fourier transform of the central 32 lines, the middle graph and image show the replacement of the central 32 lines of the dynamic image into the remaining lines of the reference image from Figure 7-1. The bottom graph and image show reconstruction using the RIGR technique from the central 32 lines of the dynamic image with basis functions derived from the reference image. While all three techniques are able to distinguish the transmural defect, RIGR provides visibly sharper edges to the LV blood pool with significantly less artefact. For purposes, display the images on the right have been cropped and this region is shown as dotted lines on the graphs on the left

To compare reconstruction results for subtle image details, Figure 7-4 illustrates a pair of images showing a small subendocardial defect in the antero-lateral wall. The layout of the image is similar to that of Figure 7-1, but now with the phase encode direction rotated by 90°, *i.e.*, along the horizontal direction. The corresponding image reconstruction results with 16 and 32 phase encoding steps are shown in Figure 7-5 and Figure 7-6, respectively. It is evident that as the image details get smaller, RIGR seems to retain these details more faithfully.

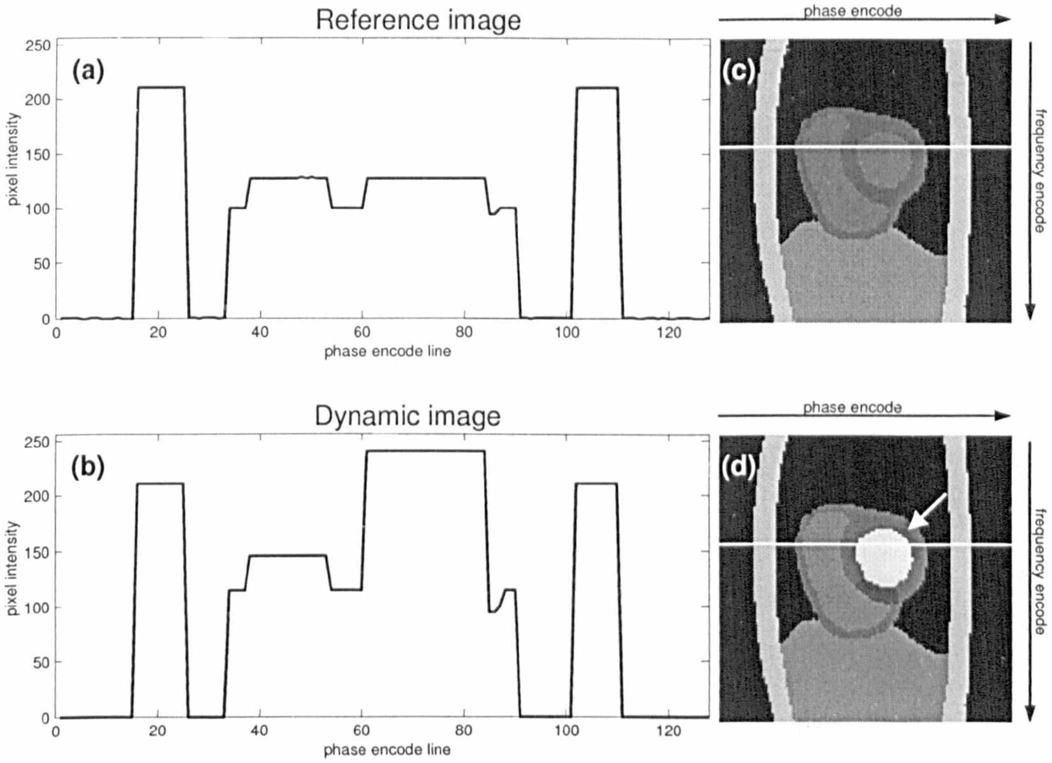

Figure 7-4 Two images from a synthetic myocardial perfusion sequence. The reference image is an image from late in the sequence and the dynamic image as the contrast agent enters the myocardial tissue. In the dynamic image a subendocardial defect is shown in the antero-lateral wall (pointed by the arrow). The graphs show the pixel intensity values for the line shown across the image in the phase encode direction. The most notable difference between the reference and dynamic image in the graph is the enhancement of the blood pool of the LV and hypo-enhancement of the subendocardial perfusion defect (phase encode line ~85).

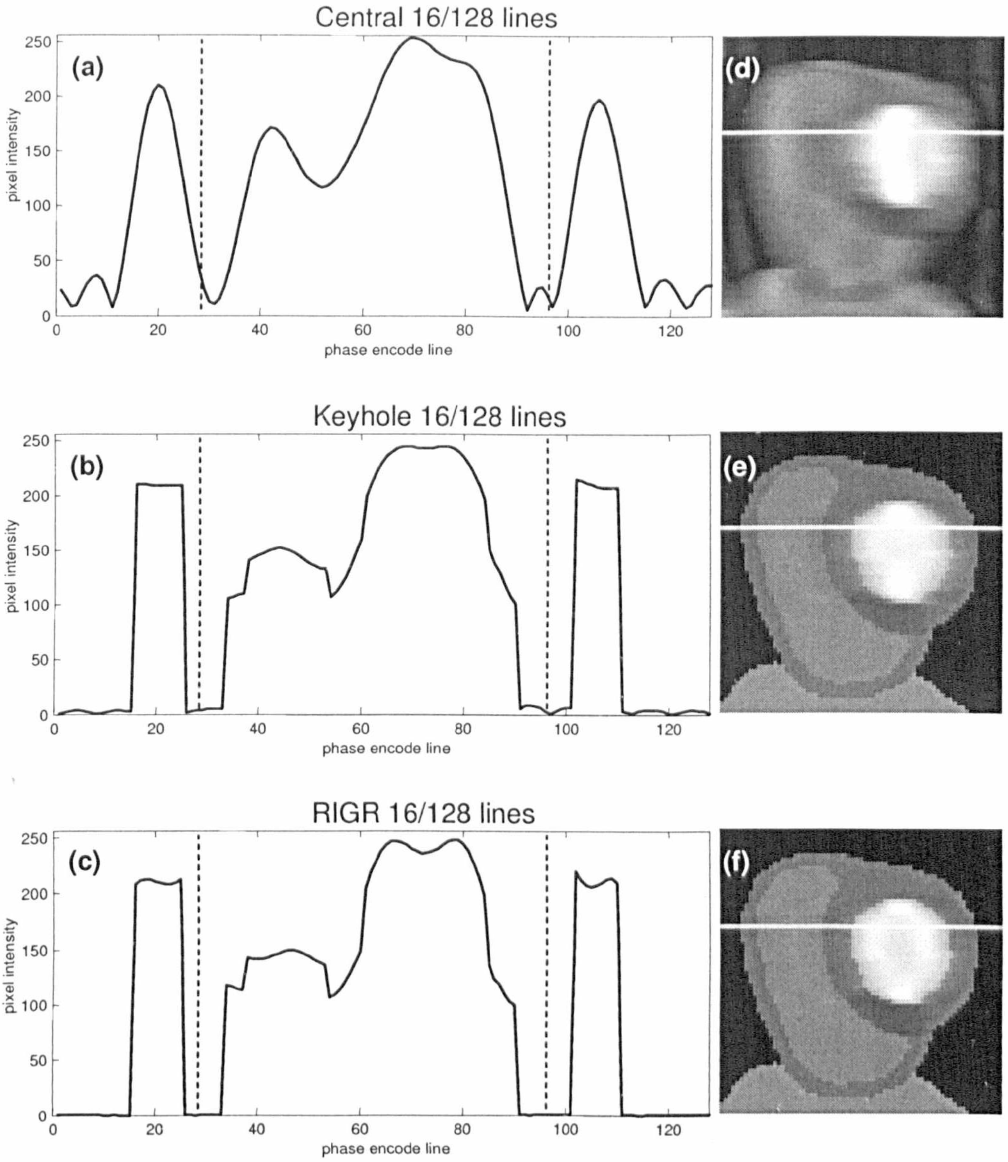

Figure 7-5 Reconstruction of the dynamic image from Figure 7-4 by using only 16 of the 128 phase encode lines. The top graph and image show a simple Fourier transform of the central 16 lines, the middle graph and image show the replacement of the central 16 lines of the dynamic image into the remaining lines of the reference image from Figure 7-4. The bottom graph and image show reconstruction using the RIGR technique from the central 16 lines of the dynamic image with basis functions derived from the reference image. For display purposes, the images on the right have been cropped and this region is shown as dotted lines on the graphs on the left

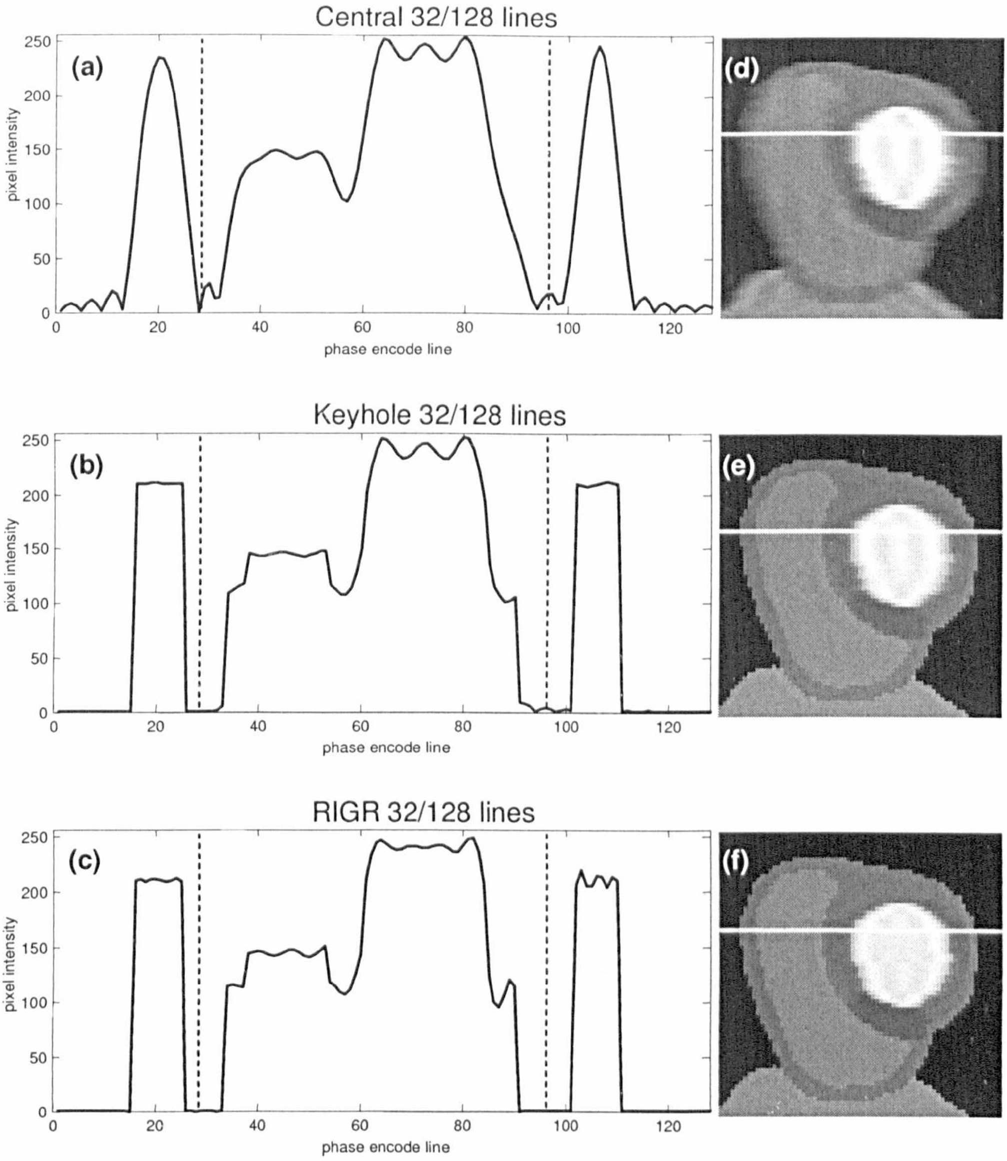

Figure 7-6 Reconstruction of the dynamic image from Figure 7-4 by using only 32 of the 128 phase encode lines. The top graph and image show a simple Fourier transform of the central 32 lines, the middle graph and image show the replacement of the central 32 lines of the dynamic image into the remaining lines of the reference image from Figure 7-4. The bottom graph and image show reconstruction using the RIGR technique from the central 32 lines of the dynamic image with basis functions derived from the reference image. It is clear that the RIGR technique provides a clearer endocardial border in the LV with fewer artefacts in the blood pool than the keyhole technique and is also able to distinguish the subendocardial defect from the dynamic image in Figure 7-4. For display purposes, the images on the right have been cropped and this region is shown as dotted lines on the graphs on the left.

The above simulation results with synthetic data demonstrate the benefit of using reference images for reconstructing dynamic data sets. In addition, subtle differences between the keyhole technique and RIGR technique are highlighted with the RIGR technique better able to reconstruct contrast changes of small regions of the image. This shows clear advantages for the RIGR technique over the keyhole technique. As expected, due to the more data consistent estimation of the high frequency components the image retains small image details well. The main limitation of the RIGR technique for first pass myocardial perfusion assessment is the effects of motion as this causes significant differences in the high frequency information between the reference data and the dynamic data.

To demonstrate the potential problems associated with RIGR, Figure 7-7 demonstrates the different reconstruction result for a small subendocardial defect when different reference images are used. For Series 1, the reference image does not clearly capture the regional borders associated with the defect, which results in significant blurring at the subendocardial border. This demonstrates the importance in choosing the reference image in practical applications. Depending on the size of the *k*-space used, the RIGR method is generally suitable for depicting small dynamic regions.

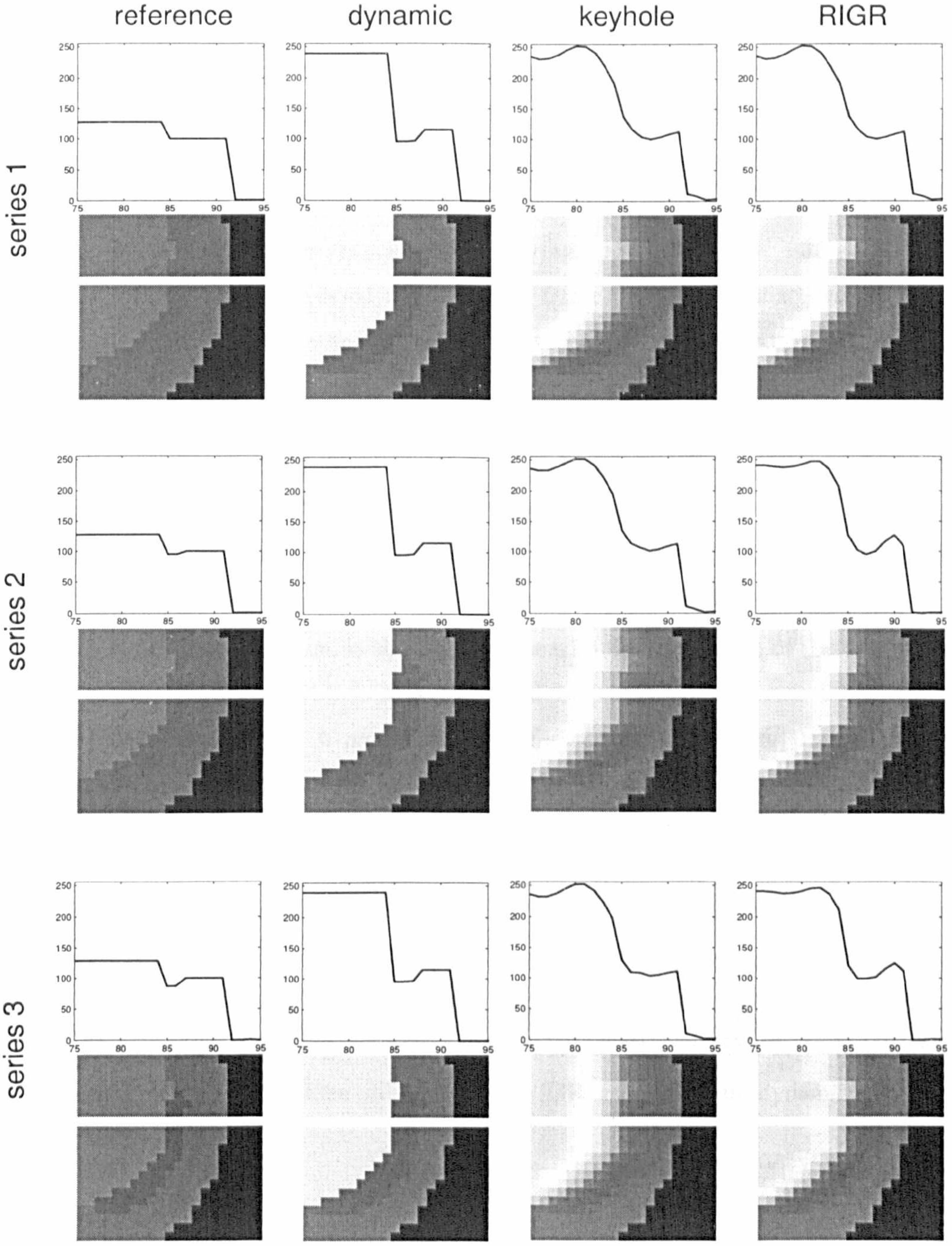

Figure 7-7 The effect of small detail in the reference image on the reconstruction quality of the keyhole and RIGR methods. Series 1,2 and 3 are identical but for the contrast of the subendocardial defect in the reference image. With RIGR, due to the way that the basis functions are derived, when the high-resolution details are not clearly present in the reference image, significant blurring can be observed. This is evident from the above figure in the clarity of the small subendocardial border reconstructed. Depending on the size of the *k*-space used, the RIGR method is generally suitable for depicting small dynamic regions.

7.3.2 RIGR for myocardial perfusion with free breathing

While the benefits of RIGR are clear with static contrast enhanced studies, the method has inherent difficulties for dealing with motion. This is due to inconsistency within the high-resolution information between the reference image and the dynamic images. To study the effects of this, we use the RIGR technique to reconstruct a sequence of contrast enhanced first pass myocardial perfusion images acquired during free breathing, with data acquired as in Chapter 6. Images are processed with the final frame of the 50 cardiac cycle sequence chosen as the reference image and 28 central phase encode lines of the full 112 used for reconstructing the dynamic sequence.

Figure 7-8 shows seven frames from the complete sequence. The value of the diaphragmatic respiratory navigator directly preceding the acquisition is shown so that the correspondence between respiratory position and artefact can be observed. We have selected a small region of the image for observation and error analysis containing the heart. The fully encoded, as well as the RIGR reconstruction, is shown, together with the subtraction of the two images. Artefact in the RIGR reconstruction is clear and in particular, in frame 29 where the navigator position differs by 6 *mm* from the reference image used to define the basis functions. While the contrast characteristics of frame 20 differ significantly to that of the reference image, little artefact is created due to the lack of corresponding motion.

Figure 7-9 shows the mean squared subtraction error for this sequence along with the respiratory position as measured by the diaphragmatic respiratory navigator. It is clear that the amount of error is strongly correlated with respiratory position, particularly in the early and late frames where changing relative contrast plays little part. This is to be expected, which highlights the difficulties in using the RIGR method with dynamic sequences including respiratory motion.

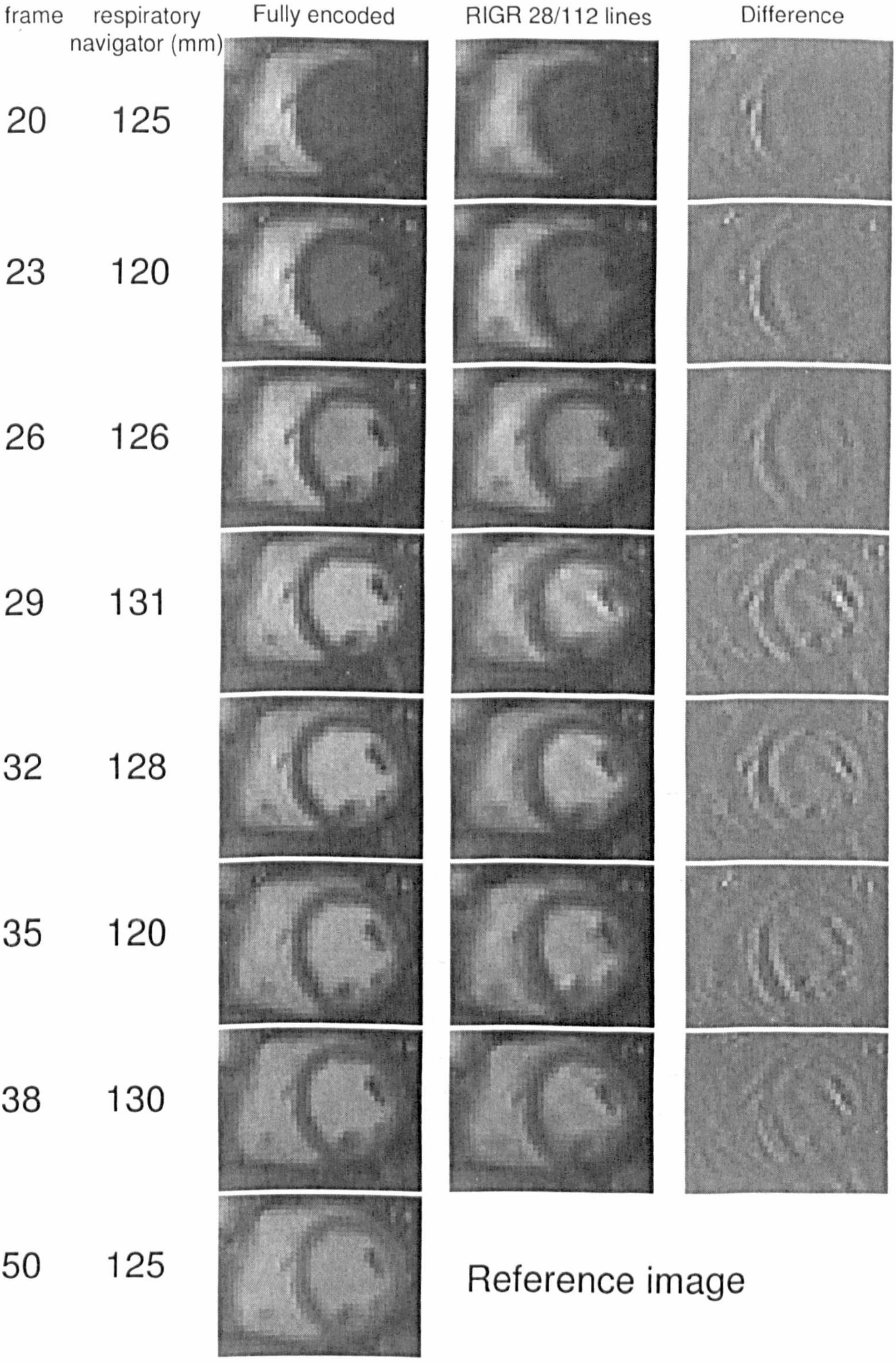
frame
respiratory navigator (mm)
Fully encoded
RIGR 28/112 lines
Difference
20 125
23 120
26 126
29 131
32 128
35 120
38 130
50 125
Reference image

Figure 7-8 Seven frames from a first pass myocardial perfusion sequence acquired during free breathing. Each frame is shown with the value of the diaphragmatic respiratory navigator acquired directly preceding the image acquisition. The fully encoded reconstruction with 112 phase encode lines and the RIGR reconstruction using only 28 dynamic phase encodings are shown side by side with the direct subtraction image showing resulting artefact. At the bottom, the static reference image (frame 50) is also shown.

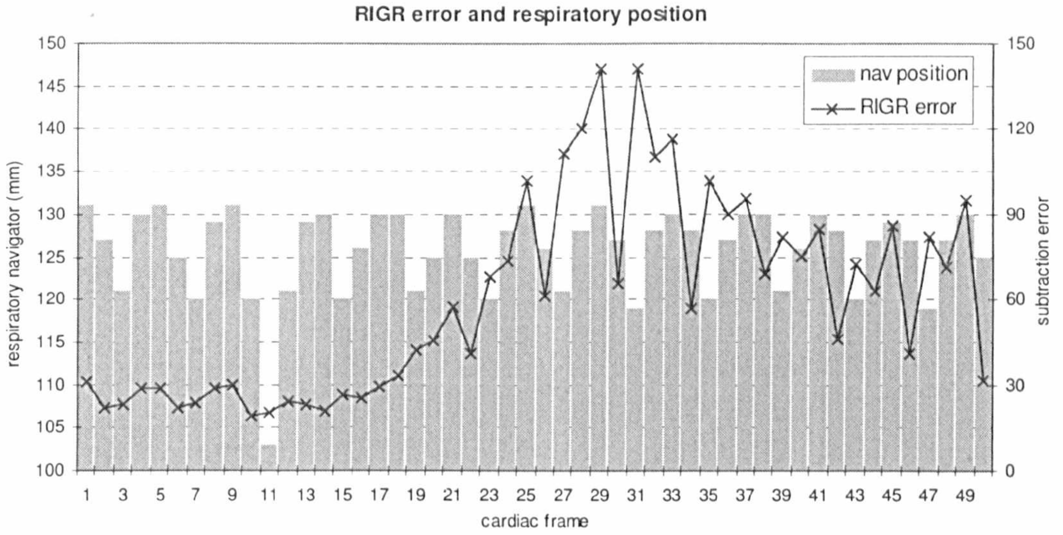

Figure 7-9 For a single subject shown in Figure 7-8, the diaphragmatic respiratory navigator reading, and the subtraction error result from a fully encoded image sequence is shown for each cardiac cycle.

7.4 RR-RIGR for myocardial perfusion imaging

In the previous chapter, we looked at a method to reduce temporal redundancies in a dynamic imaging sequence in the presence of respiratory motion. Here we attempt to apply the same principles to reduce the artefact present in the RIGR reconstruction. The main steps of RR-RIGR are similar in principal to RR-UNFOLD. Diaphragmatic navigator echoes are used to split the perfusion imaging series into different sub-series (bins) so that within each bin the anatomical structures are spatially static. The dynamic information within the sub-series is limited to varying contrast uptake amongst different anatomical regions. No pre-scan is used to determine the bin limits as this was found to provide little benefit with RR-UNFOLD. During the passage of the contrast agent bolus, reduced *k*-space data is limited to symmetrically acquired central *k*-space lines. Subsequent to the perfusion scan, a complete fully encoded static image is acquired with suitable contrast as a consequence of residual contrast agent in the tissue and blood pool. In post processing, this fully sampled static image is used to determine suitable coefficients for a class of basis functions able to represent the data with a reduced number of phase encode lines. The high-resolution dynamic image sequence is then reconstructed from the acquired dynamic *k*-space data.

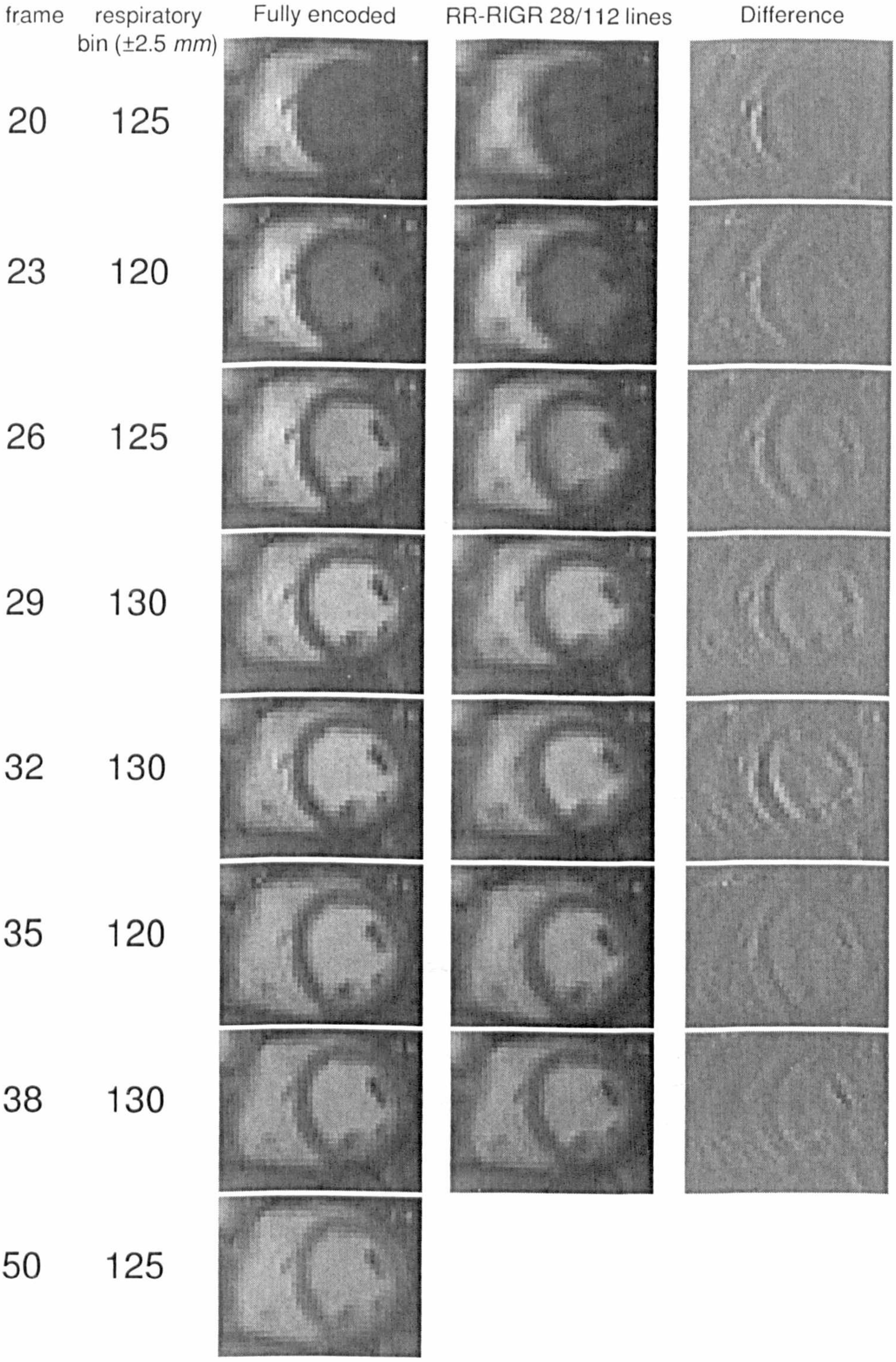
frame
respiratory bin (±2.5 mm)
Fully encoded
RR-RIGR 28/112 lines
Difference
20
125
23
120
26
125
29
130
32
130
35
120
38
130
50
125

Figure 7-10 Seven frames from a first pass myocardial perfusion sequence acquired during free breathing. Each frame is shown with the central value of the respiratory bin used for reconstruction of the image. The fully encoded reconstruction with 112 phase encode lines and the RR-RIGR reconstruction using only 28 dynamic phase encodings are shown side by side. The RR-RIGR image is reconstructed with the static data from the final frame within its respiratory bin, not necessarily frame 50. Frame 20 and 26 use frame 50 for reconstruction resulting in exactly the same reconstruction as in Figure 7-8. It is clear that significantly fewer artefacts are created using this technique as shown in frames 29, 32, 35 and 38. This is further highlighted by the difference images on the right.

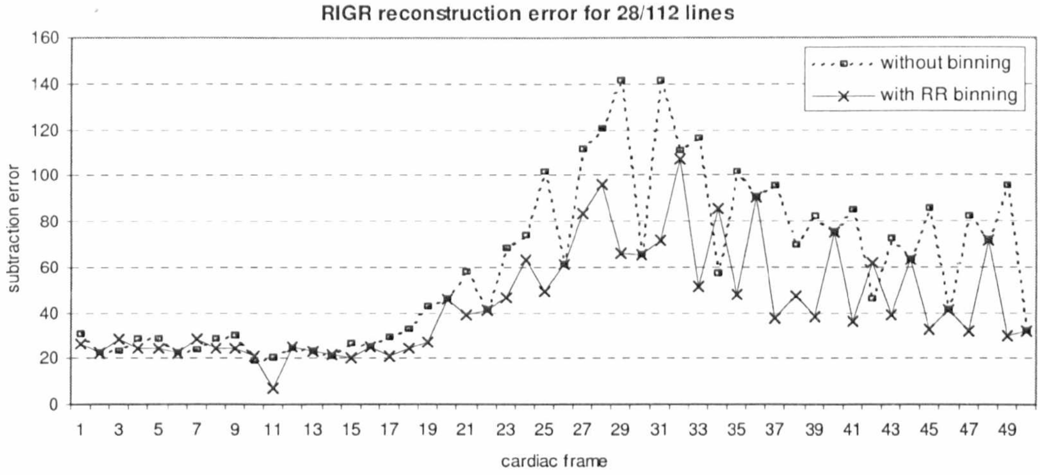

Figure 7-11 Mean square subtraction error is shown for each frame of the myocardial perfusion sequence reconstructed with the RIGR technique using 28/112 dynamic phase encode lines. Two variations of this are shown, the method without binning uses the final frame (50) as a static reference image for the calculation of the required basis functions for the generalised series reconstruction. With RR binning, the data is separated into 5 *mm* bins and the final image from each of these bins is used as a static reference image.

Figure 7-10 shows the corresponding frames from the RIGR reconstruction with the use of respiratory reordering (RR-RIGR). Rather than displaying the respiratory position, we now display the respiratory bin used for reconstruction. When compared with Figure 7-8, it is clear that the level of artefact has been reduced with frame 29 significantly clearer. Figure 7-11 shows the effect on the subtraction error over all 50 cardiac cycles. Many frames reamin the same as they belong to the same bin as frame 50 so are reconstructed with exactly the same information in both cases, whereas other frames show reduced subtraction error due to the use of a static reference image with more similar high frequency information. The use of RR-RIGR has significantly reduced the error throughout the sequence with around a 50% reduction for frame 29.

7.4.1 Comparison of RR-RIGR with RR-UNFOLD

To compare the effectiveness of the RR-RIGR technique with that of RR-UNFOLD, a study is carried out using the same patient data sets as used in the previous chapter. Each bin has been selected in an identical manner with RR-UNFOLD and RR-RIGR. Reconstruction of the RR-UNFOLD technique is based on 56 phase encode lines for each cardiac phase out of a possible 112, with the addition of 6 extra central phase encode lines for preservation of dynamic contrast information. The RIGR reconstruction uses 56 central phase encoding steps for each dynamic image.

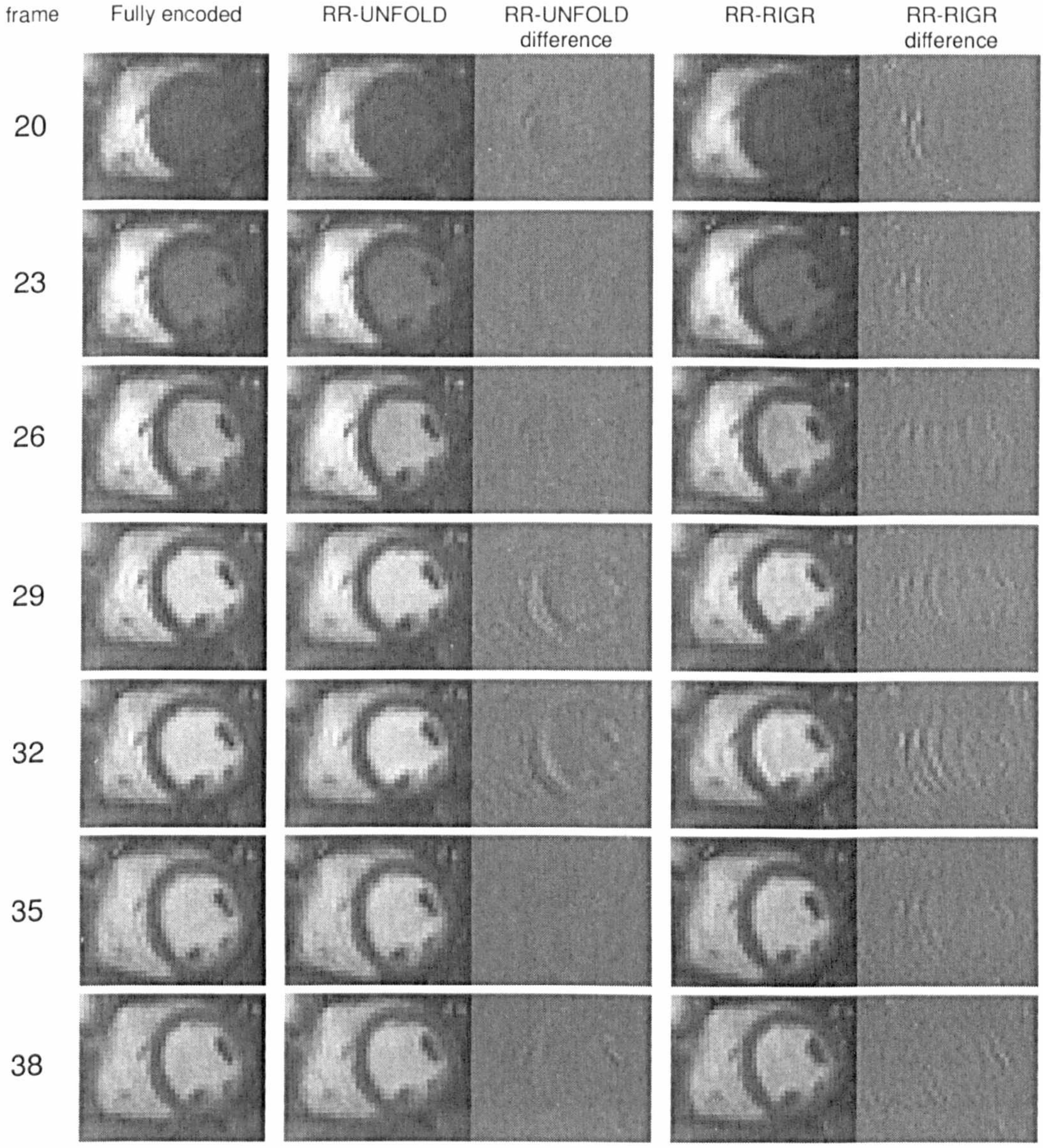

Figure 7-12 Seven frames from a first pass myocardial perfusion sequence acquired during free breathing (subject 1). The fully encoded reconstruction with 112 phase encode lines is shown on the left. A reconstruction using RR-UNFOLD with 56 lines and 6 extra central phase encode lines is shown together with the subtraction difference image from the full reconstruction. Also shown is a RR-RIGR reconstruction using only 56 dynamic phase encodings. From the subtraction images the difference in the artefact created by the two techniques is clear.

Figure 7-12 uses the same subject as used previously in this chapter and compares the RR-UNFOLD method with the RR-RIGR method. It is clear that while a small amount of artefact is present in both cases, the type of artefact varies significantly. In the case of RR-UNFOLD large edge artefact is present due to remaining motion within the 5 *mm* bin. Whereas with RR-RIGR high frequency Gibbs artefact is created due to small amounts of motion within the bin. In Figure 7-13, the subtraction error is shown over all 50 cardiac cycles and it appears there is little relationship between the extent of artefact using the two techniques.

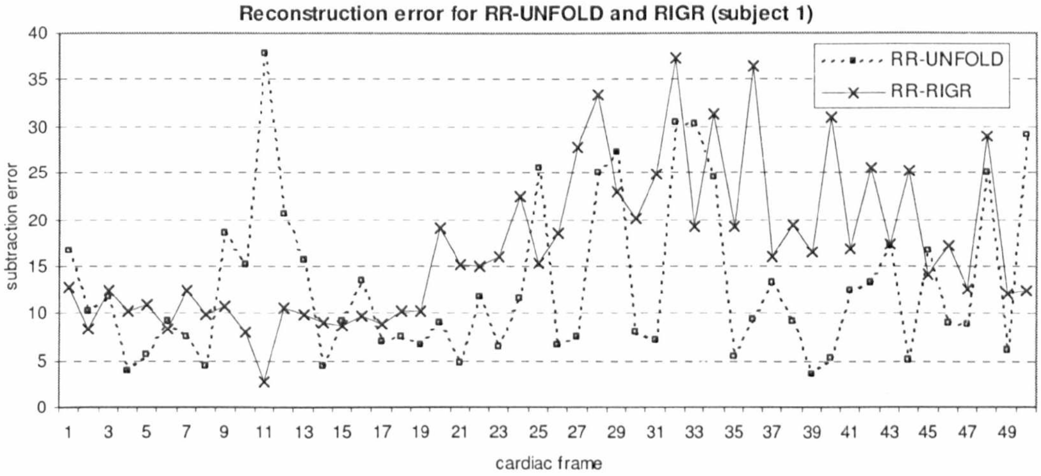

Figure 7-13 Mean square subtraction error is shown for each frame of the myocardial perfusion sequence reconstructed with the RR-UNFOLD and RR-RIGR using approximately half of the phase encode lines. It is clear that the error created differs between the two techniques.

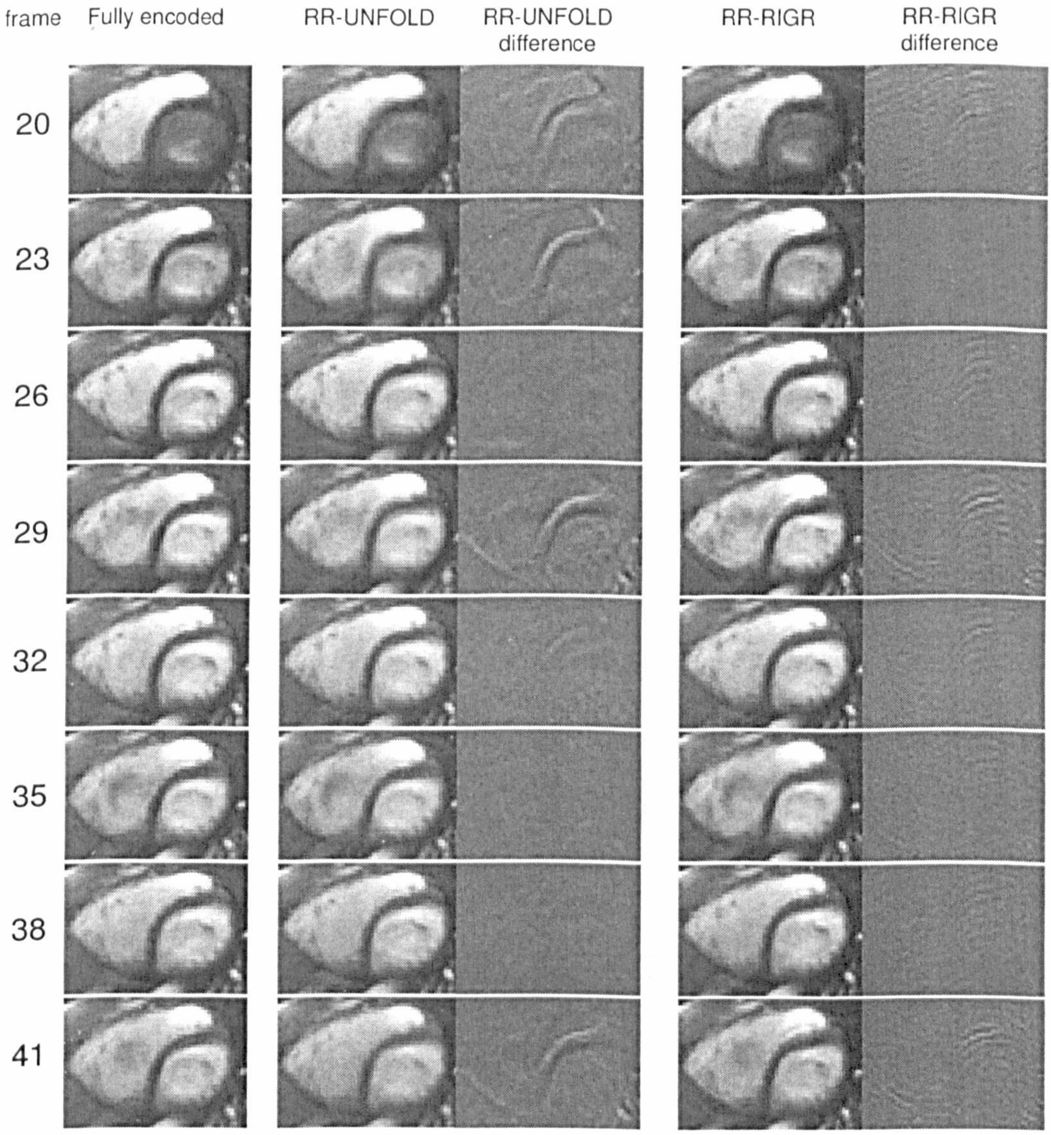
frame
Fully encoded
RR-UNFOLD
RR-UNFOLD difference
RR-RIGR
RR-RIGR difference
20
23
26
29
32
35
38
41

Figure 7-14 Eight frames from a first pass myocardial perfusion sequence acquired during free breathing (subject 2). The fully encoded reconstruction with 112 phase encode lines is shown on the left. A reconstruction using RR-UNFOLD with 56 lines and 6 extra central phase encode lines is shown together with the subtraction difference image from the full reconstruction. Also shown is a RR-RIGR reconstruction using only 56 dynamic phase encodings.

demonstrates another subject with significant artefact seen in 4 of the 8 frames. It is evident from Figure 7-15 that the RR-UNFOLD technique has had particular difficulty with reconstructing a number of frames within this sequence and the RR-RIGR has performed significantly better on these frames.

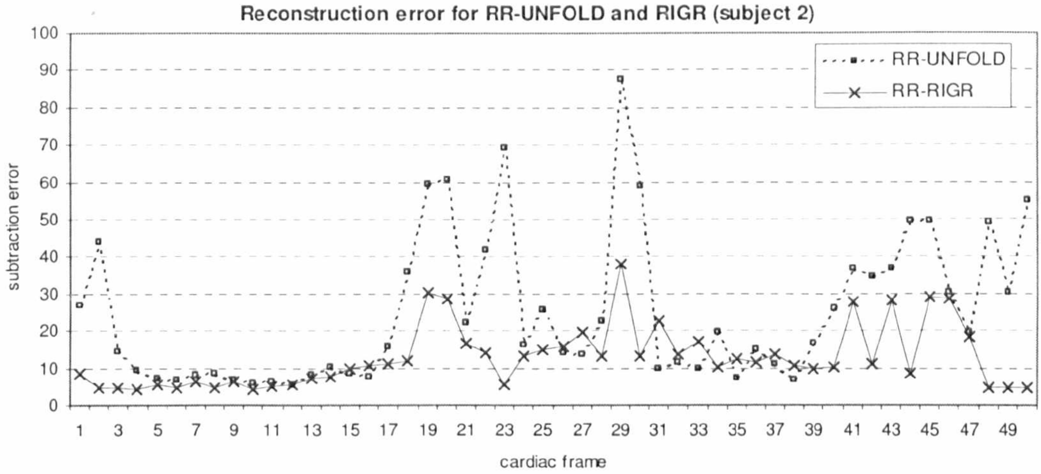

Figure 7-15 Mean square subtraction error is shown for each frame of the myocardial perfusion sequence reconstructed with the RR-UNFOLD and RR-RIGR using approximately half of the phase encode lines. In this case the error created from the RR-RIGR technique is clearly less than from the RR-UNFOLD technique.

The comparison is performed on a total of 5 subjects and mean square subtraction error for the whole sequence is shown in Table 7-1. In general the RR-UNFOLD technique is currently able to outperform the RR-RIGR method.

subject	1	2	3	4	5
RR-UNFOLD	13.00	25.09	12.18	2.35	11.87
RR-RIGR	16.85	12.90	21.02	4.82	23.22

Table 7-1 Mean subtraction error for five subjects using RR-UNFOLD with 56 lines and 6 extra central phase encode lines and RR-RIGR with 56 central phase encode lines for 5 subjects with contrast enhanced first pass myocardial perfusion imaging.

In Table 7-2, the two techniques are used to derive perfusion indices using the Perfusion plug-in of CMRtools (Imperial College, London, UK) to examine if the different type of artefact has an effect on the perfusion indices. The results show that while a difference in relative error is found between the two this varies amongst subjects and is relatively insignificant with a normal range for perfusion reserve varying between 2.5 and 4, and 20% difference is relatively small.

subject	1	2	3	4	5
RR-UNFOLD	21	9	14	11	6
RR-RIGR	18	17	24	9	10

Table 7-2 The percentage error in perfusion index (compared with full *k*-space acquisition) after applying the same processing steps to all the 5 subjects studied by using the RR-UNFOLD and RR-RIGR techniques, respectively.

7.5 Discussion and conclusions

In this chapter, we have performed detailed analysis of using RIGR for respiratory reordered myocardial perfusion imaging. Numerical analysis has shown that in terms of overall reconstruction error, the two techniques are relatively similar to each other. However, the spread of artefact is intrinsically different for the two techniques considered. From Figure 7-14, it is evident that RR-UNFOLD has a spatio-temporal smoothing effect to the perfusion sequence, and the residual error is focused on regional borders. For RR-RIGR, however, the subtraction error spreads across the image. The amount of error is also associated with the size of the respiratory bin. This is because for RR-RIGR, the basis functions are derived from the reference image, and the RIGR reconstruction method assumes that there is no relative motion between the reference and dynamic frames. For respiratory reordering, it is practically difficult to maintain small respiratory windows size whilst keeping the number of reference images to a minimum. It is therefore important to realise the potential pitfalls associated with this approach. The results from this chapter suggest that when there is sufficient SNR, the use of RR-RIGR is preferable due to its ability in localising small perfusion defects. However, when the SNR is low, the use of RR-UNFOLD is more preferable.

In this chapter, the effect of motion on RR-RIGR is demonstrated, but we did not go into depth in exploring different ways of correcting for it. In the current framework, a reference image is acquired for each respiratory bin, which is not efficient given the similarity of those images acquired. It is possible that combined with the navigator echoes, to use the low-resolution details of the dynamic image to pre-warp a single reference image to each bin before the basis function is extracted. This however, requires accurate spatial co-registration that means both in plane and through plane motion must be corrected. To further improve the accuracy of the RR-RIGR technique, it is also possible to acquire two reference images to encode the temporal dynamics of different anatomical regions [119], such that the effects discussed in Figure 7-7 can be minimised.

In conclusion, we have compared in this chapter the relative strength and drawbacks of the RR-UNFOLD and RR-RIGR techniques. Although RR-UNFOLD is currently well developed and straightforward to implement, there are a number of important potential benefits of the RR-RIGR technique. The main problem associated with the RR-RIGR approach is the acquisition of different reference images that can prolong the overall data acquisition time. The prospect of using motion registration, however, can significantly simplify the data acquisition requirement, thus making it practically more feasible. To this end, accurate motion tracking based on that described in Chapter 4 needs to be fully integrated.

Chapter 8 : Tracer Kinetic Modelling and Perfusion Analysis

8.1 Introduction

In Chapters 7 and 8, we have discussed various data acquisition considerations related to myocardial perfusion imaging, particularly the handling of respiratory induced cardiac motion in relation to RR-UNFOLD and RR-RIGR. In this chapter, we will discuss detailed quantification issues by using tracer kinetic modelling. In myocardial perfusion imaging, the contrast agent has a T1 shortening effect, which results in an increase in signal intensity in the perfused regions. Currently, perfusion image analysis is both time consuming and prone to subjective errors. In a clinical environment, qualitative visual assessment is still often used which involves a visual inspection of the image sequence to look for areas displaying abnormal enhancement. For more detailed analysis, intensity time curves need to be studied. These are obtained through the selection of regions of interest within the image. Semi quantitative analysis of these curves, typically via normalised up-slopes of the myocardial signal has produced some useful results, amongst which is the detection of microvascular dysfunction, such as the subendocardial hypo perfusion in cardiac Syndrome-X patients [72].

With the maturity of myocardial perfusion imaging, detailed quantitative analysis is becoming increasingly important, particularly in the establishment of its role in assessing regional myocardial viability and the prognosis of coronary artery and microvascular flow restrictions. The use of automatic or semi-automatic quantification techniques reduce observer bias and allows for more widespread study of the myocardial perfusion and the recognition of accepted levels of MBF for healthy and diseased tissue.

Thus far, a number of simple tracer kinetic modelling techniques have been proposed [9,15,228,229]. The use of these techniques in practice involves several major issues to ensure the validity of these models in clinical settings. When quantitative or semi quantitative approaches are employed, for example, it is important that the combination of the imaging protocol and the contrast agent dosage does not result in clipping of the peak signal intensity, particularly for the measurement of the Arterial Input Function (AIF), which is the concentration of gadolinium in the LV or aortic blood pool as a function of time during its first pass. This is due to the high concentration of the contrast agent in this region during measurement. The effects of receiver coil sensitivity must also be considered as inhomogeneities across the image can affect regional perfusion indices. As discussed in earlier chapters, accurate and efficient delineation of myocardial territories is greatly improved with myocardial motion correction. The use of modelling techniques to obtain further understanding of blood flow through the myocardial tissue with the effects of collateral circulation and the monitoring of angiogenesis is reliant on a combination of contrast agent characteristics and modelling protocol.

8.1.1 Extracellular versus intravascular contrast agent

For the measurement of first pass myocardial perfusion, it is assumed that the observed contrast enhancement is due to myocardial perfusion. Most contrast agents that have been approved for human use are extracellular Gadolinium-based agents that have a relatively short residence time in the vascular system. More recently, intravascular agents have been introduced that have longer residence times and allow extended imaging procedures without the need for repeated injections of the agent. With the standard use of extra cellular contrast agents, about half of the agent leaks into the interstitial space during the first pass of the contrast agent. Therefore, the imaged voxel intensity is dependent not only on the myocardial perfusion, but also on the size of the extra cellular space and the capillary permeability.

Intravascular contrast agents, on the other hand, normally remain confined to the intravascular space. This is a result of intravascular agents having a much larger molecular weight compared to Gd-DTPA. There are several advantages of intravascular agents. They can assess perfusion in areas of ischaemia and provide information about capillary permeability in areas of reperfusion. They can show the extent of tumour neo-vascularity and associated permeability changes. Intravascular contrast agents are of particular use in cardiac

MR for providing increased imaging contrast between blood pool and tissue in applications such as coronary artery angiography [230] and myocardial wall motion studies [231]. Thus far, several intravascular MR contrast agents have been studied for myocardial perfusion [13,232-235]. A direct comparison of Gadomer-17 and Gd-DTPA in a porcine model [236] showed similar peak contrast to noise ratios for the two agents and the absence of capillary leakage allowed for more straightforward calculation of blood flow and blood volume from the tracer kinetic modelling resulting in improved accuracy. A more recent intravascular agent, albumin targeted contrast agent, MS-325 produces a prolonged hypo-intense signal in ischaemic myocardium during stress [237]. This aids visualisation as the defect can be observed for at least 15 heartbeats. For human studies, toxicity is the major concern for intravascular agents.

8.1.2 Tracer kinetics and compartment modelling

Tracer kinetics is the study of tracer concentration or pixel intensity in relation to time. In the case of perfusion analysis, the variation of the contrast agent concentration through time within the specified regions of interest is observed. Indication of CAD may be signalled by a lack of perfusion to certain areas of the myocardium. The further study of tracer kinetics may provide a more robust and objective analysis of regional myocardial blood supply. The concept of tracer kinetic modelling is not new to imaging research and is closely related to work in other imaging modalities such as SPECT and PET.

In the analysis of tracer kinetics, assumptions must be made so that the MR data may be related to the biological region being imaged. The general assumptions made in analysing tracer kinetics are as follows

- The perfusion is constant and not affected by the tracer.
- The tracer is completely mixed with the blood.
- The concentration of the tracer can be monitored accurately.
- Recirculation of the tracer can be corrected for when present.

Under certain conditions, these assumptions may be met with myocardial perfusion CMR. The most significant of these assumptions is that the concentration of the tracer can be monitored accurately. This is dependent on a number of factors that require careful consideration. When dealing with different contrast agents, the choice of dosage and administration must be taken into account. It is also important to consider the signal characteristics of the image sequence in relation to the contrast agent. Finally, the protocol followed by the study and the residual contrast agent after repeated studies are also of significance. It has been shown that with large doses of Gd-DTPA, the concentration of the tracer is no longer linearly proportional to pixel intensity measured from MR images. Significant error can therefore be introduced.

Due to image noise, obtaining kinetic curves directly from the perfusion image series can be difficult and inaccurate. By devising a model of contrast uptake over time, the acquired data may be fitted to a model to increase the accuracy and reproducibility. The basic principle of this modelling can be shown in Figure 8-1. The output (*m*) is the curve obtained from the pixel intensity of a region of the myocardium over time. This is related to the input blood pool signal (*b*) and the impulse response of the tissue (*r*), which determines the basic characteristics of myocardial perfusion. Commonly, the concentration of the contrast agent across the blood pool is assumed to be uniform allowing for the selection of a large region of interest for sampling. The measurement of output myocardial signal needs to cater for temporal mis-registration due to respiratory motion and image SNR.

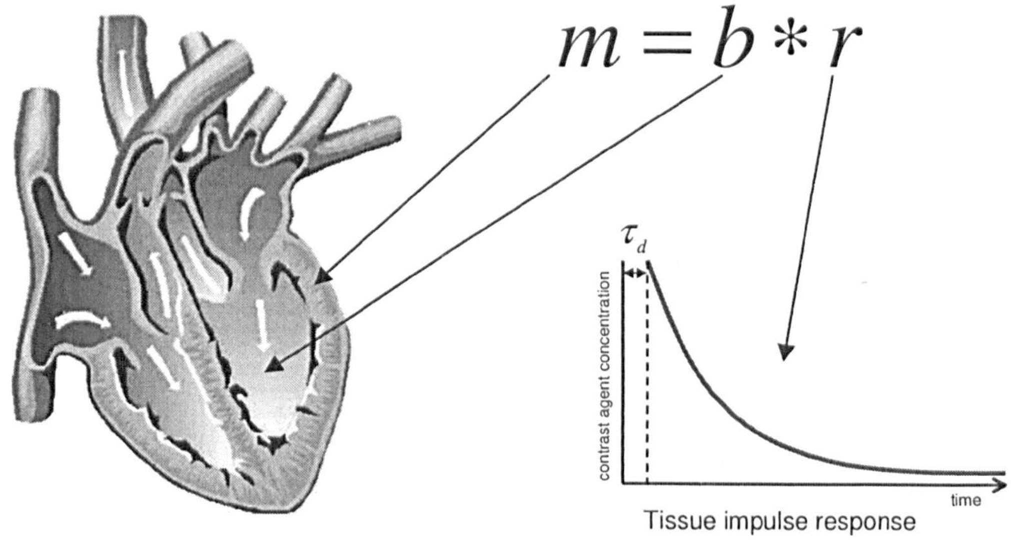

Figure 8-1 The basic perfusion model. The time intensity signal from the blood pool of the LV (b) is combined with the curve for the tissue impulse response (r) to give the time intensity signal from the myocardium. The blood pool signal is considered as the input to the system and the myocardial signal the output. The impulse response has a small time delay representing the time taken for the agent carrier to travel to the entrance of the coronary arteries.

8.1.3 Single compartment modelling

A compartment is a volume that acts kinetically like a distinct, homogenous, well-mixed container. It allows the transfer of contrast agent into or out of it. Compartment modelling is based on the assumption that specific pools can be identified and that the discharge of tracer can be described by exponential equations. The theory of compartment modelling or analysis is widely used in many branches of biology, leading to quantification of biological systems. Single compartment modelling deals with a compartment with only one well-defined input *i.e.*, a defined arterial input with the passage of the contrast medium through a single compartment.

The Fermi function

The Fermi function was first used for this type of deconvolution problem on X-ray CT [238] and has since been applied to MR myocardial perfusion analysis [15,239,240]. The definition of this function is:

$$r(t) = \frac{F}{1 + \exp[(t - \tau_0 - \tau_d) \cdot k]} \cdot \theta(t - \tau_d) \tag{8.1}$$

where τ_0, τ_d, k and F are four unknowns defining the shape of the curve, and a step function θ. In this equation $r(t)$ is the value of the Fermi function with respect to time t. F represents the flow rate and τ_0 and k control the shape of the curve. θ is a step function and introduces a delay τ_d to account for the time taken for the blood to pass from the point of measurement for the input function (*i.e.* the blood pool) to the input of the coronary arteries.

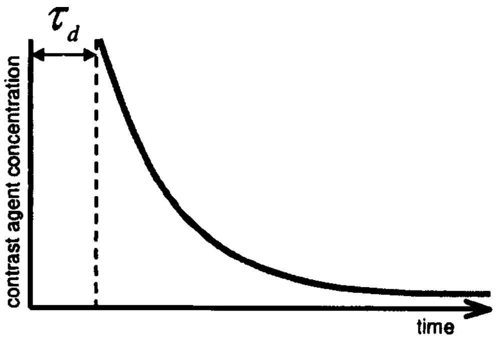

Figure 8-2 The Fermi function. This represents the impulse response of the washout properties of the contrast agent through the myocardium. The value of τ_d represents the delay due to the time taken for the bolus of contrast agent to pass from the blood pool of the LV to the entrance to the coronary arteries.

The resulting curve is shown in Figure 8-2 and this is used as a good estimate of the impulse response of the anatomical structure. In order to find the optimal model, the error between the computed output and the actual recorded output must be minimised. That is, the objective is to find

$$r(t) = f(\tau_0, \tau_d, k, F) \tag{8.2}$$

such that

$$\int [m(t) - (r(t) * b(t))]^2 \, dt \to \min \tag{8.3}$$

where $r(t)$ is a function of four unknowns. These four parameters (τ_0, τ_d, k, F) are optimised to minimise the error between the recorded myocardial signal and the convolution of the input blood pool signal and the Fermi function model. An optimisation procedure suitable for this purpose is the Levenberg-Marquardt method that is described in Appendix C.

8.1.4 Multi-compartment modelling

The single compartment modelling approach described above is generally appropriate for the first pass of contrast agent wash in. In simulations based on a multi-path and multi-tracer model, which includes parallel flow pathways to describe the effects of regional flow heterogeneity [241], the leakage of contrast agent into the interstitial space was found only to be negligible with a rapid bolus injection and normal MBF rates [242]. Following the peak of the first pass of contrast agent through the circulatory system, however, the signal generally does not return to its pre-injection baseline levels. This is due to the leakage of contrast agent into the interstitial space. When signals from the tissue of interest and the adjacent arterial bed are considered to account for this contrast agent leakage from the vascular space, a two-compartment model needs to be applied. This takes into account the volume of the vascular space and the interstitial space and the permeability surface area product of the two.

8.1.5 Factor analysis

By using the intensity variation measured from the LV blood pool as the input signal, deconvolution is required to recover the impulse response of different regions of the myocardium. In practice, the signal from the LV blood pool may be significantly attenuated at peak amplitude due to the relatively high concentration of the Gd-DTPA used. In this case, the model-based approach can introduce significant errors. Furthermore, the use of a single model for representing both normal and infarcted regions requires further justification.

Factor analysis is a valuable tool for extracting underlying characteristics of a ROI with different tissue types, from dynamic image series without prior assumptions about tissue models. An image sequence S can be represented as the sum of K underlying images (spatial distribution) a_k, each weighted by their factors (temporal distribution) f_k, as follows [243,244]

$$S(p,t) = \sum_{k=1}^{K} a_k(p) \cdot f_k(t) + e(p,t) \tag{8.4}$$

where $e(p,t)$ is the residual error and K is the number of factors kept, and usually is equal to the number of different tissue kinetics within the ROI. By neglecting the error term, the above expression can be turned into a matrix form

$$\mathbf{S} = \mathbf{FA} = \mathbf{U\Gamma V} \tag{8.5}$$

where **S** is a M×N matrix, **U** the M×K orthonormal column matrix composed of the first K principal kinetic curves, **V** the K×N orthonormal row matrix composed of K principal component images, **Γ** the K×K diagonal matrix of the K roots of eigenvalues and M and N are the number of image frames and total number of pixels within the ROI, respectively. Since there is no unique solution to the above equation, additional constraints are necessary. Among them, the positive constraint is the most commonly adopted one. It is based on the fact that there are no negative values in the actual images and the corresponding time curves, *i.e.*, factors. This can be implemented by iterative oblique rotations of the factors and the corresponding factor images.

Figure 8-3 shows eight time frames of the synthetic perfusion images with a lateral subendocardial defect and another posterior transmural defect. The first three factor images of the perfusion sequence clearly indicate different tracer kinetic behaviours of the myocardium and the exact locations of the defects.

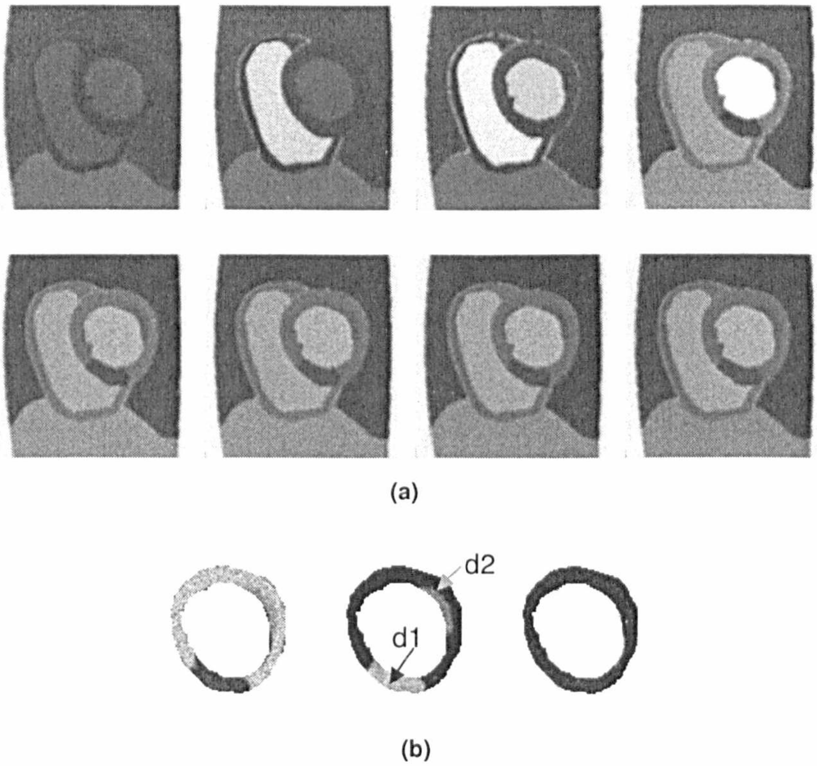

Figure 8-3 (a) Eight image frames from a synthetic perfusion sequence showing both subendocardial and transmural perfusion defects. (b) The derived factor images show different tracer characteristics of the myocardium and the locations of the defects (d1 and d2, pointed by the arrows).

8.2 Issues related to perfusion quantification

8.2.1 The deconvolution problem

The issue of myocardial perfusion quantification is in essence a deconvolution problem, and the perfusion index to be sought in this case is derived from the tissue impulse response. The method for resolving this is through the deconvolution of the two signals as shown in Figure 8-4. While this method is possible through the use of inverse Fourier transform, it can have significant numerical problems due to the potential singularities involved, as deconvolution is a differentiation process and is thus unstable when the given signals contain noise.

To deal with this problem, a method of model fitting is to be used. The purpose of this is to create a model of the impulse response, so when convolved with the input signal from the blood pool produces a curve that fits the output signal of the myocardium. During optimisation, the aim is to adjust the parameters of the impulse response model to minimise the error between the myocardial signal and the result of the convolution.

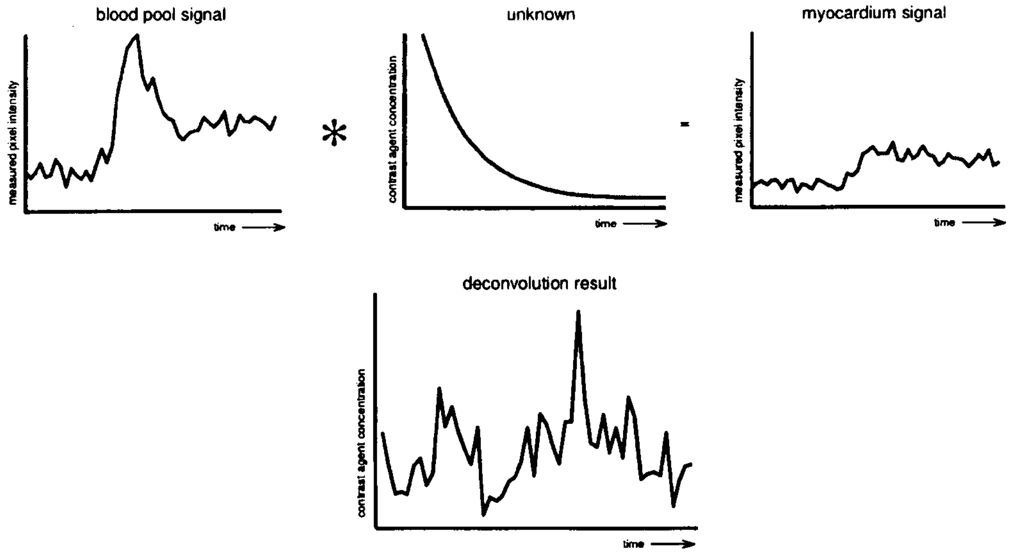

Figure 8-4 The deconvolution problem represented through time intensity curves. Given the blood pool signal and the myocardial signal as the input and output to the system. It can be seen that the myocardial signal is the result of combining the blood pool signal with the unknown system characteristics through convolution. To obtain these system characteristics, a simple deconvolution could be performed. In this case, we show the result to be dominated by noise due to the inherent differentiation process involved. It is because of this that the model fitting approach is required.

8.2.2 Perfusion indices

Clinically, a number of different indices can be used to quantify regional myocardial perfusion. Semi-quantitative indices used typically include:

Peak Signal Intensity: The maximum signal intensity attained during the first pass of the contrast agent; this can be normalised against the mean signal intensity before enhancement.

Time to peak: The time taken from the first arrival of contrast agent within the myocardium to the peak myocardial signal.

Up-slope: The first derivative of the measured signal intensity curve on the first pass of the contrast agent through the myocardial tissue. This parameter is often normalised against the up-slope of the left ventricular blood pool signal directly preceding the myocardial measurement, such that:

$$MPI = \frac{MaxSlope(m_{stress})/MaxSlope(b_{stress})}{MaxSlope(m_{rest})/MaxSlope(b_{rest})} \tag{8.6}$$

Up-slope measurement has been used extensively for the calculation of myocardial perfusion reserve indices [72,245-247]. The normalised up-slope has shown to be sensitive in the detection and extent of compromised myocardium when compared with PET [100], although underestimation of the absolute blood flow has been noted due to the low extraction fraction of MR contrast agent Gd-DTPA [248]. Potential problems with the use of normalisation via blood pool up-slope have been highlighted where broadening of the LV blood pool signal is not taken into consideration in subsequent analysis [249]. With an intravascular blood pool agent (MS-325) normalised slope has shown a valid relationship with MBF [250]. The method used a gamma variate fit to smooth the curve simplifying the determination of the maximum up-slope. It was found that taking into account the time at which the maximum up-slope is reached avoids under estimation of the perfusion reserve.

With the use of Fermi deconvolution, myocardial perfusion indices include:

Mean Transit Time (MTT)

$$MTT = \frac{\int_0^\infty r(t)\,dt}{\max_{t=0}^{\infty} r(t)} \tag{8.7}$$

The average time it takes a tracer molecule to pass through the target tissue.

Myocardial Perfusion Reserve (MPR)

$$MPR = \frac{\max_0^\infty r(t)_{stress}}{\max_0^\infty r(t)_{rest}} \tag{8.8}$$

The ratio between peak perfusion at rest, and that during stress.

8.2.3 Perfusion plug in for CMRtools

Perfusion Tools is a plug in for CMRtools (Imperial College, London, UK) developed from this research. Figure 8-5 shows a typical workflow associated with Perfusion-Tools. In (a), initial myocardial borders are traced around for determining the approximate location of the myocardium. Automatic in-plane motion correction (rigid transformations with a cross correlation similarity measure) is then performed to align the sequence of images to remove respiratory induced cardiac motion. In (b), this can be viewed as a cine and where necessary, manual corrections can be made to this result. In (c), the ROI are delineated including the AIF measurement from the blood pool and multiple myocardial regions of interest. This can optionally be subdivided into endo- and epicardial regions and the number of radial segments adjusted for each slice. At this stage, adjustment to the myocardial borders can be made on a frame-by-frame basis. In (d), time intensity curves from the chosen regions can be interactively displayed for quality assurance. Spurious frames due to gross deformation or artefact can be disabled to avoid interference with the derivation of the perfusion indices. Once this is done, Fermi deconvolution is performed for each of the selected ROI as shown in (e). In addition, a bullseye plot simultaneously shows the results from all of the slices and this can be switched between sub endocardial and subepicardial territories.

A bullseye plot is a common visualisation technique used in clinical studies with the ability to visualise the whole myocardial wall of the LV in one view. Typically, as shown in Figure 8-5 and later studies, the central region corresponds to the apical region and the outer circumference the basal region. The segments are then divided around the anterior, lateral, inferior and septal region clockwise around the display as if the heart is viewed from the base. This allows a simple display of the results, although the display tends to exaggerate the size of the basal defects and correspondingly make apical defects look smaller. For display purposes, the values are interpolated between myocardial regions.

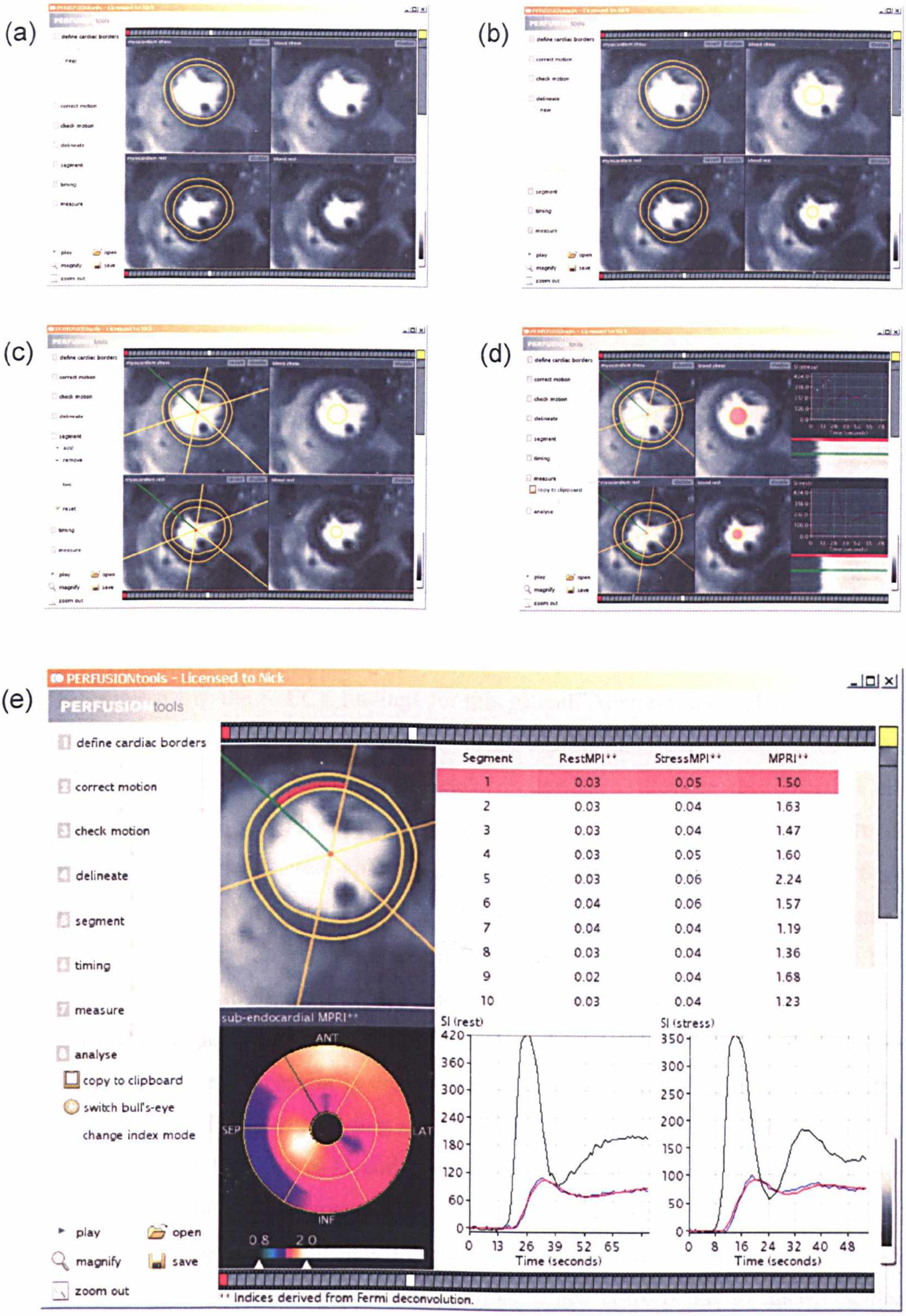
(a)
(b)
(c)
(d)
(e)
PERFUSIONtools - Licensed to Nick
PERFUSIONtools
define cardiac borders
correct motion
check motion
delineate
segment
timing
measure
analyse
copy to clipboard
switch bull's-eye
change index mode
play
open
magnify
save
zoom out
sub-endocardial MPRI**
ANT
SEP
LAT
INF
0.8
2.0
SI (rest)
420
360
300
240
180
120
60
0
0 13 26 39 52 65
Time (seconds)
SI (stress)
350
300
250
200
150
100
50
0
0 8 16 24 32 40 48
Time (seconds)

Segment	RestMPI**	StressMPI**	MPRI**
1	0.03	0.05	1.50
2	0.03	0.04	1.63
3	0.03	0.04	1.47
4	0.03	0.05	1.60
5	0.03	0.06	2.24
6	0.04	0.06	1.57
7	0.04	0.04	1.19
8	0.03	0.04	1.36
9	0.02	0.04	1.68
10	0.03	0.04	1.23

** Indices derived from Fermi deconvolution.

Figure 8-5 Example screenshots of the Perfusion plug-in for CMRtools. Myocardial borders are delineated in (a) followed by motion correction (b), ROI delineation (c) in this case 6 radial segments divided into endo- and epicardium with a circle selecting the blood pool region. Corresponding signal-time measurements are graphically shown in (d) with the blood pool region shown in red and the selected myocardial region in green. In the final stage, this data is used to calculate myocardial perfusion indices (e) and displayed in a bullseye plot (the subendocardium is currently displayed). For the region selected, the myocardial perfusion index is shown at both rest and stress along with the corresponding curves and the final myocardial perfusion reserve index (MPRi). 10 of the 12 measurements are shown with a scroll bar to view the remaining data entries.

8.3 Clinical case studies

CMRtools is currently being used with our collaborators at the Royal Brompton Hospital. In order to outline the clinical value of the described modelling technique, we describe in this section three patients who have undergone SPECT, X-ray angiography, MR myocardial perfusion and late enhancement studies.

8.3.1 Patient 1

This is a 79-year-old male, who had a ventricular fibrillation arrest and was resuscitated on the way to accident and emergency. After resuscitation his ECG was of a left bundle branch block pattern, consistent with previous or recent infarction. Thrombolysis was given as clinically it was thought an ongoing infarction was probable. He was subsequently transferred to the coronary care unit and stabilized.

Figure 8-6 summarises the SPECT findings for this patient. At stress, there is absent uptake in the antero-apical region with hypo-perfusion of the septum and moderate reduction in the whole of the inferior wall. Antero-lateral uptake is normal. Following rest injection the antero-apical region and septum improve partially and the inferior wall returns to normal. Therefore partial thickness antero-apical and septal and inferior infarction with at least moderate ischaemia superimposed. Figure 8-7 shows the corresponding X-ray angiogram of the left coronary artery with an unobstructed LCX but a sub-totally occluded LAD. The angiogram of the RCA in Figure 8-8 shows an occlusion proximally. Sample images from the MR myocardial perfusion study obtained with a Hybrid EPI sequence are shown in Figure 8-9 with hypo-enhancement in the inferior wall basally and infero-septal wall in the mid ventricular slice. The corresponding polar bullseye plot from MR perfusion analysis is shown in Figure 8-10. In Figure 8-11 and Figure 8-12, the curves for two contrasting ROI's are shown demonstrating the accuracy of the curve fitting and the contrasting uptake curves. Finally, the late enhancement images in Figure 8-13 illustrates hypo-enhancement ~5 minutes following the contrast agent administration, which corresponds to microvascular obstruction. For this patient, no hypo-enhancement in the initial late enhancement image (~10mins) was observed, but after a further delay (~30mins) there was hyper-enhancement seen in the septal subendocardium. This was due to the microvascular obstruction delaying contrast enhancement early; with time, contrast does reach this recent infarction. This represents recent and ongoing myocytes necrosis rather than myocardial fibrosis. The lack of perfusion to the anterior, septal and inferior walls ties in with blockages in LAD and RCA.

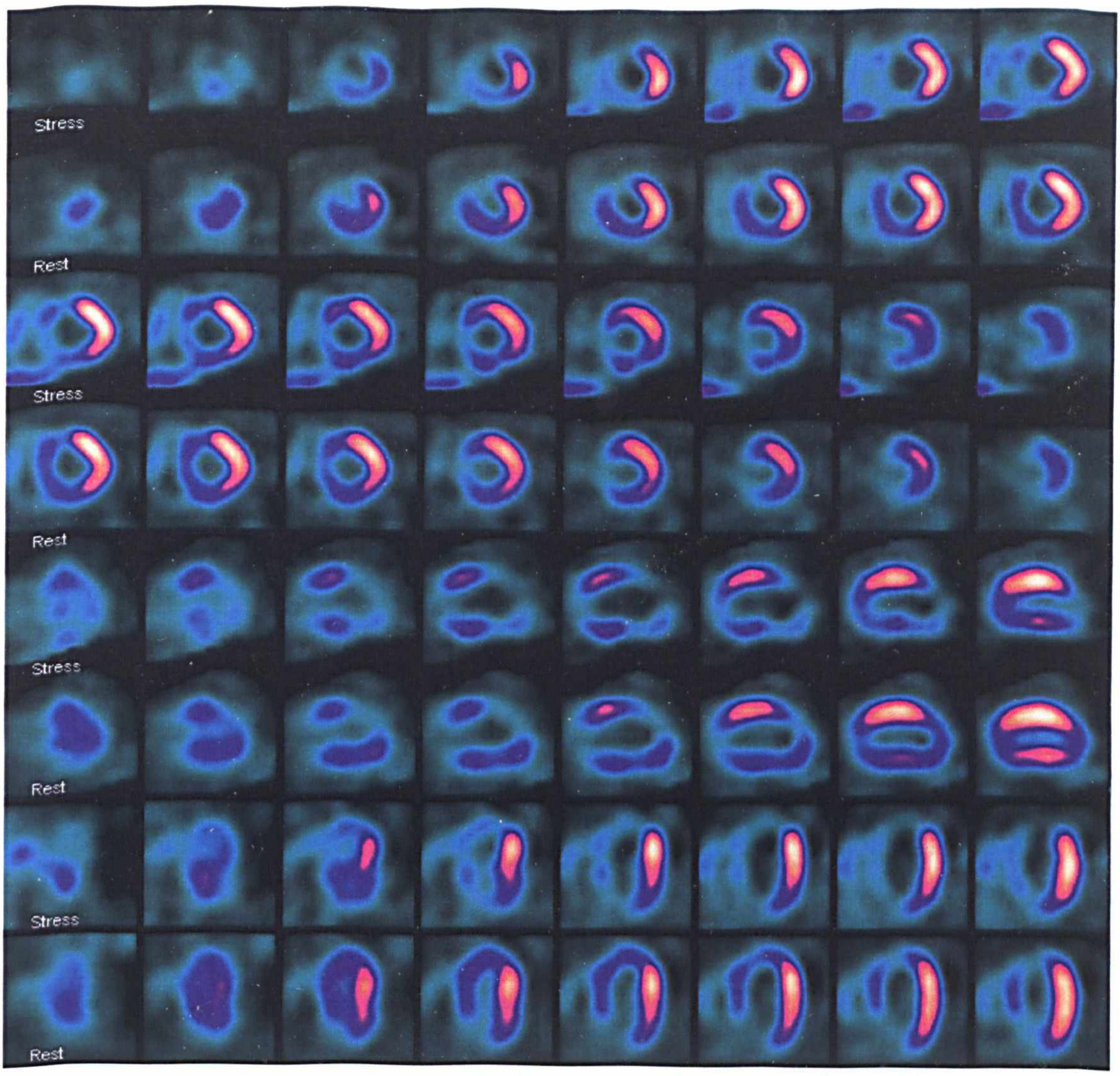

Figure 8-6 A summary of SPECT findings for patient 1. Four views are shown, at the top eight time series images at stress and rest of a basal slice, below stress and rest of a mid ventricular slice then a HLA view and a VLA view. At stress, there is absent uptake in the antero-apical region with severe reduction of uptake in the septum and moderate reduction in the whole of the inferior wall. Antero-lateral uptake is normal. Following rest injection the antero-apical region and septum improve partially and the inferior wall returns to normal.

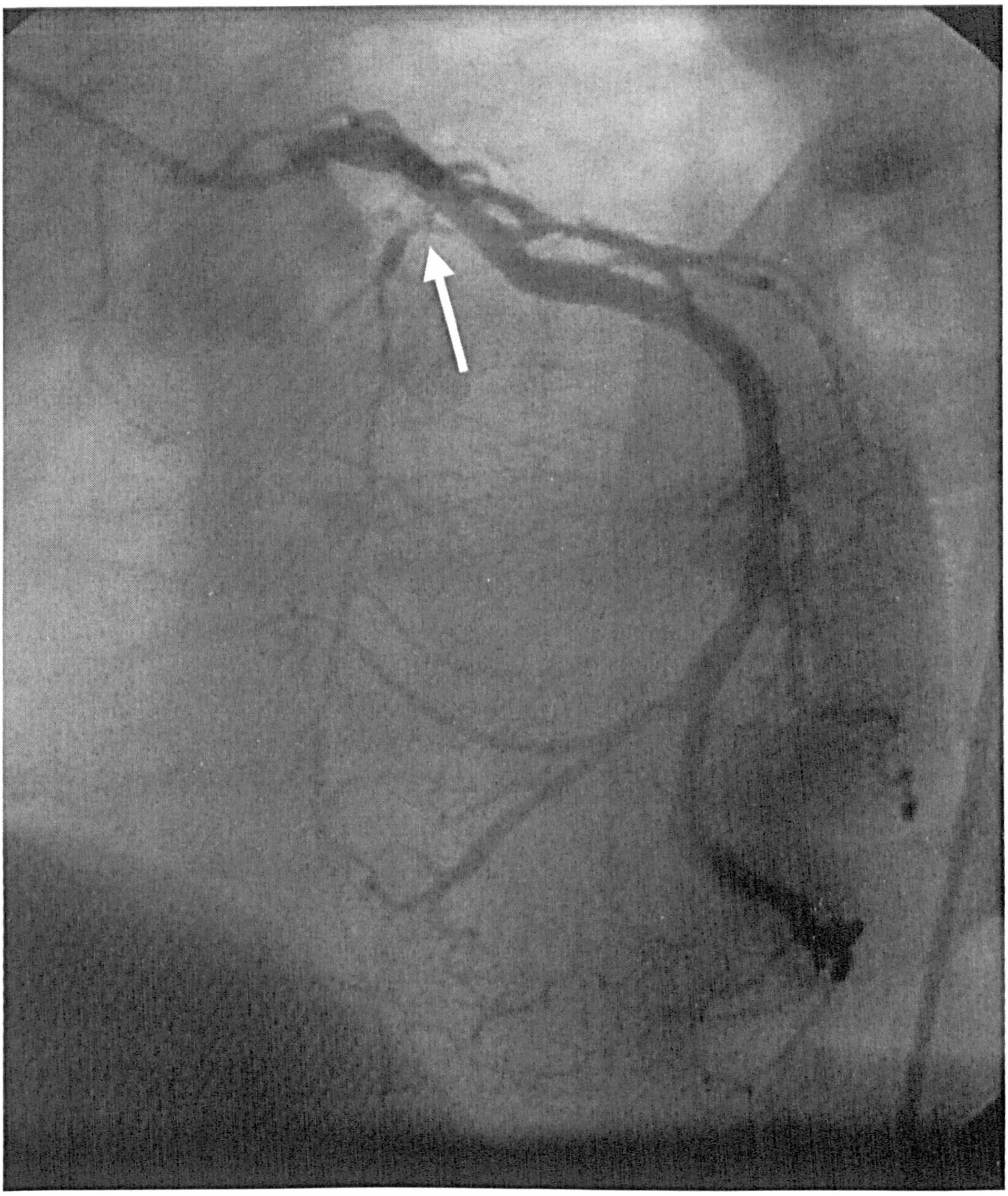

Figure 8-7 X-ray angiography of the left coronary artery of patient 1, showing the LAD sub-totally occluded whilst the LCX is unobstructed.

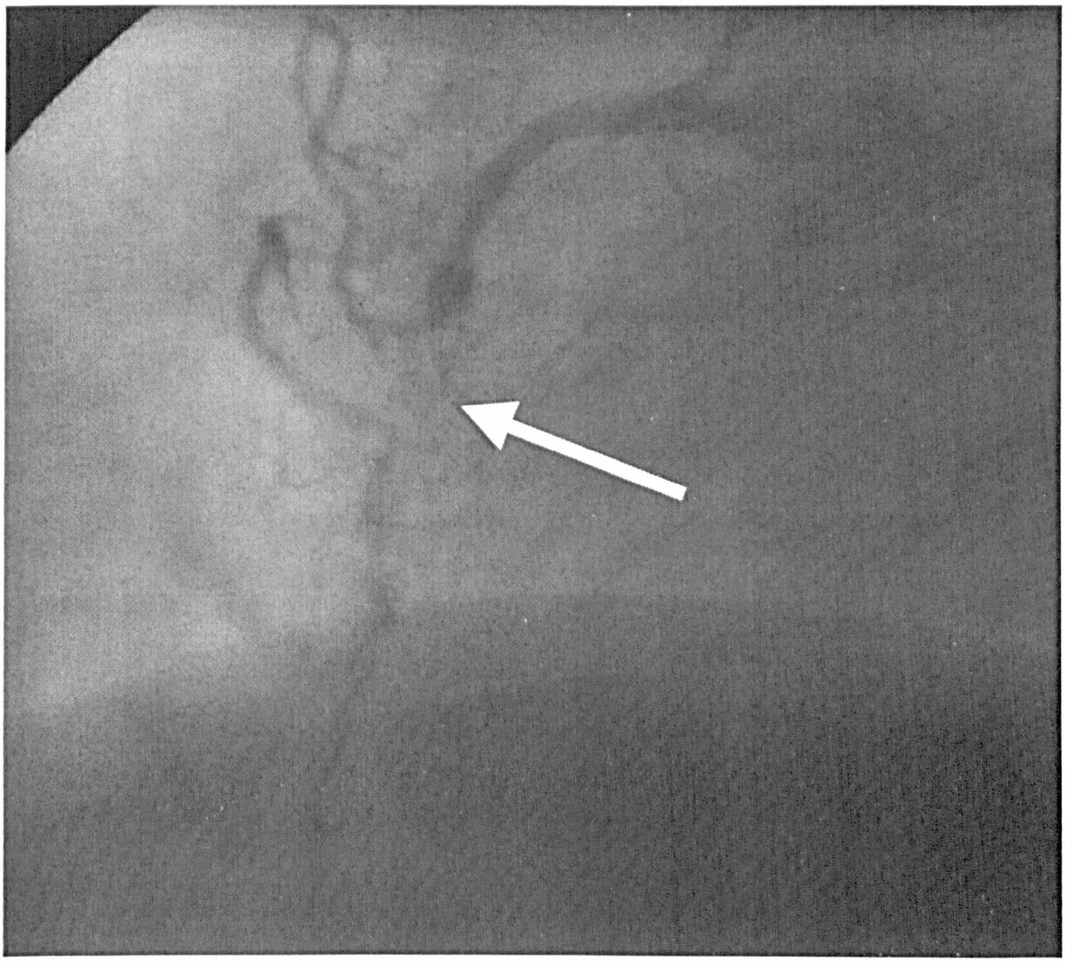

Figure 8-8 X-ray angiography of the RCA of patient 1, showing the proximal occlusion as marked by the arrow.

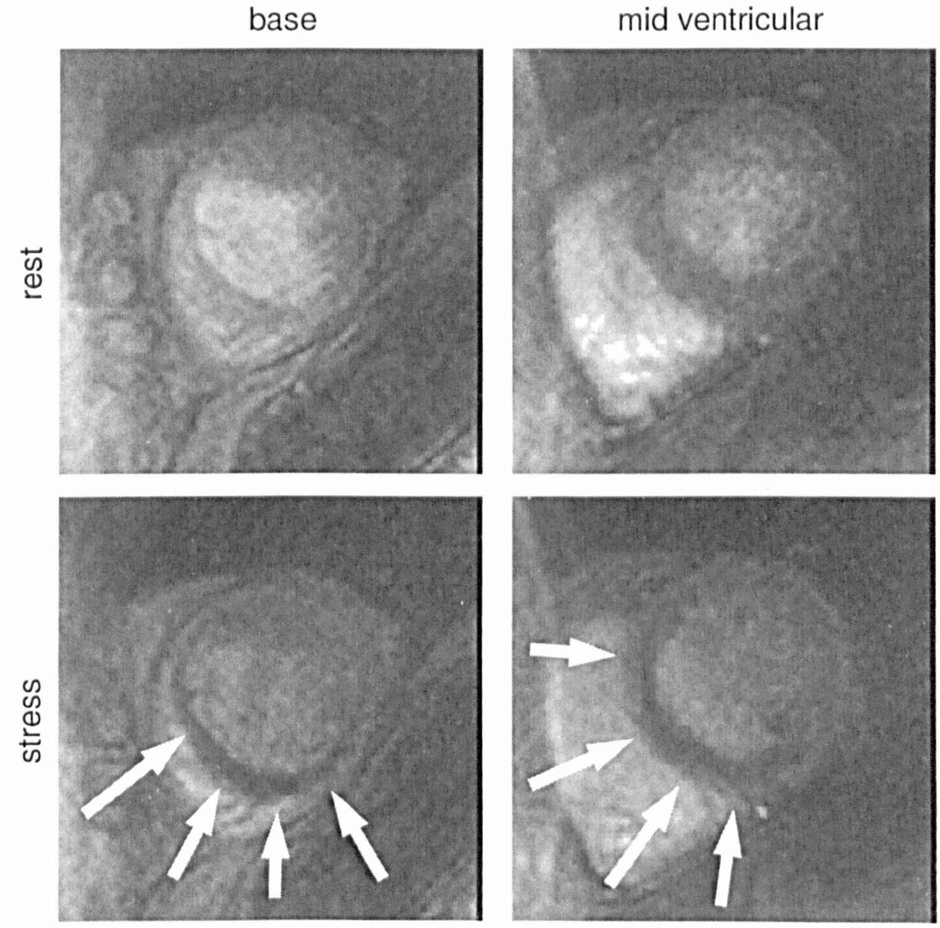
base
mid ventricular
rest
stress

Figure 8-9 Images from the first pass MR perfusion sequence of patient 1 showing hypo-perfusion of the anterior, inferior and septal walls, predominantly in the subendocardium.

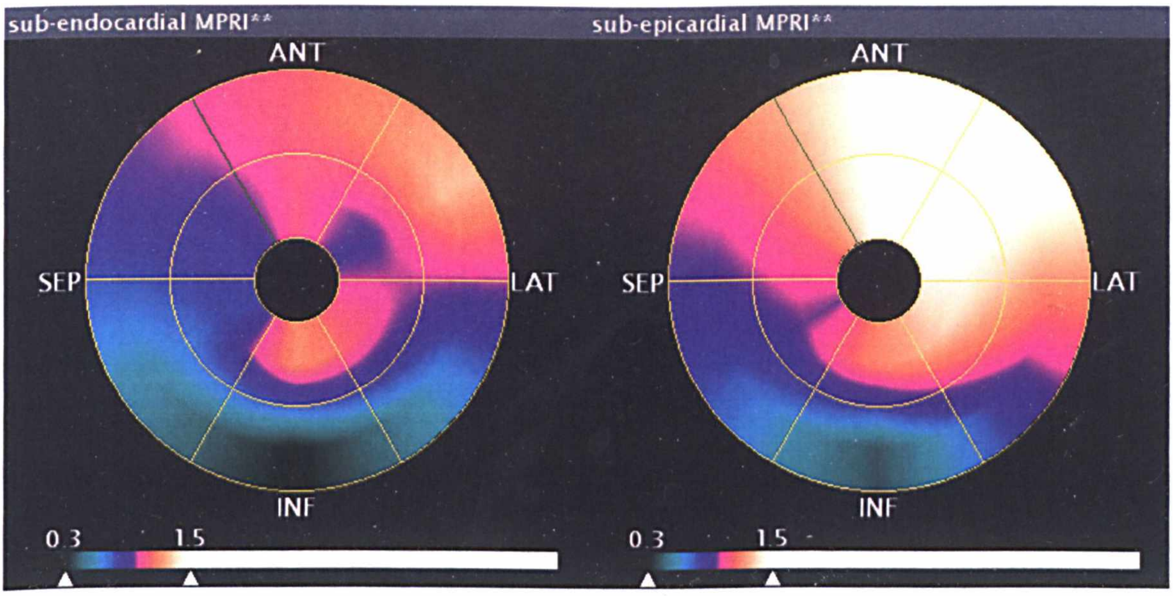

Figure 8-10 The bullseye plots of the first pass perfusion distribution corresponding to results in Figure 8-9 of patient 1. Severely reduced MPR Index (MPRi) values for the inferior wall is seen in the basal slice spreading around to the septal wall in the mid ventricular slice.

From the figures shown, the relative sparing of the mid-ventricular wall is consistent with the angiogram showing a large dominant circumflex vessel. It is likely the RCA was small prior to its occlusion. This is likely to be a chronic occlusion in the light of the early gadolinium images, with the LAD occlusion being the most recent event. The thallium and MR perfusion imaging give comparable results. However, the MR late enhancement images identify the coronary territory responsible for the presentation. Despite the RCA having the chronic occlusion it doesn't seem to have developed any collateral circulation to the distal territory, reflecting the dominance of the circumflex vessel in supplying this territory.

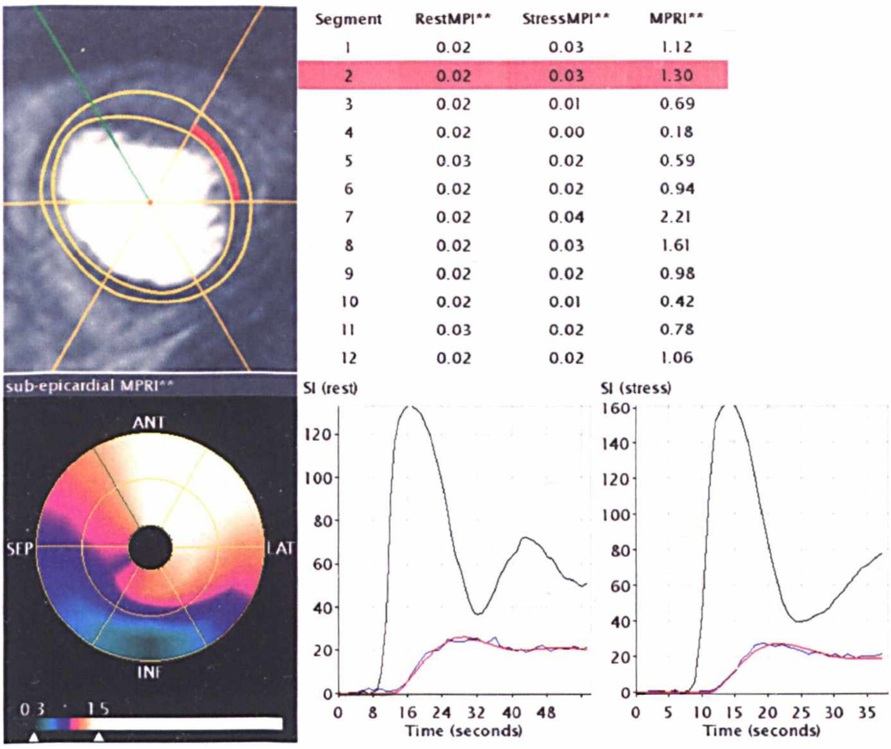

Segment	RestMPI**	StressMPI**	MPRI**
1	0.02	0.03	1.12
2	0.02	0.03	1.30
3	0.02	0.01	0.69
4	0.02	0.00	0.18
5	0.03	0.02	0.59
6	0.02	0.02	0.94
7	0.02	0.04	2.21
8	0.02	0.03	1.61
9	0.02	0.02	0.98
10	0.02	0.01	0.42
11	0.03	0.02	0.78
12	0.02	0.02	1.06

sub-epicardial MPRI**
ANT
SEP
LAT
INF
0.3
1.5
SI (rest)
0
20
40
60
80
100
120
0 8 16 24 32 40 48
Time (seconds)
SI (stress)
0
20
40
60
80
100
120
140
160
0 5 10 15 20 25 30 35
Time (seconds)

Figure 8-11 The intermediate modelling results for Segment 2 of Figure 8-9 of patient 1, demonstrating normal perfusion uptake of this subendocardial segment.

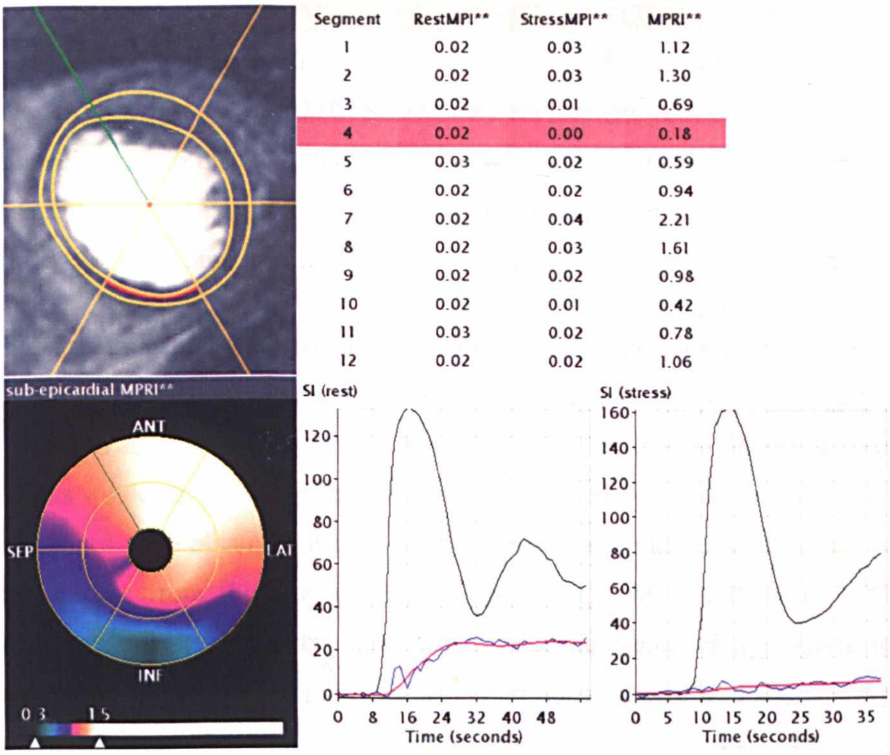

Segment	RestMPI**	StressMPI**	MPRI**
1	0.02	0.03	1.12
2	0.02	0.03	1.30
3	0.02	0.01	0.69
4	0.02	0.00	0.18
5	0.03	0.02	0.59
6	0.02	0.02	0.94
7	0.02	0.04	2.21
8	0.02	0.03	1.61
9	0.02	0.02	0.98
10	0.02	0.01	0.42
11	0.03	0.02	0.78
12	0.02	0.02	1.06

sub-epicardial MPRI**
ANT
SEP
LAT
INF
0.3
1.5
SI (rest)
0
20
40
60
80
100
120
0 8 16 24 32 40 48
Time (seconds)
SI (stress)
0
20
40
60
80
100
120
140
160
0 5 10 15 20 25 30 35
Time (seconds)

Figure 8-12 The intermediate modelling results for Segment 4 of Figure 8-9 of patient 1, demonstrating hypo-enhancement in the inferior wall.

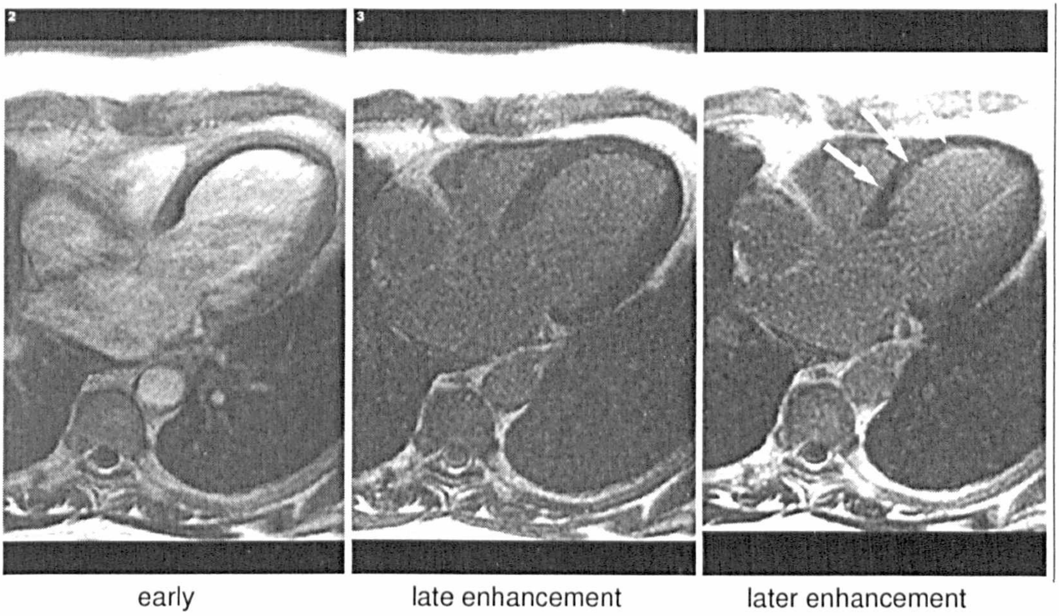

Figure 8-13 Late enhancement images of patient 1 at five weeks following presentation with ventricular fibrillation and myocardial infarction, showing septal hypo-enhancement. In the context of a recent infarction, this demonstrates microvascular obstruction and is therefore the territory responsible for their presentation.

8.3.2 Patient 2

This is a 76-year-old male with angina, who has previously undergone coronary artery bypass grafting performed in 1991. Subsequent angiography showed he had a blocked saphenous vein graft to the RCA and percutaneous coronary intervention was performed to the stenosed LCX saphenous vein graft in 2002. The patient has normal left and right ventricular systolic function, and no significant valvular stenosis or regurgitation.

The SPECT assessment results are shown in Figure 8-14, illustrating the partial thickness basal inferior myocardial infarction with moderate inducible ischaemia of the mid and distal inferior wall. An additional area of moderate ischaemia is evident in the distal anterior wall and apex; this would suggest an increased likelihood of future coronary events. MR first pass perfusion images were obtained using a hybrid EPI sequence at rest and during adenosine stress and images from this are shown in Figure 8-15. At rest there is homogenous myocardial perfusion, and at stress there is an inducible region of hypo-perfusion, most marked within the infero-septal region, but also in the antero lateral wall and lateral papillary muscles. The corresponding bullseye plot from MR perfusion analysis is shown in Figure 8-16. Following gadolinium injection there is subendocardial late myocardial enhancement of the inferior wall consistent with previous myocardial infarction as shown in Figure 8-17. The remaining myocardium is viable.

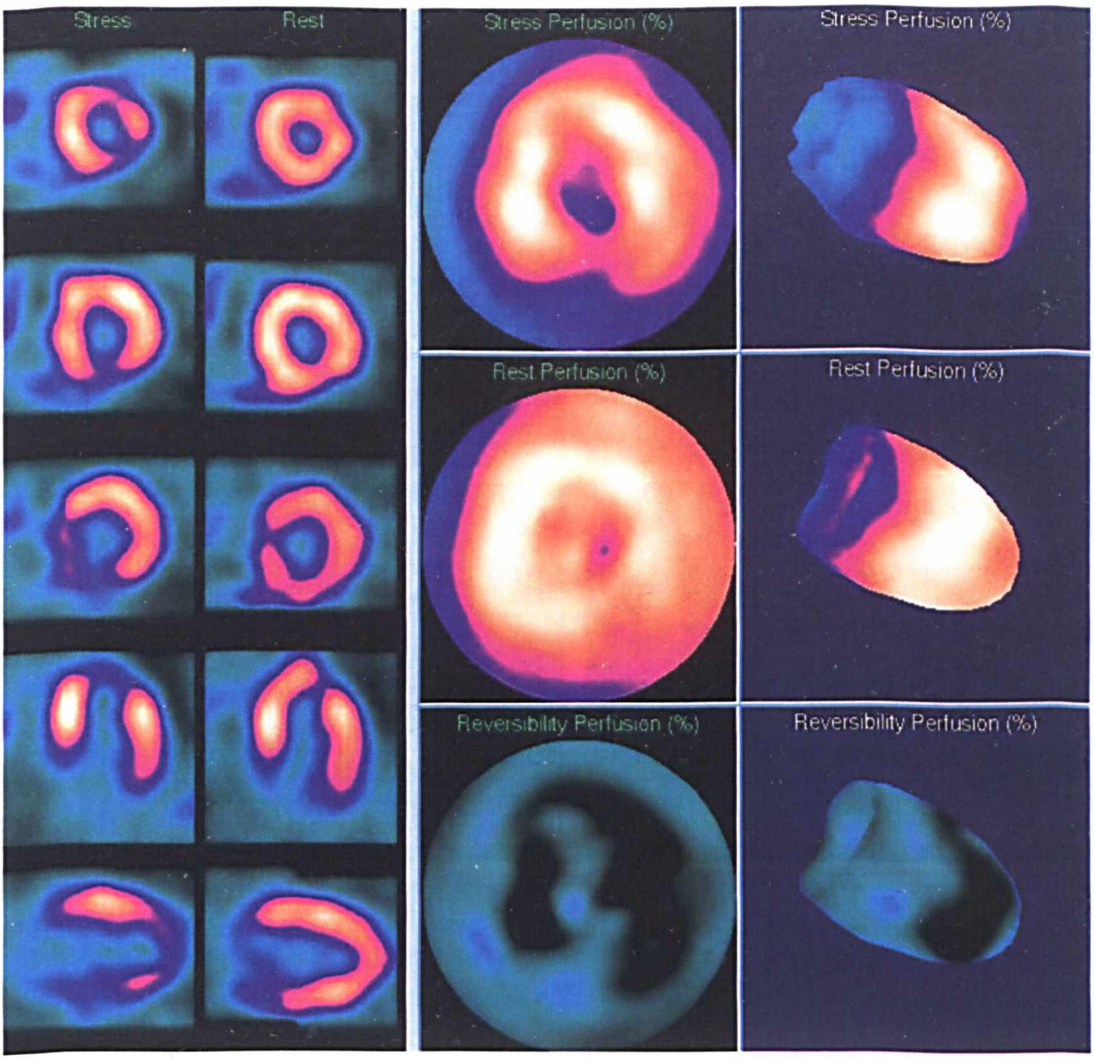
Stress
Rest
Stress Perfusion (%)
Stress Perfusion (%)
Rest Perfusion (%)
Rest Perfusion (%)
Reversibility Perfusion (%)
Reversibility Perfusion (%)

Figure 8-14 SPECT assessment of patient 2 showing partial thickness basal inferior myocardial infarction with moderate inducible ischaemia of the mid and apical inferior wall. The views on the left show from the top, apical, mid ventricular and basal short axis slices of the LV, followed by a HLA and VLA view. In the central column bullseye plots, and on the right a 3D visualisation of the LV are shown with a measure of reversibility based on the rest and stress findings.

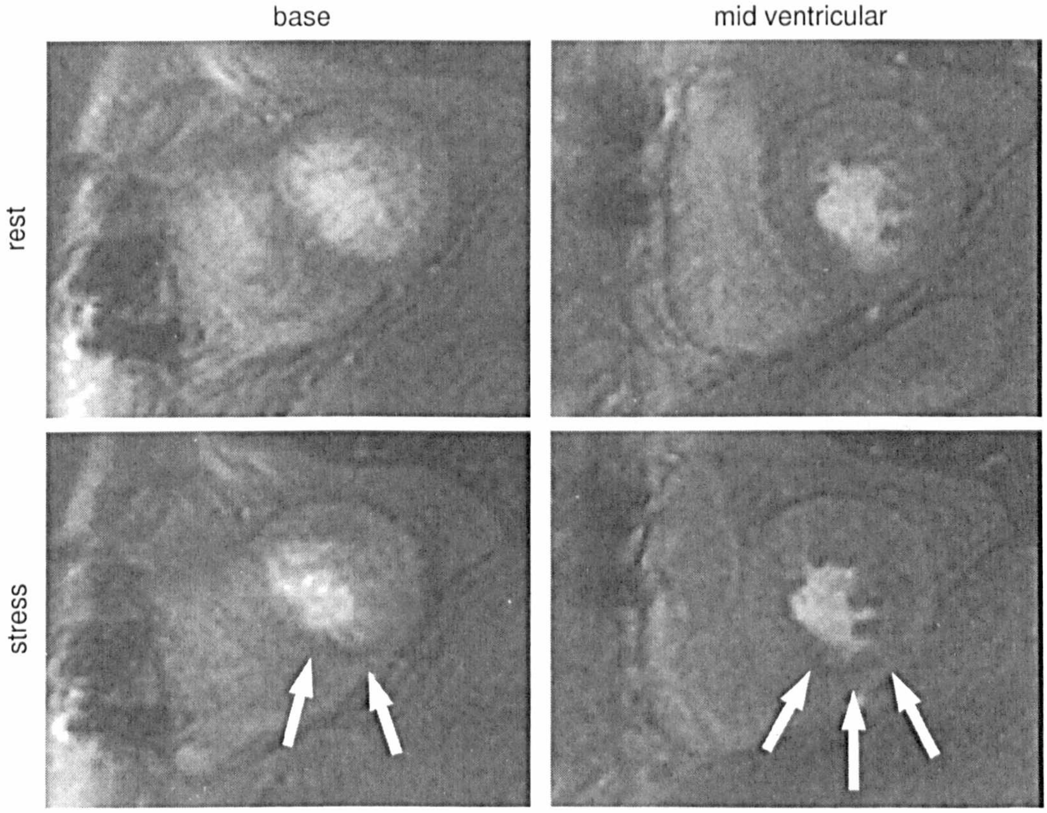
base
mid ventricular
rest
stress

Figure 8-15 MR first pass perfusion assessment of patient 2 with arrows identifying hypo-perfusion of the inferior, infero-septal and lateral walls at stress.

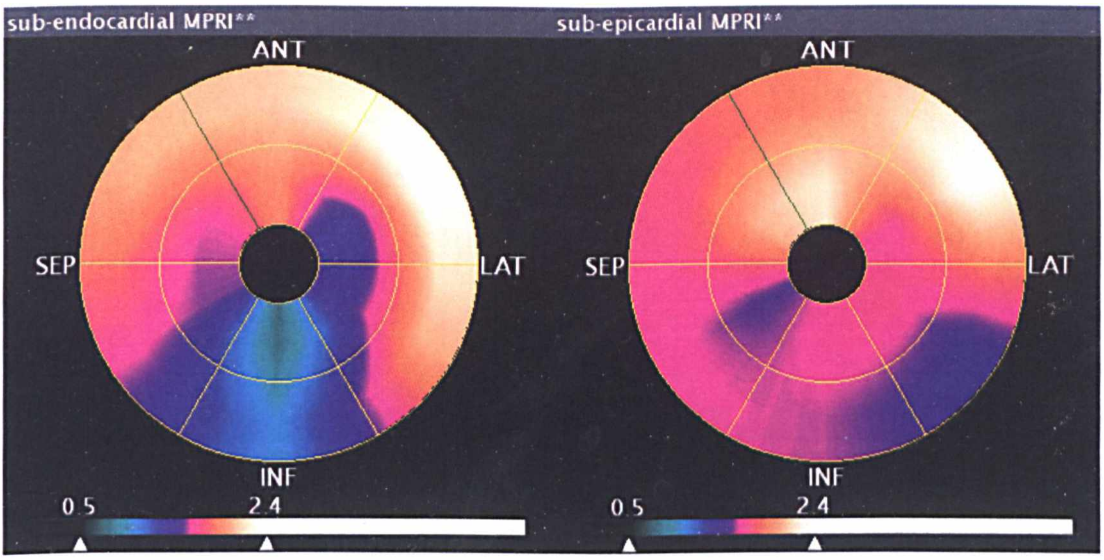
sub-endocardial MPRI**
ANT
SEP
LAT
INF
0.5
2.4
sub-epicardial MPRI**
ANT
SEP
LAT
INF
0.5
2.4

Figure 8-16 Bullseye plots from the MR assessment of patient 2 clearly showing the subendocardial perfusion defect in the inferior wall spreading to the infero-septal wall and lateral wall of the mid ventricular slice (shown as the inner ring).

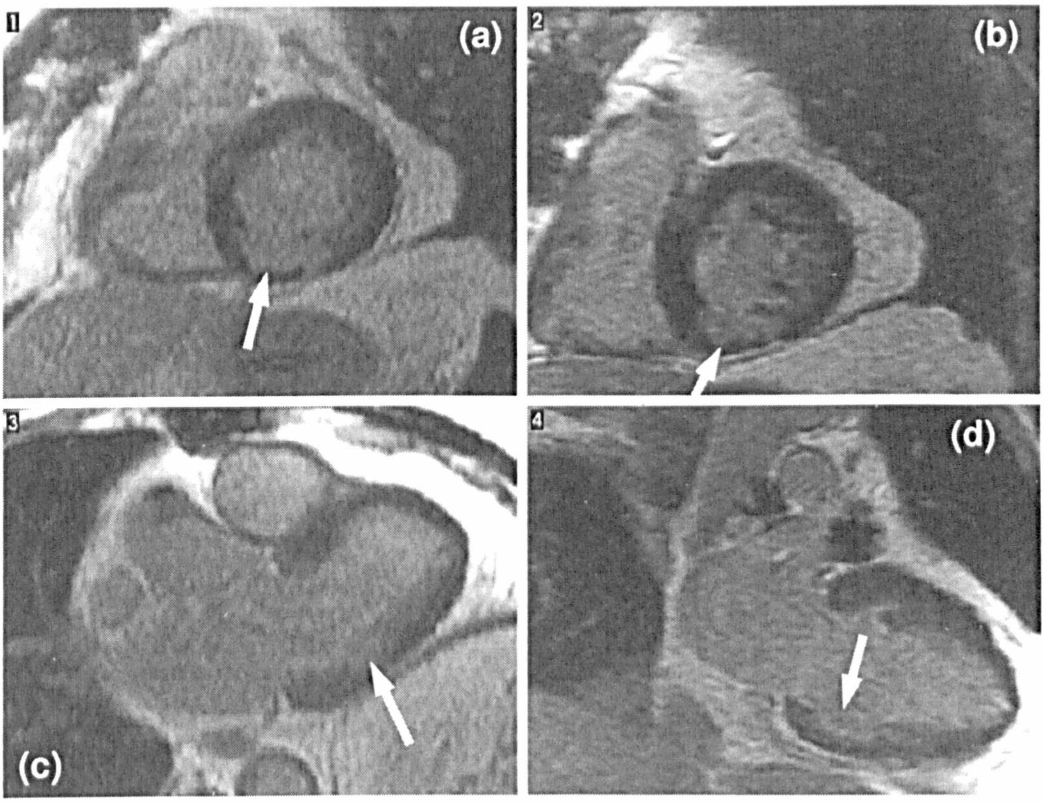

Figure 8-17 Late enhancement images of patient 2 showing subendocardial infarction of the inferior wall. The arrows identify the late enhancement in the (a) short axis basal slice (b) short axis mid slice (c) LV outflow tract and (d) VLA views.

In conclusion, this patient has normal ventricular systolic function, a subendocardial infarction of the basal and mid inferior wall and inducible ischaemia mainly affecting the infero-septal region, but with additional mild ischaemia of the antero-lateral wall and lateral papillary muscles. This was present in both the SPECT and CMR studies.

8.3.3 Patient 3

This is a 51-year-old male with a previous inferior myocardial infarction. The patient has an occluded RCA, and LAD stenoses of 50%. He has experienced ongoing angina, and had a negative exercise treadmill test on recent admission. CMR examination of the patient has shown mildly a dilated LV. The inferior wall is severely hypo-kinetic with a limited segment of akinesia at the basal inferior wall. There is no significant valvular stenosis or regurgitation. First pass MR perfusion images were obtained at rest and during adenosine stress; images were acquired with a TSENSE [251] EPI sequence as described in section 3.4.2. Examples of the perfusion image series are shown in Figure 8-18, showing the coverage of the LV. The bullseye plots in Figure 8-19 show an inducible area of hypo-perfusion within the inferior and infero-septal walls. Furthermore, they also depict the less severe inducible hypo-perfusion of the septum and anterior wall, particularly at a mid ventricular level. However, perfusion of the lateral walls appears homogeneous. Following gadolinium injection shown in Figure 8-20, there was late myocardial enhancement of the basal inferior wall in a near transmural distribution. This extends into the inferior septum. These findings correspond well to angiogram findings as shown in Figure 8-21 and Figure 8-22, demonstrating the occlusion of RCA and the moderate stenosis of the LAD.

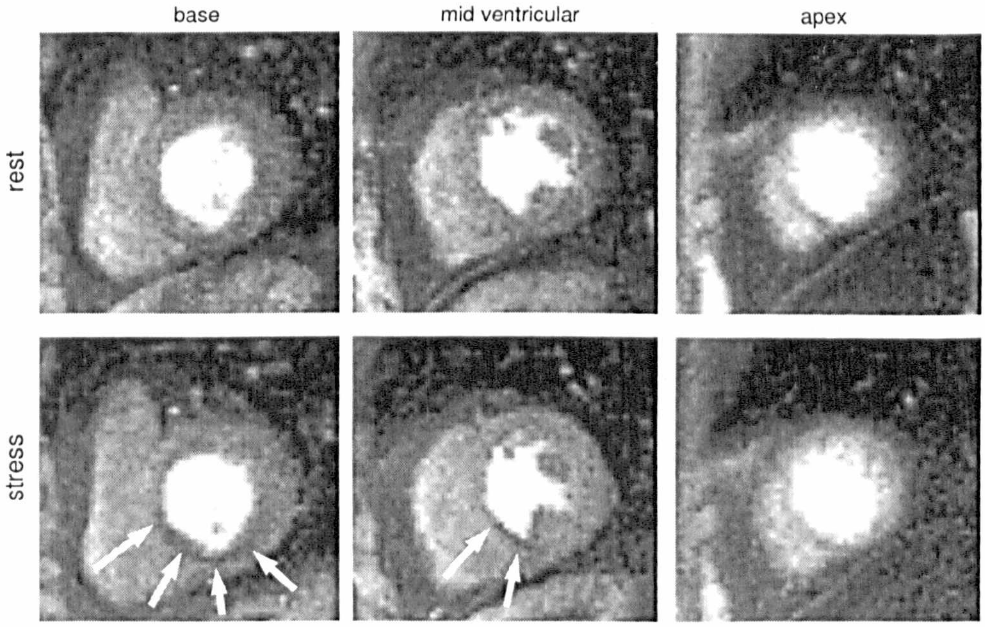

Figure 8-18 CMR perfusion images of patient 3 obtained with the TSENSE EPI sequence. Images taken during adenosine hyperaemia show an area of hypo-perfusion within the inferior and infero-septal wall in the basal and mid ventricular slices. In the basal slice this extends further in to the septum and antero-septal wall. Therefore the distribution of this inducible defect would suggest that more than one coronary territory is affected, most likely the RCA and to a lesser extent the LAD vessel.

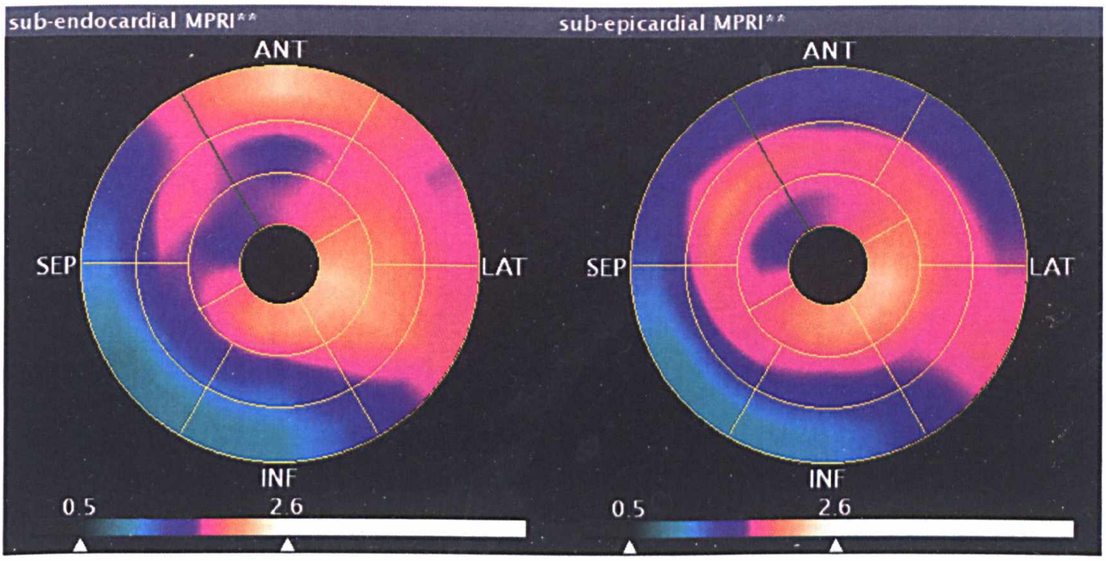
sub-endocardial MPRI**
ANT
SEP
LAT
INF
0.5
2.6
sub-epicardial MPRI**
ANT
SEP
LAT
INF
0.5
2.6

Figure 8-19 Polar plots of MPRi values for patient 3 graphically illustrate the severe inducible hypo-perfusion of the inferior and infero-septal walls in green, particularly at the base of the ventricle. Furthermore, they also depict the less severe inducible hypo-perfusion of the septum and anterior wall, particularly at a mid ventricular level.

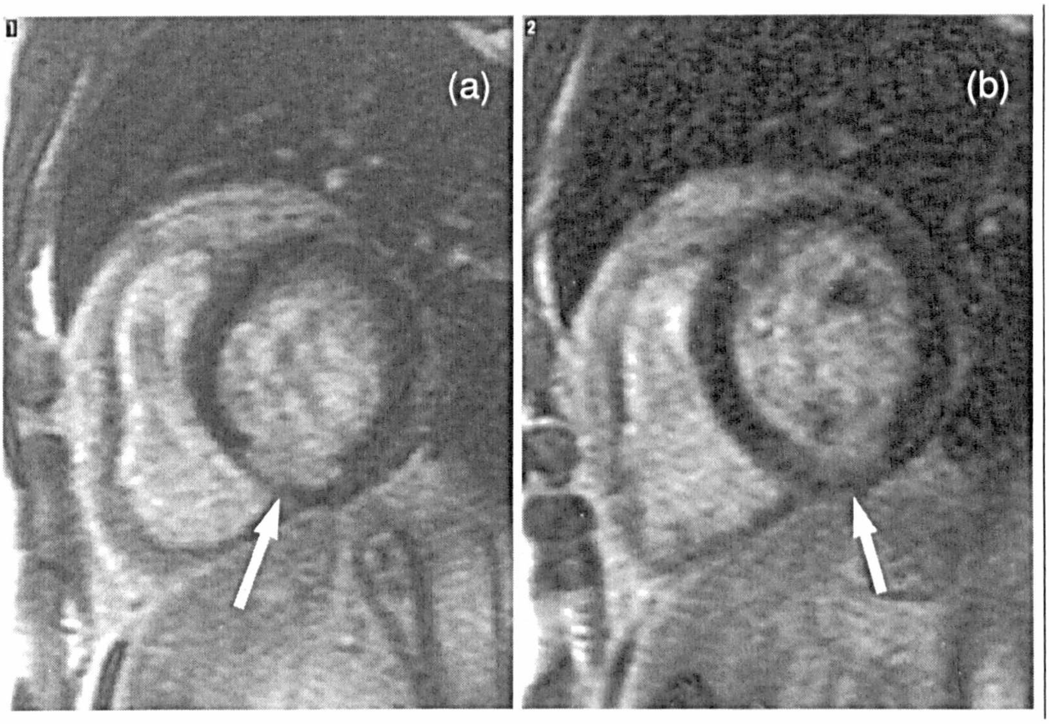

Figure 8-20 Late enhancement images for patient 3 showing subendocardial infarction of the inferior wall. The arrows identify the late enhancement in the (a) short axis basal slice (b) short axis mid slice.

The MR perfusion study in this case predicted that the anterior wall and to a greater extent the inferior wall were supplied by stenosed arteries. On angiography, this confirmed the RCA occlusion with distal collaterals and the moderately stenosed LAD. The significance of the severe infero-basal perfusion defect when compared to the inferior wall at a mid ventricular level may be the collateral vessels, seen on angiography, refilling the distal vessel.

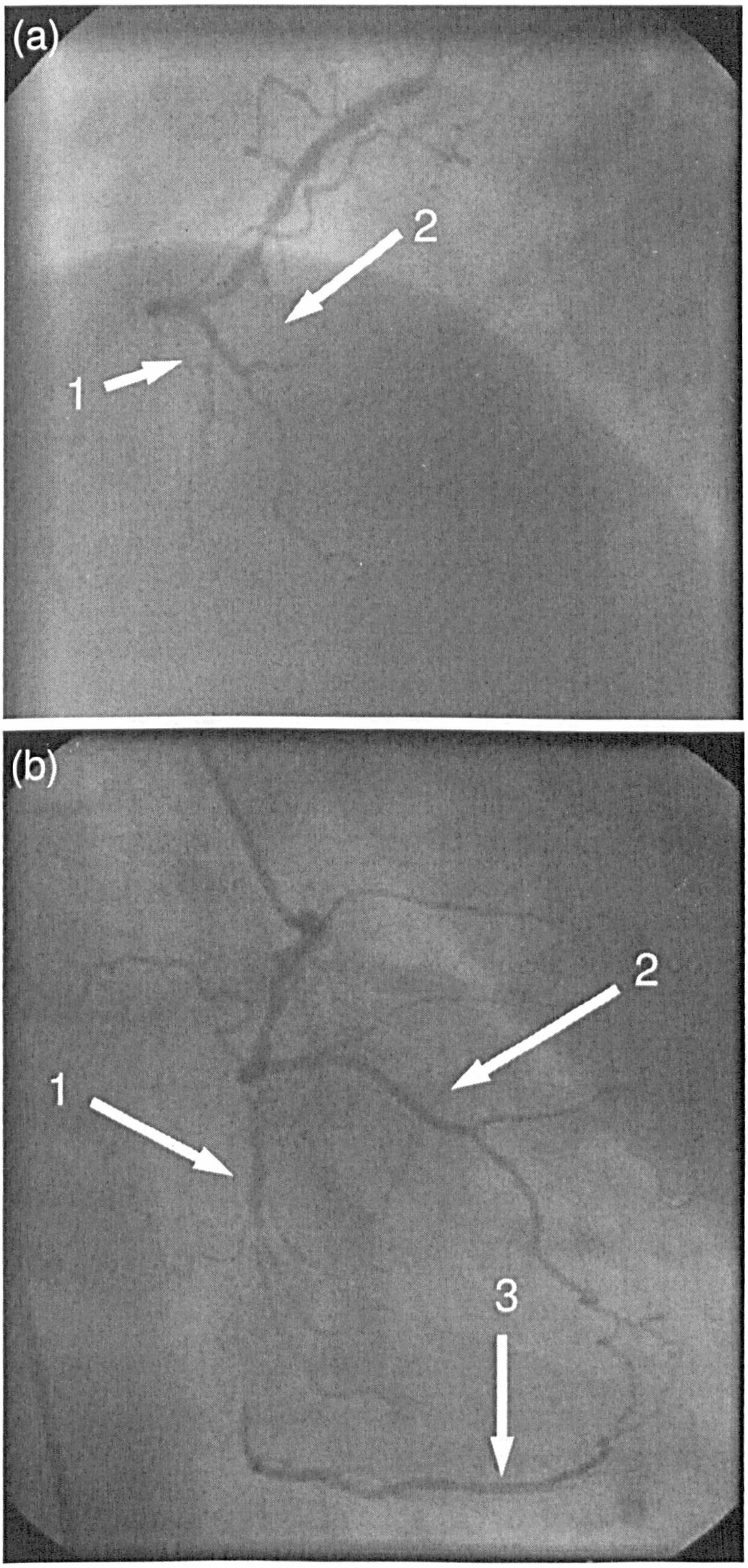

Figure 8-21 Left anterior oblique (a) and right anterior oblique (b) projections of the RCA of patient 3. Showing occlusion of the main vessel (1), and a large collateral vessel (2) that distally refills the occluded vessel (3).

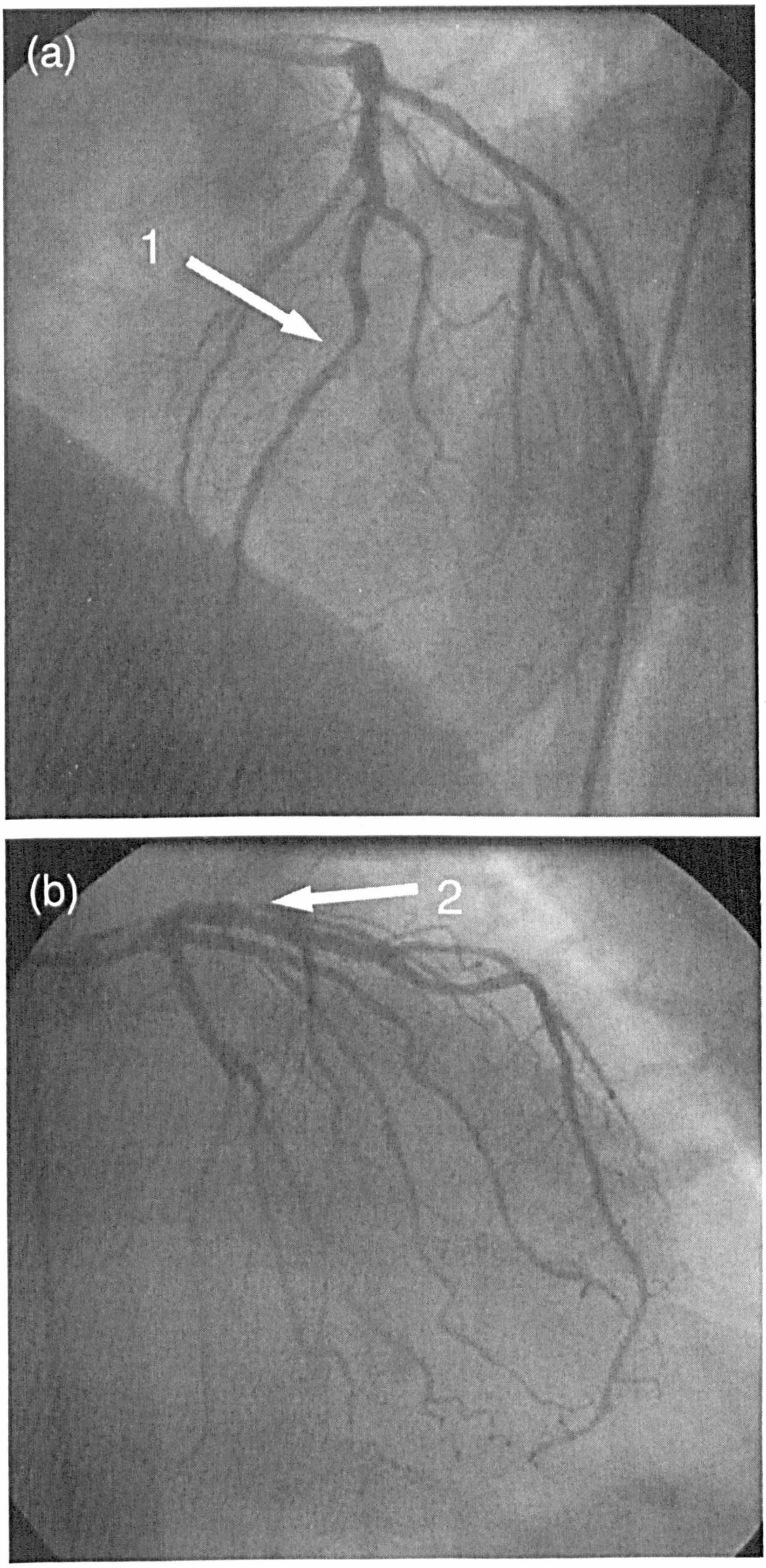

Figure 8-22 Left anterior oblique cranial (a) and left anterior oblique (b) projections of the LAD artery of patient 3. Arrows 1 and 2 depict 50% of luminal diameter stenoses of the mid and proximal vessel respectively.

8.4 Interstudy reproducibility

To further assess the clinical value of the proposed modelling technique, a reproducibility study of MR myocardial perfusion was carried out with statistics derived from both normalised up-slope and indices measured directly from the optimised Fermi function tissue impulse response curve [252]. The study included seven normal volunteers and nine patients with CAD; all underwent rest and adenosine stress perfusion CMR studies on two separate visits. A single mid-ventricular short axis (SA) slice was studied on each visit using a fast low-angle shot (FLASH) sequence. The global and regional MPRi were calculated using two methods: constrained deconvolution with the Fermi function and normalised up-slopes. The same ROI's were used by the two analysis techniques. Figure 8-23 is a scatterplot of the global MPRi measurement, calculated by normalised up-slopes. Figure 8-24 is a scatterplot of the global MPRi measurement, calculated by Fermi deconvolution. The reproducibility of MPRi measurements was superior with Fermi deconvolution over normalised up-slopes for global analysis (coefficient of variation 21% vs 41%, P=0.02). The reproducibility of MPRi was similar in normal volunteers and in patients with CAD (coefficient of variation 21% vs 23%, P=0.88). The study concluded that quantitative first-pass perfusion CMR has reasonable reproducibility for measuring MPRi using Fermi deconvolution. The reproducibility is less good using normalised up-slopes.

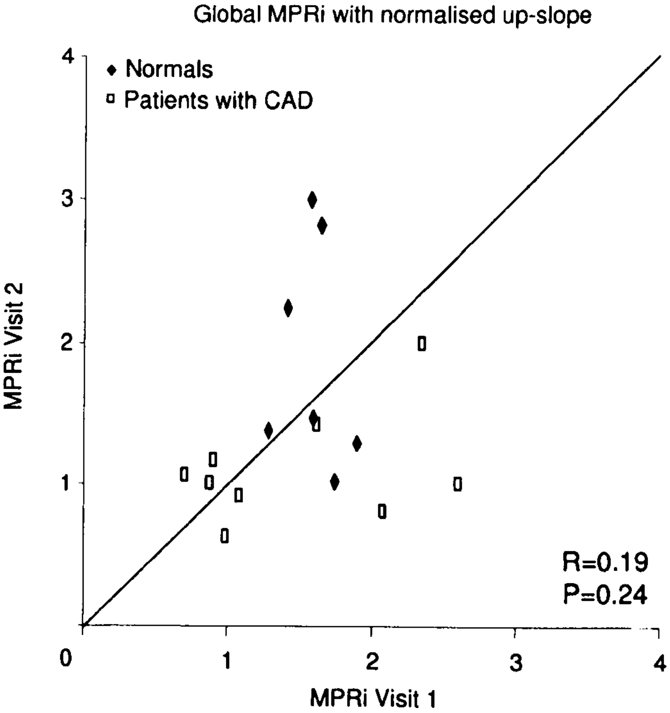

Figure 8-23 A scatterplot of the global MPRi measurement, calculated by the maximum up-slope of the myocardial signal normalised against the maximum upslope of the blood pool signal.

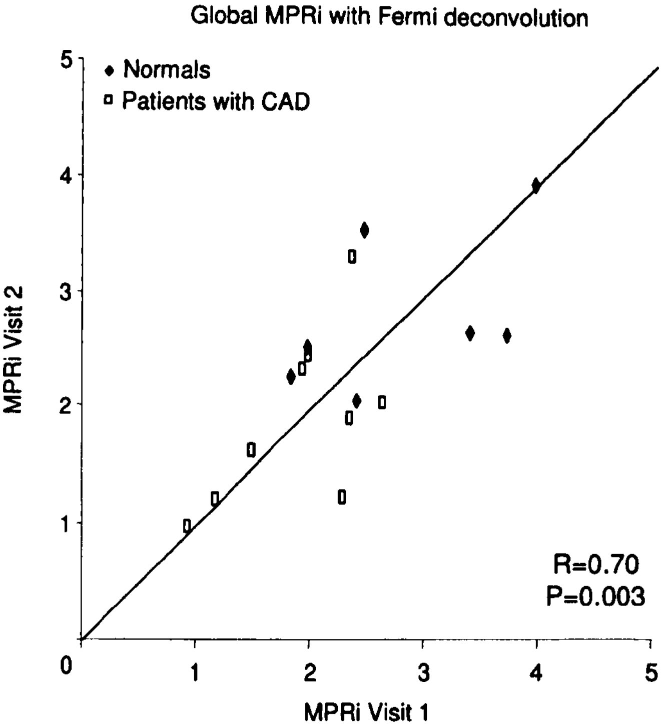

Figure 8-24 A scatterplot of the global MPRi measurement, calculated by Fermi deconvolution. The reproducibility of MPRi was similar in normal volunteers and in patients with CAD (CoV 21% vs 23%, P=0.88).

8.5 Conclusions

With rapid acquisition and correction for cardiac and respiratory motion, the final stage of the assessment of myocardial perfusion with MR is the derivation of quantitative regional perfusion indices for determining myocardial perfusion reserve. Quantitative perfusion indices greatly improve the capabilities of MR myocardial perfusion for assessing CAD and facilitate further research into coronary and microvascular dysfunction. This chapter presents the issues involved in tracer kinetic modelling and the development of a practical platform for routine clinical use.

In perfusion imaging, the choice of contrast agent is critical to the subsequent analysis. While intra vascular contrast agents provide a simplified and potentially more accurate method of measuring MBF, currently extra cellular contrast agents are commonly used clinically. For the derivation of the impulse response of the coronary flow, accurate acquisition of the AIF is as important as the acquisition of the myocardial signal. This, however, can prove difficult due to the contrasting signal characteristics often resulting in clipping of the AIF due to saturation of the T1 signal.

With the use of an extra cellular contrast agent, the leakage of contrast agent into the interstitial space is detrimental to the single compartment modelling technique although promising results have been shown with these techniques. As an example of this, Fermi function deconvolution has been implemented. Three case studies are presented for patients with CAD and results are compared to those derived from other imaging modalities. In this chapter it has been shown that the use of a quantitative measure of myocardial perfusion indices facilitates interstudy comparison and that the direct deconvolution result was more reliable than the normalised up-slope measure.

Chapter 9 : Discussions and Conclusions

In clinical cardiology, the importance of CMR in assessing morphology, function, and blood flow has been increasingly recognised. With the recent development of ultra-fast CMR techniques, it is now possible to observe the first pass of an administered contrast agent for the non-invasive evaluation of perfusion abnormalities in the myocardium. In this thesis, we have addressed some of the major technical issues related to CMR myocardial perfusion. It is part of our continuing effort in establishing detailed quantitative assessment of myocardial perfusion for the early detection of CAD, as well as prognostic evaluation of patients with known cardiac ischaemia.

In this thesis, we have outlined the clinical background of myocardial perfusion imaging, as well as the basic pathophysiology of myocardial infarction and the development of imaging techniques for quantifying myocardial perfusion abnormalities. We have also provided a relatively comprehensive comparison of the relative strength and potential pitfalls of different imaging techniques for quantifying myocardial perfusion, highlighting the potential of CMR perfusion in a clinical setting, and the technical challenges we have to overcome. The approaches we have used in this thesis are mainly based on exploiting the information content of the *k*-space data, and we have reviewed some of the commonly used *k*-space acquisition techniques that have been developed over the years, including Keyhole, BRISK, BLAST, *k-t* BLAST, UNFOLD, and RIGR. We have also described the basic concept of parallel imaging techniques including SMASH and SENSE which highlights their potential value in myocardial perfusion imaging.

The main contribution of the thesis is the development of the motion-decoupling framework and the use of PLSR for predictive motion modelling. We have also developed novel RR-UNFOLD and RR-RIGR perfusion image acquisition techniques, which both give a near two-fold increase in scan efficiency. To outline the clinical value of the techniques proposed, particularly the use of tracer kinetic modelling, we also provided detailed quantitative analysis and a reproducibility study involving both patients and normal subjects.

9.1 Effective cardiac motion modelling

In CMR, the management of acyclic motion due to respiration is driven by the ongoing demand for assessing cardiovascular anatomy and function with higher image resolution. Although the use of breath-holding effectively freezes respiration, the need to limit the duration of data acquisition to that of a comfortable breath-holding period imposes significant limitations on the image quality. A further drive in CMR towards enhanced spatial resolution and scan efficiency with improved motion adaptation is the recent development in prospective motion tracking. Although imaging with real-time tracking and adaptation has shown great promise in a number of clinical applications, existing research has shown that reliable motion prediction is a significant challenge. The implementation of adaptive tracking over a large range of motion requires an accurate understanding of the intrinsic relationship between the motion of the target anatomical structure and respiration, as many of the existing techniques for adaptive tracking only permit modest increases in the acceptable respiratory range. This relationship has been found to be subject specific and recent 3D studies have confirmed the significance of inter-subject variability as well as the need for in situ subject specific motion modelling. For this thesis, our emphasis has been placed on the use of real-time surface measurable signals to perform accurate motion prediction. The predictive motion modelling method developed is designed for extracting intrinsic relationships between 3D cardiac deformation due to respiration and multiple 1D real-time measurable surface intensity traces. The strength of this approach is that it does not require the interleaved acquisition of navigators, and thus significantly simplifies the pulse sequence design. Furthermore, it makes the technique easily transportable to other imaging modalities. For myocardial perfusion, it will allow cross modality comparison of transmural MBF distributions, particularly with 3D PET. The problem with using surface measured signals, however, is that they are strongly coupled with each other but poorly correlated with respiratory induced cardiac deformation. Numerically, this can create significant problems for recovering the inherent model that explains the causality between respiratory motion and surface deformations. With this project, a new technique of predictive cardiac motion modelling and correction based on PLSR has been developed. The key steps of the method involve initial subject specific modelling of cardiac deformation with 2D/3D imaging of the anatomical structure combined with in situ real-time measurable inputs. Registration based on FFD or finite element modelling is used to recover the underlying spatio-temporal deformation of the anatomical structure. The causality between tissue deformation and real-time measurable signals, such as surface deformation, is then extracted using PLSR. At the prediction stage, real-time measurable inputs are used to predict cardiac deformations without the need for further 2D/3D imaging, so that adaptive imaging can be performed in real-time to track the anatomical regions of interest. To validate the proposed technique and extract subject specific respiratory induced cardiac deformation patterns, 10 normal subjects were recruited for this part of the project. The method derived from this work has attracted extensive interest and further research is being carried out within the group in applying the technique for high-resolution PET reconstruction.

9.2 Fast image acquisition in the presence of respiratory motion

For 3D myocardial perfusion imaging, the use of imaging sequences such as FGRE-ET for myocardial perfusion imaging has significantly reduced the acquisition window whilst maintaining the desired spatial resolution. Further improvements in spatial resolution and 3D coverage for perfusion imaging will require making full use of the information content of the *k*-space data or the application of parallel imaging techniques [103]. For this project, we have concentrated on the former because of its ease of generalisation to other scanners. Techniques such as BRISK and BLAST can potentially be adapted for this purpose. Previously, unaliasing by UNFOLD has been used for perfusion imaging. The technique attempts to encode spatial information into redundant regions of *k-t* space. Initial experience has shown promising practical value of the technique for breath-hold myocardial perfusion imaging by doubling the scan efficiency, which can be used either to increase the spatial resolution/coverage or to decrease the acquisition window. For perfusion imaging with free breathing, however, the technique suffers from significant motion artefacts and blurring due to respiratory induced motion. With this thesis, we have developed a new prospective *k*-space reordering method for UNFOLD to eliminate respiratory induced motion artefact. The method uses real-time diaphragm navigator echoes to ensure temporal filtering of UNFOLD is carried out on a series of images that are spatially registered. The method entails a prospective re-binning algorithm for the creation of multiple image sub-series related to different levels of respiratory motion.

The basic principle of UNFOLD is based on temporal filtering to resolve spatial aliasing within the FOV caused by a reduction in the density of *k*-space sampling. The method assumes that the dynamic structure under consideration is slowly varying throughout the imaging series, and therefore carries a low temporal frequency component. A reduction in the density of the *k*-space sampling reduces the distance between the central peaks of the PSF resulting in aliased reconstructions of the PSF image overlapping onto the central FOV. By shifting the sampling function in the phase encode direction through time we introduce a linear phase shift in the PSF. This has the effect of altering the phase through time of all but the central peak of the PSF, thus introducing a temporal frequency phase modulation that effectively labels the overlapping reconstructions. The use of UNFOLD for myocardial perfusion imaging is currently faced with two major problems. First, the transit of the contrast bolus within the blood pool at the up-slope of the contrast intake is rapid, which can result in sharp signal intensity changes. Second, respiratory induced cardiac deformation between cardiac cycles can be significant. Both of these introduce high temporal frequency components, thus compromising the basic condition for UNFOLD to be effective. The associated artefact is normally manifested as an attenuation of the contrast bolus signal and aliased edges from the chest wall as well as borders between the blood pool and myocardium. The elimination of respiratory motion and the restoration of tracer kinetics are therefore essential to performing UNFOLD for myocardial perfusion quantification. The main steps of our method involve the use of prospective diaphragmatic navigator echoes to split the perfusion imaging series into different sub-series (bins) so that within each bin the anatomical structures are spatially static. Since all bins are created dynamically during acquisition, post-processing of the contents of the bins is necessary before image series reconstruction. The principle behind this post processing step is to increase the contents of a bin to a suitable size for UNFOLD to be successfully applied. This is achieved either through the reuse of current frames within the bin or the recruitment of frames from neighbouring bins. The frames recruited must adhere to the required phase shifting pattern selected during the acquisition. In this way, we are able to optimise the result of UNFOLD for each bin by making use of the extra information we have from the full series. By splitting up the image series into spatially registered subsets, respiratory motion induced artefact can be eliminated in the reconstructed images. Finally, since UNFOLD works by eliminating temporal changes in pixel intensity at the Nyquist frequency, which has the effect of smoothing out sharp signal intensity changes between adjacent images within each bin, correction for dynamic tracer uptake was applied. This is important to myocardial perfusion quantification as distortion to the contrast information is especially pronounced during contrast uptake, as by reordering we have effectively introduced sharper intensity changes.

Validation of the proposed technique was performed in two stages. A detailed study of the technique for 10 normal subjects without the administration of contrast agent allowed for the assessment of RR-UNFOLD on the removal of motion artefact. Following this, the method was applied to 10 patients. This was used to determine the effects of the changing image intensity through time on the success of RR-UNFOLD. It also provides a means of determining the optimum number of extra central *k*-lines required to maintain the contrast agent intensity through time. For quantifying image artefact, the image series reconstructed with full *k*-space encoding was used as a gold standard and the sum of the squared subtraction error was calculated for different reconstruction methods used. Results from this study have shown that RR-UNFOLD significantly extends the applicability of UNFOLD to perfusion imaging, which brings a 40% reduction in image artefact when the same amount of *k*-space information is used.

Further improvement of the technique by using reconstruction with RIGR was also pursued. While the RR-RIGR technique does not clearly improve upon the RR-UNFOLD technique, it is a promising area for further development as the acquisition is able to focus data acquisition solely on the dynamic contrast enhancement. A significant challenge of the RIGR approach is the need to acquire fully encoded reference images, and with the binning procedure applied this requires multiple fully encoded reference images, limiting the potential application of the two reference RIGR which is better able to model dynamic behaviour in the derivation of the basis functions. A method of efficiently acquiring these reference images would provide a useful addition to this technique, as the closer to the main scan that these can be obtained, the better the chance of the smaller defects still having a subtle edge component for inclusion in the basis functions. With the proposed RR-UNFOLD and RR-RIGR, the scan efficiency achieved can be used in couple with CMR hardware improvement for extending the 3D spatial coverage and shortening the data acquisition window for providing detailed information on regional myocardial perfusion abnormality. One of the key limiting factors of quantitative myocardial perfusion CMR lies in the accuracy of the AIF for tracer kinetic modelling. Since the completion of the work reported in this thesis, we have developed an accurate method for deriving AIF in the presence of high-dose Gd-DTPA.

9.3 Future work

The contribution of this thesis to MR imaging is not limited to myocardial perfusion analysis. The PLSR predictive motion-modelling scheme can be applied to a range of cardiac imaging tasks and offers potential for use in other modalities. This, however, requires significant further development with the identification of suitable external motion measures ideally compatible with MR as well as other modalities such as PET and Ultrasound. The optimal location as well as the number of measures must also be investigated, currently free form deformation with B-splines. For use in myocardial perfusion, the method could be combined with the cardiac contractile motion tracking as described in Chapter 4 to provide real time slice tracking for free breathing myocardial perfusion imaging. This could also be applied to coronary imaging and other dynamic imaging studies of the heart such as flow measurement. The respiratory reordering has shown to be effective with the use of UNFOLD but further development of the RR-RIGR technique could potentially offer a more consistent solution to this problem increasing the efficiency of the data acquisition. Other possible *k*-space acquisition schemes could be explored with the use of respiratory reordering and the use of PLSR for more sensitive motion modelling.

For tracer kinetic modelling, further work is required to improve the technique. For this thesis, a rather simple Fermi function deconvolution was performed as it allowed a proven modelling technique to be applied in a clinical setting. In addition, the rapid progress of imaging sequences and imaging protocol applied to MR perfusion makes the more detailed modelling of the system characteristics difficult to assess with the variation in acquisition. By choosing a simple approach more consistency can be expected. For this reason the development of the model free approach would be a useful area of future work. Recent work in model independent deconvolution techniques has shown the importance of bolus transit in the ventricle and its effect on perfusion quantification. The model free method simplifies the estimation of MBF by the determination of an impulse response function [253,254]. The deconvolution of the myocardial signal is solved with a B-spline representation of the tissue impulse response, and Tikhonov-Philips regularisation. This effectively applies *a priori* continuity and smoothness constraints while limiting the degrees of freedom, although no further assumptions about the shape of the curve are made. The estimates for MBF produced by this method correlate well with results based on radioisotope labelled micro spheres. This model independent approach is advantageous for a number of reasons. The method limits the number of required prior assumptions so minimising the user interaction necessary to determine the myocardial impulse response. In addition, recent modelling of collateral circulation has identified a delay due to the time taken for blood to arrive at tissue fed by collaterals. Previous model based approaches perform poorly if this delay is incorrectly determined where model independent analysis is able to clearly represent this in changes of the impulse response shape due to its greater flexibility. Further studies in this area, combined with accurate motion management will provide further insight into the quantification process.

The main beneficiaries of a well-developed MR myocardial perfusion imaging examination are the patients and the research community. For the patients, the test will be more reliable, faster, safer and more sensitive to early coronary disease. CMR myocardial perfusion imaging achieves a high resolution that enables the definition of subendocardial perfusion defects, which occur much earlier in the course of development of CAD, and manifest in functional microvascular disorders such as Syndrome-X. The method involves no radiation burden and is ideally suited to repeated studies and research. Three-dimensional high-resolution perfusion imaging is important in the assessment of emerging gene therapies and other interventions designed to improve regional MBF. The novelty of the work reported in this thesis lies in its close integration of new CMR sequence design, information theory and post- processing. Current approaches of image registration rarely rely on modifying the imaging protocol to simplify the problem at hand. The use of predictive motion tracking, for example, allows cross-modality reconstruction of patient specific models for dense motion field prediction, which after initial modelling can be used in real-time prospective motion tracking or correction. This will facilitate combining CMR for developing new methods of cardiac PET imaging, allowing more detailed assessment of transmural MBF distributions that is free from motion averaging. This will in turn enhance the accuracy of the perfusion CMR technique by using 3D PET as a reference for developing improved tracer kinetic modelling and regional myocardial perfusion assessment. The technique is also expected to be valuable to other imaging and therapeutic modalities such as intensity modulated radiation therapy, a promising tool for dose escalation in the management of mobile thoracic and abdominal lesions, where respiration-induced organ motion may greatly degrade the effectiveness and efficiency of the treatment.

As stated in the introduction of the thesis, the work reported in this thesis is motivated by the fact that non-invasive evaluation of cardiac perfusion abnormalities before pathologic effects occur, or as follow-up to therapy, is important to the management of patients with CAD. Early reperfusion of ischaemic myocardium has been shown to have a positive reversal effect on the ischaemic myocardium, which reduces mortality and morbidity. Differentiation of ischaemic but viable myocardium from infarcted regions requires detailed global quantitative assessment and modelling of myocardial perfusion characteristics. CMR allows for the acquisition of images of the myocardium with relatively high spatial resolution, thus allowing the transmural extent of myocardial ischaemia to be determined. The work presented in this thesis combines information theory, CMR sequence design, image processing, motion modelling and simulation. It is an interdisciplinary effort made possible by the unique facilities at the Royal Society/Wolfson Foundation Medical Image Computing Laboratory at Imperial College London.

Appendix A : The NIPALS algorithm

The solution to the equations presented in Chapter 6 can be solved iteratively through the NIPALS method [214]. The MATLAB (Mathworks, Natick, MA) implementation of this algorithm is provided below. Each execution of the loop extracts a latent variable of the data. The loop terminates when the required number of latent variables are extracted or when A, M or B reduces to (or close to) zero, which implies the current number of factors suitably represents the data.

A.1 MATLAB implementation

```
function [ C ] = nipals( X, Y, c, S )
%  NIPALS: Matlab implementation of the NIPALS algorithm
%  This algorithm is used for calculating the coefficient matrix C
%  for use in the PLSR algorithm

  % X and Y have already been zero mean'd and scaled.

  % step 1, Initialise A = X'Y, M=X'X, B=I
    A = X'*Y;
    M = X'*X;
    B = eye(size(X,2));

  % step 2, for k=1 to c, begin iteration
    for k=1:c
  % step 3, Compute coefficient loading vector qk, being the first
  % eigenvector of A'A
        [ Va Ea ] = eig( A'*A );
        Q(:,k) = Va(:,size(Va,1));

  % step 4, Compute weighting (column) vector wk=BAqk, normalise wk = wk / ||wk||
        W(:,k) = B * A * Q(:,k);
        W(:,k) = W(:,k)/(sqrt(W(:,k)'*W(:,k)));

  % step 5, Compute factor loading vector (column) pk = M wk/f, where f=wk' M wk
        f = W(:,k)' * M * W(:,k);
        P(:,k) = M * W(:,k) / f;

  % step 6, Renew the coefficient loading vector qk as qk = A' wk/f
        Q(:,k) = A' * W(:,k) / f ;

  % step 7, Renewal for A and M: A=A-f pk qk', M=M-f pk pk'
        A = A - f * P(:,k) * Q(:,k)';
        M = M - f * P(:,k) * P(:,k)';

  % step 8, Renewal for B: B=B-wk pk'
        B = B - W(:,k) * P(:,k)';

  % step 9, If k>c or M vanishes, stop iteration; otherwise return to step 3.
        if sum(sum(abs(M))) < 1e-10, break, end
        if sum(sum(abs(B))) < 1e-10, break, end
    end

  % Calculate C the regression matrix in Y=XC+E
    C = W * Q';

End
```

Appendix B : PLSR with a 2D CMR myocardial perfusion sequence*

B.1 Introduction

MR myocardial perfusion imaging is a relatively new technique for distinguishing ischaemic myocardium from healthy tissue [7,73]. It offers the possibility of non-invasively determining the location and extent of ischaemia or infarction at transmural resolutions. First-pass techniques using fast gradient echo (turboFLASH) or EPI sequences are now common practice in clinical research and quantitative results have been achieved in animal studies with intravascular agents (polylysine-Gd-DTPA) as a macromolecular blood pool marker [12,75,76]. At the same time, semi-quantitative results have also been established in humans with conventional extracellular agents (Gd-DTPA). Either approach has an impact on the detailed characterisation of the relationship between functional and perfusion abnormalities.

For first-pass perfusion imaging, a complete 2D or volumetric data set has to be acquired for each cardiac cycle [13,74,78]. Cardiac and respiratory induced motion is a major problem during both imaging and subsequent perfusion analysis. With standard perfusion sequences, a typical single slice short axis image of the myocardium may take about 100 *ms* to acquire. Even with limited coverage of three to four slices of the LV, the acquisition window within each cardiac cycle can still become excessive. During this period, cardiac motion can cause the myocardium imaged through different image planes to be mis-registered, *i.e.*, some parts of the myocardium may be imaged multiple times whereas other parts may be missed out completely. This type of mis-registration is difficult to correct for by using post-processing techniques. In a previous study, we have proposed a novel 4D motion-decoupling technique based on the use of motion tagging and slice tracking [255]. This has simplified the problem to multiple 2D temporal free-form image registration tasks. In this case, the deformation within the imaging plane is normally caused by respiration during the acquisition period, typically lasting for about 50 cardiac cycles. Breath-holding has been suggested, but for most patients, particularly those with CAD, this has proven to be impractical. This renders accurate image registration of cardiac deformation a crucial step in the quantification of perfusion indices. Thus far, several image registration approaches have been proposed for in-plane motion correction [195,256]. The purpose of this paper is to introduce the concept of partial-least-squares-regression (PLSR) [218] to derive intrinsic characteristics of the deformation model both for improving the internal consistency of the registration process and for predicting myocardial deformation due to respiration.

---

* Gao JX, Ablitt NA, Elkington A, Yang GZ, Deformation Modelling Based on PLSR for Cardiac Magnetic Resonance Perfusion Imaging, MICCAI (1) 2002: 612-619.

B.2 Materials and methods

B.2.1 Myocardial motion prediction

Existing research in cardiac imaging has shown that there is significant correlation between myocardial deformation and respiratory motion patterns. In MR coronary imaging, for example, respiratory navigators have been extensively used to sample the movement of the diaphragm in order to predict the distortion of the epicardial surface, thus allowing real-time adaptive tracking of the coronary arteries to avoid the use of breath-holding for patient studies. Research has also shown that the internal correlation between respiration and cardiac deformation is subject specific, but intra-patient characteristics remain relatively consistent throughout the imaging period. Inspired by these findings, we propose to use the varying intensity distribution of the chest and diaphragm as predictors of myocardial deformation.

Historically, models for respiratory induced cardiac motion have been based on cardiac landmarks. This has the advantage of simplifying the derivation of motion models but has the major drawbacks in accuracy. Respiratory motion and its induced cardiac deformation are highly complex. In our proposed motion prediction model, principal modes of intensity variation related to the diaphragm and chest are extracted to correlate with deformation vectors of the myocardium, leading to a reliable motion prediction approach. Figure B-1 illustrates the basic concepts involved in the motion prediction model. The use of free-form image registration allows the extraction of intra-frame tissue deformation, resulting in a dense displacement vector field within the image plane. To relate motion fields reflecting respiration to those of cardiac deformation, non-linear correlation techniques need to be employed. This, however, is not trivial especially when the model parameters are unknown and patient specific. By observing the fact that there is a large amount of redundancies and internal correlations in intensity distribution of the chest wall and the motion vectors of the myocardium, PLSR can be applied.

In PLSR, PCA is first applied to extract the intrinsic patterns, *i.e.* latent factors, of the original data sets. Then the focus is put on these latent factors rather than the original data that carries redundancies. A relationship can subsequently be established between these latent factors through linear regression. In practice, this is implemented as a learning process, *i.e.*, by feeding the model with both input (intensity distributions around the chest wall and diaphragm) and observed output (motion vectors of myocardial deformation). Since intra-patient motion characteristics are relatively consistent throughout the imaging period, a short segment of the image sequence can be used for extracting the deformation model such that cardiac deformation can be automatically predicted from the intensity variations at the chest wall or the diaphragm. This removes the need of using image registration for the remaining images within the sequence. Of course, the same process can also be used for processing the entire sequence during learning so as to derive an internally consistent motion model to regulate the deformation vectors calculated from the registration algorithm.

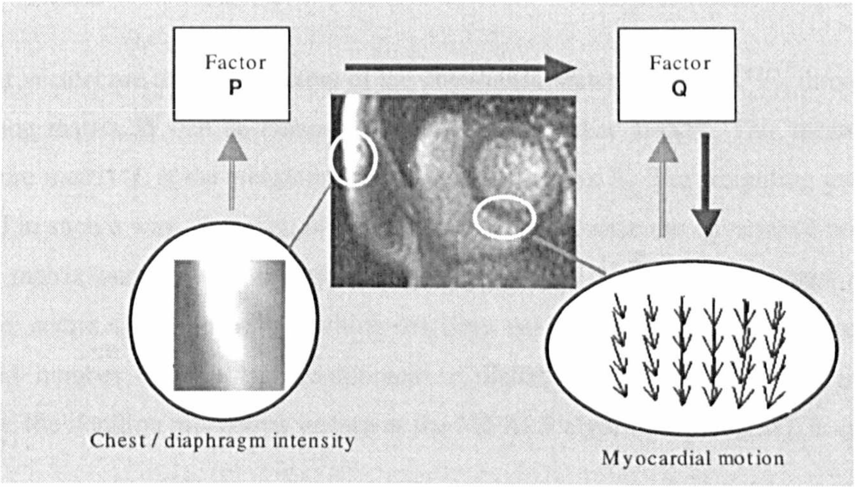

Figure B-1 A schematic illustration of using PLSR for deformation modelling. In this example, multiple measurements of the intensity distribution near the chest wall, reordered as long vectors, are used as the input, from which input latent factors are extracted. A similar process is also applied to the observed output data, in this case the deformation vectors derived from normal free-form image registration. A model that reflects the intrinsic correlation between input/output can then be derived from these factors. At the prediction stage, the path along the dark arrows is followed, *i.e.*, myocardial deformation can be directly predicted from the intensity pattern measured at the chest wall.

B.2.2 PLSR implementation

Let **X** denote the intensity pattern of the chest wall and/or the diaphragm, **Y** the free-form deformation vectors of the myocardium, each with a dimensionality of p and m. When n image frames are used for learning, their intrinsic relationship can be expressed as

$$\mathbf{Y} = \mathbf{XC} + \mathbf{E} \tag{B.1}$$

where **C** is a p by m coefficient matrix, **E** represents noise and higher order terms that are not accounted for in the above relationship, with the same rank of **Y**. In PLSR, both the input **X** and output **Y** are used for extracting the factors, also called scores, in forming the coefficient matrix **C**. The regression is implemented based on these factors rather than the original input and output matrix themselves. That is, PCA is applied to decompose **X** and **Y** as

$$\mathbf{X} = \mathbf{TP} + \mathbf{E}_1 \tag{B.2}$$

$$\mathbf{Y} = \mathbf{TQ} + \mathbf{E}_2 \tag{B.3}$$

In Equation (B.2) and (B.3), **T** is the factor score matrix of n by c, **P** the factor loading matrix of c by p, **Q** the coefficient loading matrix of c by m, here c is the number of predominant latent vectors kept in the PCA computation; and $\mathbf{E}_1$ and $\mathbf{E}_2$ represent, respectively, parts of **X** and **Y** that are unaccounted for, with the same ranks as of **X** and **Y**.

The latent vectors are the eigenvectors of the covariance matrix $(\mathbf{X'Y})'(\mathbf{X'Y})$, through which a weighting matrix **W** can be computed iteratively such that $\mathbf{T}=\mathbf{XW}$. This means that the factor score matrix **T** is the weighting result of input matrix **X**. The weighting matrix **W** is generated in such a way, that each of its columns will maximize the covariance between the response matrix and the corresponding factor scores. By applying a standard regression procedure, matrix **Q** can be derived which describes the relationship between **Y** and **T**. For a predefined number of principal components c, usually much less than the number of predictors, the iteration procedure, known as the NIPALS algorithm [257,258], is as follows:

```
1. Initialise $\mathbf{A}=X'Y$, $\mathbf{M}=X'X$, $\mathbf{B}=\mathbf{I}$;
2. For $k=1$ to $c$, begin iteration:
3. Compute coefficient loading vector $\mathbf{q}_k$, being the first eigenvector of $\mathbf{A}'\mathbf{A}$;
4. Compute weighting (column) vector $wk=\mathbf{BAq}_k$, normalize $\mathbf{w}_k=\mathbf{w}_k/\|\mathbf{w}_k\|$;
5. Compute factor loading vector (column) $\mathbf{p}_k=\mathbf{Mw}_k/f$, where $f=\mathbf{w}_k'\mathbf{Mw}_k$;
6. Renew the coefficient loading vector $\mathbf{q}_k$ as $\mathbf{q}_k=\mathbf{A}'\mathbf{w}_k/f$;
7. Renewal for A and M: $\mathbf{A}=\mathbf{A}-f\mathbf{p}_k\mathbf{q}_k'$, $\mathbf{M}=\mathbf{M}-f\mathbf{p}_k\mathbf{p}_k'$;
8. Renewal for B: $\mathbf{B}=\mathbf{B}-\mathbf{w}_k\mathbf{p}_k'$;
9. If $k>c$ or M vanishes, stop iteration; otherwise return to step 3.
```

where $\mathbf{p}_k$, $\mathbf{q}_k$,$\mathbf{w}_k$ are the vectors of the corresponding matrix **P**, **Q** and **W**. Once **P**, **Q** and **W** are computed, the regression matrix in equation (1) can be determined by $\mathbf{C}=\mathbf{WQ}$.

The above computation corresponds to a learning process. For new image frames, the myocardial motion can then be predicted according to the motion of the chest and/or diaphragm with the established regression matrix **C**. In the current study, we used 40% of the image frames located at the end of the perfusion sequence for learning. Only the first five principal components of the covariance matrix are kept in extracting the regression matrix **C**, since they cover around 90% or more of total covariance.

B.2.3 Validation and *in vivo* data acquisition

To validate the effectiveness of the proposed model extraction scheme for motion prediction, a simulated MR myocardial perfusion image sequence has been created. This data set is used to validate the registration process in a situation where the correct deformation is known. This also allows us to test the method in a variety of different conditions. The structure of the image is based on an example short axis slice of the heart. The images consist of 6 anatomical features: myocardium of the LV, myocardium of the RV, blood pool of the LV, blood pool of the RV, the diaphragm, the chest wall. Additionally to this we have two distinct defects in the myocardium of the LV these being a subendocardial defect and a transmural defect. This gives nine distinct regions that are spatially defined by a static bitmap image. The temporal intensity of these regions is defined by time series curves based on real values from example data sets. Subsequently to this the image sequence is warped so as to simulate respiratory motion. This motion vector is based on a real motion vector from the inverse of the motion vector produced from the registration of a real sequence. This dataset is used to evaluate the proposed 2D free form registration, self-adaptive learning and prediction with PLSR. After numerical verification, nine *in vivo* data sets acquired from patients with known CAD were used to further validate the proposed technique. These images were obtained using a 1.5T Siemens Sonata scanner (200 *T/m/s*; 40 *mT/m*) with a four-element phased-array receiver coil. The first-pass perfusion data was acquired with a FLASH sequence (Tr=3.7 *ms*) that consists of three saturation-recovery short-axis slices per cardiac cycle, for 50 cycles during the first-pass of Gd-DTPA (cubital vein, 0.1 *mmol/kg*, 3 *ml/s*) with a FOV of 400 *mm* (128 pixels) by 300 *mm* (64 pixels).

The accuracy of the deformation correction technique for the patient data sets was assessed by two independent observers by using an image analysis package (CMRtools, Imperial College). The scoring was done through the measurement of displacements in millimeters of predefined landmarks on the septal, anterior and posterior segments. The derived values were then averaged over the entire sequence, and between the three chosen locations.

B.3 Results

Figure B-2 illustrates the internal correlation between respiration and myocardial deformation. For simplicity, a single input trace is given and patterns of respiration at 18, 26, 31, 35, 40, and 46 cardiac cycles from the beginning of the acquisition are provided. Figure B-3 (a) demonstrates the accuracy of the free-form image registration technique and the modelling approach based on PLSR. The temporal trace of the input bolus is also provided as a reference. It is evident that the overall accuracy of the PLSR approach is significantly better than using normal registration method. The reason for the registration technique to perform poorly at the beginning the sequence is due to the application of inversion pulse where signals from the myocardium are nullified before the arrival of the contrast bolus. Figure B-3 (b) shows the corresponding assessment results for the patient data sets, illustrating the overall improvement of the motion correction results where only 40% of the image frames are used for motion prediction.

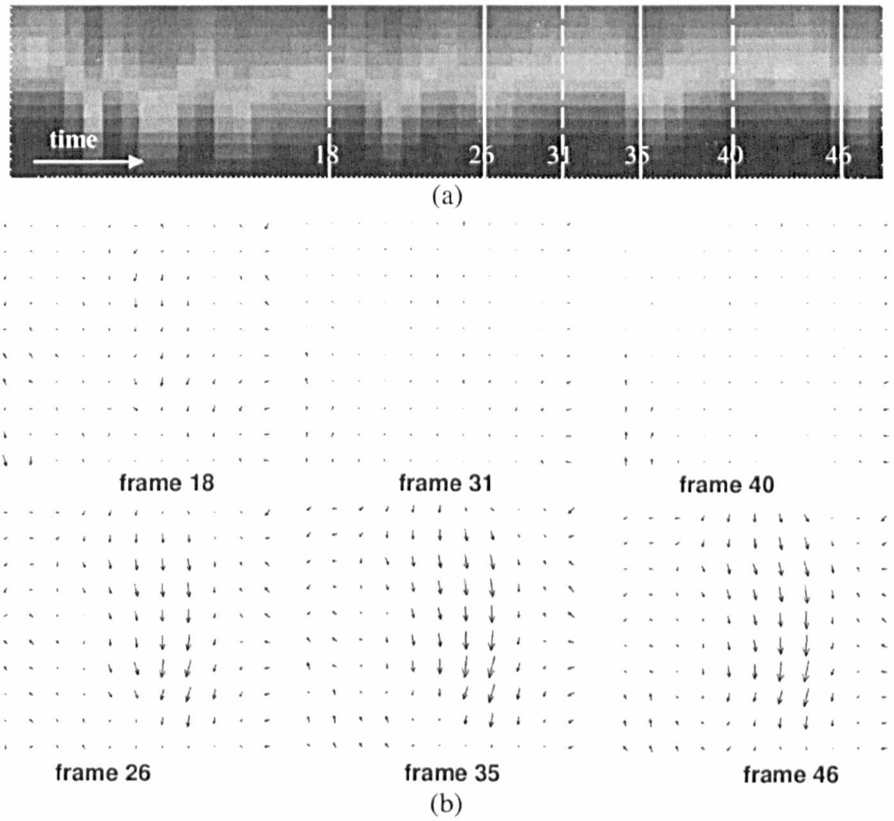

Figure B-2 A representation of the application of PLSR image registration. (a) This is a typical trace obtained from the chest wall region with displacement across the chest wall in the y-axis and time along the x-axis. Displacement fields from six frames of the sequence are shown in (b) with the similarity between the displacement and the trace evident.

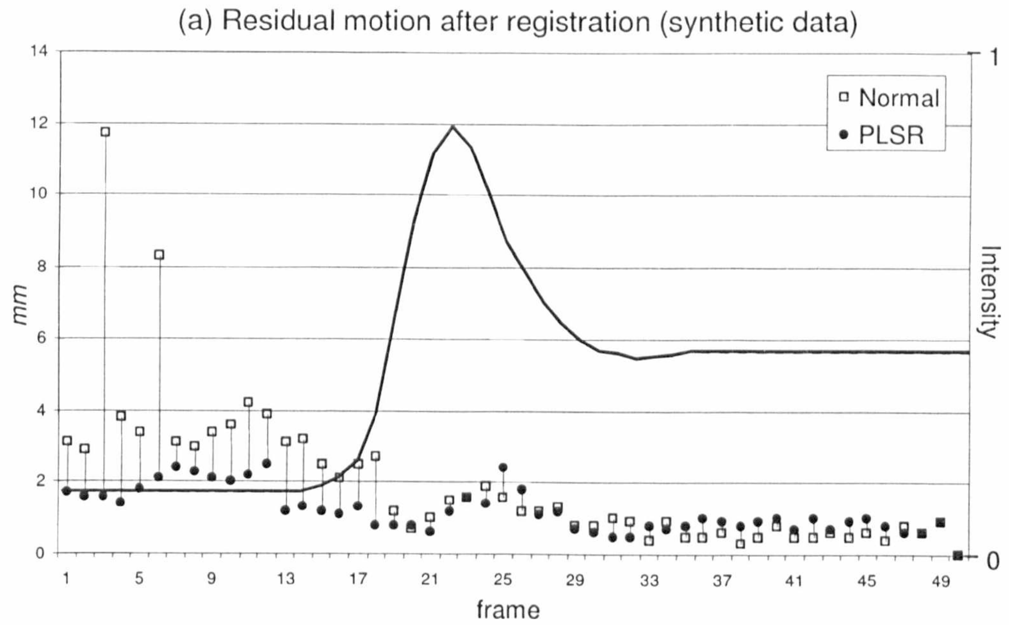
(a) Residual motion after registration (synthetic data)

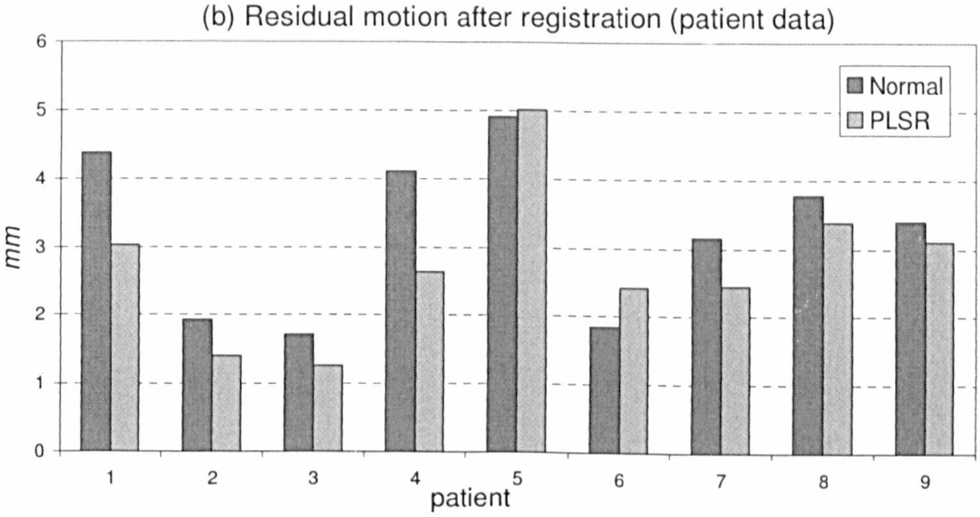
(b) Residual motion after registration (patient data)

Figure B-3 Efficiency of PLSR in image registration. The PLSR technique reduces computation by 60% as well as reducing the residual motion in the majority of cases relative to the standard method of registration on each frame. Graph (a) shows the effect over 50 frames of PLSR in comparison with a normal registration technique on synthetic data. Graph (b) shows the mean effect on 9 perfusion patients. Seven of the cases show a reduction in residual motion using the PLSR method.

B.4 Discussion and conclusions

Image registration is crucial in quantifying myocardial perfusion images. The use of conventional image registration is useful in aligning inter frame object deformations. For first-pass MR myocardial perfusion imaging, a direct application of the method can be problematic, especially before/during the arrival of the contrast bolus. During this period, the signal from the myocardium is minimum, and thus leads to large registration error. This effect has clearly been demonstrated in our simulation data as shown in Figure B-3 PLSR is a method for motion prediction where both the input and the output response data contain significant redundancies. In our study, we use the latter 40% of the total image sequence for learning, since these later images have a relatively clear structure for almost all of the anatomy. The predicted deformation distribution has shown to be reliable. This not only reduces the number of frames requiring traditional registration down to 40%, but also significantly improves the consistency of the derived deformation vectors. The study represents the first attempt of using PLSR for deformation modelling, which should have important value for other deformation prediction applications including motion adaptive radiotherapy and imaging, where the motion of the target organ can be predicted from externally measurable signals.

Appendix C : Levenberg-Marquardt minimisation

Levenberg-Marquardt minimisation is a method first derived by Levenberg [259] and then later derived in a similar manner while taking a different approach by Marquardt [260]. It is an iterative approach for solving non-linear least square problems of parameter estimation. Marquardt's method aims to tend to the Gauss method in the neighbourhood of the minimum of the ordinary least squares norm, and tend to the steepest descent method in the neighbourhood of the initial guess used for the iterative procedure.

The method uses the available information about the distance to the optimal result in the direction determined by conventional gradient descent. While this is not precise, there is some useful information that may be obtained. This distance information is then used in determining the method of minimisation. The Levenberg-Marquardt method smoothly transfers between the gradient descent method and the Gauss as the estimated distance to the optimal result is reduced.

Levenberg-Marquardt is a popular alternative to the Gauss-Newton method of finding the minimum of a function $\mathbf{F}(x_k)$ that is a sum of squares of nonlinear functions,

$$f(x)=\frac{1}{2}\sum_{i=1}^{m}\mathbf{F}_i(x)^2 \tag{C.1}$$

Denoting the m-by-n Jacobian matrix of $\mathbf{F}(x_k)$ as $\mathbf{J}(x_k)$, the Levenberg-Marquardt method uses a search direction that is a solution of the linear set of equations

$$\left(\mathbf{J}(x_k)^T\mathbf{J}(x_k)+\lambda_k\mathbf{I}\right)d_k=-\mathbf{J}(x_k)\mathbf{F}(x_k) \tag{C.2}$$

where the scalar λ_k controls both the magnitude and direction of d_k. When λ_k is zero, the direction d_k is identical to that of the Gauss-Newton method. As λ_k tends to infinity, d_k tends toward a vector of zeros and a steepest descent direction. This implies that for some sufficiently large λ_k, the term $\mathbf{F}(x_k+d_k)<\mathbf{F}(x_k)$ holds true. The term λ_k can therefore be controlled to ensure descent even when second order terms, which restrict the efficiency of the Gauss-Newton method, are encountered. The Levenberg-Marquardt method therefore uses a search direction that is a cross between the Gauss-Newton direction and the steepest descent.

Appendix D : Journal Publications

D.1 Predictive cardiac motion modeling and correction with partial least squares regression

Ablitt NA, Gao JX, Keegan J, Stegger L, Firmin DN, Yang GZ, Predictive cardiac motion modeling and correction with partial least squares regression. IEEE Trans Med Imaging. 2004 Oct;23(10):1315-24.

10 pages

Predictive Cardiac Motion Modeling and Correction With Partial Least Squares Regression

Nicholas A. Ablitt, Jianxin Gao, Jennifer Keegan, Lars Stegger, David N. Firmin, and Guang-Zhong Yang*

Abstract—**Respiratory-induced cardiac deformation is a major problem for high-resolution cardiac imaging. This paper presents a new technique for predictive cardiac motion modeling and correction, which uses partial least squares regression to extract intrinsic relationships between three-dimensional (3-D) cardiac deformation due to respiration and multiple one-dimensional real-time measurable surface intensity traces at chest or abdomen. Despite the fact that these surface intensity traces can be strongly coupled with each other but poorly correlated with respiratory-induced cardiac deformation, we demonstrate how they can be used to accurately predict cardiac motion through the extraction of latent variables of both the input and output of the model. The proposed method allows cross-modality reconstruction of patient specific models for dense motion field prediction, which after initial modeling can be used for real-time prospective motion tracking or correction. Detailed numerical issues related to the technique are discussed and the effectiveness of the motion and deformation modeling is validated with 3-D magnetic resonance data sets acquired from ten asymptomatic subjects covering the entire respiratory range.**

Index Terms—**Cardiac imaging, image registration, partial least squares, PLSR, predictive motion modeling, respiratory motion correction.**

I. INTRODUCTION

THE management of inconsistent physiological motion is one of the major considerations of high-resolution cardiac imaging. For different imaging modalities, the effects of patient motion and its associated artifacts are well recognized. In general, patient motion can be grouped into voluntary and involuntary motions. Voluntary motion includes unpredictable movements of the patient during data acquisition, which can be avoided with patient cooperation, improved couch design, or certain levels of straining. Involuntary motion, on the other hand, involves movements of the organs such as those due to cardiac and respiratory motion. It also includes motion that is induced by physiological loadings such as stress or exercise. In practice, if the involuntary motion is cyclic, imaging motion artifact can be eliminated through the use of effective gating. Acyclic motion, however, remains a major challenge to current imaging techniques. In single photon emission computed tomography (SPECT), for example, the effect of upward creep after exercise can lead to artifact manifesting as reversible defects in the infero-septal wall [1]. For intensity modulated radiation therapy (IMRT), respiration-induced organ motion may greatly degrade the effectiveness and efficiency of the treatment [2]–[4]. Respiratory-induced cardiac deformation is also one of the main limiting factors for positron emission tomography (PET) and three-dimensional (3-D) echo-cardiography [5]–[7].

In cardiovascular magnetic resonance (MR), the management of acyclic motion due to respiration is driven by the ongoing demand for the assessment of cardiovascular anatomy and function with higher image resolution, particularly for examining vessel walls and coronary arteries [8], [9]. While the effects of cardiac motion may be dealt with by acquiring data at mid-diastole when the heart is relatively stationary, respiratory motion is more difficult to control. Although the use of breath-holding effectively freezes respiration, the need to limit the duration of data acquisition to that of a comfortable breath-holding period imposes significant limitations on the image quality [10]. The alternative technique of respiratory gating [11]–[13] requires the monitoring of respiratory patterns. This removes the need for patient cooperation but since imaging is now only performed during a small part of the respiratory cycle, the scan efficiency is considerably reduced. The strength and flexibility of cardiovascular MR in providing *in situ* respiratory motion measurements has permitted the development of a number of more advanced techniques for adapting k-space data acquisition with different levels of respiratory-induced motion [14]–[16].

A further drive in cardiovascular MR toward enhanced spatial resolution and scan efficiency with improved motion adaptation is the recent development in prospective motion tracking [17]. In its simplest form, real-time slice-following is used to shift the imaging slice for each data segment according to the respiratory position, as determined by the preceding navigator echoes [18]–[20]. The accuracy of this technique is critically dependent on the accuracy of the navigator echo to predict the cardiac motion. Locally focused imaging techniques have been proposed that use elaborated radio-frequency (RF) pulses to excite only the 3-D volume of interest to avoid pseudomotion aliasing [19]–[21]. With this scheme, it has been demonstrated that it is possible to achieve an overall scan efficiency of 90%

Manuscript received March 1, 2004; revised July 7, 2004. This work was supported in part by the Engineering and Physical Sciences Research Council and the Royal Society and the Wolfson Foundation. The Associate Editor responsible for coordinating the review of this paper and recommending its publication was W. J. Niessen. *Asterisk indicates corresponding author.*

N. A. Ablitt and J. Gao are with the Royal Society/Wolfson Foundation Medical Image Computing Laboratory, Department of Computing, Imperial College London, London SW7 2BZ, U.K.

J. Keegan and D. N. Firmin are with the Cardiovascular Magnetic Resonance Unit, Royal Brompton and Harefield NHS Trust, London SW3 6NP, U.K.

L. Stegger was with the Cardiovascular Magnetic Resonance Unit, Royal Brompton and Harefield NHS Trust, London SW3 6NP, U.K. He is now with the Department of Nuclear Medicine, University of Münster, 48129Münster, Germany.

*G.-Z. Yang is with the Royal Society/Wolfson Foundation Medical Image Computing Laboratory, Department of Computing, Imperial College London, South Kensington Campus, London SW7 2BZ, U.K. (e-mail: g.z.yang@imperial.ac.uk).

Digital Object Identifier 10.1109/TMI.2004.834622

0278-0062/04$20.00 © 2004 IEEE

without sacrificing the image quality, compared to the 60% that is achievable using the conventional approaches [20].

Although imaging with real-time tracking and adaptation has shown great promise in a number of clinical applications, existing research has shown that reliable motion prediction is a significant challenge. The implementation of adaptive tracking over a large range of motion requires an accurate understanding of the intrinsic relationship between the motion of the target anatomical structure and respiration. In coronary imaging, it has been shown that due to a failure of the linear model, or to the use of inaccurate correction factors relating the motion of the artery to that of the diaphragm, many of the existing techniques for adaptive tracking only permit modest increases in the acceptable respiratory range.

The improvement of MR hardware has allowed rapid imaging of the entire cardiac structure with much reduced imaging time. This permits a more detailed assessment of the effect of cardiac motion and deformation in response to respiratory motion. Recent study has confirmed the significance of intersubject variability and the need for *in situ* subject specific motion modeling [22], [23]. A prospective translational motion correction method based on image registration of 3-D respiratory motion data has been used to derive more accurate and subject specific motion tracking for coronary imaging [22].

The use of diaphragmatic navigators is now a popular choice for coronary imaging and the adaptation of coordinated multiple navigator traces is an ongoing research topic [24], [25]. The quest for higher image resolution as required for vessel wall imaging has called for more sensitive real-time motion measurement techniques to be explored. In cardiovascular MR, researchers are investigating the use of complementary MR-compatible sensing methods to perform real-time measurements of surface distortions due to respiration. The strength of these techniques is that they do not require the interleaved acquisition of navigators, and thus significantly simplify the pulse sequence design. Furthermore, it makes the technique easily transportable to other imaging modalities. The problem with these methods, however, is that surface measured signals are strongly coupled with each other but poorly correlated with respiratory-induced cardiac deformation. Numerically, this can create significant problems for recovering the inherent model that explains the causality between respiratory motion and surface deformations. The purpose of this paper is to present a new technique of predictive cardiac motion modeling and correction based on partial least squares regression (PLSR).

PLSR is a recent technique that generalizes and combines features from principal component analysis and multiple regression. It originated in social sciences and became popular in chemometrics, i.e., computational chemistry [26]. Its ability to extract correlation between input and output data that is itself highly collinear, allows it to deal with problems that would be inappropriate for multilinear or principal components regression. In imaging, it has also been used for analyzing spatial patterns of functional brain images [27].

The predictive motion modeling method described in this paper is designed for extracting intrinsic relationships between 3-D cardiac deformation due to respiration and multiple 1-D real-time measurable surface intensity traces. By using reconstructed 3-D image data sets, detailed numerical issues related to the technique are discussed and the effectiveness of the method is validated with data acquired from ten asymptomatic subjects using motion modeling covering the entire respiratory range.

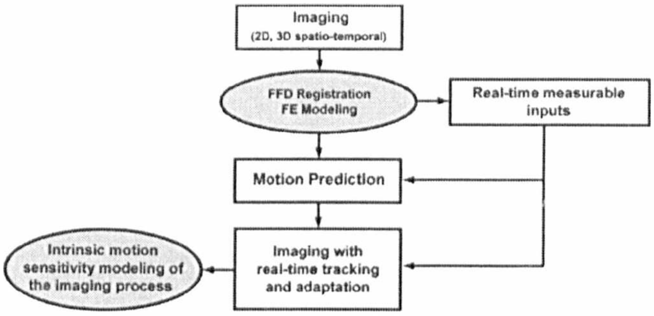
Imaging
(2D, 3D spatio-temporal)
FFD Registration
FE Modeling
Real-time measurable inputs
Motion Prediction
Intrinsic motion sensitivity modeling of the imaging process
Imaging with real-time tracking and adaptation

Fig. 1. Diagrammatic representation of the proposed predictive motion modeling scheme. Initial 2-D/3-D imaging is used along with real-time measurable inputs to create a motion model that can be used as the input to the imaging system for achieving real-time motion adaptation.

II. MATERIALS AND METHODS

The basic principle of the proposed method is shown in Fig. 1, which outlines the key steps involved. The initial subject specific modeling of cardiac deformation involves 2-D/3-D imaging of the anatomical structure combined with *in situ* real-time measurable inputs. Registration based on free-form deformation (FFD) or finite-element modeling (FEM) can be used to recover the underlying spatio-temporal deformation of the anatomical structure. The causality between tissue deformation and real-time measurable signals, such as surface deformations, is then extracted through the use of PLSR. At the prediction stage, real-time measurable inputs are used to predict cardiac deformations without the need for further 2-D/3-D imaging so that adaptive imaging can be performed in real-time to track the anatomical regions of interest.

A. Deformation Recovery With 3-D Free-Form Image Registration

To recover cardiac deformation and establish its intrinsic correlation with real-time measurable surface signals, 3-D image volumes depicting different stages of the cardiac deformation due to respiration are used. The extraction of 3-D deformation vectors was performed by using the free-form image registration method proposed in [28]. With this technique, a hierarchical transformation model of soft tissue deformation is employed, in which the global motion of the heart is modeled by an affine transformation whereas local deformation is described by free-form deformation based on B-splines. The normalized mutual information is used as a voxel-based similarity measure and registration was achieved by minimizing a cost function that encapsulates contributions associated with both the smoothness of the transformation and the overall image similarity. To ensure a good optimization performance, the algorithm worked by decoupling global and local motion such that only the affine transformation parameters are optimized initially. This was then followed by optimizing the nonaffine transformation parameters at increasing levels of resolution of the control point mesh. For this study, no manual delineation of the cardiac border was performed on the 3-D volume. To reduce the image registration time, however, we have manually trimmed the 3-D volume to a volume containing the heart at the full range of respiratory positions. The final number of control points used was $9 \times 9 \times 9$ for covering the image volume, which gives the total degrees-of-freedom of 2187. With this registration approach, the deformation of each volume in relation to a selected reference volume was characterized by the movement of control vertices of the B-splines; the associated 729 3-D vectors were used with the PLSR algorithm to determine their intrinsic relationship with real-time measurable signals associated with different levels of respiratory motion.

B. Predictive Motion Modeling and PLSR

The traditional approach of using navigator echoes only involves a single navigator trace, and the prediction of cardiac deformation in this case can be achieved via simple correlation. If multiple traces are used and by assuming that the respiratory motion components detected are linearly independent, multivariate regression may be used. When multiple surface measurements are used, however, one can no longer guarantee that these measurements are mutually independent. If we assume $\mathbf{X}$ to be the surface measurements at a given instant of the respiratory cycle (predictor) and $\mathbf{Y}$ to be the respiratory-induced cardiac motion (response), there will be a significant amount of redundancies in both $\mathbf{X}$ and $\mathbf{Y}$. This is because the FFD model used for deformation recovery involves uniformly sampled control vertices and some of the vertices may be strongly correlated depending on the cardiac structure being covered. Conversely, the placement of surface measurements for real-time monitoring of respiratory motion is difficult to control and redundancies are inevitable.

The goal of PLSR is to predict $\mathbf{Y}$ from $\mathbf{X}$ and to describe their common structure. When $\mathbf{X}$ is full rank, this can be accomplished by using ordinary multilinear regression (MLR). In practice, $\mathbf{X}$ is likely to be singular due to multicollinearity of the predictors and the regression approach is no longer feasible. To avoid this problem, one can either use stepwise methods to eliminate some predictors or apply principal component analysis to the $\mathbf{X}$ matrix to extract the principal components of $\mathbf{X}$ as regressors on $\mathbf{Y}$. Although the orthogonality of the principal components eliminates the multicollinearity problem, the issue of choosing an optimum subset of predictors remains. By contrast, PLSR regression finds components from $\mathbf{X}$ that are also relevant for $\mathbf{Y}$. Specifically, PLSR searches for a set of components called latent vectors that perform a simultaneous decomposition of $\mathbf{X}$ and $\mathbf{Y}$ with the constraint that these components explain as much as possible of the covariance between $\mathbf{X}$ and $\mathbf{Y}$ [29]. Fig. 2 illustrates a sample data set similar in spirit to the one used in [30], where 22 sample readings corresponding to input $\mathbf{X}$ with dimensions x_1 and x_2 are used. The use of principal components regression (PCR) would reveal the principal source of variation in $\mathbf{X}$ being contributed by those samples marked with solid color. A close examination of these samples has shown that although they contribute to over 99% of the variation in $\mathbf{X}$, the response of these samples are constant, and the variation in $\mathbf{X}$ is therefore not useful for predicting $\mathbf{Y}$. By contrast, the somewhat smaller variation in samples marked with open circles has a more direct relationship with variation in $\mathbf{Y}$, despite the fact that they only explain 1% of the variation in $\mathbf{X}$. In practice, it is possible that significant information for describing the variation in $\mathbf{Y}$ may be hidden in $\mathbf{X}$ to the extent that PCR may exclude this information as noise. In PLSR, we seek the direction in the space of $\mathbf{X}$, which yields the biggest covariance between $\mathbf{X}$ and $\mathbf{Y}$. The method examines both the $\mathbf{X}$ and $\mathbf{Y}$ data and extracts the factors that are significant to both of them. The factors extracted are in order of significance, by evaluating $\mathbf{X}^{\mathrm{T}}\mathbf{Y}$, the primary factor with which $\mathbf{X}$ determines the variation in $\mathbf{Y}$ in Fig. 2 corresponds to the open circles.

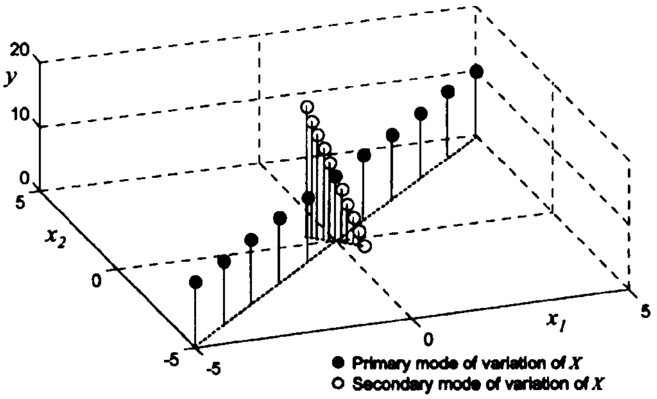

Fig. 2. Example data set illustrating the basic concept of PLSR. The input data has two variables x_1 and x_2, and these are plotted against the output variable y. The solid circles show the primary mode of variation in $\mathbf{X}$ while the open circles show the secondary mode of variation. After applying PCA on $\mathbf{X}$, it is found that the solid circles represent around 99% of the variation. The graph shows that although the solid circles represent the majority of the variation within $\mathbf{X}$, they do not help to describe the variation in $\mathbf{Y}$. In fact, the variation present in the open circles, while only representing 1% of the variation in $\mathbf{X}$, is the only useful information in describing the variation in $\mathbf{Y}$.

Let's assume that the dimension used to describe the distribution of myocardial deformation is q and the dimension used to describe each surface measurement for the respiratory motion is p. When a total number of m experiments are performed to extract the relationship between $\mathbf{X}$ and $\mathbf{Y}$, the size of the matrices will be $m \times p$ and $m \times q$ for $\mathbf{X}$ and $\mathbf{Y}$, respectively. With PLSR, both the predictor and response matrices are decomposed, such that

$$\mathbf{X}_c = \mathbf{T}\mathbf{P}^{\mathrm{T}} + \mathbf{E} \tag{1}$$

$$\mathbf{Y}_c = \mathbf{U}\mathbf{Q}^{\mathrm{T}} + \mathbf{F} \tag{2}$$

where $\mathbf{P}$ is the factor loading matrix, $\mathbf{Q}$ is the coefficient loading matrix, and $\mathbf{E}$ and $\mathbf{F}$ are factors in $\mathbf{X}$ and $\mathbf{Y}$ that are not described by the PLSR model. In the above equations, $\mathbf{X}_c$ and $\mathbf{Y}_c$ represent the mean centered matrices of $\mathbf{X}$ and $\mathbf{Y}$, respectively. PLSR tries to find a score vector $\boldsymbol{t}$ in the column space of $\mathbf{X}_c$ and a score vector $\boldsymbol{u}$ in the column space of $\mathbf{Y}_c$ such that

$$\mathbf{t} = \mathbf{X}_c\mathbf{w} \tag{3}$$

$$\mathbf{u} = \mathbf{Y}_c\mathbf{q} \tag{4}$$

to give the maximal squared covariance for $(\mathbf{u}^{\mathrm{T}}\mathbf{t})^2$. That is, the process aims to maximize $(\mathbf{q}^{\mathrm{T}}\mathbf{Y}_c^{\mathrm{T}}\mathbf{X}_c\mathbf{w})^2$ subject to $|\mathbf{w}| =$

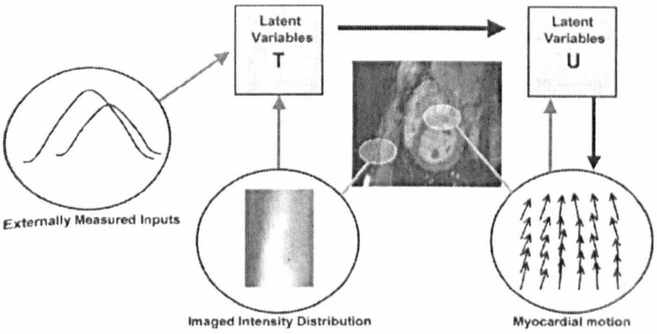

Fig. 3. Schematic diagram of the PLSR method used for deformation modeling and prediction. In this example, multiple measurements of surface intensity distributions are used as the input, from which latent variable factors are extracted. A similar process is also applied to the observed output data, in this case the deformation vectors of the heart derived from the control vertices of the free-form image registration algorithm. A model that establishes the intrinsic correlation between T and U is then derived. At the prediction stage, 3-D myocardial deformation is directly predicted from the intensity patterns measured at the chest wall, which can be performed in real-time.

$|\mathbf{q}| = 1$. The solution to this equation is given by an eigenvalue problem of $\mathbf{X}_c^T\mathbf{Y}_c$, i.e.,

$$\mathbf{X}_c^T\mathbf{Y}_c\mathbf{Y}_c^T\mathbf{X}_c\mathbf{w} = \lambda\mathbf{w} \tag{5}$$

where λ is the eigenvalue associated with $\mathbf{w}$. In essence, the method searches for a set of latent vectors that performs a simultaneous decomposition of $\mathbf{X}$ and $\mathbf{Y}$ with the constraint that these components explain as much as possible of the covariance between $\mathbf{X}$ and $\mathbf{Y}$. Rather than linking measurements $\mathbf{X}$ and $\mathbf{Y}$ directly, the method tries to establish the inner relationships between latent variables $\mathbf{T}$ and $\mathbf{U}$, derived from $\mathbf{X}$ and $\mathbf{Y}$, respectively, i.e.,

$$\mathbf{U} = \mathbf{TB} + \mathbf{U_E} \tag{6}$$

where $\mathbf{B}$ is a diagonal matrix that has the regression weights as the diagonal elements, and $\mathbf{U_E}$ is an error term similar to $\mathbf{E}$ and $\mathbf{F}$ above. When these error terms are ignored, we can obtain the predicted value of $\mathbf{Y}_c$ as

$$\mathbf{Y}_c = \mathbf{TBQ^T}. \tag{7}$$

Fig. 3 gives a schematic diagram showing how the PLSR framework is applied to the current framework for predicting myocardial deformation. The method allows for a large number of predictor variables to be used even when the principal modes of variation of the response variables are limited. It is particularly useful when the data involved is highly collinear as it accounts for redundancies in both the predictor and responses. Numerically, the solution to the equations presented above can be solved iteratively through the nonlinear iterative partial least squares (NIPALS) method [26]. The pseudocode in Fig. 4 represents the key computational steps of the NIPALS algorithm. Each execution of the loop extracts a latent variable of the data. The loop terminates when the required number of latent variables are extracted or when A, M, or B reduces to (or close to) zero, which implies the current number of factors suitably represents the data.

```
Zero-mean and scale the input X and the output Y.
Set starting matrix M=X^TX, A=X^TY and B=I.
For the required number of principal components
    Calculate the first eigenvector of A^TA, save as the first coefficient loading vector $q_1$, in row form
    Calculate the corresponding weighting vector $w_1$=B A $q_1$ in column form normalized as $w_k=w_k/||w_k||$;
    Calculate the first factor loading vector $p_1$=M$w_1$/f in column form, where f=$w_1^T$M$w_1$, and then update the coefficient loading vector $q_1$ as $q_1$=A^T$w_1$/f
    Exclude the extracted information from initial variance matrix M, co-variance matrix A and unit matrix B: A=A-f$p_1q_1$, M=M-f$p_1p_1^T$, B=B-$w_1p_1^T$;
    If either A, M or B vanishes to zero then break from loop
End loop
```

Fig. 4. Pseudocode representation of the NIPALS algorithm.

C. Image Acquisition

To extract subject specific respiratory-induced cardiac deformation patterns, ten normal subjects were recruited and underwent MR imaging on a Siemens Sonata MR scanner. The system has a field strength of 1.5 T, a peak gradient strength of 40 mT/m, and a slew rate of 200 mT/m/ms. All images were acquired in the supine position. The duration of each examination was about 20 to 25 min, depending on the heart rate. After scout scans, a segmented 3-D TrueFISP sequence was used to acquire short-axis image volumes in free breathing with navigator-echoes and data oversampling [31]. The imaging parameters used include an RF flip angle of 65°, in plane matrix size of 256 × 102, pixel size of 1.56 mm × 2.70 mm × 8.78 mm, and FOV of 400 mm × 275 mm × 123 mm. The 3-D stack comprised 14 short axis slices from the valve plane to the apex throughout the full respiratory range, covered by two k-space segments with 51 views per segment. This gave a total of 28 segments per 3-D slab. Data acquisition was repeated 20 times for a total acquisition duration of 560 cardiac cycles. The image acquisition and reconstruction procedure used are schematically illustrated in Fig. 5. A navigator echo, located perpendicular to the center of the right hemidiaphragm, preceded each segment. Data were acquired with four receiver coils. All raw data, including navigators, were stored and processed off-line. 3-D data sets were generated at different respiratory positions by means of retrospective respiratory gating using purpose-built programs written in C++ and MATLAB (Mathworks, Natick, MA). For each acquired segment, the diaphragm position was determined from the preceding navigator echo. A one-dimensional (1-D) Fourier transform of the navigator echo was smoothed by using an averaging filter (kernel size of 5), and a step function was iteratively fitted to the filtered data in the region of the liver–diaphragm–lung junction. The location of the step after the fitting procedure indicates the diaphragm position. In order to reconstruct a 3-D data set for a given respiratory position, each segment contributing to the data set was chosen from the oversampled data when the accompanying navigator echo yielded a diaphragm position nearest to the given respiratory level. The remaining oversampled data was discarded. Images were then created from the raw data by using the 3-D fast Fourier transform. Contributions from all coils were combined with an equal weight. Image sets were

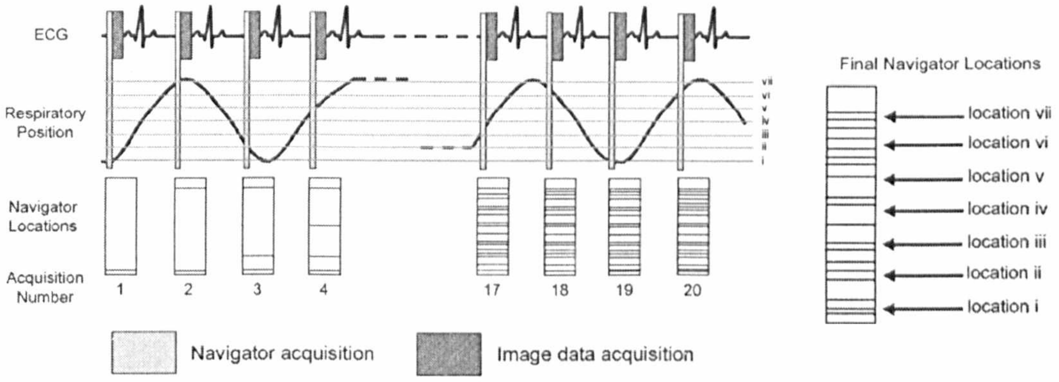

Fig. 5. Schematic diagram showing the image acquisition and reconstruction procedure for the 3-D imaging method with retrospective respiratory gating used in this study. ECG gating was used to acquire data at the same phase (early diastole) of the cardiac cycle. Prior to image data acquisition, a navigator echo was used to locate the position of the dome of the diaphragm. The figure shows the oversampling of one data segment 20 times and the corresponding navigator locations. The full 3-D acquisition requires a total of 28 data segments (14 slices × 2 segments per slice). Oversampling the data by a factor of 20 ensured that 3-D data sets could be reconstructed at a number of positions through the respiratory cycle.

created for between six and seven different respiratory positions covering from end-inspiration to end-expiration.

D. Validation

In order to validate the proposed motion prediction scheme, multiple 1-D intensity traces through the chest wall were used as the input signal to the PLSR model. Points lying on the chest wall were selected in a grid with around 25-mm spacing from the stack of 14 short axis slices. The traces were measured directly from the imaging volume in parallel to the local intensity gradient. A total of 20 measurements were made for each subject, and these intensity values were concatenated as a row vector for matrix $\mathbf{X}$ of the PLSR model. In this study, between five and seven image volumes were reconstructed for each subject to cover the entire range of respiration, which determines the number of rows used for matrices $\mathbf{X}$ and $\mathbf{Y}$ for motion prediction. The associated cardiac motion due to respiration was represented by the movements of the control vertices of the FFD model by the use of the 3-D registration scheme described in Section II-A, for which the 3-D volume corresponding to end-expiration was used as the reference. Since the control grid used was refined to $9 \times 9 \times 9$, by concatenating all their deformation values together the number of columns of $\mathbf{Y}$ was therefore 729. In this study, we performed motion prediction separately for each of the three (dx, dy, dz) deformation components.

For each subject, the accuracy of the proposed motion prediction method was assessed. The basic form of cross-validation is to divide the acquired input–output data into two parts, one for training and the other for prediction. To avoid any bias in partitioning the data, multiple permutations of this division can be performed and averaged. In this paper, leave-one-out cross-validation was used. The idea is to predict the output for each data set with learning based on both the input and output of all other data sets. The learning stage of the PLSR method was performed using all but one of the acquired respiratory positions for each result. From this learning phase, the multiple navigator trace vector for the missing volume was used to predict the motion vectors for the missing image volume. This was carried out for all available volumes of each subject. In this way, we are able to assess the ability of the method to predict the correct motion characteristics for a respiratory position not involved in the learning phase. For quantitative assessment, the predicted motion vectors were used to warp the 3-D volume so that normalized mean absolute difference could be calculated between the target and reference volumes. A small value represents a good motion prediction result.

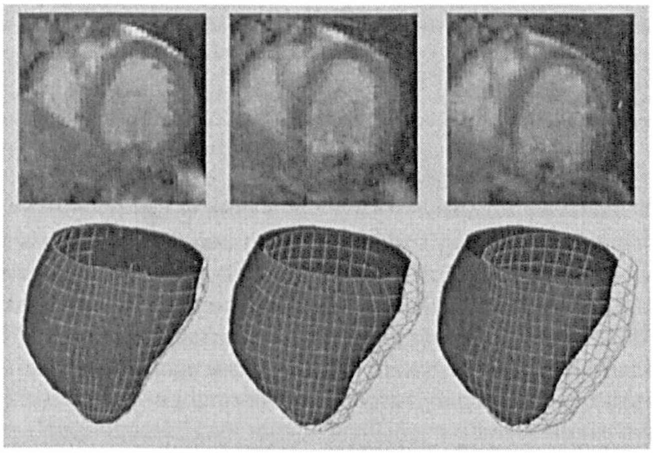

Fig. 6. Visual representation of the motion of the heart due to respiration. The solid surface of each 3-D reconstruction represents the endocardial surface at end-expiration and the meshed surface delineates the endocardial border due to respiration corresponding to diaphragm displacements of 5, 15, and 25 mm, respectively. The corresponding midventricular short axis slice of each 3-D volume is shown on the top row of the figure.

III. RESULTS

Fig. 6 illustrates the amount of cardiac deformation that can be induced at different stages of the respiratory cycle. The solid shaded surfaces represent the reference endocardial border delineated from the 3-D imaging volume corresponding to end-expiration. The meshed surfaces illustrate the deformation of the endocardial border due to respiration corresponding to diaphragm displacement values of 5, 15, and 25 mm, respectively. The corresponding midventricular slices from which these meshed surfaces have been extracted are shown on the top row of Fig. 6. The amount of cardiac motion is evident,

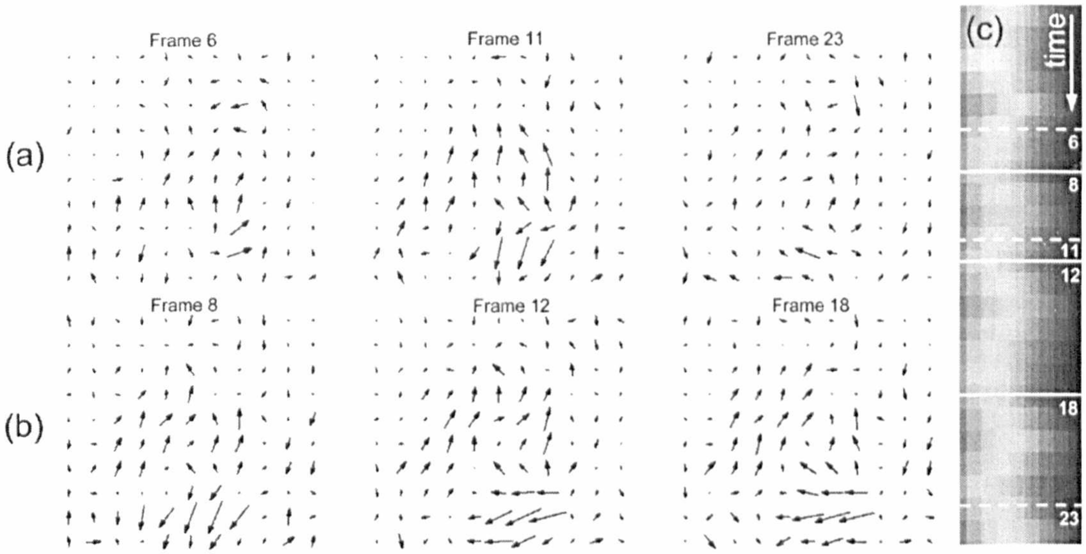

Fig. 7. Two-dimensional deformation vectors of a midventricular slice at the same phase of different cardiac cycles with varying levels of respiratory motion, and an associated intensity trace measured at the surface of the chest. (a) The deformation vectors corresponding to cardiac cycles 6, 11, and 23, as marked by the dashed lines on (c), and (b) the deformation vectors corresponding to cardiac cycles 8, 12, and 18, as marked by the solid lines on (c). These images highlight the potential inconsistencies of using single movement traces of the chest wall to predict respiratory-induced cardiac deformation as in (a) the associated cardiac deformation is different despite the fact that the intensity patterns measured at the chest wall are identical. For (b), however, there is a much closer correlation between the deformation vectors and surface traces.

TABLE I

MAXIMUM AND MINIMUM RELATIVE SUBTRACTION ERRORS NORMALIZED AGAINST THE REGISTRATION RESULT FOR MLR AND PLSR WITH AN INCREASING NUMBER OF INPUT VARIABLES

Input Variables	32 1 trace	64 2 traces	96 3 traces	128 4 traces
MLR max	5.265	5.080	5.956	5.964
MLR min	1.380	1.889	2.247	3.943
PLSR max	1.176	1.121	1.086	1.079
PLSR min	1.053	1.052	1.054	1.051

which includes bulk motion, twisting, and deformation. For this subject, the maximum cardiac displacement induced was about 15 mm.

Fig. 7 highlights the potential inconsistencies of using single movement traces of the chest wall to predict respiratory-induced cardiac deformation. Image (c) shows a sampled chest intensity trace over a number of cardiac cycles. Row (a) shows the deformation vectors of the midventricular slice corresponding to cardiac cycles 6, 11, and 23, as marked by the dashed lines in Fig. 7(c). It is evident that similar intensity patterns measured at the chest wall can result in contrastingly different deformation fields. These results confirm the uncertainties of using limited measurements of the chest wall to predict respiratory-induced cardiac deformation, as found in previous studies. For this reason, a combination of surface traces were used from a spread of locations. The use of PLSR allows the variation (or factors) from the multiple traces that are significant in determining the output to be extracted during the learning stage so that the prediction can be performed with a high level of confidence.

To assess the relative merit of the proposed PLSR method, detailed comparisons were made when different input traces are used for PLSR and MLR. The results presented in Table I are normalized with the residual errors achieved by 3-D free-form registration that is used as the gold standard for this study. A value of 1, therefore, indicates the best possible motion prediction result. It is evident that with the PLSR approach, the min/max error range is consistently small and it improves with the increasing number of traces used. For MLR, however, the error range is large and due to the collinearity of the data when a large number of input variables are used, the result deteriorates.

The proposed PLSR motion prediction technique was to rely on a large number of chest wall traces to extract their intrinsic correlation to cardiac deformations. As the inherent correlation could be significant, latent variables among these traces were extracted. For the corresponding deformation vectors of the cardiac structure, the movement of the deformation vectors of the control vertices of the FFD model were used. The same process of latent variable extraction was also applied to these deformation vectors. To illustrate the internal redundancies of the 3-D deformation vectors, Fig. 8 demonstrates the deformation patterns of layer 3, 5, and 7 of the final $9 \times 9 \times 9$ grid of a subject studied. For each image, the vectors were calculated from the PLSR coefficient matrix by keeping the first three principal components. Each row of this image represents the in-plane deformation captured by the first, second, or third principal component, respectively, where the motion vectors were amplified by $10\times$ for the second and third rows of each image as the corresponding vectors were much smaller compared to those captured by the first principal component. For each layer, the columns show the mean ± standard deviation of the in-plane deformation. The first principal component is shown to carry most of the variation demonstrating that while a large number of input factors are acquired, the majority of this information is redundant with the third mode of variation having little effect on the final result.

With the establishment of the PLSR model, it is now possible to accurately predict respiratory-induced cardiac motion

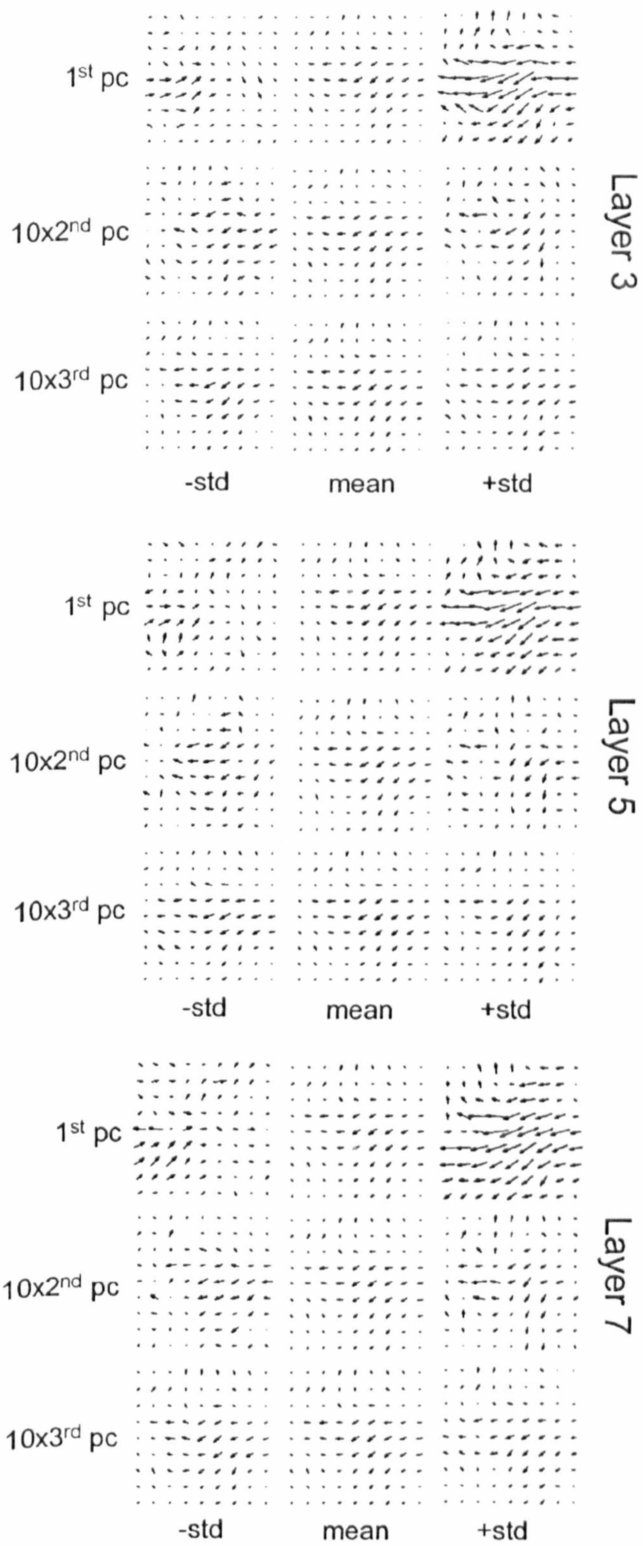

Fig. 8. Deformation patterns of layer 3, 5, and 7 of the final 9 × 9 × 9 grid of a subject studied. For each image, the vectors were calculated from the PLSR coefficient matrix by keeping the first three principal components. Each row of this image represents the in-plane deformation captured by the first, second, or third principal component, where the motion vectors were amplified by 10 × for the second and third rows of each image as the corresponding vectors were much smaller than those captured by the first principal component. For each layer, the columns show the mean ± standard deviation of the in-plane deformation.

from multiple chest wall movement traces. Fig. 9 shows an example result derived from the proposed 3-D motion prediction method. Images (a1) and (a2) represent the midventricular slices of a subject at different phases of the respiratory cycle, with the corresponding subtraction result shown in (a3). The 3-D rendition shown in (a4) highlights the amount of cardiac motion and deformation involved, where the solid and meshed surfaces represent the endocardial border of (a1) and (a2), respectively. The second row of Fig. 9 shows the result of using direct 3-D free-form image registration on these two 3-D image volumes. It is evident that the motion associated with Image (b2) has been corrected for, with the left ventricle being warped to the correct position. The quality of the registration process can be seen from the direct subtraction result and 3-D endocardial surface rendering. The final result derived from PLSR motion prediction is shown in the last row of Fig. 9. The effectiveness of the prediction algorithm is evident by comparing the result to that derived from 3-D image registration.

In order to demonstrate the fact that by using PLSR and multiple surface traces it is possible to derive results with similar accuracy to those derived by measuring diaphragmatic motion, Table II lists the mean residual errors by using these two approaches for the ten subjects studied. In this table, the residual error was measured as the normalized mean absolute intensity difference between the reference 3-D image volume timed at end-expiration and the target 3-D image volume timed at mid-respiration with 3-D warping. The normalization was done by dividing the mean absolute residual error of each method with the mean absolute error without motion correction. When applied to Fig. 9, for example, the normalized error in Image (b2) is calculated as the mean absolute value of (b3) divided by that of Image (a3). A similar value can be derived for (c2) by normalizing (c3) against (a3). This normalization process is important as for each subject the range of pixel intensities can be contrastingly different depending on the attenuation used for the RF receiver coil and the reconstruction parameters used.

In Table II, Rows P-chest and P-diaphragm represent results derived from motion prediction with PLSR from the chest wall and diaphragm, respectively. Despite the fact that the results derived from motion prediction are slightly poorer than that of 3-D image registration, it is evident that the results from P-chest and P-diaphragm are very much similar. For all the ten subjects studied, leave-one-out tests were performed for each subject with all the 3-D volumes acquired corresponding to different respiratory positions. The overall errors produced by using the proposed motion prediction technique can be assessed in Fig. 10, which provides the mean error and standard deviation for each subject based on the intensity difference criteria mentioned above. The corresponding results by using the 3-D free-form image registration are also provided for each subject as a reference. No significant difference was found between the two techniques.

To assess which surface traces are most useful for motion prediction, Fig. 11 shows the range of subtraction error values with the removal of input chest traces. The initial value (1.00) is obtained with a leave-one-out test on all ten subjects with 16 chest traces as input. Subsequently, traces are removed and a range of results are shown between the worst and best case. The optimal result is obtained with between four and ten traces remaining, the error being around 97% of the error with all 16 traces used.

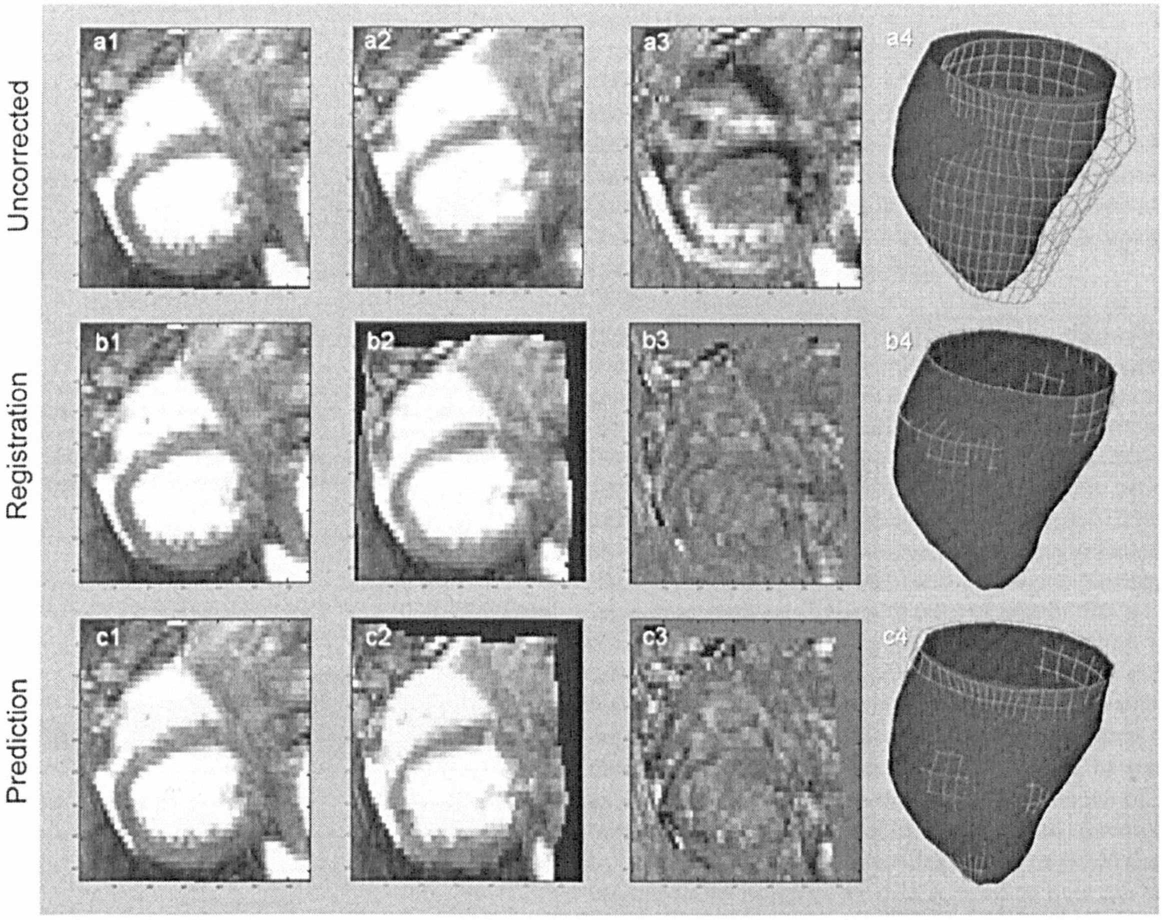

Fig. 9. Example of the results derived from the proposed 3-D motion prediction method. Images (a1) and (a2) represent the midventricular slices of a subject at different phases of the respiratory cycle with the corresponding subtraction result shown in (a3). The 3-D rendition shown in (a4) highlights the amount of cardiac motion and deformation involved, where the solid and meshed surfaces represent the endocardial border of (a1) and (a2), respectively. The second row shows the result of using direct 3-D free-form image registration to the two 3-D image volumes with (b2) representing the final warped midventricular slice. Images (b3) and (b4) show the residual error by image subtraction and 3-D rendering. The third row illustrates the same result as that of the second row but with PLSR motion prediction, demonstrating the ability of the proposed technique in accurate 3-D motion prediction.

TABLE II

MEAN RESIDUAL ERRORS AND STANDARD DEVIATIONS BY USING 3-D IMAGE REGISTRATION, 3-D MOTION PREDICTION WITH SURFACE INTENSITY TRACES (P CHEST) AND THE DOME OF THE DIAPHRAGM (P DIAPHRAGM), FOR THE TEN SUBJECTS STUDIED. THE RESULTS WERE DERIVED FROM MIDRESPIRATION AND END-EXPIRATION IMAGE VOLUMES

	1	2	3	4	5	6	7	8	9	10	**Mean**	**STD**
Registration	0.622	0.531	0.524	0.583	0.544	0.621	0.529	0.529	0.620	0.575	**0.568**	**0.042**
P chest	0.629	0.534	0.562	0.683	0.511	0.691	0.571	0.718	0.642	0.587	**0.617**	**0.065**
P diaphragm	0.624	0.531	0.572	0.750	0.553	0.662	0.550	0.718	0.643	0.587	**0.619**	**0.074**

Although being able to suggest the most useful traces for motion prediction for a particular subject at different phases of the respiratory cycle, it has been found that the permutation of the sensor position can vary across subjects. A poor selection of traces can result in a significantly worse result than from using all available traces. This justifies the use of PLSR in using a relatively large number of surface traces for reliable motion prediction despite the fact that they can be correlated and often individually of poor quality.

IV. DISCUSSIONS AND CONCLUSION

In this paper, we have presented a new technique based on surface measurable information for predicting respiratory-induced cardiac deformation. The technique relies on multiple input traces to capture the intrinsic pattern of surface deformation related to cardiac deformation. The use of PLSR effectively resolves the problem encountered by traditional regression methods in that we used the latent variables from both the input and output of the regression model to establish their inner relationships. Multicollinearity or near-linear dependence of regressors is a significant problem in regression models. The strength of the proposed PLSR approach is that it not only effectively deals with high multicollinearity of the measured signals from the chest, but also permits reliable motion prediction when the number of observations is significantly less than the observed variables as in this study, where only 6–7 different 3-D

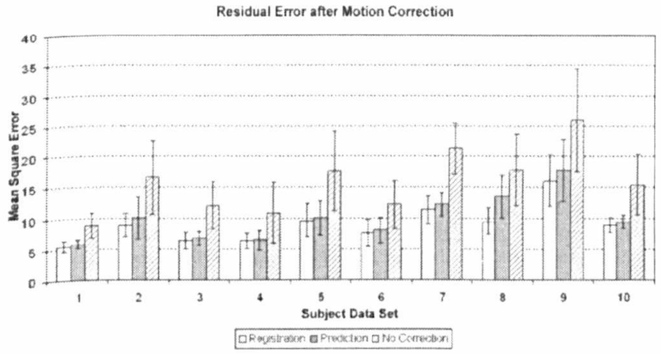

Fig. 10. Overall residual error and standard deviation of the proposed motion prediction technique for all the ten subjects studied. For residual error of the proposed PLSR method, leave-one-out error analysis is performed. The analysis covers the entire respiration range and the corresponding residual error for the 3-D image registration method is provided as a reference.

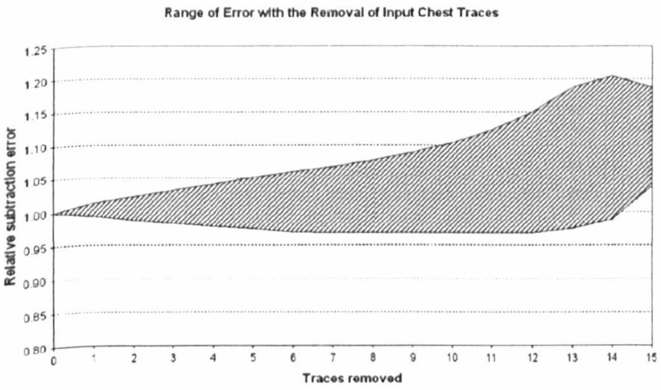

Fig. 11. Relative subtraction error after sequential removal of traces used for learning and prediction. The best and worst case is shown with all possible error values for the different number of traces shaded in between.

volumes corresponding to different respiratory positions were used. It must be mentioned, however, that the method used is fundamentally a linear technique. While it is able to deal with nonrigid 3-D motion, it is possible that for different subjects, a nonlinear relationship can exist between the measured respiratory traces and the deformation of the heart. This is true especially at the two extremes of the respiratory cycle. To cater for this problem, some of the developments in nonlinear and kernel-based PLSR approaches may be used [32]. It is worth noting that hysteresis, as observed in respiratory-induced cardiac deformation was not assessed in this study. This effect is related to the different relationship between respiration and cardiac deformation during inspiration and expiration [33]. It is not studied here due to the nature of the oversampled retrospectively gated image acquisition. The use of a single navigator to determine the respiratory gating precludes the hysteresis effect, and because of this, we are unable to assess the ability of the current framework to cope with this effect.

Subject specific respiratory patterns are a significant problem for motion management in *in vivo* imaging. Although in MR the use of navigator echoes has already improved the quality of the images acquired, particularly for capturing small mobile structures such as the coronaries, its widespread use is still hindered by its lack of general adaptivity to different imaging platforms. The results from this study suggest that being effectively a real-time technique, the proposed method is not only reasonably accurate, but also able to predict respiratory-induced cardiac motion from purely surface measurable signals. The development of a general method for 3-D motion prediction based on easily measured surface signals will have a significant impact on motion tracked imaging in MR, as well as for other parallel imaging modalities and the delivery of focused energy in the presence of physiological motion.

There are, however, a number of design issues related to the experiment that need to be recognized. First, the image acquisition for this study was based on retrospective diaphragmatic gating for acquiring 3-D volumes at different respiratory positions. The use of retrospective gating with oversampling has the advantage of being easy to implement and the data acquired corresponds to natural physiological states of the patient. The option of using breath holding was not adopted in this study as it could introduce artificial loadings to the visceral structure. The technique used, however, had a prolonged imaging time. A large oversampling factor was used to ensure that all k-space data, corresponding to different respiratory positions, was covered. Secondly, the use of diaphragmatic navigator echoes for predicting the deformation of visceral structures can itself have problems. It is possible that certain respiratory patterns can have different cardiac thoracic deformations despite the same navigator trigger response from the diaphragm. The use of 3-D volumes acquired as such is not ideal, but we are currently limited by the alternatives that are available. It is expected that by the use of parallel imaging, the data acquisition time can be significantly reduced.

It is also important to note that in this study, motion modeling and prediction are based on data that is simultaneously acquired. For the method to be used for cross-modality motion prediction, i.e., the use of MR for predictive motion modeling prior to PET imaging such that prospective motion correction can be applied, interscan inconsistencies of motion correlation will need to be further investigated. This analysis must be conducted in line with the choice of surface signal measurement techniques. In this study, we have used chest intensity profiles as a means of measuring local surface deformation. This is only to demonstrate the basic principle of the proposed motion prediction technique. In practice, more accurate imaging or nonimaging based techniques will need to be explored. These include the use of surface tension arrays to measure surface tension based on strain rather than absolute positions, or by the use of other optical/ultrasound based techniques. In these cases, modality compatibility is an important issue, especially for MR as the exclusion of ferromagnetic materials and the restriction on RF can introduce significant design problems. This is an important area to pursue given the current development in microsensor research.

It is worth noting that in the current study, we did not investigate the optimum arrangement of surface sensing locations. A detailed analysis either to determine a suitable arrangement for all subjects, or an efficient method of determining suitable locations on a subject-specific basis can potentially minimize the number of physical sensors. In conclusion, we have demonstrated an effective motion prediction technique, which after initial modeling can be used in real-time prospective motion tracking. Detailed analysis results from ten asymptomatic subjects demonstrate the accuracy and effectiveness of the proposed technique.

REFERENCES

[1] J. Friedman, K. Van Train, J. Maddahi, A. Rozanski, F. Prigent, and J. Bietendorf *et al.*, "'Upward creep' of the heart: A frequent source of false-positive reversible defects during thallium-201 stress-redistribution SPECT," *J. Nucl. Med.*, vol. 30, no. 10, pp. 1718–1722, 1989.

[2] T. Bortfeld, K. Jokivarsi, M. Goitein, J. Kung, and S. B. Jiang, "Effects of intra-fraction motion on IMRT dose delivery: Statistical analysis and simulation," *Phys. Med. Biol.*, vol. 47, pp. 2203–2220, 2002.

[3] C. R. King, J. Lehmann, J. R. Adler, and J. Hai, "CyberKnife radiotherapy for localized prostate cancer: Rationale and technical feasibility," *Technol. Cancer Res. Treat*, vol. 2, no. 1, pp. 25–30, 2003.

[4] R. George, P. J. Keall, V. R. Kini, S. S. Vedam, J. V. Siebers, and Q. Wu *et al.*, "Quantifying the effect of intrafraction motion during breast IMRT planning and dose delivery," *Med. Phys.*, vol. 30, no. 4, pp. 552–562, 2003.

[5] M. M. Ter-Pogossian, S. R. Bergmann, and B. E. Sobel, "Influence of cardiac and respiratory motion on tomographic reconstructions of the heart: Implications for quantitative nuclear cardiology," *J. Comput. Assist. Tomogr.*, vol. 6, no. 6, pp. 1148–1155, 1982.

[6] J. L. R. Andersson, B. E. Vagnhammar, and H. Schneider, "Accurate attenuation correction despite movement during PET imaging," *J. Nucl. Med.*, vol. 36, no. 4, pp. 670–678, 1995.

[7] D. Atkinson, M. Burcher, J. Declerck, and J. A. Noble, "Respiratory motion compensation for 3-D freehand echocardiography," *Ultrasound. Med. Biol.*, vol. 27, no. 12, pp. 1615–1620, 2001.

[8] W. J. Manning, M. Stuber, P. G. Danias, R. M. Botnar, S. B. Yeon, and F. C. Aepfelbacher, "Coronary magnetic resonance imaging: Current status," *Curr. Probl. Cardiol.*, vol. 27, no. 7, pp. 275–333, 2002.

[9] D. Li and V. Deshpande, "Magnetic resonance imaging of coronary arteries," *Top. Magn. Reson. Imag.*, vol. 12, no. 5, pp. 337–347, 2001.

[10] R. R. Edelman, W. J. Manning, D. Burstein, and S. Paulin, "Coronary arteries: Breath-hold MR angiography," *Radiology*, vol. 178, pp. 357–360, 1991.

[11] V. M. Runge, J. A. Clanton, C. L. Partain, and A. E. James Jr., "Respiratory gating in magnetic resonance imaging at 0.5 Tesla," *Radiology*, vol. 151, no. 2, pp. 521–523, 1984.

[12] J. N. Oshinski, L. Hofland, S. Mukundan, W. T. Dixon, W. J. Parks, and R. I. Pettigrew, "Two-dimensional coronary MR angiography without breath-holding," *Radiology*, vol. 201, pp. 737–743, 1996.

[13] R. L. Ehman and J. P. Felmlee, "Adaptive technique for high-definition MR imaging of moving structures," *Radiology*, vol. 173, no. 1, pp. 255–263, 1989.

[14] D. R. Bailes, D. J. Gilderdale, G. M. Bydder, A. G. Collins, and D. N. Firmin, "Respiratory ordered phase encoding (ROPE): A method for reducing respiratory motion artefacts in MR imaging," *J. Comput. Assist. Tomogr.*, vol. 9, no. 4, pp. 835–838, 1985.

[15] P. Jhooti, F. Wiesmann, A. M. Taylor, P. D. Gatehouse, G. Z. Yang, and J. Keegan *et al.*, "Hybrid ordered phase encoding (HOPE): An improved approach for respiratory artifact reduction," *J. Magn. Reson. Imag.*, vol. 8, no. 4, pp. 968–980, 1998.

[16] M. Weiger, P. Bornert, R. Proksa, T. Schaffter, and A. Haase, "Motion-adapted gating based on k-space weighting for reduction of respiratory motion artifacts," *Magn. Reson. Med.*, vol. 38, no. 2, pp. 322–333, 1997.

[17] P. G. Danias, M. V. McConnell, V. C. Khasgiwala, M. L. Chuang, R. R. Edelman, and W. J. Manning, "Prospective navigator correction of image position for coronary MR angiography," *Radiology*, vol. 203, pp. 733–736, 1997.

[18] M. V. McConnell, V. C. Khasgiwala, B. J. Savord, N. H. Chen, M. L. Chuang, and R. R. Edelman *et al.*, "Prospective adaptive navigator correction for breath-hold MR coronary angiography," *Magn. Reson. Med.*, vol. 37, no. 1, pp. 148–152, 1997.

[19] G. Z. Yang, P. Burger, P. D. Gatehouse, and D. N. Firmin, "Locally focused 3D coronary imaging using volume-selective RF excitation," *Magn. Reson. Med.*, vol. 41, no. 1, pp. 171–178, 1999.

[20] P. D. Gatehouse, J. Keegan, G. Z. Yang, R. H. Mohiaddin, and D. N. Firmin, "Tracking local volume 3D-echo-planar coronary artery imaging," *Magn. Reson. Med.*, vol. 46, no. 5, pp. 1031–1036, 2001.

[21] G. Z. Yang, P. D. Gatehouse, J. Keegan, R. H. Mohiaddin, and D. N. Firmin, "Three-dimensional coronary MR angiography using zonal echo-planar imaging," *Magn. Reson. Med.*, vol. 39, pp. 833–842, 1998.

[22] D. Manke, P. Rosch, K. Nehrke, P. Bornert, and O. Dossel, "Model evaluation and calibration for prospective respiratory motion correction in coronary MR angiography based on 3-D image registration," *IEEE Trans. Med. Imag.*, vol. 21, pp. 1132–1141, Sept. 2002.

[23] K. McLeish, D. L. G. Gill, D. Atkinson, J. M. Blackall, and R. Razavi, "A study of the motion and deformation of the heart due to respiration," *IEEE Trans. Med. Imag.*, vol. 21, pp. 1142–1150, Sept. 2002.

[24] D. Manke, K. Nehrke, and P. Bornert, "Novel prospective respiratory motion correction approach for free-breathing coronary MR angiography using a patient-adapted affine motion model," *Magn. Reson. Med.*, vol. 50, pp. 122–131, July 2003.

[25] T. S. Sachs, C. H. Meyer, J. M. Pauly, B. S. Hu, D. G. Nishimura, and A. Macovski, "The real-time interactive 3D-DVA for robust coronary MRA," *IEEE Trans. Med. Imag.*, vol. 19, pp. 73–79, Feb. 2000.

[26] P. Geladi and B. Kowalski, "Partial least-squares regression: A tutorial," *Anal. Chem. Acta*, vol. 185, pp. 1–17, 1986.

[27] A. R. McIntosh, F. L. Bookstein, J. V. Haxby, and C. L. Grady, "Spatial pattern analysis of functional brain images using partial least squares," *Neuroimage*, pt. 1, vol. 3, pp. 143–157, June 1996.

[28] D. Rueckert, L. I. Sonoda, C. Hayes, D. L. Hill, M. L. Leach, and D. J. Hawkes, "Nonrigid registration using free-form deformations: Application to breast MR images," *IEEE Trans. Med. Imag.*, vol. 18, pp. 712–721, Aug. 1999.

[29] H. Abdi, "Partial least squares regression (PLS-regression)," in *Encyclopedia for Research Methods for the Social Sciences*, M. Lewis-Beck, A. Bryman, and T. Futing, Eds. Thousand Oaks, CA: Sage, 2003.

[30] R. Bro, *Håndbog i Multivariabel Kalibrering* (in Danish). Copenhagen, Denmark: Jordbrugsforlaget, 1996.

[31] J. Keegan, P. D. Gatehouse, G. Z. Yang, and D. N. Firmin, "Coronary artery motion with the respiratory cycle during breath-holding and free-breathing: Implications for slice-followed coronary artery imaging," *Magn. Reson. Med.*, vol. 47, no. 3, pp. 476–481, 2002.

[32] E. Malthouse, A. Tamhane, and R. Mah, "Nonlinear partial least squares," *Comput. Chem. Eng.*, vol. 21, no. 8, pp. 875–890, 1997.

[33] K. Nehrke, P. Bornert, D. Manke, and J. C. Bock, "Free-breathing cardiac MR imaging: Study of implications of respiratory motion—initial results," *Radiology*, vol. 220, pp. 810–815, Sept. 2001.

D.2 Respiratory reordered UNFOLD perfusion imaging

Ablitt NA, Gatehouse PD, Firmin DN, Yang GZ, Respiratory reordered UNFOLD perfusion imaging, J Magn Reson Imaging. 2004 Nov;20(5):817-25.

9 pages

JOURNAL OF MAGNETIC RESONANCE IMAGING 20:817–825 (2004)

Original Research

Respiratory Reordered UNFOLD Perfusion Imaging

Nicholas A. Ablitt, MSc,[1] Peter D. Gatehouse, PhD,[2] David N. Firmin, PhD,[2] and Guang-Zhong Yang, PhD[1]*

Purpose: To propose a respiratory reordered UNFOLD (RR-UNFOLD) imaging sequence to significantly reduce the amount of *k*-space data required for first-pass MR myocardial perfusion imaging.

Materials and Methods: Rapid acquisition of high-resolution imaging data is essential to detailed quantitative analysis of first-pass myocardial perfusion. Existing MR sequences have explored the full capacity of the imaging hardware to reduce the acquisition window within each cardiac cycle while maintaining the desired spatial resolution. Further improvement in perfusion imaging will require a more efficient use of the information content of the *k*-space data. The method uses prospective diaphragmatic navigator echoes to ensure that temporal filtering of UNFOLD is carried out on a series of images that are spatially registered. An adaptive real-time rebinning algorithm is developed for the creation of static image subseries related to different levels of respiratory motion. Issues concerning the temporal smoothing of tracer kinetic signals are discussed, and a solution based on oversampling of the central *k*-space is provided. The method is assessed in 10 normal subjects without the administration of contrast agent, and further validated by administration of Gd-DTPA in 10 patients at rest.

Results: The results of this study show that RR-UNFOLD significantly extends the applicability of UNFOLD to perfusion imaging, which yields a 40% reduction in image artifact when the same amount of *k*-space information is used.

Conclusion: The scan efficiency achieved can be used in combination with MR hardware improvements for extending the three-dimensional spatial coverage and shortening the data acquisition window to provide detailed information on regional myocardial perfusion abnormalities.

Key Words: myocardial perfusion imaging; UNFOLD; navigator echoes; respiratory encode reordering; adaptive imaging; respiratory motion correction
J. Magn. Reson. Imaging 2004;20:817–825.
© 2004 Wiley-Liss, Inc.

EARLY DIAGNOSIS and localization of myocardial perfusion defects is an important step in the treatment of coronary artery disease. In recent years, the development of myocardial perfusion MR has extended the role of cardiovascular MR (CMR) in the evaluation of ischemic heart disease beyond situations in which gross myocardial changes, such as acute infarction or scarring, have already occurred. The ability to noninvasively evaluate cardiac perfusion abnormalities before pathologic effects occur, or as follow-up to therapy, is important for the management of patients with coronary artery disease. Early reperfusion of ischemic myocardium has been shown to have a positive reversal effect on the ischemic myocardium that reduces mortality and morbidity. The differentiation of ischemic but viable myocardium from infarcted regions requires a detailed global quantitative assessment and modeling of myocardial perfusion characteristics. CMR permits the acquisition of myocardial perfusion images with relatively high spatial resolution, and thus allows the transmural extent of myocardial ischemia to be determined. Thus far, the most common techniques used to assess myocardial perfusion based on first-pass imaging with CMR include turbo fast low-angle shot (turbo-FLASH) imaging (1–3), fast imaging with steady precession (trueFISP) (4) and echo-planar imaging (EPI) (5,6). Quantitative results have been achieved in animal studies with intravascular agents (polylysine-Gd-DTPA) as a macromolecular blood pool marker (7) and conventional extracellular agents (Gd-DTPA) for human studies (1,8–10). While limited multislice two-dimensional CMR perfusion studies are being increasingly used in a clinical setting to quantify gross ischemic burden, research is now directed toward complete three-dimensional coverage of the myocardium for accurate localization of the extent of possible defects. In three-dimensional myocardial perfusion imaging, one must acquire a complete volumetric data set for each cardiac cycle in order to study the first pass of the contrast bolus. This normally requires a relatively large acquisition window within each cardiac cycle to ensure a comprehensive coverage of the myocardium and reasonably high resolution of the images. With multislice imaging, long-axis cardiac motion during this large acquisition window can cause the myocardium, which is imaged in different cross-sections, to be misregistered (i.e., while some part of the myocardium may be imaged more than once, other parts may be missed completely). It is difficult to correct for this type of misregistration using postprocessing techniques. New imaging sequences, such as fast gradient echo with echo train readout

---

[1] Royal Society/Wolfson Foundation Medical Image Computing Laboratory, Imperial College of Science, Technology and Medicine, London, United Kingdom.
[2] Royal Brompton and Harefield NHS Trust, London, United Kingdom.
*Address reprint requests to: G.Z.Y., Royal Society/Wolfson Foundation MIC Laboratory, Department of Computing, 180 Queen's Gate, Imperial College, London SW7 2BZ, UK. E-mail: g.z.yang@imperial.ac.uk
Received February 9, 2004; Accepted June 23, 2004.
DOI 10.1002/jmri.20183
Published online in Wiley InterScience (www.interscience.wiley.com).

© 2004 Wiley-Liss, Inc.

(FGRE-ET) (11,12), have significantly reduced the acquisition window while maintaining the desired spatial resolution. Further improvements in perfusion imaging will require the application of parallel imaging techniques (13) or making full use of the information content of the *k*-space data. View-sharing is a common approach that involves the use of the similarity or redundancy in *k*-lines between images. Phase-encode lines, which through a Fourier transform represent image data that remain static across time, can be acquired once and shared between multiple images. Techniques such as block regional interpolation scheme for *k*-space (BRISK) (14) and broad-use linear acquisition speed-up technique (BLAST) (15) potentially can be adapted for this purpose.

More recently, unaliasing by Fourier encoding the overlaps using the temporal dimension (UNFOLD) has been used for perfusion imaging (16,17). This technique attempts to encode spatial information into redundant regions of *k*-t space. Initial experience has shown that this technique has promising practical value for breath-hold myocardial perfusion imaging because it doubles the scan efficiency, which can be used to either increase the spatial resolution/coverage or decrease the acquisition window. For perfusion imaging with free breathing, however, the technique suffers from significant motion artifacts and blurring due to respiratory-induced motion. It is generally not possible for patients to maintain a breath-hold for the duration of the perfusion scan, which typically lasts for about 50–60 heartbeats. In addition, prolonged breath-holding may alter the physiological response, which can affect the perfusion index quantification. Therefore, extensive improvement of the current UNFOLD framework is necessary before the technique can be of practical use for myocardial perfusion imaging. The purpose of this paper is to present a new prospective *k*-space reordering method for UNFOLD to eliminate respiratory-induced motion artifact. The method uses real-time diaphragm navigator echoes (18), similar to those used in CMR coronary angiography (19–21), to ensure that temporal filtering of UNFOLD is carried out on a series of images that are spatially registered. The method requires a prospective rebinning algorithm for the creation of multiple image subseries related to different levels of respiratory motion. Issues concerning the temporal smoothing of tracer kinetic signals are discussed, and a solution based on oversampling of the central *k*-space is provided. The strength of the technique is demonstrated with a detailed error analysis of 10 patients and 10 normal volunteers with UNFOLD and RR-UNFOLD simulated post-scan from the complete *k*-space data.

MATERIALS AND METHODS

UNFOLD

The principle of UNFOLD is based on temporal filtering to resolve spatial aliasing within the field of view (FOV) caused by a reduction in the density of *k*-space sampling. The method assumes that the dynamic structure under consideration is slowly varying throughout the imaging series, and therefore carries a low-temporal-frequency component (16). A reduction in the density of the *k*-space sampling reduces the distance between the central peaks of the point spread function (PSF), resulting in aliased reconstructions of the PSF image overlapping onto the central FOV. By shifting the sampling function in the phase-encode direction through time, we introduce a linear phase shift in the PSF. This has the effect of altering the phase through time of all but the central peak of the PSF, and introducing a temporal frequency phase modulation, effectively labeling the overlapping reconstructions. With this shift in the temporal-frequency spectrum, we are able to distinguish the central replica of the object from its overlapping replicas with the use of bandpass filters in the temporal-frequency domain. In the case in which the sampling function is shifted by half of its phase-encode resolution at each time-frame, we modulate the signal of the overlapping component by the Nyquist frequency while the central replica is unchanged. We achieve separation or "unfolding" by filtering out the extra information contained at each pixel location in the temporal Fourier domain before performing the inverse Fourier transform to reconstruct the image series with the overlapping component removed. A twofold reduction in the sampling function equates to a shift in the phase-encode direction by half a line for each image acquisition, which is tantamount to the shifting of one phase-encode line for a complete *k*-space acquisition in which alternate lines are obtained. We relate this to the full *k*-space acquisition by describing it as the acquisition of odd or even phase-encode lines.

The use of UNFOLD for myocardial perfusion imaging currently presents two major problems. First, the transit of the contrast bolus within the blood pool at the up-slope of the contrast intake is rapid, which can result in sharp signal intensity changes. Second, respiratory-induced cardiac deformation between cardiac cycles can be significant. Both of these introduce high-temporal-frequency components, and thus compromise the basic condition for UNFOLD to be effective. The associated artifact is normally manifested as an attenuation of the contrast bolus signal and aliased edges from the chest wall, as well as borders between the blood pool and myocardium. It is therefore essential to eliminate respiratory motion and restore tracer kinetics to perform UNFOLD for myocardial perfusion studies.

Respiratory Reordered UNFOLD (RR-UNFOLD)

The main steps of RR-UNFOLD involve the use of prospective diaphragmatic navigator echoes to split perfusion image series acquired for each cardiac cycle into different subseries (bins) so that within each bin the anatomical structures are spatially static. The method can be used for single- or multislice imaging, and images acquired within the same cardiac cycle are treated as a single *k*-space data set during the respiratory binning process. The only temporal change within the subseries is a varying contrast uptake among different anatomical regions. For each bin, a standard UNFOLD *k*-space acquisition is employed whereby, with twofold speed-up, alternating odd/even *k*-line coverage is used

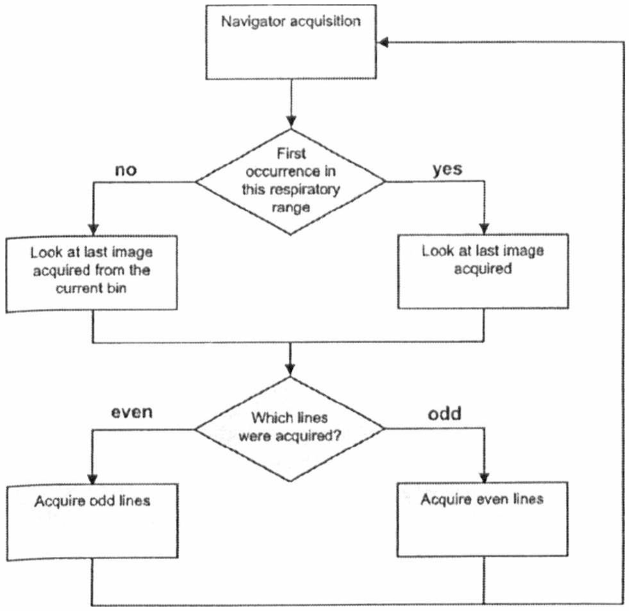
Navigator acquisition
First occurrence in this respiratory range
no
yes
Look at last image acquired from the current bin
Look at last image acquired
Which lines were acquired?
even
odd
Acquire odd lines
Acquire even lines

Figure 1. A schematic diagram showing the algorithm used for the binning, and the odd/even alternation used for RR-UNFOLD.

for successive temporal frames. For the first acquisition cycle, odd lines are obtained and inserted into a respiratory bins. Subsequently, depending on the respiratory navigator position, the associated k-space data are assigned to an appropriate respiratory bin. As the data collection progresses, the proposed technique acquires data sets with odd/even k-space coverage dictated by the RR-UNFOLD algorithm, and assigns them to the appropriate respiratory bins. There is no limit on how many images should be acquired for each bin, as the data collection process is prospective. This process is illustrated in Fig. 1.

Figure 2 schematically illustrates how this algorithm is applied with the use of a diaphragm navigator trace in which five respiratory bins are used to cover the entire respiratory range. It also demonstrates how different bins are created as time progresses. One detail of note is that when a new bin is created, the first image is chosen to be in sequence (in terms of odd/even k-line coverage) with the previous image, regardless of respiratory position. For example, when bin 2 was first created, the first image used odd k-line coverage since the previous acquisition was for bin 1 and it used even k-line coverage. This is potentially useful for dealing with bins with orphan frames (single frame within bin) during subsequent reconstruction.

With the above data acquisition scheme, it is not always possible to guarantee that each bin will contain the same number of odd/even k-space pairs for UNFOLD reconstruction. Although it is possible to use prescan navigator echoes to obtain the general statistics of the respiratory pattern and the associated respiratory range so that the derived histogram can be used to equally distribute the raw k-space data among different bins, it is not practical in patient studies since the administration of Gd-DTPA and Adenosine for pharmacological stress can significantly alter the respiratory patterns of the patient during data acquisition. In this study, a fixed respiratory window size was used to dynamically create all the necessary bins used for RR-UNFOLD, as indicated in Fig. 1. A typical respiratory window size is in the range of 5 mm, and with this approach the method is immune to respiratory drifts since new bins are created on the fly when necessary.

Image Series Reconstruction After Rebinning

The image series created by the above rebinning process cannot be used directly for reconstruction because nonuniform breathing patterns can result in bins with too few images for UNFOLD reconstruction. The number of bins created depends on the respiratory range of the subject during acquisition, and the size of the window for each bin. Because of the way in which UNFOLD is implemented, certain restrictions are imposed on the contents of each bin (i.e., each bin must contain at least four images because fewer than this will make it impossible to separate the aliased image from the original image in the temporal-frequency domain, since we are

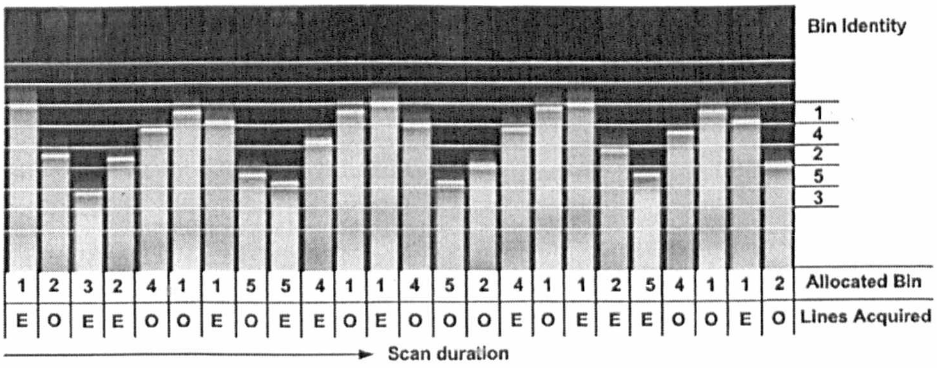

Figure 2. A sample navigator trace with a respiratory window of 5 mm for each of the bins used for RR-UNFOLD. A new bin is created in real time at the first instance of a navigator edge being located within the specified window, and from there each further instance of a navigator edge within the required bin alternates the acquisition of odd (O) and even (E) k-space encoding steps. When a new bin is created, the first image is always chosen to be in sequence (in terms of odd/even k-line coverage) with the previous image, regardless of respiratory position.

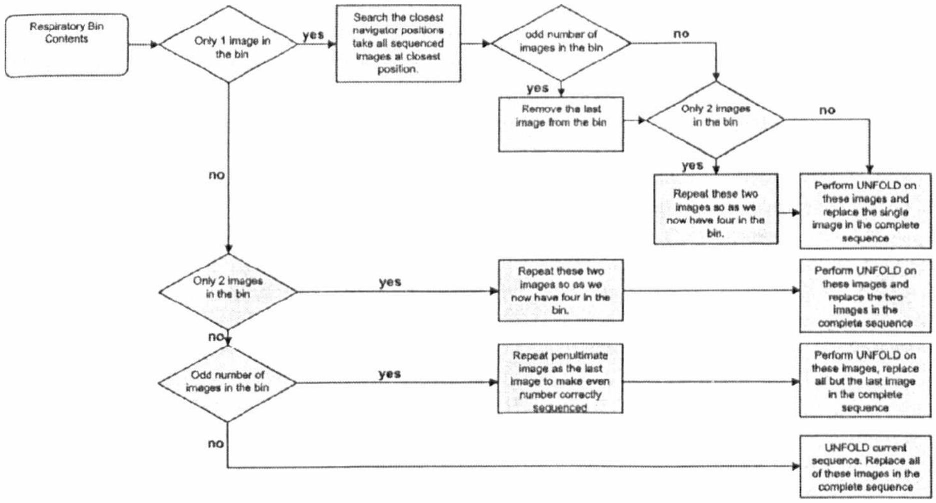
Respiratory Bin Contents
Only 1 image in the bin
yes
Search the closest navigator positions take all sequenced images at closest position.
odd number of images in the bin
no
yes
Remove the last image from the bin
Only 2 images in the bin
no
yes
Repeat these two images so as we now have four in the bin.
Perform UNFOLD on these images and replace the single image in the complete sequence
no
Only 2 images in the bin
yes
Repeat these two images so as we now have four in the bin.
Perform UNFOLD on these images and replace the two images in the complete sequence
no
Odd number of images in the bin
yes
Repeat penultimate image as the last image to make even number correctly sequenced
Perform UNFOLD on these images, replace all but the last image in the complete sequence
no
UNFOLD current sequence. Replace all of these images in the complete sequence

Figure 3. A schematic diagram showing all the processing steps involved in preprocessing the *k*-space data within each bin before UNFOLD reconstruction is applied.

unable to distinguish sufficient temporal frequencies). In addition, because of the way in which Fourier temporal filtering is used, we must have an even number of images within each bin. To correct for these problems, we supplement each bin with additional frames before applying the UNFOLD method. Since all bins are created dynamically during acquisition, there are four possible cases that must be considered. The basic steps involved in the proposed method are shown in Fig. 3. For example, when there is only one frame in the bin, images from the closest navigator position that are in odd/even sequence are appended to the bin. Further processing is then applied to ensure that the bin with padding has a minimum of four images with all of the odd/even acquisitions paired before conventional UNFOLD reconstruction is used. When there are only two images in the bin, the existing data in the bin are duplicated before reconstruction. The third case in Fig. 3 deals with situations in which there are an odd number of frames within the bin. In this case, the penultimate image is copied as the last image to complete the odd/even sequence. Finally, if none of the above applies, conventional UNFOLD reconstruction is applied directly.

The purpose of this postprocessing step is to increase the contents of a bin to a suitable size for the successful application of UNFOLD. This is achieved either by reusing the current frames within the bin, or recruiting frames from neighboring bins. The frames recruited must adhere to the required phase-shifting pattern selected during the acquisition (in our case, odd and even phase-encode lines). From this, we keep the reconstructions for the frames originally contained within the bin and add them to the final series, while those from additional "borrowed" frames are discarded. In this way, we are able to optimize the result of the UNFOLD procedure for each bin by making use of the extra information we have from the full series.

Restoration of the Tracer Kinetic Signal

By splitting up the image series into spatially registered series, respiratory motion-induced artifact can be eliminated in the reconstructed images. However, UNFOLD works by eliminating temporal changes in pixel intensity at the Nyquist frequency, which has the effect of smoothing out sharp signal intensity changes between adjacent images within each bin. With respiratory reordering, this smoothing effect is amplified for each bin, since successive images are acquired with the same respiratory position but are not temporally immediately adjacent to each other. This is especially pronounced during contrast uptake, since by reordering we have effectively introduced sharper intensity changes. To reintroduce the correct intensities within the image, extra central phase-encode *k*-lines are acquired to reintroduce the low-frequency spatial intensity information. While the outer *k*-space lines contain the high-spatial-frequency information, such as edges and noise, the central lines predominantly determine the low-spatial-frequency information, such as regions of intensity, and are therefore highly significant in representing the contrast agent present in the blood pool and myocardium. During the acquisition, *k*-space is filled with alternate lines in the phase-encode direction for the outer region, and full coverage in the central region. This is equivalent to acquiring extra central phase-encode lines to complete the subsampled coverage in the central region. This additional sampling can be substituted into the *k*-space series after the application of RR-UNFOLD to correct for excessive temporal smoothing due to out-of-sequence UNFOLD reconstruction.

Image Acquisition

To study in detail the effectiveness of the reordering scheme for motion artifact removal, and the robustness of the rebinning algorithm for free-breathing perfusion imaging, we applied a trueFISP perfusion sequence to 10 normal subjects (age = 24 ± 3 years) and 10 patients (age = 54 ± 18 years) with clinical referrals for late gadolinium myocardial viability assessment with written consent. In each cardiac cycle, the navigator column was formed immediately before the trueFISP image by the intersection of 90° and 180° 10-mm-thick slice-selective RF pulses, avoiding the heart, and positioned along the head–foot direction through the dome of the diaphragm. For navigator echoes, a frequency-encoded readout of 256 points was used to cover a 400-mm range, which was then interpolated to 1-mm resolution during reconstruction for display and edge position measurement.

For each subject, images covering 50 cardiac cycles were acquired. For each cardiac cycle, the navigator was followed by complete *k*-space coverage of single-slice trueFISP imaging, which, to avoid cardiac motion, was run as late as possible in the cardiac cycle (typically starting about 400–500 msec after the R-wave, depending on the patient's R-R interval and variability). The total image duration was 260 msec from the start of the nonselective saturation pulse to the end of the single-shot trueFISP sequence. Since Gd-DTPA was not used in the normal volunteers, the saturation pulse was turned off. Other imaging parameters included a 140-msec saturation recovery delay, 0.1-mmol/kg Gd-DTPA dose injected at ≈3 mL/sec followed by a 10-mL saline flush, 10-mm slice, 40–60° flip angle (SAR limited), 370 mm (FE) × 288 mm (PE) FOV (both scaled up sometimes for bigger patients), 144 (FE) × 112 (PE) uninterpolated unfiltered pixels in the image, full *ky* coverage in linear order over *ky* vs. time, and 2.2-msec repeat time between the trueFISP RF pulses. All images were acquired on a SIEMENS 1.5T Sonata scanner with a peak gradient strength of 40 mT/m and peak slew rate of 200 mT/m/msec. The full *k*-space data were stored, and subsequently phase-encode lines were zero-filled to simulate the UNFOLD and RR-UNFOLD acquisition.

Error Analysis

Validation of the proposed technique was performed in two stages. A detailed study of the technique on 10 normal subjects without the administration of contrast agent allowed for the assessment of RR-UNFOLD in the removal of motion artifact. Following this, the method was applied to 10 patients for further assessment of the quantitative errors associated with perfusion index calculation under normal CMR perfusion settings. The aim of the patient study was to determine the effects of the changing image intensity through time on the success of RR-UNFOLD. By using full *k*-space coverage in the acquisition stage, we were also able to determine the optimum number of extra central *k*-lines required to maintain the contrast agent intensity through time. For quantifying image artifact, the image series reconstructed with full *k*-space encoding was used as a gold standard, and the sum of the squared subtraction error was calculated for the different reconstruction methods used.

RESULTS

Figure 4 illustrates the image artifact introduced by applying the original UNFOLD and the proposed RR-UNFOLD methods (with and without intensity correction) to a perfusion sequence. It is evident that with UNFOLD, significant motion blurring and movement artifacts are present. Before the restoration of the tracer kinetic signal, the proposed RR-UNFOLD method eliminates motion artifact and restricts the difference between the reconstructed images and those with fully encoded data to temporal intensity attenuation only. This attenuation can be corrected for by the use of extra central *k*-lines. This is demonstrated in Fig. 5, where signal intensity curves from regions within the blood pool and myocardium are provided to illustrate the effectiveness of the proposed intensity correction method. It is evident that by using extra central *k*-lines with RR-UNFOLD, the reconstructed perfusion image series is very close to the result obtained with full *k*-space encoding. In the examples shown in Fig. 5, only six extra central *k*-lines were used, which represents a 45% reduction in imaging acquisition time.

To obtain a more quantitative assessment of the errors introduced by the proposed RR-UNFOLD technique, we conducted the following experiments to analyze the effect of the window width of each bin and the number of extra *k*-lines used for RR-UNFOLD reconstruction: Figure 6 illustrates the amount of reduction in image artifact with RR-UNFOLD compared to UNFOLD when different window sizes (bin width) were used during data acquisition. To make the comparison fair, the extra central *k*-lines were also used for UNFOLD reconstruction, and the ratio of image artifact between the two was used for Fig. 6a and b. For normal volunteers with no Gd-DTPA injection, the amount of image artifact mainly reflects the effectiveness of the binning algorithm for respiratory motion correction, whereas for patients, this is associated with the combined effect of motion and contrast uptake restoration. As expected, smaller respiratory windows are advantageous for motion correction, whereas for normal perfusion sequences in the presence of Gd-DTPA bolus, a window size of 5 mm is optimal. Overall, the average image artifact was reduced to 60% of the UNFOLD technique when the same number of *k*-space encoding lines were used. This reduction is significant for quantifying subtle perfusion defects in clinical applications.

The graph in Fig. 7 illustrates the reduction in image artifact with RR-UNFOLD when different numbers of central *k*-lines, ranging from 1 to 20, were used to reconstruct the data sets for the 10 patients studied. For this analysis, the navigator window size used for each bin was fixed at 5 mm. As before, all values provided are represented as the amount of artifact reduction achieved with RR-UNFOLD compared to normal UNFOLD. It is evident that the error reduces rapidly with the first five extra lines, and after this point the reduction in image artifact is marginal. A good compromise between image quality and scan efficiency is to use six extra central lines for the present imaging sequence, with which the artifact is reduced to 30% of the normal UNFOLD method.

To help relate the above image artifact ratio to the actual improvement in the visual quality of the reconstructed images, Fig. 4 provides an example image series obtained by using the optimum parameter settings determined above (i.e., the navigator window size and the number of extra central *k*-lines were set to be 5 mm and six, respectively). Four frames from a perfusion

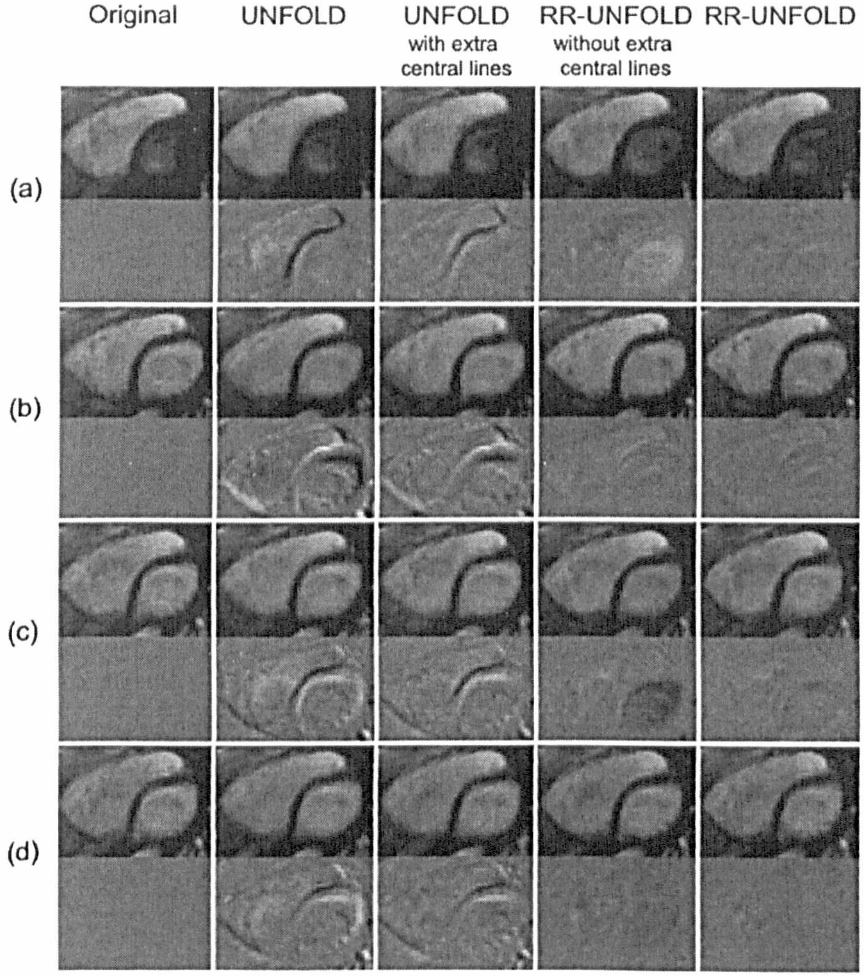

Figure 4. Four frames from a perfusion sequence of a patient showing the image artifact introduced by the use of different reconstruction techniques: original fully encoded images (first column), conventional UNFOLD reconstructed images (second column), conventional UNFOLD with extra central *k*-lines (third column), RR-UNFOLD reconstructed images (prior to tracer intensity correction; fourth column), and RR-UNFOLD (fifth column). Rows a–d show the results for different time frames and the corresponding subtraction errors compared to the original fully encoded image.

image series are shown for one of the patients studied. Each frame was reconstructed using five different methods, with the respective subtraction images demonstrating the difference between the original image and the reconstruction results. It can be seen that UNFOLD introduces a large amount of spatial motion artifact even with the addition of the six extra central *k*-lines. While RR-UNFOLD almost entirely eliminates this edge artifact, it suffers from low-frequency image intensity artifact. With the use of RR-UNFOLD with the additional six extra central *k*-lines, we are able to eliminate both types of artifact from the final reduced *k*-space reconstruction. This acquisition gives a 45% saving in *k*-space coverage, with an average reduction in artifact of 72% ± 8% over the UNFOLD method.

Finally, the effect of RR-UNFOLD on the accuracy of the derived perfusion index was analyzed for the 10 patients studied. We analyzed the image series using CMRtools (Imperial College, London, UK), and a model-based approach based on Fermi deconvolution (9) was used to fit the signal time course curves. Six transmural regions of interest (ROIs) were selected in addition to the blood pool from the short-axis slice of the myocardium. The image series full *k*-space acquisition was then automatically aligned with image registration to correct for rigid body motion. Manual adjustment was applied when necessary if the automatic registration was suboptimal. We analyzed the resulting time series curves by deconvolving the myocardial signal with that of the blood pool. The same analysis, including the same motion correction parameters, was applied to RR-UNFOLD reconstructed data. We used the normalized slope as the perfusion index for the 10 patients studied (Fig. 8 gives regional values for one of the patients studied). It is evident that the error from normal UNFOLD ranges from 25% to 71%, whereas with RR-UNFOLD the maximum error is only 14%. Figure 9 illustrates the mean absolute error of the perfusion index obtained with conventional UNFOLD and the proposed RR-UNFOLD technique with a 5-mm bin width and six extra central lines for all of the 10 patients studied. The average error of the two techniques was 25% and 9%, respectively.

DISCUSSION

In this study, we have presented a new RR-UNFOLD technique for myocardial perfusion imaging. The relative strength and potential pitfalls of the techniques were assessed in detail, and the results demonstrate the potential clinical value of the technique. The method achieved an overall 45% reduction in image acquisition time, and significantly reduced image artifacts compared to UNFOLD, based on the trueFISP per-

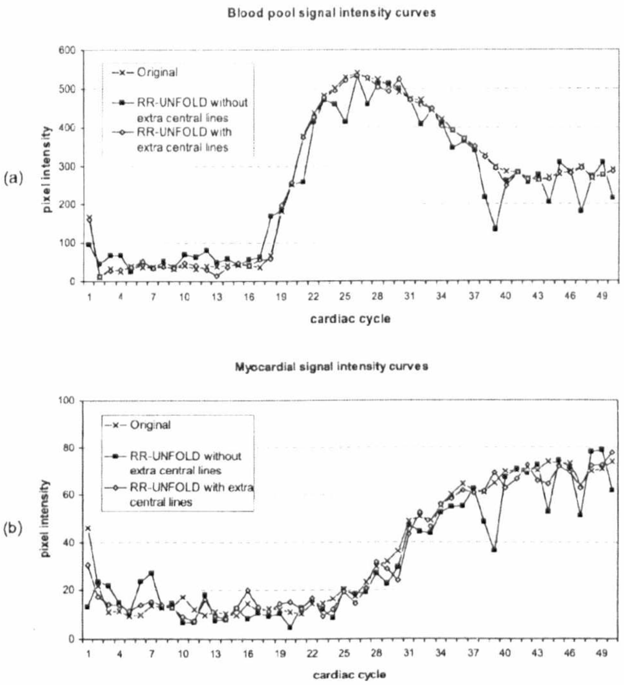

Figure 5. ROI signal intensity curves showing the effectiveness of signal intensity correction by the introduction of extra central k-space encoding lines for RR-UNFOLD. The three intensity curves of each figure show the signal derived from images with and without central k-space encoding measured within the blood pool and myocardium, respectively, compared to those from the original fully encoded perfusion image sequence.

fusion sequence used. One of the major advantages of the proposed method is its simplicity, in terms of both respiratory motion correction and data reconstruction. The method involves only minor changes to the sequence design if prospective navigator echoes are available on the CMR system. The rebinning algorithm proposed is straightforward to implement, and our study involving both normal subjects and patients demonstrates the robustness of the technique in dealing with different respiratory patterns.

For this study, the bin used for each image subseries was created dynamically, which made the technique resilient to changes in respiratory patterns. It is worth noting that for the results presented here, a fixed respiratory window was used for all of the bins. This introduced a non-equal distribution of the number of images in each bin, since for normal respiratory patterns the dwell time at end-expiration and -inspiration can be extensive. Although the rebinning algorithm proposed can effectively deal with this issue, certain optimizations, such as using variable window sizes at different phases of the respiratory cycle, can be introduced. Furthermore, it is also important to consider the respiration speed during data acquisition given that in perfusion imaging the acquisition window is long compared to that in conventional imaging, due to the complete spatial coverage required for every cardiac cycle. This effect is most pronounced at mid-respiration, when the speed of the diaphragm movement is at its maximum. An optimized solution to these issues, however, is not trivial and will require prior knowledge of subject-specific respiratory patterns. Although one can acquire this information, to some extent, by using prescans so that the respiratory patterns are monitored for a short period of time before actual perfusion imaging is performed, it is difficult to put this into practice because respiratory patterns change during the course of image acquisition, especially when pharmacological stress is used to assess the perfusion reserve.

It is worth noting that although all results shown in this paper are based on a trueFISP perfusion sequence, the method is applicable to general perfusion sequences. Our results show that RR-UNFOLD significantly extends the applicability of UNFOLD to perfusion imaging, and yields a 40% reduction in image artifact (or a 70% reduction if the extra central k-lines are not used for UNFOLD reconstruction). The scan efficiency achieved can be used to extend the three-dimensional spatial coverage or to shorten the acquisition window of the perfusion sequence, both of which are fundamental to the accuracy of the CMR technique in providing detailed information on regional myocardial perfusion ab-

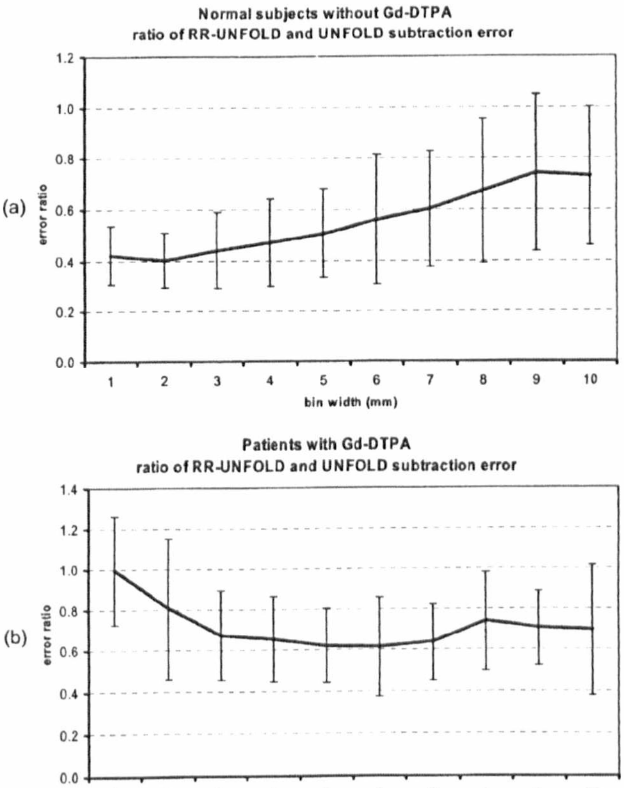

Figure 6. The ratio of subtraction errors between RR-UNFOLD and conventional UNFOLD for normal subjects **(a)** and patients **(b)** studied when different respiratory window sizes are used for each bin. In both figures, the same k-space data with extra central lines were used for RR-UNFOLD and conventional UNFOLD techniques. An error ratio of less than 1.0 indicates an improved artifact suppression of the RR-UNFOLD technique. The solid curve demonstrates the mean error ratio, and the vertical bars indicate the standard deviation (SD).

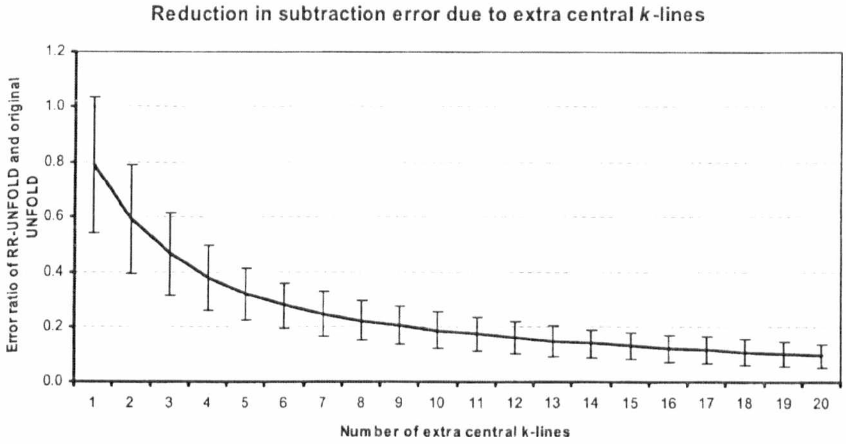

Figure 7. The reduction in error (mean and SD of the 10 patients studied) represented as a ratio of RR-UNFOLD against normal UNFOLD when different numbers of extra central *k*-lines are used.

normality. The reduction in the acquisition window is particularly important for three-dimensional perfusion imaging with multislice coverage, since misregistration due to materials moving in or out of the imaging plane caused by cardiac- and respiratory-induced long-axis motion is particularly difficult to rectify, and it cannot be restored by postprocessing techniques. The proposed technique is therefore valuable for accurately quantifying perfusion so as to extend the role of CMR in managing patients with suspected coronary artery disease, and following up patients with known ischemic defects.

The reduction in *k*-space coverage can be used in different ways. The 45% reduction in *k*-space coverage required may allow an almost twofold increase in myocardial coverage. This, paired with the latest imaging sequences (13), would allow the possibility of several short-axis myocardial slices and the acquisition of long-axis slices for greater apical coverage. With a multislice image acquisition, the navigator would be acquired prior to image data acquisition for each cardiac cycle as with single-slice imaging. Binning would then be applied in a similar manner to single-slice imaging.

It is important to note that for this study the prescribed dose of contrast agent (0.1 mmol/kg of Gd-DTPA) is likely to result in signal-clipping of the arterial input function. For this study, we concentrated mainly on the measurement errors by using the same experiment setting but with a different reconstruction (i.e., full acquisition, traditional UNFOLD, and RR-UNFOLD imaging techniques). The study of the arterial input function under high-dose Gd-DTPA imaging and its impact on perfusion index quantification, as well the avoidance of nonlinear response-induced errors are active fields of research in MR myocardial perfusion (22).

While the results for RR-UNFOLD show marked improvements in accuracy for the perfusion index measured by the normalized slope in comparison with UNFOLD, in two instances RR-UNFOLD actually produced greater error in the measured perfusion index value (patient 1 increased from 8% to 12%, and patient 6 increased from 12% to 23%, as shown in Fig. 9). In the case of patient 1, both UNFOLD and RR-UNFOLD provided acceptable error of around 10%. For patient 6, however, the error is significant. This is attributed to the poor navigator trace from the patient, which when used with RR-UNFOLD degrades the consistency of the *k*-space data and actually increases the image artifact.

In summary, we have developed an effective way to extend the UNFOLD framework for myocardial perfusion imaging. We demonstrated the strength of the technique with in vivo data acquired from both normal subjects and patients referred for myocardial viability assessment. The method provides a near twofold increase in imaging efficiency, with only minor deterioration in image quality compared to full *k*-space coverage. Furthermore, the method is relatively simple to imple-

Segment	UNFOLD	RR-UNFOLD
1	1.25	0.95
2	1.42	1.14
3	1.28	1.00
4	1.32	1.03
5	1.36	1.00
6	1.71	1.05

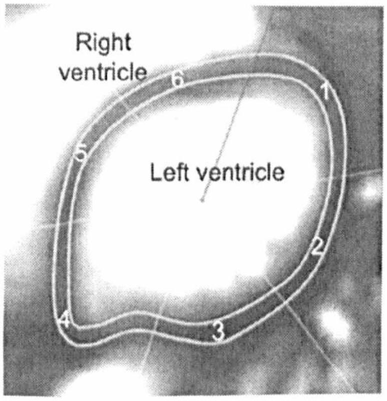

Figure 8. Perfusion index calculated for six midventricular segments of a patient, demonstrating the effect of RR-UNFOLD and conventional UNFOLD for myocardial perfusion quantification. Relative values between reduced *k*-space reconstructions and the original data are shown for UNFOLD and RR-UNFOLD, where 1.0 indicates no change in perfusion index. With UNFOLD, the derived perfusion index has an error range of 25–71%, whereas for RR-UNFOLD the error range is kept within 14%.

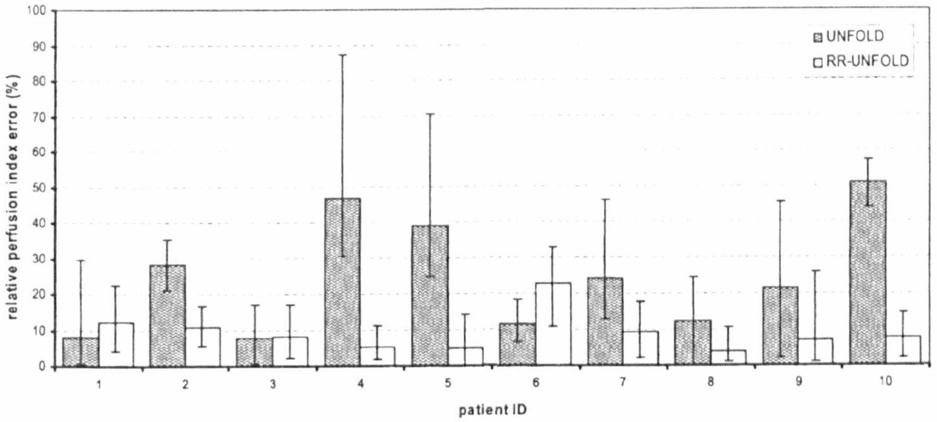

Figure 9. The relative error in the perfusion index after the same processing steps as in Fig. 8 are applied to the 10 patients studied with the UNFOLD and RR-UNFOLD techniques. The mean absolute error of the perfusion index, and minimum/maximum absolute error of the perfusion index are shown for each patient.

ment and can be applied to most of the current state-of-the-art CMR scanners.

REFERENCES

1. Wilke N, Simm C, Zhang J, et al. Contrast-enhanced first-pass myocardial perfusion imaging: correlation between myocardial blood flow in dogs at rest and during hyperemia. Magn Reson Med 1993;29:485–497.
2. Tsekos NV, Zhang Y, Merkle H, et al. Fast anatomical imaging of the heart and assessment of myocardial perfusion with arrhythmia insensitive magnetization preparation. Magn Reson Med 1995;34: 530–536.
3. Wilke N, Jerosch-Herold M, Wang Y, et al. Myocardial perfusion reserve: assessment with multisection, quantitative, first-pass MR imaging. Radiology 1997;204:373–384.
4. Schreiber WG, Schmitt M, Kalden P, Mohrs OK, Kreitner KF, Thelen M. Dynamic contrast-enhanced myocardial perfusion imaging using saturation-prepared TrueFISP. J Magn Reson Imaging 2002;16: 641–652.
5. Edelman RR, Li W. Contrast-enhanced echo-planar MR imaging of myocardial perfusion: preliminary study in humans. Radiology 1994;190:771–777.
6. Schwitter J, Debatin JF, von Schulthess GK, McKinnon GC. Normal myocardial perfusion assessed with multishot echo-planar imaging. Magn Reson Med 1997;37:140–147.
7. Wilke N, Kroll K, Merkle H, et al. Regional myocardial blood volume and flow: first-pass MR imaging with polylysine-Gd-DTPA. J Magn Reson Imaging 1995;5:227–237.
8. Larsson HB, Fritz-Hansen T, Rostrup E, Sondergaard L, Ring P, Henriksen O. Myocardial perfusion modeling using MRI. Magn Reson Med 1996;35:716–726.
9. Jerosch-Herold M, Wilke N, Stillman AE. Magnetic resonance quantification of the myocardial perfusion reserve with a Fermi function model for constrained deconvolution. Med Physiol 1998; 25:73–84.
10. Manning WJ, Atkinson DJ, Grossman W, Paulin S, Edelman RR. First-pass nuclear magnetic resonance imaging studies using gadolinium-DTPA in patients with coronary artery disease. J Am Coll Cardiol 1991;18:959–965.
11. Ding S, Wolff SD, Epstein FH. Improved coverage in dynamic contrast-enhanced cardiac MRI using interleaved gradient-echo EPI. Magn Reson Med 1998;39:514–519.
12. Epstein FH, London JF, Peters DC, et al. Multislice first-pass cardiac perfusion MRI: validation in a model of myocardial infarction. Magn Reson Med 2002;47:482–491.
13. Zhang Q, Crowe ME, Chung YC, Simonetti OP. Acceleration techniques combined with TrueFISP for rapid first-pass myocardial perfusion imaging. In: Proceedings of the 11th Annual Meeting of ISMRM, Toronto, Canada, 2003. p 1665.
14. Doyle M, Walsh EG, Blackwell GG, Pohost GM. Block regional interpolation scheme for k-space (BRISK): a rapid cardiac imaging technique. Magn Reson Med 1995;33:163–170.
15. Tsao J, Behnia B, Webb AG. Unifying linear prior-information-driven methods for accelerated image acquisition. Magn Reson Med 2001;46:652–660.
16. Madore B, Glover GH, Pelc NJ. Unaliasing by Fourier-encoding the overlaps using the temporal dimension (UNFOLD), applied to cardiac imaging and fMRI. Magn Reson Med 1999;42:813–828.
17. Di Bella EV, Wu YJ, Alexander AL, Parker DL, Green D, McGann CJ. Comparison of temporal filtering methods for dynamic contrast MRI myocardial perfusion studies. Magn Reson Med 2003;49:895–902.
18. Ehman RL, Felmlee JP. Adaptive technique for high-definition MR imaging of moving structures. Radiology 1989;173:255–263.
19. Wang Y, Rossman PJ, Grimm RC, Riederer SJ, Ehman RL. Navigator-echo-based real-time respiratory gating and triggering for reduction of respiration effects in three-dimensional coronary MR angiography. Radiology 1996;198:55–60.
20. McConnell MV, Khasgiwala VC, Savord BJ, et al. Prospective adaptive navigator correction for breath-hold coronary angiography. Magn Reson Med 1997;37:148–152.
21. Keegan J, Gatehouse PD, Taylor AM, Yang GZ, Jhooti P, Firmin DN. Coronary artery imaging in a 0.5-Tesla scanner: implementation of real-time, navigator echo-controlled segmented k-space FLASH and interleaved spiral sequences. Magn Reson Med 1999;41:392–399.
22. Gatehouse PD, Elkington AG, Ablitt NA, Yang GZ, Pennell DJ, Firmin DN. Accurate assessment of the arterial input function during high-dose myocardial perfusion cardiovascular magnetic resonance. J Magn Reson Imaging 2004;20:39–45.

D.3 Accurate assessment of the arterial input function during high-dose myocardial perfusion cardiovascular magnetic resonance

Gatehouse PD, Elkington AG, Ablitt NA, Yang GZ, Pennell DJ, Firmin DN. Accurate assessment of the arterial input function during high-dose myocardial perfusion cardiovascular magnetic resonance. J Magn Reson Imaging. 2004 Jul;20(1):39-45.

7 pages

JOURNAL OF MAGNETIC RESONANCE IMAGING 20:39–45 (2004)

Original Research

Accurate Assessment of the Arterial Input Function during High-Dose Myocardial Perfusion Cardiovascular Magnetic Resonance

Peter D. Gatehouse, PhD,[1] Andrew G. Elkington, BSc, MRCP,[1] Nicholas A. Ablitt, PhD,[2] Guang-Zhong Yang, PhD,[2] Dudley J. Pennell, MD, FRCP,[1] and David N. Firmin, PhD[1]*

Purpose: To develop a method for accurate measurement of the arterial input function (AIF) during high-dose, single-injection, quantitative T1-weighted myocardial perfusion cardiovascular magnetic resonance (CMR).

Materials and Methods: Fast injection of high-dose gadolinium with highly T1 sensitive myocardial perfusion imaging is normally incompatible with quantitative perfusion modeling because of distortion of the peak of the AIF caused by full recovery of the blood magnetization. We describe a new method that for each cardiac cycle uses a low-resolution short-axis (SA) image with a short saturation-recovery time immediately after the R-wave in order to measure the left ventricular (LV) blood pool signal, which is followed by a single SA high-resolution image with a long saturation-recovery time in order to measure the myocardial signal with high sensitivity. Fifteen subjects were studied. Using the new method, we compared the myocardial perfusion reserve (MPR) with that obtained from the dual-bolus technique (a low-dose bolus to measure the blood pool signal and a high-dose bolus to measure the myocardial signal).

Results: A small significant difference was found between MPRs calculated using the new method and the MPRs calculated using the dual-bolus method.

Conclusion: This new method for measuring the AIF introduced no major error, while removing the practical difficulties of the dual-bolus approach. This suggests that quantification of the MPR can be achieved using the simple high-dose single-bolus technique, which could also image multiple myocardial slices.

Key Words: heart; magnetic resonance; myocardial perfusion; gadolinium; first-pass; arterial input function
J. Magn. Reson. Imaging 2004;20:39–45.
© 2004 Wiley-Liss, Inc.

QUANTITATIVE MYOCARDIAL perfusion cardiovascular magnetic resonance (CMR) requires measurement of the arterial input function (AIF), which is the concentration of gadolinium in the left ventricular (LV) or aortic blood pool as a function of time during its first pass. T1-weighted contrast is typically achieved by applying an inversion or saturation pulse before each image, saturation being generally preferred because of its immunity to cardiac interval variability. A long recovery delay (time from saturation pulse to the beginning of the readout) and high gadolinium dose are required for high T1 sensitivity and good myocardial signal intensity. However, a high gadolinium concentration causes full magnetization recovery with a long saturation delay (Fig. 1a), which may cause clipping of the AIF, and further increases in gadolinium concentration may even reduce the signal by T2* effects (1). The clipping of the AIF results in an underestimation of the AIF. Therefore, for accurate measurement of the myocardial perfusion reserve (MPR), it is preferable to use a low dose (Fig. 1b). This tension between the need for high-dose gadolinium for good myocardial response and low-dose gadolinium for accurate measurement of the AIF has not been adequately resolved to date. Previous proposed solutions include the T1-FARM (fast acquisition relaxation mapping) method (2), which computes a T1 map from two full-resolution images with response covering both the AIF and the myocardial tissue enhancement, and the dual-bolus technique (3), with a low dose for the AIF, followed by a large dose for the myocardium (i.e., the blood curve from Fig. 1b and the myocardial curve from Fig. 1a). However, both techniques have problems: the T1-FARM method has a low signal-to-noise ratio (SNR) and long imaging time, and the dual-bolus method is complicated to perform and care has to be taken to ensure the boluses are reproducible. In a third approach, using dual-inversion-time imaging for work on water exchange across the capillary wall, a 20-msec inversion recovery time gave the undistorted AIF, while both 20 and 600 msec were obtained in the myocardium (4), an approach similar to the method described in this article, except that the resolution was the same in both images. In a fourth method, multiple inversion times have been used for accurate multislice

---

[1] Cardiovascular Magnetic Resonance Unit, Royal Brompton Hospital, London, UK.
[2] Department of Computing, Imperial College, London, UK.
Peter D. Gatehouse and Andrew G. Elkington are joint first authors.
*Address reprint requests to: D.F., Cardiovascular Magnetic Resonance Unit, Royal Brompton Hospital, Sydney Street, London SW3 6NP, UK. E-mail: d.firmin@ic.ac.uk
Received May 5, 2003; Accepted February 2, 2004.
DOI 10.1002/jmri.20054
Published online in Wiley InterScience (www.interscience.wiley.com).

© 2004 Wiley-Liss, Inc.

myocardial T1 measurements, but have so far been acquired too slowly to follow first-pass perfusion (5).

Longitudinal magnetization recovery is partially suppressed by fast-low-angle shot (FLASH) imaging (7) (Fig. 1) with the consequence, for longer T1 values, that most of the longitudinal magnetization recovery occurs between saturation and the start of FLASH imaging, with small further recovery in the remaining time before central k-space acquisition. For this reason, the saturation-recovery delay in the Materials and Methods section is defined as the recovery time before imaging starts. The remaining delay before central raw data acquisition is available from the sequence parameters. A simple exponential recovery model based on a single recovery time should be modified according to Larsson et al (7).

This work describes a new approach to the problem of accurate blood and myocardial measurements in high-dose fast-injection perfusion CMR. It compares MPR measurements by the new approach with those made using the dual-bolus technique (3).

MATERIALS AND METHODS

A 1.5-T scanner (Siemens Sonata) with four-channel body array coil and gradient performance up to 40 mT/m and 200 T/m/second was used, with a FLASH prototype sequence (Siemens IDEA pulse sequence programming software) modified to acquire two different resolution images of the same slice within each cardiac cycle. A single-shot image was obtained immediately after the R-wave, which was designed for measurement of LV blood pool signal with only low resolution. Single-shot FLASH was used to acquire 48 × 64 k-cells at field of view (FOV) = 30 × 40 cm, short saturation-recovery time = 3.4 msec (time from the 1-msec nonselective saturation pulse to the first FLASH excitation pulse), short TE = 0.5 msec, TR = 1 msec, linear ky order, no ky offset, and 3900 Hz/pixel, overall aiming for a response covering the peak blood gadolinium concentration. Figure 1c demonstrates how this low-resolution sequence acquires an accurate AIF with high-dose (0.1 mmol/kg) injection of gadolinium. The same 0.16-msec 10° flip angle slice-selective radio frequency (RF) pulse was used for this sequence and for the high-resolution FLASH sequence described below. Neither sequence used a partial echo. The increased possibility of signal dephasing by T2* within the large voxels of this image was partly offset by the very short TE. The effect of T2* was evaluated in vivo by comparing the peak signal with the unsaturated signal level prior to contrast agent injection.

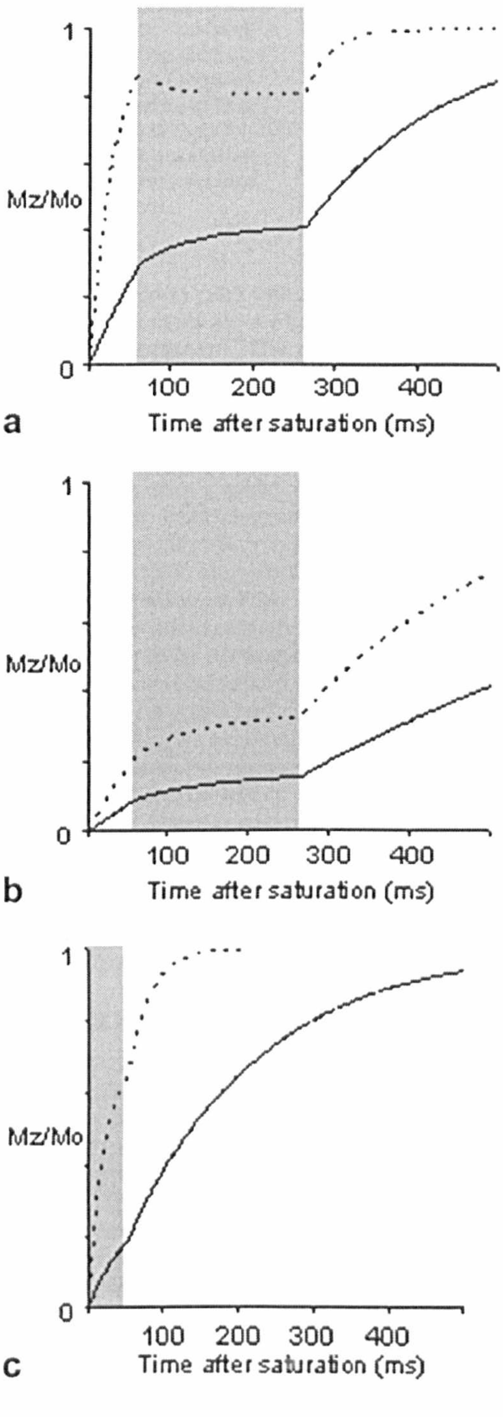

Figure 1. Longitudinal magnetization (Mz) after saturation during gadolinium first pass. The broken line is the recovery curve for blood and the solid line is the recovery curve for myocardium. The magnetization was simulated using sequence parameters and the doses given in the Materials and Methods section, using the following estimated peak contrast agent concentrations: 7 mM high-dose blood, 1 mM myocardium, 0.7 mM low-dose blood, and 0.1 mM myocardium. The gray block shows the time of the FLASH sequence. **a:** Long saturation-recovery-delay high-dose FLASH perfusion; the blood pool (T1 ≈ 30 msec) has fully recovered by the time of image acquisition, meaning that the AIF is clipped. Myocardial SNR is high (T1 ≈ 175 msec). **b:** Long saturation-recovery-delay low-dose FLASH perfusion; the blood pool has not fully recovered (T1 ≈ 250 msec) and the AIF is not clipped. Myocardial SNR is low (T1 ≈ 640 msec) **c:** Short saturation-recovery low-resolution high-dose FLASH perfusion; the blood pool (T1 ≈ 30 msec) has not fully recovered and the AIF is not clipped.

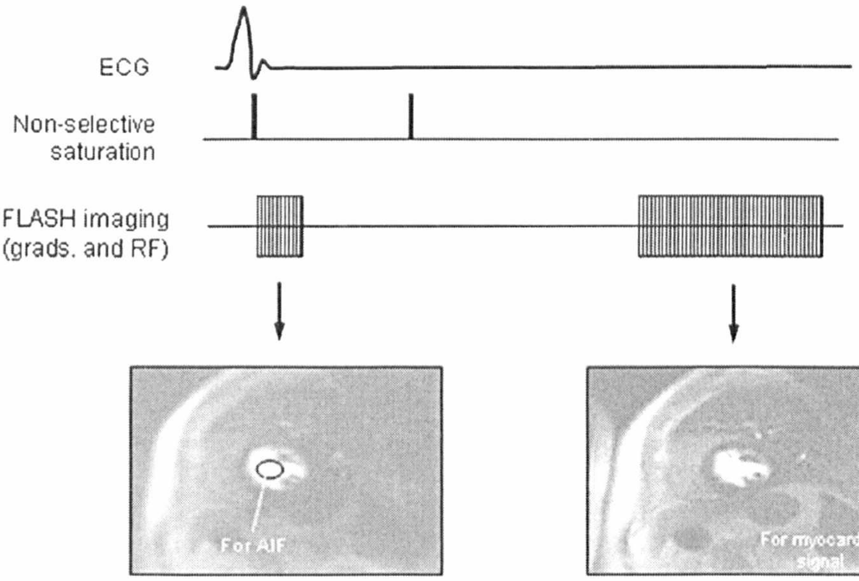

Figure 2. The dual-resolution perfusion sequence method. Immediately following each R-wave the fast low-resolution FLASH sequence is run, to provide the AIF, which is then followed by the high-resolution FLASH sequence to measure the myocardial signal.

The 48-msec blood pool image was followed later in the same cardiac cycle by a FLASH image for myocardial signal measurement. The myocardial imaging sequence was saturation-recovery high-resolution single-shot FLASH acquiring 108 × 256 k-cells in the same plane and FOV as the low-resolution image, with imaging time = 201 msec, long saturation-recovery time = 63.4 msec from the 1-msec nonselective saturation pulse to the first FLASH excitation pulse, TE = 1.2 msec, flip angle = 10°, TR = 1.86 msec, linear ky order, no ky offset, and 1500 Hz/pixel. Due to its long imaging time, the high-resolution FLASH was run in late diastole for minimal cardiac motion (Fig. 2). The long FLASH image was required by an ongoing research protocol to which this work was attached, but a single AIF image per cycle by the new method could apply to multislice myocardial imaging by any sequence. Images were obtained by magnitude reconstruction; both raw data arrays were zero-filled to 128 × 256 before fast Fourier transform. In the low-resolution blood pool images, Gibbs truncation artifacts were seen, but this did not interfere with blood pool analysis. The T1 sensitivities of the low-resolution and high-resolution FLASH sequences were compared using diluted contrast agent in saline in 60-mm-diameter bottles.

Subjects and Protocol

The new method was evaluated in 15 subjects. All patients gave informed consent and the project was approved by the local ethics committee. Volunteers were requested to abstain from caffeine consumption or other adenosine antagonists on the day of scanning. A mid-ventricular short-axis (SA) plane was selected and images were acquired for 50 cardiac cycles, during peripheral injection of the contrast agent through an 18-G cannula at 7 mL/second by power injection (Medrad) into the antecubital fossa. For the dual-bolus approach, the gadolinium contrast agent (Omniscan, Nycomed) was diluted to 0.05 M in saline, resulting in identical fluid volumes of injection for the low-dose (0.01 mmol/kg) and high-dose (0.1 mmol/kg) perfusion runs. After each injection, the lines were flushed with normal saline. The contrast agent was selected for its low viscosity before dilution, so that the two injections should be as similar and rapid as possible. The low dose was injected approximately 2 minutes before the high-dose injection. The power injector had two syringes (designed for contrast agent and saline), which were used for 0.05 and 0.5 M contrast agent in this work. Because no saline flush could be delivered, a fixed 5-mL line volume was preloaded with saline, and an additional 5-mL injection volume to that required for the dose was programmed to ensure complete dose delivery. The subjects were requested to hold their breath from the start of the perfusion sequence for as long as possible. After the rest study, adenosine was infused at 140 μg/minute/kg for four minutes and the full dual-bolus technique was repeated. The time between the rest and stress studies was 20–25 minutes. Each subject received a total of 0.22 mmol/kg of gadolinium contrast agent for this comparison protocol.

During each injection of low-dose (LD) and high-dose (HD) gadolinium, two series of perfusion images were obtained: low resolution with low T1 sensitivity (LT) and high resolution with high T1 sensitivity (HT). Four series of perfusion images were therefore obtained at rest and repeated under stress. The four series (Fig. 3) are identified as follows: low-dose LT (LDLT) and low-dose HT (LDHT); high-dose LT (HDLT) and high-dose HT (HDHT). The LDLT images were not used since virtually no contrast enhancement was present. The first image of each series was acquired without saturation pulses to act as a reference for the full recovery level.

Analysis

For the AIF measurements, a 20-mm-diameter region of interest (ROI) was selected in the LV blood pool during the LDHT, HDLT, and HDHT series. For a total of 30

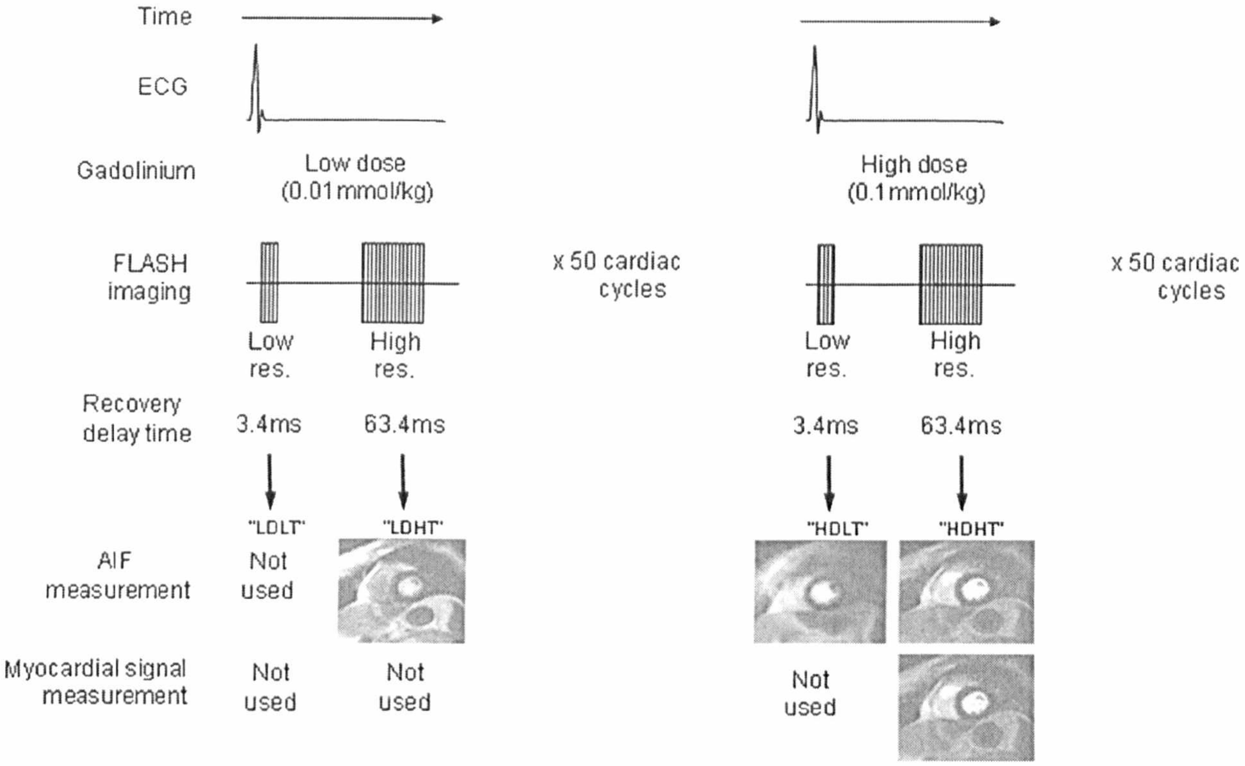

Figure 3. Diagram illustrating the sequences and images acquired. In each subject low-resolution and high-resolution images were acquired with low and high doses of gadolinium at rest and stress. This allowed three measurements of the AIF, only two of which were used in MPR calculations: low-dose low T1 sensitivity (LDLT) (unused), low-dose high T1 sensitivity (LDHT), high-dose low T1 sensitivity (HDLT), and high-dose high T1 sensitivity (HDHT). The HDHT AIF was used only to illustrate the clipping problem.

first-pass perfusion studies, the three versions of the AIF were assessed by plotting their baseline and peak values compared to the reference full recovery level. Only the AIFs from the LDHT and HDLT series were used for MPR analysis by deconvolution. The HDHT AIF was available gratis during the myocardium imaging and was used only to illustrate the clipping problem. For the myocardial signal response, the ROI included the entire myocardium in the HDHT images. The ROIs were moved manually to follow any in-plane respiratory motion.

All of the measurements were performed at rest and stress on each subject. Receiver gain and image reconstruction settings did not change. For each of the two blood input measurement methods with each myocardial region, MPR was calculated using constrained deconvolution with a Fermi function model (6) using in-house designed software (CMRtools, Imperial College, London, UK). A linear dependence of ROI magnitude on contrast agent concentration was assumed, and the baseline ROI value before bolus arrival was subtracted from the input function. The MPR values obtained using the different input functions were compared using the Wilcoxon matched-pairs test.

RESULTS

The Gd phantom results (Fig. 4) showed 90% of full recovery for the low- and high-resolution sequences at 14 and 4 mM concentrations of contrast agent, respectively.

Figure 5 shows one subject's resting examples of the AIFs measured from the HDHT, LDHT, and HDLT images. Peak clipping distorted the HDHT AIF (clipping, arrowed). Normal T1 recovery of blood during the 63.4-msec saturation-recovery time of the LDHT images explained their higher baseline mean ROI before bolus arrival, compared to the 3.4-msec saturation-recovery low-T1-sensitivity HDLT images. For the stress perfusion measurement (Fig. 6), the remaining contrast agent from the rest measurement typically increased

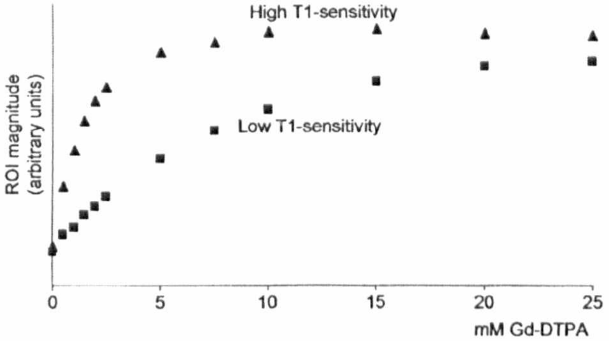

Figure 4. The T1 sensitivity of the two FLASH sequences for contrast agent diluted in saline.

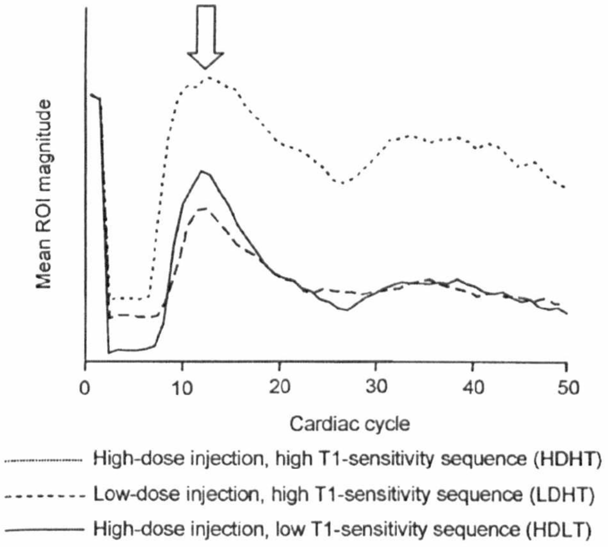

Figure 5. Rest Gd bolus measurements: the saturation pulse was turned off for the first images (see Materials and Methods), giving a full recovery value in the absence of Gd. Each method was scaled by its full recovery value to the same starting value. Full recovery caused clipping of the HDHT response (arrow) at a value higher than the initial value because of the small inherent T1 sensitivity of the FLASH image without a saturation pulse. The LDHT and HDLT responses are not clipped, but they differ in shape because they were obtained during two separate injections at low and high doses, and they differ in amplitude because of their different doses and T1 sensitivities. Except for the higher baseline of the high-T1-sensitivity response caused by the normal blood T1, and its peak clipping, the two AIFs obtained during the high-dose injection are similar on a beat-to-beat time-scale.

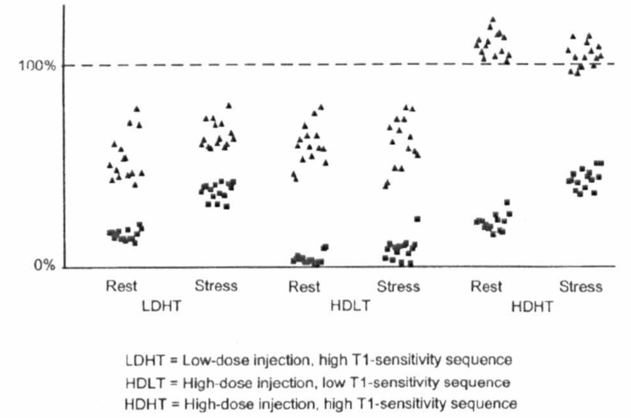

Figure 7. The AIF baseline (square) and peak (triangle) values of ROI mean magnitude, at rest and stress, for all 15 patients with all three methods. The 100% reference level was measured from the images acquired with no saturation pulse.

this baseline and swamped the response to the low-dose injection, whereas the HDLT measurement was relatively unaffected by this problem. Figure 7 shows the AIFs at baseline and peak for the 15 subjects at rest and stress. The 100% reference level was measured from the image acquired with no saturation pulse. In the HDHT image, designed to measure myocardial signal response, full recovery caused the blood signal to reach its maximum at contrast agent concentrations lower than the peak; this peak clipping effect is not to be confused with any maximum pixel value clipping by image reconstruction and display software. At high levels of Gd, this level exceeded the 100% reference due to the T1 sensitivity of the FLASH sequence itself. For the LDHT and HDLT methods, taking each AIF amplitude = peak − baseline, the AIF amplitudes were compared (Fig. 8), where linear regression analyses showed a

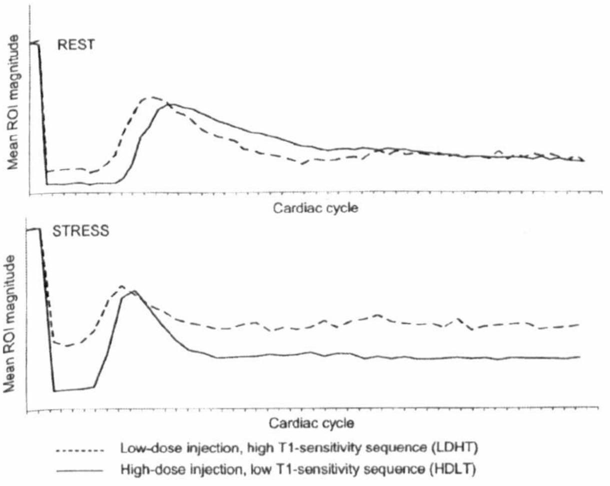

Figure 6. The effect of the remaining contrast agent on AIF measurements in the same subject. The second (stress) LDHT AIF is most affected by the remaining contrast agent from the first (rest) scan.

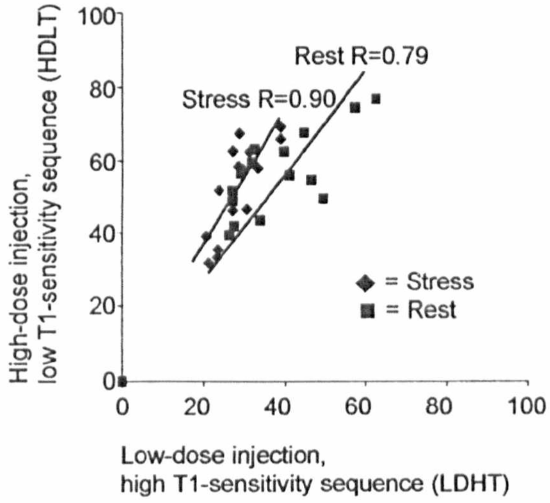

Figure 8. Comparison of the AIF amplitudes (= peak − baseline, from uncalibrated ROI mean magnitudes in the left ventricle) measured by the HDLT and LDHT methods. One hundred percent on the axes represents an amplitude equal to the reference level of Fig. 7. There is a reduction in the AIF amplitude measured by the LDHT method at stress compared to rest. Linear regression fits are shown separately for rest and stress.

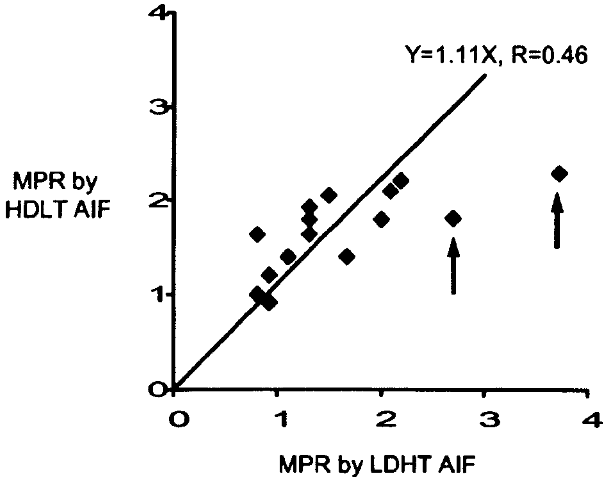

Figure 9. Comparison of MPR values calculated using AIFs measured from the new method HDLT images and the dual-bolus method LDHT images. In two cases (arrowed), the signal from the residual gadolinium from the first rest study was particularly high, and therefore the stress low-dose input was underestimated, resulting in a high LDHT MPR being calculated. Omitting these two points, the results showed an 11% overestimate of the MPR by the HDLT AIF, which has not been explained.

close agreement between the AIF amplitudes by the two methods. A change in the response of the LDHT method between rest and stress is apparent from Fig. 8 (see Discussion section).

For the 15 subjects, the MPR values (Fig. 9) using the LDHT and HDLT methods appear to demonstrate two effects. First, in some subjects the MPR calculated was markedly higher using the LDHT rather than the HDLT for the AIF (arrows). Second, eliminating the two most evident outliers, the MPR was higher using the HDLT AIF method (MPR by HDLT = 1.11 (± 0.07) × MPR by LDHT).

In one extra subject, to examine possible T2* effects during the high-dose first pass, the mean ROI blood signal was measured (Fig. 10) in the ascending aorta using the HDLT sequence alone without saturation pulses. It showed no drop in the signal, unlike the neighboring caval vein. Furthermore, on the HDLT AIFs (Fig. 7) the consistent occurrence of peak bolus amplitudes approximately 50% to 60% of full recovery indicated that no severe T2* loss occurred. Finally, the phantom results (Fig. 4) were obtained from small bottles approximating diastolic LV blood cavity dimensions.

DISCUSSION

Accurate AIF measurement should avoid a concentration and T1 sensitivity arrangement that makes use of near full recovery, where the distorted response to [Gd] effectively clips the peak. The phantom experiments demonstrated how the dual-bolus and dual-T1-sensitivity methods avoid the problem: for an estimated peak concentration of 5 mM, the high-T1-sensitivity sequence exceeded 90% recovery, whereas the low-T1-sensitivity sequence was approximately 50% recovered. The dual-bolus method implemented here at 0.01 mmol/kg would result in an estimated 0.5 mM peak concentration, which drove the high-T1-sensitivity sequence to approximately 40% recovery. Although the HDLT and LDHT methods therefore had similar responses, no attempt was made to make them match precisely.

The reasonable in vivo agreement between the proposed new method and the dual-bolus method suggests that the new approach may be valuable because of the problems of using the dual-bolus approach. In spite of careful efforts to use the same injection volume and viscosity for both low and high doses, differences may still have occurred between the injections of the dual-bolus approach, such as cardiac timing and effects of breath holding on venous return. This concern remains even if the dual-bolus method is performed with more practical ease.

An additional problem with the dual-bolus technique is that the second low-dose bolus, given during adenosine infusion, is prone to being swamped by the residual gadolinium from the rest perfusion study. This effect may explain the two points arrowed on Fig. 9: in these two cases, the level of residual gadolinium from the first rest study remained high at the time of commencing the stress study. The residual Gd had a greater effect on the high-T1-sensitivity image (LDHT image) used for the dual-bolus technique for stress than it had upon the low-T1-sensitivity image (HDLT image). In Fig. 6, the residual Gd elevated the initial LDHT baseline before the arrival of the new Gd bolus injection and shifted the response to the Gd bolus further up the recovery curve than during the rest study. (The simple linear conversion of pixel magnitude to contrast agent concentration after baseline subtraction underestimated the AIF when the pixel magnitudes were higher up the curve toward full recovery.) It appears likely that the stress AIF was therefore sometimes underestimated by the LDHT images, as indicated by Fig. 8. Consequently, the MPR could be overestimated using this AIF, compared to using the AIF from HDLT images. Finally, omitting the points most obviously overestimated by the MPR calculated using the LDHT AIF, the

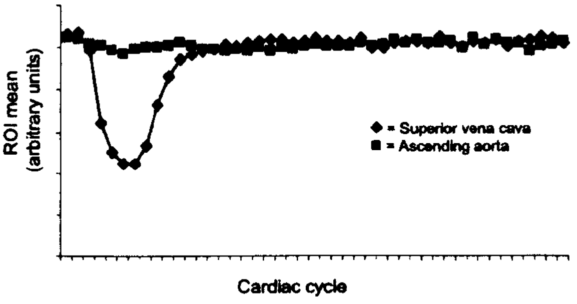

Figure 10. High-dose contrast agent first pass imaged by the low-resolution low-T1-sensitivity sequence (HDLT images). The T2* effect of the peak concentration reduced the signal in the superior vena cava, while no effect was seen in the neighboring ascending aorta.

results showed an 11% overestimate of the MPR by the HDLT AIF. The discrepancy in these results has not been explained. For each purpose (blood and myocardium T1 assessment), there is a limited range of saturation-recovery times that avoid peak AIF clipping while maximizing the sensitivity, and the calibration images obtained without saturation pulses at the start assisted in evaluating this range. We found empirically that 3.4-msec saturation-recovery delay worked well for LV blood pool with the injection parameters used. For the myocardium, a long saturation-recovery delay such as 63.4 msec might allow complete recovery of the vascular volume; however, the vascular volume is a small fraction (13 mL/100 g) of the myocardium, of which mainly the arterial (15%) and capillary (5%) components may contribute to a small multicompartment error in the myocardial mean ROI signal as a function of extracellular contrast agent concentration (7). Further concerns exist about the potential breakdown of the fast-exchange assumption at high concentrations of gadolinium; at the highest gadolinium concentrations in the extravascular extracellular volume (the interstitial fluid), the rate at which water protons are exchanged between extracellular and intracellular volumes may be slow compared to the relaxation time in the interstitial fluid, so that the tissue magnetization now has two separate extravascular components, and its longitudinal magnetization recovery cannot be modeled as a single exponential term (4,8). If this complex issue, where work is still in progress, is assumed to have a negligible impact, a final possible source of distortion must be considered for high-dose high-T1-sensitivity myocardial imaging. If the contrast agent in the interstitial fluid reached such a high concentration that its magnetization recovered fully in 63.4 msec after saturation, this method would have introduced myocardial response clipping; however, the initial calibration images with the saturation switched off proved that this limit was not reached even at the peak stress perfusion.

At 3.4-msec saturation-recovery delay, longitudinal magnetization in some regions of the HDLT images was partially saturated, and in other regions it had been driven negative and not yet recovered through zero. This effect was observed prior to the contrast agent injection, and the described regions could be shifted by changing the transmitter calibration—it was thought due to B_1 nonuniformity and inherent sensitivity of saturation to B_1 calibration (9). The nonuniform saturation was more apparent using the short saturation-recovery delay of 3.4 msec than the long recovery delay, when all relevant regions of the FOV had recovered through zero. The spatial effectiveness of the saturation varied between subjects, varying with tissue absorption and B1 calibration. In extreme cases the relationship between ROI magnitude and contrast agent concentration in the high-dose low-T1-sensitivity image was distorted (by a zero-crossing having lost the sign of the magnitude).

In conclusion, although the use of short saturation-recovery delay to reduce peak distortion of the AIF is well known, and the overestimation compared to the dual-bolus method in this work could not be explained, the proposed new method provided this data during the same first-pass of gadolinium as a highly sensitive high-resolution myocardial measurement. The new method may also apply to normalized upslope analysis. For multislice imaging, one AIF image by the new method may replace AIFs from the myocardial slices, where peak clipping may still occur at lower T1 sensitivity than in this work. The separate blood imaging sequence also provides new flexibility, e.g., the position of the separate blood measurement (10) or no longer needing a bright blood signal in the myocardial image.

REFERENCES

1. Neimatallah MA, Chenevert TL, Carlos RC, et al. Subclavian MR arteriography: reduction of susceptibility artefact with short echo time and dilute gadopentetate dimeglumine. Radiology 2000;217: 581-586.
2. Bellamy DD, Pereira RS, McKenzie CA, et al. Gd-DTPA bolus tracking in the myocardium using T1 fast acquisition relaxation mapping (T1 FARM). Magn Reson Med 2001;46:555–564.
3. Christian TF, Aletras AH, Balaban RS, Arai AE. Absolute quantification of high contrast dose perfusion imaging can be repeated at two hours despite elevated baseline T_1 relaxivity [Abstract]. In: Proceedings of the 5th Annual Meeting of the Society for Cardiovascular Magnetic Resonance, Florida, 2002. p 93.
4. Larsson HBW, Rosenbaum S, Fritz-Hansen T. Quantification of the effect of water exchange in dynamic contrast MRI perfusion measurements in the brain and heart. Magn Reson Med 2001;46:272–281.
5. Ridgway JP, Radjenovic A, Higgins DM, Kassner A, Sivananthan UM. A fast, multiple-slice, multiple-point method for the determination of T_1 relaxation time for use in quantitative myocardial perfusion measurement [Abstract]. In: Proceedings of the 9th Annual Meeting of ISMRM, Glasgow, Scotland, 2001. p 1905.
6. Jerosch-Herold M, Wilke N, Stillman AE, Wilson RF. Magnetic resonance quantification of the myocardial perfusion reserve with a Fermi function model for constrained deconvolution. Med Phys 1998;25:73–84.
7. Larsson HBW, Fritz-Hansen T, Rostrup E, Sondergaard L, Ring P, Henriksen O. Myocardial perfusion modeling using MRI. Magn Reson Med 1996;35:716-726.
8. Donahue KM, Burstein D, Manning WJ, Gray ML. Studies of Gd-DTPA relaxivity and proton exchange rates in tissue. Magn Reson Med 1994;32:66-76.
9. Venkatesan R, Lin W, Haacke EM. Accurate determination of spin-density and T1 in the presence of RF-field inhomogeneities and flip-angle miscalibration. Magn Reson Med 1998;40:592-602.
10. Schmitt M, Mohrs OK, Petersen SE, et al. Systematic investigation of the influence of arterial input function on quantitative evaluation of myocardial blood flow with contrast enhanced MRI [Abstract]. In: Proceedings of the 10th Annual Meeting of ISMRM, Honolulu, 2002. p 1606.

References

1 Huang SC, Schwaiger M, Carson RE, Carson J, Hansen H, Selin C, Hoffman EJ, MacDonald N, Schelbert HR, Phelps ME. Quantitative measurement of myocardial blood flow with oxygen-15 water and positron computed tomography: an assessment of potential and problems. *J Nucl Med* 1985 Jun;26(6):616-25.

2 Bol A, Melin JA, Vanoverschelde JL, Baudhuin T, Vogelaers D, De Pauw M, Michel C, Luxen A, Labar D, Cogneau M, et al. Direct comparison of [13N] ammonia and [15O] water estimates of perfusion with quantification of regional blood flow by microspheres. *Circulation* 1993 Feb;87(2):512-25.

3 Lammertsma AA, De Silva R, Araujo LI, Jones T. Measurement of regional myocardial blood flow using C15O2 and positron emission tomography: comparison of tracer models. *Clin Phys Physiol Meas.* 1992 Feb; 13(1): 1-20.

4 Nitzsche EU, Choi Y, Czernin J, Hoh CK, Huang SC, Schelbert HR. Noninvasive quantification of myocardial blood flow in humans. A direct comparison of the [13N]ammonia and the [15O]water techniques. *Circulation.* 1996 Jun 1;93(11):2000-6.

5 Sieswerda GT, Yang L, Boo MB, Kamp O. Real-time perfusion imaging: a new echocardiographic technique for simultaneous evaluation of myocardial perfusion and contraction. *Echocardiography.* 2003 Aug; 20(6): 545-55.

6 Peltier M, Vancraeynest D, Pasquet A, Ay T, Roelants V, D'hondt AM, Melin JA, Vanoverschelde JL. Assessment of the physiologic significance of coronary disease with dipyridamole real-time myocardial contrast echocardiography. Comparison with technetium-99m sestamibi single-photon emission computed tomography and quantitative coronary angiography. *J Am Coll Cardiol.* 2004 Jan 21; 43(2): 257-64.

7 Wilke N, Simm C, Zhang J, Ellermann J, Ya X, Merkle H, Path G, Ludemann H, Bache RJ, Ugurbil K. Contrast-enhanced first pass myocardial perfusion imaging: correlation between myocardial blood flow in dogs at rest and during hyperemia. *Magn Reson Med.* 1993 Apr;29(4):485-97.

8 Tsekos NV, Zhang Y, Merkle H, Wilke N, Jerosch-Herold M, Stillman A, Ugurbil K. Fast anatomical imaging of the heart and assessment of myocardial perfusion with arrhythmia insensitive magnetization preparation. *Magn Reson Med.* 1995 Oct;34(4):530-6.

9 Wilke N, Jerosch-Herold M, Wang Y, Huang Y, Christensen BV, Stillman AE, Ugurbil K, McDonald K, Wilson RF. Myocardial perfusion reserve: assessment with multisection, quantitative, first-pass MR imaging. *Radiology.* 1997 Aug;204(2):373-84.

10 Schreiber WG, Schmitt M, Kalden P, Mohrs OK, Kreitner KF, Thelen M. Dynamic contrast-enhanced myocardial perfusion imaging using saturation-prepared TrueFISP. *J Magn Reson Imaging.* 2002 Dec;16(6):641-52.

11 Edelman RR, Li W. Contrast-enhanced echo-planar MR imaging of myocardial perfusion: preliminary study in humans. *Radiology.* 1994 Mar;190(3):771-7.

12 Schwitter J, Debatin JF, von Schulthess GK, McKinnon GC. Normal myocardial perfusion assessed with multishot echo-planar imaging. *Magn Reson Med.* 1997 Jan;37(1):140-7.

13 Wilke N, Kroll K, Merkle H, Wang Y, Ishibashi Y, Xu Y, Zhang J, Jerosch-Herold M, Muhler A, Stillman AE, *et al.* Regional myocardial blood volume and flow: first-pass MR imaging with polylysine-Gd-DTPA. *J Magn Reson Imaging.* 1995 Mar-Apr; 5(2): 227-37.

14 Larsson HB, Fritz-Hansen T, Rostrup E, Sondergaard L, Ring P, Henriksen O. Myocardial perfusion modeling using MRI. *Magn Reson Med.* 1996 May; 35(5): 716-26.

15 Jerosch-Herold M, Wilke N, Stillman AE. Magnetic resonance quantification of the myocardial perfusion reserve with a Fermi function model for constrained deconvolution. *Med Phys.* 1998 Jan; 25(1): 73-84.

16 Manning WJ, Atkinson DJ, Grossman W, Paulin S, Edelman RR. First-pass nuclear magnetic resonance imaging studies using gadolinium-DTPA in patients with coronary artery disease. J *Am Coll Cardiol.* 1991 Oct; 18(4): 959-65.

17 American Heart Association. Heart Disease and Stroke Statistics — 2004 Update. Dallas, Tex.: *American Heart Association*; 2003.

18 Marks AR, Marx SO. Cardiac contraction and relaxation: Molecular and cellular physiology. *Essential Cardiology: Principles and Practice*, (2001), 22-37.

19 Scanlon PJ, Faxon DP, Audet AM, Carabello B, Dehmer GJ, Eagle KA, Legako RD, Leon DF, Murray JA, Nissen SE, Pepine CJ, Watson RM, Ritchie JL, Gibbons RJ, Cheitlin MD, Gardner TJ, Garson A Jr, Russell RO Jr, Ryan TJ, Smith SC Jr. ACC/AHA guidelines for coronary angiography. A report of the American College of Cardiology/American Heart Association Task Force on practice guidelines (Committee on Coronary Angiography). Developed in collaboration with the Society for Cardiac Angiography and Interventions. *J Am Coll Cardiol.* 1999 May;33(6):1756-824.

20 Schaper W, Binz K, Sass S, Winkler B. Influence of collateral blood flow and of variations in MV02 on tissue-ATP content in ischemic and infracted myocardium. *J Mol Cell Cardiol,* 1987; 19: 19-37.

21 Fliss H, Gattinger D. Apoptosis in ischemic and reperfused rat myocardium. *Circ Res* 1996 Nov;79(5):949-56.

22 Majno G, Joris I. Cell, Tissues, and Disease: principles of general pathology, (1996), Chap 5, 175-227.

23 Majno G, Joris I. Cell, Tissues, and Disease: principles of general pathology, (1996), Chap 24, 675-711.

24 Cerqueira MD, Weissman NJ, Dilsizian V, Jacobs AK, Kaul S, Laskey WK, Pennell DJ, Rumberger JA, Ryan T, Verani MS. Standardized myocardial segmentation and nomenclature for tomographic imaging of the heart: a statement for healthcare professionals from the Cardiac Imaging Committee of the Council on Clinical Cardiology of the American Heart Association. *Circulation.* 2002 Jan 29;105(4):539-42.

25 Jain D, Zaret BL. Coronary blood flow and myocardial ischemia, Essential Cardiology: Principles and Practice, (2001), 422-436.

26 Wilke NM, Jerosch-Herold M, Zenovich A, Stillman AE. Magnetic resonance first-pass myocardial perfusion imaging: clinical validation and future applications. *J Magn Reson Imaging* 1999 Nov;10(5):676-85.

27 Jerosch-Herold M, Hu X, Murthy NS, Seethamraju RT. Time delay for arrival of MR contrast agent in collateral-dependent myocardium. *IEEE Trans Med Imaging.* 2004 Jul;23(7):881-90.

28 Fuchs S, Baffour R, Zhou YF, Shou M, Pierre A, Tio FO, Weissman NJ, Leon MB, Epstein SE, Kornowski R. Transendocardial delivery of autologous bone marrow enhances collateral perfusion and regional function in pigs with chronic experimental myocardial ischemia. *J Am Coll Cardiol* 2001 May;37(6):1726-32.

29 Rajanayagam MA, Shou M, Thirumurti V, Lazarous DF, Quyyumi AA, Goncalves L, Stiber J, Epstein SE, Unger EF. Intracoronary basic fibroblast growth factor enhances myocardial collateral perfusion in dogs. *J Am Coll Cardiol* 2000 Feb;35(2):519-26.

30 Gibson RS, Watson DD, Craddock GB, Crampton RS, Kaiser DL, Denny MJ, Beller GA. Prediction of cardiac events after uncomplicated myocardial infarction: A prospective study comparing predischarge exercise thallium-201 scintigraphy and coronary angiography. *Circulation* 1983 Aug;68(2):321-36.

31 The Multicentre Postinfarction Research Group. Risk stratification and survival after myocardial infarction. *N Engl J Med* 1983; 309: 331-6.

32 Ladenheim ML, Kotler TS, Pollock BH, Berman DS, Diamond GA. Incremental prognostic power of clinical history, exercise electrocardiography and myocardial perfusion scintigraphy in suspected coronary artery disease. *Am J Cardiol* 1987; 59: 270-7.

33 Kaul S, Lilly DR, Gascho JA, Watson DD, Gibson RS, Oliner CA, Ryan JM, Beller GA. Prognostic utility of the exercise thallium-201 test in ambulatory patients with chest pain: comparison with cardiac catheterisation. *Circulation* 1988 Apr;77(4):745-58.

34 Machecourt J, Longere P, Fagret D, Vanzetto G, Wolf JE, Polidori C, Comet M, Denis B. Prognostic value of thallium-201 single-photon emission computed tomographic myocardial perfusion imaging according to extent of myocardial defect. Study in 1,926 patients with follow-up at 33 months. *J Am Coll Cardiol* 1994 Apr;23(5):1096-106.

35 Hachamovitch R, Berman DS, Shaw LJ, Kiat H, Cohen I, Cabico JA, Friedman J, Diamond GA. Incremental prognostic value of myocardial perfusion single photon emission computed tomography for the prediction of cardiac death. Differential stratification for risk of cardiac death and myocardial infarction. *Circulation* 1998 Feb 17;97(6):535-43.

36 Verani MS, Mahmarian JJ, Hixson JB, Boyce TM, Staudacher RA. Diagnosis of coronary arteery disease by controlled coronary vasodilation with adensoine and thallium-201 scintigraphy in patients unable to exercise. *Circulation* 1990; 82(1): 80-7.

37 DePuey EG. How to detect and avoid myocardial perfusion SPECT artifacts. *J Nucl Med.* 1994 Apr;35(4):699-702.

38 DePuey EG, Garcia EV. Optimal specificity of thallium-201 SPECT through recognition of imaging artifacts. *J Nucl Med.* 1989 Apr;30(4):441-9.

39 Taillefer R, DePuey EG, Udelson JE, Beller GA, Benjamin C, Gagnon A. Comparison between the end-diastolic images and the summed images of gated 99mTc-sestamibi SPECT perfusion study in detection of coronary artery disease in women. *J Nucl Cardiol.* 1999 Mar-Apr;6(2):169-76.

40 Tan P, Bailey DL, Meikle SR, Eberl S, Fulton RR, Hutton BF. A scanning line source for simultaneous emission and transmission measurements in SPECT. *J Nucl Med.* 1993 Oct;34(10):1752-60.

41 Hendel RC, Berman DS, Cullom SJ, Follansbee W, Heller GV, Kiat H, Groch MW, Mahmarian JJ. Multicenter clinical trial to evaluate the efficacy of correction for photon attenuation and scatter in SPECT myocardial perfusion imaging. *Circulation.* 1999 Jun 1;99(21):2742-9.

42 Camici PG. Positron emission tomography and myocardial imaging. *Heart.* 2000 Apr;83(4):475-80.

43 Bergmann SR, Herrero P, Markham J, Weinheimer CJ, Walsh MN. Noninvasive quantitation of myocardial blood flow in human subjects with oxygen-15-labeled water and positron emission tomography. *J Am Coll Cardiol* 1989 Sep;14(3):639-52.

44 Iida H, Kanno I, Takahashi A, Miura S, Murakami M, Takahashi K, Ono Y, Shishido F, Inugami A, Tomura N, et al. Measurement of absolute myocardial blood flow with H215O and dynamic positron-emission tomography. Strategy for quantification in relation to the partial-volume effect. *Circulation* 1988 Jul;78(1):104-15.

45 Araujo LI, Lammertsma AA, Rhodes CG, McFalls EO, Iida H, Rechavia E, Galassi A, De Silva R, Jones T, Maseri A. Noninvasive quantitation of regional myocardial blood flow in cornary artery disease with oxygen-15-labeled carbon dioxide inhalation and positron emission tomography. *Circulation* 1991 Mar;83(3):875-85.

46 Iida H, Takahashi A, Tamura Y, Ono Y, Lammertsma AA. Myocardial blood flow: comparison of oxygen-15-water bolus injection, slow infusion and oxygen-15-carbon dioxide slow inhalation. *J Nucl Med* 1995 Jan;36(1):78-85.

47 Hermansen F, Ashburner J, Spinks TJ, Kooner JS, Camici P G , Lammertsma AA. Generation of myocardial factor images directly from the dynamic oxygen-15-water scan without use of an oxygen-15-carbon monoxide blood-pool scan. *J Nucl Med* 1998 Oct;39(10):1696-702.

48 Hermansen F, Rosen SD, Fath-Ordoubadi F, Kooner JS, Clark JC, Camici PG, Lammertsma AA. Measurement of myocardial blood flow with oxygen-15 labelled water: comparison of different administration protocols. *Eur J Nucl Med* 1998 Jul;25(7):751-9.

49 Kaul S, Kelly P, Oliner JD, Glasheen WP, Keller MW, Watson DD. Assessment of regional myocardial blood flow with myocardial contrast two-dimensional echocardiography. *J Am Coll Cardiol* 1989 Feb;13(2):468-82.

50 Ito H, Tomooka T, Sakai N, Yu H, Higashino Y, Fujii K, Masuyama T, Kitabatake A, Minamino T. Lack of myocardial perfusion immediately after successful thrombolysis a predictor of poor recovery of left ventricular function in anterior myocardial infarction. *Circulation* 1992 May;85(5):1699-705.

51 Villanueva FS, Glasheen WP, Sklenar J, Kaul S. Characterization of spatial patterns of flow within the reperfused myocardium by myocardial contrast echocardiography. *Circulation* 1993 Dec;88(6):2596-606.

52 Ragosta M, Camarano G, Kaul S, Powers ER, Sarembock IJ, Gimple LW. Microvascular integrity indicates myocellular viability in patients with recent myocardial infarction. New insights using myocardial contrast echocardiography. *Circulation* 1994 Jun;89(6):2562-9.

53 Meza MF, Kates MA, Barbee RW, Revall S, Perry B, Murgo JP, Cheirif J. Combination of dobutamine and myocardial contrast echocardiography to differentiate postischemic from infarcted myocardium. *J Am Coll Cardiol* 1997 Apr;29(5):974-84.

54 Kaul S, Senior R, Dittrich H, Raval U, Khattar R, Lahiri A. Detection of coronary artery disease with myocardial contrast echocardiography: comparison with 99m Tc-sestamibi single-photon emission computed tomography. *Circulation* 1997 Aug 5;96(3):785-92.

55 Jucquois I, Nihoyannopoulos P, D'Hondt AM, Roelants V, Robert A, Melin JA, Glass D, Vanoverschelde JL. Comparison of myocardial contrast echocrdiography with NC100100 and Tc-99m sestamibi single photon emission computed tomography for detection of resting

myocardial perfusion abnormalities in patients with previous myocardial infarction. *Heart* 2000 May;83(5):518-24.

56 Wei K, Jayaweera AR, Firoozan S, Linka A, Skyba DM, Kaul S. Quantification of myocardial blood flow with ultrasound-induced destruction of microbubbles administered as a constant venous infusion. *Circulation* 1998 Feb 10;97(5):473-83.

57 Ohmori K, Cotter B, Leistad E, Bhargava V, Wolf PL, Mizushige K, DeMaria AN. Assessment of Myocardial Postreperfusion Viability by Intravenous Myocardial Contrast Echocardiography. Analysis of the Intensity and Texture of Opacification. *Circulation* 2001 Apr 17;103(15):2021-7.

58 Wei K, Ragosta M, Thorpe J, Coggins M, Moos S, Kaul S. Noninvasive quantification of coronary blood flow reserve in humans using myocardial contrast echocardiography. *Circulation.* 2001 May 29;103(21):2560-5.

59 Lafitte S, Masugata H, Peters B, Togni M, Strachan M, Yao B, Kwan OL, DeMaria AN. Accuracy and reproducibility of coronary flow rate assessment by real-time contrast echocardiography: in vitro and in vivo studies. *J Am Soc Echocardiogr.* 2001 Oct;14(10):1010-9.

60 Leong-Poi H, Le E, Rim SJ, Sakuma T, Kaul S, Wei K. Quantification of myocardial perfusion and determination of coronary stenosis severity during hyperemia using real-time myocardial contrast echocardiography. *J Am Soc Echocardiogr.* 2001 Dec;14(12):1173-82.

61 Ludman PF, Coats AJ, Burger P, Yang GZ, Poole-Wilson PA, Underwood SR, Rees RS. Validation of measurement of regional myocardial perfusion in humans by ultrafast x-ray computed tomography. *Am J Card Imaging* 1993 Dec;7(4):267-79.

62 Gould RG. Perfusion quantification by ultrafast computed tomography. *Invest Radiol* 1992 Dec;27 Suppl 2:S18-21.

63 Rumberger JA, Bell MR. Measurement of myocardial perfusion and cardiac output using intravenous injection methods by ultrafast (cine) computed tomography. *Invest Radiol* 1992 Dec;27 Suppl 2:S40-6.

64 Wolfkiel CJ, Ferguson JL, Chomka EV, Law WR, Labin IN, Tenzer ML, Booker M, Brundage BH. Measurement of myocardial blood flow by ultrafast computed tomography. *Circulation* 1987 Dec;76(6):1262-73.

65 Schmermund A, Bell MR, Lerman LO, Ritman EL, Rumberger JA. Quantitative Evaluation of Regional Myocardial Perfusion Using Fast X-Ray Computed Tomography. *Herz* 1997 Feb;22(1):29-39.

66 Rumberger JA, Feiring AJ, Lipton MJ, Higgins CB, Ell SR, Marcus ML. Use of ultrafast computed tomography to quantitate regional myocardial perfusion: a preliminary report. *J Am Coll Cardiol* 1987 Jan;9(1):59-69.

67 Rodriguez-Porcel M, Lerman A, Best PJ, Krier JD, Napoli C, Lerman LO. Hypercholesterolemia impairs myocardial perfusion and permeability: role of oxidative stress and endogenous scavenging activity. *J Am Coll Cardiol* 2001 Feb;37(2):608-15.

68 Da Silva AJ, Tang HR, Wong KH, Wu MC, Dae MW, Hasegawa BH. Absolute quantification of regional myocardial uptake of Tc-sestamibi with SPECT: experimental validation in a porcine model. *J Nucl Med* 2001 May;42(5):772-9.

69 Da Silva AJ, Tang HR, Wong KH, Wu MC, Dae MW, Hasegawa BH. Absolute *in vivo* quantitation of myocardial activity. *IEEE Trans on Nuc Sci*, Volume 47, Issue 3 III, June 2000, Pages 1093-1098.

70 Budoff MJ, Gillespie R, Georgiou D, Narahara KA, French WJ, Mena I, Brundage BH. Comparison of exercise electron beam computed tomography and sestamibi in the evaluation of coronary artery disease. *Am J Cardiol* 1998 Mar 15;81(6):682-7

71 Wagner A, Mahrholdt H, Holly TA, Elliott MD, Regenfus M, Parker M, Klocke FJ, Bonow RO, Kim RJ, Judd RM. Contrast-enhanced MRI and routine single photon emission computed tomography (SPECT) perfusion imaging for detection of subendocardial myocardial infarcts: an imaging study. *Lancet.* 2003 Feb 1;361(9355):374-9.

72 Panting JR, Gatehouse PD, Yang GZ, Grothues F, Firmin DN, Collins P, Pennell DJ. Abnormal subendocardial perfusion in cardiac syndrome X detected by cardiovascular magnetic resonance imaging. *N Engl J Med.* 2002 Jun 20;346(25):1948-53.

73 Wilke N, Jerosch-Herold M, Stillman AE, Kroll K, Tsekos N, Merkle H, Parrish T, Hu X, Wang Y, Bassingthwaighte J, et al. Concepts of myocardial perfusion imaging in magnetic resonance imaging. *Magn Reson Q* 1994 Dec;10(4):249-86.

74 Cullen JH, Horsfield MA, Reek CR, Cherryman GR, Barnett DB, Samani NJ. A myocardial perfusion reserve index in humans using first_pass contrast_enhanced magnetic resonance imaging. *J Am Coll Cardiol* 1999 Apr;33(5):1386-94.

75 Keijer JT, van Rossum AC, van Eenige MJ, Karreman AJ, Hofman MB, Valk J, Visser CA. Semiquantitation of regional myocardial blood flow in normal human subjects by first_pass magnetic resonance imaging. *Am Heart J* 1995 Oct;130(4):893-901.

76 Beache GM, Kulke SF, Kantor HL, Niemi P, Campbell TA, Chesler DA, Gewirtz H, Rosen BR, Brady TJ, Weisskoff RM. Imaging perfusion deficits in ischemic heart disease with susceptibility-enhanced T2-weighted MRI: preliminary human studies. *Magn Reson Imaging* 1998;16(1):19-27.

77 Ding S, Wolff SD, Epstein FH. Improved coverage in dynamic contrast-enhanced cardiac MRI using interleaved gradient-echo EPI. *Magn Reson Med* 1998 Apr;39(4):514-9.

78 Larsson HBW, Stubgaard M, Søndergaard L, Henriksen O. *In vivo* quantification of the unidirectional influx constant for Gd-DTPA diffusion across the myocardial capillaries with MR imaging. *J Magn Reson Imaging* 1994 May-Jun;4(3):433-40.

79 Dendale P, Franken PR, Block P, Pratikakis Y, De Roos A. Contrast enhanced and functional magnetic resonance imaging for the detection of viable myocardium after infarction. *Am Heart* J 1998 May;135(5 Pt 1):875-80.

80 Kim RJ, Wu E, Rafael A, Chen EL, Parker MA, Simonetti O, Klocke FJ, Bonow RO, Judd RM. The use of contrast enhanced magnetic resonance imaging to identify reversible myocardial dysfunction. *N Engl J Med* 2000 Nov 16;343(20):1445-53.

81 Wendland MF, Saeed M, Lauerma K, de Crespigny A, Moseley ME, Higgins CB. Endogenous susceptibility contrast in myocardium during apnea measured using gradient recalled echo planar imaging. *Magn Reson Med* 1993 Feb;29(2):273-6.

82 Atalay MK, Forder JR, Chacko VP, Kawamoto S, Zerhouni EA. Oxygenation in the rabbit myocardium: assessment with susceptibility-dependent MR imaging. *Radiology* 1993 Dec;189(3):759-64.

83 Balaban RS, Taylor JF, Turner R. Effect of cardiac flow on gradient recalled echo images of the canine heart. *NMR Biomed* 1994 Mar;7(1-2):89-95.

84 Niemi P, Poncelet BP, Kwong KK, Weisskoff RM, Rosen BR, Brady TJ, Kantor HL. Myocardial intensity changes associated with flow stimulation in blood oxygenation sensitive magnetic resonance imaging. *Magn Reson Med* 1996 Jul;36(1):78-82.

85 Li D, Dhawale P, Rubin PJ, Haacke EM, Gropler RJ. Myocardial signal response to dipyridamole and dobutamine: demonstration of the BOLD effect using a double-echo gradient-echo sequence. *Magn Reson Med* 1996 Jul;36(1):16-20.

86 Li D, Oellerich WF, Beck G, Gropler RJ. Assessment of myocardial response to pharmacologic interventions using an improved MR imaging technique to estimate T2 values. *Am J Roentgenol* 1999 Jan;172(1):141-5.

87 Wacker CM, Bock M, Hartlep AW, Beck G, van Kaick G, Ertl G, Bauer WR, Schad LR. Changes in myocardial oxygenation and perfusion under pharmacological stress with dipyridamole: assessment using T*2 and T1 measurements. *Magn Reson Med* 1999 Apr;41(4):686-95.

88 Atalay MK, Reeder SB, Zerhouni EA, Forder JR. Blood oxygenation dependence of T1 and T2 in the isolated, perfused rabbit heart at 4.7T. *Magn Reson Med* 1995 Oct;34(4):623-7.

89 Reeder SB, Holmes AA, McVeigh ER, Forder JR. Simultaneous noninvasive determination of regional myocardial perfusion and oxygen content in rabbits: toward direct measurement of myocardial oxygen consumption at MR imaging. *Radiology* 1999 Sep;212(3):739-47.

90 Wright KB, Klocke FJ, Deshpande VS, Zheng J, Harris KR, Tang R, Finn JP, Li D. Assessment of regional differences in myocardial blood flow using T2-weighted 3D BOLD imaging. *Magn Reson Med* 2001 Sep;46(3):573-8

91 Klein C, Nekolla SG, Bengel FM, Momose M, Sammer A, Haas F, Schnackenburg B, Delius W, Mudra H, Wolfram D, Schwaiger M. Assessment of myocardial viability with contrast-enhanced magnetic resonance imaging: comparison with positron emission tomography. *Circulation.* 2002 Jan 15;105(2):162-7.

92 Crnac J, Schmidt MC, Theissen P, Sechtem U. Assessment of myocardial perfusion by magnetic resonance imaging. *Herz* 1997 Feb;22(1):16-28.

93 Frahm J, Haase A, Matthaei D. Rapid NMR imaging of dynamic processes using the FLASH technique. *Magn Reson Med* 1986 Apr;3(2):321-7.

94 Haase A, Matthaei D, Hanicke W, Frahm J. Dynamic digital subtraction imaging using fast low-angle shot MR movie sequence. *Radiology* 1986 Aug;160(2):537-41

95 McKinnon GC. Ultrafast interleaved gradient-echo-planar imaging on a standard scanner. *Magn Reson Med.* 1993 Nov;30(5):609-16.

96 Epstein FH, Wolff SD, Arai AE. Segmented *k*-space fast cardiac imaging using an echo-train readout. *Magn Reson Med.* 1999 Mar;41(3):609-13.

97 Reeder SB, Atalar E, Faranesh AZ, McVeigh ER. Multi-echo segmented *k*-space imaging: an optimized hybrid sequence for ultrafast cardiac imaging. *Magn Reson Med.* 1999 Feb;41(2):375-85.

98 Epstein FH, Arai AE. Optimization of fast cardiac imaging using an echo-train readout. *J Magn Reson Imaging.* 2000 Feb;11(2):75-80.

99 Epstein FH, London JF, Peters DC, Goncalves LM, Agyeman K, Taylor J, Balaban RS, Arai AE. Multislice first-pass cardiac perfusion MRI: validation in a model of myocardial infarction. *Magn Reson Med.* 2002 Mar;47(3):482-91.

100 Schwitter J, Nanz D, Kneifel S, Bertschinger K, Buchi M, Knusel PR, Marincek B, Luscher TF, von Schulthess GK. Assessment of myocardial perfusion in coronary artery disease by magnetic resonance: a comparison with positron emission tomography and coronary angiography. *Circulation.* 2001 May 8;103(18):2230-5.

101 Oppelt A, Graumann R, Barfuss H, Fischer H, Hartl W, Schajor W. FISP: eine neue schnelle Pulssequenz für die Kernspintomographie. *Electromedica* 1986; 54:15--18.

102 Barkhausen J, Ruehm SG, Goyen M, Buck T, Laub G, Debatin JF. MR evaluation of ventricular function: true fast imaging with steady-state precession versus fast low-angle shot cine MR imaging: feasibility study. *Radiology.* 2001 Apr;219(1):264-9.

103 Zhang Q, Crowe ME, Chung YC, Simonetti OP. Acceleration Techniques Combined with TrueFISP for Rapid First-Pass Myocardial Perfusion Imaging. *Proc. Intl. Soc. Mag. Reson. Med. 11* (2003). 1665.

104 Xiang QS, Henkelman RM. *K*-space description for MR imaging of dynamic objects. *Magn Reson Med.* 1993 Mar;29(3):422-8.

105 McGibney G, Smith MR, Nichols ST, Crawley A. Quantitative evaluation of several partial Fourier reconstruction algorithms used in MRI. *Magn Reson Med.* 1993 Jul;30(1):51-9.

106 van Vaals JJ, Brummer ME, Dixon WT, Tuithof HH, Engels H, Nelson RC, Gerety BM, Chezmar JL, den Boer JA. "Keyhole" method for accelerating imaging of contrast agent uptake. *J Magn Reson Imaging.* 1993 Jul-Aug;3(4):671-5.

107 Jones RA, Haraldseth O, Muller TB, Rinck PA, Oksendal AN. *k*-space substitution: a novel dynamic imaging technique. *Magn Reson Med.* 1993 Jun;29(6):830-4.

108 Bishop JE, Santyr GE, Kelcz F, Plewes DB. Limitations of the keyhole technique for quantitative dynamic contrast-enhanced breast MRI. *J Magn Reson Imaging.* 1997 Jul-Aug;7(4):716-23.

109 Liang ZP. Lauterbur PC. An efficient method for dynamic magnetic resonance imaging. *IEEE Trans Med Imaging.* 1994 Dec;13(4):677-86.

110 Zientara GP, Panych LP, Jolesz FA. Dynamically adaptive MRI with encoding by singular value decomposition. *Magn Reson Med.* 1994 Aug;32(2):268-74.

111 Panych LP, Oesterle C, Zientara GP, Hennig J. Implementation of a fast gradient-echo SVD encoding technique for dynamic imaging. *Magn Reson Med.* 1996 Apr;35(4):554-62.

112 Doyle M, Walsh EG, Blackwell GG, Pohost GM. Block regional interpolation scheme for *k*-space (BRISK): a rapid cardiac imaging technique. *Magn Reson Med.* 1995 Feb;33(2):163-70.

113 Madore B, Glover GH, Pelc NJ. Unaliasing by fourier-encoding the overlaps using the temporal dimension (UNFOLD), applied to cardiac imaging and fMRI. *Magn Reson Med.* 1999 Nov;42(5):813-28.

114 Epstein FH, Kellman P, McVeigh ER. First pass cardiac MRI using UNFOLD. In: *Proceedings of RSNA*, Chicago 2000, 379.

115 Di Bella EV, Wu YJ, Alexander AL, Parker DL, Green D, McGann CJ. Comparison of temporal filtering methods for dynamic contrast MRI myocardial perfusion studies. *Magn Reson Med.* 2003 May;49(5):895-902.

116 Rehwald WG, Kim RJ, Simonetti OP, Laub G, Judd RM. Theory of high-speed MR imaging of the human heart with the selective line acquisition mode. *Radiology.* 2001 Aug;220(2):540-7.

117 Rehwald WG, Kim RJ, Judd RM. Rapid cine MRI of the human heart using reconstruction by estimation of lines and inhibition of fold-in. *Magn Reson Med.* 2002 May;47(5):844-9.

118 Tsao J, Behnia B, Webb AG. Unifying linear prior-information-driven methods for accelerated image acquisition. *Magn Reson Med.* 2001 Oct;46(4):652-60.

119 Hanson JM, Liang ZP, Wiener EC, Lauterbur PC. Fast dynamic imaging using two reference images. *Magn Reson Med.* 1996 Jul;36(1):172-5.

120 Hu X. Simpler locally focused tomography in MR imaging. *J Magn Reson Imaging.* 1994 Jan-Feb;4(1):103-4.

121 Hu X, Parrish T. Reduction of field of view for dynamic imaging. *Magn Reson Med.* 1994 Jun;31(6):691-4.

122 Tsao J, Boesiger P, Pruessmann KP. *k-t* BLAST and *k-t* SENSE: dynamic MRI with high frame rate exploiting spatiotemporal correlations. *Magn Reson Med.* 2003 Nov;50(5):1031-42.

123 Kozerke S, Tsao J, Razavi R, Boesiger P. Accelerating cardiac cine 3D imaging using *k-t* BLAST. *Magn Reson Med.* 2004 Jul;52(1):19-26.

124 Cao Y, Levin DN, Yao L. Locally focused MRI. *Magn Reson Med.* 1995 Dec;34(6):858-67.

125 Cao Y, Levin DN. MR imaging with spatially variable resolution. *J Magn Reson Imaging.* 1992 Nov-Dec;2(6):701-9.

126 Yao L, Cao Y, Levin DN. 2D locally focused MRI: applications to dynamic and spectroscopic imaging. *Magn Reson Med.* 1996 Dec;36(6):834-46.

127 Fredrickson JO, Pelc NJ. Temporal resolution improvement in dynamic imaging. *Magn Reson Med.* 1996 Apr;35(4):621-5.

128 Scheffler K, Hennig J. Reduced circular field-of-view imaging. *Magn Reson Med.* 1998 Sep;40(3):474-80.

129 Parrish TB, Hu X. Hybrid technique for dynamic imaging. *Magn Reson Med.* 2000 Jul;44(1):51-5.

130 Yang GZ, Burger P, Gatehouse PD, Firmin DN. Locally focused 3D coronary imaging using volume-selective RF excitation. *Magn Reson Med.* 1999 Jan;41(1):171-8.

131 Sodickson DK, Manning WJ. Simultaneous acquisition of spatial harmonics (SMASH): fast imaging with radiofrequency coil arrays. *Magn Reson Med.* 1997 Oct;38(4):591-603.

132 Jakob PM, Griswold MA, Edelman RR, Manning WJ, Sodickson DK. Accelerated cardiac imaging using the SMASH technique. *J Cardiovasc Magn Reson.* 1999;1(2):153-7.

133 Griswold MA, Jakob PM, Chen Q, Goldfarb JW, Manning WJ, Edelman RR, Sodickson DK. Resolution enhancement in single-shot imaging using simultaneous acquisition of spatial harmonics (SMASH). *Magn Reson Med.* 1999 Jun;41(6):1236-45.

134 Sodickson DK. Tailored SMASH image reconstructions for robust in vivo parallel MR imaging. *Magn Reson Med.* 2000 Aug;44(2):243-51.

135 McKenzie CA, Yeh EN, Sodickson DK. Improved spatial harmonic selection for SMASH image reconstructions. *Magn Reson Med.* 2001 Oct;46(4):831-6.

136 Sodickson DK, McKenzie CA, Ohliger MA, Yeh EN, Price MD. Recent advances in image reconstruction, coil sensitivity calibration, and coil array design for SMASH and generalized parallel MRI. *MAGMA*. 2002 Jan;13(3):158-63.

137 Jakob PM, Griswold MA, Edelman RR, Sodickson DK. AUTO-SMASH: a self-calibrating technique for SMASH imaging. SiMultaneous Acquisition of Spatial Harmonics. *MAGMA*. 1998 Nov;7(1):42-54.

138 Heidemann RM, Griswold MA, Haase A, Jakob PM. VD-AUTO-SMASH imaging. *Magn Reson Med.* 2001 Jun;45(6):1066-74.

139 Tsao J. On the UNFOLD method. *Magn Reson Med.* 2002 Jan;47(1):202-7.

140 Pruessmann KP, Weiger M, Scheidegger MB, Boesiger P. SENSE: sensitivity encoding for fast MRI. *Magn Reson Med.* 1999 Nov;42(5):952-62.

141 Madore B, Pelc NJ. SMASH and SENSE: experimental and numerical comparisons. *Magn Reson Med.* 2001 Jun;45(6):1103-11.

142 Weiger M, Pruessmann KP, Boesiger P. Cardiac real-time imaging using SENSE. SENSitivity Encoding scheme. *Magn Reson Med.* 2000 Feb;43(2):177-84.

143 Kellman P, Epstein FH, McVeigh ER. Adaptive sensitivity encoding incorporating temporal filtering (TSENSE). *Magn Reson Med.* 2001 May;45(5):846-52.

144 Guttman MA, Kellman P, Dick AJ, Lederman RJ, McVeigh ER. Real-time accelerated interactive MRI with adaptive TSENSE and UNFOLD. *Magn Reson Med.* 2003 Aug;50(2):315-21.

145 Kellman P, Derbyshire JA, Agyeman KO, McVeigh ER, Arai AE. Extended coverage first-pass perfusion imaging using slice-interleaved TSENSE. *Magn Reson Med.* 2004 Jan;51(1):200-4.

146 Madore B. Using UNFOLD to remove artifacts in parallel imaging and in partial-Fourier imaging. *Magn Reson Med.* 2002 Sep;48(3):493-501.

147 Sodickson DK, McKenzie CA. A generalized approach to parallel magnetic resonance imaging. *Med Phys.* 2001 Aug;28(8):1629-43.

148 Griswold MA, Jakob PM, Nittka M, Goldfarb JW, Haase A. Partially parallel imaging with localized sensitivities (PILS). *Magn Reson Med.* 2000 Oct;44(4):602-9.

149 Griswold MA, Jakob PM, Heidemann RM, Nittka M, Jellus V, Wang J, Kiefer B, Haase A. Generalized autocalibrating partially parallel acquisitions (GRAPPA). *Magn Reson Med.* 2002 Jun;47(6):1202-10.

150 Lanzer P, Barta C, Botvinick EH, Wiesendanger HU, Modin G, Higgins CB. ECG-synchronized cardiac MR imaging: method and evaluation. *Radiology.* 1985 Jun;155(3):681-6.

151 Thompson RB, McVeigh ER. Flow-gated phase-contrast MRI using radial acquisitions. *Magn Reson Med.* 2004 Sep;52(3):598-604.

152 Larson AC, White RD, Laub G, McVeigh ER, Li D, Simonetti OP. Self-gated cardiac cine MRI. *Magn Reson Med.* 2004 Jan;51(1):93-102.

153 McLeish K, Gill DLG, Atkinson D, Blackall JM, Razavi R. A Study of the motion and deformation of the heart due to respiration. *IEEE Trans Med Imaging.* 2002; 21(9): 1142-1150.

154 Oshinski JN, Hofland L, Mukundan S Jr, Dixon WT, Parks WJ, Pettigrew RI. Two-dimensional coronary MR angiography without breath holding. *Radiology.* 1996 Dec;201(3):737-43.

155 Felblinger J, Boesch C. Amplitude demodulation of the electrocardiogram signal (ECG) for respiration monitoring and compensation during MR examinations. *Magn Reson Med.* 1997 Jul;38(1):129-36.

156 Wang Y, Riederer SJ, Ehman RL. Respiratory motion of the heart: kinematics and the implications for the spatial resolution in coronary imaging. *Magn Reson Med.* 1995;33(5):713-719.

157 Ehman RL, Felmlee JP. Adaptive technique for high-definition MR imaging of moving structures. *Radiology.* 1989;173(1):255-263.

158 Nehrke K, Bornert P, Groen J, Smink J, Bock JC. On the performance and accuracy of 2D navigator pulses. *Magn Reson Imaging.* 1999 Oct;17(8):1173-81.

159 Wang Y, Rossman PJ, Grimm RC, Riederer SJ, Ehman RL. Navigator-echo-based real-time respiratory gating and triggering for reduction of respiration effects in three-dimensional coronary MR angiography. *Radiology.* 1996 Jan; 198(1): 55-60.

160 McConnell MV, Khasgiwala VC, Savord BJ, Chen MH, Chuang ML, Edelman RR, Manning WJ. Prospective adaptive navigator correction for breath-hold MR coronary angiography. *Magn Reson Med.* 1997 Jan;37(1):148-52.

161 Keegan J, Gatehouse PD, Taylor AM, Yang GZ, Jhooti P, Firmin DN. Coronary artery imaging in a 0.5-Tesla scanner: implementation of real-time, navigator echo-controlled segmented *k*-space FLASH and interleaved-spiral sequences. *Magn Reson Med.* 1999 Feb;41(2):392-9.

162 Korin HW, Ehman RL, Riederer SJ, Felmlee JP, Grimm RC. Respiratory kinematics of the upper abdominal organs: a quantitative study. *Magn Reson Med.* 1992 Jan;23(1):172-8.

163 Gierada DS, Curtin JJ, Erickson SJ, Prost RW, Strandt JA, Goodman LR. Diaphragmatic motion: fast gradient-recalled-echo MR imaging in healthy subjects. *Radiology.* 1995 Mar;194(3):879-84.

164 Taylor AM, Jhooti P, Wiesmann F, Keegan J, Firmin DN, Pennell DJ. MR navigator-echo monitoring of temporal changes in diaphragm position: implications for MR coronary angiography. *J Magn Reson Imaging.* 1997 Jul-Aug;7(4):629-36.

165 Holland AE, Goldfarb JW, Edelman RR. Diaphragmatic and cardiac motion during suspended breathing: preliminary experience and implications for breath-hold MR imaging. *Radiology.* 1998 Nov;209(2):483-9.

166 Nehrke K, Bornert P, Manke D, Bock JC. Free-breathing cardiac MR imaging: study of implications of respiratory motion--initial results. *Radiology.* 2001 Sep;220(3):810-5.

167 Friedman J, Van Train K, Maddahi J, Rozanski A, Prigent F, Bietendorf J, Waxman A, Berman DS. "Upward creep" of the heart: a frequent source of false-positive reversible defects during thallium-201 stress-redistribution SPECT. *J Nucl Med.* 1989 Oct;30(10):1718-22.

168 Ter-Pogossian MM, Bergmann SR, Sobel BE. Influence of cardiac and respiratory motion on tomographic reconstructions of the heart: Implications for quantitative nuclear cardiology. *J Comput Assist Tomogr.* 1982; 6(6):1148–1155.

169 Andersson JLR, Vagnhammar BE, Schneider H. Accurate attenuation correction despite movement during PET imaging. *J Nucl Med.* 1995; 36(4):670–678.

170 Atkinson D, Burcher M, Declerck J, Noble JA. Respiratory motion compensation for 3-D freehand echocardiography. *Ultrasound in Medicine & Biology.* 2001; 27(12):1615-1620.

171 Edelman RR, Manning WJ, Burstein D, Paulin S. Coronary arteries: breath-hold MR angiography. *Radiology* 1991; 178: 357-360.

172 Ferrigno M, Hickey DD, Liner MH, Lundgren CE. Cardiac performance in humans during breath holding. *J Appl Physiol.* 1986 Jun;60(6):1871-7

173 Paulev P, Wetterqvist H. Cardiac output during breath-holding in man. *Scand J Clin Lab Invest.* 1968;22(2):115-23.

174 Runge VM, Clanton JA, Partain CL, James AE Jr. Respiratory gating in magnetic resonance imaging at 0.5 Tesla. *Radiology.* 1984;151(2):521-523.

175 Ehman RL, McNamara MT, Pallack M, Hricak H, Higgins CB. Magnetic resonance imaging with respiratory gating: techniques and advantages. *AJR Am J Roentgenol.* 1984 Dec;143(6):1175-82.

176 Sachs TS, Meyer CH, Hu BS, Kohli J, Nishimura DG, Macovski A. Real-time motion detection in spiral MRI using navigators. *Magn Reson Med.* 1994 Nov;32(5):639-45.

177 Liu YL, Riederer SJ, Rossman PJ, Grimm RC, Debbins JP, Ehman RL. A monitoring, feedback, and triggering system for reproducible breath-hold MR imaging. *Magn Reson Med.* 1993 Oct;30(4):507-11.

178 Wang Y, Christy PS, Korosec FR, Alley MT, Grist TM, Polzin JA, Mistretta CA. Coronary MRI with a respiratory feedback monitor: the 2D imaging case. *Magn Reson Med.* 1995 Jan;33(1):116-21.

179 Wang Y, Grimm RC, Rossman PJ, Debbins JP, Riederer SJ, Ehman RL. 3D coronary MR angiography in multiple breath-holds using a respiratory feedback monitor. *Magn Reson Med.* 1995 Jul;34(1):11-6.

180 Taylor AM, Keegan J, Jhooti P, Gatehouse PD, Firmin DN, Pennell DJ. Differences between normal subjects and patients with coronary artery disease for three different MR coronary angiography respiratory suppression techniques. *J Magn Reson Imaging.* 1999 Jun;9(6):786-93.

181 Danias PG, McConnell MV, Khasgiwala VC, Chuang ML, Edelman RR, Manning WJ. Prospective navigator correction of image position for coronary MR angiography. *Radiology* 1997; 203: 733-736.

182 Gatehouse PD, Keegan J, Yang GZ, Mohiaddin RH, Firmin DN. Tracking local volume 3D-echo-planar coronary artery imaging. *Magn Reson Med.* 2001; 46(5):1031-1036.

183 Stuber M, Botnar RM, Danias PG, Sodickson DK, Kissinger KV, van Cauteren M, Becker J, Manning WJ. Double-oblique free-breathing high resolution three-dimensional coronary magnetic resonance angiography. *J Am Coll Cardiol.* 1999; 34: 524–531, 1999.

184 Bornert P, Aldefeld B, Nehrke K. Improved 3D spiral imaging for coronary MR angiography. *Magn Reson Med.* 2001; 45(1): 172–175.

185 Yang GZ, Gatehouse PD, Keegan J, Mohiaddin RH, Firmin DN. Three-dimensional coronary MR angiography using zonal echo-planar imaging. *Magn Reson Med.* 1998; 39: 833-842.

186 Taylor AM, Keegan J, Jhooti P, Firmin DN, Pennell DJ. Calculation of a subject-specific adaptive motion-correction factor for improved real-time navigator echo-gated magnetic resonance coronary angiography. *J Cardiovasc Magn Reson.* 1999; 1(2):131-138.

187 Nagel E, Bornstedt A, Schnackenburg B, Hug J, Oswald H, Fleck E. Optimization of realtime adaptive navigator correction for 3D magnetic resonance coronary angiography. *Magn Reson Med.* 1999; 42(2):408-411.

188 Kyriakos WE, Panych LP, Zientara GP, Jolesz FA. Implementation of a reduced field-of-view method for dynamic MR imaging using navigator echoes. *J Magn Reson Imaging.* 1997 Mar-Apr;7(2):376-81.

189 Bailes DR, Gilderdale DJ, Bydder GM, Collins AG, Firmin DN. Respiratory ordered phase encoding (ROPE): a method for reducing respiratory motion artefacts in MR imaging. *J Comput Assist Tomogr.* 1985 Jul-Aug;9(4):835-8.

190 Haacke EM, Patrick JL. Reducing motion artifacts in two-dimensional Fourier transform imaging. *Magn Reson Imaging.* 1986;4(4):359-76.

191 Korin HW, Riederer SJ, Bampton AE, Ehman RL. Altered phase-encoding order for reduced sensitivity to motion in three-dimensional MR imaging. *J Magn Reson Imaging.* 1992 Nov-Dec;2(6):687-93.

192 Jhooti P, Wiesmann F, Taylor AM, Gatehouse PD, Yang GZ, Keegan J, Pennell DJ, Firmin DN. Hybrid ordered phase encoding (HOPE): an improved approach for respiratory artifact reduction. *J Magn Reson Imaging.* 1998 Jul-Aug;8(4):968-80.

193 Jhooti P, Gatehouse PD, Keegan J, Bunce NH, Taylor AM, Firmin DN. Phase ordering with automatic window selection (PAWS): a novel motion-resistant technique for 3D coronary imaging. *Magn Reson Med.* 2000 Mar;43(3):470-80.

194 Weiger M, Bornert P, Proksa R, Schaffter T, Haase A. Motion-adapted gating based on *k*-space weighting for reduction of respiratory motion artifacts. *Magn Reson Med.* 1997; 38(2): 322-333.

195 Delzescaux T, Frouin F, De Cesare A, Philipp-Foliguet S, Zeboudj R, Janier M, Todd-Pokropek A, Herment A. Adaptive and self-evaluating registration method for myocardial perfusion assessment. *MAGMA* 2001 Aug;13(1):28-39.

196 Yang GZ, Burger P, Panting J, Gatehouse PD, Rueckert D, Pennell DJ, Firmin DN. Motion and deformation tracking for short-axis echo-planar myocardial perfusion imaging. *Med Image Anal.* 1998 Sep;2(3):285-302

197 C. Dornier, M. K. Ivancevic, P. Thévenaz, M. Unser, J. Vallée, Accurate MR cardiac perfusion analysis by using a multiresolution B-splines registration algorithm, 700, *ISMRM* 2003.

198 Collins DL, Peters TM, Evans AC. An automated 3D non-linear deformation procedure for determination of gross morphometric variability in human brain. Proc. 3rd *International Conference Visualization in Biomedical Computing* (VBC '94), pages 180-190, Rochester, MN, 1994.

199 Bookstein FL. Principal Warps: Thin-plate splines and the decomposition of deformations. *IEEE Trans on Patt Analys and Mach Intell,* 11(6):567-585,1989.

200 Lee S, Wolberg G, Shin SY. Scattered data interpolation with multilevel B-splines. *IEEE Trans Visualization Comput Graph.* 1997 Jul;3:228-244.

201 Rueckert D, Sonoda LI, Hayes C, Hill DL, Leach MO, Hawkes DJ. Nonrigid registration using free-form deformations: application to breast MR images. *IEEE Trans Med Imaging.* 1999 Aug;18(8):712-21.

202 Mortenson ME. Geometric Modeling, John Wiley & Sons, New York, 1985.

203 Viola PA, Wells WM, Alignment by maximization of mutual information. in Proc. of *5th Int. Conf. on Computer Vision*, MIT, volume 1, pp. 16--23, 1995.

204 Maes F, Collignon A, Vandermeulen D, Marchal G, Suetens P. Multimodality image registration by maximization of mutual information. *IEEE Trans Med Imaging* 1997 Apr;16(2):187-98.

205 Studholme C, Hawkes DJ, Hill DLG, A Normalised Entropy Measure of 3D Medical Image Analysis, Proceedings of *SPIE Medical Imaging* , San Diego Ca., Feb 1998.

206 Sachs TS, Meyer CH, Pauly JM, Hu BS, Nishimura DG, Macovski A. The real-time interactive 3-D-DVA for robust coronary MRA. *IEEE Trans Med Imaging.* 2000 Feb;19(2):73-9.

207 Manke D, Nehrke K, Bornert P. Novel prospective respiratory motion correction approach for free-breathing coronary MR angiography using a patient-adapted affine motion model. Magn Reson Med. 2003 Jul;50(1):122-31.

208 Bortfeld T, Jokivarsi K, Goitein M, Kung J, Jiang SB. Effects of intra-fraction motion on IMRT dose delivery: statistical analysis and simulation. *Phys. Med. Biol.* 2002; 47:2203–2220.

209 King CR, Lehmann J, Adler JR, Hai J. CyberKnife radiotherapy for localized prostate cancer: rationale and technical feasibility. *Technol Cancer Res Treat.* 2003; 2(1):25-30.

210 George R, Keall PJ, Kini VR, Vedam SS, Siebers JV, Wu Q, Lauterbach MH, Arthur DW, Mohan R. Quantifying the effect of intrafraction motion during breast IMRT planning and dose delivery. *Med Phys.* 2003; 30(4):552-562.

211 Manning WJ, Stuber M, Danias PG, Botnar RM, Yeon SB, Aepfelbacher FC. Coronary magnetic resonance imaging: current status. *Curr Probl Cardiol.* 2002; 27(7):275-333.

212 Li D, Deshpande V. Magnetic resonance imaging of coronary arteries. *Top Magn Reson Imaging.* 2001; 12(5):337-347.

213 McLeish K, Gill DLG, Atkinson D, Blackall JM, Razavi R. A Study of the motion and deformation of the heart due to respiration. *IEEE Trans Med Imaging.* 2002; 21(9): 1142-1150.

214 Geladi P, Kowalski B. Partial least-squares regression: a tutorial, *Analytic Chemica Acta,* 1986; 185:1-17.

215 McIntosh AR, Bookstein FL, Haxby JV, Grady CL. Spatial pattern analysis of functional brain images using partial least squares, *Neuroimage,* 1996 Jun;3(3 Pt 1):143-57.

216 Abdi H (2003). Partial least squares regression (PLS-regression), in M. Lewis-Beck, A. Bryman, T. Futing (Eds): *Encyclopedia for research methods for the social sciences.* Thousand Oaks (CA): Sage.

217 Bro R, *Håndbog i Multivariabel Kalibrering,* Copenhagen, Jordbrugsforlaget, 1996. (in Danish).

218 Wold, H. Soft modelling with latent variables: the nonlinear iterative partial least squares approach. *Perspectives in probability and Statistics*: Papers in honour of M.S. Barlett, (J. Gani, ed). London: Academic Press. 1975: 114-142.

219 Keegan J, Gatehouse PD, Yang GZ, Firmin DN. Coronary artery motion with the respiratory cycle during breath-holding and free-breathing: implications for slice-followed coronary artery imaging. *Magn Reson Med.* 2002; 47(3): 476-481.

220 Malthouse E, Tamhane A, Mah R. Nonlinear partial least squares. *Computers in Chemical Engineering.* 1997; 21(8): 875-890.

221 Webb AG, Liang ZP, Magin RL, Lauterbur PC. Applications of reduced-encoding MR imaging with generalized-series reconstruction (RIGR). *J Magn Reson Imaging.* 1993 Nov-Dec;3(6):925-8.

222 Chandra S, Liang ZP, Webb A, Lee H, Morris HD, Lauterbur PC. Application of reduced-encoding imaging with generalized-series reconstruction (RIGR) in dynamic MR imaging. *J Magn Reson Imaging.* 1996 Sep-Oct;6(5):783-97.

223 Hanson JM, Liang ZP, Magin RL, Duerk JL, Lauterbur PC. A comparison of RIGR and SVD dynamic imaging methods. *Magn Reson Med.* 1997 Jul;38(1):161-7.

224 Merrifield R, Keegan J, Firmin D, Yang GZ. Reduced *k*-space encoding for dual-contrast TrueFISP imaging. *Magn Reson Med.* 2003 Mar;49(3):595-8.

225 Hsu EW, Henriquez CS. Myocardial fiber orientation mapping using reduced encoding diffusion tensor imaging. *J Cardiovasc Magn Reson.* 2001;3(4):339-47.

226 Liang ZP, Madore B, Glover GH, Pelc NJ. Fast algorithms for GS-model-based image reconstruction in data-sharing Fourier imaging. *IEEE Trans Med Imaging.* 2003 Aug;22(8):1026-30.

227 Formiconi AR, Piccolomini EL,Martini S, Zama F, Zanghirati G, Numerical methods and software for functional magnetic resonance images reconstruction, Annali dell'Università di Ferrara, sez. VII Scienze Matematiche, suppl. vol. XLVI, Ferrara , 2000.

228 Jerosch-Herold M, Wilke N. MR first pass imaging: quantitative assessment of transmural perfusion and collateral flow. *Int J Card Imaging.* 1997 Jun;13(3):205-18.

229 Muhling OM, Dickson ME, Zenovich A, Huang Y, Wilson BV, Wilson RF, Anand IS, Seethamraju RT, Jerosch-Herold M, Wilke NM. Quantitative magnetic resonance first-pass perfusion analysis: inter- and intraobserver agreement. *J Cardiovasc Magn Reson.* 2001;3(3):247-56.

230 Li D, Zheng J, Weinmann HJ. Contrast-enhanced MR imaging of coronary arteries: comparison of intra- and extravascular contrast agents in swine. *Radiology.* 2001 Mar;218(3):670-8.

231 Stillman AE, Wilke N, Jerosch-Herold M., Use of an intravascular T1 contrast agent to improve MR cine myocardial-blood pool definition in man. *J Magn Reson Imaging.* 1997 Jul-Aug;7(4):765-7.

232 Wiener EC, Brechbiel MW, Brothers H, Magin RL, Gansow OA, Tomalia DA, Lauterbur PC. Dendrimer-based metal chelates: a new class of magnetic resonance imaging contrast agents. *Magn Reson Med.* 1994 Jan;31(1):1-8.

233 Canet E, Revel D, Forrat R, Baldy-Porcher C, de Lorgeril M, Sebbag L, Vallee JP, Didier D, Amiel M. Superparamagnetic iron oxide particles and positive enhancement for myocardial perfusion studies assessed by subsecond T1-weighted MRI. *Magn Reson Imaging.* 1993;11(8):1139-45.

234 Schmiedl U, Ogan MD, Moseley ME, Brasch RC. Comparison of the contrast-enhancing properties of albumin-(Gd-DTPA) and Gd-DTPA at 2.0 T: and experimental study in rats. *AJR Am J Roentgenol.* 1986 Dec;147(6):1263-70.

235 Kroll K, Wilke N, Jerosch-Herold M, Wang Y, Zhang Y, Bache RJ, Bassingthwaighte JB. Modeling regional myocardial flows from residue functions of an intravascular indicator. *Am J Physiol.* 1996 Oct;271(4 Pt 2):H1643-55.

236 Jerosch-Herold M, Wilke N, Wang Y, Gong GR, Mansoor AM, Huang H, Gurchumelidze S, Stillman AE. Direct comparison of an intravascular and an extracellular contrast agent for quantification of myocardial perfusion. Cardiac MRI Group. *Int J Card Imaging*. 1999 Dec;15(6):453-64.

237 Kraitchman DL, Chin BB, Heldman AW, Solaiyappan M, Bluemke DA. MRI detection of myocardial perfusion defects due to coronary artery stenosis with MS-325. *J Magn Reson Imaging*. 2002 Feb;15(2):149-58.

238 Axel L. Tissue mean transit time from dynamic computed tomography by a simple deconvolution technique. *Invest Radiol* 1983 Jan-Feb;18(1):94-9.

239 Wilke N, Jerosch-Herold M, Wang Y, *et al.* Myocardial perfusion reserve: assessment with multisection, quantitative, first-pass MR imaging. *Radiology* 1997;204:373–384.

240 Muehling OM, Jerosch-Herold M, Panse P, Zenovich A, Wilson BV, Wilson RF, Wilke N. Regional heterogeneity of myocardial perfusion in healthy human myocardium: assessment with magnetic resonance perfusion imaging. *J Cardiovasc Magn Reson.* 2004;6(2):499-507.

241 Bassingthwaighte JB, Goresky CA. Modeling in the analysis of solute and water exchange in the microvasculature. In: Renkin EM, Michel CC, ed. Handbook of Physiology – The Cardiovascular System. Bethesda, MD:AmPhysiol Soc, 1984: 549–626.

242 Jerosch-Herold M, Wilke N, Stillman AE, Muehler A, Wang Y. Functional myocardial perfusion maps from MR first pass images. Society of Magnetic Resonance, 3rd Annual Meeting, Nice, 1995; 459.

243 Buvat I, Benali H, Paola RD. Statistical distribution of factors and factor images in factor analysis of medical image sequences. *Phys Med Biol.* 1998; 43: 1695–1711.

244 Martel AL, Moody AR, Allder SJ, Delay GS, Morgan PS. Extracting parametric images from dynamic contrast-enhanced MRI studies of the brain using factor analysis. *Med Img Analysis,* 2001; 5: 29-39.

245 Eichenberger AC, Schuiki E, Kochli VD, Amann FW, McKinnon GC, von Schulthess GK. Ischemic heart disease: assessment with gadolinium-enhanced ultrafast MR imaging and dipyridamole stress. *J Magn Reson Imaging.* 1994 May-Jun;4(3):425-31.

246 Al-Saadi N, Nagel E, Gross M, Bornstedt A, Schnackenburg B, Klein C, Klimek W, Oswald H, Fleck E. Noninvasive detection of myocardial ischemia from perfusion reserve based on cardiovascular magnetic resonance. *Circulation.* 2000 Mar 28;101(12):1379-83.

247 Al-Saadi N, Nagel E, Gross M, Schnackenburg B, Paetsch I, Klein C, Fleck E. Improvement of myocardial perfusion reserve early after coronary intervention: assessment with cardiac magnetic resonance imaging. *J Am Coll Cardiol.* 2000 Nov 1;36(5):1557-64.

248 Ibrahim T, Nekolla SG, Schreiber K, Odaka K, Volz S, Mehilli J, Guthlin M, Delius W, Schwaiger M. Assessment of coronary flow reserve: comparison between contrast-enhanced magnetic resonance imaging and positron emission tomography. *J Am Coll Cardiol.* 2002 Mar 6;39(5):864-70.

249 Kraitchman DL, Boston RC. Where does normalization fail in cardiac perfusion MRI? [abstract]. Proceedings of the 10th Annual Meeting of the ISMRM 2002:1608 (Hawaii).

250 Jerosch-Herold M, Hu X, Murthy NS, Rickers C, Stillman AE. Magnetic resonance imaging of myocardial contrast enhancement with MS-325 and its relation to myocardial blood flow and the perfusion reserve. *J Magn Reson Imaging.* 2003 Nov;18(5):544-54.

251 Kellman P, Zhang Q, Larson AC, Simonetti OP, McVeigh ER, Arai AE. Cardiac first-pass perfusion MRI using 3D trueFISP parallel imaging using TSENSE. *Proc Intl Soc Mag Reson Med* 11, 2004. (Kyoto)

252 Elkington AG, Gatehouse PD, Ablitt N, Yang GZ, Firmin DN, Pennell DJ. Interstudy reproducibility of quantitative perfusion Cardiovascular Magnetic Resonance, (under review) *J Magn Reson Imaging.*

253 Jerosch-Herold M, Swingen C, Teja-Seethamraju R, Model-Independent Quantification of Myocardial Blood Flow with Extracellular Contrast Agents: The Central Volume Principle Revisited, *Proc. Intl. Soc. Mag. Reson. Med.* 10 (2002).

254 Jerosch-Herold M, Swingen C, Seethamraju RT. Myocardial blood flow quantification with MRI by model-independent deconvolution. *Med Phys.* 2002 May;29(5):886-97.

255 Ablitt N, Gao JX, Gatehouse P, Yang GZ. Motion Decoupling and Registration for 3D Magnetic Resonance Myocardial Perfusion Imaging. The 2002 International Conference on Computational Science. Amsterdam, The Netherlands.

256 Veeser S, Dunn MJ, Yang GZ. Multiresolution image registration for two-dimensional gel electrophoresis. *Proteomics.* 2001; 1: 856-870.

257 Bhupinder S. Dayal, Jhon F. MacGregor. Recursive exponentially weighted PLS and its applications to adaptive control and prediction. *J Proc Cont.* 1997; 7: 169-179.

258 Blanco M, Coello J, Elaamrani M, Iturriaga H, Maspoch S. Partial least-squares regression for the quantitation of pharmaceutical dosages in control analyses. *J Pharm. Biomed Anal.* 1996; 15: 329-338.

259 Levenberg K. A method for the solution of certain problems in least squares. *Quart. Appl. Math.* 2, 164-168, 1944.

260 Marquardt D. An algorithm for least-squares estimation of nonlinear parameters. *SIAM J. Appl. Math.* 11, 431-441, 1963.